IntechOpen

Bringing Thermoelectricity into Reality

Edited by Patricia Aranguren

BRINGING THERMOELECTRICITY INTO REALITY

Edited by **Patricia Aranguren**

Bringing Thermoelectricity into Reality
http://dx.doi.org/10.5772/intechopen.71354
Edited by Patricia Aranguren

Contributors

Bo Li, Kuo Huang, Yuying Yan, Jaime Álvarez Quintana, Angel Fabian, Himanshu Dehra, Diana Enescu, Raghied Atta, Duraisamy Sivaprahasam, Harish Subramaniam, Raghavan Gopalan, Govindhan Sundararajan, Pavel Shiriaev, Konstantin Shishov, Roman Poshekhonov, Alexey Osipkov, Thiago Antonini Alves, Paulo Santos, Larissa Krambeck, Miguel Angel Olivares-Robles, Arturo Monedero Khouri, Federico Vazquez, Isaac Rodríguez-Vargas, Aldo Figueroa, Iván Rivera, Jaziel Alberto Rojas, Roberto Palma, Emma Moliner, Josep Forner-Escrig, Leyre Catalan, Miguel Araiz, Óscar Herrero, Gurutze Perez, Antonio Rodriguez, Pablo Eduardo Ruiz-Ortega, Jose Antonio Alonso, Javier Gainza, Federico Serrano-Sánchez, Mouna Gharsallah, Manuel Funes, Felix Carrascoso, Norbert Nemes, Oscar Dura, Jose Luis Martinez, Matthew Grayson, Qing Shao, Boya Cui, Yang Tang, Xueting Yan, Chuanle Zhou, Jin-Lian Hu, Qian Wu, Gilad Guttmann, Yaniv Gelbstein

Notice

Statements and opinions expressed in the chapters are these of the individual contributors and not necessarily those of the editors or publisher. No responsibility is accepted for the accuracy of information contained in the published chapters. The publisher assumes no responsibility for any damage or injury to persons or property arising out of the use of any materials, instructions, methods or ideas contained in the book.

First published in London, United Kingdom, 2018 by IntechOpen
eBook (PDF) Published by IntechOpen, 2019
IntechOpen is the global imprint of INTECHOPEN LIMITED, registered in England and Wales, registration number: 11086078, The Shard, 25th floor, 32 London Bridge Street
London, SE19SG – United Kingdom
Printed in Croatia

British Library Cataloguing-in-Publication Data
A catalogue record for this book is available from the British Library

Additional hard and PDF copies can be obtained from orders@intechopen.com

Bringing Thermoelectricity into Reality
Edited by Patricia Aranguren

p. cm.

Print ISBN 978-1-78923-440-4

Online ISBN 978-1-78923-441-1

eBook (PDF) ISBN 978-1-83881-565-3

Meet the editor

Dr. Patricia Aranguren completed her PhD degree focusing on thermoelectric generation applications from the Public University of Navarre (Spain) in 2015. Her research interests are heat transfer optimization and thermoelectricity. She is a recipient of the "Graduate Student Award" by the "International Thermoelectric Society" in recognition of her outstanding research trajectory in the field of thermoelectrics. On two further occasions, she has been awarded the "Best Contribution Award" of the International Thermoelectric Society during the celebration of Annual International Conferences on Thermoelectrics. Until now, she has published 13 manuscripts in peer-reviewed international journals and 1 book chapter, and participated in 28 contributions presented at international conferences. She also serves as a reviewer of many international journals.

Contents

Preface

The disproportionate use of fossil fuels has turned into a serious environmental issue. Consequently, global warming, greenhouse gas emissions, climate change, ozone layer depletion, and acid rain are frequently heard terms from the media. Also, fossil fuel reserves are limited, and strict environmental regulations are appearing. Thus, we are encountering one of the biggest challenges of the twenty-first century, satisfying the energy demand with respect to the environment. This fact brings an intense activity directed to obtain a rational use of traditional fuels, reduce the greenhouse gas emissions, and stimulate the research of alternative energy sources.

Despite the complexity of the actual energy problem, as scientific, technological, economic, environmental, sociological, and political aspects are involved, new intensive activities focused on two directives have been encouraged. The intelligent use of energy, boosting savings, avoiding overspending, and developing more efficient equipment; and the development of renewable energy production, an intense activity which has increased a 220% of the global renewable power capacity in the last 10 years.

Thermoelectricity is one of the technologies, which contributes to the reduction in the impact of the use of fossil fuels, as it contributes to the better use of traditional fuels, improving the efficiency of the processes. Thermoelectricity is an emerging technology, due to its capacity to convert heat into electricity or produce cooling or heating effects out of electricity without the necessity of refrigerants. The solid state of thermoelectric devices eliminates the moving parts, chemical reactions, and the presence of refrigerants. Hence, maintenance as well as the harmful emissions to the environment is cancelled. Longer lives are achieved due to the safe operation.

Thermoelectric generators harvest heat, especially waste heat, to produce electricity. Waste heat is defined as the by-product heat, which is produced by a process that is not used by but is emitted to the ambient. Today, the amount of waste heat produced is disproportionate; 40% of the primary energy used in the industrialized countries is emitted to the ambient as waste heat. Most of this heat corresponds to low-grade heat, complicating its reuse. However, thermoelectricity is a very promising technology to recover this kind of heat. Likewise, thermoelectric coolers and heaters do not need refrigerants and therefore eliminate greenhouse gas emissions and hence do not contribute to the global warming. Accordingly, the electrical energy generation from waste heat and the cooling or heating without the necessity of refrigerants contribute to a more sustainable world.

Unfortunately, the efficiency of thermoelectric generators, coolers, and heaters is still very low, and therefore, great efforts are being made to improve their efficiency. The study of novel thermoelectric materials, the development of computational models, the design of

proper assemblies, and the optimization of thermal designs, among others, are currently being studied by the scientists. This book includes the previously mentioned aspects categorized into four sections:

- Advanced Thermoelectric Materials
- Building Up the Devices: Material Properties, Modeling, Geometry, and Assembly Optimization
- Thermoelectric Generation: Automotive Waste Heat Recovery
- Thermoelectric Cooling: Principles, Effects, Optimization and Applications

I believe that the information contained in this book will help researchers and scientists to develop the definitive thermoelectric application applied to everyday life, boosting thermoelectricity to the visible plane.

I am very thankful to all the authors who have contributed to this book, and without whom it would not have been possible to gather all the wisdom. I hope that the coordinating efforts would serve to bring thermoelectricity into reality.

Dr. Patricia Aranguren
Public University of Navarre
Pamplona, Spain

Section 1

Advanced Thermoelectric Materials

Chapter 1

Nanostructured Thermoelectric Chalcogenides

Javier Gainza, Federico Serrano-Sánchez,
Mouna Gharsallah, Manuel Funes, Félix Carrascoso,
Norbert M. Nemes, Oscar J. Dura,
José L. Martínez and José A. Alonso

Additional information is available at the end of the chapter

http://dx.doi.org/10.5772/intechopen.75442

Abstract

Thermoelectric materials are outstanding to transform temperature differences directly and reversibly into electrical voltage. Exploiting waste heat recovery as a source of power generation could help towards energy sustainability. Recently, the SnSe semiconductor was identified, in single-crystal form, as a mid-temperature thermoelectric material with record high figure of merit, high power factor and surprisingly low thermal conductivity. We describe the preparation of polycrystals of alloys of SnSe obtained by arc-melting; a rapid synthesis that results in strongly nanostructured samples with low thermal conductivity, advantageous for thermoelectricity, approaching the amorphous limit, around 0.3–0.5 W/mK. An initial screening of novel samples $Sn_{1-x}M_xSe$, by alloying with 3d and 4d transition metals such as M = Mn, Y, Ag, Mo, Cd or Au, provides for a means to optimize the power factor. M=Mo, Ag, with excellent values, are described in detail with characterization by x-ray powder diffraction (XRD), scanning electron microscopy (SEM), and electronic and thermal transport measurements. Rietveld analysis of XRD data demonstrates near-perfect stoichiometries of the above-mentioned alloys. SEM analysis shows stacking of nanosized sheets, with large surfaces parallel to layered slabs. An apparatus was developed for the simultaneous measurement of the Seebeck coefficient and electric conductivity at elevated temperatures.

Keywords: thermoelectrics, nanostructuration, lattice thermal conductivity, thermopower, SnSe alloying

1. Introduction

Thermoelectric materials hold a tantalizing promise of greater energy efficiency by providing a robust and clean option for waste heat recovery and conversion to useful electrical energy through the Seebeck effect [1–5]. However, existing materials have poor thermoelectric efficiency. This is related to the inherent difficulty to obtain, at the same time, a high electrical conductivity, a low thermal one, and a very high Seebeck voltage. Thermoelectric materials are characterized, for research purposes, by the thermoelectric figure of merit, $zT = \frac{\sigma S^2}{\kappa} T$, combining into a dimensionless number the Seebeck coefficient, S (the larger, the better), the electrical conductivity, σ (the larger, the better, to minimize waste through Joule-heating), the thermal conductivity, κ (the smaller, the better, to minimize thermally shorting the temperature gradient giving the Seebeck voltage), and the absolute temperature, T. Unfortunately, the character of these properties pulls against the optimization of the figure of merit. While σ is directly proportional to the carrier concentration n, the Seebeck coefficient is inversely proportional to it ($n^{-2/3}$), a common rule for doped semiconductors known since the 1950s as the Pisarenko relation, after Mr. N. L. Pisarenko [6]. Moreover, the Wiedemann-Franz law establishes a direct relationship between σ and the electronic contribution to the thermal conductivity (κ_{ele}) [7, 8]. Usually, the thermoelectric properties are described as:

$$S = \frac{8\pi^2 k_B^2 m^* T}{3e h^2} \left(\frac{\pi}{3n}\right)^{\frac{2}{3}} \tag{1}$$

$$\sigma = \mu e n \tag{2}$$

$$\kappa_{tot} = \kappa_{latt} + \kappa_{ele} = L\sigma T = L\mu e n T \tag{3}$$

A zT above 4 would be desirable for economically viable thermoelectric modules for waste heat recovery, for example, in automotive applications. Yet, current state-of-the-art materials have zT limited to around 2, with commercial materials limited to 1. Furthermore, p- and n-type thermoelectric materials with similar figure of merit, and electrical, thermal, and mechanical characteristics, in the same temperature range are necessary for their implementation. Nonetheless, much effort has gone into developing cost-effective devices for different applications [9–12]. For instance, as potential candidates for gas heat recovery, automobile exhaust thermoelectric generators (AETEG) were first studied in 1963, and they have been thoroughly investigated since then reaching 400 W and 5% efficiency in current Bi_2Te_3-based modules [12–14]. A recent report on AETEG for military SUV applications shows an output power up to 646 W and 1.03% efficiency, which meets the electrical requirements for automotive applications [13]. Another applicability of thermoelectric modules is found as Solar-Heat-Pipe-Thermoelectric-Generator hybrid systems for combined power generation and hot water production in the high-temperature range [11].

Thermoelectric materials are typically degenerately doped semiconductors, often of heavy p-block elements, such as SiGe, Bi_2Te_3, PbTe, and $CoSb_3$ [15–17]. However, recently, a zT as

large as 2.6 was reported above 900 K in an overlooked semiconductor, SnSe [18]. This value was found in a single crystal of SnSe along one crystallographic direction, above a structural phase transition, just below the melting point. Later reports in single crystals found smaller values, and in polycrystalline samples only zT = 1.0 [19–21]. Nevertheless, SnSe is a very promising thermoelectric. As a semiconductor, SnSe was disregarded due to its complicated orthorhombic structure. It consists of puckered layers, quite analogous to black phosphorus, and it has a small bandgap of 0.61 eV, quite sought after among optoelectronic 2D materials [22].

One reason for the high zT of SnSe has to do with its low thermal conductivity. Nevertheless, a further reduction by nanostructuring is highly desirable. According to the Wiedemann-Franz law [7], the thermal conductivity of SnSe is overwhelmingly determined by the lattice thermal conductivity because of its inherently low electrical conductivity. Thus, doping can be used to increase σ through the charge density, and in turn zT. However, following the Pisarenko relation [23], the Seebeck coefficient will decrease with increasing charge concentration. Thus, an optimum must be found of the power-factor, σS^2. Furthermore, an intense controversy arose about the actual thermal conductivity of the material, with values reported anywhere between 0.2 and 1.0 W m^{-1} K^{-1} [18, 19, 21, 24–31]. Numerous different explanations have been proposed for such values, as surface oxidation, exact stoichiometry, porosity, morphology, and crystal defects of the samples. Thermoelectric devices made of this material have not been described yet despite the fact that SnSe presents one of the highest figures of merit, and only a few attempts proving the interface bonding properties for high-temperature modules have been reported [32, 33].

There have been several reports on doped SnSe, with silver, iodine, bismuth, or sodium [19–21, 24, 34, 35]. These can be used to select the type of carriers, since a useful thermoelectric device must contain both p- and n-type thermo-elements. What is common in these studies is that the dopant concentration reaches no more than a few percent. Our group has reported on alloying SnSe with p-block elements, such as Ge, In, and Pb, using arc-melting [36–39]. The arc-melting technique has several advantages for SnSe, and some drawbacks. It is a very fast, one-step synthesis method that avoids the costly and time-consuming steps of spark plasma sintering (SPS), yet produces dense pellets [40]. Crucially, it yields highly nanostructured materials because of the rapid melting and quenching. It also allows for alloying at much higher concentrations. As a drawback, we find our polycrystalline samples to have notoriously low electrical conductivity at room temperature, and also much lower charge carrier density than would be expected from the huge amount of dopants. These are likely related to surface oxidation of the grain boundaries and to charge-trapping at defects.

Here we report on a general survey of alloying SnSe with *d*-block elements. As a quick screening tool, we employed the room temperature Seebeck coefficient and electrical conductivity. As a rule of thumb, we looked for indications of the Pisarenko relation at work: dopants that, at some concentration, can yield highly conducting samples, usually with almost zero Seebeck coefficient, whereas the pure or lightly doped SnSe is a bad conductor with large Seebeck effect. We characterized every composition by laboratory x-ray diffraction to check for phase purity and changes in the lattice constant, a good indication that some of the dopants indeed entered the crystal structure. For some samples, we also measured the Seebeck coefficient and

electrical conductivity at high temperatures (a much more laborious task), where SnSe would perform as a thermoelectric. In particular, we looked for n-type alloys with negative Seebeck coefficient. We also characterized the thermal conductivity of a few selected samples.

2. Experimental section

2.1. Preparation by arc-melting

Tin selenide alloys with various dopings were prepared in an Edmund Buhler mini-arc MAM-1 furnace (**Figure 1a**). Stoichiometric amounts of ground mixture of reacting elements were pelletized in a glove box. Pellets were molten under Ar atmosphere in a water-cooled Cu crucible (**Figure 1b**), leading to ingots of intermetallic characteristics (**Figure 1c**), which were partially ground to powder for structural characterization. The Seebeck coefficient and electrical and thermal conductivities were measured in disk-shaped specimens obtained by pressing the arc-molten ingots under 200 MPa at ambient temperature in a cylindrical die.

2.2. Structural characterization

Laboratory x-ray diffraction (XRD) was used to characterize the as grown samples (in powder form), for phase identification and for assessment of the phase purity, using a Brucker D8 diffractometer (40 kV, 30 mA), controlled by a DIFFRACTPLUS software, in Bragg-Brentano reflection geometry with CuKα radiation (λ = 1.5418 Å), between 10 and 64° in 2θ°. The resulting diffractograms were evaluated by Rietveld method with the FULLPROF program [41]. A pseudo-Voigt profile function was used for the line shape of the diffraction peaks. The following parameters were refined: half-width, pseudo-Voigt, zero shift, background points, and scale factor. Crucially, unit-cell parameters and positional and overall thermal displacement parameters were also refined for XRD data. A preferred orientation correction was applied, considering platelets perpendicular to [100] direction for SnSe-related alloys.

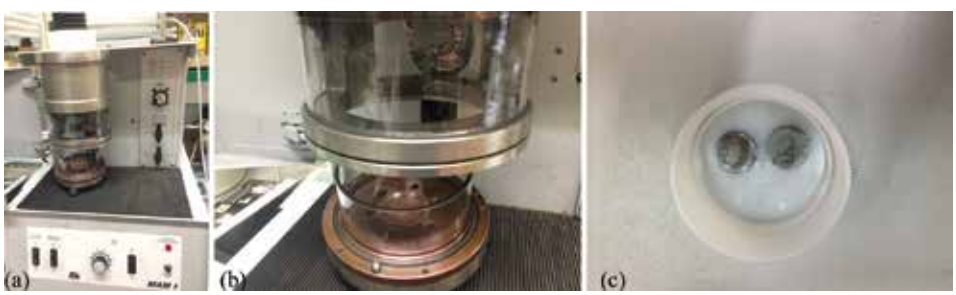

Figure 1. (a) Images of the mini arc furnace and (b) its water-cooled copper crucible, for synthesis of SnSe alloys materials. Pellets of powders of starting material are molten and then quenched in this crucible. (c) Typical disks of as-grown and then pressed intermetallic alloys.

2.3. Microstructural characterization

Surface texture of as-grown pellets was studied by scanning electron microscopy (SEM) in a table-top Hitachi TM-1000 microscope. This microscope, best used for middle and low resolutions with high acceleration voltage, is chiefly used to scan with low magnification to select interesting zones and to study obtain topographical information, with large depth of field, thanks to its sensitivity to surface characteristics.

2.4. Seebeck measurements in home-made apparatus

Measurement of the Seebeck coefficient seems simple: create a temperature gradient and measure the induced voltage. Yet, at elevated temperatures, this poses a challenge, mainly due to large and hard to control temperature gradients.

In many of the instruments used for Seebeck measurement, the most important systematic errors originate in the great difficulty to detect temperatures at exactly the same spot where the voltage difference is observed. Furthermore, the strong chemical and metallurgic reactivity of typical thermoelectric materials at elevated temperatures limits the choice of materials for constructing the instrument. For example, Pt is typically used at high temperatures as an inert and useful material without second thought, but it is out of the question for many thermoelectric alloys of heavy p-block elements. Instead, niobium or tungsten is recommended [42].

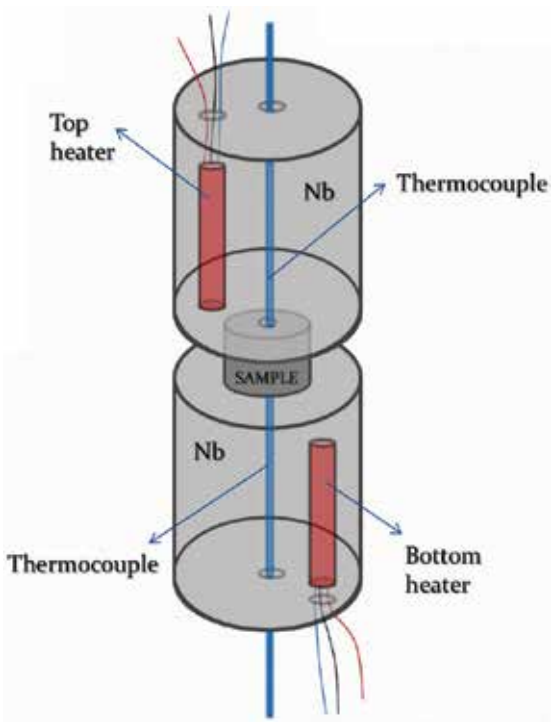

Figure 2. Scheme of the Seebeck measurement apparatus: Two blocks of niobium (Nb) with inner cartridge heaters (with built-in thermocouples), and home-made thermocouples (in contact with the sample).

We try to minimize all the possible errors that could arise during the measurement; for that, we designed a slightly modified device recently published [42]. Using this apparatus, we can measure the Seebeck coefficient from room temperature up to around 950 K. **Figures 2** and **3** show the design scheme of the measurement device. This instrument is composed of two home-made thermocouples, pressed into contact with the sample with springs outside the furnace, two blocks of niobium (Nb), also pressed to the sample by springs, with inner cartridge heaters (with built-in thermocouples), and a tubular furnace with yet another thermocouple.

When high temperature measurements are planned, the system is placed in a vacuum chamber equipped with a turbo-pump, which can reach a vacuum of around 1×10^{-6} mbar. The baseplate is water-cooled in order to provide better control at high temperatures.

Home-made thermocouples are used to measure the temperature of the sample at either side and also the Seebeck voltage. Their election is guided by the need to use inert chemical materials at high temperature against typical compounds in many thermoelectric materials, such as Sn, Pb, Te, and Se. This is the reason we chose thermocouples made of a niobium and chromel combination, ensuring that the Nb wires are in contact with the sample [27, 33], which allows us to reach temperatures near up to 950 K without reactions between samples and thermocouples.

The blocks are built of niobium because i) of its chemical inertness to chalcogenides and pnictides and ii) this metal has a good thermal conductivity, which is important since the heaters are inside them. As an added advantage, the Nb blocks can act as current injection contacts in a 4-point measurement of sample resistance, with the Nb wires of the thermocouples acting as voltage leads, providing an estimate of the electrical conductivity of the material. Although this is not the best geometry to ensure reliable absolute values (the samples have large cross section and are short, just the opposite of what one would desire for 4-point resistivity), it is

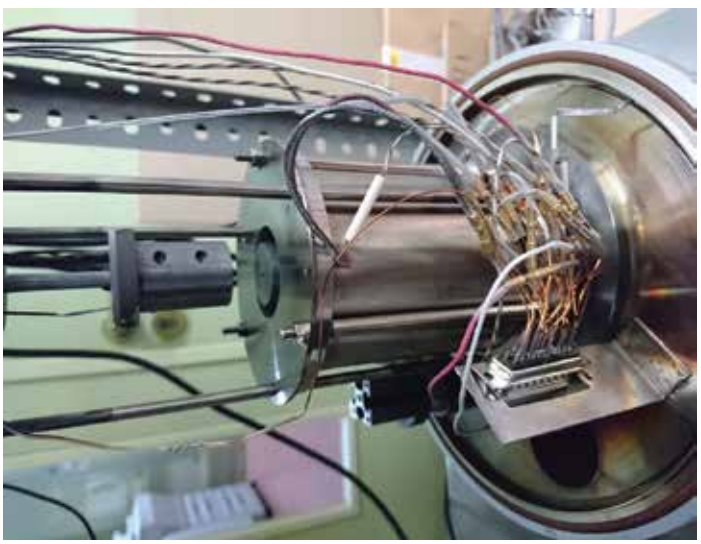

Figure 3. View of the measurement setup, showing the upper and lower Nb pistons and the radiation furnace, which would be shifted upwards during the measurements.

useful to gauge the behavior of the conductivity at higher temperatures. For more reliable absolute conductivity values, we estimated the geometric factor of this setup using a pellet of typical dimensions of our samples (10 mm diameter and 2 mm height) of a commercial Bi_2Te_3 ingot manufactured by TECTEG MFR, by comparing to a conventional in-line 4-point measurement of a $10 \times 2 \times 2$ mm^3 bar cut from the same pellet.

We use a Keithley-2700 scanning multimeter to measure the Seebeck voltage, the thermocouples monitoring the sample temperature, and a Pt sensor used for a numerical "cold" junction compensation. Three independent West-P6100 PID controllers are used to measure and control the cartridge heaters and the furnace. They provide an analog DC programming output of 0–5 V amplified by DeltaES150 DC power supplies. The advantage of this somewhat costlier power control is that the Seebeck voltages and resistivity are less affected by the electronic noise from the heaters. Measurement errors associated with the Seebeck coefficients are close to ~5%, while resistivity error is strongly dependent on the magnitude of the resistance, varying from 20% for low resistances in the mΩ range to negligible errors for values around 1 Ω.

Since typical thermoelectric pellets have resistances in the mΩ range, they are measured using a combination of Keithley Current Source 6221A and a KeithleyNanovoltmeter 2182A. Data acquisition and temperature control are handled by LabVIEW program, which communicates via GPIB with multimeter/nanovoltmeter and via RS485 serial protocol with PID controllers. The whole setup is shown in **Figure 4**.

Figure 4. High temperature Seebeck measurement system: The electronics in the top shelf, the vacuum chamber (with the sample inside) in the back, and the computer with the control-software.

3. Results and discussion

3.1. XRD characterization

Materials of the series $Sn_{1-x}M_xSe$ (M = Ti, Cr, Mn, Zn, Mo, Ag, Cd, Au) were prepared by a simple and straightforward arc-melting technique, yielding highly textured SnSe-type samples. About 2 g ingots were obtained in each case; a part was ground to powder for structural characterization, the remaining pellet was used for transport measurements. XRD patterns are all characteristic of the orthorhombic GeSe structural type, and can be Rietveld-refined in the orthorhombic *Pnma* space group. Both Sn(M) and Se atoms occupy 4*c* (x, ¼, z) positions. Dopant M atoms are distributed at random at Sn positions: different occupation tests were performed in the refinement, verifying M inclusion in the Sn sublattice. **Table 1** includes the unit-cell parameter and volume for each sample; the left panel of **Figure 5a** illustrates the quality of the fit for $Sn_{0.9}Mo_{0.1}Se$, with good discrepancy factors (R_p = 2.29%, R_{wp} = 3.07%, R_{exp} = 1.73%, χ^2 = 3.26, R_{Bragg} = 4.42%). The structure consists of trigonal pyramids $Sn(M)Se_3$ forming double layers perpendicular to the [100] direction, as shown in **Figure 5b**.

Figure 6 illustrates, as an example, the unit cell-volume variation for some selected M dopant atoms. A contraction of the cell is observed when Ag is introduced at Sn positions (**Figure 6a**), whereas the cell volume expands as Ti is introduced in the crystal structure (**Figure 6b**), as a consequence of the different ionic radii of the concerned atoms. In either case, the unit-cell variation assesses the incorporation of the dopant atoms in the crystal structure, discarding the inclusion of spurious phases in the grain boundaries or as secondary phases.

3.2. Scanning electron microscopy (SEM)

The layered crystal structure of SnSe-type compounds, containing strong covalent bonds within the layers, and much weaker interactions between adjacent layers, promotes the easy cleavage of materials. The arc-furnace procedure, involving a fast quenching of the samples from the molten state, drives a peculiar microstructure consisting of piles of stacking sheets, as shown in **Figure 7**.

Illustrated for M = Mn and M = Cd, the same typical microstructure is observed for all the samples. We find individual sheets with thickness below 0.1 μm (typically 20 to 40 nm). This micro- or nanostructuration has strong influence on the thermoelectric properties, especially the many surface boundaries that are responsible for scattering of both charge carriers and phonons (i.e. the electrical and the thermal conductivity).

3.3. Transport measurements

The Seebeck coefficient and electrical conductivity were measured in coin-shaped pellets of 12 mm diameter in the home-made device described before. **Table 1** includes the thermopower and electrical conductivity at room temperature (RT) for all the studied samples, which is useful

Material	Seebeck coefficient (μV/K)	Electrical conductivity (S/m)	Lattice constant a (Å)	Lattice constant b (Å)	Lattice constant c (Å)	Volume (Å^3)
SnSe	403	13	11.500 (2)	4.151 (1)	4.443 (1)	212.04 (9)
SnSe (SPS)	316	0.7	11.502 (2)	4.1539 (8)	4.4441 (9)	212.33 (7)
$Sn_{0.9}Y_{0.1}Se$	−81	6	11.503 (3)	4.157 (1)	4.436 (2)	212.1 (1)
$Sn_{0.95}Ti_{0.05}Se$	12	111	11.497 (2)	4.1531 (8)	4.443 (1)	212.14 (7)
$Sn_{0.90}Ti_{0.10}Se$			11.523 (7)	4.165 (3)	4.430 (3)	212.6 (3)
$Sn_{0.85}Ti_{0.15}Se$	7	2841	11.508 (4)	4.155 (1)	4.448 (2)	212.7 (1)
$Sn_{0.95}Cr_{0.05}Se$	−2	174	11.494 (3)	4.151 (1)	4.440 (1)	211.8 (1)
$Sn_{0.9}Cr_{0.1}Se$	−5	251	11.495 (3)	4.151 (1)	4.441 (1)	211.9 (1)
$Sn_{0.99}Mo_{0.01}Se$	480	4	11.492 (2)	4.1516 (7)	4.4424 (9)	211.94 (6)
$Sn_{0.97}Mo_{0.03}Se$	500	8	11.502 (2)	4.1560 (8)	4.446 (1)	212.53 (7)
$Sn_{0.95}Mo_{0.05}Se$	280	15	11.499 (2)	4.1529 (8)	4.445 (1)	212.29 (7)
$Sn_{0.9}Mo_{0.1}Se$	442	3	11.502 (2)	4.1523(8)	4.445 (1)	212.29 (7)
$Sn_{0.8}Mo_{0.2}Se$	404	8	11.504 (2)	4.1553 (9)	4.445 (1)	212.51 (8)
$Sn_{0.7}Mo_{0.3}Se$	357	47	11.504 (2)	4.155 (1)	4.444 (1)	212.41 (8)
$Sn_{0.99}Mn_{0.01}Se$	453	42	11.509 (2)	4.1558 (8)	4.447 (1)	212.72 (8)
$Sn_{0.99}Ag_{0.01}Se$	220	330	11.505 (2)	4.155 (1)	4.446 (1)	212.57 (9)
$Sn_{0.97}Ag_{0.03}Se$	161	111	11.500 (2)	4.1553 (9)	4.445 (1)	212.42 (8)
$Sn_{0.95}Ag_{0.05}Se$	112	276	11.502 (2)	4.155(1)	4.445 (1)	212.40 (9)
$Sn_{0.9}Ag_{0.1}Se$	123	3411	11.496 (4)	4.152 (2)	4.441 (2)	212.0 (2)
$Sn_{0.99}Au_{0.01}Se$	368	224	11.506 (3)	4.155 (1)	4.446 (1)	212.6 (1)
$Sn_{0.9}Zn_{0.1}Se$	432	18	11.500 (4)	4.154 (1)	4.444 (2)	212.3 (1)
$Sn_{0.99}Cd_{0.01}Se$	590	2	11.502 (3)	4.153 (1)	4.443 (2)	212.2 (1)
$Sn_{0.97}Cd_{0.03}Se$	640	0.7	11.497 (3)	4.152 (1)	4.440 (2)	211.9 (1)
$Sn_{0.95}Cd_{0.05}Se$	549	4	11.503 (3)	4.154 (1)	4.441 (1)	212.2 (1)
$Sn_{0.9}Cd_{0.1}Se$	482	23	11.513 (3)	4.161 (1)	4.444 (2)	212.9 (1)
$Sn_{0.8}Cd_{0.2}Se$	508	6	11.506 (3)	4.156 (1)	4.441 (2)	212.4 (1)

Table 1. Seebeck coefficient, electrical conductivity, and unit cell parameters of the different $Sn_{1-x}M_xSe$ alloys measured at room temperature.

as a preliminary screening in order to avoid particularly time-consuming high-temperature measurements. For the sake of comparison, some samples were also prepared by ball milling followed by SPS processes; inferior (lower) Seebeck coefficients and (considerably lower) electrical conductivities were invariably obtained, proving the excellence of the arc-melting procedure

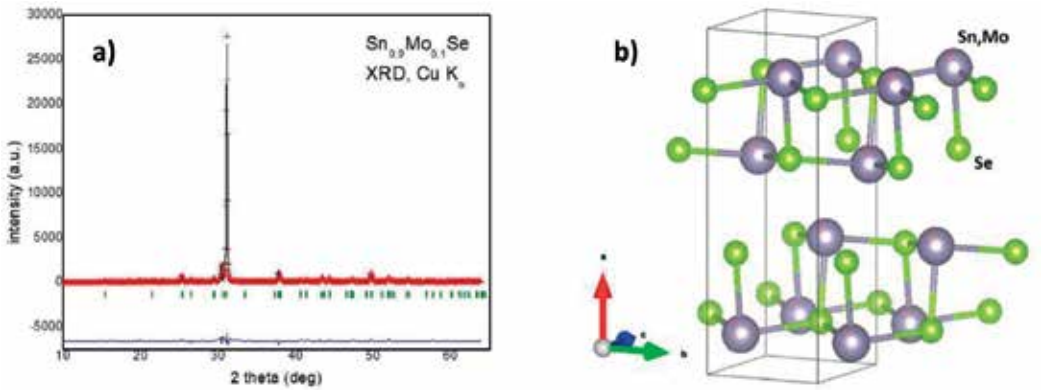

Figure 5. (a) XRD pattern and its Rietveld-refinement of $Sn_{0.9}Mo_{0.1}Se$, showing an excellent agreement between observed (crosses) and calculated (black line) profiles. (b) View of the $Sn_{1-x}Mo_xSe$ crystal structure, highlighting the layers of $Sn(Mo)Se_3$polyhedra perpendicular to **a** axis.

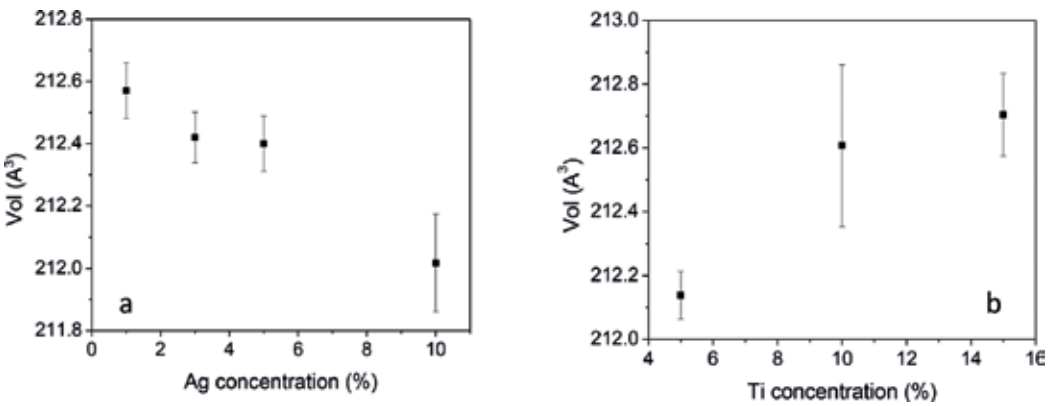

Figure 6. Unit-cell volume variation with the concentration of dopant element for (a) Ag and (b) Ti.

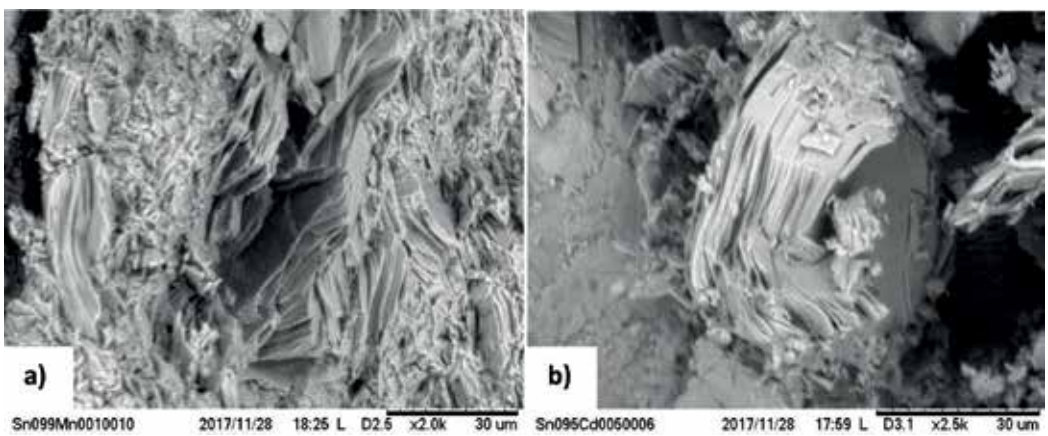

Figure 7. SEM image of as-grown $Sn_{1-x}M_xSe$, exhibiting nanostructuration, consisting of piles of nanometric platelets (perpendicular to [100] direction) taken with (a) 2000 magnification for M = Mn and (b) 2500 magnification for M = Cd.

reported here. Some samples were subsequently chosen for a more detailed high temperature study, up to 950 K.

As mentioned in the Introduction, pure tin selenide has good thermoelectric properties at high temperature [18]. However, in our screening we focus on the room temperature properties, and although we observed a high Seebeck coefficient, its electrical conductivity turned out to be much lower, by one or two orders of magnitude, than in single crystals. A good reference value for the electrical conductivity would be above 1000 S/m. Our approach has been to enhance this state of affairs by doping SnSe with adequate elements to boost the RT electrical conductivity, while keeping a good Seebeck coefficient. The thermoelectric performance is certainly enhanced at elevated temperature, as we indeed observe here. In addition, doping elements that yield almost zero Seebeck coefficient but good electrical conductivity are very promising for further optimization at much lower doping concentrations, such as the case of Ti, or Cr.

From **Table 1**, it is noteworthy that certain doping elements such as Mo or Cd are able to enhance the RT Seebeck coefficient to as high as 480 μV/K ($Mo_{0.01}$), 500 μV/K ($Mo_{0.03}$), 590 μV/K ($Cd_{0.01}$) or even 640 μV/K ($Cd_{0.03}$), while other elements such as Cr kill the thermoelectric performance (−2 μV/K for $Cr_{0.05}$). The microscopic origin of this behavior is beyond this study, since our aim was the preliminary identification of those doping elements that induce a better performance. Some selected samples with promising properties were studied above room temperature and are described in the following sections.

3.3.1. $Sn_{0.9}Y_{0.1}Se$

Starting from the left of the periodic table, we have alloyed SnSe with 10% yttrium, to obtain $Sn_{0.9}Y_{0.1}Se$. Interestingly, it turns out to be an n-type semiconductor, with negative Seebeck coefficient, at room temperature. The thermal evolution of the Seebeck coefficient and the electrical conductivity are shown in **Figure 8a**.

The Seebeck coefficient changes sign around 600 K. This sign change is reversible, reproducible in the same sample, and was observed in several specimens. The explanation has to do with a scenario where negative and positive carriers coexist in the material. At lower temperatures electrons are the majority carriers and holes the minority carriers. At higher temperatures, more holes are excited, in such a way that holes become the majority carriers, dominating their contribution to the Seebeck effect, turning it positive. This might happen, for example, if a narrow band of defects lies near the top of the valence band with the Fermi-level trapped near its bottom.

The electrical conductivity of $Sn_{0.9}Y_{0.1}Se$ rises exponentially with temperature, corresponding to a thermally activated semiconductor with an activation energy of E_g~0.2 eV, obtained from the inset of **Figure 8c**. The excellent fit shows that, despite the geometry utilized in the home-made apparatus, it provides highly reliable temperature-dependent relative conductivity values. Such a small band-gap is not intrinsic to pure SnSe. It may correspond to the above-mentioned defect band. Another possibility is that the electrical conductivity, invariably poor in arc-melting produced SnSe, and its alloys, at room temperature [36–39], is limited by intergrain hopping with activation energy of around 0.2 eV.

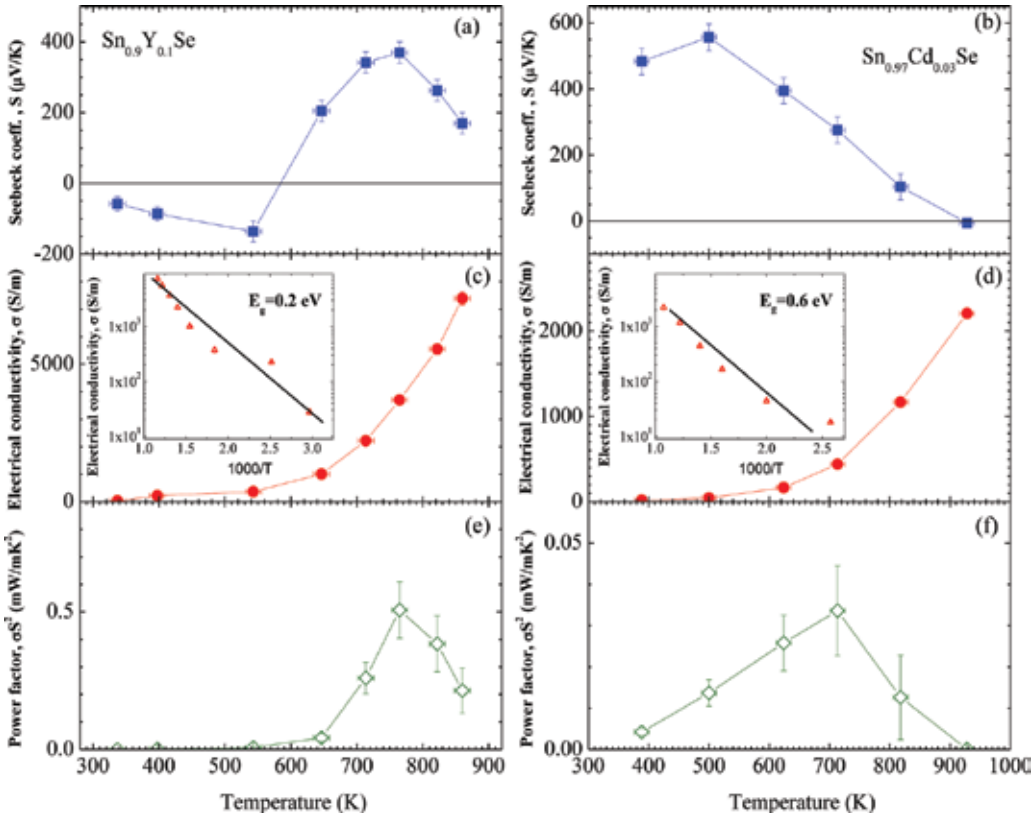

Figure 8. (a) Seebeck coefficient, (c) electrical conductivity, (e) power factor of $Sn_{0.9}Y_{0.1}Se$, and (b) Seebeck coefficient, (d) electrical conductivity, (f) power factor of $Sn_{0.97}Cd_{0.03}Se$ and insert in (d) inverse semilog-plot of electrical conductivity indicating a gap.

The power factor reaches a maximum of 0.5 mW/mK² at around 800 K. As we will show below and have published before [36–39], the thermal conductivity for SnSe alloys produced by arc-melting is less than 0.5 W/mK, indicating a possible figure of merit zT > 0.8 for $Sn_{0.9}Y_{0.1}Se$.

3.3.2. $Sn_{0.97}Cd_{0.03}Se$

As an alloy with contrasting behavior, we show the transport properties of $Sn_{0.97}Cd_{0.03}Se$ (**Figure 8b**, **d**, **f**). The cadmium-doped SnSe is the system with the highest Seebeck coefficients in this study (**Table 1**). Conversely, the electrical conductivity is very poor at RT, but there is an extraordinary increase with temperature, as illustrated in **Figure 8** on the right (middle panel). Both the large Seebeck coefficient and the low electrical conductivity indicate very low charge concentration. The steady decrease of the Seebeck coefficient (highest at 500 K with 570 μV/K) accompanied by the rapid increase of the electrical conductivity is another manifestation of the Pisarenko relationship [6]. The exponential temperature dependence of σ indicates a gap of E_g = 0.6 eV. This is very similar to the intrinsic gap of SnSe. We can conclude from this study that Cd is unlikely to be a useful dopant for SnSe

since its power factor is rather small, probably because of a lack of effective charge transfer (i.e. doping).

3.3.3. $Sn_{0.95}Mo_{0.05}Se$

We have prepared a series of molybdenum-alloyed SnSe samples at various concentrations, from 1% up to 30% Mo. According to the change of lattice parameters, Mo clearly enters the SnSe structure. However, the dependence of any of the properties studied (Seebeck coefficient, electrical conductivity, unit-cell volume) vary non-monotonously, thus the use of Mo as an alloying element is questionable. Without more detailed structural studies it is impossible to assess whether Mo indeed incorporates at the nominal compositions into SnSe. For 5% Mo-doped SnSe, the temperature-dependent Seebeck coefficient is shown in **Figure 9a**. The Seebeck coefficient is positive and reaches a maximum of 400 μV/K around 700 K. While the samples are rather resistive at room temperature, we observed an abrupt increment of the electrical conductivity at 800 K, reaching values up to perhaps 10,000 S/m (not shown).

3.3.4. $Sn_{0.99}Mn_{0.01}Se$

For SnSe doped with 1% manganese (**Figure 9b**), we also find an abrupt change of sign of the Seebeck coefficient, as described above for $Sn_{0.9}Y_{0.1}Se$. However, for Mn-doped SnSe the thermoelectric power is positive at low temperatures, and inverts above 630 K. A similar explanation considering two types of charge carriers may be invoked here. Importantly, this behavior is intrinsic to the material, not an effect of thermally induced chemical changes, as it is reversible, and reproducible in several thermal cycles. Therefore, Mn-doping provides a high temperature n-type SnSe thermoelectric element.

3.3.5. $Sn_{0.9}Ag_{0.1}Se$

The Ag-doped SnSe system is an example where the interplay of the Seebeck coefficient and electrical conductivity follows the Pisarenko relation, in **Table 1**. For low Ag-doping the Seebeck coefficient is around 200 μV/K at room temperature with an electrical conductivity

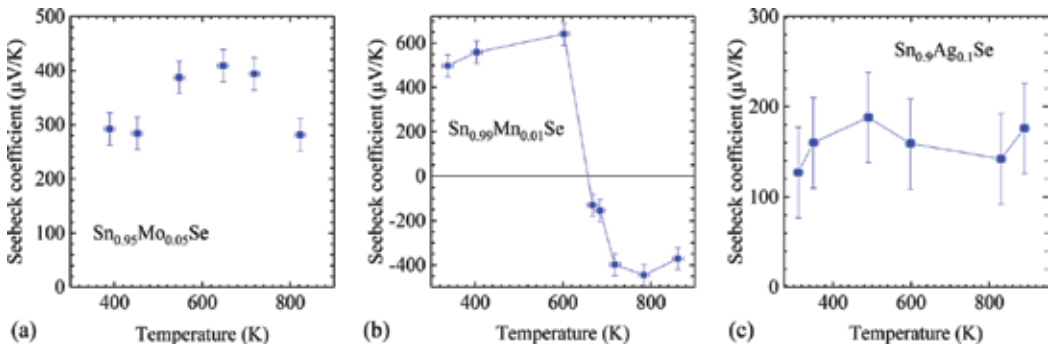

Figure 9. Seebeck coefficient of (a) $Sn_{0.95}Mo_{0.05}Se$, (b) $Sn_{0.99}Mn_{0.01}Se$, and (c) $Sn_{0.9}Ag_{0.1}Se$.

around 100 S/m, but for 10% Ag (itself difficult to stabilize by other methods [21]), while the Seebeck coefficient halves, σ shoots up to above 3000 S/m. That the Ag indeed enters the structure at such high doping levels is shown up by the continuous decrease of the unit-cell volume in **Figure 6a**. A σ increase of several orders of magnitude with respect to the RT value was observed above 800 K. The Seebeck coefficient remained stable between 150 and 200 μV/K (within the error bars), indicating that the conductivity is limited by intergrain boundaries. This effect is seen also in the small gap of a gold-doped alloy (**Figure 10**), as well as in the Y-doped sample in **Figure 8c**.

3.3.6. $Sn_{0.99}Au_{0.01}Se$

Gold doping is a yet-unexplored alternative to silver doping. The transport results corresponding to SnSe doped with 1% Au are shown in **Figure 10**. The Seebeck coefficient increases

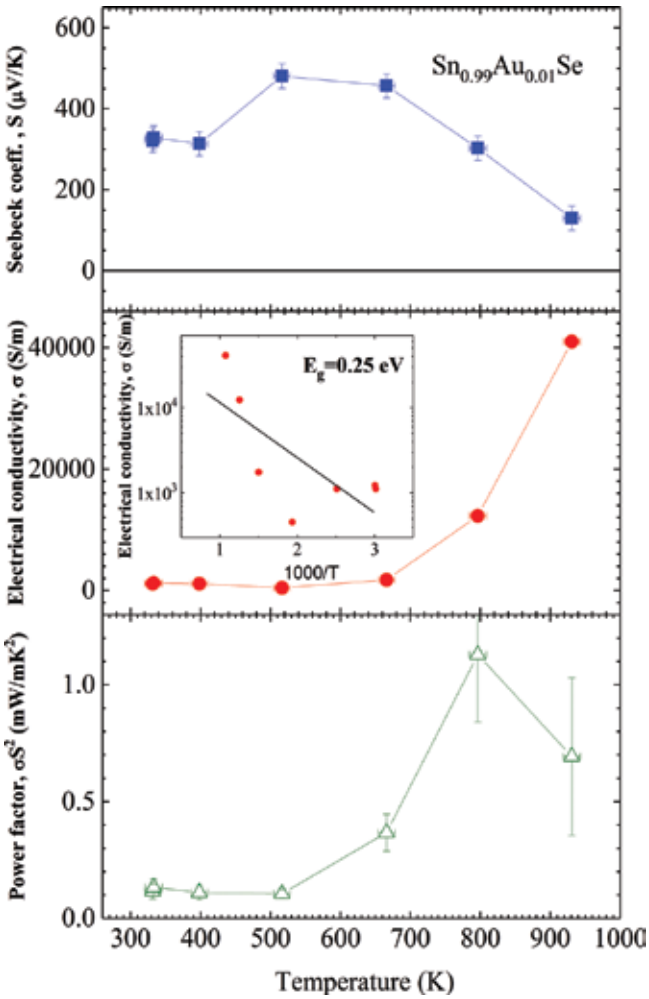

Figure 10. $Sn_{0.99}Au_{0.01}Se$: (top) Seebeck coefficient, (middle) electrical conductivity, (bottom) power factor, and (insert) inverse semilog plot of electrical conductivity indicating a gap.

up to a maximum at 500 K reaching 500 μV/K. The ambient electrical conductivity is noticeably lower than for Ag, yet it steadily increases with temperature reaching 40,000 S/m at 950 K, with a maximum power factor around 800 K above 1 mW/mK², thus implying a maximum zT up to 1.5 (this surprising value requires more careful verification of the resistivity measurements). The exponential increase of sigma indicates a gap of Eg = 0.25 eV, similar to the one seen in the Y-doped sample in **Figure 8**. Such a small gap, together with the relatively constant Seebeck coefficient, indicates that it is not the charge concentration increase, but thermally activated intergrain hopping limits the electrical conductivity in arc-molten SnSe.

3.4. Thermal conductivity

Figure 11 illustrates the total thermal conductivity (κ) obtained by laser-flash diffusivity method for two selected thermoelectric compounds: $Sn_{0.99}Mn_{0.01}Se$ and $Sn_{0.95}Ti_{0.05}Se$; in our experience, SnSe alloys prepared by arc-melting have similar thermal conductivities, and these values are representative for other alloys and different compositions.

Both SnSe alloys display remarkably low thermal conductivities at high-temperature region. At room temperature the thermal conductivities are 0.95 and 0.88 W/mK for the Mn and Ti alloys, respectively. These decrease further with increasing temperature, reaching 0.4 W/mK at 675 K. Both electron and phonon transport contribute to the total thermal conductivity, denoted as lattice thermal conductivity (κ_{lat}) due to phonon transport, and charge thermal conductivity (κ_{ch}) due to thermal transport of charges (electrons and/or holes). With the use

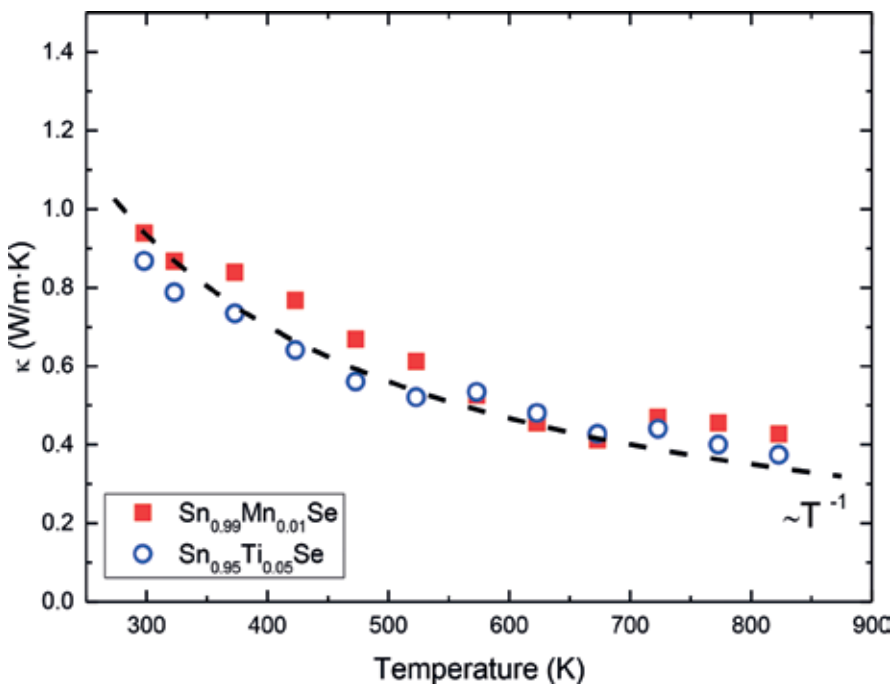

Figure 11. Thermal conductivity of $Sn_{0.99}Mn_{0.01}Se$ and $Sn_{0.95}Ti_{0.05}Se$ obtained by laser flash diffusivity. The black-dashed line indicates the classical behavior, $\kappa \sim T^{-1}$, due to the phonon-phonon interaction.

of the Wiedemann-Franz law [7], we can estimate charge contribution to the thermal conductivity as a function of temperature, $\kappa_{ch} = L_0 T\sigma$, with L_0 the Lorentz number and σ the electrical conductivity. For the highly resistive SnSe and its alloys, total thermal conductivity is dominated by the lattice thermal conductivity by a factor of 10,000:1. The temperature dependence of the lattice thermal conductivity follows the T^{-1} trend (black-dashed line in **Figure 11**), showing that the phonon-phonon interaction dominates in this temperature range.

The extremely low thermal conductivities observed in all the materials of the different doped series reported here afford considerably high figures of merit, zT.

4. Conclusion

We propose arc-melting technique as a fast one-step process to elaborate nanostructured intermetallic alloys of the $Sn_{1-x}M_xSe$ family (M: transition metals). All the specimens show a peculiar microstructure consisting of stacks of nanosheets. The presence of many extended grain boundaries perturbs the propagation of phonons and brings about extremely low thermal conductivities, around 0.5 W/mK. Using as quick screening tool the RT Seebeck coefficient and electrical conductivity, our preliminary survey of different SnSe-related transition metal alloys shows very distinct behaviors: certain doping elements such as Mo or Cd are able to enhance the RT Seebeck coefficient to values as high as 640 μV/K (3% Cd), while other elements such as Cr practically kill the thermoelectric performance (−2 μV/K for 5% Cr). The microscopic origin of this diverse behavior is far from being understood. Crucially, we find that some dopants, such as Y and Mn, can provide n-type alloys with a change of sign of the Seebeck coefficient. $Sn_{0.90}Y_{0.10}Se$ is n-type at low temperature and changes to p-type around 600 K. This sign change is reversible, and this behavior was reproduced in several specimens. The opposite behavior is observed for $Sn_{0.99}Mn_{0.01}Se$, which changes from p-type to n-type above 630 K. Many materials showed evidence of the Pisarenko relationship at work: dopants that, at some concentration, can yield highly conducting samples, usually with almost zero Seebeck coefficient, whereas for pure or lightly doped SnSe alloys bad conduction with large Seebeck effects are observed. This rich phenomenology can be useful as a guide for further, deeper research. We also describe an instrument to characterize the high-temperature Seebeck coefficient and electrical conductivity in disk-shaped pellets directly obtained from the intermetallic ingots. Problems with alloying of the samples at high temperature are avoided by the use of Nb pistons and Nb-based thermocouples that are chemically inert to reactive p-block elements. This is shown to be essential for the accuracy and reproducibility of the measurements, avoiding the degradation of the materials after thermally cycling up to 950 K.

In the context of thermoelectric devices, our finding of stable n-type doped SnSe at elevated temperatures prepared by a straightforward method would allow the use of SnSe derivatives for high-temperature applications. Thermoelectric devices require both n- and p-type semiconductors with matching thermoelectric, electronic, and mechanical properties, and this material system based on SnSe alloys could find application, for example, in the exhaust heat recovery or in solar-hybrid TEG applications.

Acknowledgements

We thank the financial support of the Spanish Ministry of Science and Innovation to the project MAT2017–84496-R.

Author details

Javier Gainza[1], Federico Serrano-Sánchez[1], Mouna Gharsallah[1,2], Manuel Funes[1], Félix Carrascoso[1], Norbert M. Nemes[3], Oscar J. Dura[4], José L. Martínez[1] and José A. Alonso[1]*

*Address all correspondence to: ja.alonso@icmm.csic.es

1 Instituto de Ciencia de Materiales de Madrid, C.S.I.C., Madrid, Spain

2 National School of Engineers, Sfax University, Tunisia

3 Departamento de Física de Materiales, Universidad Complutense de Madrid, Madrid, Spain

4 Departamento Física Aplicada and INEI, Universidad de Castilla La Mancha, Ciudad Real, Spain

References

[1] Rowe DM. CRC Handbook of Thermoelectrics. CRD Press; 1995. DOI: 10.1201/9781420049718.ch3

[2] Goldsmid HJ. Introduction to thermoelectricity. SSMATERIALS, volume 121. Springer-Verlag Berlin Heidelberg; 2016. DOI: 10.1007/978-3-662-49256-7

[3] Chen G, Dresselhaus MS, Dresselhaus G, et al. Recent developments in thermoelectric materials. International Materials Review. 2003;**48**:45-66. DOI: 10.1179/095066003225010182

[4] Nolas GS, Sharp J, Goldsmid HJ. Thermoelectrics: Basic Principles and New Materials Developments. New York: Springer; 2001

[5] Rull-Bravo M, Moure A, Fernández JF, Martín-González M. Skutterudites as thermoelectric materials: Revisited. RSC Advances. 2015;**5**:41653-41667. DOI: 10.1039/C5RA03942H

[6] Ioffe AF. Physics of Semiconductors. New York: Academic Press; 1960

[7] Zaitsev VK, Fedorov MI, Eremin IS, Gurieva EA, Rowe DW. Thermoelectrics Handbook: Macro to Nano. Boca Ratonp: CRC press; 2006

[8] Kim HS, Gibbs ZM, Tang Y, et al. Characterization of Lorenz number with Seebeck coefficient measurement. APL Mater. 2015;**3**:41506. DOI: 10.1063/1.4908244

[9] DiSalvo F. Thermoelectric cooling and power generation. Science. 1999;**285**:703-706. DOI: 10.1126/science.285.5428.703

[10] Zebarjadi M, Esfarjani K, Dresselhaus MS, et al. Perspectives on thermoelectrics: From fundamentals to device applications. Energy & Environmental Science. 2012;**5**:5147-5162. DOI: 10.1039/C1EE02497C

[11] Ong KS. Review of solar, heat pipe and thermoelectric hybrid systems for power generation and heating. International Journal of Low-Carbon Technologies. 2015;**11**:460-465. DOI: 10.1093/ijlct/ctv022

[12] Orr B, Akbarzadeh A, Mochizuki M, Singh R. A review of car waste heat recovery systems utilising thermoelectric generators and heat pipes. Applied Thermal Engineering. 2016;**101**:490-495. DOI: 10.1016/j.applthermaleng.2015.10.081

[13] Quan R, Liu G, Wang C, et al. Performance investigation of an exhaust thermoelectric generator for military SUV application. Coatings. 2018;**8**:45. DOI: 10.3390/coatings8010045

[14] Kumar S, Heister SD, Xu X, et al. Thermoelectric generators for automotive waste heat recovery systems part I: Numerical modeling and baseline model analysis. Journal of Electronic Materials. 2013;**42**:665-674. DOI: 10.1007/s11664-013-2471-9

[15] Nolas GS, Poon J, Kanatzidis M. Recent developments in bulk thermoelectric materials. MRS Bulletin. 2006;**31**:199-205. DOI: 10.1557/mrs2006.45

[16] Zhang X, Zhao L-D. Thermoelectric materials: Energy conversion between heat and electricity. Journal of Materials. 2015;**1**:92-105. DOI: 10.1016/j.jmat.2015.01.001

[17] Snyder GJ, Toberer ES. Complex thermoelectric materials. Nature Materials. 2008;**7**:105-114. DOI: 10.1038/nmat2090

[18] Zhao L-D, Lo S-H, Zhang Y, et al. Ultralow thermal conductivity and high thermoelectric figure of merit in SnSe crystals. Nature. 2014;**508**:373-377. DOI: 10.1038/nature13184

[19] Sassi S, Candolfi C, Vaney JB, et al. Assessment of the thermoelectric performance of polycrystalline p -type SnSe. Applied Physics Letters. 2014;**104**:212105. DOI: 10.1063/1.4880817

[20] Chen S, Cai K, Zhao W. The effect of Te doping on the electronic structure and thermoelectric properties of SnSe. Physica B: Condensed Matter. 2012;**407**:4154-4159. DOI: 10.1016/j.physb.2012.06.041

[21] Chen C-L, Wang H, Chen Y-Y, et al. Thermoelectric properties of p-type polycrystalline SnSe doped with Ag. Journal of Materials Chemistry A. 2014;**2**:11171-11176. DOI: 10.1039/c4ta01643b

[22] Castellanos-Gomez A. Black phosphorus: Narrow gap, wide applications. Journal of Physical Chemistry Letters. 2015;**6**:4280-4291. DOI: 10.1021/acs.jpclett.5b01686

[23] Heremans JP, Wiendlocha B, Chamoire AM. Resonant levels in bulk thermoelectric semiconductors. Energy & Environmental Science. 2012;**5**:5510-5530. DOI: 10.1039/C1EE02612G

[24] Zhang Q, Chere EK, Sun J, et al. Studies on thermoelectric properties of n-type polycrystalline SnSe1-xSx by iodine doping. Advanced Energy Materials. 2015;**5**:1500360. DOI: 10.1002/aenm.201500360

[25] Kutorasinski K, Wiendlocha B, Kaprzyk S, Tobola J. Electronic structure and thermoelectric properties of n- and p-type SnSe from first-principles calculations. Physical Review B. 2015;**91**:1-12. DOI: 10.1103/PhysRevB.91.205201

[26] Li CW, Hong J, May AF, et al. Orbitally driven giant phonon anharmonicity in SnSe. Nature Physics. 2015;**11**:1-8. DOI: 10.1038/nphys3492

[27] Guo R, Wang X, Kuang Y, Huang B. First-principles study of anisotropic thermoelectric transport properties of IV–VI semiconductor compounds SnSe and SnS. Physical Review B: Condensed Matter and Materials Physics. 2015;**92**:1-13. DOI: 10.1103/PhysRevB.92.115202

[28] Fu Y, Xu J, Liu G-Q, et al. Enhanced thermoelectric performance in p-type polycrystalline SnSe benefiting from texture modulation. Journal of Materials Chemistry C. 2016;**4**:1201-1207. DOI: 10.1039/C5TC03652F

[29] Zhao L-D, Chang C, Tan G, Kanatzidis M. SnSe: A remarkable new thermoelectric material. Energy & Environmental Science. 2016;**9**(10):15-17. DOI: 10.1039/C6EE01755J

[30] Peng K, Lu X, Zhan H, et al. Broad temperature plateau for high ZTs in heavily doped p-type SnSe single crystals. Energy & Environmental Science. 2016;**9**:454-460. DOI: 10.1039/C5EE03366G

[31] Chen YX, Ge ZH, Yin M, et al. Understanding of the extremely low thermal conductivity in high-performance polycrystalline SnSe through potassium doping. Advanced Functional Materials. 2016;**26**:6836-6845. DOI: 10.1002/adfm.201602652

[32] Dai XQ, Wang XL, Li W, Wang TX. Electronic properties of the SnSe-metal contacts: First-principles study. Chinese Physics B. 2015;**24**:7-12. DOI: 10.1088/1674-1056/24/11/117308

[33] Kim Y, Yoon G, Cho BJ, Park SH. Multi-layer metallization structure development for highly efficient polycrystalline SnSe thermoelectric devices. Applied Sciences. 2017;**7**: 1116. DOI: 10.3390/app7111116

[34] Zhao L, Tan G, Hao S, et al. Ultrahigh power factor and thermoelectric performance in hole-doped single-crystal SnSe. Science. 2016;**351**:141. DOI: 10.1126/science.aad3749

[35] Duong AT, Nguyen VQ, Duvjir G, et al. Achieving ZT = 2.2 with Bi-doped n-type SnSe single crystals. Nature Communications. 2016;**7**:1-6. DOI: 10.1038/ncomms13713

[36] Serrano-Sánchez F, Gharsallah M, Bermúdez J, et al. Nanostructured state-of-the-art thermoelectric materials prepared by straight-forward arc-melting method. Thermoelectrics for Power Generation – A Look at Trends in the Technology. InTech-Open Access Publisher; December 21, 2016. http://www.intechopen.com/books/thermoelectrics-for-power-generation-a-look-at-trends-in-the-technology DOI: 10.5772/65115

[37] Serrano-Sánchez F, Gharsallah M, Nemes NM, et al. Record Seebeck coefficient and extremely low thermal conductivity in nanostructured SnSe. Applied Physics Letters. 2015;**106**:83902. DOI: 10.1063/1.4913260

[38] Serrano-Sanchez F, Nemes NM, Dura OJ, et al. Structural phase transition in polycrystalline SnSe: A neutron diffraction study in correlation with thermoelectric properties. Journal of Applied Crystallography. 2016;**49**:2138-2144. DOI: 10.1107/S1600576716015405

[39] Gharsallah M, Serrano-Sánchez F, Nemes NM, et al. Giant seebeck effect in Ge-doped SnSe. Scientific Reports. 2016;**6**:26774. DOI: 10.1038/srep26774

[40] Lan Y, Minnich AJ, Chen G, Ren Z. Enhancement of thermoelectric figure-of-merit by a bulk Nanostructuring approach. Advanced Functional Materials. 2010;**20**:357-376. DOI: 10.1002/adfm.200901512

[41] Rodríguez-Carvajal J. Recent advances in magnetic structure determination by neutron powder diffraction. Physics B. 1993;**192**:55-69. DOI: 10.1016/0921-4526(93)90108-I

[42] Iwanaga S, Toberer ES, Lalonde A, Snyder GJ. A high temperature apparatus for measurement of the Seebeck coefficient. The Review of Scientific Instruments. 2011;**82**:63905. DOI: 10.1063/1.3601358

Chapter 2

Thermoelectric Textile Materials

Qian Wu and Jinlian Hu

Additional information is available at the end of the chapter

http://dx.doi.org/10.5772/intechopen.75474

Abstract

Textile, as an intimate partner of human body, shows promising application in wearable thermoelectrics for body heat conversion. Compared with other widely studied flexible film thermoelectric materials, textiles having better air-permeability, wearability, and flexibility are more suitable for wearable electronics. In the past few years, many researches have focused on the design and fabrication of textile-based thermoelectric materials and generators. By integrating with high performance inorganic semiconductors and conductive polymers, fabrics or fibers will be given thermoelectric properties. Technologies of coating, printing, and even thermal drawing can be adopted in the fabrication of textile thermoelectric materials. With great design flexibility, various flexible textile generator structures can be obtained by using yarns or fabrics as thermoelectric legs, which will bring new inspirations for the future development of flexible thermoelectrics.

Keywords: thermoelectric, textile, flexible, wearable, fiber

1. Introduction

Recently, the rapid development of wearable electronic devices such as smart watches, wrist bands, smart glasses, and electronic skins has attracted extensive research interest of self-powered and wearable technologies [1, 2]. Energy harvesting technologies such as solar cell, piezoelectric, triboelectric, and thermoelectric technologies can be utilized to meet the requirement of self-powered system [3–7]. As one of the most promising energy harvesting strategies, thermoelectric technology has received extensive research attentions in recent years. In a thermoelectric system, heat especially waste heat, such as human body heat, geothermal energy, solar thermal energy, and the residual heat of motor engines, can be directly converted into electrical energy without any pollution [8]. A typical thermoelectric generator (TEG) is composed of several p-type and n-type thermoelectric materials connected parallelly

with conductors. When temperature difference exists between the two sides of thermoelectric materials, the charge carriers in the materials will be driven to flow from the hot side to the cold side, and thus a thermo-voltage can be formed. As key components in a thermoelectric system, the energy conversion efficiency of a thermoelectric material can be evaluated by a thermoelectric figure of merit, also called ZT value [9]. As shown in Eq. (1).

$$ZT = \frac{\sigma S^2}{\kappa} T \tag{1}$$

In this equation, σ is electrical conductivity, S is Seebeck coefficient, κ is thermal conductivity, T is absolute temperature, and ZT is a dimensionless value without upper limit. The value of $S^2\sigma$ is called power factor, which also can be used to represent the thermoelectric performance of materials where the impact of thermal conductivity is secondary. For example, in polymer-based thermoelectric materials, power factor is widely used, since most polymers have much lower thermal conductivity than inorganic semiconductors and then their thermoelectric performance will be mainly decided by the power factor.

Now, two main strategies can be adopted to improve the efficiency of thermoelectric system. One is to increase the ZT value of the thermoelectric materials, and the other is to adjust the structure of TEG for better utilization of heat energy. In past few years, the thermoelectric efficiency of bulk inorganic metal alloys has been improved significantly. A record-breaking high ZT of 2.6 achieved by SnSe single crystals at 923 K was reported in 2014, which gives thermoelectric generators a better application prospect in future [10]. Meanwhile, a new solar heat TEG system has been developed. By combining solar heat collection and thermoelectric conversion technologies, the new system could possess a peak efficiency of 7.4% [11].

Nowadays, with the rapid development of wearable and flexible electronics, the field of flexible thermoelectric materials and generators were growing dramatically. Various flexible thermoelectric materials were developed in form of films, papers, fabrics, and even fibers. Thermoelectric films are most studied among them, while the research about thermoelectric fabrics and fibers are just beginning very recently. Generally, these flexible thermoelectric materials are mostly made by organic polymers or polymer/inorganic semiconductor composites, so that they are easier to fabricate on large scales. However, the thermoelectric efficiency of these polymer-based flexible materials is much lower than the inorganic semiconductors. Hence, the methods to further improve the thermoelectric efficiency of these flexible materials will still be a hot research issue in future.

Although fabrics, fibers and polymer films are all flexible materials, textile thermoelectric materials have exhibited more competitive characteristics than simple films, especially on the wearable application. Textiles composed of different sets of fibers and yarns have excellent structure design flexibility, which allows them to meet the requirement of flexible, wearable, nontoxic, light weight, and even washable for wearable devices so that we can utilize our human body heat as power source. Until now, many pioneering research works have been conducted on this area and showed gratifying results. Therefore, in this chapter, the development of these textile thermoelectric materials and generators will be thoroughly described.

http://dx.doi.org/10.5772/intechopen.75474

2. Textile thermoelectric materials

Textile is an ideal candidate to utilize our human body heat to generate power due to its excellent flexibility, wearability, comfort, and air-permeability properties, especially compared with those rigid bulk electronic materials and impermeable polymer-based flexible films. Thus, it is promising to develop textile material-based thermoelectric materials and generators to utilize our body heat. In the past few years, many research works have been done on both textile thermoelectric materials and fabric generators, which have paved the way and given us inspirations for future wearable thermoelectric systems.

2.1. Fabric-based thermoelectric materials

Fabric finishing and coating are mature technologies in textile industry that can be easily used for large-scale production. Thus, it is a cost-effective and practical way to added effective thermoelectric materials on fabrics for both organic and inorganic materials. In 2015, Yong Du et al. prepared a textile thermoelectric material by coating commercial polyester fabrics with PEDOT:PSS [12]. Their adopted a simple dip coating process to fabricate textiles with thermoelectric functions. **Figure 1** shows the dip coating process the prepared thermoelectric textile strip by Tong Lin. P-type PEDOT:PSS doped with DMSO was acted as effective thermoelectric materials. Commercial available polyester fabric was used as a flexible substrate. Both advantages of textiles and PEDOT:PSS were utilized. The prepared textile materials exhibit electrical conductivities ranged from 0.5–3 S/cm and Seebeck coefficient of 15.3–16.3 μV/K at 300 K. The highest power factor of 0.045 $\mu Wm^{-1} K^{-2}$ was achieved at 390 K. Although the thermoelectric efficiency of this flexible textile thermoelectric material is not quite satisfied, this is

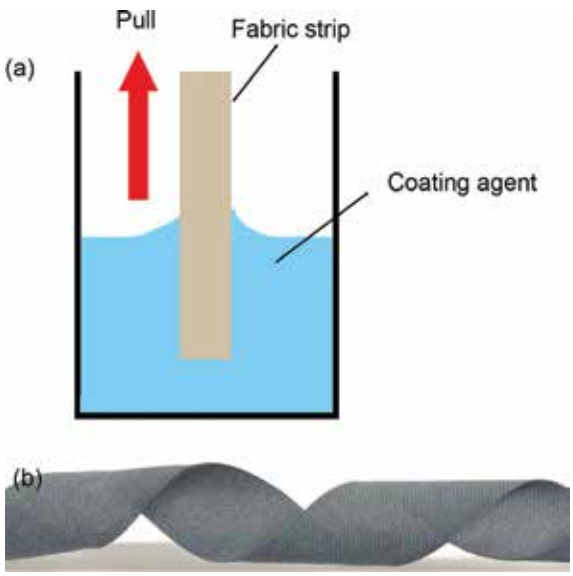

Figure 1. (a) A dip coating process and (b) PEDOT:PSS coated polyester fabric by Yong Du et al. [12].

still an initial attempt to applying fabrics into thermoelectric application. The low efficiency may also attribute to the used organic polymer thermoelectric materials. Choosing high efficient inorganic semiconductors especially their nano-sized counterparts as fabric coating materials, the thermoelectric efficiency coated fabrics could be further improved.

Another example is to use nano inorganic materials to produce thermoelectric fabric. In 2015, Chongjian Zhou et al. prepared a thermoelectric fabric made by inorganic nanowires and organic polymer composite [13]. A simple five-step vacuum filtration process was employed. $Cu_{1.75}Te$ nanowires sheet was fabricated by filtration, hot press, and annealing first, and then PVDF solution was drop cast on the nanowire sheet. After a heating process, a flexible composite material was formed. The composite structure and prepared fabric film are shown in **Figure 2**. The prepared flexible fabric film has a high electrical conductivity of 2490 S/cm, and a Seebeck coefficient of 9.6 μV/K at room temperature, which resulted in a power factor of 23 $\mu Wm^{-1} K^2$. The performance of prepared fabric could keep steady after 300 cycles of bending tests. The results indicate that this easy to scale-up method is effective to fabricate flexible thermoelectric fabric and can be extended to other effective inorganic materials such as Bi_2Te_3, Ag_2Te, or Ag_2Se nanowires.

The preparation of fabric thermoelectric materials is simple and very easy to fabricate on large scale. The integration of inorganic high performance thermoelectric materials would give fabrics better thermoelectric performance than organic polymers. Although fabrics usually have the same 2D flat structure as polymer films, porous fabric structures would have better air-permeability and wearable comfort than polymer films, which is more appropriate for wearable devices.

2.2. Fiber/yarn-based thermoelectric materials

In addition to fabrics, fibers and/or yarns can be also fabricated into thermoelectric materials. Since fibers and yarns are the structural basis of fabrics, to offer fibers and yarns thermoelectric properties other than fabric itself will give more design flexibility for flexible textile TEGs. In 2012, Daxin Liang et al. reported a fiber thermoelectric material. PbTe nanocrystals were coated onto glass fibers via a dip coating process [14], as shown in **Figure 3**. The PbTe nanocrystal coated fibers have an electrical conductivity of 104.4 S/m, Seebeck Coefficient 1201.7 $\mu V \cdot K^{-1}$, and thermal conductivity of 0.228 $W \cdot m^{-1} \cdot K^{-1}$ at 300 K. The resulted power factor is 0.15 $mW \cdot m^{-1} \cdot K^{-2}$ at 300 K. It should be noted that the thin coating layer would lower the electrical conductivity of PbTe nanocrystals compared with PbTe bulk crystals.

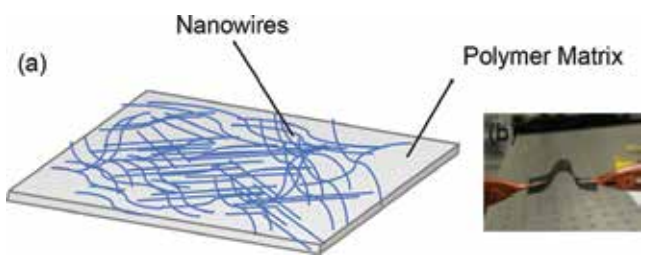

Figure 2. (a) The composite film structure and (b) the picture of flexible fabric film prepared by Chongjian Zhou et al. [13].

http://dx.doi.org/10.5772/intechopen.75474

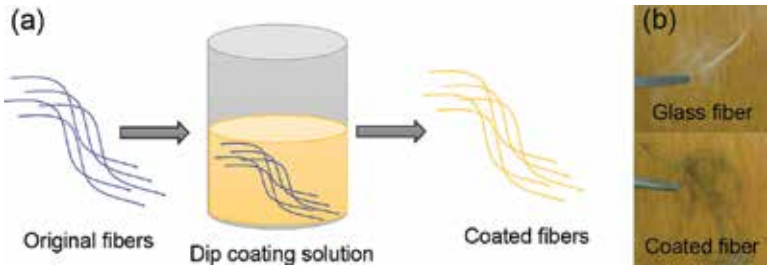

Figure 3. (a) Dip coating process of fibers and (b) comparison of uncoated and coated glass fibers made by Daxin Liang et al. [14].

In 2016, we proposed a water-processable thermoelectric coating material made of waterborne polyurethane, MWCNT, and PEDOT:PSS composite [15]. The optimal electrical conductivity and Seebeck coefficient could achieve ~13,826 S/m and ~10 μV/K at room temperature respectively, and the resulted power factor is about ~1.41 $\mu Wm^{-1} K^{-2}$. Compared with other organic-solvent-based thermoelectric polymers, this water-based composite exhibits satisfactory thermoelectric performance and good processability. Then, we coated the prepared water-based composite on polyester and cotton yarns respectively, as shown in **Figure 4**. The results show that the fabricated thermoelectric composite can be successfully coated on textile yarns, and polyester filament is more suitable as coating substrate than staple cotton yarn. Besides, these coated yarns can be treated as thermoelectric legs and were further used to fabricate fabric TEG.

In 2016, Jae Ah Lee et al. using electro-spinning technology to fabricate thermoelectric nanofibers and then twisted into yarns [16]. Polyacrylonitrile (PAN) nanofiber sheets were electrospun on two parallel wire collectors. Bi_2Te_3 and Sb_2Te_3 were selected as n-type and p-type thermoelectric materials, and deposited on two sides of the PAN sheets. After a twisting process, thermoelectric yarns can be formed, as shown in **Figure 5**. The highly porous structure of the electrospun yarns are quite resistant to mechanical damage, which enables the yarns to be knitted and woven into fabrics without the significant changes in their electrical conductivity and thermopowers.

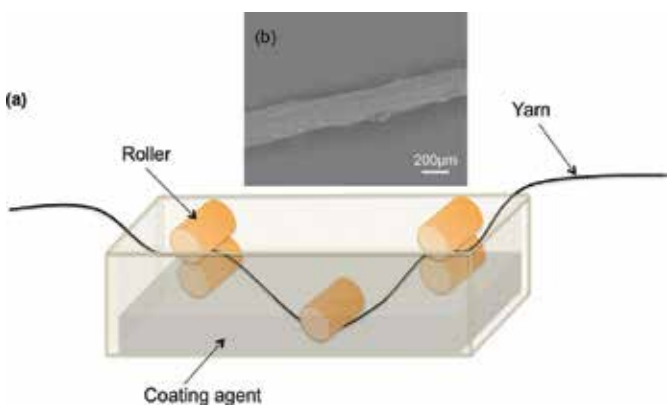

Figure 4. (a) Yarn coating process and (b) polyester yarn coated with waterborne polyurethane thermoelectric composites made by Jinlian Hu [15].

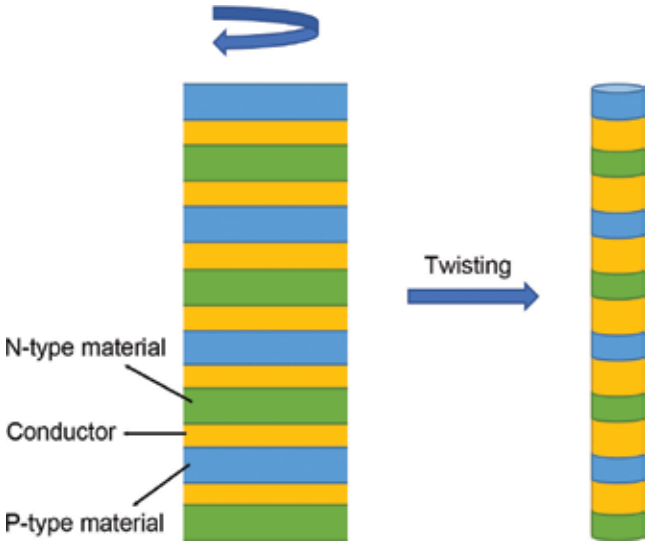

Figure 5. Schematic illustration of the conversion of thermoelectric sheet into a yarn.

The studies of yarn and fiber thermoelectric materials are just beginning. The same coating process of fabrics can be further used to prepare fiber and yarn thermoelectric materials. Additionally, more complicated fabrication technique such as electrospinning and twisting process can also be adopted to prepare fiber and yarn materials with better performance. It can be imagined that there will be more ingenious methods in future to fabricate high performance thermoelectric fiber or yarn materials, so that a fully textile-based thermoelectric generator can be achieved.

3. Textile thermoelectric generators

Generally, a traditional inorganic TEG possesses a sandwich structure. Several n-type and p-type thermoelectric bulk materials are alternatively arranged and connected in series with conductors in the middle part of TEG. Ceramics are used at the top and bottom layers to avoid short-circuit between the metal interconnects. This sandwich structure helps to maintain an excellent heat exchange with surroundings. Temperature difference will be generated along the thickness direction of sandwich TEG, which is necessary for wearable thermoelectrics to some extent. However, it is difficult to apply this sandwich structure in flexible film materials. The structure of a typical organic film TEG is a two-dimensional plane. Although p-type and n-type film thermoelectric legs are still alternatively connected in series by flexible conductors, the temperature difference in this structure will only exists along the film length direction rather than along the thickness direction, since the dimension limitation in film thickness direction cannot sustain the temperature difference. Thus, the flexible 2D film generator will be challenged in wearable application. Textiles TEG with various structure design flexibility may provide one solution for this problem.

3.1. Two-dimensional textile TEGs

A 2D flat TEG structure is also adopted in the first generation of textile TEGs. In 2012, C. A. Hewitt et al. developed a PVDF/CNT composite-based fabric TEG. Several n-type and p-type CNT composite films were alternatively arranged between the insulated PVDF films. The PVDF films are shorter than the CNT composite films. Thus, n-type and p-type CNT composites could form p-n junctions to connect the generator legs by hot press the stacked films, and resemble a felt fabric TEG [17]. The schematic structure of they prepared fabric TEG is shown in **Figure 6**. The prepared TEG composed of 72 layers fabric could generate power about 137 nW with an internal resistance of 1270 Ω.

In 2015, Yong Du et al. prepared a 2D fabric TEG by using PEDOT:PSS coated polyester fabric strips [12]. To fabricate the TEG, a whole PEDOT:PSS coated polyester fabric was cut into several strips first. Then, these strips were further adhered on a polyester fabric substrate by silver paint and connected in series with silver wires. Thus, a fabric TEG only composed of p-type materials can be prepared. The TEG arrangement is shown in **Figure 7**. Temperature difference will generate along the fabric length direction. The fabric TEG prototype consisting of five fabric strips could generate 4.3 mV when temperature difference ΔT is 75.2 K. The maximum output power P_{max} could achieve 12.29 nW.

The same arrangement can also be achieved by thermoelectric yarns. In 2017, Ryan et al. reported a highly durable thermoelectric silk yarn made by dyeing with PEDOT:PSS, which could be produced with a length of up to 40 m and keep steady after repeated machine washing and drying [18]. Then, they embroidered these yarns into a felted wool fabric substrate and connected them end-to-end with silver wires to form a fabric TEG. The structure is illustrated in **Figure 8**. In an in-plane fabric TEG prototype composed of 26 yarn legs, the internal resistance is about 8.7 KΩ, and the output voltage of $V_{out}/\Delta T$ is about 313 μV K^{-1} when temperature difference ΔT is about 120°C. An output current of 1.25 μA can be observed when ΔT is 66°C, and resulted a maximum power output P_{max} of ~12 nW.

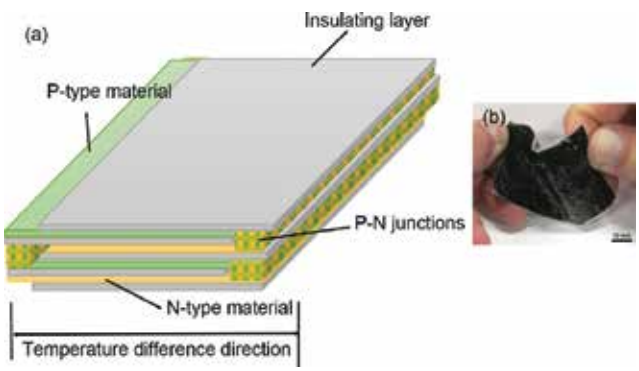

Figure 6. (a) Alternative arranged multilayer fabric TEG structure and (b) fabric film TEG prepared by Hewitt et al. [17].

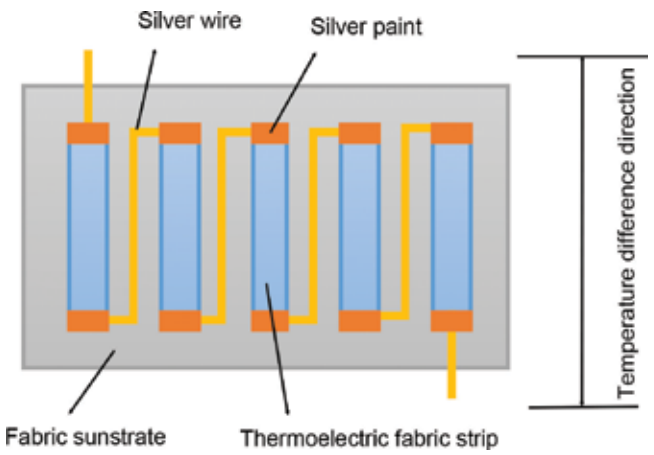

Figure 7. Arrangement of 2D fabric TEG composed of only p-type materials.

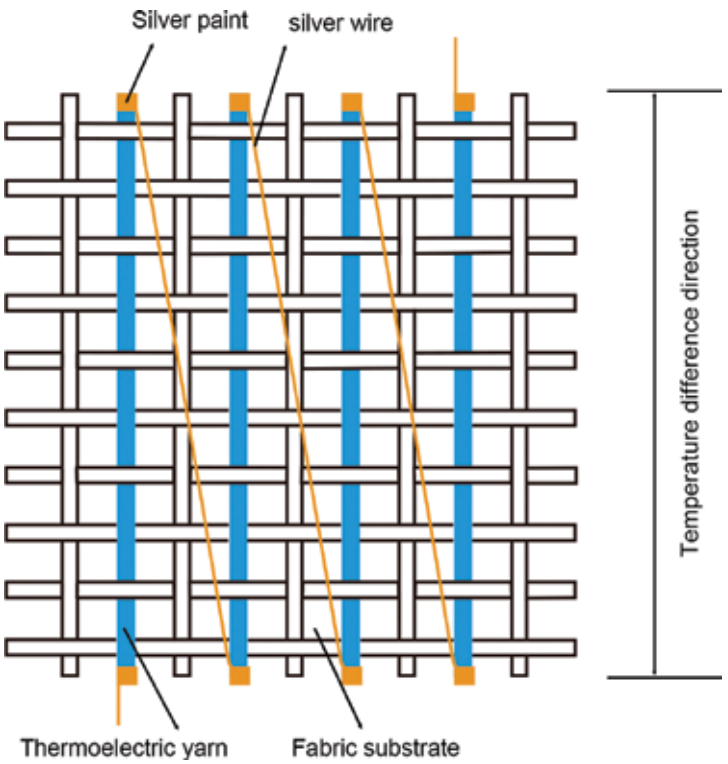

Figure 8. Thermoelectric yarn arrangement in a fabric substrate.

In general, 2D fabric TEG is a first attempt to apply textile structures to the design of flexible TEGs. Although these initial 2D fabric TEGs have almost the same in-plane structure with film TEGs, fabric TEGs can be easily rolled up, bent, twisted, and are permeable to air and moisture, making them more flexible and comfort to wear.

3.2. Three-dimensional textile TEGs

In addition to the initial 2D textile TEG structures, researchers also developed several 3D textile TEGs similar to the classical sandwich bulk TEG. In 2014, Kim et al. fabricated a wearable TEG on a glass fabric by screen-printing technology [19]. The device structure and is shown in **Figure 9**. The inorganic Bi_2Te_3 and Sb_2Te_3 thermoelectric materials were printed on a glass fabric substrate first. Then, the fabric containing an array of eight thermocouples was connected by several cooper foils, and finally encapsulated with PDMS. The fabricated TEG exhibits a high output power density of 3.8 $mWcm^{-2}$ and 28 mWg^{-1} at $\Delta T = 50$ K. Besides, the TEG could endure repeated bending for 120 cycles.

Another research reported a silk fabric-based TEG similar to the Kim's structure in 2016. Zhisong Lu et al. deposited nanostructured Bi_2Te_3 and Sb_2Te_3 synthesized by hydrothermal method on two sides of a commercial available silk fabric [20]. The deposited p-type and n-type thermoelectric materials were further connected with silver foils to form a flexible TEG using a similar arrangement of Kim et al. [19]. The prototype containing 12 thermocouples could generate a maximum thermos-voltage of ~10 mV and output power of ~15 nw under a temperature difference of 35 K. The power output performance can sustain stable even during 100 cycles of bending and twisting.

Jae Ah Lee et al. using textile structure designed a new type of fabric TEG, which can utilize thermal energy along fabric thickness direction. Both knitting and weaving technology can be employed to fabricate this fabric TEG [16]. Several p-type and n-type yarns prepared by electro-spinning were arranged in the fabric according to the predesigned patterns. In knitted structure, p-type and n-type yarns were alternatively arranged and connected in series. In a plain weave structure, several single yarns containing metallic connected n-type and p-type components were woven into fabrics with insulating yarns. In addition, these single yarns should be carefully placed in correct way to ensure the right contact between p-n junctions and hot/cold surfaces. **Figure 10** illustrates the fabric TEG in knitted and woven structures respectively. The best output power of the prepared fabric TEG could achieve 8.56 Wm^{-2} at a temperature difference of 200°C. This study is the first attempt to utilize fabric structures to realize textile TEG that suitable for fabric thickness power generation.

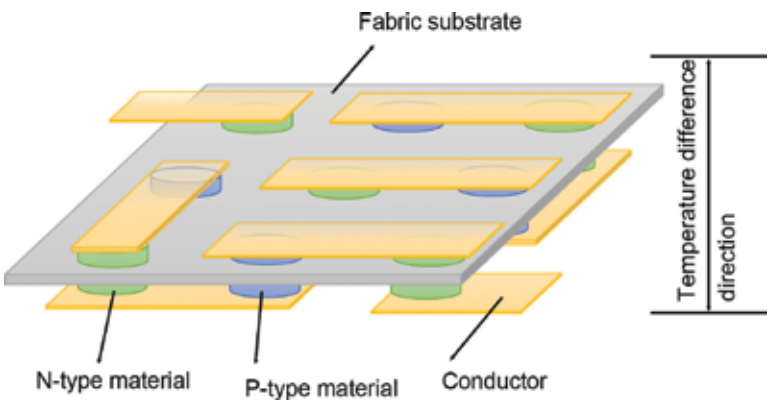

Figure 9. Arrangement of fabric TEG that allowing generate temperature difference along fabric thickness direction.

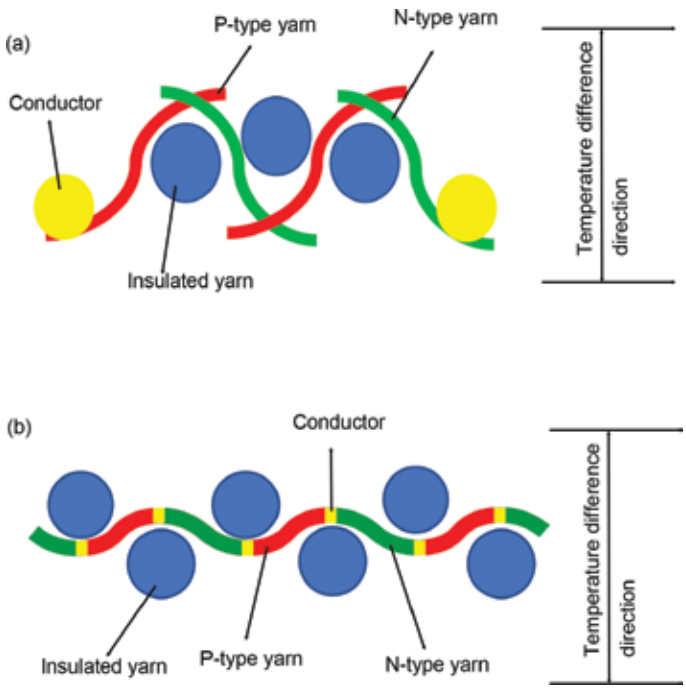

Figure 10. (a) Thermoelectric yarn arrangement in knitted fabric structure and (b) thermoelectric yarn arrangement in woven fabric.

In the following 2017, we designed a new flexible 3D fabric TEG which have a sandwich structure, so that the temperature difference could be generated along fabric thickness direction [21]. A 3D spacer fabric is composed of two separate fabric layers on the top and bottom of the fabric, and a set of pile yarns in the middle used to connected the top and bottom fabric layers. Compared with 2D materials, the sandwich 3D structure has more dimensions in thickness direction, so that the temperature difference can be sustained along the fabric thickness direction, and the flexibility of the TEG can be retained due to its fabric nature. Therefore, 3D fabric would be a good candidate as substrate for flexible and wearable TEG. **Figures 3–5** show the designed 3D fabric TEG. A prototype was fabricated by embroidered p-type and n-type coated polyester yarns into a 3D spacer fabric. The 3D fabric TEG consisting of 10 couples of thermoelectric yarns would generate a thermo-voltage of ~800 μV and output power of ~2.6 nW at a temperature difference of 66 K.

3.3. Other textile TEGs

There are also some new creative textile TEGs developed very recently. In 2017, Ting Zhang et al. demonstrated a novel crystalline ultralong thermoelectric fiber and two TEG prototypes [22]. Thermal drawing technology was employed to integrate high performance thermoelectric materials in a fiber-like carrier, which is also a physical thermal size-reduction strategy. P-type $Bi_{0.5}Sb_{1.5}Te_3$ and n-type Bi_2Se_3 nanowires were used as core thermoelectric materials, and borosilicate glass tube with a T_g slightly higher than the thermoelectric nanowires were

used as cladding materials to form a core-shell structure fiber. The fabricated thermoelectric fibers are long, flexible, intrinsically crystalline, and mechanically stable, which can be further applied in flexible TEGs. The two pairs of p-n fibers composed TEG has an internal resistance of 410 Ω, and could generate an open-circuit voltage of 24.2 mV, a short-circuit current of 59.1 μA, and a maximum output power of 0.36 μW, when applying a temperature difference of 50 K. To demonstrate the advantages of fiber's length and flexibility, a thermoelectric cup and a thermoelectric pipe were fabricated by wrapping several pairs of p-n thermoelectric fibers on the curved surface.

In 2016, Abu Raihan Mohammad Siddique et al. employed a manual dispenser printing technique to fabricate a flexible fabric TEG [23]. $(0.98Bi,0.02Sb)_2(0.9Te,0.1Se)_3$ was used as n-type material, $(0.25Bi,0.75Sb)_2(0.95Te,0.05Se)_3$ was used as p-type material. Two TEG prototypes containing 12 pairs of p-n thermoelectric materials were fabricated by printing the selected thermoelectric materials on polyester fabric. The fabricated prototypes consisting 12 pairs of n-type and p-type legs and connected in series with silver wires. The best open circuit voltage and output power were 23.9 mV and 3.107 nW, respectively, under a temperature difference of 22.5°C. The wearing test on human body proves that the fabricated prototypes are very flexible, twistable, and durable with the substrate as well as conforming well to the human body.

In 2017, Jaeyoo Choi et al. reported a flexible and ultralight TEG-based on carbon nanotube yarn (CNTY) with excellent thermoelectric performance [24]. A high electrical conductivity of 3147 S/cm was achieved by a highly aligned CNTY, which has increased longitudinal carrier mobility. In their work, the CNTY exhibits multifunction in the TEG. N- and p-types dopants of polyethylenimine and $FeCl_3$ were alternatively doped into CNTY to generate n- and p-type legs in the CNTY device respectively. Between the doped regions, highly conductive undoped CNTY regions were acted as electrodes to connect and minimize the circuit resistance. Thus an all-carbon TEG without additional metal deposition process can be formed. A prepared TEG prototype containing 60 pairs of n- and p-type doped CNTY exhibits the maximum power density of 10.85 and 697 μW/g at $\triangle$T of 5 and 40 K, respectively.

Screen printing technology is a low-cost fabrication technique that is applicable to large scale production. Zhuo Cao et al. demonstrated that screen printing technology can be used to fabricate BiTe/SbTe-based TEGs for room temperature energy harvesting applications on flexible substrate [25]. Although the fabricated TEG contained only eight pairs of thermoelectric legs, the screen printing process and materials flexibility allow longer strips with larger numbers of thermocouples to be connected in series and rolled up to form a coil TEG and enabling the power output to be increased. Thus, it is also a practical fabrication method to prepare fabric-based TEGs on large scale.

Besides the thermoelectric performance of thermoelectric materials, temperature difference is also an important impact factor on the thermoelectric efficiency of TEGs. A higher $\triangle$T would increase the output power of TEGs. However, the temperature difference between human body and environment are usually in the range of 1.5–4.1°C, which is unfavorable for body heat utilization. It is necessary to find ways to enlarge the temperature difference for wearable TEGs. In 2017, Yeon Soo Jung et al. proposed a novel approach to increase the $\triangle$T

of conventional wearable TEGs, they present a wearable solar TEG possessing a high $\triangle T$ value of ~20.9°C by introducing a local solar absorber and thermoelectric legs on a polyimide substrate [26]. The prepared solar absorber is composed of a five-period Ti/MgF_2 superlattice. The structure and thickness of each layer was carefully designed to absorb sunlight at maximum extent. A dispenser printing technique was employed to prepare thermoelectric legs on the substrate. The n- and p-type ink were made by alloyed BiTe-based powders and Sb_2Te_3-based sintering additive dispersed in glycerol. A wearable TEG prototype consisting of 10 pairs of thermoelectric legs exhibits an open circuit voltage of 55.15 mV and an output power of 4.44 μW when exposed to sunlight. The generated high $\triangle T$ of ~20.9°C between the hot solar absorber and cold edges is also the highest $\triangle T$ value of all wearable TEGs reported to date. In 2016, Melissa Hyland et al. also reported a wearable TEG device with optimized heat spreaders to increase the $\triangle T$ of wearable TEG [27]. The integration of heat spreader would improve the dissipation of heat and cooling throughout the wearable TEG. In their design, a three-layered device structure were used. Two flat heat spreaders were equipped on the top and bottom of TEG respectively. The sandwich structure was chosen as the final design due to its high efficiency and low form factor.

4. Conclusion

With the rapid growth in wearable and flexible electronics, the demand in flexible self-power technologies are also increased. Thermoelectric energy conversion technology shows great potential in make use of our human body heat to generate power, which would be an ideal power source candidate for wearable electronic systems. In most of the developed flexible thermoelectric materials and generators, textile-based thermoelectric materials and TEG have unique advantage in body heat energy conversion due to their excellent air permeability, flexibility, and wearing comfort, especially for natural materials such as silk and cotton, which shows good biocompatibility. Therefore, a fabric-based thermoelectric generator with great wearability would overcome the wearable difficulty of existing organic film generators, which shows promising application in flexible and wearable self-powered electronic systems by harvesting body heat to generate electricity. In the past years of study, many textile thermoelectric materials were prepared in forms of fibers and fabrics including some traditional inorganic semiconductors and the newly developed organic polymers and composites. Compared with 2D fabrics, fiber-based thermoelectric legs would give more design flexibility for the flexible TEGs. Besides, some pioneering researches also designed and fabricated several novel textile TEGs with excellent flexibility and thermoelectric performance. Various TEG structures such as 2D generator making use of in-plane temperature difference and 3D generators generating temperature difference along fabric thickness directions are included. These textile-based TEGs with multiple structures are more practical and suitable for wearing than the previous widely studied film TEG, which shows promising application in future self-powered wearable system driven by body heat. The study of flexible and wearable thermoelectric materials and generators is just beginning. The efficiency of textile thermoelectric materials and generator need to be further improved for real application. These creative works bring many inspirations for the future explorations in thermoelectric field.

Acknowledgements

This work was supported by University Research Grants Council, PolyU 5162/12E, Shen Zhen Government Key Incubation Fund, JC201104210132A, National Key Technology R & D Program Project, The Ministry of Science and Technology of P.R.C, 2012BAI17B06, and National Natural Science Foundation of China, 51673162.

Conflict of interest

There are no conflicts of interest to declare.

Author details

Qian Wu[1] and Jinlian Hu[2]*

*Address all correspondence to: jin-lian.hu@polyu.edu.hk

1 School of Textile Science and Engineering, Xi'an Polytechnic University, Xi'an, Shaanxi, China

2 Institute of Textiles and Clothing, The Hong Kong Polytechnic University, Kowloon, Hong Kong

References

[1] Stoppa M, Chiolerio A. Wearable electronics and smart textiles: A critical review. Sensors [Internet]. Jul 2014;**14**(7):11957-11992. Available from: http://www.mdpi.com/1424-8220/14/7/11957/

[2] Mukhopadhyay SC. Wearable sensors for human activity monitoring: A review. IEEE Sensors Journal [Internet]. Dec 9, 2014;**15**(3):1321-1330. Available from: http://ieeexplore.ieee.org/document/6974987/

[3] Shaikh FK, Zeadally S. Energy harvesting in wireless sensor networks: A comprehensive review. Renewable and Sustainable Energy Reviews (Elsevier). Mar 1, 2016;**55**(C):1041-1054

[4] Cha Y, Hong S. Energy harvesting from walking motion of a humanoid robot using a piezoelectric composite. Smart Materials and Structures (IOP Publishing). Sep 3, 2016;**25**(10):1-5

[5] Bogue R. Energy harvesting: A review of recent developments. Sensor Review [Internet]. Jan 19, 2015;**35**(1):1-5. Available from: http://www.emeraldinsight.com/doi/abs/10.1108/SR-05-2014-652

[6] Myers A, Hodges R, Jur JS. Human and environmental analysis of wearable thermal energy harvesting. Energy Conversion and Management (Elsevier Ltd). Jul 1, 2017;**143**: 218-226

[7] Leonov V. Energy harvesting for self-powered wearable devices. In: Wearable Monitoring Systems. Boston, MA: Springer US; 2010. pp. 27-49

[8] Tritt TM. Thermoelectric phenomena, materials, and applications. Annual Review of Materials Research [Internet]. Aug 4, 2011;**41**(1):433-448. Available from: http://www.annualreviews.org/doi/10.1146/annurev-matsci-062910-100453

[9] Rowe DM. CRC Handbook of Thermoelectrics. Boca Raton: CRC Press; 2005. 1-15 p

[10] Zhao L-D, Lo S-H, Zhang Y, Sun H, Tan G, Uher C, et al. Ultralow thermal conductivity and high thermoelectric figure of merit in SnSe crystals. Nature (Nature Publishing Group). Apr 9, 2014;**508**(7496):373-377

[11] Kraemer D, Jie Q, McEnaney K, Cao F, Liu W, Weinstein LA, et al. Concentrating solar thermoelectric generators with a peak efficiency of 7.4%. Nature Energy (Nature Publishing Group). Sep 19, 2016;**1**(11):16153-16158

[12] Du Y, Cai K, Chen S, Wang H, Shen SZ, Donelson R, et al. Thermoelectric fabrics: Toward power generating clothing. Scientific Reports [Internet]. Mar 23, 2015;**5**(1):448-6416 Available from: http://www.nature.com/articles/srep06411

[13] Zhou C, Dun C, Wang Q, Wang K, Shi Z, Carroll DL, et al. Nanowires as building blocks to fabricate flexible thermoelectric fabric: The case of copper telluride nanowires. ACS Applied Materials & Interfaces [Internet]. Sep 21, 2015;**7**(38):21015-21020 Available from: http://pubs.acs.org/doi/10.1021/acsami.5b07144

[14] Liang D, Yang H, Finefrock SW, Wu Y. Flexible nanocrystal-coated glass fibers for high-performance thermoelectric energy harvesting. Nano Letters [Internet]. Jan 27, 2012;**12**(4):2140-2145 Available from: http://pubs.acs.org/doi/abs/10.1021/nl300524j

[15] Wu Q, Hu J. Waterborne polyurethane based thermoelectric composites and their application potential in wearable thermoelectric textiles. Composites Part B (Elsevier Ltd). Dec 15, 2016;**107**(C):59-66

[16] Lee JA, Aliev AE, Bykova JS, de Andrade MJ, Kim D, Sim HJ, et al. Woven-yarn thermoelectric textiles. Advanced Materials. Apr 25, 2016;**28**(25):5038-5044

[17] Hewitt CA, Kaiser AB, Roth S, Craps M, Czerw R, Carroll DL. Multilayered carbon nanotube/polymer composite based thermoelectric fabrics. Nano Letters [Internet]. Feb 7, 2012;**12**(3):1307-1310 Available from: http://pubs.acs.org/doi/abs/10.1021/nl203806q

[18] Ryan JD, Mengistie DA, Gabrielsson R, Lund A, Müller C. Machine-washable PEDOT:PSS dyed silk yarns for electronic textiles. ACS Applied Materials & Interfaces. Mar 2, 2017; **9**(10):9045-9050

[19] Kim SJ, We JH, Cho BJ. A wearable thermoelectric generator fabricated on a glass fabric. Energy & Environmental Science [Internet]. 2014;**7**(6):1959-1957 Available from: http://xlink.rsc.org/?DOI=c4ee00242c

[20] Lu Z, Zhang H, Mao C, Li CM. Silk fabric-based wearable thermoelectric generator for energy harvesting from the human body. Applied Energy [Internet]. Feb 2016;**164**(C):57-63 Available from: http://dx.doi.org/10.1016/j.apenergy.2015.11.038

[21] Wu Q, Hu J. A novel design for a wearable thermoelectric generator based on 3D fabric structure. Smart Mater Struct (IOP Publishing). Mar 27, 2017;**26**(4):045037-045039

[22] Zhang T, Li K, Zhang J, Chen M, Wang Z, Ma S, et al. High-performance, flexible, and ultralong crystalline thermoelectric fibers. Nano Energy (Elsevier Ltd). Nov 1, 2017;**41**:35-42

[23] Siddique ARM, Rabari R, Mahmud S, Van Heyst B. Thermal energy harvesting from the human body using flexible thermoelectric generator (FTEG) fabricated by a dispenser printing technique. Energy (Elsevier Ltd). Nov 15, 2016;**115**(Part 1):1081-1091

[24] Choi J, Jung Y, Yang SJ, Oh JY, Oh J, Jo K, et al. Flexible and robust thermoelectric generators based on all-carbon nanotube yarn without metal electrodes. ACS Nano. Aug 10, 2017;**11**(8):7608-7614

[25] Cao Z, Koukharenko E, Tudor MJ, Torah RN, Beeby SP. Flexible screen printed thermoelectric generator with enhanced processes and materials. Sensors and Actuators A: Physical [Internet]. Feb 2016;**238**:196-206. Available from: http://dx.doi.org/10.1016/j.sna.2015.12.016

[26] Jung YS, Jeong DH, Kang SB, Kim F, Jeong MH, Lee K-S, et al. Wearable solar thermoelectric generator driven by unprecedentedly high temperature difference. Nano Energy (Elsevier Ltd). Oct 1, 2017;**40**:663-672

[27] Hyland M, Hunter H, Liu J, Veety E, Vashaee D. Wearable thermoelectric generators for human body heat harvesting. Applied Energy (Elsevier Ltd). Nov 15, 2016;**182**(C):518-524

Chapter 3

Thermoelectricity from Macro to Nanoscale: Wave Behaviour and Non-Local Effects

Aldo Figueroa Lara, Iván Rivera Islas,
Víctor Hernández García,
Jaziel Rojas Guadarrama and
Federico Vázquez Hurtado

Additional information is available at the end of the chapter

http://dx.doi.org/10.5772/intechopen.75998

Abstract

In this chapter, the physical principles to be taken into account in thermoelectricity at the nanometre scale are discussed. We argue that the numerical methods must also be adapted to the emergence of new physical behaviours at that scale, namely, wave propagation of heat, diffusive-ballistic transition, nonlocal effects, among others. It is first shown that thermoelectric phenomena at the nanoscale can be described by introducing thermodynamic inertia and nonlocal effects. The transport equations are obtained from the thermodynamics of irreversible processes. After this, we introduce the Spectral Chebyshev Collocation method as a well-suited numerical method to deal with the new physical behaviours appearing at the nanoscale. We then show the use of these formalisms to analyse specific and interesting aspects of the optimization of pulsed thermoelectricity and coupled thermoelectric modules.

Keywords: electrothermal, pulsed thermoelectricity, nanometre length scale, heat wave propagation, size effects, thermal optimization, coupled thermoelectric modules

1. Introduction: irreversible thermodynamics of thermoelectricity

Heat, electron and hole transport and generation-recombination of electron-hole pairs are processes which determine the functioning of thermoelectric devices. In this section, the principles of irreversible thermodynamics of modelling of thermoelectric phenomena are exposed. The contributions to the entropy production in the stationary state due to the dissipative

effects associated with electron and hole transport, generation-recombination of electron–hole pairs as well as heat transport are analysed.

The operation of thermoelectric devices occurs on the basis of the so-called cross effects. On the one hand, the Seebeck effect which arises when an external temperature difference is applied leading to a charge flux and, on the other hand, the Peltier effect which causes thermal fluxes in the presence of an applied voltage [1, 2]. This is also connected with the Joule and Thomson effects arising with the electrical current together with the non-equilibrium electrons and holes and electron–hole recombination phenomena. The latter becomes a thermal source causing an internal energy heterogeneity described through the internal energy balance equation [3].

The importance of electron–hole recombination must be remarked since the optimization of the device must be achieved in the regime of bipolar transport [4]. In this context, the problem of heat dissipation and its removal concerns the parameters that characterize the work of the device. When the dimension of the device goes to the nanometric length scale, nonlocal and memory effects must be taken into account [5]. This is achieved through the introduction of thermodynamic inertia in the constitutive equations of the dissipative fluxes and local dependence of transport coefficients, respectively. In the following, the constitutive equations of dissipative fluxes will be derived from the very principles of irreversible thermodynamics [6]. Then nonlocal and inertial effects will be introduced.

Let us consider the system constituted by two species (electron and holes) and the lattice. Firstly, define the electron and hole densities by $n\left(\vec{r},t\right)$ and $p\left(\vec{r},t\right)$. The continuity equations for the electrons (electric charge $-q$) and holes (electric charge $+q$) are given by

$$q\frac{\partial n}{\partial t}-\nabla\cdot\vec{J}_n=-qR, \tag{1}$$

$$q\frac{\partial p}{\partial t}+\nabla\cdot\vec{J}_p=-qR, \tag{2}$$

where $\vec{J}_n$ and $\vec{J}_p$ are electric charge fluxes of electrons and holes, respectively, q is the elementary electric charge and R is the balance of generation and recombination of electron–hole pairs processes. Now we write the balance equation of total internal energy$u$ including the contribution of electrons u_n, holes $u_p$and the lattice u_L:

$$\frac{\partial u}{\partial t}+\nabla\cdot\vec{J^u}=-\vec{E}\cdot\left(\vec{J}_n-\vec{J}_p\right)+P, \tag{3}$$

with $u=u_n+u_p+u_L$ and $\vec{J^u}=\vec{J}^u_n+\vec{J}^u_p+\vec{J}^u_L$ the total internal energy flux. The total electric field (external plus self-consistent field) is represented by $\vec{E}$. Finally, P is a source term which can include light energy transference to the lattice and other processes. We use the expression for the Gibbs equation for each of the components of the system in order to find the balance

equation of the total entropy density. We begin by writing the corresponding Gibbs equation for electrons, holes and the lattice. They are

$$\begin{aligned} T_n ds_n &= du_n - \Phi_n dn, \\ T_p ds_p &= du_p + \Phi_p dp, \\ T_L ds_L &= du_L, \end{aligned} \tag{4}$$

In these equations, Φ_x is the electrochemical potential of species $x = n, p$. Explicit expressions for the electrochemical potentials are the following.

$$\begin{aligned} \Phi_n &= \nu_n - q\varphi, \\ \Phi_p &= \nu_p + q\varphi \end{aligned} \tag{5}$$

being φ the total electric potential (external plus self-consistent field). At this point, it is convenient to mention that the self-consistent electric field is given by Poisson's equation:

$$\nabla \cdot \left(\varepsilon \nabla \varphi_s\right) = q\left(N_A^- + N_D^+ + n - p\right), \tag{6}$$

where ε is the permittivity constant and N_A^-, N_D^+ are the densities of ionized acceptors and donors, respectively. It is now assumed that the components of the system are in thermal equilibrium, that is, $T_n = T_p = T_L \equiv T$. The sum of Eqs. (4) yields the balance equation for the total entropy density. One gets

$$\frac{\partial s_T}{\partial t} + \nabla \cdot \vec{J}_T^{\,s} = \vec{J}_T^{\,s} \cdot \nabla\left(\frac{1}{T}\right) + \frac{1}{T} J_n \cdot \vec{E}_n^{\,\prime} + \frac{1}{T} J_p \cdot \vec{E}_p^{\,\prime} + R\left(\frac{\Phi_n - \Phi_p}{T}\right) + \frac{P}{T}. \tag{7}$$

In obtaining Eq. (7) use has been made of Eqs. (1–3). The total entropy density s_T in Eq. (7) is then given by.

$$s_T = s_n + s_p + s_L. \tag{8}$$

The total entropy flux $\vec{J}_T^{\,s}$ has been defined as

$$\vec{J}_T^{\,s} = \frac{1}{T}\left(\vec{J}_q + q^{-1}\Phi_n \vec{J}_n + q^{-1}\Phi_p \vec{J}_p\right), \tag{9}$$

and the heat flux $\vec{J}_q$ becomes:

$$\vec{J}_q = \vec{J}^u. \tag{10}$$

The field $\vec{E}_x^{\,\prime}$ in Eq. (7) is a generalized electric field given by $\vec{E}_x^{\,\prime} = q^{-1}\nabla\Phi_x \mp \vec{E}$, with $x = n, p$.

The right-hand side of Eq. (7), excepting the term P/T, is the entropy generation term divided by the temperature, that is,

$$T\sigma = \vec{J}_n \cdot \vec{E}_n' + \vec{J}_p \cdot \vec{E}_p' - \vec{J}_T^s \cdot \nabla T + R\left(\Phi_n - \Phi_p\right), \tag{11}$$

and it has the form $\sum \vec{J}_i \cdot \vec{X}_i$, where $\vec{J}_i$ and $\vec{X}_i$ are generalized fluxes and thermodynamic forces, respectively. This allows us to identify the dissipative fluxes, and therefore, the origin of irreversibilities in the system. The generalized fluxes are $\left(\vec{J}_n, \vec{J}_p, \vec{J}_T^s, R\right)$ and the corresponding forces $\left(\vec{E}_n', \vec{E}_p', \nabla T, \Phi_n - \Phi_p\right)$.

The second law of thermodynamics demands that $\sigma > 0$. This condition is satisfied if the thermodynamic forces and fluxes are linearly related as follows:

$$\begin{pmatrix} \vec{J}_n \\ \vec{J}_p \\ \vec{J}_T^s \\ R \end{pmatrix} = \begin{pmatrix} L_{nn} & 0 & L_{ns} & 0 \\ 0 & L_{pp} & L_{ps} & 0 \\ L_{sn} & L_{sp} & L_{ss} & 0 \\ 0 & 0 & 0 & L_{RR} \end{pmatrix} \begin{pmatrix} \vec{E}_n' \\ \vec{E}_p' \\ \nabla T \\ \Phi_n - \Phi_p \end{pmatrix}, \tag{12}$$

where the coefficients L_{xy} are the so called Onsager coefficients. They are determined through phenomenological arguments and obey the reciprocity Onsager relations, namely, $L_{xy} = L_{yx}$, with $x, y = n, p, s, R$. Eq. (12) are the constitutive equations of the system which make complete the description offered by Eqs. (1–3, 6) together with the caloric equation $u_T = c_V T$, where c_V is the specific heat at constant volume. The constitutive equation, Eq. (12), contain well-known phenomenological laws: Ohm, Fourier, Fick, and Peltier and Seebeck effects. In the following section, we expose some additional considerations to be taken into account when the dimensions of the thermoelectric systems are in the nanometric length scale.

2. Non-local and memory effects

In this section, we address the problem of heat transport in a thermoelectric nanoscaled layer when an electric current circulates through it. At that length scale, nonlocal and memory effects must be included. The former are due to size effects on the transport coefficients when going to the nanometric scale and the second one become from the thermodynamic inertia of the system. Let us consider the thermoelectric system shown in **Figure 1**, and let us pay attention to one of the semiconductor branches, the n type for instance.

The analysis of heat transport in that element of the device of **Figure 1** is based on the constitutive equations obtained in Section 1, Eqs. (12). The equations explicitly read [7–9]

$$\tau_{eff} \frac{\partial q}{\partial t} + q = -[K(L) + \Pi S_E(L)\sigma(L)] \frac{\partial T}{\partial x} - \Pi\sigma(L) \frac{\partial V}{\partial x}, \tag{13}$$

$$\tau_J \frac{\partial J}{\partial t} + J = -S_E(L)\sigma(L) \frac{\partial T}{\partial x} - \sigma(L) \frac{\partial V}{\partial x}, \tag{14}$$

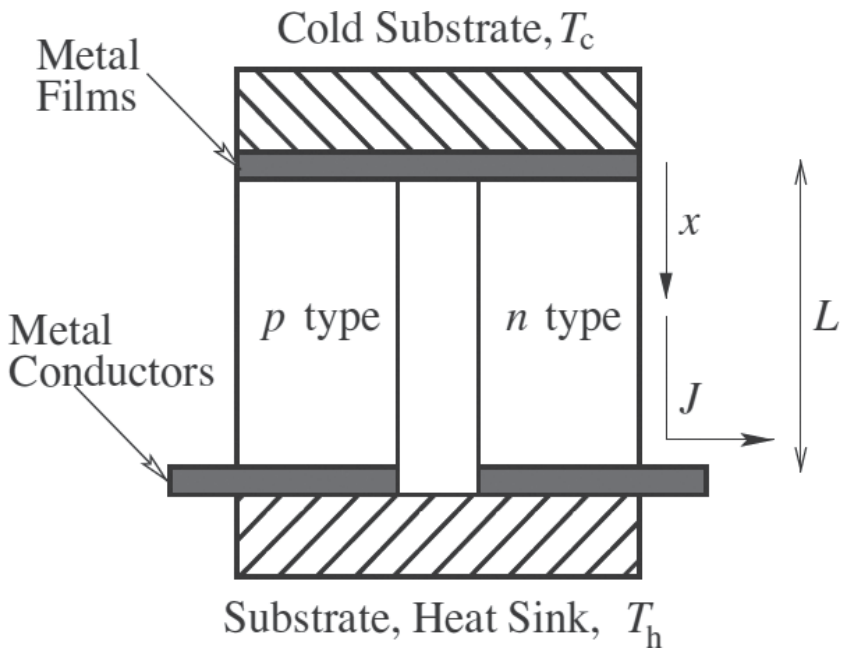

Figure 1. Thermoelectric couple system. From Ref. [5].

where for the sake of simplicity, we have denoted the heat and electric charge fluxes as q and J, respectively. Inertia and no locality were introduced through the time derivatives of the heat and electric charge fluxes and the dependence of the transport and thermoelectric coefficients on the width of the layer, respectively. The equations have been written in one spatial coordinate since if the length L goes to the nanometric scale, the dimensions of the branch n in the y and z directions become much larger than L. The times τ_{eff} and τ_J are the relaxation times of the heat and electric charge fluxes, respectively. K, σ and S_E are the thermal conductivity, the electric conductivity and the Seebeck coefficient, respectively. In Eqs. (13) and (14), they are denoted to depend on the length L. Expressions for the transport coefficients as functions of L are obtained within the higher order dissipative fluxes framework of extended irreversible thermodynamics [10, 11]. The expressions are the following

$$K(L) = \frac{K_0 L^2}{2\pi^2 l_p^2}\left(\sqrt{1+4\pi^2\left(\frac{l_p}{L}\right)^2}-1\right), \tag{15}$$

$$\sigma(L) = \frac{\sigma_0 L^2}{2\pi^2 l_e^2}\left(\sqrt{1+4\pi^2\left(\frac{l_e}{L}\right)^2}-1\right), \tag{16}$$

$$S_E(L) = \frac{4\pi^2 S_0 l_e^2}{3L^2}\left(\frac{2\pi(l_e/L)}{\arctan(2\pi(l_e/L))}-1\right)^{-1}, \tag{17}$$

with l_p and l_e the mean free path of heat and electric charge carriers, respectively. K_0, σ_0 and S_0 are the bulk thermal conductivity, electric conductivity and Seebeck coefficient, respectively. A hyperbolic-type transport equation for temperature can be obtained by introducing Eqs. (13)–(14) in Eq. (3) (with $P = 0$) and using the caloric equation for the inner energy. The procedure may be followed in Appendix A of reference [5]. The resulting equation is

$$\alpha_{eff}\frac{\partial^2 T}{\partial t^2}+\frac{\partial T}{\partial t}=\nu\frac{\partial^2 T}{\partial x^2}+\beta J^2+\varsigma J\frac{\partial}{\partial t}\left(\frac{\partial T}{x}\right), \tag{18}$$

where the dimensionless coefficients are defined as follows:

$$\begin{aligned}\alpha_{eff}&=\frac{\tau_{eff}}{\tau},\ \nu=\frac{K(L)\tau}{\rho C_v L^2},\\ \beta&=\frac{\tau J_0^2}{\rho C_v \sigma(L) T_h},\ \varsigma=\frac{J_0\tau_{eff}S_E(L)}{\rho C_v L}.\end{aligned} \tag{19}$$

The characteristic time $\tau=\frac{\pi^2 L^2 \rho C_v}{4K(L)}$ is the diffusion time and T_h is a reference temperature. Equation (18) is here solved numerically for a thermoelectric thin film (in the branch n, see **Figure 1**) subjected to a Dirichlet boundary condition in the hot side of the thermoelectric device and a Robin type one in the cold side. We choose the space domain as $-1\le x\le 1$, in such a way that boundary conditions can be written as:

$$\left.\frac{\partial T}{\partial x}\right|_{x=-1}=\gamma JT,\ T(1)=1, \tag{20}$$

where the dimensionless coefficient γ is defined as $\gamma = S_E(L)J_0L/(2K(L))$. As the initial condition, we state that the device is at room temperature, that is, $T(x,0)=1$. Eq. (18) shows step-solutions which are very challenging numerically speaking. Thus, it was solved by using the numerical code based on the Spectral Chebyshev Collocation method described in Section 3. In **Figure 2a**, it is shown the time evolution of the cold temperature towards the stationary state. Since Silicon is a basic material for short and long scale devices, our departing results come from considering doped Silicon as working material, whose properties have been published before in [12]: $K_0 = 149\ \mathrm{Wm^{-1}\ K^{-1}}$, $\sigma_0 = 35.5\times10^3\ \Omega^{-1}\ \mathrm{m^{-1}}$, $S_E = 440\times10^{-6}\ \mathrm{V\ K^{-1}}$ and $a_E = 88\times10^{-6}\ \mathrm{m^2\ s^{-1}}$, where a_E is the thermal diffusivity. The mean free path of the heat carriers and their mean velocity are [10] $l_p = 40\mathrm{nm}$ and $v = 3K/\rho C_p l_p$, respectively. The mean free path of electric charge carriers was assumed to be of the order of the lattice constant of Silicon $l_e = 0.5$ nm. As hot side temperature, we use $T_h = 373.1$ K [12]. We present the results without further discussion. The temperature starts to decrease once the electric current is applied. The transient to the stationary strongly depends on L. As it can be appreciated in **Figure 2a**, as the Knudsen numbers δ (defined as l_p/L) increases the wave behaviour appears. On the contrary, for small δ, the steady state is reached quickly through a relaxation process without any oscillation. The minimum reached temperature is about 160 K when $\delta = 4$. The response of the system to a short electric pulse superimposed to the stationary state obtained

http://dx.doi.org/10.5772/intechopen.75998

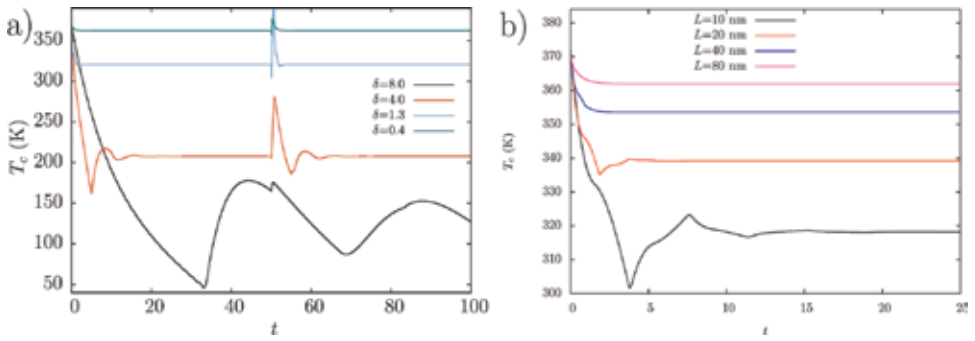

Figure 2. (a) Cold side temperature T_c as a function of time t for different δ. From Ref. [5]. (b) Cold side temperature T_c as a function of time t for different L. In this case, there is no applied squared electric pulse and size effects on Seebeck coefficient have been omitted. From Ref. [13]. The initial temperature in both cases (a) and (b) is 373.1 K.

with the optimal electric current was also studied. The squared electric pulse with magnitude 3.5 is applied at time $t = 50$. The wave behaviour of temperature produces subsequent supercooling transient process once the electric current pulse has been applied. The duration of it exceeds the duration of the supercooling obtained with the pulse. The minimum reached temperature is about 300 K when $\delta = 4$. In **Figure 2a**, it can also be seen an overheating after the application of the current pulse (which occurs at the dimensionless time 50). This effect is due to the thermal inertia, and it is more pronounced for small values of L for which the thermal inertia plays a more important role. **Figure 2b** shows the evolution to the stationary state by omitting in the calculations the effect of the size L on the Seebeck coefficient given by Eq. (17). The oscillating decay for small values of L remains but, interestingly, the minimum temperature reached is much higher than that reached when the effect of the size L on the Seebeck coefficient is included by means of Eq. (17). Thus, the thermal efficiency of the cooling, measured by the temperature difference reached, is much greater due to the influence of the size on the Seebeck coefficient.

3. Computational methods

In this section, we present a couple of numerical methods in order to solve the hyperbolic transport equation (Eq. (18)) that models the heat transport in thermoelectric thin layers. Since Eq. (18) cannot be solved analytically, a numerical approach must be accomplished. Typically, low-order numerical methods such as finite differences (FD) are used. However, because of the high temporal gradients (due to the source term with crossed derivatives) for the small scales in the problem, that is, when the heat wave propagation or *ballistic* transport is present, the FD method fails in providing satisfactory results. As commented previously, this kind of equations is very challenging and we opt for a high-order numerical method in order to find its solution. High-order (or spectral) methods have previously been used to study heat transport based on the Maxwell-Cattaneo-Vernotte equation giving a hyperbolic transport equation in macroscopic systems [14, 15] and in some microscopic devices [16]. Thus, in this section, we discuss

the numerical approximations of the one-dimensional hyperbolic heat transport equation for a low- and a high-order schemes.

3.1. Finite differences

The code for the finite differences scheme is a standard one. It considers a forward difference and a second-order central differences for the first and second derivatives in time, respectively. In turn, for the second-order spatial derivative, a second-order central differences was used as well. The grid points were uniformly spaced, the time integration was an explicit with constant time step.

3.2. Spectral Chebyshev collocation

The high-order numerical code is based on the Spectral Chebyshev Collocation (SCC) method. The method departs by establishing a partial sum of Chebyshev polynomials. The partial sum is then considered to represent the solution of a partial differential equation (PDE). The solution of the PDE equation is satisfied exactly at the Gauss-Lobatto collocation points

$$x_i = \cos\left(\frac{i\pi}{N}\right), \qquad i = 1, \ \ldots, \ N-1, \tag{21}$$

where N denotes the number of points or the size of the grid. Thus, the solution is in the domain of the standard Chebyshev polynomials, that is $\{x \mid -1 < x < 1\}$. The partial sum of Chebyshev polynomials was inserted in the spatial derivatives of Eq. (18) obtaining expanded derivative matrices. The obtained coefficient equation system was solved by the matrix-diagonalization method in the physical space directly. A further explanation of the SCC method is found in [17, 18]. In order to compare directly with FD scheme, a coordinate transformation to interval to $0 < x < 1$ was done. The time marching scheme was the same as the FD method.

3.3. Comparison

Figure 3a presents the steady-state temperature as a function of the spatial x-coordinate in the thermoelectric film for the micro-scale. We can easily observe that the temperature difference between the hot (T_h) and cold (T_c) sides is about 3.1 degrees. Because of the *Joule effect,* the temperature profile is parabolic. The cold side temperature T_c as a function of time is shown in **Figure 4b**. The departing point is the initial condition when T_c = 373.1 K, then the cooling Peltier effect acts till the temperature reaches the steady state T_c = 370 K. We can observe (in **Figure 3**) that both numerical schemes agree quantitatively in the steady state spatial distribution as well as modelling the transitory state. If we define the error between both solutions as

$$\varepsilon = \max \ |u_{FD} - u_{SCC} \ |. \tag{22}$$

The maximum error for the steady profile (**Figure 3**a) with $N = 30$ is $\varepsilon = 8.6 \times 10^{-5}$, and the error for the transitory is one order of magnitude higher, that is $\varepsilon = 2.5 \times 10^{-4}$ which is acceptable.

As the length of the system L diminishes, reaching the nanoscale, the steady state is a line with positive slope, see **Figure 4a**, whereas the wave heat transport is clearly visible during the transient, showing a damped harmonic oscillation, see **Figure 4b**. At this scale, the α_{eff} coefficient in the heat Eq. (18) becomes important, and thus, the wave term becomes dominant, see **Table 1**. The overall error for the steady-state solution is acceptable ($\varepsilon = 9.8 \times 10^{-5}$). However, it is considerable larger ($\varepsilon = 6 \times 10^{-3}$) for the transient. Finally, we can conclude that the SCC technique is more robust since the convergence of the solution is assured with smaller grid points than the FD method.

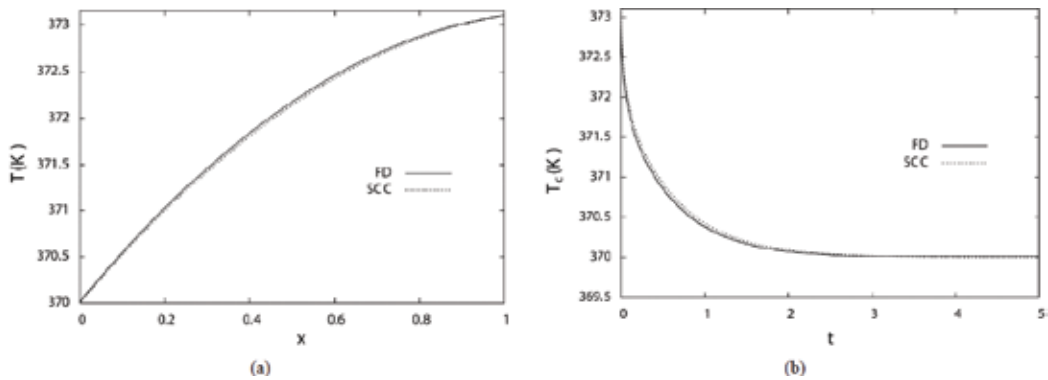

Figure 3. Comparison of the numerical schemes in the micro-scale. (a) Steady-state temperature profile; (b) transient of the cold side. From Ref. [19].

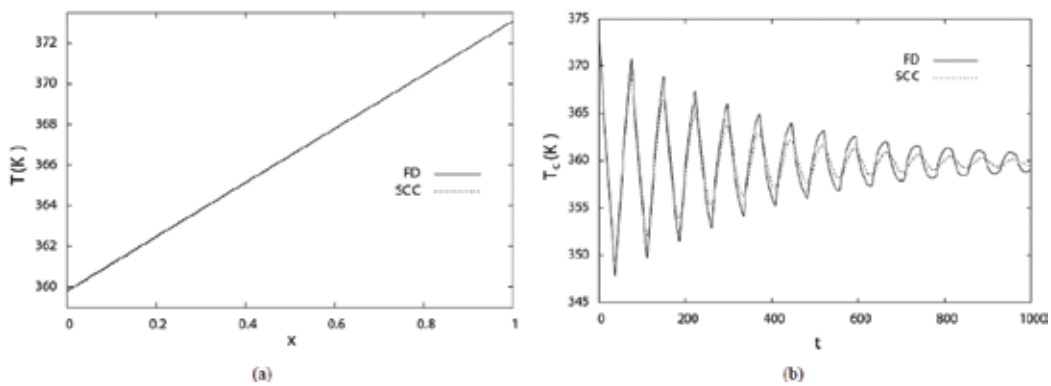

Figure 4. Comparison of the numerical schemes in the nanoscale. (a) Steady-state temperature profile; (b) transient of the cold side. From Ref. [19].

L(m)	α_{eff}	β	γ
1×10^{-4}	2.16×10^{-8}	7.81×10^{-3}	7.38×10^{-3}
1×10^{-5}	2.16×10^{-6}	7.81×10^{-5}	7.38×10^{-4}
1×10^{-6}	2.16×10^{-4}	8.27×10^{-7}	7.82×10^{-5}
1×10^{-7}	2.16×10^{-2}	2.39×10^{-8}	2.26×10^{-5}
1×10^{-8}	2.16×10^{0}	2.00×10^{-9}	1.89×10^{-5}
1×10^{-9}	2.16×10^{2}	1.97×10^{-10}	1.85×10^{-5}

Table 1. Dimensionless coefficients in Eqs. (18) and (20) as a function of the length of the system.

4. Optimal performance of thin thermoelectric layers

The control of heat in the nanoscale could have important consequences in applications as refrigeration, energy generation, energy transport and others. So, nanophonics has become a very active field of theoretical, computational and experimental research in the last 15 years. Many questions about the use of non-equilibrium thermodynamics principles at the micro and the nanoscale are being discussed, and several issues should be solved to make devices at those scales a matter of practical use. Particularly, devices in the micro and nanometric length scales work at high frequencies and they generate heat fluxes that can be in the order of thousands of watts per square centimetre. These irreversible processes elevate temperature reducing the device's life time. This makes necessary the study of those operating conditions producing less dissipation, which often correspond to the minimum entropy production. Here we describe the effects of the width on the time evolution of temperature in thin thermoelectric layers and, particularly, on the thermal figure of merit and the entropy generation. The analysis is based on hyperbolic-type Eq. (18) describing the time evolution of dissipative flows including size effects on the thermal and electric conductivities. The hyperbolic Eq. (18) was solved with a numerical code explained in Section 3. The transition from the diffusive heat transport to the wave propagation regime is controlled by the system's size when going from the micro to the nanometric scale of lengths.

When applying an electrical current to the thermoelectric system in order to obtain the maximum gradient between boundaries, the temperature distribution along the system's length is parabolic as it can be seen in **Figure 5a**. Such current is named the optimal electrical current. In turn, the entropy generation is a parabolic decaying function showing its higher value at the cold end of the device. It is important to note that these profiles are invariant to the device length when applying the optimal current. **Figure 5b** shows the dependence of the temperature difference between the boundaries of the thermoelectric (Eq. (23)), the thermal figure of merit (Eq. (24)), the entropy generation (Eq. (25)), and, as functions of the length's device (inset):

$$\Delta T = T_h - T_c, \tag{23}$$

$$ZT_h = \frac{2T_h \Delta T}{(T_h - \Delta T)^2}, \tag{24}$$

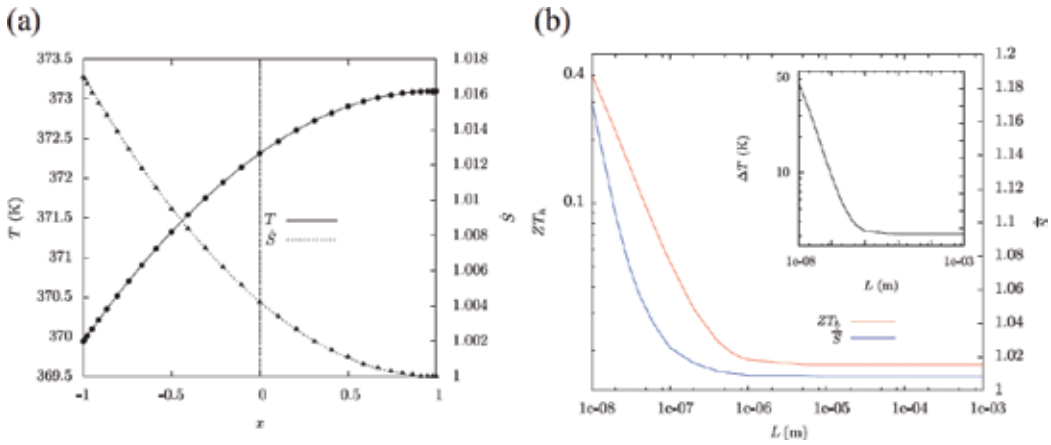

Figure 5. Temperature T and entropy generation S profiles. Lines and dots denote the exact and numerical solutions, respectively. $J_0 = 5.7785x10^7$ A/m2, $L = 1.0x10^{-4}$ m. (b) Temperature difference between boundaries ΔT, thermal figure of merit ZT_h and total entropy generation S as a function of L using the optimal electrical current. From Ref. [13].

$$\dot{S}(x) = S_J \frac{J^2}{T} + S_F \frac{1}{T^2}\left(\frac{dT}{dx}\right)^2, \tag{25}$$

where the coefficients are $S_J = {J_0}^2/\sigma T_h$ and $S_F = K/l^2$. In **Figure 5b**, we can note that devices with $L < 10^{-6}$ m increase their thermal figure of merit, from $ZT_h = 0.017$ (for $L < 10^{-6}$ m) to $ZT_h \approx 0.4$ for $L < 10^{-8}$ m.

We find that the steady-state thermal figure of merit (TFM) improves as the width goes to the nanoscale while the entropy generation increases. We identify a transition at a length of the order of the mean free path of heat carriers; in silicon it is about 40 nm. When going from the micro to the nanoscale, this transition is featured by an abrupt increment of both the total entropy production and the TFM. Above L = 40 nm, the heat transfer is dominated by diffusive processes; below this value, it is in the form of heat waves. The wave heat transport is clearly visible in the nonstationary process. An interesting study of the ballistic-diffusive transition in metals controlled by the wave number vector can be seen in [20].

5. Pulsed thermoelectric phenomena in thin films

As it was shown in Section 2, pulsed regimes produce a lower temperature than that obtained in the stationary state even with the optimal electric current for both uniform and non-uniform materials. This phenomenon is due to the fact that the Peltier effect occurs mainly at the cold junction while Joule heating is distributed in the bulk introducing a difference in the time taken by each one to influence the cold side of the device. The cold temperature is first changed by the Peltier effect and after diffusion Joule heat reaches the cold junction affecting it. Some

examples of devices which need to be overcooled during a short time are mid-IR laser gas sensors [21], condensation hygrometers and microelectronic processors generating hotspots [22–26]. The effect of the pulse form has been widely studied in macroscale of lengths. It has been shown that by applying a quadratic pulse form, the supercooling effect can be improved over other forms [27]. Some other pulse forms present additional advantages [28, 29]. Here we explore the influence of the electric pulse shape in the supercooling effect when the dimensions of the thermoelectric device go to the submicrometre length scale. We study the effects of the shape of the electric pulse on the maximum diminishing of temperature by applying pulses in the form t^a with a being a power going from 0 to 10.

In **Figure 6**, it can be seen the different shapes of the imposed electric pulse as a function of time. The duration in all cases is 0.163 and the maximum magnitude 3.5 over the stationary electric density (with normalized magnitude of one). The values are the optimal in order to obtain the maximum supercooling for the squared shape (t^0). In the same figure, t^0 denotes the squared-shape pulse.

In **Figure 7**, it can be seen the time evolution of the temperature during the supercooling at the cold side T_c of the thermoelectric for two distinct thickness of the film, namely, (a) $L = 1 \times 10^{-4}$ m and (b) $L = 1 \times 10^{-8}$ m. Each curve corresponds to one of the shaped pulses accordingly with the notation of **Figure 6**. The curves in **Figure 7a** reproduces the previous result found in [23]

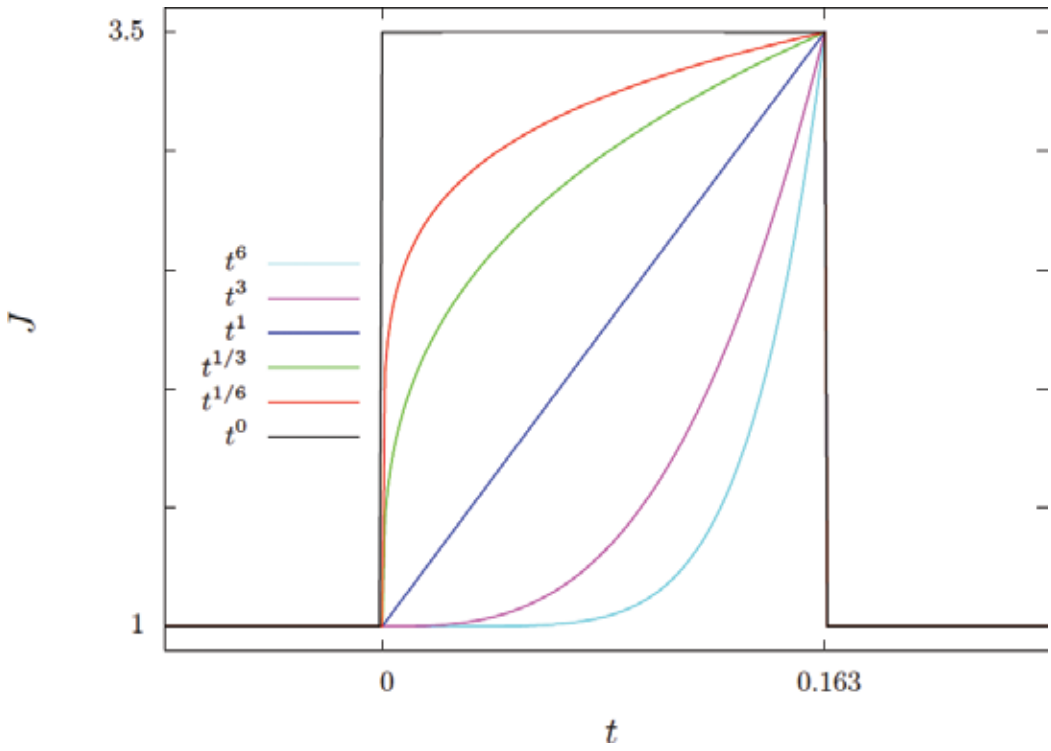

Figure 6. Pulsed electric density current as a function of time. Different pulse shapes are used in optimizing the supercooling effect. From Ref. [30].

http://dx.doi.org/10.5772/intechopen.75998

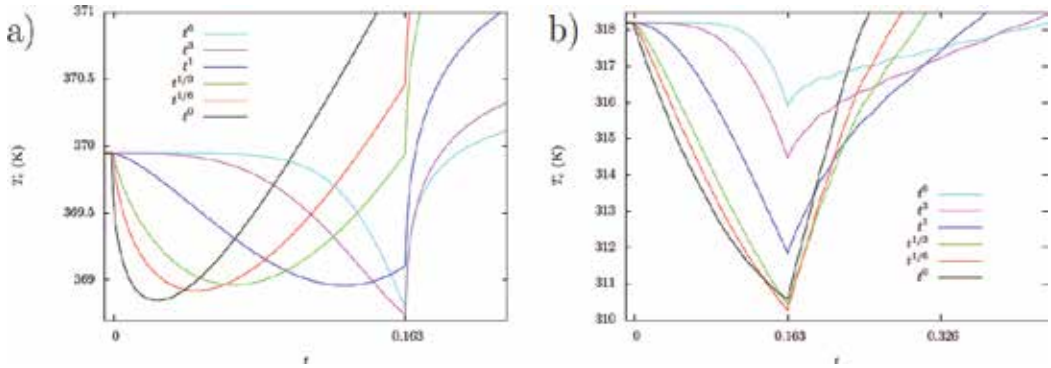

Figure 7. Cold side temperature T_c as a function of time t for due to pulse shapes: (a) Microscale and (b) nanoscale. Fractional pulse shapes perform better at the nanoscale. From Ref. [30].

(microscopic case). The curves in **Figure 7b** are the result of the present analysis. It is remarkable the fact that the super cooling effect is about eight times larger at nanometric than at micrometric scale.

Pulses with a *fractionary* number perform better for *nanoscaled* devices, whereas those with *a* bigger than unity do it for *microscaled* ones. We also find that the supercooling effect is improved by a factor of 6.6 over long length scale devices in the best performances and that the elapsed supercooling time for the *nanoscaled* devices equals the best of the *microscaled* ones.

6. Coupled thermoelectric modules

Thermoelectric systems are efficient devices for small size cooling objectives. Thus, this section is devoted to study the thermal performance of system composed of two thermoelectric devices. As a first step, a theoretical model of the heat transport in both thermoelectric devices will be developed. As a second step, the theoretical results will be compared with experimental data. Similar experimental devices have been previously reported in the literature [31–36]. However, we use a local approach instead of global energy balances, which allow us to obtain spatial distributions of the main physical properties.

6.1. Experimental procedure

The experimental set-up is conformed by a two-stage Peltier cooler, that is, two thermoelectric modules connected electrically independent and thermally in series, see **Figure 8**. The modules (with side length L = 30 mm and width h = 3.6 mm) are denoted by M in the figure and are made of Bismuth Telluride alloys. The two-stage system is located on a metal plate (15 × 8 cm). The plate is kept at a constant temperature by the contact with hot water, which is continuously forced to circulate by a pump in a rectangular frame where the hot plate is located. The pump is a LMI MILTON ROY Microprocessor dosing and is denoted by B. The modules are operated by an electric current I from a BK PRECISION 1696 DC power supply V. The electric currents are in the range 0 < I < 1.517 A. Avoiding the transient, the temperature on top of module one M_1 was

measured with a thermocouple (K type, Extech 470 True RMS Multimeter). Silitek thermal paste was used for the joints between the thermocouple and the cold wall, and the two modules. The latter is for avoiding the thermal decoupling of joints. When the two-stage system is turned on, the temperature in the cold wall is diminished because the modules generate a heat flow from the cold to hot wall. The error in the temperature data was obtained by adjusting a normal distribution to the data at same points.

6.2. Mathematical model

The heat transport problem can be reduced by considering only the heat flux in a branch (n type) of the thin thermoelectric modules, see **Figure 9**. An electric current I_i, i = 1, 2, is injected through each of the thermoelectric modules. The system is thus subjected to a Dirichlet boundary condition in the hot side at T_h, and a Robin type one in the cold side T_c, see Eq. (20).

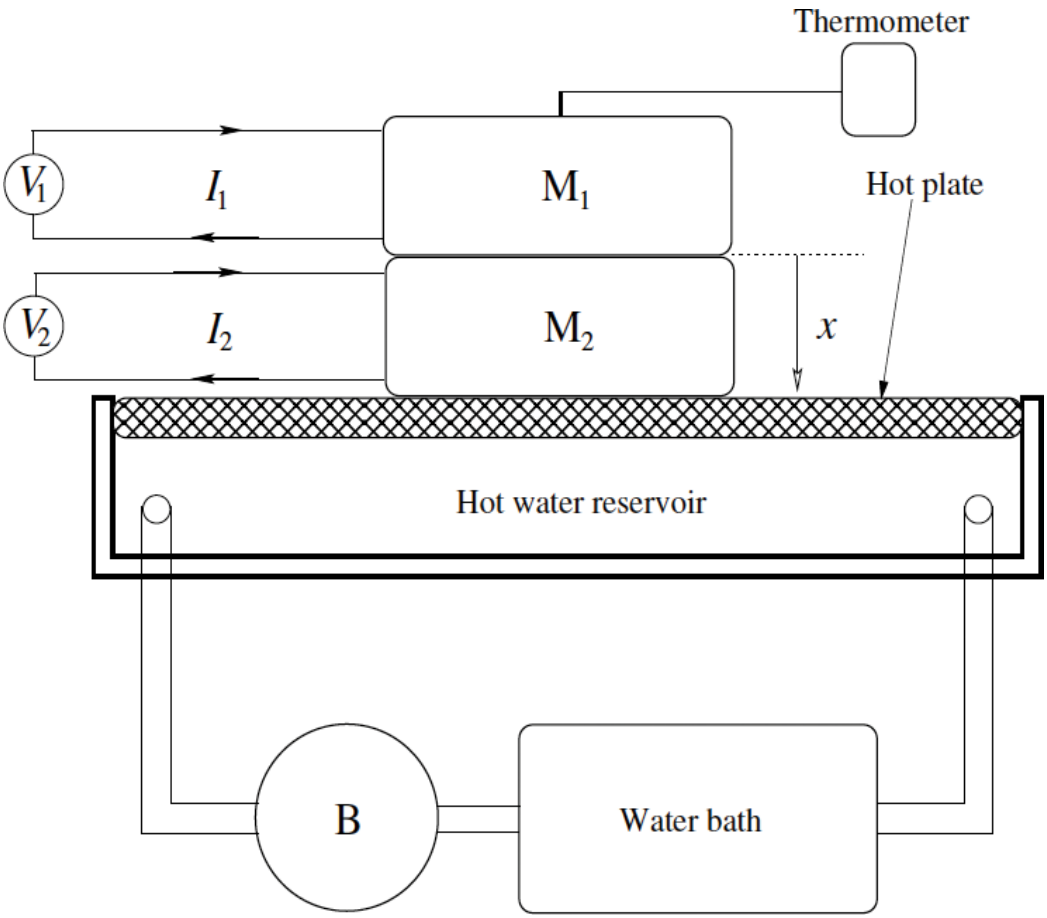

Figure 8. Scheme of two coupled thermoelectric devices. This study is devoted to the thermal analysis of the thermoelectric materials denoted by n type. The devices are actioned by injecting an electric current I_i. The thickness (width) is denoted by L_i. The i denotes the first (1) and second (2) device. From Ref. [37].

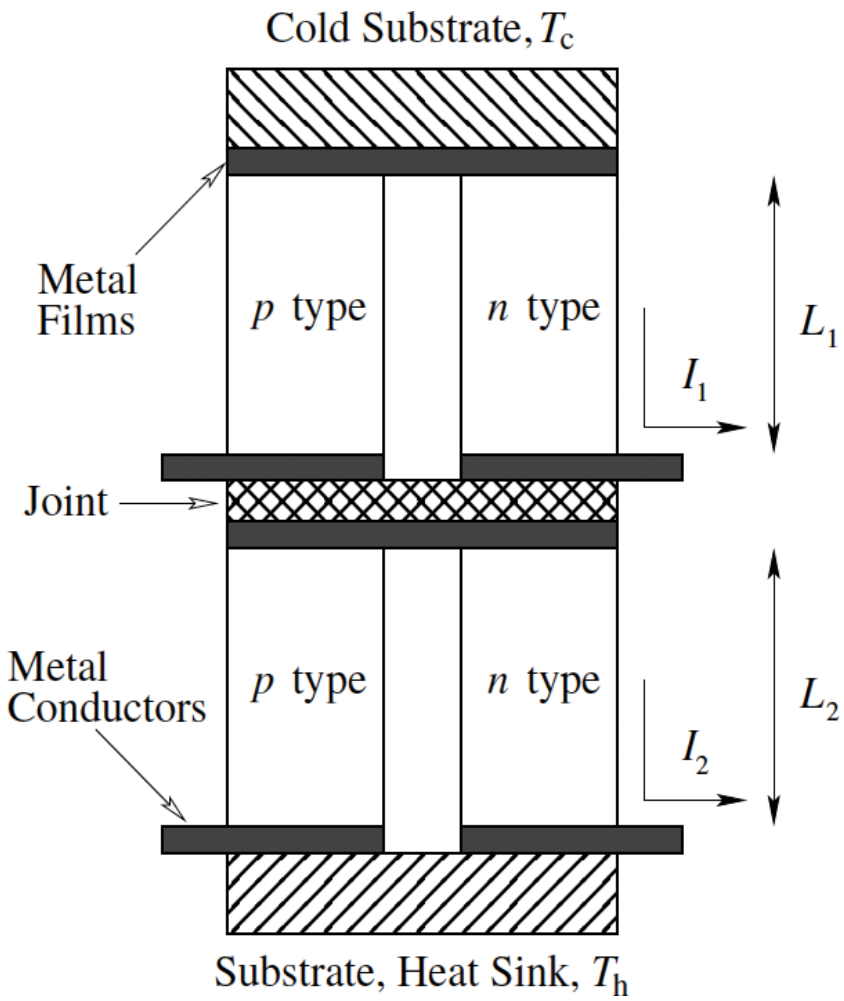

Figure 9. Scheme of two coupled thermoelectric devices. This study is devoted to the thermal analysis of the thermoelectric materials denoted by n type. The devices are actioned by injecting an electric current I_i. The thickness (width) is denoted by L_i. The i denotes the first (1) and second (2) device. From Ref. [37].

At this point we assume that each of the thermoelectric modules behaves independent, as the single thermoelectric case (Eq. (18)), and they only share a common boundary. The heat transport for the coupled system is modelled by a system of two one-dimensional differential equations, each for every thermoelectric module

$$0 = \nu_1 \frac{d^2 T_1}{dx^2} + \beta_1 {J_1}^2, 0 = \nu_2 \frac{d^2 T_2}{dx^2} + \beta_2 {J_2}^2. \tag{26}$$

The subscript denotes the first (1) and second (2) modules. The boundary conditions for the cold and hot sides are, respectively,

$$\left[\frac{dT_1}{dx}\right]_{x=-1} = \gamma_1 J_1 T_1(-1), T_2(1) = 1. \tag{27}$$

While the coupling boundary conditions are

$$\gamma_1 J_1 T_1(0) - \left[\frac{dT_1}{dx}\right]_{x=0} = \delta L \delta K \gamma_2 J_2 T_2(0) - \delta L \delta K \left[\frac{dT_2}{dx}\right]_{x=0}, T_1(0) = T_2(0), \tag{28}$$

being $\delta L = L_1/L_2$ and $\delta K = K_2/K_1$the ratios between the lengths and the thermal conductivities of modules 1 and 2, respectively. The coupling boundaries at $x = 0$ are obtained from a heat balance and by equalling the temperatures of both devices. The solution to the system of Eqs. (26) reads

$$T_1(x) = a_1 x^2 + b_1 x + c_1, T_2(x) = a_2 x^2 + b_2 x + c_2, \tag{29}$$

where the coefficients a_i, b_i and c_i are given by.

$$a_i = -\frac{\beta_i J_i^2}{2\nu_i}, c_1 = \frac{\delta L \delta K (a_2 - 1) + \dfrac{a_1(2 + \gamma_1 J_1)}{1 + \gamma_1 J_1}}{\dfrac{(\gamma_1 J_1)^2}{1 + \gamma_1 J_1} - \delta L \delta K (1 + \gamma_2 J_2)} = c_2,$$
$$b_2 = 1 - a_2 - c_2, b_1 = c_1(\gamma_1 J_1 - \delta L \delta K \gamma_2 J_2) + \delta L \delta K b_2. \tag{30}$$

The difference of temperature between the hot and cold side is

$$\Delta T_{coupled} = T_2(1) - T_1(-1). \tag{31}$$

6.3. Comparison

Before presenting and discussing the theoretical results, the experimental measurements for a single and a coupled system are shown in **Figure 10a**, **b**. **Figure 10a** shows the temperature difference between the hot and cold sides ΔT as a function of the circulating electric current for a single thermoelectric device. A parabolic behaviour with a maximum $\Delta T \approx 25$ K can be appreciated. **Figure 10b** presents elliptic isocurves of ΔT as function of the two electric currents, in the case that the system is composed of two thermoelectric modules. For this array, the maximum of the temperature difference is $\Delta T \approx 34$ K, that is, nine degrees of extra cooling are obtained when using two thermoelectric modules instead of a single one. For both cases, the single and two thermoelectric module system, the electric current is normalized with $I_0 = 0.93$ A, which is the optimal current for a single module.

Figure 10c shows the temperature difference ΔT between the hot and cold sides as a function of the electric current for a single thermoelectric device. This result can be compared with the experiment, **Figure 10a**, and the parabolic behaviour with a maximum is found. **Figure 10d** makes evident the dependence of ΔT when the system is composed on two thermoelectric

http://dx.doi.org/10.5772/intechopen.75998

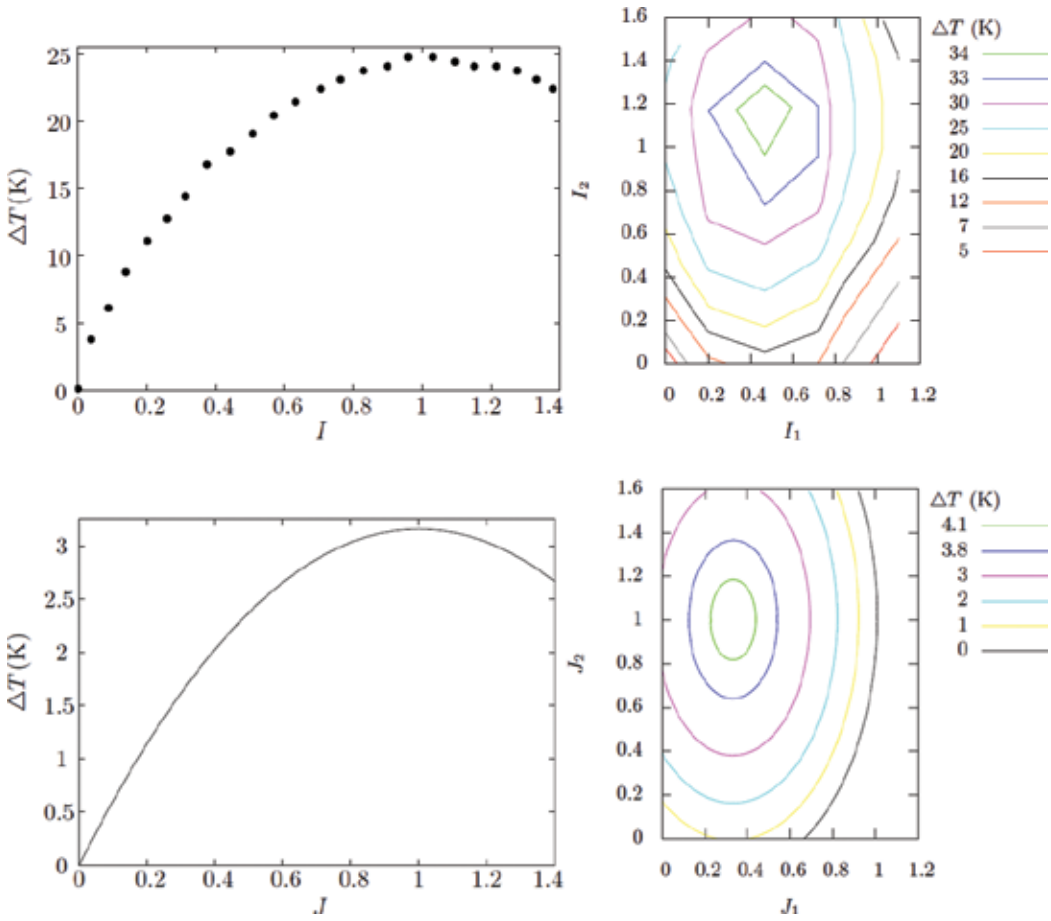

Figure 10. Temperature gradient ΔT as function of the electric current. (a) and (c) Single device. (b) and (d) Coupled devices. First row, experimental measurements from reference [37]. Second row, theoretical predictions from Ref. [37].

devices, presenting elliptic isocurves. Theoretical results (**Figure 10c**, **d**) obtained from the simple model discussed before agree qualitatively with the experimental ones (**Figure 10a**, **b**) showing a maximum $\Delta T$for certain values of the electric currents. Since the theoretical model used to get **Figure 10c**, **d** is a one-dimensional representation of a three-dimensional problem, a quantitatively comparison is far from reflecting the experimental measurements. However, if we calculate the percentage of the maximum extra cooling obtained when using two thermoelectric modules instead of a single one, that is $\left(\Delta T_{coupled} - \Delta T_{\text{single}}\right)/\Delta T_{\text{single}}$, we find that it is the same for both the experimental and the theoretical results. The maximum extra cooling that could be reached is 36%.

Some conclusions derived from the above are the following. First, the theoretical solutions of the temperature difference between the hot and the cold sides show a good qualitative agreement with the experimental measurements. Second, an optimal cooling with respect to the electric currents circulating through the modules has been found. Finally, an improvement of

36% in the performance, measured as mentioned above, of the coupled thermoelectric modules with respect to a single thermoelectric module is theoretically predicted. The analysis made in this section can be useful for the design of thermoelectric coolers.

7. Discussion and conclusions

We have analysed different aspects of the performance of thermoelectric films when an electric current flows through them, maintaining one of their sides at a constant temperature. First, we considered the effects of the size of the film on the Seebeck coefficient and the thermal and electrical conductivities as well as thermal inertia. This forms the basis for all the analysis of the problem of reducing the dimensions to the nanoscale. The introduction of such effects was done through the use of Eqs. (15)–(17) in the constitutive equations of the irreversible thermodynamics of electric charge and heat transport, Eqs. (12). When the latter are combined with the conservation equations of charge and energy, Eqs. (1)–(3), we arrive at the heat transport equation that was used systematically throughout the development of the analysis, Eq. (18). The different effects studied, namely, the wave behaviour of the propagation of heat, the response of the material to a pulse of electric current, the coupling of thermoelectric couples, the transition from the diffusive regime of heat transport to wave propagation, and so on were explained in terms of Eq. (18). The conclusions were diverse: (1)

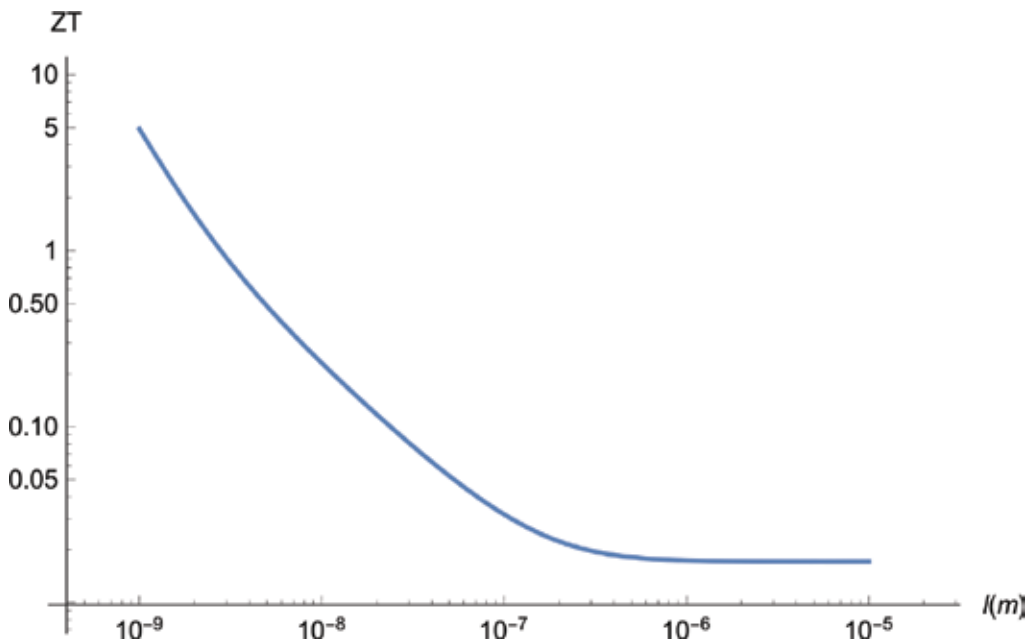

Figure 11. Effect of Eqs. (15)–(17), which describe the variation of the transport and thermoelectric coefficients with the size of the material l, on the thermoelectric figure of merit defined as usual: $ZT = \sigma S_E^2 T/K$.

thermodynamic inertia improves the thermal performance of a cooler, (2) the transition from diffusive transport to wave propagation of heat is controlled by the size of the thermoelectric material, (3) in the operating pulsed mode in a cooler, the shape of the electrical pulse is crucial for its thermal performance, (4) it is always possible to find values of the thermal parameters of a device that optimize its performance, (5) the operation of thermoelectric systems is closely related to the production of entropy in the system. Behind all these behaviours is the combined effect of the reduction of the thermal and electrical conductivities of the material and the increase of the Seebeck coefficient with the reduction of the dimensions. To close this section we show in **Figure 11** the behaviour of the thermoelectric figure of merit, $ZT = \sigma S_E^2 T/K$, when the thickness of a doped silicon semiconductor film decreases towards the nanoscale of lengths. As can be seen in the figure, the increase in the Seebeck coefficient dominates the reduction of thermal and electrical conductivities. The net effect is the increase of the thermoelectric figure of merit. Notably, the figure at a length of $l = 10^{-9}m$ is greater than that at $l = 10^{-5}m$ by a factor of 287.

8. Perspectives

Undoubtedly, a work perspective in thermoelectric power generation and refrigeration systems is to bring to the nanoscale the dimensions of the elements that make up structured systems. There is a lot of work done in systems composed or structured from elements in the millimetric escale of lengths or in larger scales [38], but a very promising perspective is the construction of those energy converting systems from nano-components such as for instance, the case of 1D phononic crystals. Several problems on thermoelectric phenomena that require attention when going from the macro to the nanoscale are: effects of size on the thermoelectric properties of the components of the nanostructured systems, the wave character of the propagation of heat and the phenomena of thermal interference and resonance, the effect of wave propagation of heat in pulsed systems, the effects of size on irreversible processes, the simultaneous consideration of the effects of size and the temperature dependence of the properties of materials, the effect of thermal inertia on the wave propagation of heat. It is also necessary to study the relationship between entropy generation and thermoelectric conversion efficiency and between structure and efficiency. In relation to this, a working hypothesis is that it is possible to find a structure that minimizes the production of entropy and to exploit interference and resonance phenomena to improve the thermoelectric energy conversion efficiency.

Acknowledgements

F.V. and A.F. acknowledge financial support from CONACYT-México under contracts 183358 and 258623, respectively. F.V. also thanks the project “Fronteras de la Ciencia” 367. A. F. also thanks the Cátedras program from CONACYT.

Conflict of interest

We declare that there is no conflict of interest.

Author details

Aldo Figueroa Lara, Iván Rivera Islas, Víctor Hernández García, Jaziel Rojas Guadarrama and Federico Vázquez Hurtado*

*Address all correspondence to: vazquez@uaem.mx

Centro de Investigación en Ciencias, Universidad Autónoma del Estado de Morelos, Cuernavaca, Morelos, Mexico

References

[1] Gurevich YG, Logvinov GN. Physics of thermoelectric cooling. Semiconductor Science and Technology. 2005;**20**:R57-R64

[2] Gurevich YG, Velázquez-Pérez JE. The role of non-equilibrium charge carriers in thermoelectric cooling. Journal of Applied Physics. 2013;**114**:033704

[3] Logvinov GN, Velázquez JE, Lashkevych IM, Gurevich YG. Heating and cooling in semiconductor structures by an electric current. Applied Physics Letters. 2006;**89**:092118

[4] Titov OY, Velázquez-Perez JE, Gurevich YG. Mechanisms of the thermal electromotive force, heating and cooling in semiconductor structures. International Journal of Thermal Sciences. 2015;**92**:44-49

[5] Vázquez F, Figueroa A, Rodríguez-Vargas I. Nonlocal and memory effects in nanoscaled thermoelectric layers. Journal of Applied Physics. 2017;**121**:014311

[6] de Groot SR, Mazur P. Non-equilibrium Thermodynamics, Vol. 014311. New York: Dover; 1984

[7] Jou D, Casas-Vazquez J, Lebon G. Extended Irreversible Thermodynamics. 4th ed. Berlin: Springer; 2010

[8] Jou D, Cimmelli V, Sellito A. Nonlocal heat transport with phonons and electrons: Application to metallic nanowires. International Journal of Heat and Mass Transfer. 2012;**55**: 2338-2344

[9] Sellito A, Cimmelli V, Jou D. Analysis of three nonlinear effects in a continuum approach to heat transport in nanosystems. Physica D. 2012;**241**:1344-1350

[10] Alvarez FX, Jou D. Memory and nonlocal effects in heat transport: From diffusive to ballistic regimes. Applied Physics Letters. 2007;**90**:1-3

[11] Lebon G, Machrafi H, Grmela M. An extended irreversible thermodynamic modelling of size-dependent thermal conductivity of spherical nanoparticles dispersed in homogeneous media. Proceedings of the Royal Society of London. Series A. 2015;**471**:20150144

[12] Zhou Q, Bian Z, Shakouri A. Pulsed cooling of inhomogeneous thermoelectric materials. Journal of Physics D: Applied Physics. 2007;**40**:4376-4381

[13] Figueroa A, Vázquez F. Optimal performance and entropy generation transition from micro to nanoscaled thermoelectric layers. International Journal of Heat and Mass Transfer. 2014;**71**:724-731

[14] Sarra SA. Spectral methods with postprocessing for numerical hyperbolic heat transfer. Numerical Heat Transfer, Part A: Applications. 2003;**43**:717-730

[15] Dorao SA. Simulation of thermal disturbances with finite wave speeds using a high order method. Journal of Computational and Applied Mathematics. 2009;**231**:637-647

[16] Ilegbusi OJ, Ümit-Coşkun A, Yener Y. Application of spectral methods to thermal analysis of nanoscale electronic devices. Numerical Heat Transfer, Part A: Applications. 2002;**41**:711-724

[17] Zhao S, Yedlin MJ. A new iterative chebyshev spectral method for solving the elliptic equation $\nabla \cdot (\sigma \nabla u) = f$. Journal of Computational Physics. 1994;**113**:215-223

[18] Peyret R. Spectral Methods for Incompressible Viscous Flow. 5th ed. New York: Springer; 2002

[19] Figueroa A, Vázquez F. Spectral and finite difference solutions of the hyperbolic heat transport equations for thermoelectric thin films. Applied Mathematics. 2013;**4**:22-27

[20] Ezzahri Y, Shakouri A. Ballistic and diffusive transport of energy and heat in metals. Physical Review B. 2009;**79**:184303

[21] Snyder GJ, Fleurial JP, Caillat T, Yang R, Chen G. Supercooling of Peltier cooler using a current pulse. Journal of Applied Physics. 2002;**92**:1564

[22] Gupta MP, Sayer M, Mukhopadhyay S, Kumar S. On-chip Peltier cooling using current pulse. In: 12th IEEE Intersociety Conference on Thermal and Thermomechanical Phenomena in Electronic Systems (ITherm); 2010. pp. 1-7

[23] Gupta MP, Sayer M-H, Mukhopadhyay S, Kumar S. Ultrathin thermoelectric devices for on-chip Peltier Cooling. IEEE Transactions on Components, Packaging and Manufacturing Technology. 2011;**1**:1395-1405

[24] Alexandrov B, Sullivan Satish Kumar O, Mukhopadhyay S. Prospects of active cooling with integrated super-lattice based thin-film thermoelectric devices for mitigating hotspot challenges in microprocessors. In: 17th Asia and South Pacific Design Automation Conference (ASP-DAC); 2012. pp. 633-638

[25] Manno M, Wang P, Bar-Cohen A. Anticipatory thermoelectric cooling of a transient Germanium hotspot. In: ASME 2013 International Technical Conference and Exhibition

on Packaging and Integration of Electronic and Photonic Microsystems. Vol. 2; 2013. V002T08A038

[26] Chowdhury I, Prasher R, Lofgreen K, Chrysler G, Narasimhan S, Mahajan R, Koester D, Alley R, Venkatasubramanian R. On-chip cooling by superlattice-based thin-film thermoelectrics. Nature Nanotechnology. 2009;**4**:235-238

[27] Thonhauser T, Mahan GD, Zikatanov L, Roe J. Improved supercooling in transient thermoelectrics. Applied Physics Letters. 2004;**85**:3247-3249

[28] Mao JN, Chen HX, Jia H, Qian XL. The transient behaviour of Peltier junctions pulsed with supercooling. Journal of Applied Physics. 2012;**112**:014514

[29] Ma M, Yu J. A numerical study on the temperature overshoot characteristic of a realistic thermoelectric module under current pulse operation. International Journal of Heat and Mass Transfer. 2014;**72**:234-241

[30] Rivera I, Figueroa A, Vázquez F. Optimization of supercooling effect in nanoscaled thermoelectric layers. Communications in Applied and Industrial Mathematics. 2016;**7**(2):98-110

[31] Yang B, Liu JL, Wang KL, Chen G. Simultaneous measurements of Seebeck coefficient and thermal conductivity across superlattice. Applied Physics Letters. 2002;**80**:1758-1760

[32] Bian Z, Zhang Y, Schmidt H, Shakouri A. Thin film ZT characterization using transient Harman technique. In: Proceedings of the 2005 International Conference on Thermoelectrics (University of California). Vol. 76; 2005

[33] Volklein F, Min G, Rowe DM. Modelling of a microelectromechanical thermoelectric cooler. Sensors and Actuators. 2006;**75**:95-101

[34] Shin W, Ishikawa M, Nishibori M, Izu N, Itoh T, Matsubara I. High-temperature thermoelectric measurement of B-doped SiGe and Si thin films. Materials Transactions. 2009;**50**: 1596-1602

[35] Ma Y, Ahlberg E, Sun Y, Iversen BB, Palmqvist AEC. Thermoelectric properties of thin films of bismuth telluride electrochemically deposited on stainless steel substrates. Electrochimica Acta. 2011;**56**:4216-4223

[36] Wojtas N, Grab M, Glatz W, Hierold C. Stacked micro heat exchange system for optimized thermal coupling of microTEGs. Journal of Electronic Materials. 2013;**42**:2103-2109

[37] Rojas JA, Rivera I, Figueroa A, Vázquez F. Coupled thermoelectric devices: Theory and experiment. Entropy. 2016;**18**(255):1-9

[38] LinGen C, FanKai1 M, FengRui S. Thermodynamic analyses and optimization for thermoelectric devices: The state of the arts. Science China Technological Sciences. 2016;**59**:442-455

Section 2

Building Up the Devices: Material Properties, Modeling, Geometry and Assembly Optimization

Chapter 4

Mechanical Properties of Thermoelectric Materials for Practical Applications

Gilad M. Guttmann and Yaniv Gelbstein

Additional information is available at the end of the chapter

http://dx.doi.org/10.5772/intechopen.75476

Abstract

Thermoelectric (TE) direct conversion of thermal energy into electricity is a novel renewable energy conversion method currently at a technological readiness level of 3–5 approaching laboratory prototypes. While approaching practical thermoelectric devices, an increase in the thermoelectric element's efficiency is needed at the entire service temperature range. Yet, the main focus of research was concentrated on the electronic properties of the materials, while research on the mechanical properties was left behind. As it is shown in this chapter, knowing and controlling the mechanical properties of TE materials are paramount necessities for approaching practical TEGs. The material's elastic constants, strength and fracture toughness are the most crucial parameters for designing of practical devices. The elastic constants provide understanding about the material's stiffness, while strength provides the loading conditions in which the material will keep its original shape. Knowing the fracture toughness provides the stress envelope in which the material could operate and its susceptibility to inherent fabrication faults. The characterization methods of these properties are varied and may be physical or pure mechanical in nature. It is the authors opinion to prefer the mechanical methods, so the results obtained will describe more accurately the material's response to mechanical loading.

Keywords: thermoelectric applications, thermoelectric materials, TEG prototype, mechanical properties, fracture toughness

1. Introduction

The demand for clean and reliable energy-harvesting technologies over the past few decades has led researchers to focus much on thermoelectric power generation (TEG) techniques. The thermoelectric effects (namely Peltier and Seebeck effects) exhibit the ability of a material

subjected to temperature gradient, to mobilize charge carriers within its volume. The right connection of two such materials can be used for building a TEG module which is reliable, quiet (due to no moving parts), and most importantly scalable. Such TEG modules had been used for the past 40 or so years as reliable power generators in top-edge technology systems at remote terrestrial and extra-terrestrial locations in NASA's systems. Furthermore, one can take advantage of the thermoelectric (TE) effects and tailor other types of modules for different applications, in a wide range of operating temperatures, such as cooling systems in cars (enhancing the coefficient of performance, COP, of the entire cooling system and car performance), harvesting residual heat from solar systems and photo-voltaic conversion cells, and harvesting residual heat from heat exchangers and converting it to useful electricity at industry, power supply modules for onsite sensor systems, and even wearable devices (if incorporated in organic films).

The energy conversion efficiency is a fraction of the Carnot efficiency and determined by the dimensionless figure of merit (ZT), which is defined as $ZT = \alpha^2 T/\rho\kappa$, where α, T, ρ, and κ are the Seebeck coefficient, absolute temperature, electrical resistivity, and thermal conductivity, respectively. While most of the research in the past 15 years was focused on improving the ZT of materials (and hence the efficiency), a little focus was given to the mechanical evaluation and reliability of these materials. Therefore, much work of evaluating the material properties in the mechanical, thermomechanical, and fatigue fields is still to be done while paying attention to the TEG whole-module integrity challenges such as thermal stability and metalized contact layer durability [1, 2].

From the physics standpoint both transport and mechanical properties originate at the atomic level. The mechanical response of the material mainly depends on the atomic bonding between the atoms from which it is constructed. An atomic bond is basically the sharing of electron(s) between two or more adjacent particles (nonmetals for covalent bond, ions for ionic bond, or atom nucleus for metals). The cohesive energy (E_C) between two particles is a measure of the work required for their separation and is a result of the repulsive and attractive forces between the two, which depend on the particle masses (the same force law as in gravity). The distance between two particles where the potential energy is minimal defines the cohesive energy of the two. The stronger the cohesive energy, the stronger the bond between the particles and more work is required for breaking the bonds. The gradient of force per small change of distance between the particles is defined as Young's modulus. The material strength is the force required to break atomic bonds and forcing a plastic and constant change in the material volume. The material compressibility, better known for its reciprocal—bulk modulus (B), is a measure for the material's resistance to hydrostatic compression. Many researchers tried over the years to find relations between the cohesive energy and bulk modulus to other various physical properties of the material (such as melting temperature, atomic volume, lattice constants, Debye temperature, etc.). Such specific connections will undoubtedly be restricted to a group of materials with similar structure, bond type, or other physicochemical property. Recently, after the examination of a large reported database on the physical properties of about 30 metals, it was realized that a correlation between the bulk modulus and the cohesive energy density (the atomic cohesive energy divided over the atomic volume—E_C/V) can be made [3]. Such a correlation opens the possibilities of correlating the other elastic constants

of the material including Young's modulus to other physical properties and therefore interlinking the material transport and electric properties with the mechanical ones on the atomic level.

The above long list of different suggested applications for TEGs is to show the wide range of service conditions that these generators will need to withstand. Such applications may vary from static operating conditions with a low number of thermal cycles and low operating temperatures, via higher temperature amplitudes and frequencies and up to dynamic applications with a high number of cycles, high thermal amplitudes, and occasional mechanical impacts.

Furthermore, the TEG service conditions necessarily subject the materials to wide temperature ranges and gradients within the materials themselves, so any mechanical characterization of TE materials should also concern the temperature dependence of the property. One such work was conducted measuring Young's modulus temperature dependence of LAST (Pb-Sb-Ag-Te) [4] between room temperature and 823 K and found an inverse relation between Young's modulus and the temperature.

In order to advance the development of thermoelectric modules for approaching practical applications, the design of future modules must take into account the mechanical properties of the involved materials for assuring adherence to the service conditions. Such design approaches based on finite element analysis, carried out for different applications, were reported [5–8]. Such analyses are essential while designing a specific TE device and give the ability to play with different parameters without the need of physical construction—saving money, time, man power, and materials in the process. Any simulation of the mechanical performance most definitely requires the values of the material's elastic constants (Young's, bulk, shear, Poisson's ratio) and strengths for the very least.

Measuring or evaluating correctly the mechanical properties of TE materials has the potential to bridge between the atomic (mechanical) and physical (electronic/transport) understanding of these materials to the fully developed working modules that will be optimal from both ends standpoint. That way, the material selection for the proper usage will be much easier and efficient.

Therefore, in order to achieve optimal operational TEGs, further evaluation and maximization of the following mechanical properties—elastic modulus, strength, hardness, fracture toughness, fatigue resistance (fatigue limit), and thermal fatigue resistance—are required at the entire operational temperature range (depending on the application). These are not the only mechanical properties at question but are the major ones that will provide both scientists and manufacturers with sufficient data to improve and further proceed to practical TEGs. As it will be clarified in detail, characterizing these few mechanical properties is handful enough for the time being.

2. Mechanical properties

All the mechanical property results for most of the currently investigated TE materials reported in this chapter are summarized in **Table 1** for convenience.

Material	Reference	Type	ZT_{max}	E sonic (GPa)	ν Poisson's ratio	E mechanical (GPa)	σ (MPa)	Hv (GPa)	K_I (MPa × m$^{1/2}$)	VIF constant
PbTe		p	0.8	27.7				0.41	0.35	
GeTe	—	p	0.8	57.0	0.27	77 (a)	168 (a)	1.16	0.39 (i)	0.0319
GeTe + 10% Ag	—	p	0.5	48.8	0.29	65 (a)	216 (a)	1.41	0.41 (i)	0.0319
GeTe + 10% Cu	—	p	0.7	60.7	0.26		239 (a)	1.59	0.44 (i)	0.0319
GeTe + 4% at Bi_2Te_3 + 10% Ag	—	p	0.7	49.4	0.28	59 (a)	221 (a)	1.58	0.48 (i)	0.0319
GeTe + 4% at Bi_2Te_3	—	p	0.6	47.8	0.26	79 (a)	176 (a)	1.62	0.54 (i)	0.0319
GeTe + 4% at Bi_2Te_3 + 10% Cu	—	p	0.7	62.7	0.25	63 (a)	204 (a)	1.78	0.56 (i)	0.0319
Zn_4Sb_3	[9]	p		71.7	0.26		56.6 (a)	2.2–2.3	0.8–1.2 (i)	0.016
$Si_{0.8}Ge_{0.2}$	[10]	n	0.9	143	0.23		86 (c)	14.5 (i)	1 (i)	0.0089
$Si_{80}Ge_{20}$	[11]	p				135 (b)	108 (c)	9 (i)	1.66 (i)	0.0089
Bi_2Te_3	[12]	n	1	32			62 (a)	0.62–0.79 (i)	1.1 (i)	unknown
Mg_2Si	[13]	n	1	117				5.3 (i)	1.25 (i)	0.016
$Yb_{0.35}Co_4Sb_{12}$	[14]	n	0.35–1	135	0.20		111	8 (i)	1.7 (i)	unknown
$Ca_3Co_4O_9$	[15]	p				84 (b)	320 (C)	2.6 (ii)	2.8 (iii)	
$CoSb_3$	[16]	n		136	0.14–0.25	92 (a)	766 (a); 86 (c)		1.7 (iii)	
$CeFe_3RuSb_3$	[16]	p		133	0.22–0.29	115 (a)	657 (a); 37 (c)		1.1–2.8 (iii)	
Bi_3Se_2Te	[17]					197.2 (b)		5.6 (ii)	2.4–2.6 (ii)	0.016
Bi_2Te_3	[18]	p			0.25	127.5 (b)		4.02 (ii)		
$Hf_{0.44}Zr_{0.44}Ti_{0.12}CoSb_{0.8}Sn_{0.2}$	[19]	p				221.0 (b)		12.8 (ii)		
$Hf_{0.25}Zr_{0.75}NiSn_{0.99}Sb_{0.01}$	[19]	n				186.5 (b)		9.1 (ii)		

Material	Reference	Type	ZT_{max}	E sonic (GPa)	ν Poisson's ratio	E mechanical (GPa)	σ (MPa)	Hv (GPa)	K_I (MPa × m$^{1/2}$)	VIF constant
$Bi_{0.4}Sb_{1.6}Te3$	[19]	*p*				41.5 (b)		1.1 (ii)		
$Bi_2Te_{2.7}Se_{0.3}$	[19]	*n*				38.8 (b)		1.2 (ii)		
$Ce_{0.45}Nd_{0.45}Fe_{3.5}Co_{0.5}Sb_{12}$	[19]	*p*				129.7 (b)		5.6 (ii)		
$Yb_{0.35}Co_4Sb_{12}$	[19]	*n*				136.9 (b)		5.8 (ii)		
$Si_{0.8}Ge_{0.2}P_2$	[19]	n				166.3 (b)		10.8 (ii)		
$Si_{0.8}Ge_{0.2}B_5$	[19]	*p*				155.6 (b)		10.7 (ii)		
$In_{0.005}PbSe$	[19]	*p*				65.9 (b)		0.6 (ii)		
$Bi_xSb_{2-x}Te$	[20]	*p*	1.4			42.1 (b)		1.6 (ii)		
$Ba_8Al_{15}Si_{31}$	[21]		0.4	96.88	0.25	109.7 (b)			1.1	0.018
MnSi	[22]	*p*	0.6			160(a); 182 (b)	1083 (a); 178 (c)	11.85 (i)	1.63 (i)	0.16
$Mg_2Si_{1-x}Sn_x$	[22]	*n*	1.1			83 (a); 58 (b)	492 (a); 79 (c)	3.54 (i)	0.99 (i)	0.16

(a) = compression; (b) = nanoindentation; (c) = flexural; (i) = Vickers Indentation Fracture; (ii) = nanoindentation; (iii) = other method from ASTM C 1421

ZT_{max} is the material's maximal figure of merit; *Esonic,* Young's modulus as measured by sonic method; ν, Poisson's ratio; *E mechanical*, Young's modulus as measured in a mechanical testing method; σ, maximum strength as measured by mechanical testing method; *Hv*, hardness Vickers; K_{VIF}, fracture toughness; VIF constant, the constant used in the Vickers Indentation Fracture equation to calculate the fracture toughness.

Table 1. Summary of the mechanical properties of various TE materials reported in the study.

http://dx.doi.org/10.5772/intechopen.75476

2.1. Elastic modulus

Young's modulus, frequently designated as E, is the most common and known member of a family of elastic constants that describe the elastic response of a material. Other constants are the shear modulus (G), Poisson's ratio (v), bulk modulus (B), and Lame's constant (λ). These constants are manifestation of the minimum free energy between the atoms that construct the material and therefore depend on the material's atomic composition and structure. They describe the elastic response of a solid to different imposed mechanical stresses and can be used as indicators of phase transition of the material with changing of temperature or pressure [23].

Young's modulus describes the material's elastic response to a uniaxial loading (either tension or compression) and gives the linear proportion of increase in the stress while increasing the displacement on the material. It is the same as with a spring's constant and obeys Hook's law (Eq. (1))

$$\sigma = E \cdot \varepsilon \tag{1}$$

where σ is the measured stress (Pa), E is Young's modulus (Pa), and ε is the displacement (mm/mm). So by studying the stress-strain curve of a material under uniaxial loading, the material's Young's modulus can be determined by measuring the initial linear slope of the curvature. As long as the material is subjected to stresses at the elastic range and do not undergo any plastic deformation, Young's modulus is a good indicator for the general stiffness of the material.

A different characterization technique of the elastic modulus is by measuring the time of flight of transverse and shear waves (see **Figure 1**) in a material (ASTM D 2845 [24]). This test method is good for estimating the elastic constants of the material—especially in the case of brittle nature materials or low-volume productions (where standard mechanical specimens for tensile/compression could not be fabricated). In contrast to mechanical testing where the

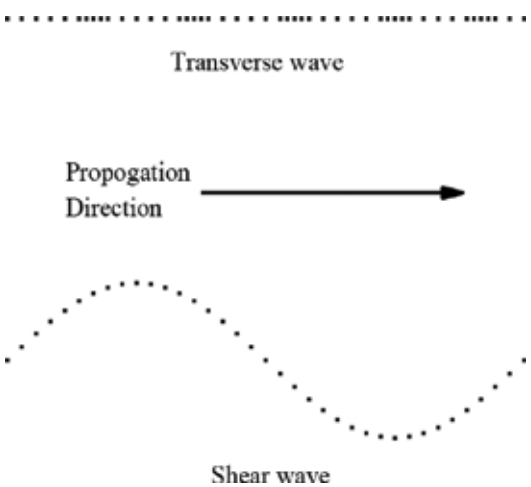

Figure 1. A schematic presentation of transverse and shear sound waves.

elastic response of the material to applied external stresses is measured in the case of time of flight, the sound velocity of elastic waves propagation through (transverse) and along (shear) the material is being characterized.

Each sound wave is excited within the material by a piezoelectric transducer working in the ultrasonic range (above 20 kHz). Usually, the same transducer can excite and receive sound waves, and a record of the voltage as a function of time can be plotted. A repetitive pattern is recorded with a decreasing amplitude, due to inelastic interactions in the material (heat generation, absorption).

Measuring the time difference between identical points in the repetitive pattern and dividing it by the specimen geometry allow measuring the sound velocity (V_L for transverse wave and V_S for shear wave). Then, the elastic constants could be evaluated using the following equations[1] [24]:

$$E = \frac{\left[\rho V_s^2 (3 V_L^2 - 4 V_s^2)\right]}{(V_L^2 - V_s^2)} \tag{2}$$

$$\nu = \frac{(V_L^2 - 2 V_s^2)}{\left[2(V_L^2 - V_s^2)\right]} \tag{3}$$

where ρ is the material density (gr/m^3), E is Young's modulus (Pa), and ν is Poisson's ratio.

A comparison of Young's modulus values measured by the sonic and mechanical methods has shown that some difference in results (up to 30%) may exist [25, 26]. The sonic-based method is less prone and sensitive to internal defects within the material's volume (up to the case where such defects affect the measured sound velocity) than the mechanical method. From this, it can be concluded that the sonic evaluation of Young's modulus will be used to distinguish between different TE material systems, but mechanical values, which are more sensitive and indicative for the actual external stresses that will be applied upon the materials, will be more suitable for the mechanical design of modules and for comparing fabrication procedures.

Investigating the elastic modulus values of different TE materials reported in the study reveals that most of the TE materials exhibit values close to common engineering metals in the range of several tens of GPa and up to 200 GPa (for a comparison, ~70 GPa is characteristic for Al alloys and ~200 GPa for steels) [27, 28]. This fact can ease some of the concerns while modeling and designing of future TE devices, because the stiffness of the different materials is not poles apart from one another.

Bismuth telluride (Bi_2Te_3)-based TE alloys exhibit the lowest and highest reported elastic modulus values, as low as ~40 GPa and up to ~200 GPa, depending on the exact alloying and fabrication procedure [12, 18]. Lead telluride (PbTe)-based alloys (which is the most researched alloy system) exhibit modulus values of ~60 GPa [1]. More advanced and recent alloys such as

[1]Here, the calculations for Young's modulus and Poisson's ratio are brought. Calculations for the other elastic constants can be found at the ASTM standard [9].

skutterudites exhibit values of ~100 GPa [19], silicon germanium (SiGe)-based alloys exhibit values of ~150 GPa [10, 11, 19], and half-Heusler alloys can even reach ~200 GPa [19].

These values show the versatility of the material systems and research opportunities while involving different alloying and fabrication procedures, highlighting the major role of the involved materials at the mechanical design stage.

2.2. Strength

Strength is defined as the stress that the material can withstand under any loading condition before any permanent change is introduced to the material. It is common to differentiate between several specific strength definitions of materials (see **Figure 2**). The first is the *yield strength,* which is defined as the stress at which the material undergoes a uniform plastic deformation (most common in metals), which means that after the load is removed, the material will not regain its full initial shape. The second is the *ultimate strength,* which is the maximal stress that the material can withstand after which a plastic deformation becomes local at the weakest site in the material (for ductile materials). The third is the *fracture strength,* which is the stress at which all of the plastic deformation are exploited and defect in the material coalescence and concluded in a final fracture of the material. In the case of materials with a brittle nature, the ultimate strength usually coincides with the final fracture.

In order to measure the material's strength, one must subject it to external loading, preferably in only one axis. The most common test is the tensile test at which a specimen is held at the testing machine and the external forces elongate the specimen and further open any defect present in the material. Therefore, the tensile test is very sensitive to the specimen fabrication method and its associated defects.

On the other end, a compression test can be performed, at which the external forces act in the direction to decrease the volume of the specimen and to stop any propagation of defects

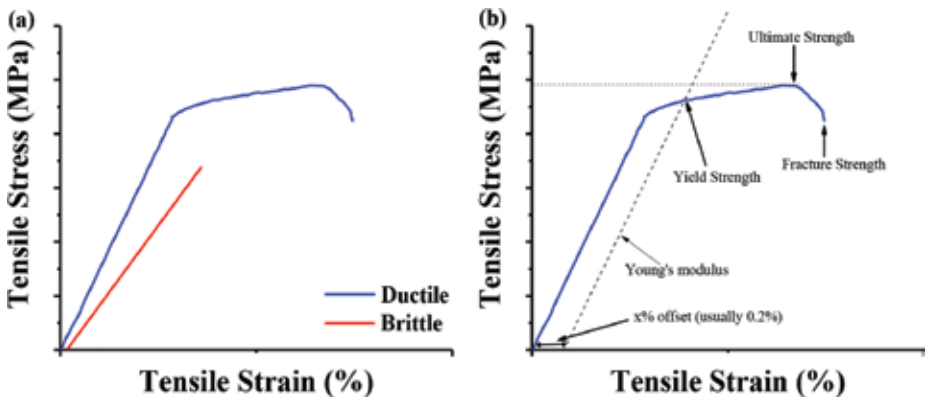

Figure 2. A schematic stress-strain curve: (a) ductile versus brittle material and (b) strength definitions.

in the material. The compression test is very common in the ceramics and semiconducting material classes in which minimization of the results deviation due to material's defects is significant.

Most TE materials are brittle in nature, meaning that their majority do not show any signs of plastic deformation (and therefore no yield strength), and fracture is rather catastrophic. Bi_2Te_3 and its alloys have the longest history of utilization for direct energy conversion, and hence their mechanical strength received early attention. Such ingots made by conventional zone-melting growth exhibited only 10–20 MPa flexural fracture strength [1]. A low mechanical strength of TE materials not only results in failure during element fabrication but also limits the degree of miniaturization which is required among others for TE modules for microelectronics [1]. Enhancing the material strength can be achieved by engineering the material microstructure in the micron and submicron scales. Furthermore, experiments were also made trying to incorporate nano-particles or wires for producing composite materials [13, 29]. The latter fabrication approach usually results in lower ZT of the materials with enhanced mechanical properties, which are associated with the strengthening components, without any significant contribution to the TE performance.

The reported fracture strength of most of the TE materials is in the range of 60–200 MPa, much depending on the testing method (lower values for the flexural test and higher values in the case of compression). Skutterudites and half-Heusler materials show the highest reported strengths in the range of 600–800 MPa [16, 17].

2.3. Hardness

Hardness is a material quality rather than a physical property (here to say that this value has no real meaning for itself, but only in a comparison to other materials or metallurgical states) that defines the material's resistance to penetration. There are several scales of hardness being used in materials science and engineering, where the most common are the ***Rockwell*** and ***Brinell*** scales usually used on metals and the ***Vickers*** scale that are also common in ceramics. The scales differ from each other by four parameters: (1) indenter geometry and compositions, (2) applied load during the test, (3) dwell time at maximal load, and (4) means of result interpretation. For instance, Rockwell hardness is determined using either a diamond cone indenter or a stainless steel ball (1/16″) under a load ranging from 15 to 150 kgf. The resulting hardness is a measure of the depth the indenter makes into the material. On the other hand, Vickers hardness is obtained by measuring the mean diagonals of an indent resulting by a square-based pyramid with a head angle of 136° made of diamond and loads ranging from several grams (micro-hardness) up to 120 kgf. Some overlap between the different scales can be found so a comparison could be made.

Notice that hardness is also an indicator for the material's resistance to wear. If the material is too soft, the surface is easily damaged during handling or device assembly.

Comparison made between hardness values obtained by micro-hardness and nano-indentation (further explanation in Section 2.4.2) found that the latter may result in 10–30% higher

values than the first, especially in materials exhibiting plasticity and has a low ratio of yield strength to Young's modulus. These conditions lead to a pileup of the plastically deformed surface at the edges of the indenter during the nano-indentation test, which in result make the affective contact area, between the indenter and the material's surface. The hardness result is determined by dividing the maximal applied force by the apparent contact area measured after the load has removed, without taking into account the pileup [30]. Therefore, nano-indentation values must be corrected in such cases. Later report comparing both of the techniques for a TE material (*n*-type LAST) [31] found that the values obtained by both of the techniques are in a very good agreement and in the range of 0.6–0.8 GPa. Such values (at the range of ~1 GPa) were reported for the most common TE materials at the early years (see **Table 1** at the beginning of the chapter). Higher values were reported more recently for different materials upon fabrication changes. SiGe and half-Heusler alloys were reported to exhibit a hardness of ~14 GPa [19].

2.4. Fracture toughness

Fracture toughness is the material's ability to adhere loading at the presence of inherent flaws before catastrophic failure will occur. For a brittle material (here to say without the ability for plastic deformation at the crack tip), the fracture toughness K_c (MPa·√m) reflects the flaw tolerance which is typically dependent on the preexisting flaw length, a_c(m), as indicated in Eq. (4)

$$K_c = Y \cdot \sigma_c \sqrt{\pi a_c} \tag{4}$$

where Y is a dimensionless geometric factor and σ_c is the critical fracture strength (MPa). Materials with high K_c can withstand higher thermal or mechanical loads.

Conventional fracture toughness tests are conducted on large specimens with fatigue crack introduced into them so to create as close as possible conditions to those defined by the linear elastic fracture mechanics (LEFM) [32, 33]. This means that the plasticity at the crack front and tri-axiality are limited (small-scale yield conditions) due to the restraining volume of the specimen. ASTM E 399 [34] standard states five types of specimens and loading setups that stand in these conditions. In the test itself, the specimen is subjected to tensile or flexural loading up to fracture while the load and crack opening displacement (COD) [16] are recorded. After the test concluded, the recordings are postprocessed by the method given in the ASTM standard in order to evaluate the fracture toughness of the material. After writing that, most of the TE material nowadays suffer from low-volume fabrication, and specimens adequate with ASTM E 399 could not be machined. Therefore, most of the published data of fracture toughness were measured by different methods—the ***Vickers Indentation Hardness***, ***Chevron Notch Flexure*** (detailed in ASTM C 1421 [35]), and recently a growing number of reports where ***nano-indentation*** had been used [19–22]. Another method, which was never utilized with TE materials, is the ***Chevron Notch Fracture Toughness*** (also known as the short rod) [36].

2.4.1. Vickers indentation hardness as a measure of the fracture toughness

In the case of ceramics and other materials with a brittle nature where fabrication is hard or costly, an emerging test method is based on the evaluation of the fracture toughness using the Vickers Indentation Hardness test through the cracking at the indentation edges. First

suggested by Swain and Lawn [37], a general equation relating the hardness and fracture toughness is in the form described in Eq. (5)

$$K_R = \xi \left(\frac{E}{H}\right)^n P C_0^{-3/2} \quad (5)$$

where K_R is the fracture toughness (Pa·√m); ξ, dimensionless material constant which describes its resistance to crack propagation; E, Young's modulus (Pa); H, Vickers hardness number (Pa); P, the load applied in the hardness test (Pa); C_0, half of the surface crack length (m); n, equation constant which is dependent on the data fitting of the results (0.4–0.5).

This common, cheap, and easy testing method requires only slightly different result interpretation procedure compared to measuring Vickers Hardness number alone. Furthermore, much of the values reported in the study for TE materials were obtained by this technique and can be compared. The disadvantages are the large standard deviation in the results (which can be corrected while using large sample size) and the uncertainty in the fracture mechanisms for each material which results in diverse experimental equations for K_{IC} [38]. The two known crack shapes upon fracture under the Vickers indent are the ***Median*** (half-penny) and ***Palmqvist*** [38] (see **Figure 3**). The median type suggests that the surface cracks from the hardness indentation are interconnected in the specimen depth, while in the Palmqvist type, each crack is independent. It is common to differentiate between the two shapes by measuring the ratio between the crack's length (2c) and the indent's diagonal (2a). If the ratio is larger than 2, it is common to relate it to the median shape, else it is Palmqvist. So far in the study, most of the equations that correlate hardness with fracture toughness are based on a numerical fitting of experimental data and are material-dependent. A short list of such equations is described in **Table 2**. The decision of which equation is the most appropriate upon developing of new materials is to be made with much care. One should be aware of the different equations offered based on their origin and the nature of cracking in the tested material (median or Palmqvist). As up to date, there is no sufficient data and comparison between values obtained by this test method and others for any given material to conform and favor one equation over the others. One reported comparison between the three methods for evaluating the fracture toughness of skutterudites [39] has found that this technique is inadequate in a comparison to the Chevron Notch Flexure method.

Fracture toughness of several common TE materials (such as Bi_2Te_3 and GeTe) tested by this test method showed values in the range of ~0.4–1 MPa√m [1, 13], while $Si_{0.8}Ge_{0.2}$ showed a fracture toughness of ~1.6 MPa√m [12] and the highest reported value is of 1.7 MPa√m for $Yb_{0.35}Co_4Sb_{12}$ [15].

2.4.2. Nanoindentation

Nano-indentation utilizes atomic force microscope (AFM) to basically perform a hardness test. The system records the depth of the indenter as a response to a very small load (up to about 1000 mN) applied over a small contact area size (at the range of few nm^2), resulting in a load-displacement curve, where the displacement is the penetration depth of the indenter into the material. Following the test, the indentation geometry is also measured and evaluated as a complementary data. This means that nano-indentation can be used to evaluate all of the abovementioned mechanical properties, starting with the elastic ***Young's modulus***, going

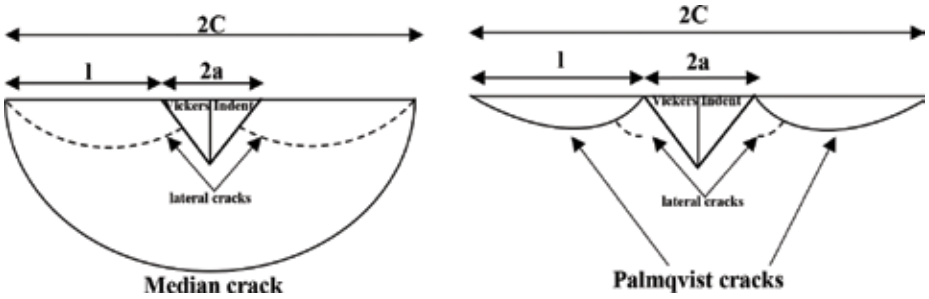

Figure 3. A schematic representation of median and Palmqvist cracks.

#	Equation	Crack type	Reference
1	$K_{IC} = 0.016\left(\frac{E}{H_V}\right)^{1/2}\frac{P}{C^{3/2}}$	Median	[40]
2	$K_{IC} = 0.0752\frac{P}{C^{3/2}}$	Median	[41]
3	$K_{IC} = 0.0089\left(\frac{E}{H_V}\right)^{2/5}\left(\frac{P}{a\,C^{1/2}}\right)$	Palmqvist	[42]
4	$K_{IC} = 0.0319\frac{P}{a\,C_0^{1/2}}$	Palmqvist	[43]

Table 2. Hardness and fracture toughness relations.

through the **yield** *and* **ultimate stresses,** and up to ***hardness*** and ***fracture toughness***. Due to the small sampling area, this technique is ideal for the measurement of materials with low fabrication volumes and such that consist micro- or sub-micron features in their structure (as in the case of many of the recently developed TE materials). In spite of these advantages, the small measured area possesses a major limitation due to the fact that in order to evaluate the macroscopic properties of the material, it is paramount to make a large number of measurements to eliminate any micro-feature dependence and to acquire the average macroscopic property. Furthermore, AFM testing systems are not available for any material's manufacturer and not even at any research center. AFM should be operated by an experienced and educated man power in order to acquire believable results (with low values of uncertainties and errors [44]) and to reduce the wearing of the system, which is quite expensive to maintain (mainly due to indenters' high fabrication costs). For further reading and understanding of nano-indentation, the reader may read the following reference [21].

Several TE materials were evaluated by this testing method and reported recently, such as $Ba_8Al_{15}Si_{31}$ [19] which was reported to have Young's modulus of 109.7 GPa (about 10% higher than the value calculated from time-of-flight measurements) and Vickers hardness of 634 HV which is in a good agreement to the micro-hardness value. Also, *p*- and *n*-type half-Haussler [19] compositions showed Young's modulus of 221 and 186 GPa and a hardness of 12.8 and 9.1 GPa, respectively. Other materials that were measured by this technique can be found in [17]. Although reports using this technique can be found with an increasing amount over the years, it was rarely applied for fracture toughness assessment as was recently applied for Bi_3Se_2Te with Young's modulus of 197.2 GPa, a hardness of 5.6 GPa, and a fracture toughness of 2.4–2.6 MPa√m [32].

2.4.3. Chevron notch fracture toughness (short rod)

This method, first introduced by Barker in 1977 [36] and more recently standardized in ASTM B 771 [45], measures the fracture toughness of both ductile and brittle materials using a Chevron Notch rod-type specimen subjected to tension loading. The specimen is loaded until a small load drop is recorded, indicating an initiation and propagation of a crack well prior to a catastrophic fracture. The ASTM standard differentiates between smooth growing crack and a discontinuous growing crack, so that ceramics and semiconductors that has some degree of plasticity can be handled as well. After the test is concluded, the recorded data are processed to evaluate the fracture toughness of the material, if all of the validation criteria of the standard are met. This testing method, if carried out correctly, has the advantage of directly measuring the material's fracture toughness, even on miniature-size specimens with the aid of testing jigs and setup such as "Fracjack" [35]. Yet, for obtaining adequate results, the specimen's fabrication must be in a high quality and machining should be made by skilled technicians, due to the fact that the required standard specimen includes many details (see **Figure 4**) and most of the ceramic and semiconducting materials suffer from poor machinability. Furthermore, the results interpretation must be carried out by an experienced man power so that no other errors and uncertainties will affect the calculated results. Up to date, as far as we know, no TE materials tested by this technique were reported. To the authors' best experience, such a test method could provide the most accurate fracture toughness values of TE materials directly with little uncertainties and without the need to evaluate it from other types of testing and based on data fitting from other material systems, especially if adequate test setup for ultra-small-sized samples is prepared.

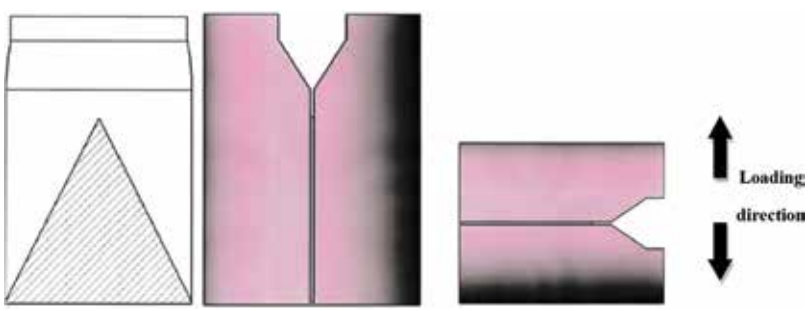

Figure 4. Short-rod specimen geometry and loading setup.

2.5. Thermal shock and fatigue

Due to the fact that TE service conditions include thermal cycles, it is also highly important that such materials will have thermal shock and fatigue resistance. *Thermal shock resistance* is the material's ability to adhere the thermal stresses introduced into it by a sudden increase in temperature as can be calculated by Eq. (6)

$$\sigma_{thermal} = \alpha E \Delta T \tag{6}$$

where $\sigma_{thermal}$ is the thermal stress (Pa), α is the coefficient of thermal expansion (CTE) (1/k), E is Young's modulus (Pa), and ΔT is the temperature difference on the material (k).

For the case where the thermal stress is lower than the yield/fracture stress, then the material will sustain the shock. Therefore, thermal shock could be connected and evaluated via other material's mechanical properties such as Young's modulus, Poisson's ratio, and fracture stress and other thermal properties based on the thermoelastic approach as being expressed in Eq. (7)

$$R' = \frac{\sigma_f(1-\nu)\kappa}{\alpha E} \tag{7}$$

where R' is the thermal shock resistance (W/m), σ_f is the material's fracture stress (Pa), ν is Poisson's ratio, and κ is the total thermal conductivity (W/m·k). The higher the R' value, the greater the resistance.

Thermal fatigue is the material's capability to adhere to multiple cycles of heating and cooling. As the material is capable to withstand higher number of cycles, it is said that it has a higher thermal fatigue resistance. The only way to measure this property is currently to subject such a material to thermal cycles and to evaluate its consistency every few cycles.

As of the current time, according to our knowledge, there are no references in the study concerning these properties with the actual measured values, and the few that mention them do so only in a theoretical fashion as stated earlier.

3. Summary

Mechanical properties of materials represent the material's responses to different loading conditions and are macroscopic representations of the atomic bonding between the atoms from which they are constructed. It was suggested that the cohesive energy (E_C) between two particles can be linked to the elastic constants of the materials and other various physical properties (such as melting temperature, atomic volume, lattice constants, and Debye temperature). Such a correlation opens the possibility of interlinking the material's electronic transport properties with the mechanical ones on the atomic level.

Measuring or evaluating correctly the mechanical properties of TE materials has the potential to bridge between the atomic (mechanical) and physical (electronic/transport) understanding of these materials to the fully developed working modules that will be optimal from both ends standpoint. That way, the material selection for the proper use will be much easier and efficient.

As it was shown in this review, knowing and controlling the mechanical properties of TE materials are paramount necessities for approaching practical TEGs and moving the entire TE technology onward in the Technological Readiness Level (TRL) scale. The material's elastic constants (e.g., Young's modulus and Poisson's ratio), strength, and fracture toughness are the most crucial for the designing practical devices (using finite element analysis). In such an approach, adequate modeling of TEGs could be prepared with lower experimental intervals while saving both money, time, materials, and man power. The elastic constants can provide

the understanding about the material's stiffness, while the strength provides the loading conditions in which the material will maintain its original shape. Knowing the fracture toughness will provide the stress envelope in which the material could operate and its susceptibility to inherent fabrication faults.

Characterizing these mechanical properties (elastic constants, strengths, and fracture toughness) is handful enough and will provide both scientists and manufacturers sufficient data to improve and further proceed to practical TEGs. Characterization methods of these properties are varied with pros and cons to each. It is the authors' opinion to prefer the mechanical methods over the physical ones (such as in the case of Young's modulus measurement by sonic waves), so the results obtained will more accurately describe the material's response to mechanical loading. In evaluating the material's strength, it will be best to choose the type of testing method in which the loading conditions are as close as possible to the expected service conditions of the material. In order to establish a coherent database for all of the developed materials, it will be adequate to test all of these materials under compression and flexural conditions. This is due to the fact that most of the currently available published were obtained following compression conditions, and for the reason, flexure conditions are more susceptible to defect in the material. For measuring fracture toughness, it seems to be wise to choose other testing methods than the Vickers Indentation Fracture, which is prone to errors and uncertainties. It may be applied for a qualitative evaluation of the property as required for distinguishing between fabrication parameters, but for quantitative modeling and calculations, it will be better to use the testing method reported in the standards such as ASTM C 1421 [36] and ASTM B 771 [36].

The abovementioned mechanical properties are not the only mechanical properties at question but also the major ones that should to be evaluated. A more detailed mechanical design will require also the characterization of the fatigue limit and thermal fatigue resistance depending on the expected service conditions of the developed practical TE devices.

Acknowledgements

The authors would like to thank the Ministry of National Infrastructures, Energy and Water Resources for granting this project, grant no. 215-11-022.

Author details

Gilad M. Guttmann[1]* and Yaniv Gelbstein[2]

*Address all correspondence to: gilad.guttmann@gmail.com

1 Department of Materials Engineering, Nuclear Research Center Negev, Beer-Sheva, Israel

2 Department of Materials Engineering, Ben-Gurion University of the Negev, Beer-Sheva, Israel

References

[1] Liu W, Jie Q, Kim HS, Materialia R-Z. Current progress and future challenges in thermoelectric power generation: From materials to devices. Acta Materialia. 2015

[2] Snyder G, Toberer E. Complex thermoelectric materials. Nature Materials. 2008;**7**(2): 105-114

[3] Wacke S, Górecki T, Górecki C, Książek K. Relations between the cohesive energy, atomic volume, bulk modulus and sound velocity in metals. Journal of Physics Conference Series. 2011;**289**(1):012020

[4] Ren F, Case ED, Timm EJ, Lara-Curzio E, Trejo RM. Anomalous temperature-dependent Young's modulus of a cast LAST (Pb–Sb–Ag–Te) thermoelectric material. Acta Materialia. 2010;**58**(1):31-38

[5] Barako M, Park W, Marconnet A, Asheghi M, Goodson K. Thermal cycling, mechanical degradation, and the effective figure of merit of a thermoelectric module. Journal of Electronic Materials. 2013;**42**(3):372-381

[6] Ziabari A, Suhir E, Shakouri A. Minimizing thermally induced interfacial shearing stress in a thermoelectric module with low fractional area coverage. Microelectronics Journal. 2014;**45**(5):547-553

[7] Liao L-L, Dai M-J, Liu C-K, Chiang K-N. Thermo-electric finite element analysis and characteristic of thermoelectric generator with intermetallic compound. Microelectronic Engineering. 2014;**120**:194-199

[8] Mansouri N, Timm E, Schock H, Sahoo D, Kotrba A. Development of a circular thermoelectric Skutterudite couple using compression technology. Journal of Energy Resources Technology. 2016;**138**(5):052003

[9] Ur S-C, Nash P, Schwarz R. Mechanical and thermoelectric properties of Zn4Sb3 and Zn4Sb3+Zn directly synthesized using elemental powders. Metals and Materials International. 2005;**11**(6):435-441

[10] Kallel AC, Roux G, Martin CL. Thermoelectric and mechanical properties of a hot pressed nanostructured n-type Si80Ge20 alloy. Materials Science and Engineering. 2013; **564**:65-70

[11] Bathula S, Jayasimhadri M, Dhar A. Mechanical properties and microstructure of spark plasma sintered nanostructured p-type SiGe thermoelectric alloys. Materials and Design. 2015;**87**:414-420

[12] Zhao L-D, Zhang B-P, Li J-F, Zhou M, Liu W-S, Liu J. Thermoelectric and mechanical properties of nano-SiC-dispersed Bi2Te3 fabricated by mechanical alloying and spark plasma sintering. Journal of Alloys and Compounds. 2008;**455**(1-2):259-264

[13] Schmidt R, Fan X, Case E, Sarac P. Mechanical properties of Mg2Si thermoelectric materials with the addition of 0-4 vol% silicon carbide nanoparticles (SiCNP). Journal of Materials Science. 2015;**50**(11):4034-4046

[14] Case ED. Thermomechanical Properties of Thermoelectric Materials. Boca Raton, FL: CRC Press; 2012

[15] Kenfaui D, Chateigner D, Gomina M, Noudem J. Texture, mechanical and thermoelectric properties of Ca3Co4O9 ceramics. Journal of Alloys and Compounds. 2010; **490**(1-2):472-479

[16] Ravi V, Firdosy S, Caillat T, Conference L-B. Mechanical properties of thermoelectric skutterudites. AIP Conference. 2008

[17] Le P, Luo C-W, Jian S-R, Lin T-C, Yang P-F. Nanomechanical properties and fracture toughness of Bi3Se2Te thin films grown using pulsed laser deposition. Materials Chemistry and Physics. 2016;**182**:72-76

[18] Tasi C-H, Tseng Y-C, Jian S-R, Liao Y-Y, Lin C-M, Yang P-F, et al. Nanomechanical properties of Bi2Te3 thin films by nanoindentation. Journal of Alloys and Compounds. 2015;**619**:834-838

[19] He R, Gahlawat S, Guo C, Chen S, Dahal T, Zhang H, et al. Studies on mechanical properties of thermoelectric materials by nanoindentation. Physica Status Solidi. 2015; **212**(10):2191-2195

[20] Li G, Gadelrab K, Souier T, Potapov P, Chen G, Chiesa M. Mechanical properties of BixSb2−xTe3 nanostructured thermoelectric material. Nanotechnology. Nanotechnology. 2012;**23**(6):065703

[21] Anno H, Ueda T, Hirata S, Kameyama T, Iida T, Kogo Y. Mechanical properties of thermoelectric Ba8Al15Si31 Clathrate prepared by combining arc melting and spark plasma sintering techniques. Journal of Electronic Materials. 2016;**45**(3):1803-1812

[22] Gelbstein Y, Tunbridge J, Dixon R, Reece M, Ning H, Gilchrist R, et al. Physical, mechanical, and structural properties of highly efficient nanostructured n- and p-Silicides for practical thermoelectric applications. Journal of Electronic Materials. 2014;**43**(6):1703-1711

[23] Maynard J. Resonant ultrasound. Spectroscopy. 1998:132-142

[24] International A. ASTM D2845: Standard Test Method for Laboratory Determination of Pulse Velocities and Ultrasonic Elastic Constants of Rock. ASTM International; 2008

[25] Aksel C, Riley F. Young's modulus measurements of magnesia–spinel composites using load–deflection curves, sonic modulus, strain gauges and Rayleigh waves. Journal of the European Ceramic Society. 2003;**23**(16):3089-3096

[26] Plachy T, Pavel, Michal. Comparison of Two Experimental Techniques for Determination of Young's Modulus of Concrete Specimens. In: Cornelia A, Valeri, Emil, Monica, Nikos, editors. Puerto De La Cruz, Tenerife, Canary Islands, Spain: WSEAS Press; 14AD. pp. 68-71

[27] International A. Metals handbook: 01 - properties and selection: Irons, steels, and high-performance alloys. 9th ed. ASM International; 2004

[28] International A. Metals handbook: 02 - properties and selection: Nonferrous alloys and special-purpose materials. 9th ed. ASM International; 2004

[29] Schmidt R, Case E, Zhao L-D, Kanatzidis M. Mechanical properties of low-cost, earth-abundant chalcogenide thermoelectric materials, PbSe and PbS, with additions of 0-4% CdS or ZnS. Journal of Materials Science. 2015;**50**(4):1770-1782

[30] Qian L, Li M, Zhou Z, Yang H, Shi X. Comparison of nano-indentation hardness to microhardness. Surface and Coatings Technology. 2005;**195**(2-3):264-271

[31] Ren F, Case ED, Timm EJ, Schock HJ. Hardness as a function of composition for n-type LAST thermoelectric material. Journal of Alloys and Compounds. 2008;**455**(1-2):340-345

[32] Barker LM. A simplified method for measuring plane strain fracture toughness. Engineering Fracture Mechanics. 1977;**9**(2):361-369

[33] Barker LM. Of and evaluation B-F. Comparisons of fracture toughness measurements by the short rod and ASTM standard method of test for plane-strain fracture toughness of metallic materials (E 399). Journal of Testing and Evaluation. 1980

[34] International A. ASTM E 399: Standard Test Method for Linear- Elastic Plane Strain Fracture Toughness Kic of Metallic Materials. ASTM International; 2012

[35] International A. ASTM C 1421: Standard Test Methods for Determination of Fracture Toughness of Advanced Ceramics at Ambient Temperatures. ASTM International; 2010

[36] International A. ASTM B 771: Standard Test Method for Short Rod Fracture Toughness of Cemented Carbides. ASTM International; 2011

[37] Swain MV, Lawn BR. Indentation fracture in brittle rocks and glasses. International Journal of Rock Mechanics and Mining Science and Geomechanics Abstracts. 1976; **13**(11):311-319

[38] Medeiros EE, Dias A. Experimental and Numerical Analysis of Vickers Hardness Testing

[39] Eilertsen J, Subramanian MA, Kruzic JJ. Fracture toughness of Co4Sb12 and In0.1Co4-Sb12 thermoelectric skutterudites evaluated by three methods. Journal of Alloys and Compounds. 2013;**552**:492-498

[40] Anstis GR, Chantikul P, Lawn BR, Marshall DB. A critical evaluation of indentation techniques for measuring fracture toughness: I, direct crack measurements. Journal of the American Ceramic Society. 1981;**64**(9):533-538

[41] Evans A, Charles E. Fracture toughness determinations by indentation. Journal of the American Ceramic Society. 1976;**59**(7-8):371-372

[42] Niihara K, Morena R. Evaluation of KIc of brittle solids by the indentation method with low crack-to-indent ratios. Journal of Materials Science. 1982

[43] Menčík J. Nanoindentation in Materials Science. 2012

[44] Fischer-Cripps A. Nanoindentation. Springer Science + Busniess Media

[45] Barker LM. Evaluation of a New Fracture Toughness Measuring Technique, and Adaptation of the Technique to Use Ultra-Small Specimens; 1979

Chapter 5

Introduction to ($p \times n$)-Type Transverse Thermoelectrics

Matthew Grayson, Qing Shao, Boya Cui, Yang Tang, Xueting Yan and Chuanle Zhou

Additional information is available at the end of the chapter

http://dx.doi.org/10.5772/intechopen.78718

Abstract

This chapter will review ($p \times n$)-type transverse thermoelectrics (TTE). Starting with the device advantages of single-leg ($p \times n$)-type TTE's over other thermoelectric paradigms, the theory of ($p \times n$)-type TTE materials is given. Then, the figure of merit, transport equations, and thermoelectric tensors are derived for an anisotropic effective-mass model in bulk three-dimensional materials (3D), quasi-two-dimensional (2D), and quasi-one-dimensional (1D) materials. This chapter concludes with a discussion of the cooling power for transverse thermoelectrics in terms of universal heat flux and electric field scales. The importance of anisotropic ambipolar conductivity for ($p \times n$)-type TTEs highlights the need to explore noncubic, narrow-gap semiconductor or semimetallic candidate materials.

Keywords: transverse thermoelectrics, Seebeck tensor, transport equations, transverse thermoelectric figure of merit, transverse cooling power

1. Introduction

The paradigm of ($p \times n$)-type transverse thermoelectrics (TTE) [1–3] occurs in an anisotropic semiconductor or semimetal with *p*-type Seebeck response along one axis and *n*-type Seebeck orthogonal, whereby an appropriately applied electric current at an angle with respect to these axes can induce a *purely orthogonal* heat flow (the transverse Peltier effect), or conversely, an applied temperature gradient can generate a *purely orthogonal* electric field (the transverse Seebeck effect).

Transverse thermoelectric effects in general [4–6] require a broken symmetry to generate the necessary *off-diagonal* component in the Seebeck tensor. An off-diagonal component of the

Seebeck tensor S_{xy} describes, for example, an x-direction gradient in the electrochemical potential $\nabla_x V$ that results from a transverse y-direction temperature gradient $\nabla_y T$, expressed as

$$S_{xy} = -\frac{\nabla_x V}{\nabla_y T} \tag{1}$$

within the full tensor expression

$$\nabla_i V = -\sum_j S_{ij} \nabla_j T \tag{2}$$

where $i, j \in (x, y, z)$. The Kelvin relations show how the corresponding transverse Peltier coefficient is related to the transverse Seebeck coefficient:

$$\pi_{xy} = S_{xy} T \tag{3}$$

For standard thermoelectrics (called "longitudinal thermoelectrics" in the present context), the Seebeck tensor is typically assumed to be diagonal and isotropic, and intentionally doped to be unipolar (entirely n-type or p-type), with no off-diagonal terms. Although many materials found in standard thermoelectrics are anisotropic in their crystalline form, for optimal thermoelectric performance these crystals are typically crushed into a powder and sintered into a dense randomly oriented polycrystal with many grain boundaries to reduce thermal conductivity, resulting in a macroscopically isotropic Seebeck tensor. For example, even if the original crystals were to have a Seebeck tensor $\mathbf{S_0}$ that was anisotropic,

$$S_0 = \begin{bmatrix} S_{xx} & 0 & 0 \\ 0 & S_{yy} & 0 \\ 0 & 0 & S_{zz} \end{bmatrix} \tag{4}$$

the resulting Seebeck tensor S_{snt} of the sintered polycrystal of randomly oriented grains becomes isotropic,

$$S_{snt} = \begin{bmatrix} S_{tr} & 0 & 0 \\ 0 & S_{tr} & 0 \\ 0 & 0 & S_{tr} \end{bmatrix}. \tag{5}$$

If the thermal conductivity of the original crystal is approximately isotropic, or if the subsequent sintered material is dominated by grain boundary scattering, the diagonal components of the sintered Seebeck tensor can be approximated by the trace of the original anisotropic crystal, $S_{\text{tr}} = \frac{1}{3} tr(\mathbf{S_0})$.

To generate off-diagonal terms, a transport symmetry must be broken. One way to do this is with a magnetic field, which *breaks time-reversal symmetry*. According to the Nernst-Ettingshausen effect (N-E) when a magnetic field is applied to a medium with ambipolar electron and hole conduction, an antisymmetric off-diagonal Seebeck response $S_{ij} = -S_{ji} = \alpha B$ is induced proportional to the

field strength B with N-E coefficient α and $i \neq j$. For a review of the Nernst-Ettingshausen effect, please see [4, 7] and references therein. A magnetic field-induced transverse thermoelectric effect has also been observed in unipolar materials, where a "spin voltage" is generated orthogonal to a temperature gradient, named spin Seebeck effect [8–11].

Similarly, *structural asymmetry* can cause nonzero off-diagonal Seebeck terms, provided the asymmetry is maintained at a macroscopic scale. For example, sintering of randomly oriented polycrystals is disallowed, but in certain cases, twinned polycrystals with common c-axis alignment might still manifest the necessary anisotropy. If the diagonal Seebeck tensor elements S_{ii} and S_{jj} in Eq. (4) are not equal, a simple rotation $\mathbf{R}$ can induce symmetric nonzero off-diagonal terms $S_{ij} = +S_{ji}$ for $i \neq j$. With appropriate choice of the rotation tensor $\mathbf{R}$, the off-diagonal terms become

$$S_{ij} = -\sum_{k} R_{ik}^{-1} S_{kk} R_{kj} \tag{6}$$

Note that a *purely* p- or n-type *unipolar* material can never generate *purely* orthogonal Seebeck response—any transverse Seebeck will always be accompanied by a finite longitudinal Seebeck response. Such unipolar transverse Seebeck effects have been observed and studied, for example, in Refs. [12–16].

A more interesting structural asymmetry is one that includes an ambipolar Seebeck tensor, whereby the diagonalized Seebeck tensor elements S_{xx}, S_{yy}, and S_{zz} in Eq. (3) have at least one p-type $S > 0$ along one direction and at least one n-type $S < 0$ along another direction, as illustrated in **Figure 1**.

In such a material, there *does* exists a rotation $\mathbf{R}$ such that the Seebeck response is *purely orthogonal*, such that an applied thermal gradient can induce a purely orthogonal electric field, or equivalently,

$$\nabla T \cdot \nabla V = 0 \tag{7}$$

where ∇V is determined from ∇T via Eq. (2). A well-documented example of such a transverse thermoelectric is the composite multilayered transverse thermoelectric [4–6, 17, 21, 22] (see **Figure 3**), whereby a sequence of macroscopic alternating n- (typically metallic or semimetallic) and p-type (semiconducting) layers create the necessary structural asymmetry. Orthogonal to the layers, electrical and thermal resistance is in series from adjacent p- to n-layers, whereas parallel to the layers, the electrical and thermal conduction is in parallel.

The most recent addition to the lexicon of transverse thermoelectric phenomena is single crystals that themselves possess orthogonal p- and n-type Seebeck components, and which the authors have dubbed "($p \times n$)-type" [1, 2]. The cause of such ambipolar behavior is fundamentally different from that of the composite multilayered materials, since the ($p \times n$)-type materials are bulk crystals, and thus both the electrical and thermal conductions are in parallel in *all* directions. Although this may seem like a trivial distinction, the consequences are profound. Once a bulk crystal is solely responsible for the ambipolar Seebeck tensor, this material can be scaled to arbitrary size—large or small—allowing one to envision both sheets

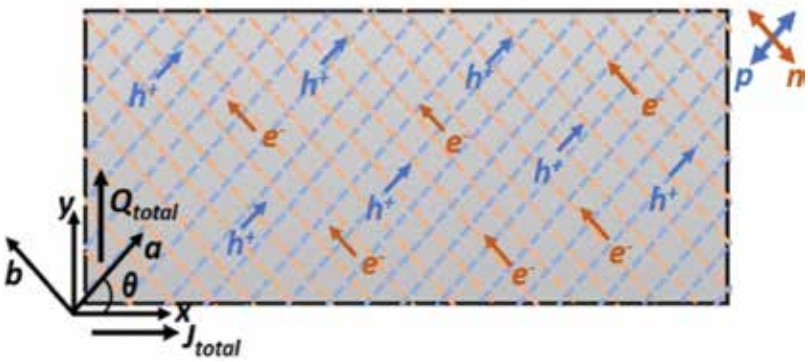

Figure 1. The ($p \times n$)-type thermoelectrics have p-type dominant conduction and Seebeck coefficient along the a-axis, where holes are the main charge carriers to transport (blue dashed lines), and n-type-dominant conduction and Seebeck coefficient along the orthogonal b-axis, where electrons are the main charge carriers to transport (orange dashed lines). The ($p \times n$)-type character is notated by the blue and orange crossed arrow symbol at the upper right. The movement of electrons (orange arrows) and holes (blue arrows) in orthogonal directions results in net charge current J_x to the right and net particle or heat flow Q_y up. The carrier transport shown in this figure can be driven either by drift due to an electric field along the $+x$ direction or by diffusion due to a temperature gradient along the $-y$ direction. As shown at the bottom left corner of this figure, the rotation angle between x-y transport coordinate system and a-b crystal axis coordinate system is θ.

of active cooling layers as well as microscale cooling applications for integrated thermal management. Furthermore, because such ambipolar materials operate close to the intrinsic limit with minimal doping, there is no danger of dopant freeze-out; thus, these materials can be expected to achieve transverse thermoelectric performance at arbitrarily low temperatures, provided that the band gap is of order the operation temperature. Finally, the ($p \times n$)-type materials continue to have the same structural advantage of all transverse phenomena, namely that they can be implemented as single-leg devices, allowing for improved cooling differentials in tapered structures [19] as well as geometric implementation in other unconventional geometries that standard thermoelectrics cannot achieve.

Because the underlying phenomenology of these ($p \times n$)-type transverse thermoelectrics materials has only recently been introduced, their band characteristics are just now being explored theoretically and experimentally. Section 2 reviews intuition behind how ($p \times n$)-type materials function in simple devices, while Section 3 reviews the key band-theoretical equations for generating the necessary ambipolar Seebeck tensor in bulk materials from a simple effective mass model for 3D bulk semiconductors. Because quasi-2D and quasi-1D materials represent extreme limits of anisotropic band structure, the equations for calculating Seebeck tensors in such limits are also provided. Section 4 reviews how the transverse figure of merit is optimized for transverse materials in general, and Section 5 identifies the cooling power for devices made of such transverse materials.

2. ($p \times n$)-type transverse thermoelectric devices

($p \times n$)-Type transverse thermoelectrics have potential device advantages over other thermoelectric solutions when considering microscale devices or cryogenic operation. Conventional

http://dx.doi.org/10.5772/intechopen.78718

longitudinal thermoelectric devices (**Figure 2**) [6] or multilayer composite transverse thermoelectrics (**Figure 3**) [4, 5, 17] require at least one component with extrinsic *p*- or *n*-type doping, which limits their use at cryogenic temperatures since the dopants freeze out. A typical minimum operation temperature is $T = 150$ K. Similarly, the minimum device size is limited for the multileg structure of conventional longitudinal thermoelectric in **Figure 2**. And for multilayer composite transverse thermoelectrics of **Figure 3**, the macroscopic stacked sublayers set a minimum device size on the order of centimeters. For this reason, submillimeter scale devices are not feasible with either of the above thermoelectric paradigms.

On the other hand, ($p \times n$)-type transverse thermoelectric bulk materials have distinct advantages in the cryogenic and size-scaling regimes since they operate as nominally undoped, single-leg devices. Transverse thermoelectric bulk materials have optimal performance near intrinsic doping with ambipolar electron and hole transport. As a consequence, narrow gap ($p \times n$)-type materials should be able to work at arbitrarily low temperatures down to the cryogenic limit. The single-leg geometry also makes it straightforward to scale up to unconventional sheet-like geometries or to scale down to microscale devices since the full thermoelectric function is contained within a single material.

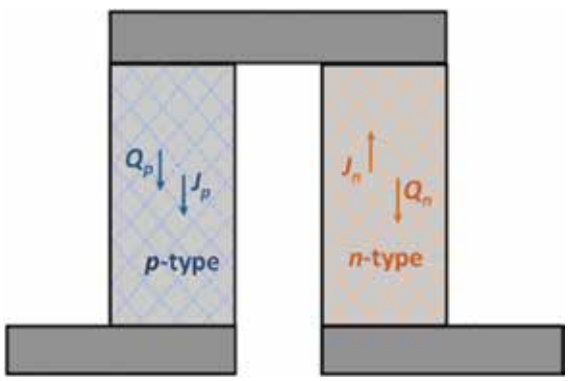

Figure 2. The conventional thermoelectric heat pump or Peltier refrigerator with one *p*-type leg and the other *n*-type leg will drive heat flow $\boldsymbol{Q}$ parallel or antiparallel, respectively, to the conventional electrical current $\boldsymbol{J}$. Solid gray rectangles represent metal contacts.

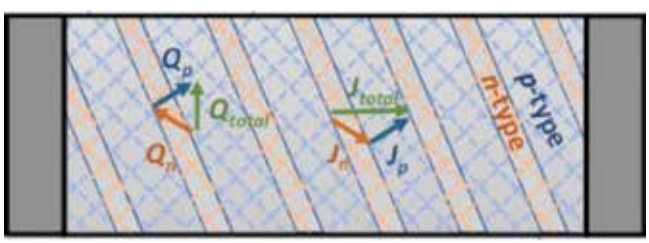

Figure 3. Stacked multilayer synthetic transverse thermoelectric. Alternating layers of *p*-type semiconductor and *n*-type (semi)metal create a stacked composite whose behavior in a tilted electric field results in skewed electron and hole currents within each layer, giving a net transverse Seebeck effect. Solid gray rectangles represent metal contacts.

There are additional device advantages to single-leg thermoelectrics that result from the reduced fabrication complexity. For conventional two-leg thermoelectric devices, it is known that by stacking thermoelectric units one on top of the other with ever smaller areas, the resulting thermoelectric cascade can achieve a lower base temperature than a single stage, alone. When longitudinal thermoelectrics require multiple devices and multiple stages [18] to create such a cascade structure, transverse thermoelectrics can achieve the same "cascade" function by simply tapering a single thermoelectric leg [19]. The result acts as an "infinite-stage" Peltier refrigerator, which achieves superior cooling efficiency compared to the multiple discrete-element cascade stages by simply tapering a piece of transverse thermoelectric as a trapezoid or exponential taper. The tapering strategy allows one to achieve enhanced temperature differences even with a somewhat smaller transverse figure of merit $z_{xy}T$ [1, 19].

A typical longitudinal thermoelectric device structure is shown in **Figure 2**. As can be observed from the schematic diagram, each thermocouple unit has two legs, one *p*-type leg and one *n*-type leg. For Peltier refrigeration, the common side of both legs on the top is connected to the object to be cooled while the other side is connected to the heat sink. Following the flow of heat Q_p and Q_n in each leg, the top junction is cooled and the heat is transferred to the bottom heat sink.

The TTE unit in **Figure 4**, on the other hand, is made of one single material. Depending on the direction of current flow, only one kind of charge carrier, holes or electrons, will dominate conduction within each leg. For instance, we can observe electron current J_n in the right branch and hole current J_p in the left counterpart. Moreover, the heat current of both legs is flowing downward, just like the heat flow of the conventional device.

As demonstrated in **Figure 5**, a simpler single-leg geometry is possible with transverse thermoelectrics. With the electrons and holes, transportation directions of the $p \times n$-type transverse thermoelectric are indicated with the crossed-arrow symbol on the upper right. The macroscopic transport of charge and heat is a vector sum of the net electron-hole electrical and heat currents, respectively. This picture depicts net charge current J_x to the right and net heat current Q_y up.

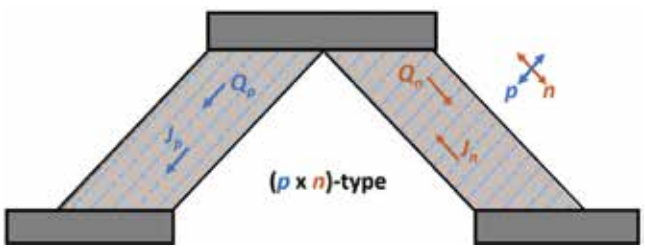

Figure 4. Sketch of $p \times n$-type transverse thermoelectrics in a device structure mimicking that of the standard double-leg thermoelectric device in **Figure 2**. Here, the same material can be used for both legs, as long as the crystal axis is oriented parallel to the *p*-type direction for the *p*-leg current J_p and parallel to the *n*-type direction for the *n*-leg current J_n. Solid gray rectangles represent metal contacts.

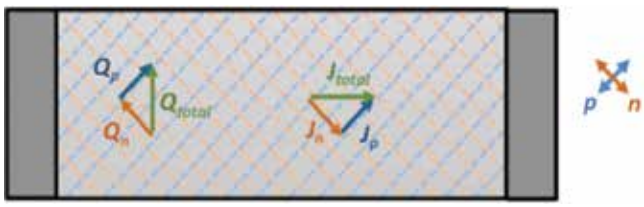

Figure 5. Microscopic electron-hole picture of the $p \times n$-type transverse thermoelectric depicts net charge current J_{total} to the right, and net particle or heat current Q_{total} up, based on the vector sum of charge current of holes Q_p and charge current of electrons Q_n, heat current of holes J_p and heat current of electrons J_n. Solid gray rectangles represent metal contacts.

An important quantity in comparing different transverse thermoelectric materials is the transverse figure of merit $z_{xy}T$, which is used in the expressions of device efficiency and performance (see Section 5). For transverse materials, the dimensionless figure of merit $z_{xy}T$ is given as:

$$z_{xy}T = \frac{{S_{xy}}^2}{\rho_{xx}\kappa_{yy}}T \tag{8}$$

In the transverse figure of merit expression above, the off-diagonal Seebeck element S_{xy} in the numerator is clearly the relevant component for generating a transverse thermoelectric response. In the denominator, to minimize Joule heating along the x-direction of current flow, a small resistivity component ρ_{xx} is needed; and to minimize passive return of Fourier heat in the y-direction of the temperature differential, a small thermal conductivity κ_{yy} is needed. Note that for longitudinal thermoelectrics, the expression for zT typically includes the conductivity in the numerator since the scalar equation $\sigma = 1/\rho$ is valid. However, when solving for transverse thermoelectric tensors, which by necessity have anisotropic conductivities, one must take care to calculate the resistivity component and place it in the denominator of the expression above, since, in general $\sigma_{xx} \neq 1/\rho_{xx}$.

3. Seebeck tensor of ($p \times n$)-type transverse thermoelectrics

3.1. Thermoelectric tensors definition

Below, we derive how parallel anisotropic electron and hole conductivity give rise to the observed transverse thermoelectric behavior in ($p \times n$)-type thermoelectrics. For an intrinsic semiconductor with anisotropic conductivity, we describe the electrical conductivity of the separate electron and hole bands with tensors $\boldsymbol{\sigma_n}$ and $\boldsymbol{\sigma_p}$ and the Seebeck response with tensors as $\mathbf{s_n}$ and $\mathbf{s_p}$. Considering the conduction along the two principal axes of interest

labeled $\boldsymbol{a}$ and $\boldsymbol{b}$, which manifest the transport anisotropy, we obtain the following diagonal matrices:

$$\begin{aligned} \sigma_n &= \begin{bmatrix} \sigma_{n,aa} & 0 \\ 0 & \sigma_{n,bb} \end{bmatrix}, \quad \sigma_p = \begin{bmatrix} \sigma_{p,aa} & 0 \\ 0 & \sigma_{p,bb} \end{bmatrix} \\ s_{\mathrm{n}} &= \begin{bmatrix} s_n & 0 \\ 0 & s_n \end{bmatrix}, \qquad s_p = \begin{bmatrix} s_p & 0 \\ 0 & s_p \end{bmatrix}, \end{aligned} \tag{9}$$

where the diagonal elements satisfy $s_n < 0$, $s_p > 0$. Note that single-band Seebeck tensors $\mathbf{s}_n$ and $\mathbf{s}_p$ are typically isotropic, but conductivity tensors $\boldsymbol{\sigma}_n$ and $\boldsymbol{\sigma}_p$ can be strongly anisotropic (see Sections 3.3–3.5). The total conductivity tensor $\boldsymbol{\Sigma}$ and total resistivity tensor $\mathbf{P}$ are related by $\boldsymbol{\Sigma} = \mathbf{P}^{-1} = \boldsymbol{\sigma}_n + \boldsymbol{\sigma}_p$.

The total Seebeck tensor for the two-band system is defined as the weighted sum of the single-band Seebeck tensors by the conductivity tensors:

$$\mathbf{S} = \left(\boldsymbol{\sigma}_p + \boldsymbol{\sigma}_n\right)^{-1}\left(\boldsymbol{\sigma}_p s_p + \boldsymbol{\sigma}_n s_n\right) \tag{10}$$

We remark again that this *parallel conduction* of bands within the same material is fundamentally different from stacked synthetic multilayer transverse thermoelectrics of **Figure 3** in which the out-of-plane Seebeck arises from *series* electrical and thermal *resistances* of two different materials. From Eq. (10), if oppositely charged carriers dominate conduction along a and b, respectively, the total Seebeck coefficients in the two orthogonal directions will have opposite signs. If we assume that p-type conduction dominates along $a-$ and n-type, conduction dominates along b, then the total Seebeck tensor is

$$\boldsymbol{S} = \begin{bmatrix} S_{p,aa} & 0 \\ 0 & S_{n,bb} \end{bmatrix}, \tag{11}$$

with elements

$$\begin{aligned} S_{p,aa} &= \frac{S_p\sigma_{p,aa} + S_n\sigma_{n,aa}}{\sigma_{p,aa} + \sigma_{n,aa}} > 0, \\ S_{n,bb} &= \frac{S_p\sigma_{p,bb} + S_n\sigma_{n,bb}}{\sigma_{p,bb} + \sigma_{n,bb}} < 0, \end{aligned} \tag{12}$$

where the first inequality is valid provided that p-type conduction in the a-direction is sufficiently dominant $\sigma_{p,aa}/\sigma_{n,aa} > \left|\frac{s_n}{s_p}\right|$, and the second valid provided n-type conduction in the b-direction is sufficiently dominant $\sigma_{n,bb}/\sigma_{p,bb} > |s_p/s_n|$. The result is the desired ambipolar Seebeck tensor where one of the diagonal elements has opposite sign.

When transverse thermoelectric materials are cut into a shape such that the transport directions x, y are at an angle θ to the principal axes a and b, as shown in **Figure 1**, the Seebeck tensor in the x-y transport basis can yield the necessary off-diagonal terms:

$$\begin{aligned}\mathbf{S}' &= \begin{bmatrix}\cos\theta & -\sin\theta \\ \sin\theta & \cos\theta\end{bmatrix}\begin{bmatrix}S_{p,aa} & 0 \\ 0 & S_{n,bb}\end{bmatrix}\begin{bmatrix}\cos\theta & \sin\theta \\ -\sin\theta & \cos\theta\end{bmatrix} \\ &= \begin{bmatrix}\cos^2\theta S_{p,aa} + \sin^2\theta S_{n,bb} & \sin\theta\cos\theta\left(S_{p,aa} - S_{n,bb}\right) \\ \sin\theta\cos\theta\left(S_{p,aa} - S_{n,bb}\right) & \cos^2\theta S_{n,bb} + \sin^2\theta S_{p,aa}\end{bmatrix} \\ &= \begin{bmatrix}S_{xx} & S_{xy} \\ S_{yx} & S_{yy}\end{bmatrix}\end{aligned} \tag{13}$$

This nonzero off-diagonal component of the Seebeck tensor S_{xy} in the transport basis is the essential prerequisite for any transverse thermoelectric effect.

3.2. Thermoelectric tensor calculation

In the following, we will demonstrate how the anisotropic electrical transport tensors of each separate band can be calculated. Standard longitudinal thermoelectric devices have both heat and electrical current flowing along the same axis, so their electrical resistivity, thermal conductivity, and Seebeck coefficient can be treated as scalars. In contrast, the thermoelectric properties in an anisotropic thermoelectric material must be described by tensors for the electrical conductivity $\boldsymbol{\sigma}$, the Seebeck coefficient $\boldsymbol{S}$ and the thermal conductivity $\boldsymbol{\kappa}$. The anisotropic transport tensors of each electron or hole band can be calculated according to the material's band structure, and then the equations of the previous section can be used to determine the total Seebeck and resistivity tensors of the two-band system. Because the compounds of interest tend to be highly anisotropic, in addition to the 3D effective mass model, we will also consider the case of quasi-2D and quasi-1D materials, which host effective mass band-conduction along two axes or one axis, respectively, and hopping transport along the remaining orthogonal axes.

We, therefore, perform a complete derivation of the thermoelectric tensor components from first principles corresponding to 3D, 2D, and 1D anisotropic transport scenarios. The thermal conductivity tensor $\boldsymbol{\kappa}$ is ideally obtained from experimental measurements of the material of interest, whereas transport tensors of the Seebeck $\boldsymbol{S}$ and electrical resistivity $\boldsymbol{\rho}$ can be calculated with simple assumptions outlined below if the band structure is known. The derivation of thermoelectric equations uses the intuitive notations borrowed from Chambers [20] except that instead of scalar coefficients, here, we show the complete tensor derivations.

When both an electric field $\mathbf{E}$ and a temperature gradient $\mathbf{G} = -\nabla T$ are present, the electrical current $\mathbf{J}$ and heat flow $\mathbf{Q}$ are given by

$$\begin{aligned}\mathbf{J} &= \boldsymbol{\sigma}\mathbf{E} + \mathbf{C}\mathbf{G} \\ \mathbf{Q} &= \mathbf{D}\mathbf{E} + \boldsymbol{\kappa}\mathbf{G}\end{aligned} \tag{14}$$

where $\boldsymbol{\sigma}$ is the electrical conductivity tensor, $\boldsymbol{\kappa}$ is the thermal conductivity tensor , $\boldsymbol{D}$ is related to the Peltier tensor $\boldsymbol{\Pi}$ and $\boldsymbol{\sigma}$ by $\boldsymbol{\Pi} = \mathbf{D}\boldsymbol{\sigma}^{-1}$, $\mathbf{C}$ is related to the Seebeck tensor $\boldsymbol{S}$ and $\boldsymbol{\sigma}$ by $\mathbf{S} = \mathbf{C}\boldsymbol{\sigma}^{-1}$, and $\mathbf{S}$ follows the Kelvin relation $\mathbf{S} = \boldsymbol{\Pi}/T = \mathbf{D}\boldsymbol{\sigma}^{-1}/T$. These equations are typically transformed so that $\boldsymbol{J}$ and $\boldsymbol{G}$ are the independent variables

$$\begin{aligned}\mathbf{E} &= \boldsymbol{\rho}\mathbf{J} - \mathbf{S}\mathbf{G} \\ \mathbf{Q} &= \boldsymbol{\Pi}\mathbf{J} + \boldsymbol{\kappa}^{\mathbf{c}}\mathbf{G}.\end{aligned} \tag{15}$$

where $\boldsymbol{\rho}=\boldsymbol{\sigma}^{-1}$ is the electrical resistivity tensor, and the normally measured open circuit thermal conductivity $\boldsymbol{\kappa}^{\mathbf{c}}$ is defined as $\boldsymbol{\kappa}^{\mathbf{c}}=\boldsymbol{\kappa}-\boldsymbol{\sigma}\mathbf{S}\boldsymbol{\Pi}$.

$\boldsymbol{\sigma}$ and $\mathbf{D}$ tensor components σ_{ij} and D_{ij} can be calculated from the band structure

$$\sigma_{ij} = \int_0^\infty d\epsilon \frac{\partial f_0}{\partial \epsilon}\sigma_{ij}(\epsilon) \tag{16}$$

$$\sigma_{ij}(\epsilon) = \frac{e^2}{4\pi^3\hbar}\int \frac{v_{ki}}{|v_k|}v_{kj}\tau_k dS_k \tag{17}$$

$$D_{ij} = \int d\epsilon \frac{\partial f_0}{\partial \epsilon}D_{ij}(\epsilon) \tag{18}$$

$$D_{ij}(\epsilon) = \frac{1}{e}(\epsilon - \mu)\sigma_{ij}(\epsilon) \tag{19}$$

where ϵ is the carrier energy relative to the edge of the energy band, $f_0(\epsilon) = 1/\left(1 + e^{-\epsilon/k_B T}\right)$ is the Fermi-Dirac distribution function, e is the electron charge, and E_F is the chemical potential. We assume that the scattering time $\tau = \gamma\epsilon^s$ obeys a power law in the energy of the carrier relative to the band minimum with exponent s. $\boldsymbol{v}_{\mathbf{k}}$ is the carrier velocity vector for wave vector $\mathbf{k}$, which is defined as $v_{\boldsymbol{k}}=v_{\mathbf{k}a}\hat{\boldsymbol{a}}+v_{\mathbf{k}b}\hat{\boldsymbol{b}}+v_{\mathbf{k}c}\hat{\boldsymbol{c}}$ with each velocity component $v_{ki} = \frac{d\epsilon}{\hbar dk_i}$. S_k is the equienergy k-space surface area at energy ϵ and wave vector k. The indices i, j, l in the subscripts represent three orthogonal crystal axes a, b, and c.

In the next subsections, we will analyze 3D, 2D, and 1D transport and deduce their thermoelectric tensors. The 3D anisotropic case is for anisotropic effective mass in bulk materials, e.g., an ellipsoidal effective mass such as in noncubic lattices. The 2D anisotropic case is relevant for quasi-2D materials and can be found in parallel quantum wells or weakly coupled superlattice layers with approximately infinite cross-plane effective mass. The 1D anisotropic case can be applied to quasi-1D materials or arrays of nanowires or nanotubes, which have weak tunnel coupling in two directions.

3.3. Three-dimensional transport

For a general orthorhombic lattice, the carrier energy relative to the band edge in a given energy band can be expressed with a three-dimensional (3D) effective mass approximation:

$$\epsilon = \frac{\hbar^2 k_a^2}{2m_a} + \frac{\hbar^2 k_b^2}{2m_b} + \frac{\hbar^2 k_c^2}{2m_c} \tag{20}$$

where m_i is the effective mass in the i direction. In spherical coordinates, the wave vectors and the velocity are as follows:

$$k_a = \frac{\sqrt{2m_a\epsilon}}{\hbar}\sin\alpha\cos\phi \tag{21}$$

$$k_b = \frac{\sqrt{2m_b\epsilon}}{\hbar}\sin\alpha\sin\phi \tag{22}$$

$$k_c = \frac{\sqrt{2m_c\epsilon}}{\hbar}\cos\alpha \tag{23}$$

$$\nu_k = \sqrt{\frac{2\epsilon}{m_a}}\sin\alpha\cos\phi\hat{a} + \sqrt{\frac{2\epsilon}{m_b}}\sin\alpha\sin\phi\hat{b} + \sqrt{\frac{2\epsilon}{m_c}}\cos\alpha\hat{c} \tag{24}$$

where α is the polar angle and ϕ is the azimuthal angle.

If the principle axes of mass anisotropy are chosen as the coordinate, then the transport tensors are all diagonal, and the diagonal components of the energy-dependent 3D conductivity become as

$$\begin{aligned}\sigma_{ii}^{3D}(\epsilon) &= \frac{e^2}{4\pi^3\hbar}\int_0^{2\pi} d\phi \int_0^{\pi} d\alpha \frac{v_{ki}}{|v_k|} v_{ki}\tau_k dS_k \\ &= \frac{e^2\gamma\epsilon^s}{4\pi^3\hbar}\int_0^{2\pi} d\phi \int_0^{\pi} d\alpha \frac{v_{ki}^2 \frac{2\epsilon\sqrt{m_i m_j m_l}}{\hbar}\sqrt{\frac{\sin^2\alpha\cos^2\phi}{m_i} + \frac{\sin^2\alpha\sin^2\phi}{m_j} + \frac{\cos^2\alpha}{m_l}}}{\sqrt{2\epsilon}\sqrt{\frac{\sin^2\alpha\cos^2\phi}{m_i} + \frac{\sin^2\alpha\sin^2\phi}{m_j} + \frac{\cos^2\alpha}{m_l}}} \\ &= \frac{2\sqrt{2}e^2\gamma}{3\pi^2\hbar^3}\sqrt{\frac{m_j m_l}{m_i}}\epsilon^{s+3/2}\end{aligned} \tag{25}$$

Integrating this expression in Eq. (16) yields the final conductivity tensor:

$$\sigma_{ii}^{3D} = \frac{2\sqrt{2}e^2\gamma}{3\pi^2\hbar^3}\sqrt{\frac{m_j m_l}{m_i}}(k_B T)^{s+\frac{3}{2}}\Gamma\left(s+\frac{5}{2}\right)F_{\frac{3}{2}+s}\left(\frac{\mu_o}{k_B T}\right), \tag{26}$$

where $E_F = 0$ is defined at the valence band edge, E_g is the bandgap, the chemical potential μ_o is defined relative to the band edge $\mu_o = E_F - E_g$ for the conduction band and $\mu_o = -E_F$ for the valence band, and $F_n(\xi)$ is the Fermi integral $F_n(\xi) = \int_0^{\infty} \frac{t^n}{1+e^{t-\xi}}\mathrm{d}t$.

The Seebeck tensor is isotropic for a single band, and the diagonal Seebeck component is

$$S_{ii}^{3D} = \frac{1}{eT}\frac{\int d\epsilon \frac{\partial f_0}{\partial\epsilon}(\epsilon-\mu_o)\sigma_{ii}^{3D}(\epsilon)}{\sigma_{ii}^{3D}} = \frac{k_B}{e}\left[\frac{(5/2+s)F_{s+3/2}\left(\frac{\mu_o}{k_B T}\right)}{(3/2+s)F_{s+1/2}\left(\frac{\mu_o}{k_B T}\right)} - \frac{\mu_o}{k_B T}\right] \tag{27}$$

3.4. Quasi-two-dimensional transport

If carriers propagate in one direction via weak tunnel coupling, then the lattice behaves as a quasi-2D lattice or as a superlattice with weak tunneling between layers. If, for example, carriers follow the effective mass approximation in the $a-c$ plane and obey a weak-coupling model in the b direction, the following energy dispersion can be assumed as follows:

$$\epsilon = \frac{\hbar^2 k_a^2}{2m_a} + \frac{\hbar^2 k_c^2}{2m_c} + 2t_b(1 - \cos k_b d) \tag{28}$$

where d is the superlattice period or quantum well width and t_b is the nearest neighbor hopping matrix element between the weakly coupled layers. In-plane momenta are

$$\begin{aligned} k_a &= \frac{\sqrt{2m_a(\epsilon - 2t_b(1 - \cos(k_b d)))}}{\hbar}\cos\phi \\ k_c &= \frac{\sqrt{2m_c(\epsilon - 2t_b(1 - \cos(k_b d)))}}{\hbar}\sin\phi. \end{aligned} \tag{29}$$

Assuming that the in-plane mass $m_a = m_c$ and that k_r is the wave vector in $a-c$ plane, we obtain the conductivity tensor components:

$$\begin{aligned} \sigma_{aa}^{2D} = \sigma_{cc}^{2D} &= \frac{e^2\gamma}{\pi\hbar^2 d}(k_B T)^{s+1}\Gamma(s+2)F_{1+s}\left(\frac{\mu_o}{k_B T}\right) \\ \sigma_{bb}^{2D} &= \frac{2e^2\gamma m_a t_b^2 d}{\pi\hbar^4}(k_B T)^{s}\Gamma(s+1)F_{s}\left(\frac{\mu_o}{k_B T}\right) \end{aligned} \tag{30}$$

The Seebeck tensor remains diagonal with components:

$$\begin{aligned} S_{ii}^{2D} &= \frac{1}{eT}\frac{\int d\epsilon \frac{\partial f_0}{\partial \epsilon}(\epsilon - \mu_o)\sigma_{ii}^{2D}(\epsilon)}{\sigma_{ii}^{2D}} \\ &= \frac{k_B}{e}\left[\frac{(2+s)F_{s+1}\left(\frac{\mu_o}{k_B T}\right)}{(1+s)F_s\left(\frac{\mu_o}{k_B T}\right)} - \frac{\mu_o}{k_B T}\right] \end{aligned} \tag{31}$$

3.5. Quasi-one-dimensional transport

If carriers propagate in two orthogonal directions via weak tunnel coupling, the lattice is a quasi-1D lattice with weak coupling between chains. Hence, if carriers obey the effective mass approximation in the a-direction only and tunnel perpendicularly in the b- and c-directions, the following energy dispersion can be assumed:

$$\epsilon = \frac{\hbar^2 k_a^2}{2m_a} + 2t_b(1 - \cos k_b d_b) + 2t_c(1 - \cos k_c d_c) \tag{32}$$

where t_b and t_c are the nearest neighbor hopping matrix elements between the weakly coupled nanowires, and d_b and d_c are the distances between nanowires in the b- and c-directions. We can arrive at an analytical solution in the second line of $\sigma_{ii}^{1D}(\epsilon)$ derivations only under the assumption that the carrier velocity in the tunnel directions is much smaller than that in the wire direction, $|v_{ka}| \gg |v_{kb}|, |v_{kc}|$. So, the conductivity components are as follows:

$$\begin{aligned}\sigma_{aa}^{1D} &= \frac{\sqrt{2}e^2\gamma}{\pi\hbar d_b d_c\sqrt{m_a}}(k_BT)^{s+1/2}\Gamma\left(s+\frac{3}{2}\right)F_{1/2+s}\left(\frac{\mu_o}{k_BT}\right)\\ \sigma_{bb}^{1D} &= \frac{\sqrt{2}e^2\gamma t_b^2 d_b\sqrt{m_a}}{\pi\hbar^3 d_c}(k_BT)^{s-1/2}\Gamma\left(s+\frac{1}{2}\right)F_{s-1/2}\left(\frac{\mu_o}{k_BT}\right)\end{aligned} \tag{33}$$

The diagonal Seebeck tensor components are

$$\begin{aligned}S_i^{i1D} &= \frac{1}{eT}\frac{\int d\epsilon\frac{\partial f_0}{\partial\epsilon}(\epsilon-\mu_o)\sigma_i^{i1D}(\epsilon)}{\sigma_i^{i1D}}\\ &= \frac{k_B}{e}\left[\frac{(3/2+s)F_{s+1/2}\left(\frac{\mu_o}{k_BT}\right)}{(1/2+s)F_{s-1/2}\left(\frac{\mu_o}{k_BT}\right)}-\frac{\mu_o}{k_BT}\right]\end{aligned} \tag{34}$$

4. Transverse thermoelectric figure of merit $z_{xy}T$

Inserting the conductivity and Seebeck tensors for the individual bands from Sections 3.3–3.5 into Eq. (10), and then rotating according to Eq. (13), the tensor components of all transport quantities in the x-y transport basis can be determined. The transverse thermoelectric figure of merit $z_{xy}(\theta)T$ is defined as:

$$z_{xy}(\theta)T = \frac{S_{xy}^2}{\kappa_{yy}\rho_{xx}} = \frac{\sin^2\theta\cos^2\theta\left(S_{p,aa}-S_{n,bb}\right)^2}{\left(\sin^2\theta\kappa_{aa}+\cos^2\theta\kappa_{bb}\right)\left(\cos^2\theta\rho_{aa}+\sin^2\theta\rho_{bb}\right)}. \tag{35}$$

We define the angle $\theta_\perp$ as that which maximizes $z_{xy}(\theta)T$:

$$\cos^2\theta_\perp = \frac{1}{1+\sqrt{\frac{\kappa_{bb}/\kappa_{aa}}{\rho_{bb}/\rho_{aa}}}} \tag{36}$$

and the maximum value $z_\perp T$ becomes

$$z_\perp T = z_{xy}(\theta_\perp)T = \frac{\left(S_{p,aa}-S_{n,bb}\right)^2 T}{\left(\sqrt{\rho_{aa}\kappa_{aa}}+\sqrt{\rho_{bb}\kappa_{bb}}\right)^2} \tag{37}$$

Eq. (36) shows that $\theta_\perp$ is independent of the Seebeck anisotropy, and it approaches $\frac{\pi}{4}$ when the thermal conductivity anisotropy matches the resistivity anisotropy $\frac{\kappa_{bb}}{\kappa_{aa}} = \frac{\rho_{bb}}{\rho_{aa}}$.

In semiconductors, the thermal conductivity is usually dominated by the lattice thermal conductivity [2]. Therefore, under the assumption of isotropic $\boldsymbol{\kappa}$, we define a transverse power factor $PF_{\perp}$ as

$$PF_{\perp} = \frac{\left(S_{p,aa} - S_{n,bb}\right)^2}{\left(\sqrt{\rho_{aa}} + \sqrt{\rho_{bb}}\right)^2}, \tag{38}$$

where $\mathbf{S}$ and $\boldsymbol{\rho}$ tensors can be calculated by the use of semiclassical Boltzmann transport theory for the corresponding scattering mechanisms [2]. Thus, for a given band structure, $PF_{\perp}$ can be theoretically estimated to evaluate the performance of transverse thermoelectrics.

4.1. Transport equations

The current flow $\mathbf{J} = J_x\hat{\mathbf{x}}$ defines the x-axis. Eqs. (35)–(37) in general apply to all transverse thermoelectrics [4, 5, 17], but they are rederived above for completeness. The dependence of temperature on position within the transverse thermoelectric must now be carefully derived. The derivation below most closely follows that of Ref. [23] for the Nernst-Ettingshausen effect, but the errors in that reference are corrected below.

With Peltier tensor $\boldsymbol{\Pi}$, the total Peltier heat flux density becomes $\mathbf{Q}_{\Pi} = \boldsymbol{\Pi}\mathbf{J} = (T\mathbf{S})\mathbf{J}$ with longitudinal and transverse components:

$$Q_{\Pi,x} = \quad Q_{\Pi} \cdot \hat{x} = \quad \left(S_{p,aa}\cos^2\theta + S_{n,bb}\sin^2\theta\right) TJ_x \tag{39}$$

$$Q_{\Pi,y} = \quad Q_{\Pi} \cdot \hat{y} = \quad \left(S_{p,aa} - S_{n,bb}\right)\cos\theta\sin\theta\, TJ_x \tag{40}$$

The total heat flux density $\mathbf{Q} = \mathbf{Q}_{\Pi} - \boldsymbol{\kappa}^{c}\nabla T$ includes both Peltier and thermal conduction effects, $\boldsymbol{\kappa}^{c}$ as notated in Ref. [23] defines the open-circuit thermal conductivity tensor at $\mathbf{J} = 0$. The thermal gradient is orthogonal to the current density $\nabla T = \frac{dT}{dy}\hat{\mathbf{y}}$; the longitudinal electric field component E_x is constant everywhere [23]; and the heat flux component Q_y depends only on y. Therefore, the longitudinal current and transverse heat flow are

$$J_x = \frac{1}{\rho_{xx}}E_x - \frac{S_{xy}}{\rho_{xx}}\frac{dT}{dy} \tag{41}$$

$$Q_y = T\frac{S_{yx}}{\rho_{xx}}E_x - \left(1 + z_{xy}T\right)\kappa^{c}_{yy}\frac{dT}{dy} \tag{42}$$

with transverse figure of merit $z_{xy}T = \frac{S_{xy}S_{yx}T}{\rho_{xx}\kappa^{c}_{yy}}$. Steady state requires $\nabla \cdot \mathbf{J} = 0$ and $\nabla\cdot\left(\mathbf{Q} + \overline{\mu}\mathbf{J}\right) = 0$, where the scalar $\overline{\mu}$ is the electrochemical potential and $-\nabla\overline{\mu} = \mathbf{E}$ is the electric field. Longitudinal Joule heating E_xJ_x sources a divergence in the transverse heat flux density Q_y:

$$\frac{dQ_y}{dy} = E_x J_x. \tag{43}$$

Eqs. (41)–(43) define the differential equation for temperature-dependent thermoelectric coefficients:

$$\begin{aligned} 0 = {} & \frac{1}{S_{xy}S_{yx}} {E_x}^2 - \left[\frac{S_{xy}+S_{yx}}{S_{xy}S_{yx}} + \frac{dln\left(S_{yx}/\rho_{xx}\right)}{dlnT}\frac{1}{S_{xy}}\right] E_x \frac{dT}{dy} \\ & + \left[1 + \frac{dln\left(S_{yx}S_{xy}/\rho_{xx}\right)}{dlnT} + \frac{1}{z_{xy}}\frac{dln\kappa_y^{yc}}{dT}\right]\left(\frac{dT}{dy}\right)^2 + \frac{1+z_{xy}T}{z_{xy}}\frac{d^2T}{dy^2} \end{aligned} \tag{44}$$

Note for constant thermoelectric coefficients, the derivatives with respect to temperature are zero, and for transverse thermoelectrics, $S_{xy} = S_{yx}$. Eq. (44) thus becomes:

$$\left(\frac{E_x}{S_{xy}} - \frac{d}{Tdy}\right)^2 + \frac{1+z_{xy}T}{z_{xy}}\frac{d^2T}{dy^2} = 0. \tag{45}$$

This equation can be integrated to determine the temperature profile inside a rectangular solid of transverse thermoelectric material under constant current density. Note again, that unlike for the Nernst-Ettingshausen effect, the above Eq. (45) must be integrated numerically and does have an analytical solution.

5. Cooling power for transverse thermoelectrics

The cooling power for transverse Peltier refrigeration has recently been studied in detail [3]. The transport equations have no analytical solution, so the graphical results are presented here to allow simple estimations of cooling power for generic transverse thermoelectric scenarios. Here, we identify the characteristic heat flux scale and electric field scale for a transverse thermoelectric to define a normalized expression for thermoelectric transport [3]. The resulting study demonstrates the superiority of transverse thermoelectric coolers over longitudinal coolers with identical figure of merit.

One starts with the expression in Eq. (45) to identify the temperature distribution in a transverse cooler. To generalize this expression, the following heat flux and electric field scales $Q_0 = \left(\kappa_{yy}^c T_h/L\right)$ and $E_0 = \left(S_{xy}T_h/L\right)$, respectively, are introduced, generating normalized versions of the Eqs. (42) and (45):

$$Q_y^* = -\left(z_{xy}T_h\right)E^*T^* - \left(1 + \left(z_{xy}T_h\right)T^*\right)\frac{dT^*}{dy^*}, \tag{46}$$

$$0 = \left(E^* - \frac{dT^*}{dy^*}\right)^2 + \frac{1+\left(z_{xy}T_h\right)T^*}{z_{xy}T_h}\frac{d^2T^*}{d\left(y^*\right)^2}, \tag{47}$$

where $T^* = (T/T_h)$, $E^* = (E/E_0)$, $y^* = \left(\frac{y}{L_y}\right)$, and $Q^* = \left(Q_y/Q_0\right)$ are normalized temperature, electric field, y coordinate, and heat flux density, respectively. Eqs. (46) and (47) indicate that the normalized heat flux density Q_y^* and the normalized temperature profile $T^*(y^*)$ only depend on the normalized electrical field E^* and transverse figure of merit $z_{xy}T_h$. To determine the maximum normalized temperature difference, one sets the cooling power at the cold side Q_c^* to zero, to achieve $\Delta T^* = 1 - T_c^* = 1 - T^*(y^* = 1)$ whereby the optimal E^* is determined by

$$\frac{\partial \Delta Q_c^*}{\partial E^*} \mid_{E^* = E_{opt}^*} = 0 \tag{48}$$

Thus, $\Delta T_{max}^*\left(z_{xy}T_h\right)$ is only a function of $z_{xy}T_h$. Similarly, the maximum of the cooling power at the cold side $Q_c^* = Q_y^*(y^* = 1)$ for a given T_c^* can be obtained when E^* satisfies:

$$\frac{\partial \Delta T^*}{\partial E^*} \mid_{E^* = E_{opt}^*} = 0 \tag{49}$$

and $Q_{c,\,max}^*$ depends only on T_c^* and zT_h.

But because Eqs. (46)–(49) cannot be exactly solved with analytical methods, it is illustrative to plot the numerically calculated temperature profile and heat flux, and thereby investigate the cooling power of the transverse coolers.

Figure 6 shows the normalized temperature profile under the condition of maximum temperature difference ($Q_c^* = 0$) for various transverse figures of merit $z_{xy}T_h$. The temperature gradient at the hot side ($y^* = 0$) is zero, indicating that there is no net heat diffusion from the heat sink into, or out of, the device. Thus, 100% of the Peltier cooling power compensates the Joule heating in the device. The temperature gradient from the hot to the cold side becomes steeper

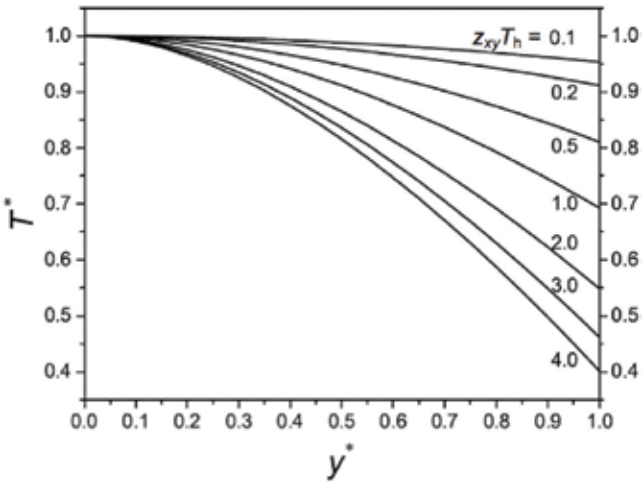

Figure 6. Normalized temperature profile of transverse thermoelectric coolers operating at maximum temperature difference for various $z_{xy}T_h$ values. At $y^* = y/L_y = 0$, the heat sink temperature $T^* = T/T_h = 1$ and at the $y^* = 1$, the cold side heat flow $Q_c = Q_y(y^* = 1) = 0$.

as $z_{xy}T_h$ increases, indicating that the higher figure of merit can compensate a larger thermal diffusive flux under larger ohmic heating. **Figure 7**, left axis, shows the dependence of the maximum temperature difference $\Delta T^* = 1 - T_c^*$ on $z_{xy}T_h$, left axis. Transverse coolers (solid line) show a larger ΔT^* than the analytically solved $\Delta T^* = 1 + \frac{1-\sqrt{1+2z_{xy}T_h}}{z_{xy}T_h}$ for longitudinal coolers (dashed line) [24]. For $z_{xy}T_h = 1$, a 30 % temperature reduction is observed for the transverse cooler, which is slightly larger than the 27 % reduction of the conventional longitudinal cooler with the same $z_{xy}T_h$. The trend becomes more obvious when an unphysically large $z_{xy}T_h$ of 4 results in a 60 % temperature reduction with the transverse cooler, whereas the longitudinal cooler achieves only 50%. Note that ΔT^*_{max} can be further increased with geometric tapering of the transverse cooler [1, 19], allowing for additional advantage over longitudinal cooling for achieving large temperature differences.

Figure 7, right axis, plots the normalized maximum cooling power $Q^*_{c,max}$ of the transverse cooler when $T_c = T_h$ as a function of $z_{xy}T_h$. Unlike the linear dependence in $Q^*_{c,max} = 1/2z_{xy}T_h$ for longitudinal coolers (dashed line) when $T_c^* = 1$, $Q^*_{c,max}$ shows a superlinear dependence on $z_{xy}T_h$ for transverse coolers (solid line), which exceeds the longitudinal limit for all $z_{xy}T_h$, approaching the longitudinal behavior only in the limit of small $z_{xy}T_h$. The cooling power enhancement in $Q^*_{c,max}$ for transverse coolers over longitudinal coolers with the same $z_{xy}T_h$ is 28 % when $z_{xy}T_h = 1$ and rapidly increases to 220 % when $z_{xy}T_h = 4$.

Figure 8 shows the cooling power $Q^*_{c,max}$ of transverse coolers as a function of T_c^* for various $z_{xy}T_h$ values. For a given $z_{xy}T_h$, the Fourier diffusion heat flow increases when T_c^* decreases; thus, a larger portion of the Peltier cooling power is used to compensate the diffusive heat flow, and the remaining cooling power at the cold side $Q^*_{c,max}$ will decrease.

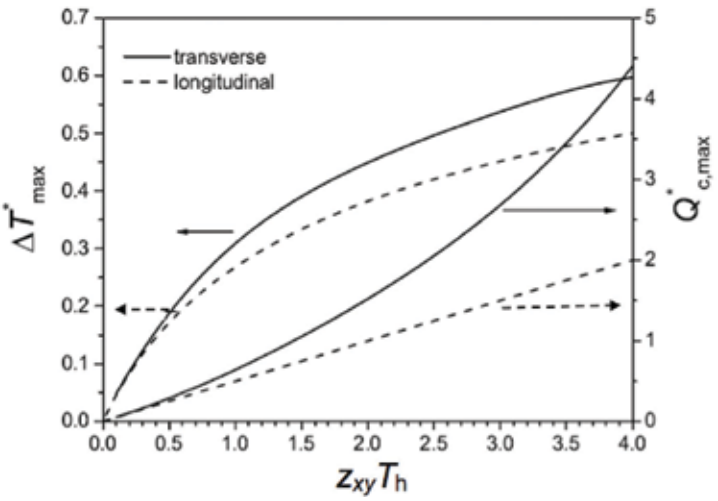

Figure 7. The dependence on $z_{xy}T$ of maximum normalized temperature difference (left axis) whereby $\Delta T^* = (T_h - T_c)/T_h$ and maximum cooling power when $T_c = T_h$ (right axis) for transverse thermoelectric coolers in comparison with longitudinal coolers. ΔT^*_{max} and $Q^*_{c,max}(T_c^* = 1)$ are numerically calculated for the transverse coolers in this study and analytically solved for the longitudinal coolers according to standard equations in the literature [1, 22, 23].

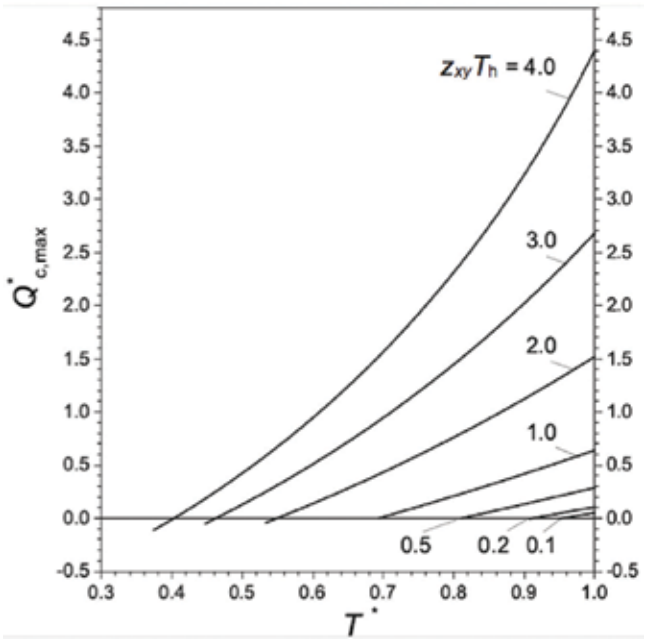

Figure 8. The maximum normalized cooling power $Q^*_{c,max}$ for transverse thermoelectric cooling as a function of the normalized cold side temperature T^*_c for various $z_{xy}T_h$ values.

The intersection of the curves with the horizontal axis and vertical axis corresponds to the maximum normalized temperature difference case and maximum cooling power case in **Figure 7**, respectively. The performance of a transverse cooler can be readily predicted from **Figure 8** for any given heat load or cold side temperature, once the scales Q_0 and E_0 are known.

6. Conclusion

This review of ($p \times n$)-transverse thermoelectrics explains the origin of materials with p-type Seebeck along one axis and n-type Seebeck orthogonal. The rigorous derivation of all thermoelectric transport tensors for anisotropic thermoelectric phenomena is given, as well as the transport equations from which one can derive all essential material performance parameters. The necessarily anisotropic band structure is expected to arise via anisotropic band or hopping conduction, whose transport tensors are derived for 3D, 2D and 1D effective mass approximations. The cooling power is expressed in a normalized notation relative to heat flux and electric field scales Q_0 and E_0 that are a function of the thermoelectric transport parameters. Numerical calculation of the maximum temperature difference and cooling power shows enhanced performance compared with longitudinal coolers with the same figure of merit. This work motivates the search for novel transverse thermoelectric materials with high figure of merit.

Acknowledgements

This work is supported by the Air Force Office of Scientific Research (AFOSR) Grant FA9550-15-1-0377 and the Institute for Sustainability and Energy at Northwestern (ISEN) Booster Award, and the work of M. Ma is supported by the China Scholarship Council program (No. 201406280070).

Author details

Matthew Grayson*, Qing Shao, Boya Cui, Yang Tang, Xueting Yan and Chuanle Zhou

*Address all correspondence to: m-grayson@northwestern.edu

Electrical Engineering and Computer Science, Northwestern University, Evanston, USA

References

[1] Zhou C, Birner S, Tang Y, Heinselman K, Grayson M. Driving perpendicular heat flow: (p × n)-type transverse thermoelectrics for microscale and cryogenic Peltier cooling. Physical Review Letters. 2013;**110**:227701

[2] Tang Y, Cui B, Zhou C, Grayson M. (p x n)-type transverse thermoelectrics: A novel type of thermal management material. Journal of Electronic Materials. 2015;**44**:2095

[3] Yang T, Ming M, Grayson M. Cooling power of transverse thermoelectrics for cryogenic cooling. In: Proceedings of the SPIE Defense + Security 98210K. International Society for Optics and Photonics; 2016

[4] Goldsmid HJ. Application of the transverse thermoelectric effects. Journal of Electronic Materials. 2011;**40**:1254

[5] Reitmaier C, Walther F, Lengfellner H. Transverse thermoelectric devices. Applied Physics A: Materials Science and Processing. 2010;**99**:717

[6] Rowe DM. Thermoelectrics Handbook: Macro to Nano. Boca Raton: CRC press; 2006

[7] Cuff KF, Horst RB, Weaver JL, Hawkins SR, Kooi CF, Enslow GM. The thermomagnetic figure of merit and Ettingshausen cooling in bi-Sb alloys. Applied Physics Letters. 1963;**2**:145

[8] Uchida K, Takahashi S, Harii K, Ieda J, Koshibae W, Ando K, Maekawa S, Saitoh E. Observation of the spin Seebeck effect. Nature. 2008;**455**:778

[9] Jaworski CM, Yang J, Mack S, Awschalom DD, Heremans JP, Myers RC. Observation of the spin-Seebeck effect in a ferromagnetic semiconductor. Nature Materials. 2010;**9**:898

[10] Uchida K, Adachi H, Ota T, Nakayama H, Maekawa S, Saitoh E. Observation of longitudinal spin-Seebeck effect in magnetic insulators. Applied Physics Letters. 2010;**97**:172505

[11] Sengupta P, Wen Y, Shi J. Spin-dependent magneto-thermopower of narrow-gap lead chalcogenide quantum wells. Scientific Reports. 2018;**8**(5972)

[12] He ZH, Ma ZG, Li QY, Luo YY, Zhang JX, Meng RL, Chu CW. Investigation of transverse Peltier effect on top-seeded melt texture $YBa_2Cu_3O_{7-\delta}$. Applied Physics Letters. 1996;**69**:3587

[13] Zhao K, Jin K-J, Huang Y-H, Lu H-B, He M, Chen Z-H, Zhou Y-L, Yang G-Z. Transient lateral photovoltaic effect in p-n heterojunctions of La0.7Sr0.3MnO_3 and Si. Physica (Amsterdam). 2006;**373B**:72

[14] Kanno T, Yotsuhashi S, Adachi H. Thermoelectric conversion via laser-induced voltage in highly textured polycrystalline Na_xCoO_2 ceramic. Applied Physics Letters. 2004;**85**:739

[15] Tang GD, Guo HH, Yang T, Zhang DW, Xu XN, Wang LY, Wang ZH, Wen HH, Zhang ZD, Du YW. Anisotropic thermopower and magnetothermopower in a misfit-layered calcium cobaltite. Applied Physics Letters. 2011;**98**:202109

[16] Kanno T, Takahashi K, Sakai A, Tamaki H, Kusada H, Yamada Y. Detection of thermal radiation, sensing of heat flux, and recovery of waste heat by the transverse thermoelectric effect. Journal of Electronic Materials. 2014;**43**:2072

[17] Babin VP, Gudkin TS, Dashevskii ZM, Dudkin LD, Iordanishvilli EK, Kaidanov VI, Kolomoets NV, Narva OM, Stilans LS. Anisotropic synthetic thermoelements and their maximum capabilities. Soviet Physics—Semiconductors. 1974;**8**:478

[18] O'Brien BJ, Wallace CS, Landecker K. Cascading of Peltier couples for thermoelectric cooling. Journal of Applied Physics. 1956;**27**:820

[19] O'Brien BJ, Wallace CS. Ettingshausen effect and thermomagnetic cooling. Journal of Applied Physics. 1958;**29**:1010

[20] Chambers RG. Electrons in Metals and Semiconductors. Chapter 10. Netherlands: Springer; 1990

[21] Kyarad A, Lengfellner H. Angle-dependent photovoltaic effect in AlCSi multilayers. Applied Physics Letters. 2005;**87**:182113

[22] Kyarad A, Lengfellner H. Transverse Peltier effect in tilted PbCBi2Te3 multilayer structures. Applied Physics Letters. 2006;**89**:192103

[23] Kooi CF, Horst RB, Cuff KF, Hawkins SR. Theory of the longitudinally isothermal Ettingshausen cooler. Journal of Applied Physics. 1963;**34**:1735

[24] Gurevich YG, Logvinov G, Fragoso OA, del Rio VJ. Lowest temperature at thermoelectric cooling. In: 4th International Conference on Electrical and Electronics Engineering; 2007

Chapter 6

Thermoelectric Devices: Influence of the Legs Geometry and Parasitic Contact Resistances on ZT

Angel Fabian-Mijangos and Jaime Alvarez-Quintana

Additional information is available at the end of the chapter

http://dx.doi.org/10.5772/intechopen.75790

Abstract

In this chapter, the impact of the shape of thermoelectric legs and parasitic contact resistances from metal electrodes and device wiring on thermoelectric figure of merit ZT is addressed. First section deals with the influence of the legs geometry on ZT. The shape of the legs is crucial in the thermoelectric performance of the thermoelectric devices. Unlike to conventional geometry thermoelectric legs, non-constant cross-section legs could help by lowering the overall thermal conductance of the device so as to increase the temperature gradient along legs, hence harnessing the Thomson effect, which is generally neglected in constant square cross-section thermoelectric legs. The final section is devoted to the electrical contact engineering of the device. Parasitic contact and wiring resistances play an important role in the performance of the device because they increase the isothermal resistance of the device. As the isothermal resistance of the device increases, the ZT decreases.

Keywords: asymmetrical legs, energy harvesting, heat recovery, heat recycling, thermoelectric module

1. Introduction

Waste heat occurs in many areas of daily life (natural and industrial processes). In general, generation of 1 W of power using the state-of-the art heat engines requires about 3 W of energy input, which results in dumping into the environment the equivalent of about 2 W of power in the form of heat. Thereby, waste heat recovery to create a source of energy is an important technology for a stable supply of electricity and environmental protection. In particular, the heat loss due to low temperature, which is below 450 K, represents a large portion of waste heat emitted from an automobile and industry. For instance, in the US manufacturing sector

alone, more than 3000 TW of waste heat energy is lost each year, an amount equivalent to more than 1.72 billion barrels of oil [1]. Hence, efficiently reclaiming even a small portion of such waste heat would itself nearly satisfy the electricity needs of the planet [2]. Thermoelectricity enabling directly converting heat into electricity using thermoelectric converters is a promising energy technology, which is under intense research to provide a solution to thermal energy recovery and management. However, wide-scale applications of this technology are limited due to the relative low thermoelectric efficiency of current materials and devices. For this reason, thermoelectric technology is only used in niche applications where its solid-state nature outweighs its poor efficiency. Therefore, an attractive and sustainable solution to the energy problem would be the development of solid-state thermoelectric devices which could help to recover this waste heat efficiently. The performance of a thermoelectric material is evaluated by the dimensionless figure of merit, ZT, which is defined as $ZT = S^2\sigma T/k$, where σ is the electrical conductivity, S is the Seebeck coefficient (i.e. thermopower), k is the thermal conductivity (often separated into the lattice thermal conductivity, k_L, and the carrier thermal conductivity, k_e), and T is the absolute temperature [3]. Good thermoelectric materials must have a high Seebeck coefficient to have high voltage output, low electrical resistivity to minimize Joule heating and low thermal conductivity to sustain large temperature gradients [4]. Clearly, the enhancement of ZT is not an easy task because these physical parameters are interdependent, and an improvement in one of these properties affects adversely another one. Hence, the development of high-efficiency thermoelectric materials and systems is very challenging. For instance, at material level recent developments in nanotechnology have led significant ZT enhancements in two-dimensional (thin films) and one-dimensional (nanowires, nanorods, nanotubes, etc.) thermoelectric materials [4–12]. In any case, although both strategies at nanoscale seems to be promising so as to increase ZT at material level, the main constraint for real applications is related to the tiny size of such nanostructures. Evidently, low-dimensional thermoelectric materials have limited applications for large-scale energy-conversion, because they are too thin to support appreciable temperature differentials [13–15]. In this sense, due to this disadvantage, researchers have been extensively focused on nanocomposites to perform nanoscale thermoelectric enhancement in bulk thermoelectric materials [13, 16–20].

On the other hand, at device level evidently the transfer from material to device affects significantly the intrinsic figure of merit of the material; hence the different materials and substrates constituting the thermoelectric device as well as its architecture play an important role in the thermoelectric figure of merit of the device, as consequence, an effective thermoelectric figure of merit lower than the intrinsic one could be presented in the thermoelectric module [21]. In this sense, significant enhancements in ZT by nanostructuring bulk materials could be seriously affected because of deficiencies during the design of thermoelectric devices. In the past, several strategies have been developed in order to improve the thermoelectric performance at device level, such strategies include filling of the empty space between thermoelectric legs with silica aerogel to minimize the thermal shunt path [22], improvement of the electrical and thermal contact between thermoelectric legs and refractory materials by using a buffer layer of carbon and Ni-Ag- based brazing material [23], even the use of thermoelectric legs modified with an organic layer has been proposed to improve the electrical contact resistance [24]. Besides, a theoretical study has proposed the cascade architectures that combine two or more

thermoelectric modules with different working temperature range in order to increase the output power of the device [25], the heat-shrink type where the module has a cross-plane heat transfer architecture similar to a conventional bulk TE module, but with heat transfer in the plane of the thin film thermoelectric elements, which assists in maintaining a significant temperature difference across the thermoelectric junctions [26], and the planar type where the thermoelectric legs are patterned onto the surface of a dielectric substrate [27, 28]. A complete review of the approaches used to enhance the thermoelectric performance in materials and devices is beyond of the scope of the present chapter; nevertheless, to explore about the strategies previously and currently proposed at the material and device level, the in-depth review can be found in the literature [29–31].

Evidently, the performance of thermoelectric devices depends on many factors, such as the temperature difference between hot and cold plates, thermoelectric legs and device material properties, as well as the configuration and arrangement of thermoelectric legs. Among these factors, the geometry and configuration of the thermoelectric legs are crucial. In this sense, several studies under a purely theoretical context have predicted the effects of varying the geometry of the legs on the thermoelectric performance of the device. For instance, it has been reported that a smaller number of shorter legs have the potential to achieve the same power per unit module area as a greater number of longer legs [32]. It has also been studied that the effect of the number of legs and their heights on the maximum output power and efficiency of the thermoelectric generator in order to find the optimum arrangements of legs [33]. Moreover, it has been analyzed that the thermoelectric performance of the device by variations in the cross-section of the legs (legs with non-constant cross sections), and predictions show that legs with trapezoid legs (linear variation cross-section) have higher nominal power density than quadratic and exponential variations in cross-sectional legs [34, 35]. In addition, the tailoring of the geometry configuration of the legs in line with the device operating conditions has also been analyzed via thermoelectric legs tapering [36], as well as the thermoelectric performance of thermoelectric generators and coolers in relation to the geometry of non-constant cross-section legs has been formulated thermodynamically [37], and via genetic algorithms [38–40] for pyramid, cylindrical, and cuboid shapes with the aim of accomplishing device geometric optimization.

As mentioned above, the design and optimization of thermoelectric legs have previously been studied theoretically. However, experimental work confirming these theoretical predictions has not been carried out so far, mainly because of the difficulties involving in fabrication of thermoelectric legs with complex geometrical structures. Section 2 of the present chapter deals with the influence of the legs geometry on ZT. Unlike conventional geometry thermoelectric legs, non-constant cross-section legs could help by lowering the overall thermal conductance of the device so as to increase the temperature gradient along legs, hence harnessing the Thomson effect, which is generally neglected in constant square cross-section thermoelectric legs as it shows a complete theoretical and experimental analysis of asymmetrical legs. Section 3 is devoted to the electrical contact engineering of the device. Parasitic contact and wiring resistances play an important role in the performance of the device because they increase the isothermal resistance of the device. Finally, in Section 4, conclusions about of the results presented in this chapter are shown.

2. Theoretical and experimental analysis of symmetrical and asymmetrical legs

According to previous theoretical studies, the investigation of the geometric structure of thermoelectric legs is essential, as their geometry affects the performance of devices. It has been reported that asymmetrical shape of thermoelectric legs can lead to a decrease in the thermal and electrical conductance, which in turn improve the Seebeck voltage due to an increase in the temperature difference [41]. In the present work, the temperature differences of the proposed asymmetrical legs are calculated by using the Fourier law. **Figure 1a** shows the proposed asymmetrical thermoelectric leg. For the sake of simplicity in the analysis, it is considered that such leg is constituted of four simpler geometrical legs connected thermally in parallel. By analyzing this simpler leg as shown in **Figure 1b**, it is possible to determine the temperature profile of the asymmetrical leg. Based on the Fourier law, the heat conduction along the simpler leg is defined by

$$\frac{dT}{dx} + \frac{\dot{Q}}{k}\left[\frac{L}{(mx+b)^2}\right] = 0 \tag{1}$$

Where, $\dot{Q}$ is the heat flux through the simpler leg, k is the thermal conductivity, $m = \tan(\theta)$ represents the slope of the pyramid, b is the half-length of the smaller cross section end, and L is the length of the sample. By solving Eq. (1) using the boundary conditions $T(x) = T_0$ at $x = x_0$, and considering the fact that four simpler legs in parallel to form a complete asymmetrical thermoelectric leg, the temperature profile of the thermoelectric leg of pyramidal shape is given by

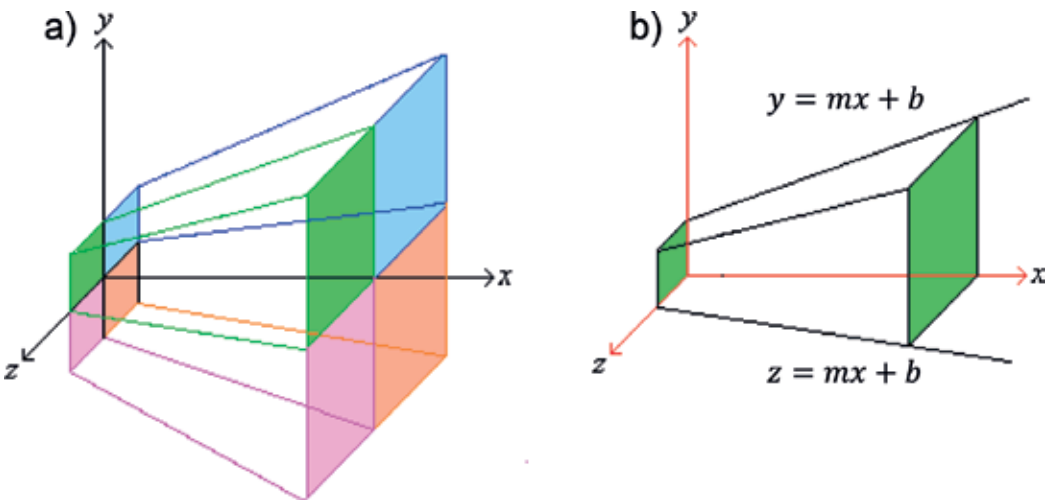

Figure 1. Schematic diagram of (a) a pyramidal-shaped thermoelectric leg and (b) simplified asymmetrical leg for modeling of the pyramidal-shaped thermoelectric legs.

$$T(x) = \frac{\dot{Q}}{4k}\left[\frac{L}{m(mx+b)}\right] - \frac{\dot{Q}}{4k}\left[\frac{L}{m(mx_0+b)}\right] + T_0 \tag{2}$$

Similarly, for a rectangular thermoelectric leg, the temperature profile is given by

$$T(x) = \frac{\dot{Q}L}{4k}\left[\frac{2x_0 - x}{a^2}\right] - \frac{\dot{Q}L}{4k}\left[\frac{x_0}{a^2}\right] + T_0 \tag{3}$$

where a is the half-length of the bigger cross-section end.

The thermoelectric modules experimentally analyzed in this chapter have rectangular thermoelectric legs based on Bi_2Te_3 with a typical dimension of around $1.7 \times 1.7 \times 2.1$ mm. Based on this dimensions and using Eqs. (2) and (3), **Figure 3a** shows the temperature profiles of an asymmetrical thermoelectric leg with a slant angle of 10° and a symmetrical thermoelectric leg under different heat fluxes, respectively. The upper solid lines (color online) represent the temperature profiles of the asymmetrical legs, whilst the lower dashed lines (color online) correspond to the temperature profiles of the symmetrical thermoelectric legs. As expected, as the heat flux decreases ($Q_1 > Q_2 > Q_3$), the temperature difference across the leg also decreases. Besides, a larger temperature difference is obtained across the asymmetrical leg as compared with the symmetrical one for a given heat flux. Therefore, by lowering the overall thermal conductance of the device via asymmetrical legs, the temperature gradient in the legs is increased, thus Seebeck voltage across terminals must be significantly increased. Besides, for simplicity it is worth to mention that the thermal conductivity k in Eqs. (2) and (3) during the modeling is taken as a constant, that is temperature independent; however, despite such simplification, uncertainty between both results is not so significant as it is seen in **Figure 2**. Hence, the main conclusions and results of the modeling are still valid.

Figure 3b shows the temperature profiles of the asymmetrical thermoelectric leg as a function of the position for different slant angles of the pyramid for a given heat flux. As expected, as the slant angle increases, the temperature difference across the leg increases; however, such increase is limited to a critical slant angle θ_c (see inset), at which a maximum temperature difference across the leg can be achieved without affect the leg length; such limit angle is given by

$$\tan(\theta_c) = \frac{a}{L} \tag{4}$$

Wherefrom, the limit angle for a thermoelectric leg with the length of 2.1 mm is around 22°, for this reason in **Figure 2b** as the slant angle achieves this value, the temperature rise increase drastically. It is worth to mention that in such modeling, convective effects were not taken into consideration because experimentally the device was tested under vacuum in order to avoid heat losses. Clearly, asymmetrical legs could help in two ways, by lowering the overall thermal conductance of the device so as to increase the temperature gradient in the legs, and by harnessing the Thomson effect, that depends on the temperature gradient in the legs and the temperature variation of Seebeck coefficient of the material in the operating temperature range, which is generally neglected in conventional rectangular thermoelectric legs. Thomson coefficient is given by $\tau(T) = TdS/dT$, when a temperature gradient is imposed on a thermoelectric material S varies from point to point along of the length of the thermoelectric element.

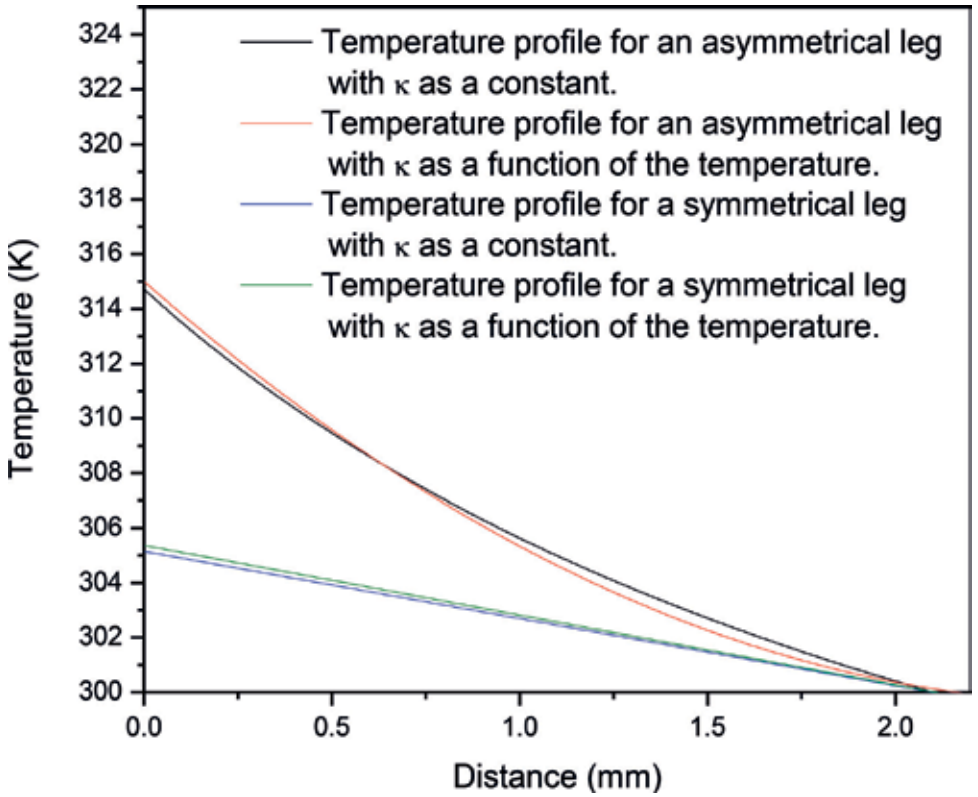

Figure 2. Comparison of temperature profiles taking κ as a function of the temperature as well as a constant, for symmetrical and asymmetrical thermoelectric legs.

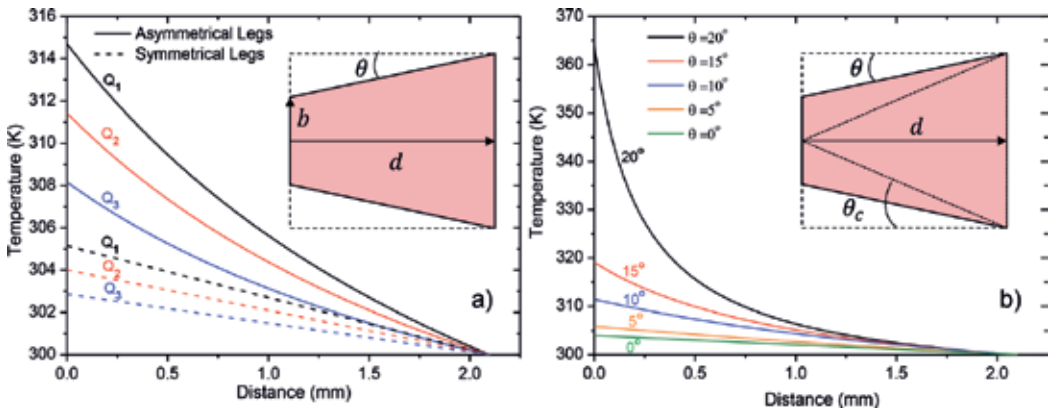

Figure 3. Temperature profiles as a function of the position for asymmetrical and rectangular thermoelectric legs at (a) different heat fluxes and at (b) different slant angle of the pyramid at room temperature.

The linear component in the temperature dependence of the intrinsic S can be taken into account so as to appear in the conventional thermal rate equations, but in fact it cancels out with the linear component of the Thomson coefficient and never appears in the thermal rate

http://dx.doi.org/10.5772/intechopen.75790

[equations 42]. Nevertheless, the nonlinear component in the temperature dependence of the intrinsic S has never been into consideration in the conventional thermal rate equations; thus when S varies nonlinearly with temperature, a portion of the nonlinear component of $\tau(T)$ remains in the thermal rate [equations 42]. Hence, when a thermoelectric element is subjected to a temperature gradient an effective Seebeck coefficient S_1 will appear. In this sense, previous experimental and analytical studies have demonstrated that an enhanced effective Seebeck coefficient can be obtained by combining the Thomson effect with the intrinsic Seebeck coefficient of a thermoelectric element because of the nonlinear changes in the intrinsic Seebeck coefficient with the temperature [43]. Hence, asymmetrical thermoelectric elements should present an enhancement in the effective Seebeck coefficient as compared to symmetrical ones because of the higher temperature gradient generated along the thermoelectric element as it is shown in **Figure 3a**.

Although in this chapter the influences of the temperature dependence of the thermal conductivity and Seebeck coefficient are not considered in the model given by Eqs. (2) and (3) for the sake of simplicity; however, the main conclusions arising from the model are still valid. In addition, a simulation study has been carried out using a finite element simulation on 3D geometries for a thermoelectric device consisting of nine pairs of pyramidal legs and rectangular legs respectively using the dedicated software "Thermoelectric module of COMSOL Multiphysics in Seebeck mode". **Figure 4a**, **b** show the simulation results of the temperature profiles and terminal voltages in the asymmetrical device respectively due to the presence of a given heat flux. For comparison, **Figure 4c**, **d** show the temperature profile and the terminal voltage in the symmetrical device respectively. Clearly, asymmetrical legs based thermoelectric device presents a higher open circuit terminal voltage than its rectangular counterpart as a consequence of the larger temperature difference generated in the legs because of their asymmetry.

The modules were made using p-type and n-Type Bi_2Te_3 thermoelectric materials available from Thermal Electronics Corp with ZT~1. For clarity, the full process so as to fabricate the thermoelectric legs is shown in **Figure 5**. The raw thermoelectric material in the form of a rod is covered by a layer of wax (wax-70) so as to hold the material in the cutting base during the cutting process, see **Figure 5a**. Then, it is cut into slices of 2.1 mm in thickness, which is the length of the thermoelectric leg as shown in **Figure 5b**. The wax is cleaned up using a warm solution of water and aquaclean-900 at a concentration of 10 mg/ml after slices cutting process as shown in **Figure 5c**. Next, a layer of Ni ranging from 0.5 and 1 μm is coated on both surfaces of the slide by electroplating. The Ni layer works as a diffusion barrier between the solder (Sn/Pb 60/40) and the thermoelectric legs, see **Figure 5d**. Prior to cutting, the Ni-electroplated slide is again fixed on a graphite plate using wax (wax-70) with the aim of keeping the legs during cutting, as you can see in **Figure 5e**. Subsequently, thermoelectric legs with the regular geometry of $1.7 \times 1.7 \times 2.1$ mm are obtained using a circular saw cutting machine (Accutom-100), see **Figure 5f**. Finally, the wax is removed from legs as previously indicated in **Figure 5c**.

In order to obtain the asymmetrical legs, a similar process as described above is employed. However, in this case, a tilted base is used to hold the graphite plate during cuttings. Hence, so as to obtain the asymmetrical geometry (truncated square pyramid), it was necessary to do a

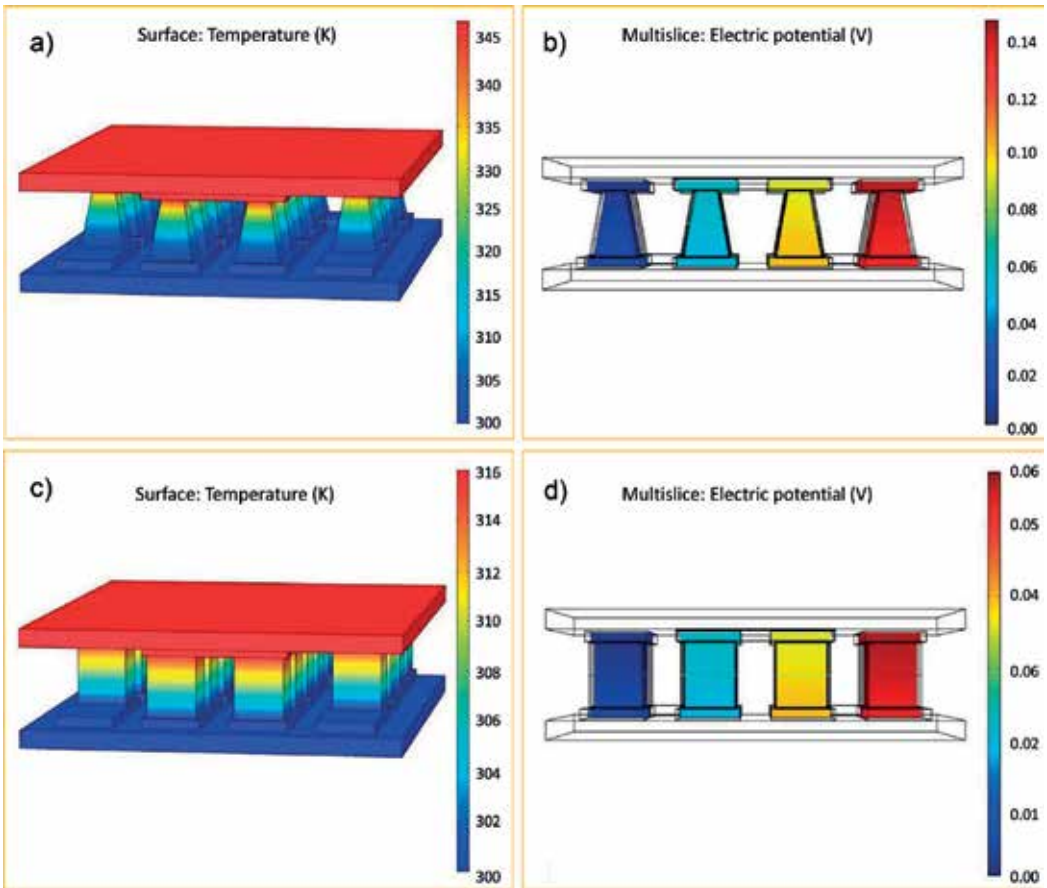

Figure 4. COMSOL simulation results: (a) temperature profile and (b) open circuit voltage for the asymmetrical thermoelectric module, (c) temperature profile and (d) open circuit voltage for the symmetrical thermoelectric module, respectively at room temperature.

cutting in every face of the rectangular leg by rotating the graphite tilted base 90° during each cutting. The slope of the base depends on the desired slant angle in the thermoelectric legs as shown in **Figure 6a**, **b**, clearly, the graphite plate is tilted at an angle of 10°. Besides, it has been attempted to fabricate the legs with a slant angle close to the critical angle of 22° so as to maximize the thermal gradient. However, it has been observed that angles higher than 10° produce legs with a small cross-section in the thin end. Such legs tend to be very fragile because of the mechanical properties of Bi_2Te_3, and they fracture during the assembling process due to the pressure and thermal treatments applied. **Figure 6c**, **d** show the side and top view of the asymmetrical legs used for the fabrication of the thermoelectric device.

Figure 7a, **b** show the images of the fabricated modules with symmetrical and asymmetrical legs, respectively, wherefrom differences in the geometry of the thermoelectric legs can be observed by comparing both images. At first instance, the performance of the devices has been evaluated by means of the hot-plate method. In such method, the thermoelectric modules are

http://dx.doi.org/10.5772/intechopen.75790

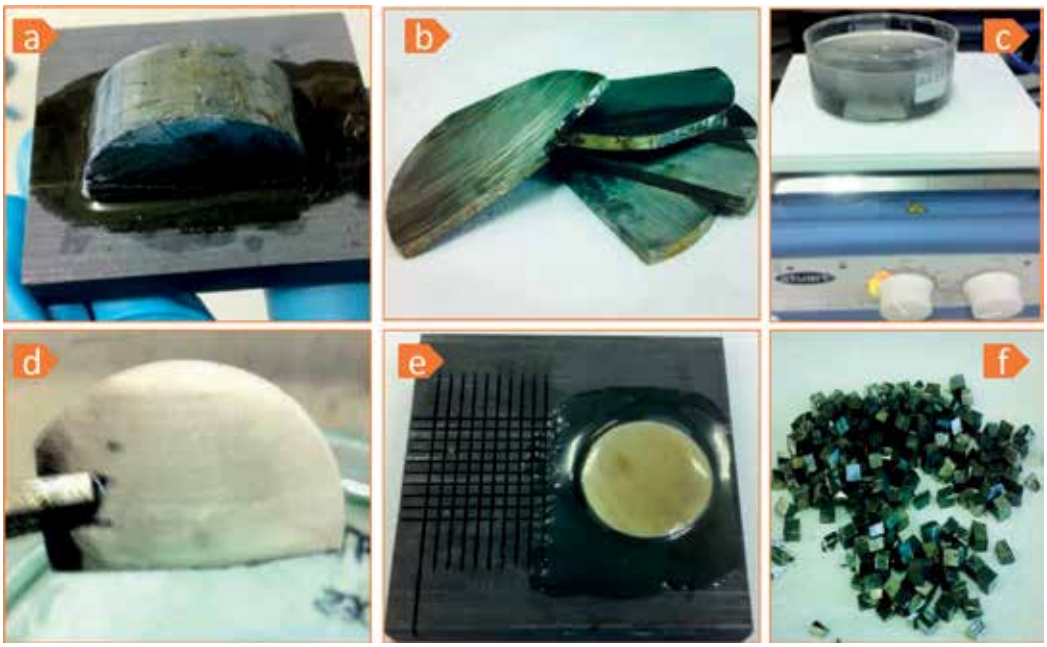

Figure 5. Steps for the fabrication of the thermoelectric legs.

installed between heating and cooling plates. Next, a dc voltage with regular increments is applied to the 130 Ω resistive heater of the heating plate by using the BK Precision 9184 dc power supply. This action induces a constant heat flow Q which flows through the test specimens in the stationary temperature state, as well as provides several temperature biases ΔT across the thermoelectric module surfaces. It is worth to note that the side of the applied heat source does not matter in symmetrical modules; however, in the asymmetrical module, the heat source must be applied necessarily on the smaller area side because it has the smallest thermal conductance along the pyramid. In **Figure 7c**, it is plotted ΔT vs Q wherefrom the slope it can be calculated the thermal resistance of the devices; evidently, the asymmetrical legs module presents a higher thermal resistance than the symmetrical legs module.

Parallel, the open circuit thermal voltage is measured along with the temperature rise across the device, such voltage is detected by using the Metrohm Autolab B. V. system; then, it is also plotted V vs Q as shown in **Figure 7d**. Again, the asymmetrical legs module presents a higher open circuit thermal voltage than its symmetrical counterpart; clearly, such enhancement must be related to the thermoelectric performance of the asymmetrical thermoelectric module. It is worth to mention that by continuing applying heat fluxes the temperature rise across the device will continue increasing, and therefore the open circuit output voltage also increases. However, if this heat flux becomes excessive, it could damage the device because of the melting of the weld joining the thermoelectric legs.

On the other hand, when a thermoelectric device is connected to any load it is desirable that such device be able to transfer the greatest amount of power to the load. In this sense, applying

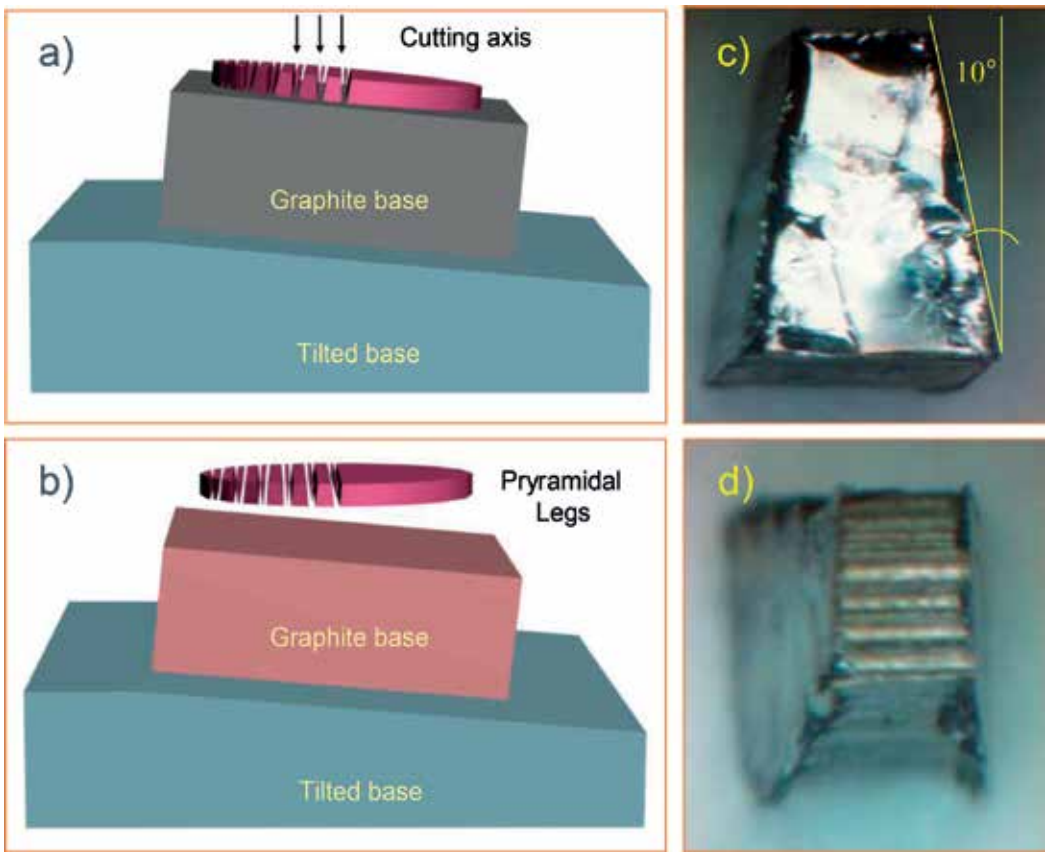

Figure 6. Schematic diagram of (a) the tilted base and (b) angled leg cutting suggested to obtain asymmetrical thermoelectric legs; micro-photographs of (c) side view and (d) top view of the thermoelectric legs.

the Theory of Maximum Power Transfer assumes a simple electrical circuit with a voltage source V which is the thermoelectric device; the source has an internal resistance R_i, a load resistance R_L, a voltage drop V_L, as shown in **Figure 8**.

The current is $I = V/(R_i + R_L)$ and the power delivered to the charge is

$$P = I^2 R_L = V^2 R_L/(R_L + R_i)^2 \tag{5}$$

Then is considered a variation in power when the load resistance R_L is changed, but internal resistance of thermoelectric device R_i as well as the voltage V are constants. When $R_L = 0$, the output power is clearly zero. Likewise, when R_L is too big, the output power is zero as well. This suggests that an intermediate value of R_L is maximum. When P is derived as a function of R_L in Eq. (5) and then it is equal to zero, it is easily shown that the maximum power is when $R_L = R_i$.

In this sense, in order to evaluate the maximum power given by the modules the maximum output power between the asymmetrical and the symmetrical modules has been evaluated by

http://dx.doi.org/10.5772/intechopen.75790

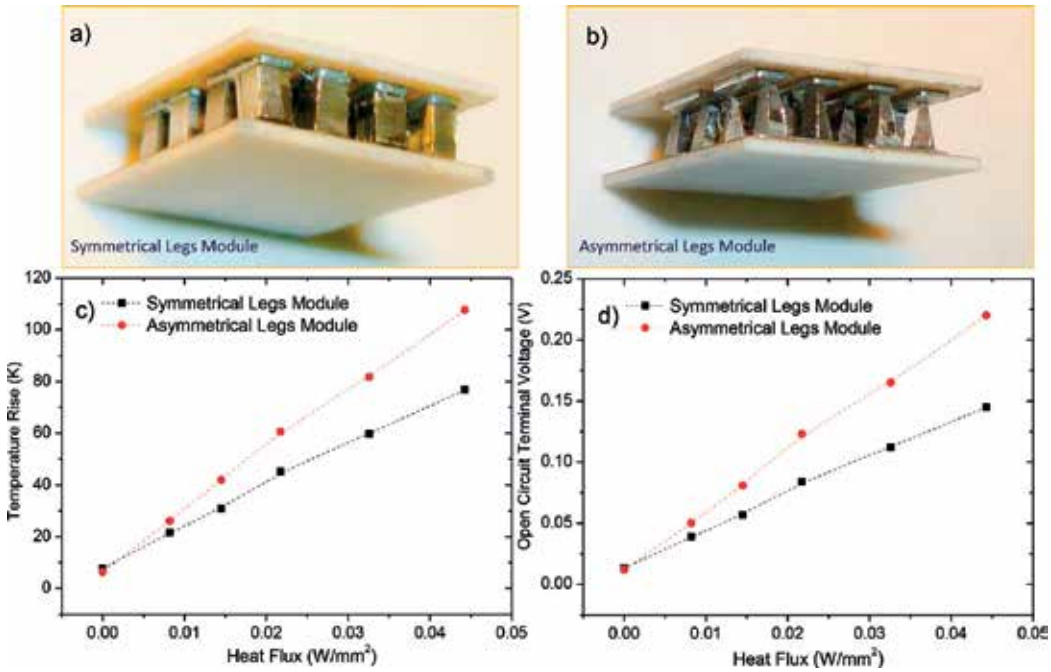

Figure 7. Photographs of the fabricated module of nine pairs of legs: (a) with symmetrical legs and (b) with asymmetrical legs; (c) temperature rise across both modules as a function of input heat flux; and (d) open circuit voltage as a function of input heat flux.

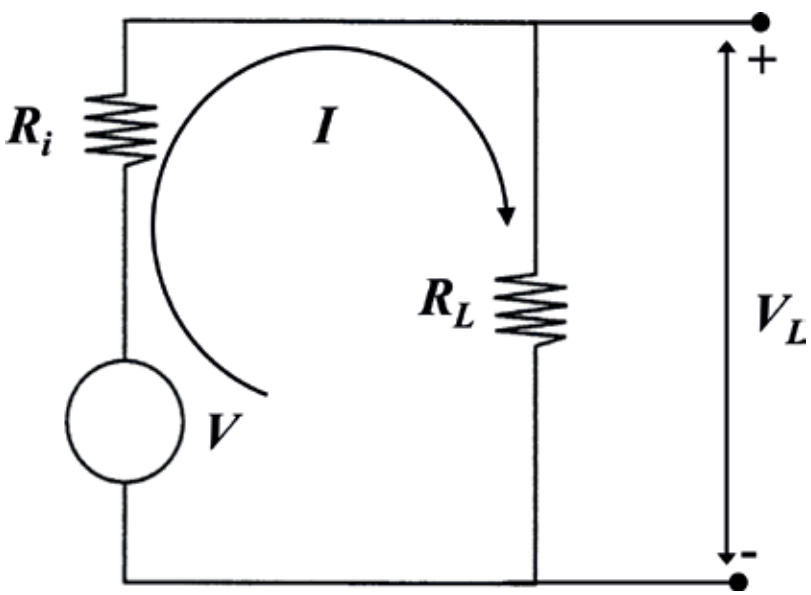

Figure 8. Basic electric circuit showing the internal resistance R_i of the thermoelectric device and the load resistance R_L.

way of the maximum power transfer theorem. In this case, an identical heat flux of around 4 mW/mm^2 was supplied to both modules by applying an electrical current of 90 mA to the Ohmic heater; once modules reached the steady state different load resistances were connected into the module and the voltage across the resistance was recorded, by using those voltages and resistances the output power was estimated. **Figure 9** shows the obtained results, it can be observed that asymmetrical module delivers more power than the symmetrical one once the load resistance equals the device internal resistance. In Fact, the asymmetrical thermoelectric module shows to have almost twofold the maximum delivered power as compared to conventional one with a constant square cross-section. Besides, by estimating the maximum available power per unit amount of material (mass of the legs) it has been obtained 433 μW/gram and 1.57 mW/gram for the symmetrical and the asymmetrical modules, respectively.

Evidently, these modules apparently present low output power, however by comparing these modules with several commercially available they have very competitive output power values [44]. For instance, by extrapolating the data shown in Ref. [44] to $\Delta T = 20°C$ a TEG module based on Bi_2Te_3 model FERROTEG 9501/71/040B with 71 pairs, and 22 mm × 22 mm generates a maximum output power around 1.5 mW. In our case, for modules with only nine pairs, we obtain 0.3 and 0.5 mW for symmetrical and asymmetrical modules, respectively. Nevertheless, by the projection of our modules to 71 pairs we would obtain 2.36 and 3.94 mW, respectively. Besides, if we compare our module against TEG-FERROTEG 9500/127/100B module based on Bi_2Te_3 with 127 pairs, and 40 × 40 mm under $\Delta T = 20°C$, which delivers an output power around 2.5 mW, we would obtain by a similar extrapolation 4.23 and 7.05 mW for symmetrical and asymmetrical modules, respectively, under $\Delta T = 20°C$. It is worth to mention that ΔT scale

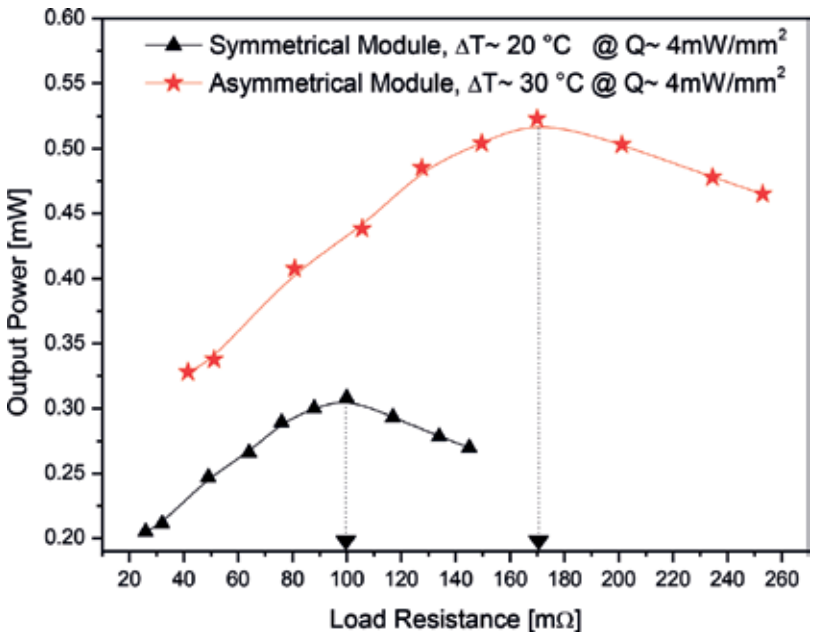

Figure 9. Output power vs load resistance for symmetrical and asymmetrical modules.

in Ref. [44] is in logarithmic scale, so it can be closely compared to $\Delta T = 20°C$ and $\Delta T = 30°C$, for the asymmetrical module.

The thermoelectric figure of merit of the fabricated modules was also evaluated by using impedance spectroscopy technique [45]. In this method, the thermoelectric figure of merit is determined by measuring the adiabatic and isothermal responses of the module under electrical excitation. Under the adiabatic condition at steady state (i.e., $\omega = 0$), the total impedance of the module can be written as [45]

$$R_{ad} = R_{te} + R_{iso} \tag{6}$$

Where R_{te} is the thermoelectric resistance, and it refers to the resistance of the device which is the result of the temperature difference induced between the ends of the sample due to the Peltier effect, R_{iso} is the isothermal resistance, and it is the resistance of the device R_{iso} excluding thermal effects but including parasitic resistances such as contact and wire resistances, R_p.

According to the Harman method, the thermoelectric figure of merit is given by the ratio between the thermoelectric resistance and the isothermal resistance of the system [46]; hence, by dividing Eq. (6) by R_{iso}, ZT is calculated as a function of adiabatic resistance R_{ad}, isothermal resistance R_{iso}, and parasitic resistance R_p:

$$ZT = \frac{R_{ad} - R_p}{R_{iso} - R_p} - 1 \tag{7}$$

As well as, in terms of the thermoelectric resistance ZT is given by

$$ZT = \frac{R_{te}}{R_{iso} - R_p} \tag{8}$$

where

$$R_p = R_c + R_w \tag{9}$$

Therefore, by using Eqs. (7) or (8), the effective thermoelectric figure of merit of a device can be accomplished. The adiabatic and isothermal resistances can be easily accessed via electrical impedance measurements [45]. Likewise, parasitic resistances R_c from module with symmetrical and asymmetrical legs are evaluated by applying Transmission Line Method (TLM) [47] and so they can be removed from ZT as it seen in Eq. (7).

During the measurements, the samples were isolated and suspended to provide adiabatic conditions in a similar way as required in the Harman method [46]. **Figure 10a**, **b** show the experimental electrical impedance curves obtained for the symmetrical and asymmetrical leg modules, respectively. In both curves, the thermoelectric, adiabatic, and isothermal resistances are indicated in order to access to their respective values. Nevertheless, it is well known that a material has more than one contribution to its impedance response, which is often the case of thermoelectric materials where thermoelectric impedance, isothermal impedance, and contact impedance have distinct contributions. Hence, one can witness more than one semi-circle, often

overlapping each other which makes impossible to distinguish them. One of the ways to model such a behavior in a simple model can be using in three series–parallel RC elements circuit. In **Figure 10a**, **b**, the solid line corresponds to the obtained fitting results. For clarity, such resistance results, as well as the effective thermoelectric figure of merit of the symmetrical and asymmetrical modules are shown in **Table 1**. Evidently, the thermoelectric figure of merit of the asymmetrical module is almost two-fold the thermoelectric figure of merit of the symmetrical module, such result confirms the enhanced thermoelectric performance of the asymmetrical module as a consequence of the larger temperature rise generated in the legs because of their asymmetry. Hence, harnessing of the Thomson coefficient via asymmetrical legs could be an important strategy in order to accomplish thermoelectric devices with enhanced performance.

On the other hand, it is worth to mention that the present experimental research is mainly focused on the development of devices for applications at room temperature (i.e. 300 K), in that case, it is not necessary to measure the temperature dependence of ZT. Besides, our devices are based on P and N-type Bi_2Te_3, it is well known that such materials present an optimal thermoelectric performance at around room temperature; hence, operation of such materials must be well below 100°C, so an operation condition above this temperature will damage the device because by applying an excessive heat flux it could damage the device due to the melting of the weld joining the thermoelectric legs. In this sense, it is not possible to operate such device under a high-temperature rise away from room temperature would affect seriously their performance.

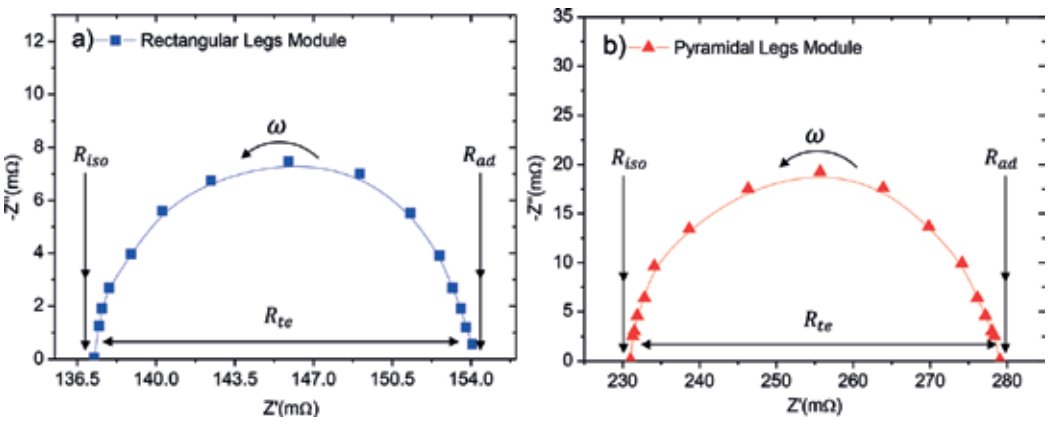

Figure 10. Experimental electrical impedance curves at room temperature for (a) symmetrical and (b) asymmetrical nine pairs of thermoelectric modules.

Module	R_{iso}(mΩ)	R_{te}(mΩ)	R_{ad}(mΩ)	R_c(mΩ)	R_w(mΩ)	ZT_c
Symmetrical	137.25	16.81	154.06	98.2	18.3	0.43
Asymmetrical	231.01	48.09	279.10	165.4	18.3	0.73

Table 1. Experimental parameters of the symmetrical and asymmetrical leg thermoelectric modules.

http://dx.doi.org/10.5772/intechopen.75790

Moreover, according to the values shown in **Table 1**, evidently, the parasitic electrical resistances play an important role in the performance of the device. For instance, if we take into consideration only parasitic contact effects (i.e. parasitic electrical contact resistance between legs and ceramic plates) and neglect the effect of parasitic resistances generated by cable wiring, a value of 0.43 and 0.73 on *ZT* is obtained.

3. Impact of parasitic contact electrical resistances on *ZT* of the thermoelectric device

Thermoelectric device engineering involves the formation of several intrinsic parasitic resistances that affect the thermoelectric module performance. In this sense, the TLM has been applied to discard the parasitic resistances and demonstrate that the increase on *ZT* of the device is mainly due to asymmetric effect in thermoelectric legs and consequently the nonlinear Thomson effect that governs them.

Figure 11a shows different lengths in the symmetrical and asymmetric thermoelectric legs as well as their respective electrical resistances as a function of length. The total measured resistance consists of several components:

$$R_T = R_{W1} + R_{C1} + R_{p-TE} + R_{C2} + R_{n-TE} + R_{C3} + R_{W2} \tag{10}$$

Where R_{W1} y R_{W2} are wiring resistances, R_{C1} y R_{C3} are contact resistances due to metal contacts, R_{C2} is associated with the metallic contact between the junction of the P-type and N-type thermoelectric legs, and $R_{P\text{-}TE}$ and $R_{N\text{-}TE}$ define the internal resistance of the P-type and N-type thermoelectric legs, respectively.

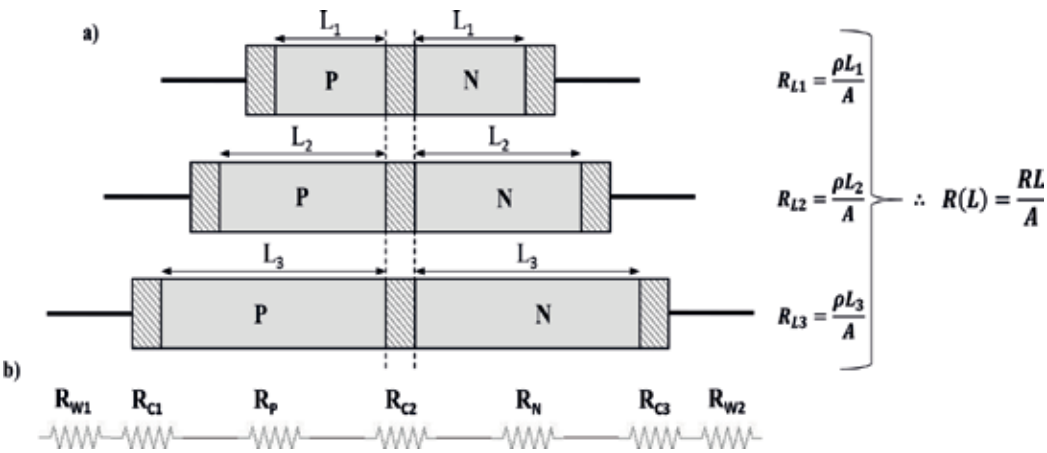

Figure 11. (a) Diagram of the variation of the length in thermoelectric couples and analysis of the electrical resistance, and (b) analogous electrical circuit of thermally coupled pairs with welding.

Therefore, the total parasitic electrical resistance Rp is given by the contact resistance Rc and the wiring resistance Rw, then Eq. (10) can be rewritten as:

$$R_p = R_w + R_c \tag{11}$$

By way of the TLM, it is possible to measure the total parasitic electrical resistance Rp. In this sense, thermoelectric legs have been fabricated with 2, 3, and 4 mm in length. The TLM is a technique used to determine the contact resistance between a metal and a semiconductor. First, the electrical resistance is measured for each length and then each resistance is presented as a function of length as shown in **Figure 12**. In the limit of a zero-length resistor, the residual resistance would be just the contact resistance. Then can be found from the graph by extrapolating back to L = 0. Then, the parasitic resistance of the P-N junction is the sum of such interceptions; hence, the total parasitic resistance of the device is estimated by multiplying this value by the number of P-N junctions in the device (in this case, 9 P-N pairs).

The total parasitic resistance *Rp* of a thermoelectric module with nine couples of symmetrical legs (see **Figure 7a**) is calculated as:

$$R_{p-symmetric} = (R_{c-P} + R_{c-N}) * 9$$

$$R_{p-symmetric} = (10.23m\Omega + 2.22m\Omega) * 9$$

$$R_{p-symmetric} = 115.29\ m\Omega$$

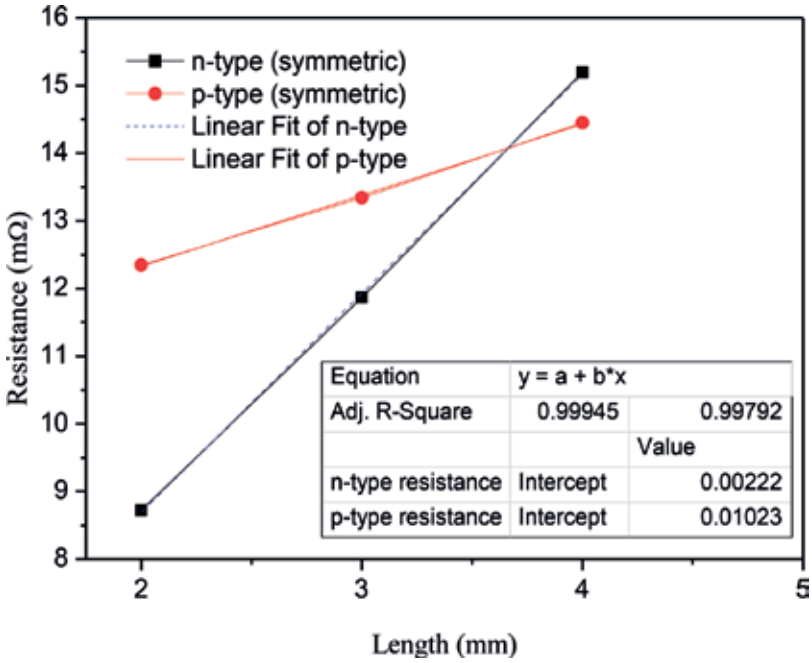

Figure 12. Electrical resistance in symmetrical thermoelectric legs as the length is increased.

http://dx.doi.org/10.5772/intechopen.75790

Where, R_{c-P} y R_{c-N} values are defined by slope interception with y-axes, as mentioned above. Such values are shown as inset table of **Figure 12**. This result is the total parasitic resistance of thermoelectric module with nine pairs that includes the wiring resistance of wire used during measurements as well as contact resistance.

In addition, by way of the four-probe AC method, it is possible to measure the wiring resistance *Rw*, as shown in **Figure 13**. Where the value *Rw* is obtained by the intersection of the adjustment with the *y*-axis as it is shown in the inset.

Now, contact resistance Rc of the thermoelectric module with symmetrical legs is calculated as:

$$R_C = R_{p-symmetric} - R_W$$

$$R_C = 115.29\ m\Omega - 18.38\ m\Omega$$

$$R_{C-symmetric} = 96.91\ m\Omega$$

By applying a similar procedure, it is possible to measure the parasitic resistance Rp using the TLM in the asymmetric device, in this case, the resistance as a function of the length is shown in **Figure 14**.

The total parasitic resistance *Rp* of a thermoelectric module with nine couples of asymmetrical legs (see **Figure 7b**) is calculated as:

$$R_{p-asymmetric} = (R_{c-P} + R_{c-N}) * 9$$

$$R_{p-asymmetric} = (17.84 m\Omega + 3.59 m\Omega) * 9$$

$$R_{p-asymmetric} = 191.97\ m\Omega$$

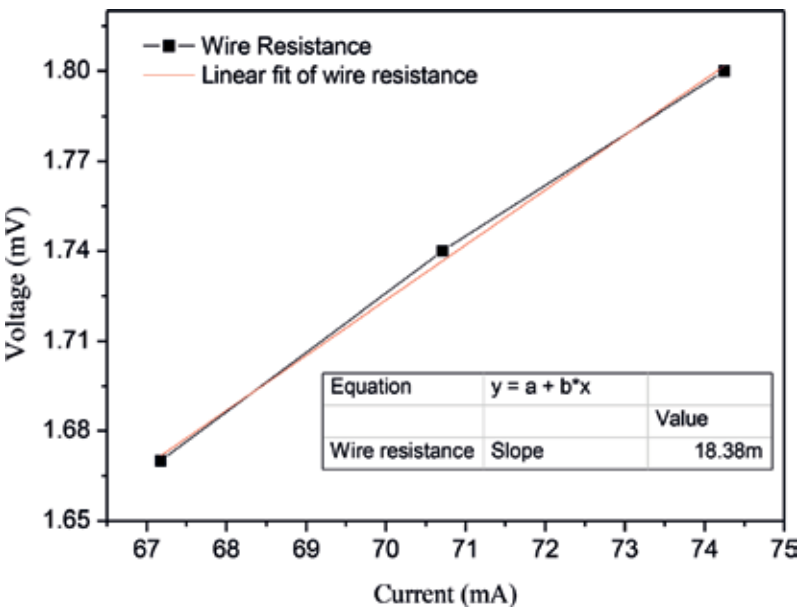

Figure 13. Wiring resistance of the wire used during thermoelectric characterization.

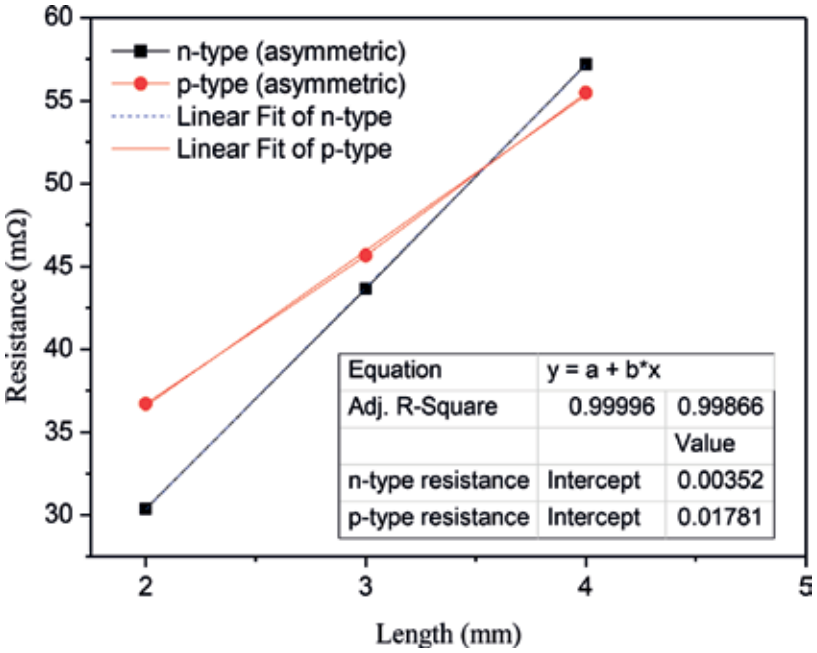

Figure 14. Electrical resistance in asymmetrical thermoelectric legs as the length is increased.

Where, R_{c-P} y R_{c-N} values are defined by slope interception with y axes. Such values are shown as inset table of **Figure 14**. This result is the total parasitic resistance of thermoelectric module with nine pairs of asymmetrical legs that includes the wiring resistance of wire used during measurements as well as contact resistance.

Now, contact resistance R_c of the thermoelectric module with asymmetrical legs is calculated as:

$$R_C = R_{p-asymmetric} - R_W$$

$$R_C = 191.97\ m\Omega - 18.38\ m\Omega$$

$$R_{C-asymmetric} = 174\ m\Omega$$

In this particular case, R_p has been obtained around 116 mΩ y 183 mΩ for the symmetrical and asymmetrical device, respectively. Using this information, ZTp can be calculated as it is shown in **Table 2**. However, by correcting such parasitic effects the estimated values on ZT_{p} are 0.79 and 1.02 for the symmetrical and asymmetrical thermoelectric modules, respectively. Thus, it is

Module	ZT_c	ZT_p
Symmetric	0.43	0.79
Asymmetric	0.73	1.02

Table 2. Effect of contact and parasitic resistances on ZT of thermoelectric modules with symmetrical and asymmetrical legs, respectively.

demonstrated that clearly parasitic electric resistance plays an important role in the performance of the thermoelectric device.

4. Conclusion

In the present chapter, it has been done an experimental demonstration of the influence of the device legs geometry as well as parasitic electrical contact resistance on ZT. Results prove that asymmetrical thermoelectric module shows to have almost twofold the thermoelectric figure of merit as compared to conventional one with a constant square cross-section. Thermal analysis of the device via analytical, as well as numerical modeling unveils an increment in the temperature gradient and Seebeck voltage across the device with asymmetrical thermoelectric legs. Such result confirms that the thermoelectric enhancement is due to the harnessing of Thompson effect which is normally neglected in rectangular legs devices. Additionally, the impact of parasitic electrical contact and wiring resistances on the thermoelectric module performance is shown. In this sense, a significant decrement on ZT due to parasitic effects is observed. Thereby, the general results of the present chapter experimentally prove that geometrical configuration of the device legs can improve significantly the thermoelectric performance of the device opening a new route to the development of enhanced performance thermoelectric modules via device engineering.

Acknowledgements

This work was supported by the National Council for Science and Technology-Conacyt Mexico, through the Grant for fundamental research No. 241597 and national issues No.1358. A.F. M. thanks to Conacyt Mexico for fellowship, as well as the thermoelectric laboratory at the Cardiff University for facilities.

Conflict of interest

Authors declare no conflicts of interest.

Author details

Angel Fabian-Mijangos[1] and Jaime Alvarez-Quintana[1,2]*

*Address all correspondence to: jaime.alvarez@cimav.edu.mx

1 Centro de Investigación en Materiales Avanzados S. C. Unidad Monterrey, Apodaca, Nuevo León, México

2 Genes-Group of Embedded Nanomaterials for Energy Scavenging, CIMAV-Unidad Monterrey, Apodaca, Nuevo León, México

References

[1] Tritt TM, Subramanian MA. Thermoelectric materials, phenomena, and applications: A bird's eye view. MRS Bulletin. 2016;**31**(3):188. DOI: 10.1557/mrs2006.44

[2] Pop E. Energy dissipation and transport in nanoscale devices. Nano Research. 2010;**3**:147-169

[3] Wang S, Fu F, She X, Zheng G, Li H, Tang X. Optimizing thermoelectric performance of Cd-doped β-Zn4Sb3 through self-adjusting carrier concentration. Intermetallics. 2011;**19**: 1823-1830

[4] Dresselhaus MS, Chen G, Tang MY, Yang RG, Lee H, Wang DZ, et al. New directions for low-dimensional thermoelectric materials. Advanced Materials. 2007;**19**:1043-1053

[5] Hicks LD, Dresselhaus MS. Thermoelectric figure of merit of a one-dimensional conductor. Physical Review B. 1993;**47**:16631-16634

[6] Hicks LD, Dresselhaus MS. Effect of quantum-well structures on the thermoelectric figure of merit. Physical Review B. 1993;**47**:12727-12731

[7] Chen G, Dresselhaus MS, Dresselhaus G, Fleurial J-P, Caillat T. Recent developments in thermoelectric materials. International Materials Review. 2003;**48**:45-66

[8] Snyder GJ, Toberer ES. Complex thermoelectric materials. Nature Materials. 2008;**7**:105-114

[9] Venkatasubramanian R, Siivola E, Colpitts T, O'Quinn B. Thin-film thermoelectric devices with high room-temperature figures of merit. Nature. 2001;**413**:597-602

[10] Sun X, Zhang Z, Dresselhaus MS. Theoretical modeling of thermoelectricity in Bi nanowires. Applied Physics Letters. 2016;**4005**:26-29

[11] Zhu T, Ertekin E. Phonon transport on two-dimensional graphene/boron nitride superlattices. Physical Review B. 2014;**90**:195209

[12] Chen Z-G, Han G, Yang L, Cheng L, Zou J. Nanostructured thermoelectric materials: Current research and future challenge. Progress in Natural Science: Materials International. 2012;**22**:535-549

[13] Poudel B, Hao Q, Ma Y, Lan Y, Minnich A, Yu B, et al. High-thermoelectric performance of nanostructured bismuth antimony telluride bulk alloys. Science. 2008;**320**:634-638

[14] Oh T-S. Thermoelectric characteristics of p-type (Bi,Sb)2Te3/(Pb,Sn)Te functional gradient materials with variation of the segment ratio. Journal of Electronic Materials. 2009;**38**(7):1041

[15] Vining CB. An inconvenient truth about thermoelectrics. Nature Materials. 2009;**8**:83-85

[16] Hsu FK. Cubic AgPbmSbTe2+m: Bulk thermoelectric materials with high figure of merit. Science. 2004;**303**:818-821

[17] Zhao XB, Ji XH, Zhang YH, Zhu TJ, Tu JP, Zhang XB, et al. Bismuth telluride nanotubes and the effects on the thermoelectric properties of nanotube-containing nanocomposites. Applied Physics Letters. 2016:062111

[18] Ni HL, Zhao XB, Zhu TJ, Ji XH, Tu JP. Synthesis and thermoelectric properties of Bi2Te3 based nanocomposites. Journal of Alloys and Compounds. 2005;**397**:317-321

[19] Slack GA, Hussain MA. The maximum possible conversion efficiency of silicon-germanium thermoelectric generators. Journal of Applied Physics. 2016;**2694**

[20] Kim W, Zide J, Gossard A, Klenov D, Stemmer S, Shakouri A, et al. Thermal conductivity reduction and thermoelectric figure of merit increase by embedding nanoparticles in crystalline semiconductors. Physical Review Letters. 2006;**96**:45901

[21] Alvarez-Quintana J. Impact of the substrate on the efficiency of thin film thermoelectric technology. Applied Thermal Engineering. 2015;**84**:206-210

[22] Salvador JR, Cho JY, Ye Z, Moczygemba JE, Thompson AJ, Sharp JW, et al. Conversion efficiency of skutterudite-based thermoelectric modules. Physical Chemistry. 2014;**16**: 12510-12520

[23] Taguchi K, Terakado K, Ogusu M, Matumoto A, Kayamoto T, Okura K, et al. Linear shaped Si-Ge thermoelectric module. In: Reference Number F2000A045 in Proceedings of Seul 2000 FISITA World Automotive Congress; 2000. pp 1-5

[24] Joshi G, He R, Engber M, Samsonidze G, Pantha T, Dahal E, et al. NbFeSb-based p-type half-Heuslers for power generation applications. Energy & Environmental Science. 2014;**7**:4070-4076

[25] Fujisaka T, Sui H, Suzuki RO. Design and numerical evaluation of Cascade-type thermoelectric modules. Journal of Electronic Materials. 2013;**42**:1688-1696

[26] Sun T, Peavey JL, David Shelby M, Ferguson S, O'Connor BT. Heat shrink formation of a corrugated thin film thermoelectric generator. Energy Conversion and Management. 2015; **103**:674-680

[27] Madan D, Chen A, Wright PK, Evans JW. Printed Se-doped MA n-type Bi2Te3 thick-film thermoelectric generators. Journal of Electronic Materials. 2012;**41**(6):1481

[28] Chen A, Madan D, Wright PK, Evans JW. Dispenser-printed planar thick-film thermoelectric energy generators. J Micromechanics Microengineering. 2011;**104006**:21

[29] Zheng XF, Liu CX, Yan YY, Wang Q. A review of thermoelectrics research – Recent developments and potentials for sustainable and renewable energy applications. Renewable and Sustainable Energy Reviews. 2014;**32**:486-503

[30] Aswal DK, Basu R, Singh A. Key issues in development of thermoelectric power generators: High figure-of-merit materials and their highly conducting interfaces with metallic interconnects. Energy Conversion and Management. 2016;**114**:50-67

[31] Hamid Elsheikh M, Shnawah DA, Sabri MFM, Said SBM, Haji Hassan M, Ali Bashir MB, et al. A review on thermoelectric renewable energy: Principle parameters that affect their performance. Renewable and Sustainable Energy Reviews. 2014;**30**:337-355

[32] Fateh H, Baker CA, Hall MJ, Shi L. High fidelity finite difference model for exploring multi-parameter thermoelectric generator design space. Applied Energy. 2014;**129**:373-383

[33] Hodes M. Optimal pellet geometries for thermoelectric power generation. IEEE Trans Components Packag Technol. 2010;**33**:307-318

[34] Sahin AZ, Yilbas BS. The thermoelement as thermoelectric power generator: Effect of leg geometry on the efficiency and power generation. Energy Conversion and Management. 2013;**65**:26-32

[35] Shi Y, Mei D, Yao Z, Wang Y, Liu H, Chen Z. Nominal power density analysis of thermoelectric pins with non-constant cross sections. Energy Conversion and Management. 2015;**97**:1-6

[36] Yilbas BS, Ali H. Thermoelectric generator performance analysis: Influence of pin tapering on the first and second law efficiencies. Energy Conversion and Management. 2015;**100**: 138-146

[37] Ali H, Sahin AZ, Yilbas BS. Thermodynamic analysis of a thermoelectric power generator in relation to geometric configuration device pins. Energy Conversion and Management. 2014;**78**:634-640

[38] Xuan XC, Ng KC, Yap C, Chua HT. Optimization of two-stage thermoelectric coolers with two design configurations. Energy Conversion and Management. 2002;**43**:2041-2052

[39] Cheng Y-H, Lin W-K. Geometric optimization of thermoelectric coolers in a confined volume using genetic algorithms. Applied Thermal Engineering. 2005;**25**:2983-2997

[40] Cheng Y-H, Shih C. Maximizing the cooling capacity and COP of two-stage thermoelectric coolers through genetic algorithm. Applied Thermal Engineering. 2006;**26**:937-947

[41] Mu Y, Chen G, Yu R, Li G, Zhai P, Li P. Effect of geometric dimensions on thermoelectric and mechanical performance for Mg2Si-based thermoelectric unicouple. Materials Science in Semiconductor Processing. 2014;**17**:21-26

[42] Ioffe AF. Semiconductor thermoelements and thermoelectric cooling. Infosearch London. 1957

[43] Yamashita O. Resultant Seebeck coefficient formulated by combining the Thomson effect with the intrinsic Seebeck coefficient of a thermoelectric element. Energy Conversion and Management. 2009;**50**(9):2394

[44] Salerno D. Ultralow voltage energy harvester uses thermoelectric generator for battery-free wireless sensor. Journal of Analog Innovation. 2010;**20**(3):1

[45] García-cañadas J, Min G. Impedance spectroscopy models for the complete characterization of thermoelectric materials. Journal of Applied Physics. 2014;**116**:174510

[46] Iwasaki H, Koyano M, Hori H. Evaluation of the figure of merit on thermoelectric materials by Harman method. Japanese Journal of Applied Physics. 2002;**41**:6606

[47] Reeves GK, Harrison HB. Obtaining the specific contact resistance from transmission line model measurements. IEEE Electron Device Letters. 1982;**3**:111-113

Chapter 7

The Importance of the Assembly in Thermoelectric Generators

Miguel Araiz, Leyre Catalan, Oscar Herrero,
Gurutze Perez and Antonio Rodriguez

Additional information is available at the end of the chapter

http://dx.doi.org/10.5772/intechopen.75697

Abstract

Generally, in the optimization of thermoelectric generators, only the heat exchangers or the thermoelectric modules themselves are taken into account. However, the assembly of the generator as a whole is of vital importance since a bad contact or a thermal bridge can waste the performance of an optimal generator. In this sense, the present chapter analyzes experimentally the use of different interface materials to reduce the thermal contact resistance between the modules and the heat exchangers, the influence of the pressure distribution in the assembly as well as the effect of different insulating materials in order to reduce the thermal bridge between the exchangers. Thus, it has been demonstrated that a good assembly requires the implementation of thermal interface materials to ensure the microscopic contact between the heat exchangers and the modules, besides a uniform clamping pressure. Nevertheless, since this is normally achieved with screws, they represent a source of thermal bridges in conjunction with the small distance between the exchangers. In order to reduce heat losses due to thermal bridges, which can represent up to one-third of the incoming heat, an increment of the distance between the exchangers and the use of an insulator is recommended.

Keywords: assembly, pressure distribution, clamping pressure, contact, thermal bridge, thermoelectric generator, thermal resistance

1. Introduction

Thermoelectric generators represent a reliable, robust and compact way for directly converting heat into electricity, as their spread use for space applications demonstrates [1]. However, these devices are hampered by their low efficiency, which has limited their expansion to civil applications.

In order to improve the efficiency of thermoelectric generators, the most common trend focuses on thermoelectric modules, the principal element of the generators since the transformation of heat into electricity is held on them thanks to Seebeck effect. A conventional module is made up of various thermocouples connected electrically in series in order to increase the operating voltage, and thermally in parallel to increase the thermal conductance. Each couple itself is typically composed of two semiconductor thermoelements (an n-type one, in which free electrons predominate, and a p-type one, dominated by free holes) united by a metal conductor. Two rigid substrates of ceramic material provide mechanical firmness to the whole system and isolate the internal circuit.

The efficiency of a thermocouple is proportional to the temperature difference among its sides, as well as to the figure of merit Z (Eq. (1)), which is a function of the Seebeck coefficients α, the thermal conductivities λ and the electrical resistivities ρ of the semiconductors that make up the thermocouple [2].

$$Z = \frac{(\alpha_p - \alpha_n)^2}{\left((\lambda_p \cdot \rho_p)^{1/2} + (\lambda_n \cdot \rho_n)^{1/2}\right)^2} \tag{1}$$

Hence, since efficiency is directly related to the capability of the materials as energy converters, there is a deep research about materials that present an equilibrium between a figure of merit as high as possible and ease of manufacturing [3–7]. Currently available thermoelectric materials present a ZT of around 1 or less, but the outlook for laboratories is to develop materials with a ZT of 2 in order to have an efficiency over 10% and become competitive with other technologies [8]. Nevertheless, this is not an easy task since the three parameters that define Z closely depend on one another [9]. Bismuth-telluride (Bi2Te3), half Heusler, skutterudites, oxides, magnesium silicides and tetrahedrites are the materials already available commercially [8].

Nonetheless, materials are not the unique tendency regarding the optimization of thermoelectric modules. It is also important to consider the geometrical configuration of the thermocouples: length, number of elements, cross-sectional area or the combination of materials within a thermocouple (the so-called segmented thermoelectric modules) among others [10–17].

Besides the improvement of thermoelectric modules, other aspects of a thermoelectric generator can be optimized in order to improve net generation. As shown in **Figure 1**, a thermoelectric generator is formed by one or multiple modules interconnected that generate electricity based on the heat received from a hot source, and emit the rest to a cold sink, which is normally the environment. Since the efficiency of the system increases as the sides of the thermoelectric modules approach the temperature of the heat source and sink, the introduction of heat exchangers between the modules and each of the thermal reservoirs becomes necessary in order to maximize the temperature difference.

In this sense, it is widely known that the optimization of heat exchangers is of utmost importance [9, 18–24]. Obtaining low thermal resistances maximizes the temperature difference, and consequently increases the efficiency of the entire generator. In fact, for a particular geometry it was demonstrated that a 10% improvement of the thermal resistance causes an increase of 8% in the electric power generation [25].

http://dx.doi.org/10.5772/intechopen.75697

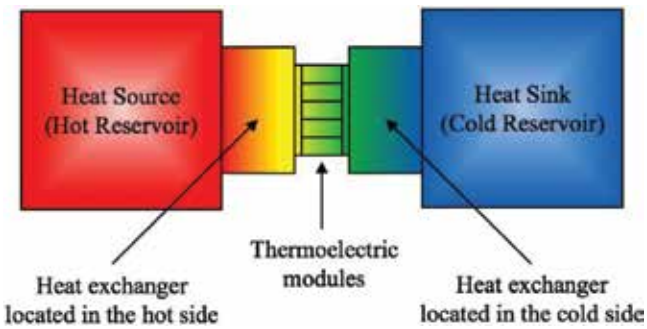

Figure 1. Basic diagram of a thermoelectric generator.

However, optimization processes often forget the assembly of the generator, i.e. how the different parts are interconnected. And this is something to definitely take into account since a poor assembly can waste the performance of the whole generator regardless having optimal modules and heat exchangers. Thus, the present chapter analyzes three different aspects that need to be considered in the assembly of a thermoelectric generator.

Section 2 deals with the interface contact, or how the microscopic unevenness can affect heat transfer. Section 3 shows the importance of having a uniform pressure distribution in order to ensure a good contact between the different parts. Section 4 explains how to reduce the thermal bridges, undesirable heat losses. Finally, Section 5 summarizes and concludes the chapter.

2. Interface contact

When two surfaces are confronted, it may seem that there exists a perfect contact among them. However, due to their roughness, surfaces are only in touch at some points, being mostly separated by air gaps that reduce the heat transmission in the interface (**Figure 2**). In thermoelectric generators, this fact attenuates the temperature difference across the thermoelectric modules, and therefore, decreases the output power. Thus, the present section explains how to quantify and improve the contact between the modules and each heat exchanger that compose a thermoelectric generator.

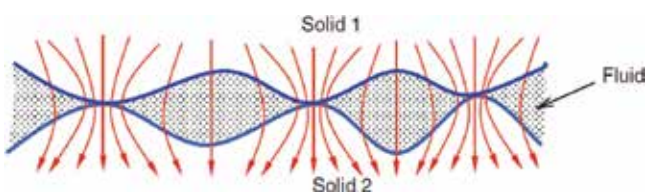

Figure 2. Representation of the interface filled with air. Red lines simulate the heat flux through the interface [26].

2.1. Thermal interface materials

In order to improve the contact and achieve a low temperature drop, thermal interface materials (TIMs) are used [27]. Their purpose consists in filling the gaps with materials that have a higher thermal conductivity than air. There are many families of thermal interface materials such as graphite sheets, thermal greases, phase change materials, indium or elastomers [28–30]. With the objective of checking if the presence of TIMs improves the real contact, this section analyzes three of the most common interface configurations for thermoelectric generators: without TIM, with graphite sheets, and with silicone thermal grease. The specific characteristics of these TIMs are described in **Table 1**.

The effect of the thermal contact is modeled through the thermal contact resistance (Eq. (2)), which depends on the temperature drop across the interface ΔT, the heat flux $\dot{Q}$ and the area A. This parameter takes into consideration that, due to imperfections in the material's surface, the real contact area is just a small fraction of the apparent contact area; and it is defined in such a way that it is also independent of the TIM's thickness, which varies with pressure.

$$R_{co} = \frac{\Delta T \cdot A}{\dot{Q}} \tag{2}$$

This thermal resistance depends on many parameters: materials of the contact (with their respective roughness, hardness, and conductivity), their geometry, interface temperature, or contact pressure among others. Therefore, it is difficult to obtain a general expression valid for all assembly possibilities and that considers all the variables. All the expressions available in the literature are restricted to particular geometries and only take into account some of the depending parameters [31–33]. In this sense, the present section focuses on obtaining the thermal contact resistance for the standard dimensions of a thermoelectric module (40×40 mm^2) depending on the clamping pressure and considering a side temperature of 100°C.

2.2. Methodology

Due to the broad parameter dependence of the thermal contact resistance, the test bench of **Figure 3b** has been used in order to measure thermal contact resistances for thermoelectric modules' dimensions in a controlled environment. This device is based on the principle of 'steady state' measurements across thermal interface material junctions.

Hence, a known heat is forced to flow through two 40×40 mm^2 reference bars (usually called fluxmeters) separated by the TIM of interest and under a certain pressure. Thanks to

	Thermal conductivity (W/m·K)	Operation temperature (°C)	Thickness (mm)
Graphite sheet	10	−40 to 400	0.127
Polydimethylsiloxane oil-based silicone thermal grease	0.41	−40 to 250	—

Table 1. Properties of thermal Interface materials.

http://dx.doi.org/10.5772/intechopen.75697

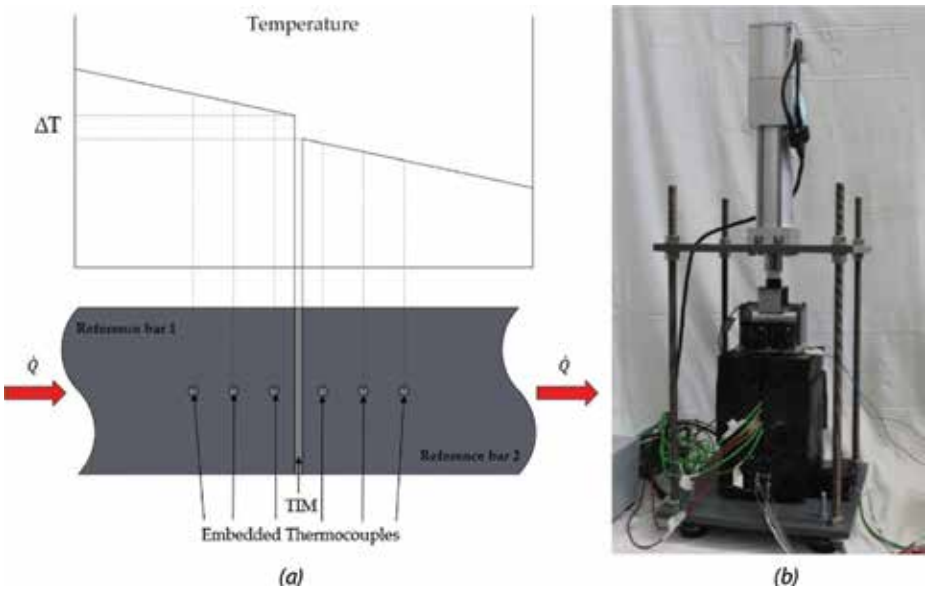

Figure 3. (a) Extrapolation method and (b) thermal contact resistance test bench for thermoelectric generation applications.

thermocouples embedded in these bars and since their conductivities are perfectly known, the temperature drop across the interface (ΔT) can be indirectly calculated by extrapolation (**Figure 3a**). Thermal contact resistance is therefore calculated with Eq. (2). Heat flux across the interface of Eq. (2) is generated by an electrical resistance and dissipated by a heat sink with a fan. Its calculation is possible thanks to the reference bars conductivity, thermocouples measurements and their distance.

Two dissimilar materials of the reference bars were used to test TIMs: highly conductive but soft 1050 Aluminum alloy and a cupper-tungsten alloy which presents an excellent relation between thermal conductivity and hardness. The specific properties (thermal conductivity, hardness, and roughness) of each of these materials are described in **Table 2**.

For each material, the three mentioned possible interfaces were studied: no TIM, graphite sheets and silicone thermal grease. All the experiments were performed under the same conditions. The only variable was pressure, one of the most influent parameters in thermal interface resistances, and which was exerted by a linear actuator. The studied pressures range between 50 and 1200 kPa because the pressure recommended by the thermoelectric modules manufacturer is around 1000 kPa [34].

Material	Thermal conductivity (W/m·K)	Hardness (HB)	Ra (μm)	Rz (μm)
Al 1050	229	21	0.090	1.275
W75Cu25	170	200	0.126	1.215

Table 2. Materials and properties of the fluxmeter bars.

In contact resistance measurement with the 'steady state method,' uncertainty calculation must be taken into account due to the large number of measures that are made. The uncertainty calculation method used is the same as other authors in the literature [35–38] when applying the same method to measure thermal contact resistances. **Table 3** shows the uncertainty values of the equipment.

2.3. Results and discussion

Firstly, results of the interface thermal resistance using aluminum bars are shown in **Figure 4a**. For all the studied interfaces, the behavior with respect pressure follows a similar trend: the thermal resistance decreases with pressure. Hence, the worst value is obtained at low pressures. In addition, it is confirmed that is better to use TIM instead of not using it; the highest thermal resistance corresponds to the absence of TIM. The thermal grease improves the contact without TIM, but when the pressure is higher, its presence is negligible. The reason is that the grease pumps out of the interface at high pressures. Therefore, thermal grease would not improve the contact in assemblies at elevated pressures. Graphite sheets seem to be better: thermal contact resistance is enhanced at every pressure point. The smallest value of thermal resistance obtained for graphite sheet is 2.19×10^{-5} K·m^2/W for the Aluminum interface at 1183 kPa.

Secondly, results of cupper-tungsten alloy bars are shown in **Figure 4b**. These bars have a higher hardness, and its influence can be observed in the results. Due to its higher hardness, thermal resistance without TIM is again the worst one and almost three times higher than with aluminum. In contrast, graphite sheet shows different results than before: its thermal resistance at low pressures is higher than thermal grease. Nevertheless, if the pressure increases, the behavior of the graphite sheets improves, being better than the thermal grease. Thus, on very hard surfaces thermal grease is very effective at low pressures due to its fluidity, and graphite sheet needs higher pressures to work well.

Hence, it can be said that thermal contact resistance must definitely be considered in thermoelectric assemblies because it produces a temperature drop across the interfaces that decreases the efficiency of thermoelectric generators. In order to reduce these thermal contact resistances, the use of thermal interface materials has been demonstrated regardless the

Measured parameter (x_i)	u_i
Temperature (thermocouple)	± 0.3 K
Temperature sensor location	± 300 μm
Force	± 0.2%
Hole distance	± 10 μm
Thermal conductivity	± 10%

Table 3. Uncertainties table.

http://dx.doi.org/10.5772/intechopen.75697

pressure. Among the studied TIMs, graphite is better for most of the cases. Nonetheless, hardness seems to be an important parameter to consider, with graphite being the most affected by this at low pressures. Thus, on very hard surfaces working with at low pressures, thermal grease presents a better behavior, reducing the temperature drop.

3. Influence of pressure distribution

Last section has shown the importance of achieving a low thermal contact resistance in the assembly of thermoelectric generators since it can affect the performance of the whole system. However, this is not always an easy task, and the introduction of thermal interface materials becomes necessary to ensure a good contact at microscopic level. Furthermore, the combination of pressure with these thermal interface materials improves even further the contact between surfaces as shown in **Figure 4**. These graphs analyze different thermal interface materials and different uniform pressure distributions. But what happens if the pressure distribution is not uniform?

Pressure distribution basically depends on the assembly, i.e. the location and the torque applied to the screws. Hence, if there is an uneven torque in the screws or if the location is not appropriate or even if the exerted torque is too big that it provokes the bending of the heat exchangers, it could happen that only some parts of the thermoelectric modules are in contact with the heat exchangers, leading to changes associated with the thermal contact resistance explained in last section [39, 40]. As a consequence, temperature mismatches appear and therefore problems of decreased power output arise [41]. Thus, although it is not normally taken into account, it is important to consider the clamping force in the assembly of thermoelectric generators [42, 43]. In this sense, the present section analyzes different screw configurations and torques to demonstrate the importance of the clamping pressure and its distribution in the assembly of thermoelectric generators.

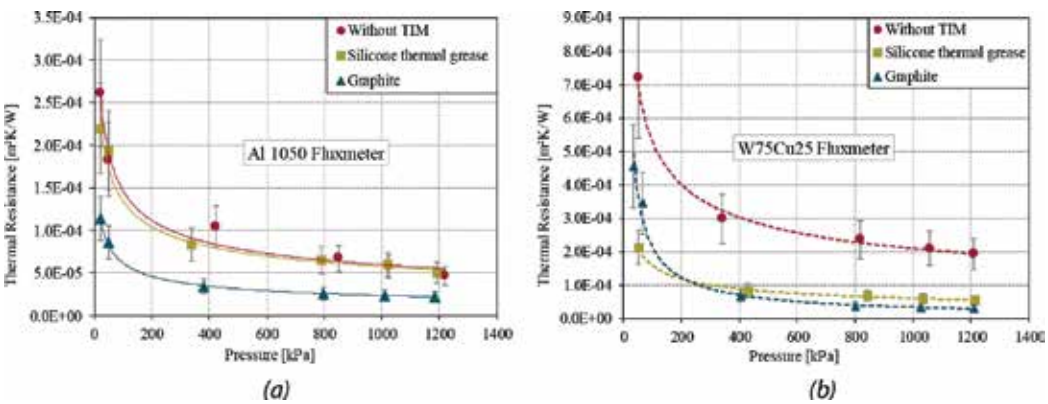

Figure 4. (a) Thermal resistance of TIMs in an aluminum interface at 100°C and (b) thermal resistance of TIMs in a copper-tungsten alloy interface at 100°C.

3.1. Methodology

3.1.1. Description of the studied configurations

In order to analyze how the pressure is distributed with regard the location of the screws and their torque, two different thermoelectric generators have been used with graphite as interface material since it has been demonstrated that it leads to better results than the other studied TIMs. In both generators, the heat source is represented by a heating plate made up of electrical resistances, in contact with the thermoelectric modules, which dissipate the non-converted heat to the ambient thanks to a fin dissipater assisted by a ventilator. The dimensions are the only difference between them. Hence, one of the generators is prepared for holding two thermoelectric modules while the bigger dimensions of the second one allows the implementation of four modules. For each generator, two possible screw configurations clamped with different torques have been analyzed. The location of the screws is depicted in **Figure 5**, while the studied torques are summarized in **Table 4**.

3.1.2. Study of the pressure distribution

Pressure distribution has been studied thanks to PRESCALE Pressure Measurement Films by Fujifilm [44]. These films change their color intensity depending on the pressure applied, changing from white to dark magenta as pressure increases. In this particular case, films ranged between 0.6 and 2.5 MPa have been used.

For each of the experiments, a film has been placed between the thermoelectric modules and the fin dissipater located at the cold side. With this film suitably located, the generator has been assembled with the corresponding torques. As a consequence, the films changed their color in those areas where more pressure was exerted. After the generator was perfectly assembled, the set was cautiously dismantled and the films analyzed. Experiments were repeated three times each in order to ensure their repetitiveness.

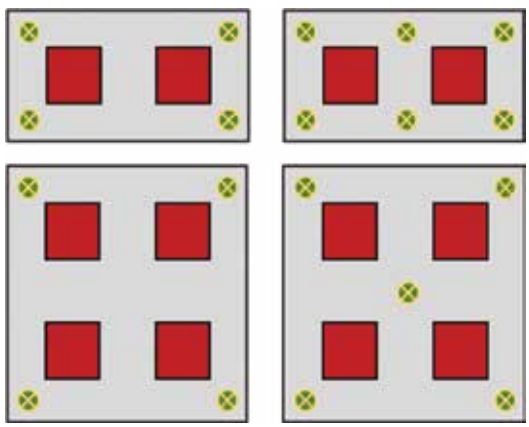

Figure 5. The four studied screw configurations for the considered thermoelectric generators.

Number of modules	Number of screws	Torque (Nm)
2	4	1
	6	1
	6	1.5
	6	2
4	4	1
	5	2

Table 4. Summary of the studied torques for the different configurations.

The analysis has been performed in two steps. On the one hand, a qualitative analysis has allowed the visual determination of the pressure distribution. On the other hand, the comparison of each of the pixels with a scale by means of the closest neighbor method has permitted a statistical analysis, with the median as the most important parameter.

3.2. Results and discussion

3.2.1. Qualitative analysis

Based on the pressure films, it is obvious that there does not exist a uniform pressure distribution in the modules. **Figure 6a** shows the distribution obtained in the configuration with two modules and four screws. As it can be observed, only those parts closer to the screws have a significant pressure. The central part of the configuration seems not to be in such a good contact due to the bending of the base of the dissipator.

If another two screws are introduced in order to reduce the mentioned bending (**Figure 6b–d**), the pressure distribution becomes more uniform. The reason why the distribution is not equally uniform at both sides of the modules is due to the different distance of the screws to the modules. Nonetheless, as expected, it is achieved a higher intensity of this pressure as the torque increases.

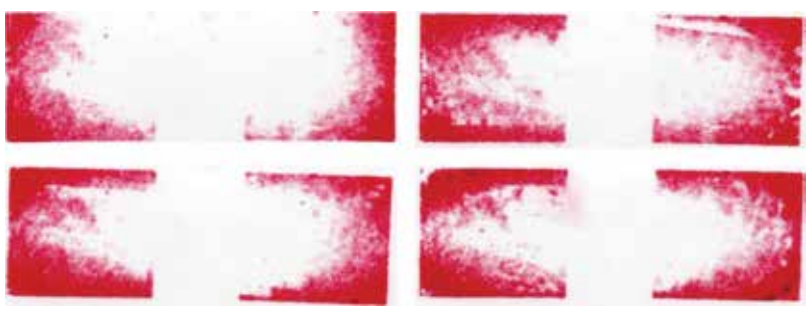

Figure 6. Pressure films for (a) 4 screws, 1 Nm; (b) 6 screws, 1 Nm; (c) 6 screws, 1.5 Nm; and (d) 6 screws, 2 Nm.

In the case of having four modules in an assembly with only four screws, the fact that pressure is not uniformly distributed becomes more noticeable. Only the four corners, where screws are actually located, are working under an appreciable pressure (**Figure 7a**).

If an additional screw is located in the center so that the bending of the dissipater is reduced and the pressure is increased in order to improve the contact, the improvements obtained are minimal (**Figure 7b**) due to the big distance between the additional screw and the modules. Thus, it is recommended that each module has its own tightening.

3.2.2. Quantitative analysis

Visual analysis of **Figures 6** and **7** states a pressure distribution which is far from uniformity. In this section, this fact is demonstrated with a statistical analysis based on the median. Since the pressure films used for the experiments are ranged from 0.6 to 2.5 MPa, those parts that work with a pressure out of scale will not be appropriately represented. Thus, the median is the most significant parameter to analyze: half of the pixels work under that pressure while the other half works above it.

On the one hand, for the heat exchanger with two modules, in the case in which there are only four screws, most of the module works under a pressure of 0.6 MPa or less. This value improves if the bending is restricted by means of an additional pair of screws located between the modules. As shown in **Figure 8**, and accordingly to the previous states, the median of the pressure increases with the torque in a proportion that seems linear.

On the other hand, in the heat exchanger with four modules, the lack of macroscopic contact is evident with the median value of 0.6 MPa, i.e. most parts of the modules have a clamping pressure of less than 0.6 MPa. Nonetheless, although the visual analysis evinces a slight improvement when the fifth screw is introduced and a more significant torque exerted, this fact is not appreciable in the median value since the range of pressures of both configurations is much lower than 0.6 MPa, the lower limit of the scale of the film.

Hence, despite not being considered a critical aspect, screw distribution and torque are aspects to definitely take into account. The assembly configuration determines the pressure

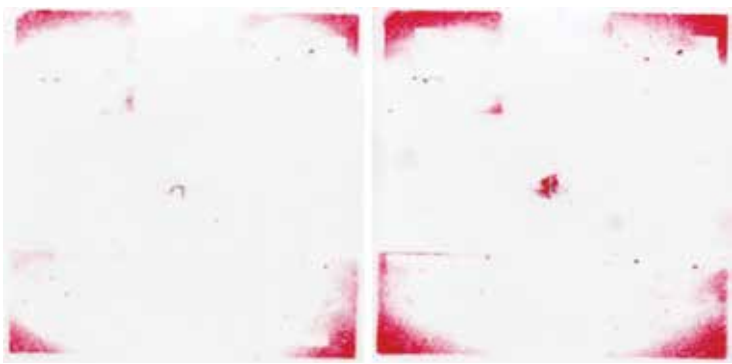

Figure 7. Pressure films for (a) four screws, 1 Nm (b) five screws, 2 Nm.

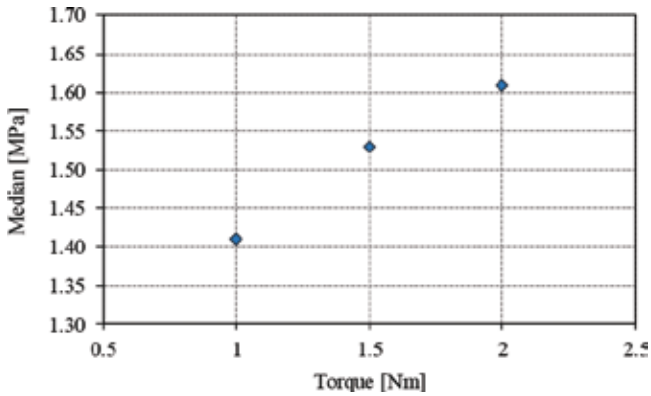

Figure 8. Median of the pressure against the applied torque for the configuration of two modules.

distribution in the modules, which is in turn related to the thermal contact resistance. If the module works under an uneven pressure distribution, the generation will be reduced, since some parts of the module can even be not in contact with the heat exchangers.

The most appropriate configuration seems that in which each module has the biggest amount of screws as close as possible to it. Furthermore, as the torque of these screws increases, the clamping pressure will get bigger as well as better distributed, and therefore, the thermal contact resistance will be reduced, leading to a better generation unless bending is provoked.

4. How to avoid thermal bridges

Last section has concluded that it is recommended to have an individual tightening of the modules in order to ensure a uniform pressure distribution that leads to a good thermal contact. In order to achieve it, screws are necessary although they represent a type of thermal bridge.

By definition, a thermal bridge is an area or component of an object which has higher thermal conductivity than the surrounding materials, creating a path of least resistance for heat transfer [45, 46]. In thermoelectric generators, there are two main sources for thermal bridges. On the one hand, the screws used to ensure a good contact and pressure distribution are normally metallic, and therefore, highly thermal conductive. In order to reduce the amount of heat lost through these screws, it is typical to use nylon washers. Nonetheless, even with this nylon rings, it is estimated that the thermal resistance of each screw is 52 K/W.

On the other hand, due to the small thickness of the thermoelectric modules (most commonly 3 mm), it can occur that part of the heat directly flows within the heat exchangers, instead of through the thermoelectric modules. Therefore, insulating materials are usually inserted between the heat exchangers.

In the present section, assuming there is a good thermal contact, three different alternatives of insulating materials that are normally used in order to avoid thermal bridges will be studied:

- Mineral wool fiber cardboard manufactured by Nefalit. This material is made up of highly thermal insulating fibers bound together with fillers. These plates are suitable for temperatures up to 750 or 1000°C and are easy to handle in the assembly. They present a thermal conductivity of 0.15 W/mK [47].
- Acrylic wool made by Flexiband: this insulating material is manufactured from pure refractory fibers which provide a low thermal conductivity (0.09 W/mK) and flexibility [48].
- Air: known as one of the best insulators, air presents a thermal conductivity of 0.024 W/mK. Nevertheless, if convection currents are created, heat transfer coefficients improve and the effective value of the thermal conductivity can be considerably increased.

4.1. Methodology

For each of these insulating materials, the assembly depicted in **Figure 9** was mounted. A heating plate acts as a heat source, providing a power, $\dot{Q}_{source}$, of 100, 150 or 200 W. This plate is in direct contact with two thermoelectric modules surrounded by the insulating material of study in each case. In the cold side of the thermoelectric modules, there is a fin dissipater assisted by a ventilator. In order to minimize direct thermal losses from the heating plate to the environment, a 50 mm layer of rock wool has been used.

Figure 9 also shows the location of the type K thermocouples installed. Hence, the three involved heat fluxes can be determined: the heat flux that goes through the modules and therefore is responsible of the electric generation, $\dot{Q}_{\mathrm{mod}}$; the heat flux lost due to the thermal bridges, $\dot{Q}_{tb}$; and the heat flux that is directly lost from the source to the ambient, $\dot{Q}_{amb}$. This last heat flux has been calculated thanks to the insulation and the ambient temperatures in conjunction with a convection coefficient of $h = 5$ W/m^2 K [49].

$$\dot{Q}_{amb} = h \cdot A \cdot \left(T_{ins} - T_{amb}\right) \tag{3}$$

In contrast, the calculation of the other two heat fluxes has required the use of a computational model. Temperatures T_c and T_h are known, but thermal resistances depend on the thermal contacts between the different parts, $R_{co,h}$ and $R_{co,c}$, as well as on the existing temperature distribution in each case. Thus, the computational model based on the finite difference method of **Figure 10** has been used. This model calculates all the possible thermal resistances of the modules, R_{mod}, and their generating voltage depending on the temperature difference and the load resistance, with an error less than 10% [50]. By comparing the experimental temperature difference and the open circuit voltage determined by the model, both the thermal contact resistances and the thermoelectric modules resistance have been estimated.

Based on them, the different heat fluxes can be computed as follows. Firstly, the heat that is supposed to flow through the modules is the heat provided by the source minus the heat directly lost to the environment.

$$\dot{Q}_h = \dot{Q}_{source} - \dot{Q}_{amb} \tag{4}$$

http://dx.doi.org/10.5772/intechopen.75697

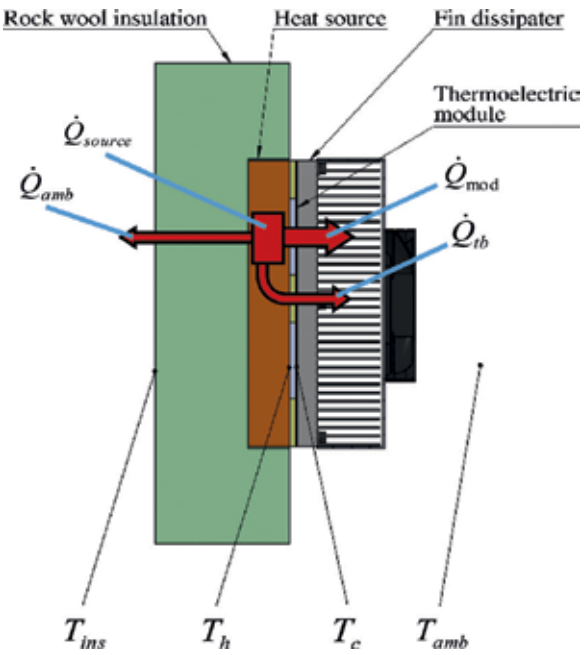

Figure 9. Schematic view of the studied configuration with specification of the position of the type K thermocouples installed and the heat fluxes considered.

Secondly, the heat that goes through the modules is computed with the mentioned thermal resistances, the measured temperature difference and the number of modules *M*.

$$\dot{Q}_{\text{mod}} = \frac{M \cdot (T_h - T_c)}{R_{co,h} + R_{\text{mod}} + R_{co,c}} \tag{5}$$

Finally, the heat that is lost in the thermal bridge can be computed as the difference between the heat that is supposed to flow through the modules, and the heat that actually passes through them.

$$\dot{Q}_{tb} = \dot{Q}_h - \dot{Q}_{\text{mod}} \tag{6}$$

Nonetheless, the percentage values of the heat that goes through the thermal bridges instead of the modules acquires more interest:

$$\%\dot{Q}_{tb} = \frac{\dot{Q}_{tb}}{\dot{Q}_h} \cdot 100 \tag{7}$$

The repetitiveness of the experiments has been ensured by means of mounting and dismounting the ensemble three times for each configuration, which also reduces the uncertainty of the measurements and the experimental procedure.

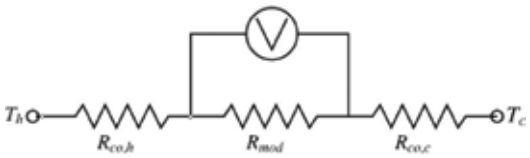

Figure 10. Thermal-electric analogy of the computational model.

4.2. Results and discussion

In a first approach, **Figure 11** shows the results obtained for the configuration in which the insulating material has the same thickness as the module, i.e. 3 mm (**Figure 12**). As it can be observed, for all the studied materials, the percentage of heat lost through the insulation increases with the heat dissipated by the source. Nonetheless, this amount differs for each material. Thus, cardboard presents the most significant heat losses, with almost 30% lost due to thermal bridges. This is the expected result since it presents the highest conductivity of the studied materials. However, despite the air having the smallest thermal resistance, the thickness between both heat exchangers is enough to create convection currents that improve the heat transfer. As a result, thermal losses with either acrylic wool or air as insulators are similar. Furthermore, it is worth mentioning that in the case of having air, which is equivalent to not putting anything, the assembly is more complicated since modules can easily move, as they are not held by the insulating material.

Since thermal losses represent a considerable part of the heat that should go through the modules, a second configuration (**Figure 13**) with a higher distance between the heat exchangers increases was also studied. Increasing the thickness of the insulation causes an increment of the thermal resistance, and therefore, thermal losses should decrease. This increment of thickness

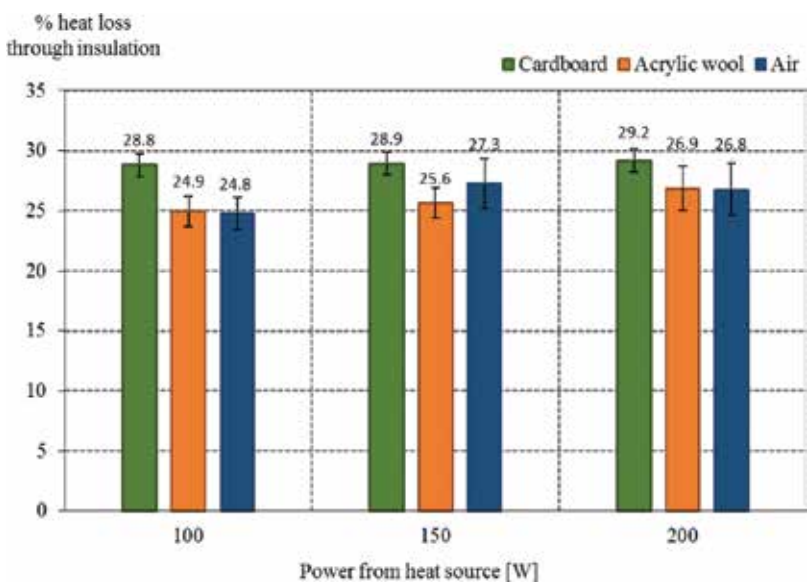

Figure 11. Percentage of heat loss through insulation for different heat powers in absence of heat extenders.

http://dx.doi.org/10.5772/intechopen.75697

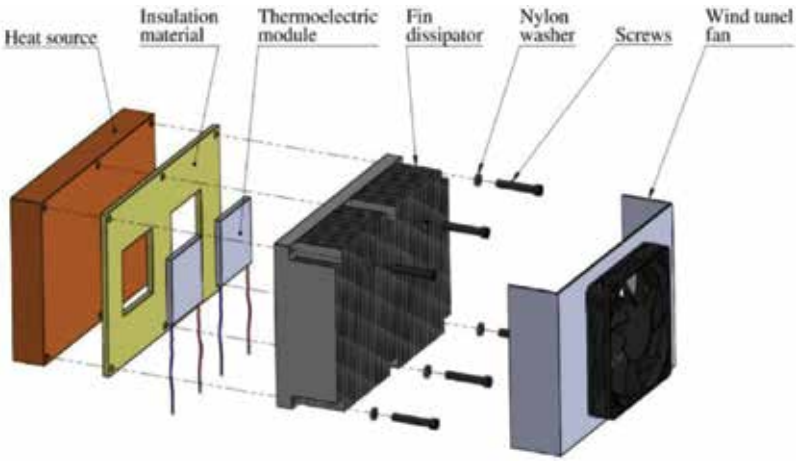

Figure 12. Exploded view of the studied generator without heat extenders.

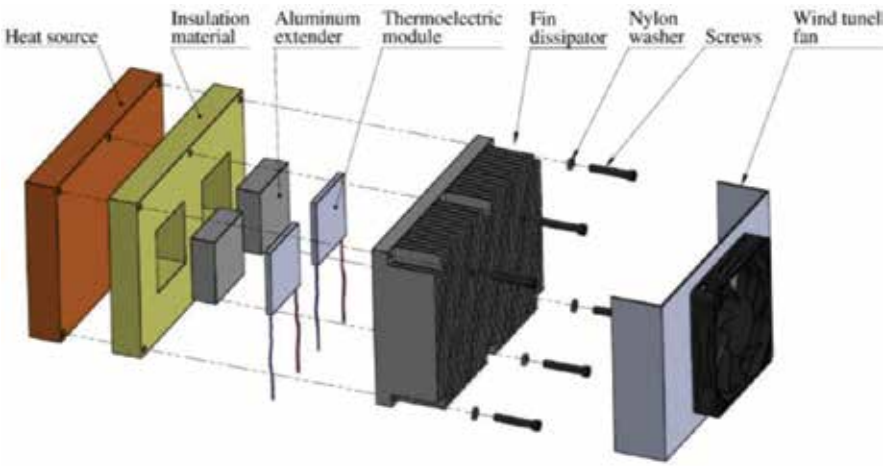

Figure 13. Exploded view of the studied generator with heat extenders.

is compensated with highly conductive aluminum heat extenders in the case of the modules. Nonetheless, this leads to two additional contacts, with their associated thermal contact resistance, which can negatively influence the thermal transfer if contact is not appropriated. In this case, graphite sheets have again been used as TIM in order to ensure the microscopic contact.

As it can be observed in **Figure 14**, the increment of distance between the heat exchangers supposes a reduction of approximately 5% in the percentage of heat that is lost due to thermal bridges since, as expected, thermal resistances of the insulation increase leading to less thermal losses. For this configuration, the tendency remains similar: heat losses increase with the power from the heat source and acrylic wool is still the best insulator and cardboard the worst. However, differences between acrylic wool and air are now more evident. Since the distance between the exchangers has increased, there is more space for the convection currents to flow, this improving the heat transfer and leading to more thermal losses.

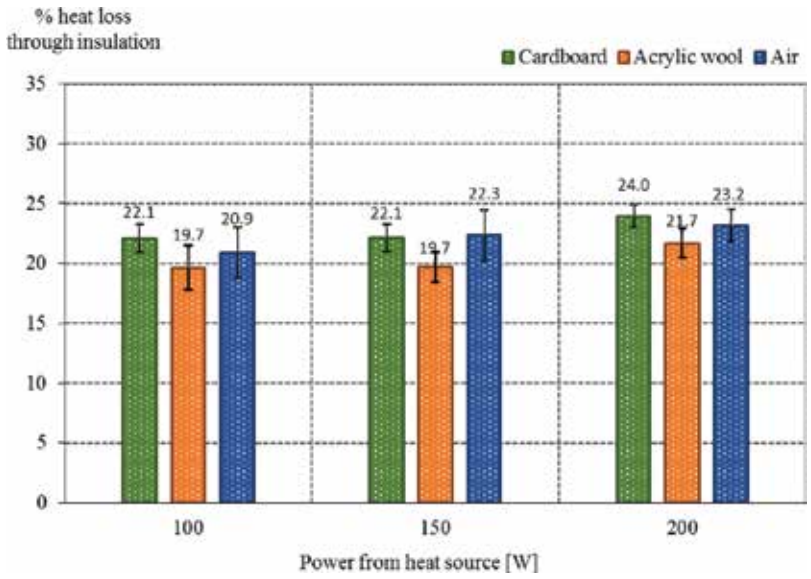

Figure 14. Percentage of heat loss through insulation for different heat powers in the case of introducing heat extenders.

In summary, losses due to thermal bridges definitely need to be taken into account: around one-fourth of the power provided from the source goes through the insulation instead of the thermoelectric modules. As a consequence, the generation is reduced.

In order to decrease the thermal losses, it has been demonstrated that it is better to increase the thickness of the insulation, despite adding two additional contacts. Among the materials studied, the best one is acrylic wool. Nonetheless, air (equivalent to not adding any insulation) should be considered, since the cost is reduced and there is not such a significant difference among them. However, it presents the disadvantage of a more complicated assembly.

5. Conclusions

Although the assembly is not generally considered in the optimization of thermoelectric generators, the present chapter has demonstrated that it is an aspect that cannot be forgotten since it deteriorates the performance of generators. Thus, the assembly needs to incorporate thermal interface materials that counteract microscopic imperfections, being graphite sheets the most recommended one between the studied. In order to ensure this microscopic contact and reduce the temperature drop that appears in the interface, it is also important to apply some pressure to the assembly. The easiest way to achieve this is the use of screws. Pressure measurement films have shown that each module needs to have its own tightening. Assemblies that share this tightening can cause a contact in only some parts of the module. However, the implementation of these screws has a counter effect: they represent a thermal bridge themselves and part of the heat is lost through them. Therefore, the insertion of nylon rings is recommended. The other important source of losses due to thermal bridges occurs between the heat exchangers, since the distance between them is too small. Placing an insulating material between the exchangers slightly reduces the losses, but it is better to

increase the distance between them with the aid of a conductive heat extender and insulate with acrylic wool. Nonetheless, if this material is not added, air has demonstrated to also be a good insulator, cheaper but which leads to a less precise assembly.

Acknowledgements

The authors are indebted to the Ministry of Economy, Industry and Competitiveness-Government of Spain and FEDER Funds for economic support of this work, included in the DPI2014-53158-R Research Project, as well as to the FPU Program of the Spanish Ministry of Education, Culture and Sport (FPU16/05203).

Nomenclature

α	Seebeck coefficient, V/K
λ	thermal conductivity, W/mK
ρ	electrical resistivity, Ωm
A	contact area, m^2
h	free convection coefficient, W/m^2K
M	number of thermoelectric modules
n	relative to type-n semiconductor
p	relative to type-p semiconductor
$\dot{Q}$	heat flux through the interface, W
$\dot{Q}_{amb}$	heat flux losses to ambient through insulation, W
$\dot{Q}_{h}$	heat through thermoelectric generator, W
$\dot{Q}_{\mathrm{mod}}$	heat through thermoelectric modules, W
$\dot{Q}_{source}$	heat provided by heating plate, W
$\dot{Q}_{tb}$	heat flux due to thermal bridges, W
R_a	arithmetical mean roughness (μm)
R_z	ten-point mean roughness (μm)
R_{co}	thermal contact resistance, Km^2/W
$R_{co,h}; R_{co,c}$	contact thermal resistance of hot and cold side, K/W
R_{mod}	thermal resistance of the modules, K/W
T_{amb}	ambient temperature, K
T_c	module cold face temperature, K

T_h	module hot face temperature, K
T_{ins}	insulation temperature, K
U_i	uncertainty in the measurement x_i
x_i	each measurement made in experiments
Z	figure of merit
ΔT	temperature drop across interface, K

Author details

Miguel Araiz[1,2]*, Leyre Catalan[1,2], Oscar Herrero[1], Gurutze Perez[1,2] and Antonio Rodriguez[1,2]

*Address all correspondence to: miguel.araiz@unavarra.es

1 Public University of Navarre, Pamplona, Spain

2 Institute of Smart Cities, Pamplona, Spain

References

[1] Abelson RD. Space Missions and Applications. Thermoelectr. Handb. Macro to nano2. 1st ed. Boca Raton: CRC Press; 2006, pp. 56.1-56.29

[2] Rowe D. General Principles and Considerations. Thermoelectr. Handb. Macro to Nano. Boca Raton: CRC Press; 2006. pp. 1.1-1.14

[3] Romanjek K, Vesin S, Aixala L, Baffie T, Bernard-Granger G, Dufourcq J. High-performance silicon–germanium-based thermoelectric modules for gas exhaust energy scavenging. Journal of Electronic Materials. 2015;**44**:2192-2202. DOI: 10.1007/s11664-015-3761-1

[4] Lee S, Lee KH, Kim YM, Kim HS, Snyder GJ, Baik S, et al. Simple and efficient synthesis of nanograin structured single phase filled skutterudite for high thermoelectric performance. Acta Materialia. 2018;**142**:8-17. DOI: 10.1016/j.actamat.2017.09.044

[5] Aswal DK, Basu R, Singh A. Key issues in development of thermoelectric power generators: High figure-of-merit materials and their highly conducting interfaces with metallic interconnects. Energy Conversion and Management. 2016;**114**:50-67. DOI: 10.1016/j.enconman.2016.01.065

[6] Gayner C, Kar KK. Recent advances in thermoelectric materials. Progress in Materials Science. 2016;**83**:330-382. DOI: 10.1016/j.pmatsci.2016.07.002

[7] Twaha S, Zhu J, Yan Y, Li B. A comprehensive review of thermoelectric technology: Materials, applications, modelling and performance improvement. Renewable and Sustainable Energy Reviews. 2016;**65**:698-726. DOI: 10.1016/j.rser.2016.07.034

[8] Champier D. Thermoelectric generators: A review of applications. Energy Conversion and Management. 2017;**140**:167-181. DOI: 10.1016/j.enconman.2017.02.070

[9] Elghool A, Basrawi F, Ibrahim TK, Habib K, Ibrahim H, Idris DMND. A review on heat sink for thermo-electric power generation: Classifications and parameters affecting performance. Energy Conversion and Management. 2017;**134**:260-277. DOI: 10.1016/j.enconman.2016.12.046

[10] Min G. Thermoelectric Modules Design Theories. Thermoelectr. Handb. Macro to Nano. 1st ed. Boca Raton: CRC Press; 2006. pp. 11.1-11.15

[11] Rowe DM, Min G. Optimisation of thermoelectric module geometry for waste heat electric power generation. Journal of Power Sources. 1992;**38**:253-259

[12] Vián JG, Astrain D, Rodríguez A, Martínez A. Computational optimization of a thermoelectric ice-maker as a function of the geometric parameters of a peltier module. Journal of Electronic Materials. 2010;**39**:1786-1791. DOI: 10.1007/s11664-010-1134-3

[13] Chen W-H, Wu P-H, Lin Y-L. Performance optimization of thermoelectric generators designed by multi-objective genetic algorithm. Applied Energy. 2018;**209**:211-223. DOI: 10.1016/j.apenergy.2017.10.094

[14] Ma Q, Fang H, Zhang M. Theoretical analysis and design optimization of thermoelectric generator. Applied Thermal Engineering. 2017;**127**:758-764. DOI: 10.1016/j.applthermaleng.2017.08.056

[15] Kishore RA, Sanghadasa M, Priya S. Optimization of segmented thermoelectric generator using Taguchi and ANOVA techniques. Scientific Reports. 2017;**7**:16746. DOI: 10.1038/s41598-017-16372-8

[16] Brownell E, Hodes M. Optimal design of thermoelectric generators embedded in a thermal resistance network. IEEE Transactions on Components, Packaging, and Manufacturing Technology. 2014;**4**:612-621. DOI: 10.1109/TCPMT.2013.2295169

[17] Aranguren P, Roch A, Stepien L, Abt M, Von Lukowicz M, Dani I, et al. Optimized design for flexible polymer thermoelectric generators. Applied Thermal Engineering. 2016;**102**:402-411. DOI: 10.1016/j.applthermaleng.2016.03.037

[18] Astrain D, Martínez Á. Heat exchangers for thermoelectric devices. Heat exchangers - Basics Design Applications. 2012:289-308. DOI: 10.5772/33464

[19] Aranguren P, Astrain D, Rodriguez A, Martinez A. Net thermoelectric power generation improvement through heat transfer optimization. Applied Thermal Engineering. 2017;**120**:496-505. DOI: 10.1016/j.applthermaleng.2017.04.022

[20] Dent Jr TJ, Agrawal AK. Role of thermal strategies in thermoelectric power generation. 50th AIAA Aerosp. Sci. Meet. Incl. New Horizons Forum Aerosp. Expo; 2012. pp. 2012-520

[21] Su CQ, Wang WS, Liu X, Deng YD. Simulation and experimental study on thermal optimization of the heat exchanger for automotive exhaust based thermoelectric generators. Case Studies in Thermal Engineering. 2014;**4**:85-91

[22] Zhou S, Sammakia BG, White B, Borgesen P, Chen C. Multiscale modeling of thermoelectric generators for conversion performance enhancement. International Journal of Heat and Mass Transfer. 2015;**81**:639-645

[23] Martínez A, Vián JG, Astrain D, Rodríguez A, Berrio I. Optimization of the heat exchangers of a thermoelectric generation system. Journal of Electronic Materials. 2010;**39**:1463-1468. DOI: 10.1007/s11664-010-1291-4

[24] Lv S, He W, Jiang Q, Hu Z, Liu X, Chen H, et al. Study of different heat exchange technologies influence on the performance of thermoelectric generators. Energy Conversion and Management. 2018;**156**:167-177. DOI: 10.1016/j.enconman.2017.11.011

[25] Astrain D, Vián JG, Martínez A, Rodríguez A. Study of the influence of heat exchangers' thermal resistances on a thermoelectric generation system. Energy. 2010;**35**:602-610. DOI: 10.1016/j.energy.2009.10.031

[26] Madhusudana CV. Thermal Contact Conductance. In: Ling FF editor. Switzerland: Springer International Publishing; 2014. DOI: 10.1007/978-3-319-01276-6. ISBN: 978-319-01275-9

[27] Sakamoto T, Iida T, Sekiguchi T, Taguchi Y, Hirayama N, Nishio K, et al. Selection and evaluation of thermal interface materials for reduction of the thermal contact resistance of thermoelectric generators. Journal of Electronic Materials. 2014;**43**:3792-3800. DOI: 10.1007/s11664-014-3165-7

[28] Prasher R. Thermal interface materials: Historical perspective, status, and future directions. Proceedings of the IEEE. 2006;**94**:1571-1586. DOI: 10.1109/JPROC.2006.879796

[29] Gwinn JP, Webb RL. Performance and testing of thermal interface materials. Microelectronics Journal. 2003;**34**:215-222. DOI: 10.1016/S0026-2692(02)00191-X

[30] Due J, Robinson AJ. Reliability of thermal interface materials: A review. Applied Thermal Engineering. 2013;**50**:455-463. DOI: 10.1016/j.applthermaleng.2012.06.013

[31] Fletcher LS. Prediction of Thermal Contact Conductance between Similar Metal Surfaces. Heat Transf. Spacecr. Therm. Control, New York: American Institute of Aeronautics and Astronautics; 1971. pp. 273-88. DOI: 10.2514/5.9781600864988.0273.0288

[32] Mikić BB. Thermal contact conductance; theoretical considerations. International Journal of Heat and Mass Transfer. 1974;**17**:205-214. DOI: 10.1016/0017-9310(74)90082-9

[33] Cooper MG, Mikic BB, Yovanovich MM. Thermal contact conductance. International Journal of Heat and Mass Transfer. 1969;**12**:2. DOI: 10.1016/0017-9310(69)90011-8

[34] Marlow Industries. Technical Data Sheet: Tg12-8-01Ls Power Generators n.d.:1-2

[35] Kempers R, Kolodner P, Lyons A, Robinson AJ. A high-precision apparatus for the characterization of thermal interface materials. The Review of Scientific Instruments. 2009;**80**:95111. DOI: 10.1063/1.3193715

[36] Smith AN, Jankowski NR, Boteler LM. Measurement of high-performance thermal interfaces using a reduced scale steady-state tester and infrared microscopy. Journal of Heat Transfer. 2016;**138**:41301. DOI: 10.1115/1.4032172

[37] Hao M, Saviers KR, Fisher TS. Design and validation of a high-temperature thermal Interface resistance measurement system. Journal of Thermal Science and Engineering Applications. 2016;**8**:31008. DOI: 10.1115/1.4033011

[38] Warzoha RJ, Smith AN, Harris M. Maximum resolution of a probe-based, steady-state thermal interface material characterization instrument. Journal of Electronic Packaging. 2016;**139**:11004. DOI: 10.1115/1.4035178

[39] Montecucco A, Buckle J, Siviter J, Knox AR. A new test rig for accurate nonparametric measurement and characterization of thermoelectric generators. Journal of Electronic Materials. 2013;**42**:1966-1973. DOI: 10.1007/s11664-013-2484-4

[40] Yeh C, Wen C, Chen Y, Yeh S, Wu C. An experimental investigation of thermal contact conductance across bolted joints. Experimental Thermal and Fluid Science. 2001;**25**:349-357. DOI: 10.1016/S0894-1777(01)00096-6

[41] Montecucco A, Siviter J, Knox AR. The effect of temperature mismatch on thermoelectric generators electrically connected in series and parallel. Applied Energy. 2014;**123**:47-54. DOI: 10.1016/j.apenergy.2014.02.030

[42] Nour Eddine A, Chalet D, Faure X, Aixala L, Chessé P. Optimization and characterization of a thermoelectric generator prototype for marine engine application. Energy. 2018;**143**:682-695. DOI: 10.1016/j.energy.2017.11.018

[43] Liu X, Li C, Deng YD, Su CQ. An energy-harvesting system using thermoelectric power generation for automotive application. International Journal of Electrical Power & Energy Systems. 2015;**67**:510-516. DOI: 10.1016/j.ijepes.2014.12.045

[44] Fujifilm. Pressure Measurement Film. n.d

[45] Binggeli C. Building Systems for Interior Designers. Hoboken, NJ, USA: John Wiley & Sons, Inc.; 2010

[46] Gorse C, Johnston D, Pritchard M. A Dictionary of Construction, Surveying and Civil Engineering. Oxford University Press; 2012. pp. 440-441. ISBN: 9780199534463

[47] Erica. Nefalit Datasheet 2018. http://www.erica.es/web/carton-fibras/ [Accessed January 31, 2018]

[48] Grupo Flexicel. Flexiband Datasheet 2018. https://www.grupoflexicel.com/pagina.php?id=15008&lang=es [Accessed January 31, 2018]

[49] Rohsenow WM, Hartnett JP, Cho YI. Handbook of Heat Transfer. 3rd ed. New York, United States: McGraw-Hill; 1985

[50] Martínez Echeverri A. Estudio y desarrollo de sistemas termoeléctricos para el aprovechamiento del calor residual en la generación de energía eléctrica. Pamplona, Spain: Universidad Publica de Navarra; 2012

Section 3

Thermoelectric Generation: Automotive Waste Heat Recovery

Chapter 8

Thermoelectric Power Generation for Heat Recovery in Automotive Industries

Bo Li, Kuo Huang and Yuying Yan

Additional information is available at the end of the chapter

http://dx.doi.org/10.5772/intechopen.75467

Abstract

Researches on integrating thermoelectric power generator into various vehicle platform have witness a surge in solid demand of improving thermal efficiency and CO_2 emission reduction from automotive industries. Many prototypes were built and tested in different segments of the car. Position at exhaust gas recirculation valve and downstream of catalyst are preferred by car manufacturers as easiness of installation. Up to 4% improvement of fuel economy has been claimed under an ideal road driving cycle. Much focuses on the lightweighting of the thermoelectric power generator whilst producing stable electric power output under an intermittent working load. However, major barriers to real application still exist due to low conversion efficiency of thermoelectric material and poor heat exchanger system design. Although heat source can be high up to 800 K, actual temperature at thermoelectric legs are much less than that. Thermal losses are inevitable through the heat exchanger route and effectiveness of heat transfer become the key to system development in future. Thermoelectric material working in higher temperature could be a breakthrough and game changer for waste heat recovery in automotive industries.

Keywords: heat enhancement, exhaust heat recovery, heat pipe, thermoelectric power generation, automotive

1. Introduction

Transport represents over a quarter of Europe's greenhouse gas emissions and is the leading cause of air pollution in cities. It has not seen the same gradual decline in emissions as other sectors. According to the research, only 30% of the energy which is generated by the fuel combustion converts into mechanical power and nearly 35% of the energy expels to the ambient through the automotive exhaust system. Stricter emission regulations position automotive

industry as primary sector to improve the propulsion efficiency, and the development of exhaust heat recovery system become imminent, especially for massive light-weight vehicle on roads. The thermoelectric power generation (TEG) technology emerges as an alternative solution to the challenge of CO_2 emission reduction in this area. However, much effort on conversion efficiency and thermal design of the TEG heat exchangers are eagerly needed, and it is essential that recover this part of waste heat effectively to contribute a higher thermal efficiency of automotive engine and better fuel economy and emission. Therefore, this chapter mainly focus on the introduction of recent TEG systems, which are developed by major car manufacturers. In addition, the discussions are introduced for longstanding problems of the heat exchanger design hindering the full integration efforts.

2. Thermoelectric generator in the automotive

In transportation, TEG system turns thermal losses in the exhaust pipe into useful electric energy. This is usually the place where thermoelectric power generator can be installed. The technology can be used either on a hybrid vehicle or a conventional one wherever parasite heat loss from internal combustion engine (ICE) can be utilised properly. And it is targeted to produce electric energy either for batteries charging or for alternator starting so far. Last decades, many pioneering projects have seen such rapid developments from lab prototype to industrial demonstrators. However, it is still too early to conclude that the technology will be adopted by car manufacturers in near future. Moreover, such technology development is also shadowed by the government regulations and strategies of full electrification in this sector over next 15–20 years. Nevertheless, there is still space for innovation and development of thermoelectric materials to take advantage of their solid-state nature, scalability and environmental friendliness in the automotive industry.

2.1. Major players in automotive TEG application

During the last decade, plenty of automotive manufacturers have invested their money on the research of waste heat recovery by using TEG systems. In this section, the TEG systems presented by some leading automotive manufacturers and component supplier will be discussed including Ford, BMW, General Motors, Faurecia, FAW China.

Ford has presented a 350 W-rated power TEG system with the central bypass functionality aiming to control the temperature on its Lincoln MKT platform with 3.0 L V-6 engine. Under US06 driving cycle, the average power output is 180 W [1], according to the test data. In addition to the experimental investigation, Ford engineers also conducted 1-D performance simulation for an existing 2.5 L gas-electric hybrid vehicle. The system simulation predicted that the potential power output for this hybrid vehicle is 300–400 W under US Environmental Protection Agency (EPA) highway driving cycle. The aim of Ford is to improve the structure of the heat exchanger to enhance the heat transfer and reduce the increment of backpressure at the same time (**Figure 1**).

After 2009, most of BMW's waste heat recovery research work focused on integrating a thermoelectric generator inside the exhaust gas recirculation (EGR) cooler system. This technology could harness up to 250 W of energy [1], which is half the on-board energy need of a 5 series

http://dx.doi.org/10.5772/intechopen.75467

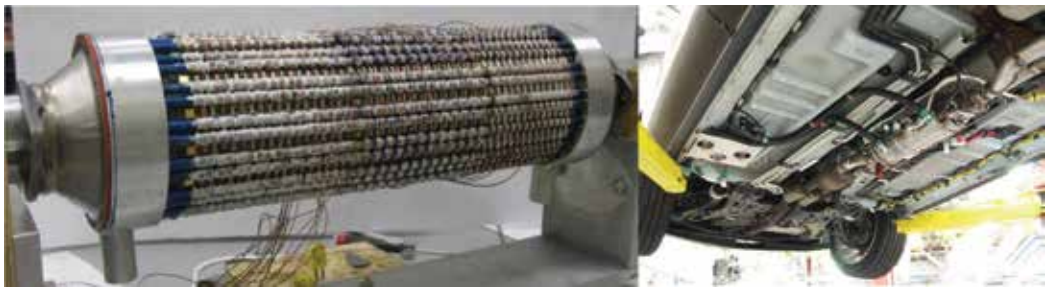

Figure 1. A prototype of Ford's thermoelectric power generator with 350 W power output [1].

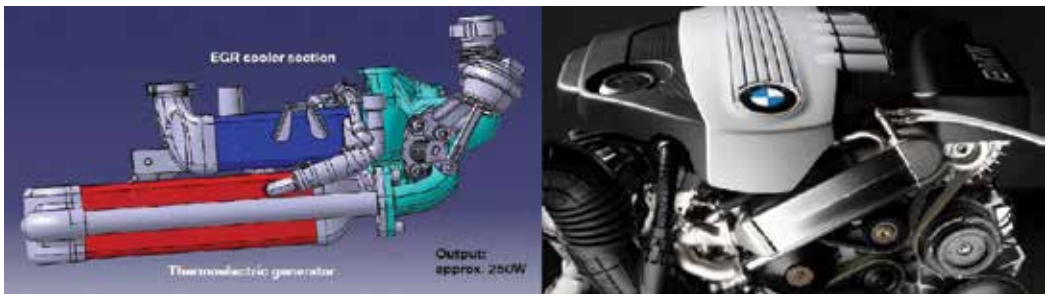

Figure 2. Thermoelectric power generator integrated with EGR cooler system.

in the 4.0 L V8 diesel engine. In terms of fuel economy, this equates to about a 2% savings in gas fuel consumption. This technology was inspired by the Radioisotope Thermoelectric Generator (RTG), which was first used in the 1960s on spacecraft by NASA (**Figure 2**).

In the past decade, General Motors has completed numerous investigation about TEG system for automobile on TE materials, system-level thermal management, efficient TEG heat exchanger design and modelling. One of the most successful achievements is the skutterudite TEMs with the figure of merit, ZT = 1.6 at 850 K [2]. This kind of TEM has a multiple filled p-n skutterudites TE materials which have been synthesised by the GM-TE material research group. A prototype of the Skutterudite-based TEG system was assembled and the experimental teat was carried out on test rig. A maximum power output of 300 W was achieved under FTP city driving cycle and 5% of fuel economy improvement is expected from this TEG system under FTP-75 driving cycle (**Figure 3**).

The feature in lightweight and highly integration is definitely welcomed by customers. A 3 kg compact TEG system was claimed by Faurecia, which made the system can be easily installed close to the engine for extreme waste heat recovery. The Faurecia TEG system claimed to be competitive among other existing systems because of faster warm-up and increased usage of the electric mode. The system can reduce the fuel consumption up to 7% as claimed. Additionally, the technology is eligible for CO_2 off-cycle credits of 1.5 g/mile in US [3].

Furthermore, this TEG system was based on a hybrid vehicle platform, Faurecia equipped the all-new Hyundai IONIQ Hybrid and plug-in Hybrid with this TEG system, offering up to 3% fuel savings, as measured on U.S. EPA Federal Test Procedure (FTP20) (**Figure 4**).

Figure 3. Skutterudite based TEG system with a rated power output of 330 W for FTP city drive cycle.

Figure 4. Faurecia offers a compact TEG system with 3 kg weight.

China First Automobile Works (FAW), as the leading vehicle manufacturer in China, has also made great effort in the waste heat recovery technologies to keep pace with the research status worldwide. FAW has proposed a novel structured concentric cylindrical TEG system, which used annular shaped TEM and combined heat pipes to enhance the heat transfer in radial direction and total filling ratio of the whole system. According to some simulation results, the peak power output can be as high as 1.2 kW under New Europe Driving Cycle (NEDC), in the same time, the power density is 800 W/m [4]. The concentric cylindrical TEG system takes the advantages of heat pipes and acquires the uniformity with the shape of exhaust pipe to make the system much easier in matching with different platform of vehicles (**Figure 5**).

2.2. The problems of scaling up

Conventional single TEG module is usually simple in a square/rectangular shape with positive/negative leads soldering on the cold side copper interconnectors. Although the common structure of thermoelectric module is rather simple, it is very difficult to configure the small modules into a large assembly. The assembling processes usually determine the working condition, the electric and thermal contacts and the final performance of the TEG. These also include the number of total TEG modules, the electric interconnections through them (serried, paralleled or hybrid), the direction of arrangement against the exhaust, the clamping method and the coolant tightness.

Usually, an electric assembly with proper sized cables is carefully designed before the structural system design. This is because that the proper electric insulation to TEG assembly is under risk of short-circuit by surrounding coolants, which may drain all the electric energy

http://dx.doi.org/10.5772/intechopen.75467

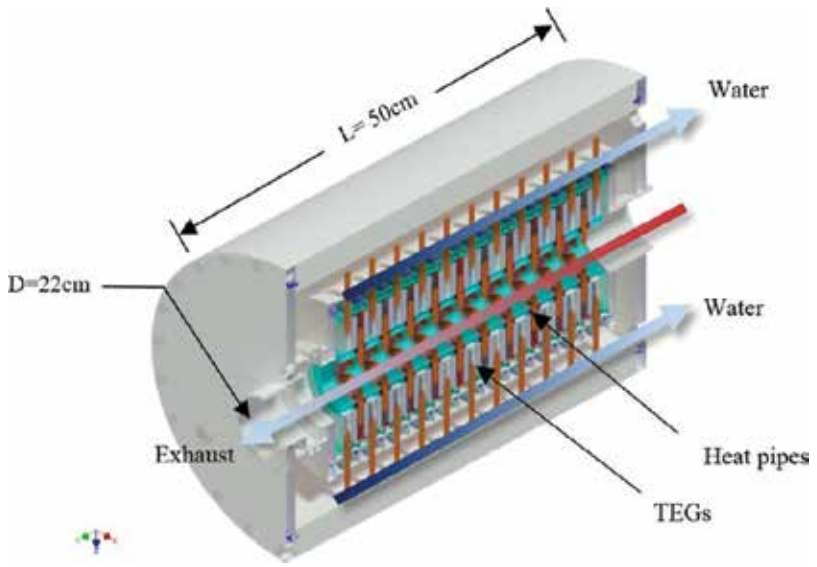

Figure 5. A heat pipe assisted and modulated TEG system offered by FAW China.

accidentally. Therefore, TEG modules should be thermally contacted other components but electrically insulated. All these issues should be carefully considered since sealing an assembly make the configuration process irreversible in most cases.

What makes the scaling up problematic is from not only TEG modules, but also the heat/cold source in the vehicle. They add extra difficulties to the final design process. As known, intermittent heat source from ICE makes heatsink temperature fluctuate. Moreover, in a typical exhaust heat recovery system, heat sink/source temperature also varies along the flow direction. Different thermoelectric materials along the exhaust flow direction may be applied in order to match each material's optimum operating temperature. The optimum operating temperature probably can be achieved by structural optimization in heatsink design. However, if the temperature varies significantly within the exhaust flow, the different types of materials should be applied to obtained higher efficiency. Additionally, sufficient thermal insulation within the whole system should be employed. Otherwise, heat leakage from the exhaust gas to the coolant will cause efficiency decline.

For example, Gao et al. [5] assessed a flat TE module with an air space in-between, which is commercially available in the market. As shown in **Figure 6**, commonly a TEM consists of several positive-type (P-type) and negative-type (N-type) that are connected by conducting strips in serials to increase the total voltage, combined with the cold and hot ceramic plates. The space between the hot and cold ceramic plates is filled by air. This air space will cause a heat loss within the TEM, as there will be heat radiation from the thermoelectric legs to the air space, which is non-negligible, even though the heat radiation is rare in TEMs. However, when it comes to the system level, a series of TEMs scaled up together, this part of radiation will cause a considerable heat loss from the hot side to cold side. As a result, the design optimization of TEM should be deliberated before the assembly of TEM.

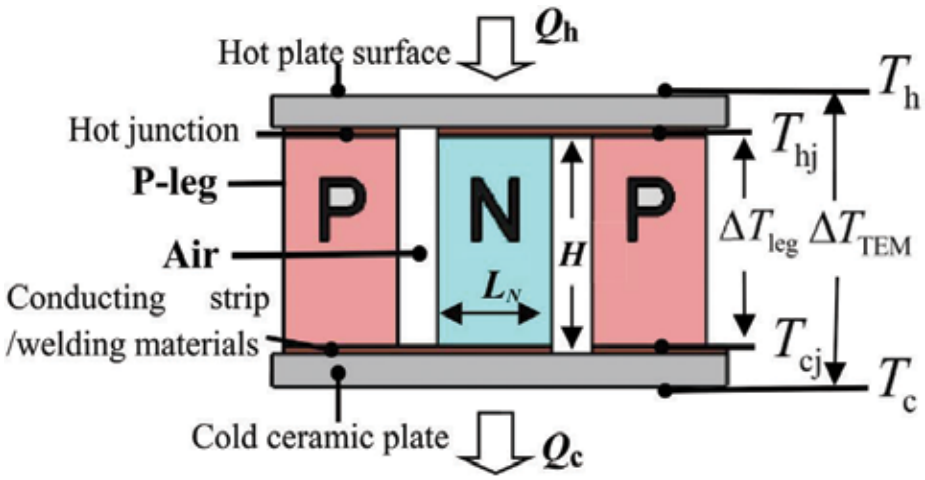

Figure 6. Mathematical models of thermoelectric module regarding the heat transfer.

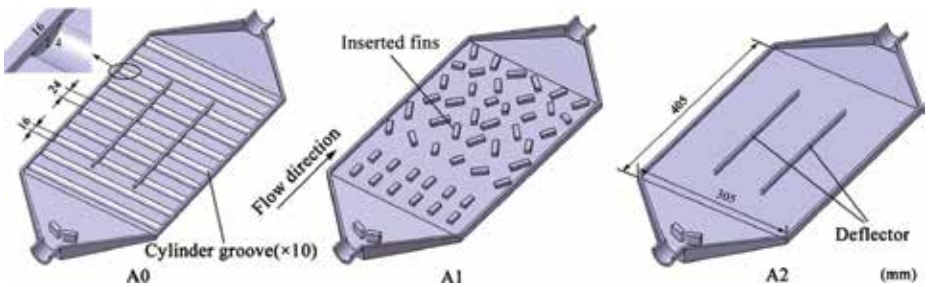

Figure 7. Topology of exhaust heat exchanger with different heat enhancement methods.

As previous researches discovered that the power output of TEG system was influenced by temperature gradient and temperature uniformity of the system significantly. Furthermore, the power output and efficiency could be improved by increasing the convection heat transfer coefficient of the high-temperature-side, but it was pricey due to the limited installation space and back pressure increment of the exhaust. Therefore, a well-designed heat exchanger will contribute to the improvement of the performance of TEG system effectively. Wang et al. [6] from Wuhan University of Technology have completed a number of investigation on the heat transfer enhancement in flat heat exchanger for TEG system [6]. The studies consisted a series of different structured heat exchanger with fins, deflectors or grooves. According to the results, by inserting fins, the heat transfer in heat exchanger could be enhanced. However it would also result in a large unwanted back pressure increment which went against to the efficiency of the engine. A heat exchanger containing cylindrical grooves on the interior surface of heat exchanger could increase the heat transfer area and enhance the turbulence intensity, meanwhile there was no additional inserts in the fluid to block the flow. Compared to flat surface, cylindrical grooves in exchanger could decrease the thermal resistance and enhance the power generation of TEG with nearly the same back pressure. Fins could greatly enhance the heat transfer and power generation of TEG, but the additional pressure loss was also great (**Figure 7**).

http://dx.doi.org/10.5772/intechopen.75467

2.3. The potential integration of TEG system with mufflers or catalytic converters

Since the economics of thermoelectric power generation depends on the nature of the heat source, there is an increasing awareness of deep integration among undergoing research projects. Moving thermoelectric power assembly closer to the ICE will certainly enhance the TEG performance. Inevitably, stricter requirements of TEG have to match working condition both muffler and thermoelectric power generators when such integration happens. One apparent advantage of such integration is the cost reduction of manufacturing.

Mufflers are used for noise reduction emitted by the exhaust of an internal combustion engine. It usually consists of several perforated tubes inside the shell. The structure of muffler is similar to the common shell and tube heat exchanger. In that case, it inspire a natural thinking of integrating two separated components into one functional device. Therefore, the integration can be achieved by redesign the muffler structure with added TEG modules on the inner surface of the shell. Double layered shell may accommodate coolant loop to cool the TEG modules. Nonetheless, both noise reduction and TEG assembly performance have to be re-evaluated under such circumstances.

At present, most of the TEGs installed in the exhaust pipe system are located after the catalyst converter. The simple reason is that the exhaust emission treatment is prior to energy recovery process. However, the high temperature will decrease roughly by 100 K through the catalyst converter. If TEG developer would like to harness higher-grade heat from exhaust, the integration with catalyst converter is sensible but difficult. Inside catalyst converter, there are two functional components including reduction and oxidation process. Both components are coated perforated structures with 600 mesh number or higher. Therefore, fundamental changes in combined structure are needed and effects of harmful gas on the TEG modules need investigation in future work.

3. Heat transfer enhancement options in vehicle

Unlike common circumstances, thermoelectric power generator in the vehicle has to work under a constant moving condition. Even if thermoelectric materials with high ZT are developed, there are still many system-level challenges to implement them into automotive applications. Especially, only ambient air is available as the eventual cold source for the thermoelectric power generator no matter what intermediate coolant adopted. Thermal systematic design is the key to match optimum heat flux between heatsinks and thermoelectric modules. Key innovations are urgently needed from not only material development but also the holistic system design. In this section, we discuss heat transfer related issues in thermoelectric modules and systems in the context of automotive applications.

3.1. Heat transfer in thermoelectric device

Layers in thermoelectric modules are thermal resistances such as interconnectors, solders and electric insulators. Considerations of minimising them without losing mechanical and electronic performance will benefit the overall system design. In exhaust pipeline, exhaust temperature ranges from 150 K to over 800 K, the added thermal protection from thermoelectric layers

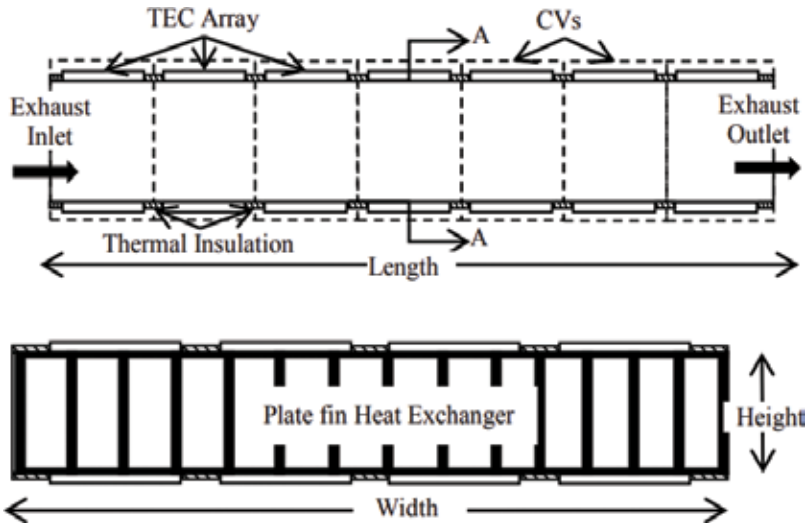

Figure 8. Schematic of TEG device configuration with plate fin heat exchanger.

inevitably become the source of parasitic loss, which leads to reduced system power output and conversion efficiency. High temperature durability for thermal layers is the key to position thermoelectric modules closer to the engine.

Kumar et al. [7] have investigated the overall heat transferred, the electrical power output, and the associated pressure drop for given inlet conditions of the exhaust gas and the available TEG volume by using a rectangular configuration TEG system. In this system each TEM is mounted on the top and the bottom surface and arranged uniformly over 80% of total surface area. The remaining 20% area and the lateral walls are thermally insulated to minimise heat leakage. As shown in figure, the plate-fin heat exchanger is applied in the TEG system and there are several transverse fins distribute along the hot channel of heat exchanger. Moreover, the inlet and outlet of the hot channel of heat exchanger are connected to the engine exhaust pipe. According to the results, TEG power output is observed to have strong relation with the mass flow rate and inlet exhaust temperature. It was found that, at the average inlet conditions, up to 64% of the inlet energy can be transferred through the thermoelectric modules, resulting in a power output of 552 W, approximately 3.33% of the inlet power (**Figure 8**).

Zhou et al. [8] proposed a newly designed TEG with cylindrical shell and straight fins to overcome the common defects of conventional TEG system. They established a two-dimensional heat transfer numerical model under steady-state conditions and utilised this model to predict the performance of the TEG system in different working conditions. As shown in figure, the newly designed TEG system is compact in structure and can be arranged between catalytic converter and the muffler to make it effective in the recovery of waste heat. The TEMs and heat transfer fins are in direct contact, avoiding the exhaust tube structural transformation, and it will not cause any influence on the engine exhaust back pressure. The cooling tubes are branches of the engine cooling system, and the engine coolant flows into the tubes to cool down the cold sides of TEM (**Figure 9**).

http://dx.doi.org/10.5772/intechopen.75467

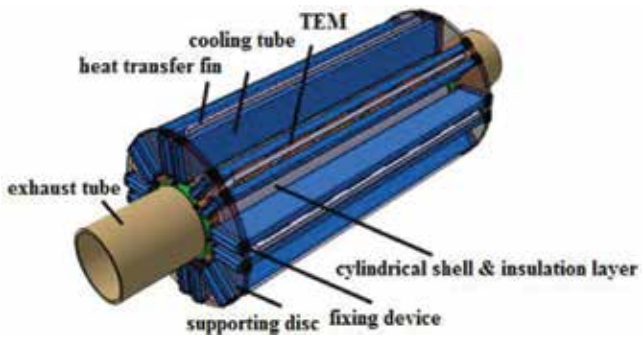

Figure 9. Radial TEG arrangements for exhaust heat recovery.

In order to enhance heat transfer between the exhaust gas and the hot side of TEM, Li et al. [9] have applied foam metal to fill in the space of the exhaust pipe. By filling foam metal within the exhaust pipe, the convective heat-transfer coefficient is increased by 4 times, meanwhile, the back pressure of the exhaust system do not boost significantly (**Figure 10**).

Another innovation may come from polymer with function of flexibility. The pipeline shape and exhaust assembly method make such demands speciously since car manufacturers are reluctant to fundamentally change the overall looking of the pipe, and it may involve the adjustment of chassis to accommodate irregular thermoelectric modules.

3.2. Heat transfer in vehicle system

When considering the installation of thermoelectric modules to the vehicle, the complexities of material configuration, clamping methods, heat sink structures, installation positions, flow resistance to the backpressure and overall cost make major car manufacturers hesitant to fully embrace this heat recovery technology. All these issues are related to the heat transfer in a powertrain system, a major research area that system specialist make enormous efforts to solve. To make use of scalable feature for large energy demands in the vehicle, careful system design are required including technical and cost considerations.

When developing a thermoelectric system including heat exchangers, heat flux through the thermoelements should be large enough to maintain the appropriate temperature difference. The general heat flux through thermoelectric legs is 100 kW/m^2, assuming that the height of thermoelectric leg is 1 mm, then the temperature gradient should be 100°C.

It could be achievable that we can deliver this level of heat flux by concentrating the heat at hot and cold side of TEM with fins or any other heat transfer enhancement methods. Therefore, the structural optimisation of TEM and heat exchanger is critical and both of them should be developed to match the high density of heat flux.

In addition to the previous work, Kumar et al. [10] have completed more investigation on the influence of heat exchanger and thermoelectric module configurations to achieve optimization of the TEG system. As shown in figure, they presented four different structured heat sinks to compare the performance between them. The topologies having a rectangular

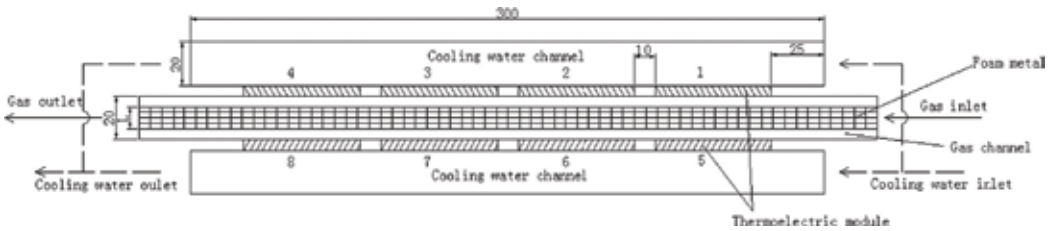

Figure 10. Heat enhancement method by filled metal foam into exhaust pipe.

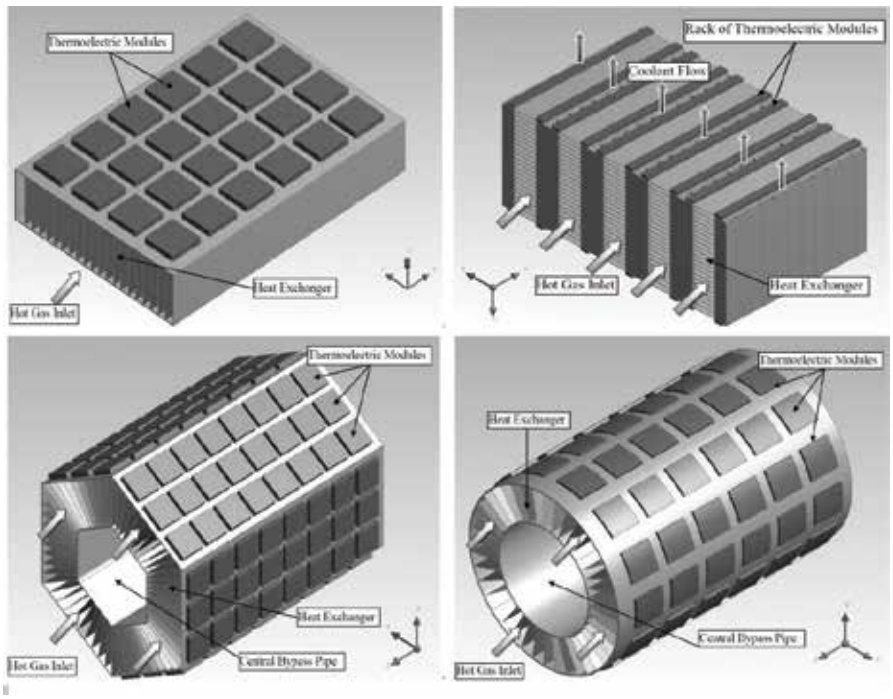

Figure 11. Various Heat exchanger structures for exhaust pipe adjustment.

box-like shape are grouped as rectangular topology. The names of the model—longitudinal and transverse—are derived from the way the TEMs are placed with respect to the exhaust flow direction. Two types of circular configuration: regular hexagon and cylinder are also presented for comparison. These models are similar to the longitudinal model except the cross-section is hexagonal or cylindrical (**Figure 11**).

All topologies behave somewhat similarly at lower numbers of TEMs in terms of electrical generation. However, the performance of the hexagonal and cylindrical topologies suffers when the number of TEMs exceeds 40 owing to large pressure drops. Overall, the transverse design shows better results in the heat enhancement and power output comparing with longitudinal designs. Furthermore, if the width of the transverse heat exchanger equals to the

http://dx.doi.org/10.5772/intechopen.75467

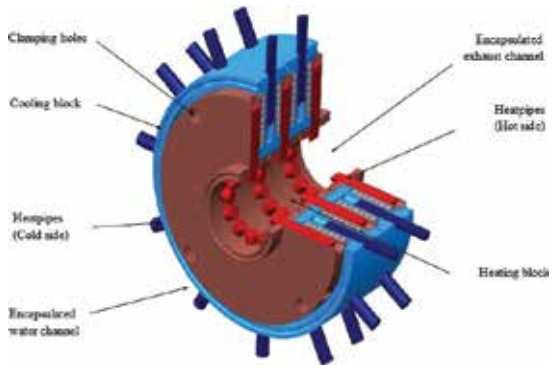

Figure 12. Simplified heat pipe assisted exhaust heat recovery system for concentric TEG device.

length of a single TEM, the TEG system will obtain the highest electrical power output with lower pressure drop among other designs.

Heat pipe-assisted heat enhancement method is approved to be an effective way to improve the TEG performance. Encapsulated heat pipes arrays in the radial direction of the exhaust pipe help to enhance heat effectively from an external fluid stream. The features of heat pipes such as temperature flattening, temperature control and thermal diode, may help TEG modules for autonomous, maintenance-free operation under fluctuating heating sources in the future. The spatial distribution of the temperature rise is considerately responsive by the variation of heating condition from exhaust streams.

In order to get a better filling ratio, Bo et al. [11] from University of Nottingham have presented a concentric cylindrical TEG system consists of a series of repeat units that are conjugated along the exhaust stream to shape of the exhaust pipe. As shown in the figure, the repeat unit is made up of four concentric TEMs, three hot plates and two cooling plates including 12 heat pipes. The exhaust stream interacts with heat pipes and transfers the heat into the TEG in the radial direction of the exhaust stream. Comparing with some commonly used TEG system, the concentric cylindrical TEG system gain a better filling ratio by such configuration. Furthermore, in this system, a compact and lightweight heat sink which is assisted by heat pipes is introduced. The merits of utilising heat pipes in the system are explored regarding the improvement of heat transfer in radial direction and the simplicity of system integration. Besides, the combination of heat pipes reduce the weight of the TEG system as well, consequently improving the fuel economy (**Figure 12**).

Lu et al. [12] investigated the effect of distribution consistency of the interceptor on the performance of heat transfer enhancement for the TEG system. The results showed the non-uniform configuration of the interceptor can lead to approximately doubled power output than smooth channel heat exchanger. However, the pressure drop which governs the pumping power of heat exchanger need to be concerned carefully (**Figure 13**).

Liu et al. [13] built a test bench for examining the performance of TEG system which is assembled into a prototype vehicle. Through the revolving drum test bench, the characteristics of

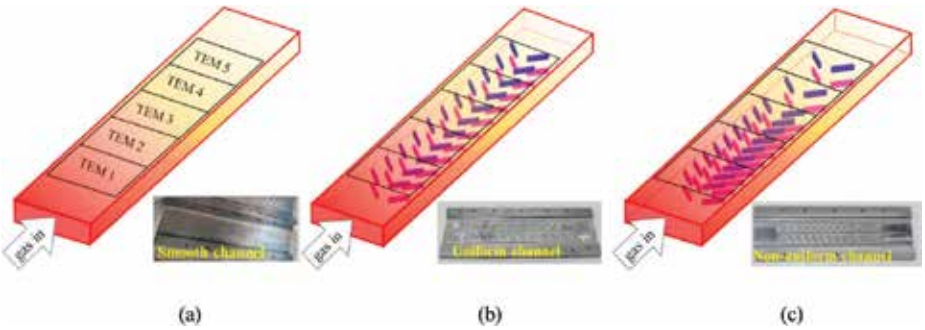

Figure 13. Fin arrangement studies for heat transfer enhancement in TEG heat exchanger.

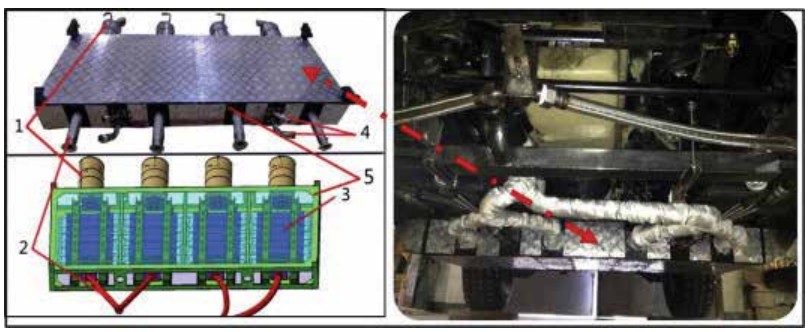

Figure 14. Multi cross flow arrangements for TEG heat exchanger.

the TEG system can be measured, and a maximum power output of 944 W was obtained, which can fulfil the power for some accessories in automotive application (**Figure 14**).

4. Challenges

High *ZT* pursued by TE community is not the only case for real automotive application. A high *ZT* with a limited temperature range is not favoured since varying heat source temperature results in low efficiency in most of time. In addition, conversion efficiency may not sit in the centre of the concern, high power density is the main factor in automotive application same as request for traction battery. Here we organised three main factors for consideration of TE selections including the limited space under chassis, the low power density and the real reliability under an all-weather condition.

4.1. Limited space

Although TEG technology is favoured in the lightweight vehicle, it is still challenge to spare a space for it. Changing the exhaust piping system is usually subject to the chassis design, which involves weight balancing, powertrain system structure and brake force distribution, etc.

Unfortunately, it is not the option for most of car manufacturers. Moreover, the TEG heat recovery system should be ideally designed in a cylindrical shape as much same as the exhaust pipe.

In order to minimising the extra coolant loop or heat sink, extra coolant pumping power should be considered when routing the loop in/out of the TEG system. A proportional electric gas valve is usually integrated with TEG system in order to adjust the bypass flow of the exhaust. In some cases, a DC-DC converter or a DC-AC converter has to be positioned close to the TEG system with extra electric cabling and connection work.

Inevitably, all the added up functional components mentioned here occupy significant space. To squeeze such TEG system into a highly-packed and harsh environment is not always an easy task for the system designers.

4.2. Power density

Power density is usually the main concerns that car manufacturers focus on. Every car manufacturer pursues highest power output in a certain weight. At present, the threshold of power output in automotive market is 1 kW per unit. In other way, the thermoelectric have to obtain at least 10 kW heat energy from the exhaust given that most of current system efficiency are less than 10%. It is a dilemma for TE material scientist and thermal system designer. To maintain such power density, system designer have to find ways to deliver sufficient heat to the TE material. Material scientist have to tune the TE into best power output capacity within a defined space.

4.3. Reliability

The lifespan of a common passenger car can reach over 25 years or more. Although no moving parts in the TEG system, TEG system exposes to an extremely varying thermal cycling condition. Tiny cracks between soldering layers and metalized layer will decrease the efficiency and cause mismatched resistive load. In addition, the clamping is prone to failure under a shock or vibration. Unfortunately, there is little research in this area but it should be included in any road test in future.

Nonetheless, considering major services in certain intervals and payback time for the customer, it is crucial for TEG developer to define the business model for selling this technology in term of installation cost and repair cost.

5. Conclusion

In this chapter, the latest progress on TEG exhaust heat recovery is introduced. The technology is still the favourite solution for lightweight vehicles until final phase-out of fuel-powered combustion engine in the middle of the twenty-first century. It is worth mentioning that automotive engineering is a process of system engineering, all the potential applicable technology should be evaluated in the context of specific vehicle platform. There is no exception for the TEG technology. Due to the nature of internal combustion engine, the heat source varies from

exhaust temperature, torque load and even climate condition. The energy demands in passenger car is very different with heavy-duty truck in respect of fuel economy. To help the decision making of go/no-go in automotive, further material researches on higher power density and economic TE material are necessary. For TEG heat recovery system, heat exchanger designers should focus on the heat enhancement to match the heat flux through TE materials.

Author details

Bo Li[1]*, Kuo Huang[1] and Yuying Yan[1,2]

*Address all correspondence to: Bo.li@nottingham.ac.uk

1 Fluids and Thermal Engineering Research Group, Faculty of Engineering, University of Nottingham, UK

2 Fluids and Thermal Engineering Research Centre, University of Nottingham Ningbo, China

References

[1] Fairbanks J. Automotive Thermoelectric Generators and HVAC [Internet]. 2013. Available from: https://energy.gov/sites/prod/files/2014/03/f13/ace00e_fairbanks_2013_o.pdf [Accessed: November 27, 2013]

[2] Crane DT. Thermoelectric Waste Heat Recovery Program for Passenger Vehicles [Internet]. 2012. Available from: https://www1.eere.energy.gov/vehiclesandfuels/pdfs/merit_review_2012/adv_combustion/ace080_lagrandeur_2012_o.pdf [Accessed: May 27, 2017]

[3] Faurecia. The Faurecia compact EHRS celebrates world first on the new Hyundai IO NIQ Hybri [Internet]. 2016. Available from: http://www.faurecia.com/en/news/faurecia-compact-ehrs-celebrates-world-first-new-hyundai-ioniq-hybrid-01032016 [Accessed: November 27, 2017]

[4] Wang X, Li B, Yan Y, Liu S, Li J. A study on heat transfer enhancement in the radial direction of gas flow for thermoelectric power generation. Applied Thermal Engineering. 2016;**102**:176-183. DOI: 10.1016/j.applthermaleng.2016.03.063

[5] Gao J, Qungui D, Chen M, Li B, Zhang D. Assessing the accuracy of mathematical models used in thermoelectric simulation: Thermal influence of insulated air zone and radiation heat. Applied Thermal Engineering. 2015;**82**:162-169. DOI: 10.1016/j.applthermaleng.2015.02.072

[6] Wang Y, Li S, Zhang Y, Yang X, Deng Y, Chuqi S. The influence of inner topology of exhaust heat exchanger and thermoelectric module distribution on the performance of automotive thermoelectric generator. Energy Conversion and Management. 2016;**126**:266-277. DOI: 10.1016/j.enconman.2016.08.009

[7] Kumar S, Heister S, Xianfan X, Salvador J, Meisner G. Thermoelectric generators for automotive waste heat recovery systems part I: Numerical modeling and baseline model analysis. Journal of Electronic Materials. 2013;**42**:665-674. DOI: 10.1007/s11664-013-2471-9

[8] Zhou M, He Y, Chen Y. A heat transfer numerical model for thermoelectric generator with cylindrical shell and straight fins under steady-state conditions. Applied Thermal Engineering. 2014;**68**:80-91. DOI: 10.1016/j.applthermaleng.2014.04.018

[9] Li Y, Wang S, Zhao Y, Lu C. Experimental study on the influence of porous foam metal filled in the core flow region on the performance of thermoelectric generators. Applied Energy. 2017;**207**:634-642

[10] Kumar S, Heister S, Xu X, Salvador J, Meisner G. Thermoelectric generators for automotive waste heat recovery systems. Part II: Parametric Evaluation and Topological Studies. Journal of Electronic Materials. 2013;**42**:944-955. DOI: 10.1007/s11664-013-2472-8

[11] Li B, Huang K, Yan Y, Li Y, Twaha S, Zhu J. Heat transfer enhancement of a modularised thermoelectric power generator for passenger vehicles. Applied Energy. 2017;**205**:868-879. DOI: 10.1016/j.apenergy.2017.08.092

[12] Lu X, Yu X, Qu Z, Wang Q, Ma T. Experimental investigation on thermoelectric generator with non-uniform hot-side heat exchanger for waste heat recovery. Energy Conversion and Management. 2017;**150**:403-414

[13] Liu X, Deng YD, Li Z, Su CQ. Performance analysis of a waste heat recovery thermoelectric generation system for automotive application. Energy Conversion and Management. 2015;**90**:121-127

Chapter 9

Automotive Waste Heat Recovery by Thermoelectric Generator Technology

Duraisamy Sivaprahasam, Subramaniam Harish,
Raghavan Gopalan and Govindhan Sundararajan

Additional information is available at the end of the chapter

http://dx.doi.org/10.5772/intechopen.75443

Abstract

Automotive exhaust thermoelectric generators (AETEG) are gaining significant importance wherein a direct conversion of exhaust waste heat into electricity allows for a reduction in fuel consumption. Over the past two decades, extensive progress has been made in materials research, modules and thermoelectric generator (TEG) system. Many prototypes using BiTe, $CoSb_3$ and half Heusler materials have been developed and tested for efficiency in different engines. The role of exhaust flow rate, temperature and heat exchanger type on the performance of AETEG is investigated deeply. This chapter reviews the progress made so far in the AETEG technology. Section 1 gives a brief introduction; section 2 gives a description of the technology and section 3, the construction details of a typical AETEG. The performance evaluation of AETEG is discussed in Section 4, application of TEG using engine coolant heat is discussed in Section 5 and TEGs for hybrid vehicles are described in Section 6. The parasitic losses due to AETEG and the conditioning of the power produced for practical applications using the maximum power point tracking technique are discussed in Sections 7 and 8, respectively. Finally, in Section 9, cost analysis and the challenges associated with the commercialization of AETEG is presented.

Keywords: thermoelectric generator, exhaust waste heat, power output, efficiency, parasitic losses

1. Introduction

Among the major contributors to the greenhouse gas emissions to the environment, automobiles make a substantial contribution to the extent of 16.4% [1]. According to the information

reported in energy technology perspective 2015, the number of light duty vehicles in the roads is expected to go up from present 900 million to 2 billion by 2050 [2]. With the global power sector moving towards clean technologies using renewable energy, the current 38% utilization of the global oil production for automotive use can increase to a significant extent. Though the advancement of electric vehicle (EV) technology is making a steady progress on one side (expected to reach 56 million passenger cars on road from the present 2 million by 2030), still it is far from making any drastic reduction in the emissions level due to transportation sector unless a radical innovation is made in the battery technology. Policies such as better urban planning that can increase the use of collective transportation and innovative technologies that can reduce the individual's vehicle need can make considerable contributions to the reduction of the CO_2 emissions. However, this requires substantial investment, and hence it is difficult to implement worldwide particularly in low and middle income countries. Implementing innovative technologies for improving automobile engine efficiency or innovations in the field of hybrid/low emissions vehicles can improve the fuel efficiency and thereby emissions can be reduced to a greater extent. Several recent developments in the engine, transmission and few ancillary systems of the vehicles show promising results. Converting a part of heat energy produced in the engine, released to the atmosphere via exhaust gas as waste heat into electricity by a thermoelectric generator (TEG) is one technology gaining a lot of attention in the past one decade though it is well explored long time back itself due to its inherent simplicity. This chapter discusses the various salient features and the progress made so far in this technology.

2. Electricity from automotive exhaust waste heat

In an internal combustion (I.C) engine, only one-third of the total heat produced in the fuel combustion is utilized for the propulsion of the vehicle while the remaining two-third goes as waste heat mainly through the exhaust gas and the engine coolant. The exhaust gas, usually at a higher temperature compared to the engine coolant which absorbs heat from engine walls, is let out in the atmosphere and the engine coolant is recirculated after cooling in the radiator. In some of the engines, particularly in diesel fuelled ones, to get better efficiency, part of the exhaust gas is cooled and mixed with air in exhaust gas recirculation (EGR) system to reduce the NO_x emissions. Turbo-charging is another technology utilizing the heat from the exhaust gas to improve the engine power. However, in all these technologies, only a small fraction of the exhaust gas or its energy is converted into useful work and remaining is let out to the atmosphere. Improving the engine performance by making use of this exhaust waste heat has been a subject of intense research in the field of energy recovery systems, exhibiting promising outcomes in the recent past.

Automotive exhaust thermoelectric generator (AETEG) technology involves converting the waste heat available in the exhaust gas into electricity that can be stored and utilized for various electrical inputs of a vehicle so that the fuel efficiency can be improved. The first such system was developed in 1963 by Neild [3] followed by Serksnis [4] in 1976. Later, Birkholz et al. in 1988 [5] and Bass et al. in 1990 [6] demonstrated AETEG using thermoelectric (TE) modules

http://dx.doi.org/10.5772/intechopen.75443

made of Fe-based and BiTe materials, respectively. Although the earliest AETEG was developed more than 50 years ago, a surge in research activities in this field has been occurring only in the past 15 years, which is evident from **Figure 1** showing the number of publications on this subject over the past five decades. Such exponential increase in the research output in recent years is mainly due to some of the path-breaking outcomes in the thermoelectric materials' properties which improved the TE figure of merit (zT) value which was <1 over a long period to more than 1. In recent years, zT ≥2 were also reported in few materials, which were achieved by engineering the microstructure of materials in different length scales [7, 8].

The thermoelectric figure of merit (zT), a dimensionless parameter indicating the thermoelectric performance of the material is defined as $zT = [(S^2\sigma).T]/\kappa$ where S is the Seebeck coefficient (V/K), σ is the electrical conductivity (S/m), κ is the thermal conductivity (W/m.K) of the material and T is the absolute temperature (K). From the mid of last decade, almost all the major automobile manufacturers in the world are associated with R&D programmes involving design, development and testing of AETEG in collaboration with the TE device manufacturers and research institutes. However, the outcomes reported so far indicates that the improvement in the fuel efficiency obtained are of very low values and even negative in some cases due to the parasitic losses associated with the TEG [9, 10]. The commercialization of AETEG, which have been projected to be feasible with improvement in efficiency of >5%, is yet to be achieved. The major bottlenecks to achieve this target are non-availability of bulk TE materials with high zT and the high cost of the currently available modules. The main contributions to the high cost of AETEG at present mostly arise from the TE modules, which are still very high compared to the practically acceptable price of less than $1/Watt. The presently available commercial modules made of Bi_2Te_3 are mostly manufactured by processes involving substantial manual operations resulting in high cost when

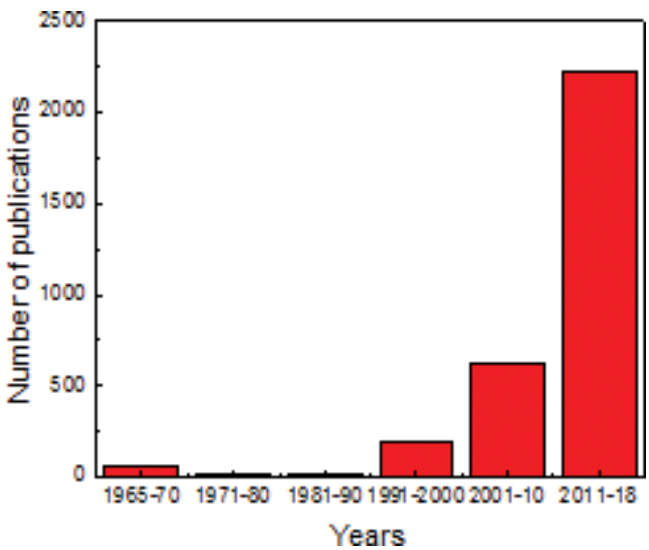

Figure 1. Number of papers published in every decade from 1965 onwards on the subject of thermoelectric generator". [data sourced from www.isiknowledge.com using the key word of 'thermoelectric generator'].

it reaches the customers. In high-temperature modules (i.e., operating temperature > 400°C), the use of rare earth elements along with intricate assembling and packaging process escalates the overall cost tremendously. Incorporation of suitable diffusion barrier layers between TE elements and metal interconnects, sealing of the complete assembly in inert gas to prevent the degradation at operating conditions etc. are some of the essential requirements for modules operating above 400°C. In spite of all these hurdles, the emergence of low-cost abundantly available materials such as tetrahedrites ($Cu_{12-x}M_xSb_4S_{13}$), Mg_2Si and $MnSi_2$ showing promising features can give the required breakthrough for commercialization.

3. Automotive exhaust thermoelectric generator system

The TEG for automobile exhaust heat conversion mainly consists of four parts, namely, TE modules, a heat exchanger to capture the heat from the flowing exhaust gas and transferring it to the hot side of the modules, heat sink to remove the heat from the cold side of the modules and assembly components. **Figure 2** shows the schematic of typical TEG arrangement for automotive exhaust waste heat conversion. In the exhaust pipe attached to the engine, the TEG is usually integrated after the catalytic converter. This is because positioning TEG before the catalytic converter can lower the exhaust gas temperature which will affect catalytic converter's performance. It is always preferable that the location of the TEG in the exhaust pipe is as close as catalytic converter since as we move away from it the temperature drops significantly. In most of the prototypes tested either in simulated or in actual driving conditions, only a TEG in the exhaust pipe alone is used. However, it is not uncommon to use two TEGs, one at the regular exhaust line and another one in the exhaust gas recirculation system (EGR) to maximize the power output.

3.1. TE modules

TE modules which are the main functional part of the AETEG are made of several pairs of p and n-type legs/elements of the thermoelectric compounds, which are connected electrically in series and thermally in parallel. The choice of the appropriate materials for modules mainly depends on (a) the optimal temperature range where zT is maximum (b) easy availability and (c) mechanical durability at the operating conditions of the TEG. The efficiency of the TE module given by.

$$\eta_{TE} = \left[(T_h - T_c)/T_h\right]^* \left\{ \sqrt{(1+zT)} - 1/\left[\sqrt{(1+zT)}\right] + T_c/T_h \right\} \quad (1)$$

where T_h, T_c are the hot and cold side temperatures of the module, T is the average temperature given by $(T_h + T_c)/2$, and zT is the figure of merit of the TE legs used.

To get the maximum efficiency in the modules, the operating temperature of the modules should be in the range where the zT of the leg materials is the highest.

Several materials with appropriate doping have been used in the modules which can be reliably employed in the typical exhaust gas temperature range which is 400–600°C for a diesel engine and 700–800°C for gasoline engine. **Table 1** gives the details of TE materials, modules and the performance of AETEG either in a simulated or actual road test conditions. In the temperature range of interest for AETEG, filled skutterudites, doped PbTe, and half-Heuslers

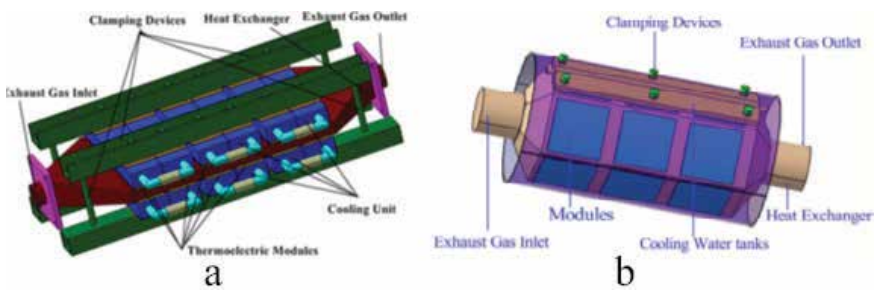

Figure 2. Schematic of the different type of TEG's arrangement [22, 36].

Sl. No	Materials	Module specifications	TEG performance	Ref.
1	Fe-based compound	—	—	[5]
2	BiTe	P_{max} ~35 W (at ΔT = 300°C) $\eta_{max.}$ 4.5%	~125 W at 112.6 km/h speed	[9]
3	BiTe	5.3 × 5.3 cm P_{module}-13 W	1.0 kW	[12]
4	B and P doped Si_2Ge	20 × 20 cm P_{max}:1.2 W (at ΔT = 563 K)	35.6 W	[13]
5	BiTe	6.2 × 6.2 × 0.5 cm (at ΔT = 563 K)	42.3 W	[14]
6	Segmented Skutterudites and Bi_2Te_3 and commercial Bi_2Te_3 modules	Mod. Size:0.24 cm^2 P_{max}~18 W (at ΔT = 560°C) $\eta_{mod.}$-6–8%	266 W at 60 km/h driving in 2 L engine.	[15]
7	Bi_2Te_3/Sb_2Te_3	$P_{nominal}$: 7 W at ΔT of 175°C	44 W using 12 modules	[16]
8	Bi_2Te_3	0.4 × 0.4 cm	75 W	[17]
9	Bi_2Te_3	4 × 4 × 0.42 cm	350 W (using 12 modules)	[18]
10	Skutterudites	—	700 W (steady state) 450 W (US06 driving cycle)	[19]
11	Half Heusler	5.26 W/cm^2 (under ΔT = 500°C)	1 kW	[20]

Table 1. Materials, modules specification, and performance of some of the AETEGs fabricated and tested in engine exhaust.

are some of the compounds showing promising results. However, the cost factor associated with these compounds because of the rare elements used makes it difficult in lowering of per Watt cost and the large-scale mass production. Apart from this, unlike the stationary or space

applications where the TEGs showed very high durability, in the case of automotive application, the modules and materials are subjected to highly fluctuating thermal and mechanical conditions which can affect its longevity. As mentioned earlier, TE legs are electrically connected in series. Hence, the failure of either a leg or the joint between leg and metallic electrodes/interconnects can result in to a complete electrical breakdown of the module. The reliability of the modules, which is affected owing to such failures occurs predominantly due to thermo-mechanical stresses created at the interface by the coefficient of thermal expansion mismatch between TE elements and interconnects. Using a fault management system which can cut off the failed module from the rest can overcome this problem in AETEG. However, such arrangement makes the system more complicated and costly. The development of a particular material system-specific design using multiphysics simulations and experiments can help in improving the reliability of the leg-interconnect joints and the interface. Another problem severely affecting the durability of the module is the loss of materials from the TE legs by sublimation under prolonged exposure to high temperatures. Coating the surface with a stable thin layer of materials with comparable thermal coefficient of expansion (CTE) or casting the space between the TE legs with highly tortuous, extremely low thermal conductivity (<0.01 W/m·K) aero-gel could reduce the sublimation loss. However, all these processes substantially add up the overall cost of the modules.

3.2. Heat exchanger

The heat exchanger is an essential element of in AETEG which determines its overall performance. Since its primary function is to extract heat from flowing exhaust gas, an optimum design and sizing are critical for delivering the maximum power output. The efficiency of the TEG (η_{TEG}) which is given by $\eta_{TEG}=\eta_{HE}\times\eta_{TE}\times\varepsilon$ where η_{HE} is the heat exchanger efficiency, η_{TE} is the conversion efficiency of the cluster of TE modules and ε is the ratio of heat transfer from modules hot side to the cold side. An ideal heat exchanger should have low weight and high η_{HE} without causing severe backpressure to the flow of the exhaust gas. The back pressure will increase the parasitic losses in the vehicle.

Thermal efficiency (η_{HE}) of the heat exchanger mainly depends on three factors: (a) type, (b) internal geometrical shape and (c) materials of construction. The types of heat exchangers are classified according to the heat transfer mechanisms and the number of fluids. Construction type and flow arrangements are some of the other parameters used for further classifications. In automotive TEG, the type of heat exchangers used are mostly indirect, contact type with direct heat transfer between different medium such as gas and solid in the hot side and solid and liquid in the cold side of the system. According to the construction type and geometrical shape classification, the heat exchangers used are mostly either box type or tubular with extended surfaces such as fins or heat pipes depending upon the space available for the integration into the vehicle [10, 11, 21].

The choice of the materials for the heat exchanger fabrication is determined by their thermal conductivity, density, and fabricability. Since most of the heat exchangers are with extended surfaces, its shell outer temperatures are significantly influenced by the thermal conductivity of the materials used. The density of the materials used decides the overall heat exchanger weight and the parasitic loss associated with it. Materials which are easy to fabricate by

http://dx.doi.org/10.5772/intechopen.75443

multiple manufacturing routes could bring in design flexibility and result in reduction of overall AETEG cost. Stainless steel, aluminum and brass are some of the heat exchanger materials used so far and tested in both diesel and gasoline engines.

The heat transfer from the exhaust gas to the outer shell of the heat exchanger where the TE modules are placed occurs by the combination of the convection and conduction mechanisms. The thermal resistance (R) for the convective heat transfer is given by R = 1/(h.A) where h is the heat transfer coefficient and A is the area of the heat transfer surface. Any internal arrangement which enhances the heat transfer area (A) increases the convective heat transfer which subsequently improves the hot side temperature (T_H). The thermal resistance for the convection mostly occurs in the boundary layer. Various kinds of fins with different shapes, dimensions, and arrangements are customarily set in the heat exchanger inside wall to enhance the turbulence resulting in the breakdown of the boundary layer. **Figure 3** shows some of the most commonly used internal arrangements in box type heat exchangers. Fishbone and inclined plate fin arrangements are some of the shapes showing high heat transfer rate from the exhaust gas with acceptable level of back pressure [22, 23]. Serial plate arrangement with the plate's direction perpendicular to the gas inlet showed the highest back pressure. Such arrangement gave backpressure as high as 190 kPa in a shell of 280 × 110 × 30 mm with inlet and outlet of 40 mm diameter [23]. An open shell metal foam filled plate heat exchanger also showed a very high efficiency of heat recovery 83.5% [24]. However, the high tortuosity of the foam structure creates an unacceptable levels of back pressure.

The temperature distribution in the heat exchanger along the exhaust flow direction usually tends to be lower in the downstream than the gas inlet region due to the heat loss to the TE module located close to the inlet [25]. Such nonuniformity in the temperature distribution reduces the power output of the modules placed beyond certain specified length in the downstream. Computational analysis carried out using different exhaust and coolant flow arrangements such as co-flow/parallel flow and counter flow suggest predicted a different overall power output [26]. However, it must be noted that a detailed experimental validation of these analyses only can confirm the preferred configuration that can maximize the overall power output.

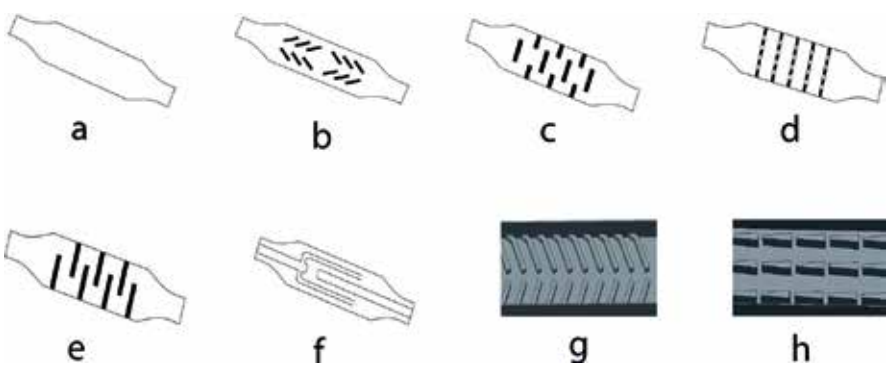

Figure 3. Different shapes of the internal arrangement for heat exchangers used in automotive TEG. (a) Empty cavity, (b) inclined plate, (c) parallel plate structure, (d) separate plate with holes, (e) serial plate structure and (f) pipe structure, (g) fish bone structure, and (h) accordion shape [23].

Using heat exchanger made of high thermal conductivity materials can improve the uniformity of the hot side surface to some extent. For example, in a study using steel and brass, Deng et al. observed better temperature uniformity in brass heat exchanger due to its higher thermal conductivity (κ_{brass}-109 W/m·K) [22]. Similarly, in a study using three-dimensional model to optimize heat exchanger parameters, Kempf et al. showed that by using silicon carbide in the heat exchanger better temperature uniformity can be achieved compared to stainless steel of 444 (SS 444) grade [25]. However, from the fabrication point of view, it will be highly cost-effective and easy to use SS than silicon carbide. The silicon carbide components are in general fabricated either by slip casting or gel-casting followed by sintering at above 2000°C. Such processes can adds up the TEG's cost significantly. The brass has higher density than SS which will increase the overall TEG's weight and the parasitic loss associated with it.

3.3. Heat sink or cold side heat exchanger

The AETEGs can be operated either at the maximum power (P_{max}) or maximum efficiency. In automotive exhaust application, it is always preferable to maximize the power output as it reduces the engine load which will improve the overall fuel efficiency. The P_{max} of a AETEG not only depends on hot side temperature (T_H) but the temperature difference (ΔT) between the hot and the cold side of the module. Hence, to maximize the power output, the cold side temperature (T_c) of the TE modules should be as low as possible. In most of the AETEGs designed, fabricated and tested in the laboratory testing conditions, the cold side temperature was controlled by using a water-cooled heat sink. However, in actual vehicles, it can be connected to the engine coolant circuit.

In the heat sink, the coolant flow is usually in the same (co-flow) or opposite (counterflow) direction to the exhaust gas flow as described in the previous section. Cross-flow and counter cross-flow arrangements are also used in few cases. The output power and the conversion efficiency of the AETEG for the various coolant flow arrangements mentioned above depends on the specific geometrical design of the cold side heat exchanger also. In the co-flow arrangement, the ΔT decreases along the streamwise direction of the exhaust gas flow as more sensible heat is absorbed and transferred to the cold side of the module tends to increase the coolant temperature. On the other hand, in counterflow arrangement, the ΔT decrease is lesser along the streamwise direction. However, to get the maximum power output in the TEG whether co-flow or counter-flow is preferable depends on the temperature and flow rate of the exhaust gas which in turn depends on the type, capacity and operating conditions of the engine.

The output power and the conversion efficiency of the AETEG for the various coolant flow configurations mentioned above depends on the specific geometrical design of the heat exchanger and heat sink combination. Su et al. performed simulation studies on different configurations of cooler design for TEG system viz., plate-shaped, stripe-shaped and diamond-shaped designs [27]. They further validated the simulation outputs with experiments and concluded that diamond-shaped design gave the highest power for a given engine speed among the three configurations for the cold side of the TEG system. They also observed that the temperature of the cold side is relatively uniform ensuring that the deviation in ΔT between the individual modules is minimal.

The cold side heat exchanger in TEG system in actual vehicle can either be a separate TEG coolant circulation system or integrated to the existing engine coolant circuit (integrated cooling

http://dx.doi.org/10.5772/intechopen.75443

system). While the separate system requires additional space and increases the overall weight of the vehicle, connecting the existing engine coolant circuit avoids these complexities. However, the cooling pump capacity and radiator size may have to be increased to accommodate the additional heat coming from the cold side of the TEG so that the overheating of the coolant can be prevented. In a combined simulation and experimental studies carried out in a 2.0 L 4 cylinder engine, Deng et al. observed that under certain vehicle operating conditions, temperature of the integrated cooling system increases and exceeds the boiling point of coolant [28].

3.4. Assembly components

The heat transfer between hot side heat exchanger and the cold side heat sink through TE modules depends on how well various components of the AETEG are assembled so that thermal contact resistance will be minimal between various interfaces. The thermal contact resistance depends on many factors: the applied contact pressure, surface roughness, the interface materials and its hardness are some of the important parameters to list. The assembly components are responsible for enforcing sufficient force over the modules sandwiched between the heat exchanger and the heat sink. The ΔT across the hot and cold side of the TE module increases typically with contact pressure as it generates more area of physical contact at the microscopic level resulting in more heat conductance through the interfaces. **Figure 4** shows the curve showing the typical variation of ΔT with applied contact pressure in a TEG with and without interface materials. [29].

In the absence of any interface materials, it can be seen that the ΔT remarkably increases with applied pressure. With the use of thermal grease at the interface, the ΔT is almost invariant. However with graphite, the most common interface material in AETEG, the ΔT was significantly

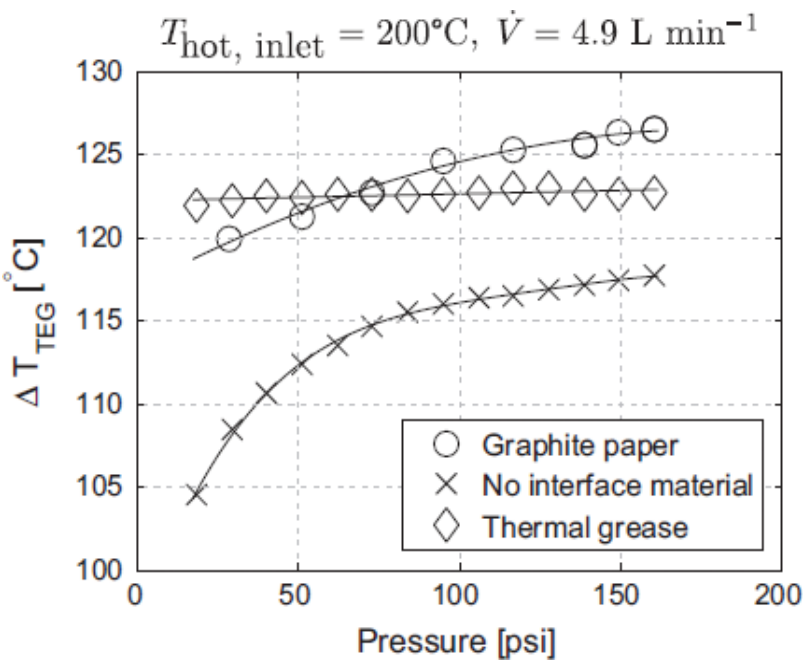

Figure 4. Variation of differential temperatures with contact pressure using different interface materials [29].

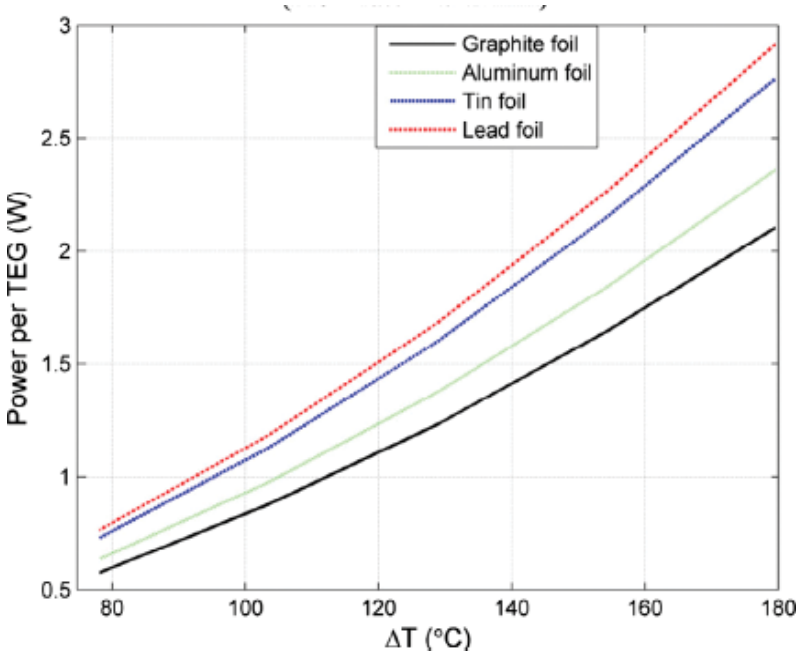

Figure 5. Estimation of the power per modules as a function of ΔT with different interface materials [28, 30].

higher than the other two for a given contact pressure particularly above 60 psi. The appropriate choice for the interface materials is the one with low hardness and high thermal conductivity. Such material will deform while applying pressure, make good contact between module and heat exchanger surfaces, and decrease the thermal contact resistance. **Figure 5** shows the comparison of the estimated power per Bi_2Te_3 modules as a function of ΔT in an investigation carried out using different interface materials [30]. Among the graphite, aluminum, tin and lead foils, the softest material lead is estimated to give lesser thermal contact resistance.

4. Performance evaluation of the AETEG

The AETEGs are usually tested for their performance by three different methods viz. (a) using a laboratory built test rig with hot gas or air as the heat source (b) in a simulated driving condition using laboratory test rig with gasoline or diesel engine and dynamometer and (c) in actual road driving test. While most of the performance tests reported so far were carried out by first or second methods, testing in actual driving conditions are very few. Such real driving conditions of a vehicle can give more realistic assessment of issues associated with this technology and its commercial feasibility.

4.1. TEG evaluation in test rig with a heat source

This test method is the ideal way of validating the design of an AETEG optimized by analytical and numerical methods. It is also a simple method to evaluate TE module reliability under the typical engine operating conditions. In AETEG, apart from the module efficiency, the power

http://dx.doi.org/10.5772/intechopen.75443

produced is determined by multiple factors such as (1) location of the TEG in the exhaust line, (2) exhaust gas flow rate and temperature, (3) locations and arrangement of modules in the TEG, (4) area of coverage of the modules in the heat exchanger/s, (5) heat sink temperatures, (6) thermal conductance at various interfaces, and (7) scheme of the modules electrical connection. Several multiphysics simulations, combining fluid mechanics, heat transfer, and thermoelectric phenomena, have been carried out to predict the influence of some of the above mentioned factors on the performance and power output of the TEG. However, the experimental validation of these predictions is very limited [31, 32]. **Figure 6** shows the image of a test rig designed and developed by this author used for evaluating the AETEG performance using hot air/gas [33]. Testing of the TEG in this test rig offers complete performance details, that is, the efficiency of the TE modules, heat exchanger, and heat sink, which will be useful for further optimization of the design before evaluating their performance in the actual engine using established driving conditions. The test rig consists of the following sub systems:

- Heat source
- Heat exchanger
- Flowmeter
- Pressure transmitter
- Differential Pressure transmitter
- Data Acquisition and Integration unit

The hot air source is a blower and heater combined unit where a high pressure blower of 4000 lpm output capacity draws in air and passes it to air heater which can heat up the air up to 400°C. The pressure of the hot gas is measured at inlet and outlet of heat exchanger using

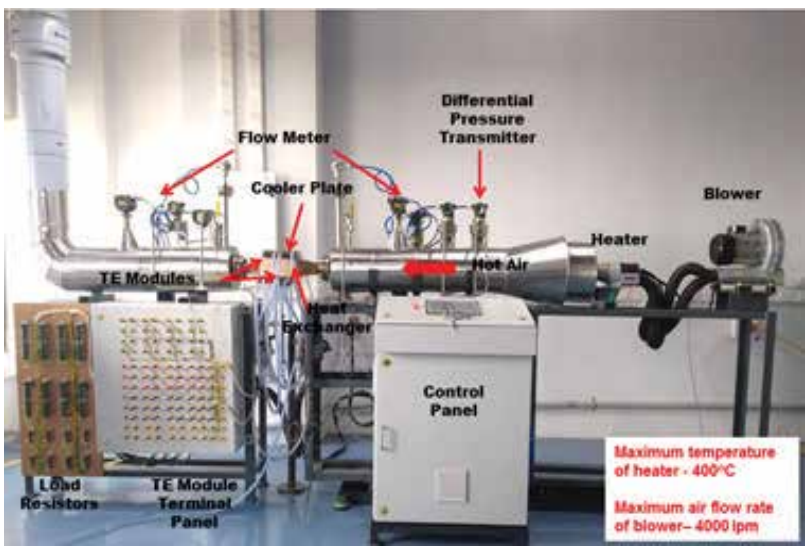

Figure 6. Photo image of the AETEG and the test rig developed at CAEM, ARCI.

a pressure transmitter and the back pressure due to the heat exchanger is measured by the differential pressure transmitter. The inlet and outlet temperatures of the hot air of the heat exchanger are measured using RTD sensors and K-type thermocouples are used for recording the temperatures on surface of heat exchanger. The data acquisition and integration unit collects the current and voltage signals from TE modules and also the pressure and flow rate signals and displays them in the display panel.

4.2. AETEG evaluation in test rig with engine exhaust

The performance evaluation of AETEGs using the engine exhaust gas has been carried out by many research groups. This method uses a test rig consisting of either a petrol or diesel engine coupled to a dynamometer to apply variable load. The testing can be carried out either in the steady state or transient condition using various engine speed and torque combinations which allows the generation of exhaust gas of different flow rates and temperatures. IC engines of different sizes ranging from 0.8 L [34] to 14 L [12] have been used in this method. In most of the works, while the heat exchanger and heat sink designs are different, the overall configuration of the AETEG prototypes is similar to one another.

The earliest attempt of building an AETEG and testing in an engine exhaust was carried out by Neild in the year 1963 [3]. Subsequently, Serksnis [4] and Birkholz [5] developed a similar system for exhaust waste conversion. Takanose and Tamakoshi developed a TEG and demonstrated it in a passenger car exhaust [35]. The system generated 100–130 W of power under various driving conditions. During the same period, Bass and his coworkers developed a 1 kW unit using 72 units of HZ-13 modules and tested in a 1.4 L Cummins diesel truck engine [12]. The BiTe modules made by Hi-Z Technology Inc. USA were arranged in a nickel steel support structure with an octahedral cross-section through which exhaust gas flows close to its internal surface. The modules cold side was cooled using an aluminum heat sink. The TEG initially generated power output of 400 W. Subsequently with several modifications in the design which resulted in better heat transfer at hot side, the TEG generated 1068 W under the engine operating condition of 300 HP and 1700 RPM. Ikoma and his co-workers from Nissan Motor Corporation, Japan developed a SiGe based AETEG fitted to the exhaust of a gasoline engine [13]. The system was made using 72 modules arranged between the rectangular cross section exhaust pipe made of SS 304 and aluminum water-cooled jacket. The TEG produced the maximum power of 35.6 W under the engine condition of 60 km/h hill climb with overall power generation efficiency of 0.1% [13]. Matsubara and his team from Science University of Tokyo, Japan [15] developed a prototype TEG and tested in a 2.0 L Toyota Estima engine using in-house manufactured segmented modules (skutterudites/Bi_2Te_3) and 4 HZ-14 modules made by Hi-Z Technology Inc., USA. The TEG produced an output power of 266 W under 60 km/h speed which is only half of the rated capability of the system. In both the abovementioned works, it was highlighted that the effectiveness of the heat exchanger and loss of heat at the various contact surfaces critically influence the power produced in the TEG.

The first qualitative assessment of the effect of AETEG system on the vehicle fuel efficiency and parasitic losses was carried but by Thatcher et al. in a 1999 model GMC Sierra light-duty pickup truck [9]. The study also emphasized the importance of the cold side temperature on the overall power output of the TEG. A 330 W capacity system built using 16 units of HZ-20 modules manufactured by Hi-Z Technology Inc., USA. The TEG produced 117 W under the

engine speed of 112.6 km/h with the hot side and coolant side of temperature around 300 and 80°C, respectively. Decreasing the cold side temperature to 15°C increased the power output to 229 W, which showed that decreasing the cold side temperature of the module appears to be more beneficial, unlike increasing the hot side temperature which may have the adverse effect on the module durability.

In a project partially funded by Swedish energy agency, with partners from Scania CV AB, Titan X, Eberspächer Exhaust Technology GmbH & Co. Germany, Swerea IVF, Gothenburg and KTH, Stockholm, a TEG system using Bi_2Te_3-based commercial modules has been designed, developed and tested in experimental hot gas test bench as well as in an actual engine exhaust [11]. The 224 modules which can be used up to 330°C are arranged in 14 modular TE units consist of hot exhaust gas and cooling water channels with counter cross-flow arrangements. At the input gas parameters of 300°C temperature and 1000 kg/h flow rate, the TEG delivered power output of 416 W. In a similar work using 1.2 L gasoline engine, a TEG designed to a nominal power of 225.6 W has produced the maximum power of 189.3 W at the engine operating conditions of 80 Nm torque, 2600 RPM speed [10]. The TEG was fabricated using 24 numbers of commercial Ferrotech SCTB NORD thermoelectric modules (Code Name TMG-241-1.4-1.2) made of BiTe-based compounds with the maximum power rating of 9.4 W. The increase in overall engine efficiency was close to 0.2%.

Zhang et al. reported the development of high temperature, high power density TEG yielding 1002.6 W power when tested in a Caterpillar diesel engine exhaust [20]. The TEG was fabricated using modules made of half-Heuslers compounds of p-type (peak ZT of 1.0 at 500°C) and n-type (peak ZT of 0.9 at 700°C) compounds. Heat exchanger with 0.2 mm thick nickel fins and aluminum cold plate with coolant flow perpendicular (cross flow) to the exhaust was used to create the temperature difference between hot and cold side of the modules. The exhaust gas of 550°C with a flow rate of 1728 kg/h generated a temperature difference 339°C of between hot and cold side. The efficiency of the individual module was around 2.1%. Liu et al. investigated an automotive TEG designed, fabricated and tested in test rig with 2.0 L naturally aspirated engine with a dynamometer and in actual road test condition in a 3.9 L engine [36]. The TEG was made of 60 modules, a brass heat exchanger and aluminum water tank as the heat sink. The maximum power output of 335.8 W under the temperature difference of 235°C with the conversion efficiency of 0.9% was obtained in the test rig. Interestingly, combining the four of the same TEGs into a single system for road test could able to generate only 390 W power as under this test conditions the exhaust heat from engine appeared to be inadequate and could able to create a temperature difference of 133°C only.

AETEG's have been investigated for the performance both in gasoline and diesel engines of various capacities and vehicles. Whether it is advantageous to use this technology for a particular kind of engine is a debatable topic. The amount of waste heat and the temperature of the exhaust gas usually is higher in the spark ignition (S.I) engine compared to compression ignition (C.I) engine. The maximum exhaust gas temperature for gasoline engines is about 700–800°C and for diesel engines is about 400–500°C at the exhaust manifold. A study carried out by Wojciechowski et al. in a single point injection 0.9 L Fiat spark ignition (gasoline) engine and 1.3 L diesel engine using BiTe-based AETEG suggests that it is more beneficial to use in spark ignition engine [16]. For a given engine power, the high output of gas flux from the diesel engine results in a low hot side temperature and hence the energy produced is lesser.

5. Automotive TEG for engine coolant waste heat conversion

Similar to the exhaust waste heat conversion, the heat in the engine coolant can also be utilized to generate power using the TEG, as nearly 30% of the energy from the fuel combustion accounts for this loss. However, the important point to be noted here is that the waste heat available in the coolant is of low grade in nature. Unlike exhaust gas, in this case the temperature and flow rate are lesser and need better heat capturing technique. Kim and his coworkers demonstrated TEG for engine coolant heat conversion using a 2.0 L passenger car engine [17]. The TEG was made of 72 BiTe modules with the hot and cold side blocks used to recover and dissipate the heat from the coolant. The cold side block was integrated with heat pipes which enhances its efficiency. Under the engine idle condition, the maximum output power of 0.4 W/module was generated which increased to 1.04 W/module under 80 km/h driving mode. The higher power obtained in the driving mode can be attributed to the lesser cold side temperature rather than hot side temperature, which shows an improvement of only 5°C. Under driving mode, the cold side temperature decreases by 25°C due to the arrangement of the heat pipes which showed better cooling performance than the radiator.

6. TEG for hybrid and electric vehicles

Hybrid vehicles consume relatively less fuel than the petrol or diesel vehicle by efficiently combining a conventional I.C engine power with the electric motor/s. The power to the drive comes from either downsized engine, motor or both depending on the driving conditions. The improvement in fuel efficiency mainly comes from operating the engine in an optimized condition with less idling, regenerative breaking, and dual power sources. Depending on the kind of the power source, the hybrid vehicles can be classified as serial hybrid, series–parallel hybrid, and plug-in hybrid. In some hybrid systems, the engine is automatically shut off during idling and restart when accelerated by integrated starter generator (ISG) thereby reducing the fuel consumption. The regenerative braking system converts the kinetic energy from the moving vehicle into electrical energy and stores it in a battery. At present, though the hybrid cars consume less fuel than conventional vehicles, there are still CO_2 emissions, the level of which may have to be reduced further to meet the futuristic goal of the allowable limit. Though, unlike in conventional I.C engines, not much work has been carried out in AETEG for the hybrid vehicles. The computational and experimental work carried out so far suggests that a notable improvement in fuel efficiency can be achieved using TEG in hybrid cars [37, 38]. Since in hybrid vehicles, the engines used are downsized, the exhaust flow rate and the temperature are expected to be low and hence using heat pipe-assisted TEG will be more suitable to maximize the power output [39].

7. Parasitic losses by TEG in vehicle

The overall effect on the fuel efficiency of the vehicle due to the incorporation of AETEG in the exhaust line not only depends on the power it produces but also on the parasitic losses associated with it during driving which has been estimated to contribute to a notable extent. The parasitic losses mainly comes from three sources viz. power required for pumping coolant into

http://dx.doi.org/10.5772/intechopen.75443

heat sink, exhaust blow-down power loss, and the rolling resistance [31]. The dominant among these three is the rolling resistance loss due to the weight of the TEG system which tends to increase with the vehicle speed.

The coolant pumping power (P_{cp}) is given by $P_{cp} \approx \rho_f \chi Q/\eta_{cp}$, where ϱ_f is the density of the coolant, χ is the loss coefficient for coolant flowing through the TEG loop, Q is the coolant flow rate, and η_{cp} is the coolant pump efficiency. The loss coefficient χ depends on Reynolds number of the fluid flow. In a typical AETEG where the coolant circuit is connected to engine coolant loop, the flow rate through the TEG will be low relative to the flow through engine coolant jacket. However, as the capacity of the TEG increases, the χ through it also will be significant.

The exhaust blow-down power, which is the power required for the engine to drive the gaseous products of the combustion through the exhaust system can change because of the flow resistance introduced by the TEG system's heat exchanger. The blow-down power can be both positive and negative depending on the power gains obtained due to AETEG. If the power produced helps to decrease the shaft power, the net blow-down power will decrease. The blow-down power given by $P=\Delta p.V_F$ is calculated from pressure drop across the TEG's heat exchanger (Δp) and the volumetric flow rate of the exhaust gas (V_F). For a given engine running at a speed (ω), the volumetric flow rate of exhaust is given by $V_F = (\pi.\omega.N_p.S.b^2)/8$ where N_p is the number of pistons, S is the piston stroke and b is the piston bore [25].

The rolling resistance is due to the weight of the AETEG system produces power loss given by $P_R = \mu_R W_T \nu/\eta_R$, where μ_R is the rolling resistance coefficient, W_T weight of the TEG system, ν is the velocity of the vehicle, and η_R driveline efficiency which is normally constant at around 0.9 [31]. An estimation in a 1.5 L car fitted with TEG tested under new European driving cycle showed that the weight penalty of TEG could be as high as 12 W/kg [47]. Therefore, the TEG requires very stringent design criteria in terms of the heat exchanger materials and TE module materials.

8. Power conditioning and maximum power point tracking

In AETEG, the output voltage changes dynamically in a nonlinear way over a wide range with the fluctuation of flow rate and temperature of exhaust gas. Therefore, a proper power conditioning circuit similar to the ones used in photovoltaic power system with a maximum power point tracking (MPPT) control is essential between the TEG and the load. A number of different power conditioning circuits for AETEG to step-up or step-down the voltage have been proposed. Some of the prominent circuits are DC-DC converters such as Ćuk converter, SEPIC converter, and Boost-buck cascade converter. MPPT is an algorithm used to operate a power system at its maximum power capability under various operating conditions. Different MPPT techniques such as load matching method, incremental conductance technique, ripple correlation, perturbation and observation (PAO) method has been developed. The PAO method is the most commonly used one due to its simplicity and system independence.

In automotive exhaust waste heat conversion, MPPT can be used, for example, between the TEG system and a battery pack so that power flow is regulated to obtain the maximum power transfer. Eakburanawat et al. proposed an MPPT technique based on feedback from battery current alone assuming constant battery voltage [40]. However, all practical batteries have a significant change

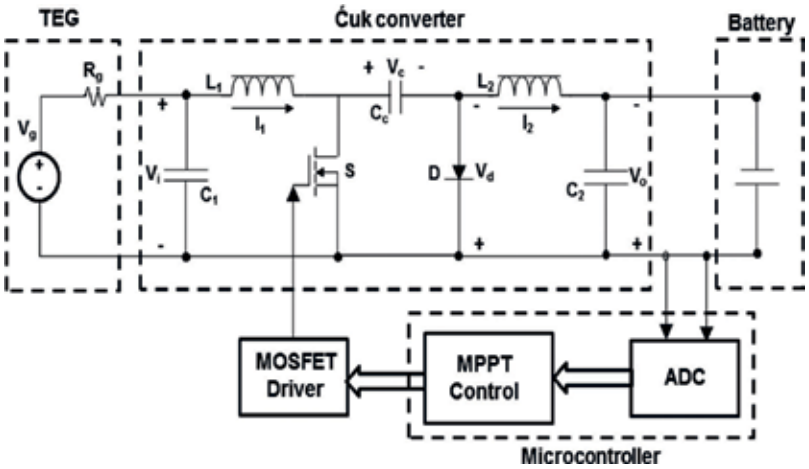

Figure 7. Schematic of power conditioning system based on battery voltage and current [40].

of terminal voltages, especially during charging, which should not be neglected. Later, Yu et al. proposed the MPPT technique based on the measurement of TEG power which is derived from its terminal voltage and current [41]. However, such maximization has not taken into account the power converter loss, which should not be a constant value. Subsequently, the same group has proposed a DC-DC Ćuk converter-based power regulation system with the MPPT technique which considers both the terminal voltage and current of the battery to maximize the TEG output power instead of using terminal voltage and current [42]. **Figure 7** shows the schematic of power conditioning scheme proposed based on battery voltage and current. The variation of battery voltage and power converter loss is also taken into account in this system.

Fang et al. proposed a novel MPPT scheme which involves the aggregated dichotomy and gradient (ADG) method for rapid tracking the maximum power in an automotive TEG [43]. They carried out the steady state and transient tracking experiments under various load conditions of dynamometer and compared the ADG method with traditional methods like single gradient method (SGM), single dichotomy method (SDM) and perturbation and observation method (PAO). The results showed that the ADG had better tracking accuracy and speed compared to the traditional methods.

9. Cost analysis of automotive TEG

Though the TEG for automotive exhaust application envisaged improving the overall fuel efficiency, the final task of implementation on commercial scale mainly depends on the cost–benefit it offers over the lifespan of a vehicle. At present, both technological and cost factors of AETEG are not in favor for such commercial realization. The major cost components in the AETEG come from modules, heat exchangers for hot and cold side, power conditioning unit with control systems, and so on. Various cost analysis studies carried out in passenger automobiles under different operating conditions suggest that the cost of the existing TE modules alone must be reduced

http://dx.doi.org/10.5772/intechopen.75443

up to 40% by using low-cost materials with higher zT [44]. In an analysis carried out in conventional vehicles operated in Korea, Bang et al. reported that the application of TEG in mid-size sedan and the medium-duty truck can save 0.15 and 1.04 kL fuel, respectively, at a driving speed of 80 km/h. Such fuel savings show that the economically acceptable costs of the TEG system for these two vehicles are 744 $/kW (mid-size sedan) and 2905 $/kW (medium duty truck) [45]. A comprehensive cost analysis of the real application scenario of automotive TEG using skutterudites module by Hendricks et al. suggests that the heat exchangers cost most often dominate the overall AETEG cost, and it is necessary to bring down from the current 10$/W to l $/W or lesser [46]. They observed that the minimum system cost is coinciding with the maximum power point which is governed by factors such as exhaust temperature, ΔT between the hot and cold side of the module, zT of the materials, thermal conductance between the hot and cold sides, heat exchanger cost factor and the parasitic losses. The rolling resistance arising due to the weight of the TEG alone would attract the penalty of a significant fraction of the power produced. In a 1.5 L engine family car tested under new European drive cycle incorporating an AETEG showed a power loss of 12 W/kg [47]. The additional load for the coolant pump for circulating the coolant to the cold side heat exchanger would further add up to the power loss. Employing low-density materials in both the heat exchanger/s and TE modules would considerably reduce the AETEG cost by decreasing its weight and parasitic losses associated with it.

10. Summary

Hydrocarbon-based fuels will continue to be a primary source of energy for transportation for the next few decades. Improving the efficiency of the vehicles by even few percentages will have a tremendous effect on the fuel savings and controlling the emissions. Automotive TEG is one potential technology which can increase the vehicle fuel efficiency. Though the technique is known for several decades, significant progress has been made in materials, modules, and systems over the past 20 years only and as of today it is far from commercialization. The high cost and low efficiency of the currently available modules make the overall cost of the TEG much higher than $1/W barrier apt for implementation this technology in vehicles. The high zT observed in several low-cost materials in recent years need to be translated into reliable high-power output modules. An innovative design which reduces the overall weight of the AETEG with improved efficiency is a key necessity to make this technology commercially successful.

Author details

Duraisamy Sivaprahasam*, Subramaniam Harish, Raghavan Gopalan and Govindhan Sundararajan

*Address all correspondence to: sprakash@arci.res.in

Centre for Automotive Energy Materials (CAEM), ARC-International, IIT Madras Research Park, Chennai, India

References

[1] Aren F, Mezzan L, Doyon A, Suzuki H, Lee K, Becker T. The Automotive CO_2 Emissions Challenge. 2020 Regulatory Scenario for Passenger Cars. Rome: Arthur D. Little; 2014). http://www.adlittle.com/downloads/tx_adlreports/ADL_AMG_2014_Automotive_CO2_Emissions_Challenge.pdf

[2] Energy Technology Perspectives 2015, International Energy Agency, France. http://www.iea.org/publications/freepublications/publication/ETP2015.pdf

[3] Neild AB Jr. Portable thermoelectric generators, Society of Automotive Engineers, New York, SAE-645 A; 1963

[4] Serksnis AW. Thermoelectric generator for automotive charging system. In: Proceedings of 11th Intersociety Conversion Engineering Conference, New York, USA. 1976. pp. 1614-1618

[5] Birkholz U, Grob E, Stohrer U, Voss K, Gruden DO, Wurster W. Conversion of waste exhaust heat in automobile using $FeSi_2$ thermoelements. Proc. 7th International Conference on Thermoelectric Energy Conversion, Arlington, USA; 1988. 124-128

[6] Bass JC, Campana RJ, Elsner NB, Thermoelectric generator for diesel trucks. Proceedings of the 10th International Conference on Thermoelectrics. Cardiff, Wales: Babrow Press; 1991

[7] Biswas K, He JQ, Blum ID, Wu CI, Hogan TP, Seidman DN, Dravid VP, Kanatzidis MG. High performance bulk thermoelectrics with all scale hierarchical architectures. Nature. 2012;**489**:414-418

[8] Zhao LD, Lo SH, Zhang YS, Sun H, Tan GJ, Uher C, Wolverton C, Dravid VP, Kanatzidis MG. Ultra low thermal conductivity and high thermoelectric figure of merit in SnSe crystals. Nature. 2014;**508**:373-377

[9] Thacher EF, Helenbrook BT, Karri MA, Richter CJ. Testing of automobile exhaust thermoelectric generator in a light truck, Proc. IMechE. Part D: Journal of Automobile Engineering. 2007;**22**:95-107

[10] Merkisz J, Fuc P, Lijewski P, Ziolkowski A, Galant M, Siedlecki M. Analysis of an increase in the efficiency of a spark ignition engine through the application of an automotive thermoelectric generator. Journal of Electronic Materials. 2016;**45**:4028-4037

[11] Frobenius F, Gaiser G, Rusche U, Welleri B. Thermoelectric generators for the integration into automotive exhaust systems for passenger cars and commercial vehicles. Journal of Electronic Materials. 2016;**45**:1433-1440

[12] Bass JC, Elsner NB, Leavitt FA. Performance of the 1 kW Thermoelectric Generator for Diesel Engines. Proc. of the 13th International Conference on Thermoelectrics, Kansas City, USA. 1994

[13] Ikoma K, Munekiyo M, Furuya K, Kobayashi M, Izumi T, Shinohara K. Thermoelectric module and generator for gasoline engine vehicles. 17th International Conference on Thermoelectrics; 1998. p 464-467

[14] Haidar JG, Ghojel JI. Waste heat recovery from the exhaust of low power diesel engine using thermoelectric generators. Proc ICT2001. 20th International Conference on Thermoelectrics (Cat. No.01TH8589). IEEE; 2001. p 413-418

[15] Matsubara K. Development of high efficient thermoelectric stack for a waste exhaust recovery of vehicle. 21st Int. Conference on Thermoelectrics, Proc. ICT 02. IEEE; 2002. p. 418-423

[16] Wojciechowski KT, Schmidt M, Zybala R, Merkisz J, Fuc P, Lijewsk P. Comparison of waste heat recovery from the exhaust of a spark ignition and a diesel engine. Journal of Electronic Materials. 2010;**39**:2034-2038

[17] Kim S, Park S, Kim S, Rhi S. A thermoelectric generator using engine coolant for light-duty internal combustion engine-powered vehicles. Journal of Electronic Materials. 2011;**40**:812-816

[18] Kim S, Won B, Rhi S, Kim S, Yoo J, Jang J. Thermoelectric power generation system for future hybrid vehicles using hot exhaust gas. Journal of Electronic Materials. 2011; **40**:778-783

[19] Crane D, Lagrandeur J, Jovovic V, Ranalli M, Adldinger M, Poliquin E, Dean J, Kossakovski D, Mazar B, Maranville C. TEG on vehicle performance and model validation and what it means for further TEG development. Journal of Electronic Materials. 2013;**42**:1582-1591

[20] Zhang Y, Cleary M, Wang X, Kempf N, Schoensee L, Yang J, Joshi G, Meda L. High temperature and high power density nanostructured thermoelectric generator for automotive waste heat recovery. Energy Conversion and Management. 2015;**105**:946-950

[21] Wang X, Li B, Yan Y, Liu S, Li J. A study on heat transfer enhancement in the radial direction of gas flow for thermoelectric power generation. Applied Thermal Engineering. 2016;**102**:176-183

[22] Deng YD, Liu X, Chen S, Tong NQ. Thermal optimization of the heat exchanger in an automotive exhaust based thermoelectric generator. Journal of Electronic Materials. 2013;**42**:1635-1640

[23] Bai S, Lu H, Wu T, Yin X, Shi X, Chen L. Numerical and experimental analysis for exhaust heat exchangers in automobile thermoelectric generators. Case Studies in Thermal Engineering. 2014;**4**:99-112

[24] Wang T, Luan W, Wang W, Tu S. Waste heat recovery through plate heat exchanger based thermoelectric generator system. Applied Energy. 2014;**136**:860-865

[25] Kempf N, Zhang Y. Design and optimization of automotive thermoelectric generators for maximum fuel efficiency improvement. Energy Conversion and Management. 2016;**121**:224-231

[26] Meng J, Wang X, Chen W. Performance investigation and design optimization of a thermoelectric generator applied in automobile exhaust waste heat recovery. Energy Conversion and Management. 2016;**120**:71-80

[27] Su CQ, Xu M, Wang WS, Deng YD, Liu X, Tang ZB. Optimization of cooling unit design for automotive exhaust-based thermoelectric generators. Journal of Electronic Materials. 2014;**44**:1876-1883

[28] Deng YD, Liu X, Chen S, Xing HB, Su CQ. Research on the compatibility of the cooling unit in an automotive exhaust-based thermoelectric generator and engine cooling system. 2013;**43**:1815-1823

[29] Bjork R, Sarhadi A, Pryds N, Lindeburg N, Viereck P. A thermoelectric power generating heat exchanger: Part I—Experimental realization. Energy Conversion and Management. 2016;**119**:473-480

[30] Sarhadi A, Bjork R, Lindeburg N, Viereck P, Pryds N. A thermoelectric power generating heat exchanger: Part II—Numerical modelling and optimization. Energy Conversion and Management. 2016;**119**:481-487

[31] Karri MA, Thacher EF, Helenbrook BT. Exhaust energy conversion by thermoelectric generator: Two case studies. Energy Conversion and Management. 2011;**52**:1596-1611

[32] Favarel C, Bedecarrats JP, Kousksou T, Champier D. Experimental analysis with numerical comparison for different thermoelectric generators configurations. Energy Conversion Management. 2016;**107**:114-122

[33] An unpublished work from our group. Centre for automotive energy materials (CAEM), ARC-International. INDIA

[34] Ramade P, Patil P, Shelar M, Chaudhary S, Yadav S, Trimbake S. Automobile exhaust thermo-electric generator design &performance analysis. International Journal of Emerging Technology and Advanced Engineering Website: www.ijetae.com. May 2014;**4**(5). ISSN 2250-2459, ISO 9001:2008 Certified Journal

[35] Takanose E, Tamakoshi H. The development of thermoelectric generator for passenger car. In: Proceedings of the 12th IEEE International Conference on Thermoelectrics, Yokohama, Japan. New York: IEEE; November 1993. pp. 467-470

[36] Liu X, Deng YD, Wang WS, Su CQ. Experimental investigation of exhaust thermoelectric system and application of vehicle. Journal of Electronic Materials. 2015;**44**:2203-2210

[37] Deng YD, Fan W, Ling K, Su CQ. A 42-V electrical and hybrid driving system based on a vehicular waste-heat thermoelectric generator. Journal of Electronic Materials. 2012;**41**:1698-1705

[38] Fang W, Quan S, Xie C, Tang X, Ran B, Jia Y. Energy optimization for a weak hybrid power system of an automobile exhaust thermoelectric generator. Journal of Electronic Materials. 2017;**46**:6617-6627

[39] Kim S, Won B, Rhi S, Kim S, Yoo J, Jang J. Thermoelectric power generation system for future hybrid vehicles using hot exhaust gas. Journal of Electronic Materials. 2011; **40**:778-783

[40] Eakburanawat J, Boonyaroonate I. Development of a thermoelectric battery charger with microcontroller based maximum power point tracking technique. Applied Energy. 2006;**83**:687-704

[41] Yu C, Chau KT, Chan CC. Thermoelectric waste heat energy recovery for hybrid electric vehicles. Paper No. 21. In: International Electric Vehicle Symposium and Exposition; 2007

[42] Yu C, Chau KT. Thermoelectric automotive waste heat energy recovery using maximum power point tracking. Energy Conversion and Management. 2009;**50**:1506-1512

[43] Fang W, Quan SH, Xie CJ, Tang XF, Wang LL. Maximum power point tracking with dichotomy and gradient method for automobile exhaust thermoelectric generators. Journal of Electronic Materials. 2016;**45**:1613-1624

[44] Kishita Y, Ohishi Y, Uwasu M, Kuroda M, Takeda H, Hara K. Evaluating the life cycle CO_2 emissions and costs of thermoelectric generators for passenger automobiles: A scenario analysis. Journal of Cleaner Production. 2016;**126**:607-619

[45] Bang S, Kim B, Youn Y, Kim YK, Wee D. Economic and environmental analysis of thermoelectric waste heat recovery in conventional vehicles operated in Korea: A model study. Journal of Electronic Materials. 2016;**45**:1956-1965

[46] Hendricks TJ, Yee C, Leblanc S. Cost scaling of a real world exhaust waste heat recovery thermoelectric generator: A deeper dive. Journal of Electronic Materials. 2016; **45**:1751-1761

[47] Rowe DM, Smith J, Thomas G, Min G. Weight penalty incurred in thermoelectric recovery of automobile exhaust. Journal of Electronic Materials. 2011;**40**:784-788

Chapter 10

Prospects and Problems of Increasing the Automotive Thermoelectric Generators Efficiency

Alexey Osipkov, Roman Poshekhonov,
Konstantin Shishov and Pavel Shiriaev

Additional information is available at the end of the chapter

http://dx.doi.org/10.5772/intechopen.76971

Abstract

The chapter considers the current state and trends in the field of heat recovery units for vehicles with internal combustion engines (ICE), including thermoelectric generators for cars, motorcycles, ships and railway transport. Based on the analysis of literature data, mathematical modeling and experimental studies, this chapter presents various designs of such generators. This research considers a heat exchange between exhaust gas (EG) and thermoelectric modules (TEM), as well as how their usage affects ICE operation. Furthermore, the chapter profoundly explores the challenges of installing thermoelectric generator (TEG) on vehicle system. In addition, the ways of increasing overall system efficiency, by optimizing the flow channel and reducing electrical power losses, are presented.

Keywords: thermoelectric generator, Seebeck effect, internal combustion engine, internal combustion engine vehicles, thermal contact resistances, heat exchange structure, automatic power management

1. Introduction

Internal combustion engines are currently the main power source for most vehicles. A significant change in the ICE share can hardly be expected in the short or medium term [1].

In 1988, in order to improve the road transport's environmental performance, the United Nations Economic Commission for Europe introduced emission standards regulation (Euro-0) that required reducing the level of carbon monoxide, nitrogen oxide and hydrocarbons in

the exhaust gases. Since then, the environmental standards are progressively becoming more stringent (Euro-6 standard is in force since 2015). In addition, the international efforts to reduce the rate of global warming resulted a new law Standard No 443/2009 by European Union, which prescribes the reduction emission of CO_2 up to 130 g/km for new passenger cars till 2015 and up to 95 g/km by end of 2021. With the passage of time every year, new restrictions are being advocated by tax policies which take into account a vehicle's environmental performance level, encourage automakers to work towards finding effective solutions to reduce harmful emissions into the atmosphere.

The activity in this area takes two directions: optimization of processes in a combustion chamber and neutralization of exhaust gases [1]. However, these developed methods can partially solve the problem of reducing harmful emissions. At the same time, the average fuel consumption for vehicle operation is 35% [2], while approximately 37% is dissipated as EG [3], which means that great potential is available for heat recovery technology.

At present numerous technical solutions are being developed for heat recovery systems. Among the most promising are the Rankine cycle, thermoelectric generator and a turbo-compound engine. All these solutions have their own merits and drawbacks [4, 5]. Numerous authors believe [6–8] that up to now the thermoelectric generator is the least developed technology. However, due to the absence of moving parts, potentially high reliability, compactness and the prospects in new thermoelectric materials over the past 20 years [9], this technology has great practical potential as an exhaust heat recovery system for ICEs.

2. ATEG research review

One of the first published works on a thermoelectric generator for vehicles was done in 1913 [10] where a thermoelectric cell based on a thermocouple wire powers lighting and ignition systems. This generator was meant to eliminate the need for a standard electromechanical alternator, thus making the electric power supply system less complex and expensive.

The first research in this area was conducted in 1961–1963 at Clarkson University (USA) by Bauer [11] and Tomarchio [12]. Bauer considered the possibility of using *PbTe*-based thermoelectric generators to recover heat in the automobile cooling system and came to the conclusion that a noticeable electric power requires a lot of thermoelectric material. Tomarchio investigated the possibility of replacing an alternator with a thermoelectric generator in the automobile exhaust system and concluded that the desired power levels in the 20–50 mph (32–80 km/h) speed range. Speeds below 20 mph require new, more efficient materials.

In the mid-1950s, research by Goldsmid [13] and Ioffe [14], the subsequent development of thermoelectric materials based on bismuth telluride solid-state solutions achieved significant development in the applications of thermoelectric effect. However, these technologies were adopted in automobile generators only in the late 1980s and early 1990s, which was apparently caused by the changes in environmental policies of different countries (the EU environmental guidelines were formulated in 1987 in The Single European Act (SEA)).

In 1988, Birkholt et al. [15]. developed automotive thermoelectric generator (ATEG) and tested on Porsche 944. It had a peak power of 58 W at 800°C temperature for hot-side heat exchanger.

Temperature difference between hot and cold side of heat exchanger was 490°C. $FeSi_2$ was used as the thermoelectric material.

Hi-Z Technology, Inc. (Hi-Z) funded by the U.S. Department of Energy (DOE) began a large-scale of research in this direction in 1987 with the aim of obtaining sufficient electric power to eliminate the need of engine driven alternators in trucks. Different locations were purposed for the TEG installation to enable heat recovery; among them were the exhaust manifold, the internal combustion engine, the intercooler and the lubrication system. The conclusion was made that the exhaust gases have the best potential for ATEG [16]. Thermoelectric materials were analyzed in terms of their effectiveness in solving this problem and the optimal materials were selected. In 1994, Hi-Z presented test results for 1 kW ATEG installed on the Cummins NTC 325 and NTC 30 engines [17]. The obtained power was 1068 W for a 300 hp. engine at 1700 rpm. The ATEG used 72 thermoelectric modules (Hi-Z-13) based on bismuth telluride with 4.5% efficiency, the hot and cold side temperatures constituted 230 and 30°C, respectively. The authors concluded that special attention must be paid to the heat exchanger configuration because of the increased sensitivity to the temperature difference between its various components and their mean temperature.

In 1998, Nissan Motor group presented ATEG test results for a 3000 mL gasoline engine with *SiGe*-based thermoelectric modules that demonstrated maximum power 35.6 W at 60 km/h on hill-climb mode with 1141°C exhaust gas temperature [18]. The total efficiency η_t of heat exchanger constituted 11% and the heat flow through the modules was converted into electricity with generated power η_p 0.9% efficiency. It was noted that by increasing 50% η_t and 5% η_p, the alternator's power would reach 950 W. It is worth to mention that a bypass was used to regulate the heat flow during the experiment.

In 1999, this group created and tested generator for 2 and 3 L gasoline engines with Hi-Z-14 modules based on Bi_2Te_3. This system demonstrated maximum power 193 W under the same operating conditions; with η_t constituting 37% and η_p 2.9% [19].

The early research in ATEG was devoted to the following issues: the total heat to electricity conversion efficiency, the dependence of the output power on the engine rpm (obtaining the maximum power at the maximum rpm), and the key directions for further work. Along with the development of more efficient thermoelectric materials, special emphasis is laid on the intensification of heat transfer processes in ATEG, especially the heat recovery in a gas heat exchanger.

In 2012, Amerigon (now Genterm) in collaboration with BMW and Ford, and the financial support from DOE presented results of their project in ATEG launched in 2004 [20]. A prototype ATEG for two passenger cars (BMW X6 and Lincoln MKT) was constructed and installed into the exhaust system behind the catalytic converter. The project focused on the effect the ATEG with an integrated bypass had on various car systems. Static and dynamic experiments were carried out, including the US06 drive cycle. Fuel efficiency was found to be 1.2% at 110 km/h. The maximum peak power for BMW X6 at 125 km/h in the stationary and dynamic modes constituted 605 and 450 W, respectively.

Between 2011 and 2015, Genterm in cooperation with BMW and Tenneco, continued work on ATEG. The aim of the new project was to achieve 5% reduction in fuel consumption over US06 cycle with the potential for efficient commercialization [21]. In the end, the average fuel

saving was 1.2% (9.2 g/mil CO_2 emission reduction) for a Ford F350 (6.2 L SOHC V8 flex fuel engine) with maximum 1160 W and average 470 W generator power over US06 cycle. At the same time, CO_2 emission increased by 0.2 g/mil for a BMW X3 28i with the ATEG. CO_2 emission increasing was explained by automobile weigh increasing and requiring more power for cooling system. These results confirm the necessity of TEG and all car systems optimization.

ATEG with Bi_2Te_3-based TEMs was developed as part of the HeatReCar [22, 23] project with Fiat and Chrysler collaboration. The system was installed onto an IVECO Daily light-duty truck with a 2.3 l diesel engine, and showed a 2.2% increase in fuel efficiency (6.7 g/km reduction in CO_2 emission) over NEDC cycle and 3.9% increase in fuel efficiency (9.6 g/km reduction in CO_2 emission) over WLTP cycle. The project also developed and tested skutterudite-based TEM for high-temperature applications.

The RENOTER project, launched in 2008 by Renault Trucks and Volvo, was aimed at creating ATEG for diesel (100–300 W depending on the driving cycle) and gasoline (up to 500 W) passenger cars, as well as for large trucks (up to 1 kW) with 0.3–1.3 $/W cost of generated electricity [24]. Apart from the heat exchanger design optimization, the project focused on the development of effective, cheap and reliable thermoelectric materials and their installation onto generators (Mg_2Si- and $MnSi_{1.77}$-based materials).

The analysis of the ATEG projects over the past 15 years reveals the drive to reduce fuel consumption or CO_2 emission, to make the design solutions economically efficient and to meet the reliability indicators. This has the following implications: ATEG must be investigated in dynamic as well as in stationary modes; tests over various operating cycles must be conducted, cheaper; less toxic materials must be used for TEM; reliability must be evaluated and maintained. Even though the projects do not always achieve their goals in full, the great potential in optimizing individual design and technological solutions is obvious.

The analysis of publications shows that the number of papers dealing with various aspects of the ATEG development is growing every year (**Figure 1**).

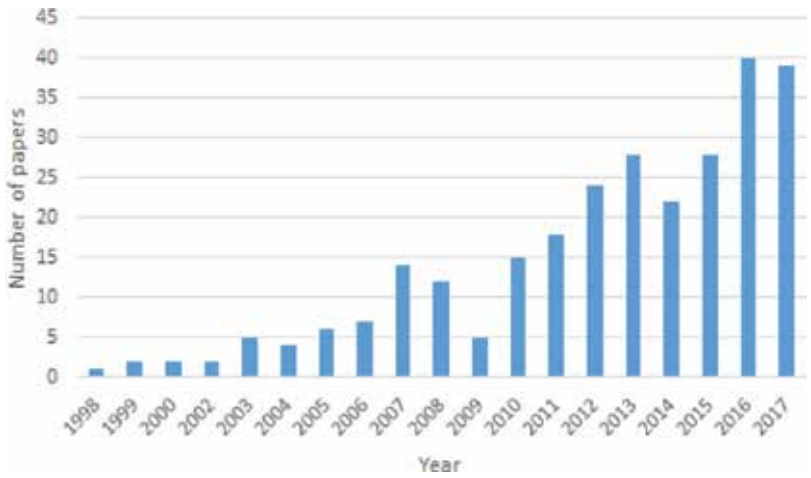

Figure 1. Research papers in ATEG (SCOPUS).

Over the past 5 years, China has become the leader in the number of publications in this field, with Wuhan University of Technology being the most active at ATEG research. In terms of publications total, the US holds the first place, with Caltech having the highest number of publications. The following organizations are playing an active part in the ATEG research: German Aerospace Center (DLR), TU Berlin, Loughborough University (UK), AGH University of Science and Technology (Poland) and Chungbuk National University (Korea). In Russia, Bauman Moscow State Technical University and Moscow Polytech are working on ATEG.

3. ATEG design

3.1. Features of technical requirements for ATEG in comparison with stationary TEGs

The increase in the electrical power of on-board equipment cannot always be achieved by installing a more efficient alternator due to the high density of the layouts of modern ICEs (this is especially true for small vehicles, for example, motorcycles). In this case, the TEG installation on the EG system can be the way out.

At the same time, in contrast to TEGs operating in stationary conditions with a constant heat flux, the effective use of TEGs for vehicles requires the solution of a number of specific tasks which must ensure:

- durability of device under variable thermal and mechanical loads associated with frequent changes in engine operating modes and vehicle vibrations;
- minimization of electric losses during various operating conditions of internal combustion engine and varying electric load;
- technological solutions must be compatible with mass production;
- optimal layout of ATEG with certain mass and dimensional constraints;
- effective convective heat transfer of TEG hot heat exchanger with a limited heat exchange surface area with low hydraulic resistance.

The solution of these problems requires a rational arrangement of TEG, parametric optimization of the quantitative TEG models taking into account multiple accompanying physical processes as well as carrying out experimental studies for quantitative verification of models and prototype tests.

3.2. General requirements for ATEG design

As a rule, ATEG has a hot heat exchanger coming through the EG and one or more TEM sections, cold heat exchanger to drain the heat into the hydraulic cooling system or directly into the external environment, the voltage stabilization system for the on-board power supply system (12 V).

ATEGs must be connected to the exhaust, power and hydraulic cooling systems of the vehicle and effectively operate with them. However, there are challenges of all these points implementation during ATEG design.

General technical requirements for ATEG:

- technological design for series production;
- reliability with frequent changes in pressure and temperature of EG;
- limitation of weight and dimensions;
- high efficiency of heat removal and heat transfer;
- low hydraulic resistance;
- no resonance frequencies in the range of 15–200 Hz.

Technical requirements differ significantly in a wide range depending on the type of vehicle. For example, the limitation for mass and dimensions for trucks is much softer, while the requirement for air resistance is much stricter than for a motorcycle.

There are conflicts of design goals. The most challenging issue is that high efficiency of heat removal can be achieved due to fins and turbulators of the EG flow, but they increase the air resistance.

Below, in this section, the known technical solutions and the structural elements used in them and requirements to them are described.

3.3. ATEG quality characteristics

The integral TEG quality characteristics are

- electric power supplied by the TEM W_{TEM};
- electric power consumption W_{need} for the operation of TEG auxiliary systems;
- total electric power produced by TEG W_{teg};
- drop pressure of a hot heat exchanger Δp_{teg};
- the efficiency of TEM η_{TEM};
- the efficiency of TEG η_{teg};
- TEG weight m_{teg}.

But these parameters can only be determined for a given engine with a selected operating mode or as the function of the flow, temperature of the EG, the flow and temperature of the liquid in the cooling system and the resistance of the electrical load R_{load} applied to the TEG.

When TEG and ICE are simultaneously considered, the quality characteristics are:

- measuring the fuel consumption of the internal combustion engine while maintaining the shaft power Δq_{fuel};
- increment of the ICE shaft power ΔW_{mech} while maintaining fuel consumption q_{fuel};
- the change in the content of toxic impurities in the EG;
- the change in the level of acoustic vibrations in the EG stream.

These values must be measured for certain operating modes of the ICE. For example, the fuel consumption and emissions into the atmosphere from passenger cars are regulated by the standards: In Europe NEDC, in US EPA Federal test FTP72/75 and JC08 in Japan. Recently, the transition to the unified standard Worldwide harmonized Light vehicles Test Procedure (WLTP) is planned. These standards describe the sequence of changes in the speed of a vehicle in typical operating modes ("Urban driving Cycle", "Extra-urban driving Cycle" and "Combined"), which is installed on a test stand. Similar standards exist for other types of vehicles.

3.4. Hot heat exchanger

Much attention is paid to the design of the ATEG hot exchanger. As a rule, the resistance of convective heat transfer is the largest in the thermal circuit of ATEG or comparable to the resistance of TEM. For example, the thermal resistance of convective heat transfer was 39–76% of the total resistance in the thermal circuit of TEG, decreasing with the growth of engine rotation n_e (**Figure 2**) in the mathematical model for TEG with hexagonal heat exchanger and longitudinal finning described in [25]. The design of the TAG is similar to the one described in article [26], but the contact resistance of the joints was also taken into account which are also very significant.

To obtain acceptable contact resistance of joints, the following actions are required: increase of holding pressure on the surface area, surface treatment of heat exchanger with low roughness and shape deviations, elimination of corrosion and thick oxide films and application of high-temperature thermal grease.

The hot TEG heat exchanger should have a large area for the installation of serial flat TEMs. Constructions with 2 [27], 4 [28] and 6 [25, 26, 29, 30] external faces are known. In **Figure 3**, the elements of TEG with such constructions are marked: 1 - hot heat exchanger; 2 - TEM; 3 - cold heat exchanger; 4 and 5 - diffuser and conceiver. Diffuser and conceiver are needed for uniform heat exchange and reduction of hydraulic resistance. The displacer 6 and the heat fins 7 serve to intensify the heat exchange.

There are known TEG versions made with several modular heat exchangers of a flat [33] or cylindrical [21] shape (**Figure 4**), the number of which must be selected for different cars, based on the consumption of EG. This greatly simplifies the design of the TEG, because the heat exchange module, with the hot and cold heat exchanger, and thermoelectric elements

have been optimized in advance. The designs with flat heat exchangers involve the use of serial TEMs and can easily be adapted to other exhaust gas temperatures by changing the TEM. The design with cylindrical modules requires manufacturing special thermocouples and is more difficult to be adapted to other temperatures. Constructions with cylindrical heat exchangers (**Figure 4b**) have a larger ratio of the area of the hot heat exchanger to the area of the cold heat exchanger, but its disadvantage is reduction of pressure in a contact area, in the case if this area is heated.

To intensify convective heat transfer in a hot heat exchanger, longitudinal [25] or oblique [29] fins and a displacer [25, 29, 30] are used, although they increase the hydraulic resistance. To reduce the length of the thermal way, the fins must run perpendicular to the plane of the heat exchanger, but in terms of manufacturability, it is convenient to make the fins in the form of folded plates [34–36] (**Figure 5a**). The heat exchanger shell can be made from cast iron or by connecting steel billets. If the fins are made from individual blanks, they must be welded to reduce thermal resistances.

The EG temperature reduces as it moves inside the hot heat exchanger. If several sections of the same TEM are used in the TEG, in order to equalize their heat flux through the different sections, it is necessary to increase the heat flux for the TEM sections located closer to the outlet. To do this, increase the area and thickness of the heat fins located closer to the outlet (**Figures 3a** and **5a**) or include water cooling towards the EG flow.

Despite the fact that the models of gas heat exchangers have been thoroughly studied [37, 38], complex geometry of the structure and nonlinearity of heat transfer in turbulent motion require the optimization of the flow channel with the use of finite volume method [27, 29] for estimating the heat flow and hydraulic resistance.

The approximate values of the pressure differences for some of the considered TEG heat exchangers for passenger cars are given in **Table 1**. The length of heat exchanger L is with lengths of diffuser and conceiver. D_p is an inside diameter of the inlet branch pipe.

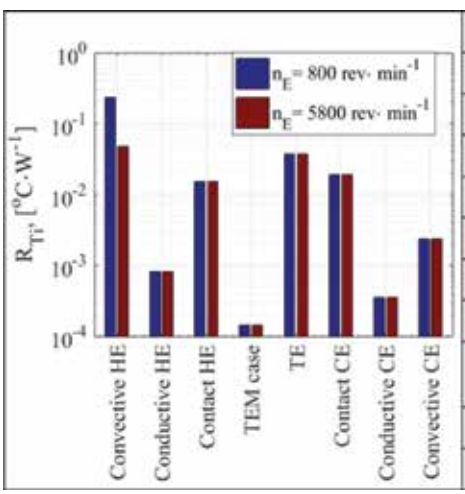

Hot exchanger (HE) - steel		
Thickness d	5	mm
Area S	0.1548	m^2
Contact resistance R_{cont}	5.67×10^{-4}	K·m^2·W^{-1}
Cold exchanger (CE) – AA6063		
Thickness d_{cold}	8	mm
Area R_{cold}	0.135	m^2
Contact resistance R_{cold}	6.37×10^{-4}	K·m^2·W^{-1}
Thermoelectric battery (TE) – PbTe, TeGa		
Thickness d_{teb}	8	mm
Area S_{teb}	0.108	m^2

Figure 2. Resistance of the components of the thermal circuit in [25], HE, hot exchanger; TE, thermoelectric element; CE, cold exchanger.

These drop pressures are quite large and can lead to a drop in the efficiency of the engine, which suggests the need for careful optimization of the flow channel taking into account its resistance to exhaust gas flow and its effect on the ICE.

According to RANS turbulent model usage [27], it is defined that the presence of numerous dimples in comparison with a flat wall allows increasing the Nusselt number Nu by 1.17–1.4 times with an increase of the Reynolds number Re from 10,000 to 25,000, but at the same time fanning friction factor f grows in 1.05–1.25 times. A single quality parameter is selected in [27] taking into account the intensification of heat exchange and the increase in friction factor:

$$P = \frac{Nu}{Nu_0}\left(\frac{f_0}{f}\right)^{1/3} \tag{1}$$

where Nu and f_0 are Nusselt number and the friction factor flow for a heat exchanger with a flat wall. According to parameter P, the heat exchanger with dimples turned out to be better than two designs with straight fins.

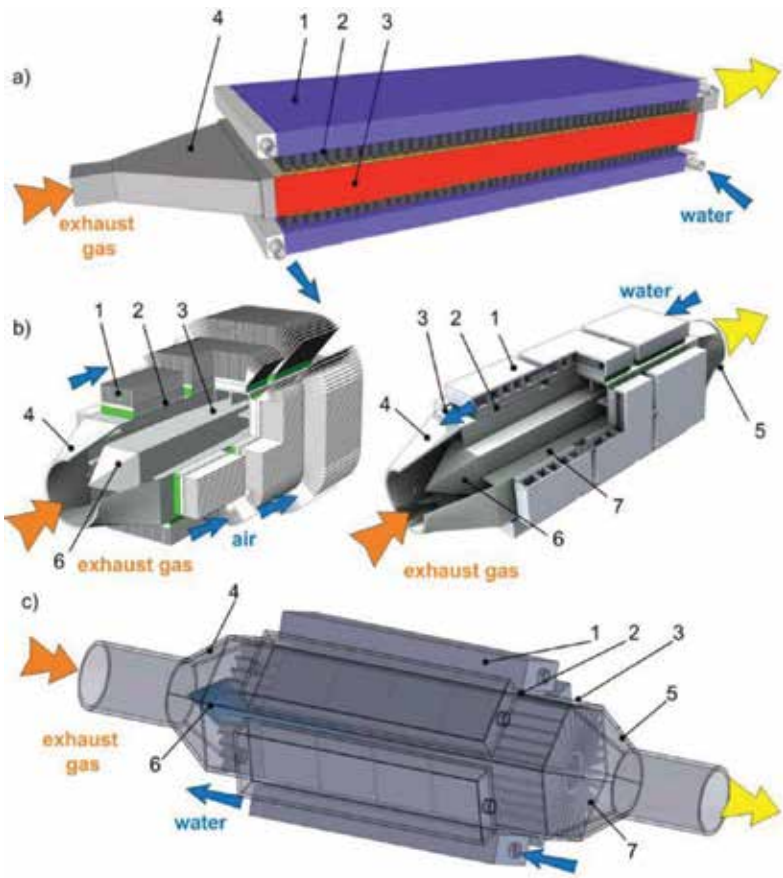

Figure 3. Constructions with flat walls of hot heat exchanger: (a) with two flat walls [31, 32]; (b) with four flat walls [28]; (c) with six walls [25, 33].

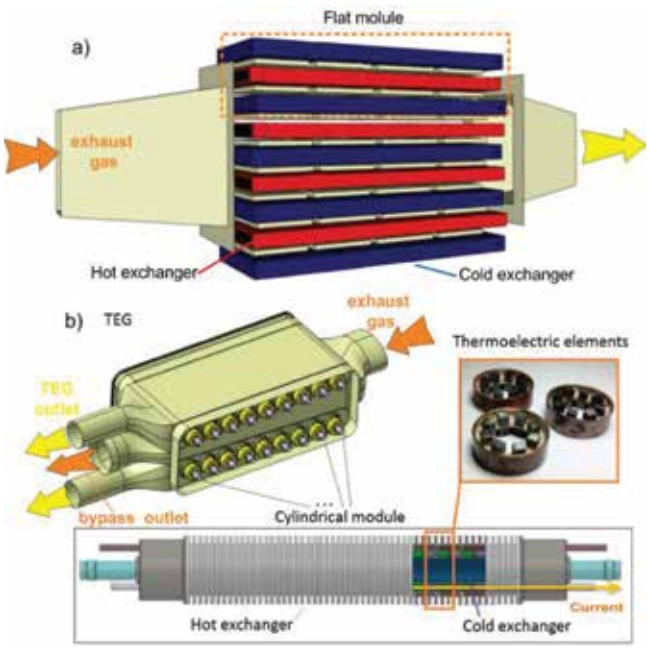

Figure 4. TEG constructions with several hot heat exchangers: (a) with flat modules [33]; (b) with cylindrical modules [21].

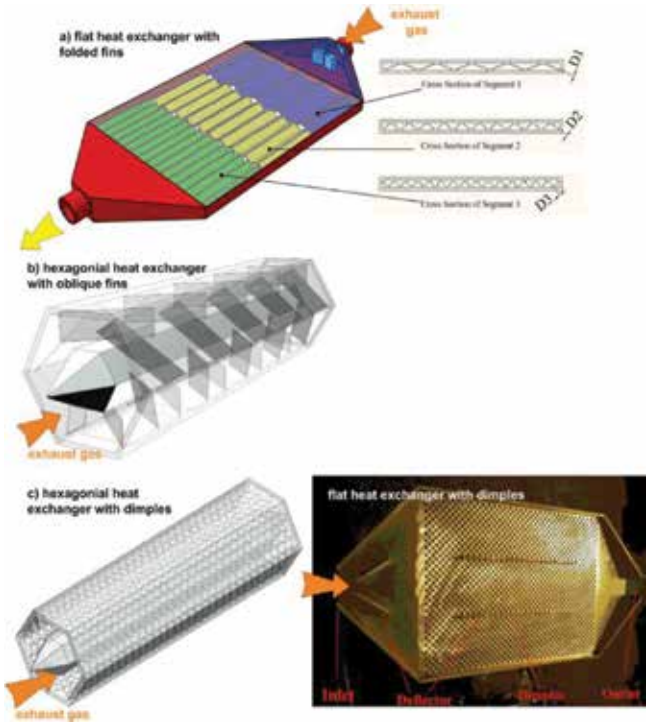

Figure 5. Thermal heat exchange intensifiers: (a) fins in the form of folded plates [35]; (b) oblique fins [29]; (c) dimpled surface [27].

Drop pressure Δp_{eg}, Pa	Flow EG Q_{eg}, L/min	Inlet EG temperature T_{EG}, K	TEM heat flow Q, W	Cross-section of heat exchanger, mm	Methods of convection intensification
100–700	1800	600	500–750	Rectangle 295 × 12 (inner sizes) L = 625, D_p=35	Flat heat exchangers with fins and dimples (**Figure 5c**) [27]
4800–5360	3920	570–870	—	Rectangle 310 × 22 (outer sizes) L = 696, D_p=50	Flat heat exchangers with folded fins (**Figure 5a**) [35]
250–450	2730	350–760	500–4200	Hexagon (side 63) L = 408, D_p = 50 inner hexahedral dispergator (side 20, length 174)	Hexagonal heat exchanger with longitudinal fins [39]
960	3650	1073	5300	Hexagon (side 62) L = 593 D_p=45 with inner hexahedral dispergator (side 29, length 513)	Hexagonal heat exchanger with flat walls [29]
1920	3650	1073	7550		Hexagonal heat exchanger with longitudinal fins [29]
2360	3650	1073	7200		Hexagonal heat exchanger with oblique fins and heat exchange intensifiers in the form of pits [29]
6420	3650	1073	8640		

Table 1. Comparison of pressure differentials in various works.

In [29], eight designs of hexagonal heat exchangers with different combinations of longitudinal, oblique fins and also with dimpless are compared based on finite volume method quantification with the use of Lam-Bremhorst $k-\varepsilon$ turbulence model. As a generalized criterion, a parameter of:

$$P = \frac{Nu}{Nu_0}\frac{\varepsilon_0}{\varepsilon} = \frac{Nu}{Nu_0}\frac{f_0}{f} \tag{2}$$

where ε is loss factor.

However, such approaches do not allow to take into account the actual drop in the engine power from the pressure drop, therefore it is necessary to introduce the ICE model and consider the mutual behavior of the internal combustion engine and ATEG, as was done in [21, 25, 30]. For this purpose, approximate dependencies of the power drop of the internal combustion engine on the volume flow EG and additional hydraulic resistance of the exhaust pipe was constructed.

Convection intensification of heat exchanger can provoke the oxidation of products due to incomplete fuel combustion (hydrocarbon and volatile organic compound), but the authors of this section are not acquainted with the quantitative studies on this issue.

Thus, the technical requirements for the hot heat exchanger are:

- low hydraulic resistance;

- ability to work at EG temperature up to 700–1000°C without corrosion and loss of load-bearing capacity;
- high efficiency of convective heat sink;
- possibility of clamping TEM with considerable efforts without heat bridges;
- it is desirable to have elastic expansion bends for temperature deformations in the heat exchanger itself and (or) in the TEM system clamping.

3.5. Thermoelectric materials and modules

The TEM is a key element of ATEG, in which, through the Seebeck effect, there is a direct conversion of the heat into electricity. The output electric power of the TEM depends on the heat flux, the temperature difference of its thermocouples, the thermal and electrical resistances in its construction, the geometry of the thermoelements which must be optimized for the given temperature conditions, the consistency of the internal resistance with the load resistance and the ZT-factor of used semiconductor materials. Moreover, ZT under optimal design is a key parameter of TEM efficiency.

Figure 6 shows the required (green line) and achievable electrical power of ATEG when it is installed in different parts of the exhaust system (close-coupled position or away from the engine). The data are given for different materials/modules for different types of cars with efficiency of the hot heat exchanger η_t of 50, 66 and 75% (C/D - mid-range class, E/F - upper/luxury class and M/J - multi-van, SUV, utilities). **Table 2** shows the efficiency of the most promising materials for use in ATEG.

The analysis of **Figure 6** shows that for achieving the required electrical power, the efficiency of the thermoelectric module, using a heat exchanger of 50%η_t, should be at least 8.2%. Increasing the

	Bi-Te(p)			Pb-Te(p)			Skutterudite(p)			HalbHeusler(p)			Na-Ca-Co-O(p)		
T_{cold} / T_{hot}	ZTavg	ZTpeak	η	ZTavg	ZTpeak	η	ZTavg	ZTpeak	η	ZTavg	ZTpeak	η	ZTavg	ZTpeak	η
[°C] / [°C]	[-]	[-]	[%]	[-]	[-]	[%]	[-]	[-]	[%]	[-]	[-]	[%]	[-]	[-]	[%]
25 / 250	1,23	1,46	10,3%	0,09	1,65	1,2%	0,44	1,06	4,9%	0,29	0,86	3,4%	0,16	0,71	2,0%
50 / 250	1,21	1,46	6,9%	0,10	1,65	1,1%	0,47	1,06	4,4%	0,30	0,86	3,1%	0,17	0,71	1,8%
50 / 500				0,41	1,65	6,8%	0,72	1,06	10,5%	0,45	0,86	7,3%	0,31	0,71	5,4%
100 / 500				0,45	1,65	6,3%	0,77	1,06	9,4%	0,48	0,86	6,6%	0,33	0,71	4,9%
100 / 600				0,65	1,65	9,5%	0,82	1,06	11,2%	0,54	0,86	8,3%	0,40	0,71	6,5%
150 / 600				0,71	1,65	8,9%	0,86	1,06	10,2%	0,57	0,86	7,5%	0,43	0,71	6,0%
	Bi-Te(p)			Pb-Te(n)			Skutterudite(n)			HalbHeusler(n)			Mg2(Sn,Si)(n)		
25 / 250	1,01	1,09	9,1%	0,51	1,41	5,5%	0,64	1,67	6,5%	0,34	0,98	3,9%	0,53	1,31	5,7%
50 / 250	1,00	1,09	7,8%	0,54	1,41	5,0%	0,67	1,67	5,8%	0,35	0,98	3,5%	0,56	1,31	5,1%
50 / 500				0,92	1,41	12,4%	0,96	1,67	12,8%	0,56	0,98	8,7%	0,84	1,31	11,6%
100 / 500				0,99	1,41	11,2%	1,01	1,67	11,4%	0,60	0,98	7,9%	0,89	1,31	10,4%
100 / 600				1,00	1,41	12,9%	1,12	1,67	13,9%	0,67	0,98	9,7%	0,97	1,31	12,6%
150 / 600				1,06	1,41	11,7%	1,18	1,67	12,5%	0,71	0,98	8,9%	1,02	1,31	11,4%
	Bi-Te(p)			Pb-Te(p)(n)			Skutterudite(p)(n)			HalbHeusler(p)(n)			Na-Ca-Co-O /Mg2(Sn,Si) (p)(n)		
25 / 250	1,12	1,27	9,7%	0,30	1,29	3,6%	0,54	1,31	5,7%	0,31	0,92	3,7%	0,35	1,01	4,0%
50 / 250	1,11	1,27	8,4%	0,32	1,29	3,2%	0,57	1,31	5,1%	0,33	0,92	3,3%	0,36	1,01	3,6%
50 / 500				0,66	1,29	9,9%	0,84	1,31	11,7%	0,51	0,92	8,0%	0,57	1,01	8,8%
100 / 500				0,72	1,29	9,0%	0,89	1,31	10,4%	0,54	0,92	7,2%	0,61	1,01	8,0%
100 / 600				0,83	1,29	11,3%	0,97	1,31	12,6%	0,61	0,92	9,0%	0,69	1,01	9,9%
150 / 600				0,89	1,29	10,4%	1,02	1,31	11,4%	0,64	0,92	8,2%	0,73	1,01	9,0%

Table 2. Efficiency of thermoelectric materials and modules on their basis [40].

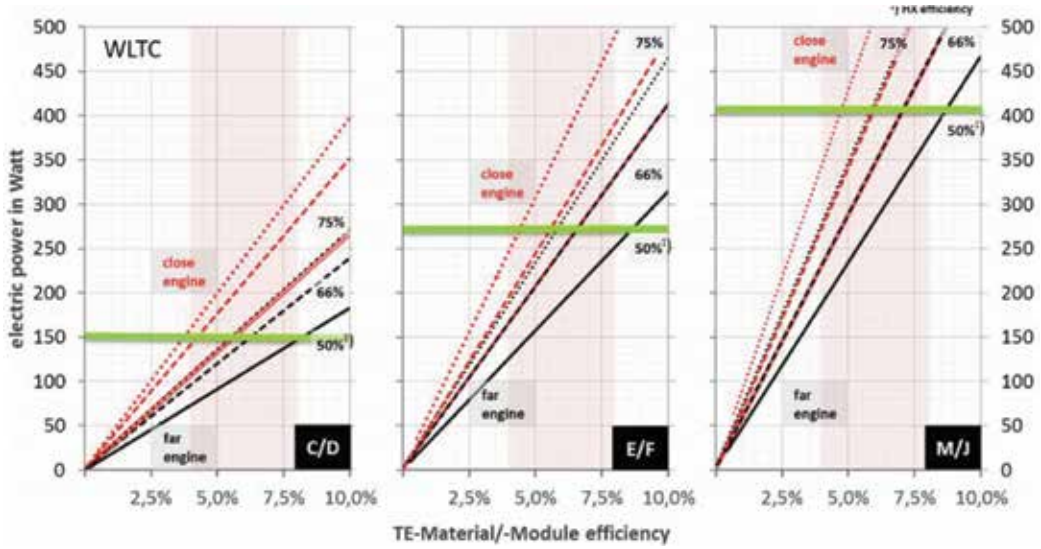

Figure 6. Necessary material/module efficiency [41].

efficiency of the heat exchanger and installing ATEG closer to the output manifold can reduce this requirement up to 5% or less. At the same time, on the basis of classical materials for which large-scale serial production is currently established (Bi_2Te_3, *PbTe*, *SiGe*), it is quite capable to satisfy these requirements. In addition, the large-scale serial production also imposes on us the friendly environmental production, non-toxic, reliability and low cost of ($/W energy) which unfortunately does not fully match with the materials above. The latter requirement is paramount. If the estimated the cost of current TEMs is 5 $/W, then economically it is necessary for ATEG, to increase the prospect of its commercialization, achieve 1 $/W [40].

Among the most promising materials—which are being actively developed and persistently being used in ATEG are the silicide, skutterudite or half-Heusler materials [40].

General technical requirements for TEMs used in ATEG can be presented:

- compactness;
- efficiency (TEM should convert as much heat as possible);
- mechanical strength in conditions of cyclic operation (heating/cooling, not less than 10,000 cycles);
- chemical stability under given temperature variables;
- shock and vibration durability in the range of 15–200 Hz;
- manufacturability and low production costs for serial production.

Existing developed ATEG mock-ups (prototypes) basically use TEMS with flat structure which thermoelectric elements are connected in series by conductor tabs commutation and clamped between two insulating ceramic or polymer plates (**Figure 7a**). Those plates are

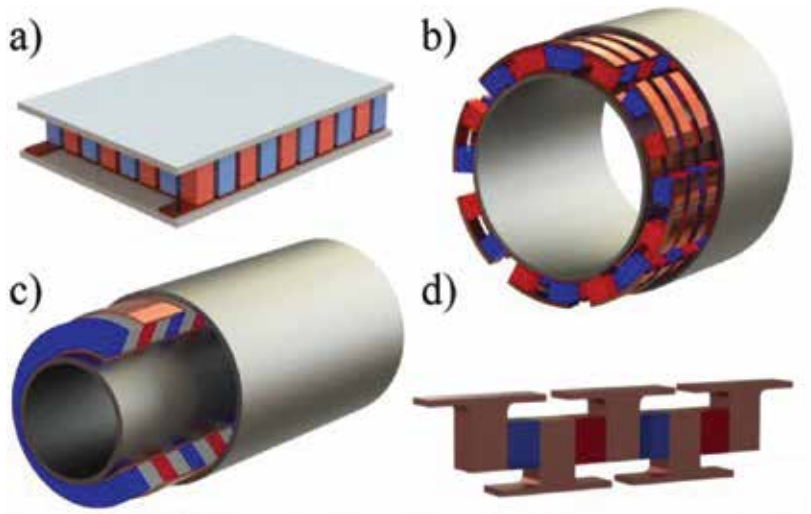

Figure 7. TEM designs: (a) with flat legs; (b) with cylindrical shape; (c) with disc shape; (d) with T-shaped conductive layers.

(cold and hot heat sides) perpendicular to heat flow. To protect from the sublimation process at high temperatures, the module can be placed in a sealed shell or coated with heat-resistant protective enamels. The use of such TEMs in ATEG presupposes the presence of flat surfaces on heat exchangers, and also requires careful study of the clamping design in order to ensure a constant and uniform effort throughout. The inability to provide such a clamp and, as a consequence, large thermal resistances forced the development of ATEG in the framework of the DOE No. DE-FC26-04NT42279 to move from a flat construction to a cylindrical one on its 4th stage [20].

The cylindrical design of ATEG with radial heat flow requires the use of tubular TEMs, in which the thermoelements can be utilized in the cylindrical (**Figure 7b**) or disc (**Figure 7c**) shapes [41]. Analogues of flat TEM with a cylindrical surface as heat exchangers can also be made. It should be noted that such TEMs will be considerably less technologically advanced than flat modules.

In view of the fact that ZTs of individual thermoelectric materials are significantly dependent on the temperature, there is a practice to use segmented thermoelements in TEMs for improving their efficiency [42, 43]. At the same time, the use of different materials with different physic-mechanical properties in the design of a thermoelement results in the need to harmonize, for example, the cross-sectional area for different materials and their thermal linear expansion coefficient (TLEC). The latter is especially important for ATEG operating under conditions of constantly changing heat flow, and also relates to the coordination of the TLEC of the p- and n-type elements and the conductive tabs for multi-segment TEMs.

An interesting design of the TEM, partially solving the problem of coordinating the material properties, was proposed in D.T. Crane et al. [44, 45]. This design with T-shaped conductive layers (**Figure 7d**), also playing the role of heat conductors, makes it possible to apply different thicknesses of elements and their different geometries, and to vary the thickness of individual segments, providing an optimal thermal operating mode for each material, therefore maximum efficiency. At the same time, attention is drawn to the stress state of the contact

between thermoelement and conductive tab, due to the fact that during compression of such thermoelement between hot and cold heat exchangers minimum thermal resistances should be ensured.

3.6. Cooling system

ATEG for heat removal must be connected to the cooling system of the car or use its own cooling system.

In the first case, the load on the regular car cooling system is increasing. In most cars, the air intake area cannot be increased without significant design changes. This circumstance limits the thermal power passing through the TEG and the electric power it generates. This obstacle can be overcome for new models of cars that would be developed taking into account the possibility of installing TEG.

In the second case, the autonomic TEG cooling system can be designed in different ways.

An independent liquid cooling system with forced circulation is relatively complex and increases mass and dimensions. The air cooling of the ribbed cold heat exchanger with an oncoming airflow can be comparable to forced liquid cooling. So in the article [28] when considering TEG models for motorcycles and snowmobiles with Yamaha WR450F motorcycle engine (a volume 0.449 mL), the values of the generated electric power of 80–105 W have been obtained at speeds of more than 40 km/h. But the protruding air radiators will inevitably degrade the aerodynamic characteristics of the vehicle.

Thermoelectric generators for internal combustion engines on water transport or snowmobiles can be installed without large and protruding cold heat exchangers due to the high efficiency of cooling by water and snow.

It should be noted that the use of an independent forced liquid cooling system requires additional energy costs for pumps, fans and valves operations. In the case of the ATEG integration into the car cooling system there is a need in the additional power for increasing cooling system productivity. In this way, the electricity generated by ATEG partly expend on the operation of the ATEG itself.

The paper [21] presents the results of the evaluation of the ATEG various components and parameters influence on CO_2 emissions for two generators installed on BMW X3 and Ford F350 cars. The energy consumption of the ATEG cooling system on the BMW X3 (**Figure 8**) averages 5.7 W in the cycle US06 (0.2 g CO_2/ mil emission increase) with an average generator power of 19.8 W. The cooling system of FORD F350 requires 25 W (0.5 g CO_2/mil emission increase) with an average generator power of 470 W under the same conditions.

In the same article [21], 23 concepts of ATEG integrating into the car cooling system are developed according to the following criteria:

- influence on engine warm-up;
- influence on engine cooling;
- influence on transmission warm-up;

- influence on transmission cooling;
- influence on TEG cooling;
- influence on warm-up of cabin heating;
- electric power consumption;
- weight and
- expected costs.

As a result, the authors choose the most optimal solution (**Figure 9**), the main idea of which is that the designer should use the extracted exhaust heat for accelerate engine warm-up, without influencing the original warm-up strategy of the cooling system.

When using forced liquid cooling (general or independent), it is necessary to provide for the regulation of the flow rate of the liquid in order to reduce the energy loss when pumping the liquid in the conditions of low thermal power passing through the TEG (for example, idling).

3.7. Cold heat exchanger

A cold heat exchanger must remove heat from the TEG into the water cooling system or directly into the external environment. The second option can be very simple and effective when cooling with snow (for snowmobiles) or with water (for hydrocycles) when the heat transfer coefficient $a_{cold} > 1000$ W/(m^2 K). Cooling by external ambient air requires the installation of numerous ribs, since in this case $a_{cold} = 20–100$ W/(m^2 K), and this strongly depends on the speed of the ambient air [28]. Installing an external ribbed air heat exchanger can increase the aerodynamic resistance of the vehicle. Even if it is a small increase in resistance—this phenomenon can offset the reduction in fuel consumption from electricity generation.

The geometry of the water heat exchanger is paid much less attention, since due to the high heat transfer coefficient there is very favorable heat removal conditions (**Figure 2**).

As an example, there are the results of ATEG calculations with air and forced water cooling, considered in the article [28] (**Figure 10a**, **b**) for Yamaha WR450F IC engine (volume 0.449 L, 9000 revmin^{-1}). **Figure 10** shows: 1 – hot heat exchanger; 2 - TEM with the height b_{te} of the thermoelement; 3 – cold heat exchanger. The air heat exchangers are considered in a motorcycle operating conditions (air flow temperature T_{air} = +20°C and speed V_{air}) and snowmachine mode (T_{air} = − 20°C and speed V_{air}).

The gas heat transfer calculations are performed with free air flow around ATEG without taking into account the geometry of the vehicle.

The different heights of thermoelements calculations allows choosing the optimal value b_{te} = 17 mm for the developed ATEG (**Figure 10d**). The generated ATEG power W_{TEG} greatly decreases with air speed V_{air} decreasing and air temperature T_{air} increasing.

At T_{air} = − 20°C and V_{air} = 100 km h^{-1} ATEG with air cooling has comparable power W_{TEG} with water cooled ATEG (**Figure 10d**). In this case, averaged in time electric power which supplies cooling systems $W_{need} = W_{TEM} - W_{TEG}$ is about 10 W or about 10% of the power produced by the optimal design.

http://dx.doi.org/10.5772/intechopen.76971

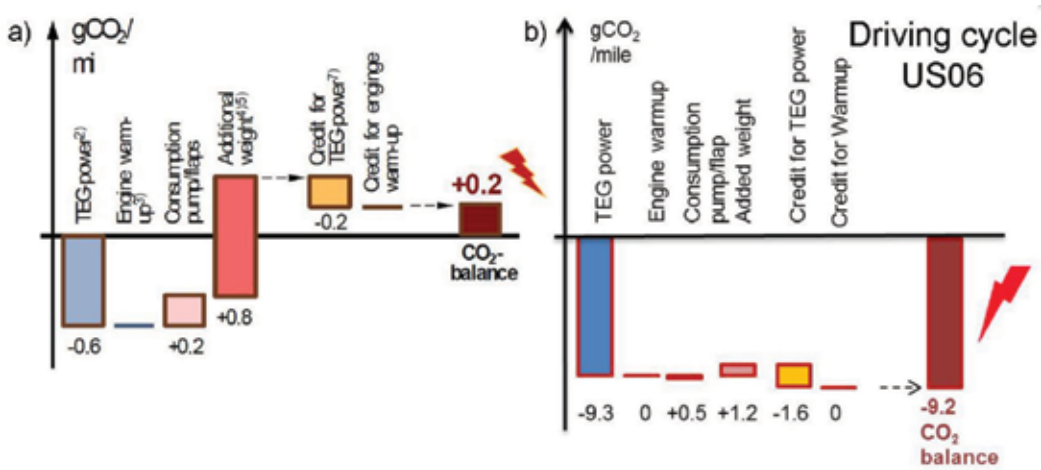

Figure 8. The results of the evaluation of the ATEG various components and parameters influence on CO_2 emissions for BMW X3 (a) and Ford F350 (b) ATEGs [21].

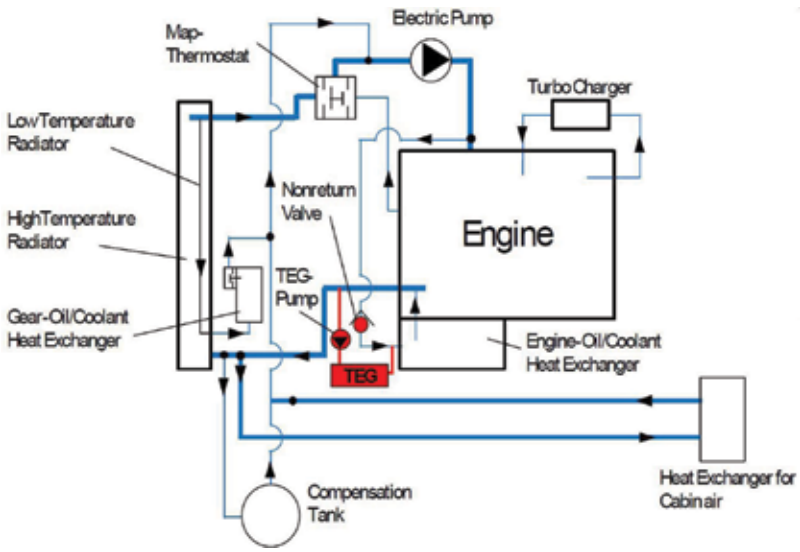

Figure 9. Coolant system of X3 xDrive28i with automatic transmission and selected concept for coolant integration [21].

Technical requirements for the cold heat exchanger:

- insignificant contact thermal resistance;
- lightweight construction;
- amount of water should be precisely defined for required cooling;
- corrosion resistance and
- when using a heat transfer fluid, the possibility of boiling, leaks, and condensation on cold parts should be avoided.

3.8. Choice of heat exchanger material

Physical requirements for the material of heat exchangers:

- high corrosion resistance;
- high thermal conductivity of the material;
- good machinability of obtaining thermal surfaces with small roughness and deviations of a shape;
- low density and/or high durability for decreasing the weight.
- for hot heat exchangers, a melting point substantially higher than the temperature of EG (700–1000°C) is needed.

Table 3 compares the properties of the materials used with pure copper, which has the greatest thermal conductivity among structural materials. Adding impurities to copper or aluminum greatly reduces thermal conductivity, but increases strength and often corrosion resistance. The density of the material ρ affects the weight and cost. The coefficient of thermal expansion α is important in calculating thermal deformations and stresses.

The thickness of metallic heat exchangers walls is usually a few millimeters and their thermal resistance is negligible. But the finned gas heat exchangers are characterized by a long thermal path, therefore a high thermal conductivity is desirable for them λ.

Copper cannot be used in a hot heat exchanger because of its low corrosive resistance in the air against CO_2 vapors and water, without protective coatings (for example, nickel). Its application could be justified for external heat exchangers, but the issue is not enough density and high cost.

Aluminum can be applicable only for cold heat exchanger due to its low melting temperature characteristic. Also aluminum is cheap and has excellent corrosion resistance. Thermal conductivity of pure technical Aluminum is very high, but even insignificant amount of impurities can reduce conductivity by 1.5–2 times. So it is necessary to carefully select the fins size for finned aluminum air cold heat exchangers.

Steel has a high melting point and density. Low-carbon steels are prone to corrosion, and stainless steels have very low thermal conductivity, limited weldability and high cost. It is possible to use special stainless steels, for example, AICI 304, used for the manufacture of mufflers and hot air ducts. But the low thermal conductivity of this steel requires the production of hot heat exchangers with short and thick fins.

Cast iron makes it possible to create complex parts with good corrosion resistance. For example, cast radiators for heating systems were widely used before. The thermal conductivity of cast iron is strongly dependent on the shape and orientation of graphite inclusions having a thermal conductivity comparable to copper. The thermal conductivity of cast iron decreases with decreasing carbon content and increasing alloying additives, especially those that reduce graphitization (Mn,Cr). Grinding the size of graphite additives increases the strength, but reduces the thermal conductivity. For the manufacture of heat exchangers by casting, EN-JL1050 and the like grades can be used. However, it is desirable to avoid overheating of parts of cast iron heat exchangers in order to avoid ferritic-austenitic transformations (723°C).

http://dx.doi.org/10.5772/intechopen.76971

Recommendations:

- cold water and air heat exchangers can be made from most of aluminum alloys.
- the finned hot heat exchangers are preferably made of low-carbon steel (possibly with anti-corrosion coatings) or cast iron (for example, Cast EN-JL1050).
- hot heat exchangers without fins or with short fins can be made by casting from cast iron or by welding from stainless steels, for example AICI 304.

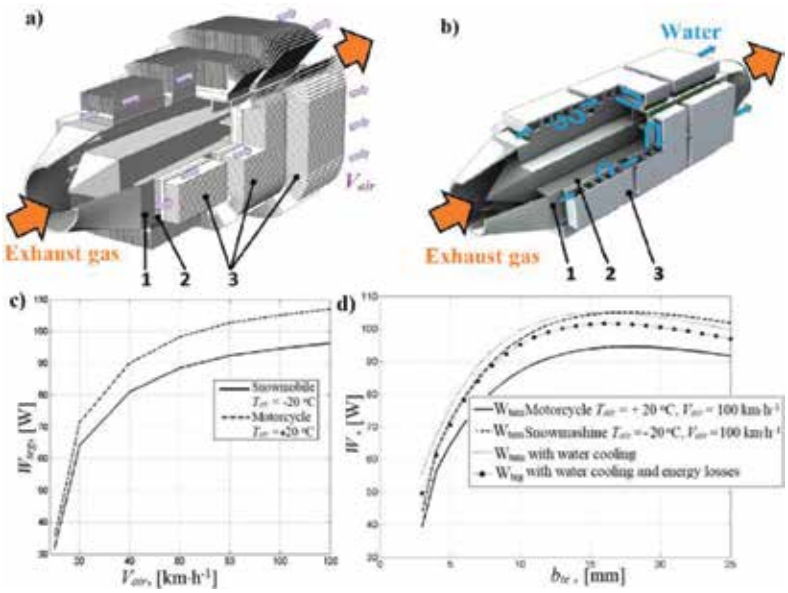

Figure 10. Comparison of TEG power with air cooling (a) and water cooling (b); temperature influence *T air* and air speed *V air* on power *W TEG* generated by ATEG (c); the influence of the thermoelement height *b te* on TEM generated power *W TEM*(d).

	Density ρ, kg·m-3	**Thermal conductivity λ,W/(m·K)**	**Thermal expansion α ·106, 1/K**	**Melt point (soludus forallow) T, K**
Pure copper	8933	400	17	1358
Pure aluminum	2702	240	24	933
Aluminum alloys	2600…2850	110–190	21–24	775–993
Low-carbon steel	7850	40–60	11–13	1425–1540
Stainless steel AICI 304	8000	17	17–18	1400
Cast EN-JL 1050	7250	42–44	13	1426

Table 3. Characteristics of materials for heat exchangers at T range 573–873 K.

3.9. Troubleshooting

This section provides general recommendations for troubleshooting issues that may occur when operating the ATEG.

Electrochemical corrosion is excluded by the selection of contacting materials with equal electrochemical potentials, qualitative isolation of electrical systems, using protective, electrically insulating or corrosion-resistant coatings and observing the pH of the coolant.

Excessive thermal deformations can lead to plastic deformation of parts and loss of flatness of contacts. It is possible to reduce the pressure force with the help of selecting the suitable materials as per their thermal expansion coefficients and using the elastic compensators for thermal deformations.

Fretting-wear occurs under the action of periodic tangential shifts on contacts. This process has not been fully studied. It can be eliminated by reducing the contact pressure (see paragraph above), using hardening or antifriction coatings or thermal grease.

The thermal contact resistance can increase due to several factors which are: oxidation, degradation of the thermal grease or reduction of the pressure during heating or cooling. Using of resistant materials, protective coatings and adjusting loads pressure can eliminate it.

Cleaning and monitoring of the pH of the coolant, selection of corrosion-resistant materials or coatings prevent heat exchangers pollution from corrosion, water deposits and soot.

4. Math modeling

It is necessary to conduct a number of tests to optimize the design of ATEG in order to increase the electric power it generates and its efficiency. Building a reliable mathematical model of the automotive thermoelectric system is the most rational solution to this problem. Detailed modeling can help to find the optimal combination of ATEG parameters. In addition, the estimation of various system parameters for existing driving cycles allows predicting the appropriateness of using a generator in a specific car model.

4.1. Structure of the mathematical model

In general, the mathematical model of ATEG should describe the behavior of a system consisting of the following components: car engine, hot heat exchanger, TEM unit, cold heat exchanger, cooling system, power control system (PCU) and consumption load. Block diagram showing the interaction of these subsystems is presented in **Figure 11**.

When simulating these subsystems, input, output impacts and parameters are set for describing the ongoing processes. The parameters include the data containing physical properties of the materials used and the geometry of system components.

As inputs to the ATEG: the temperature (T_{ex}^{in}) and mass flow (m_{ex}) of the exhaust gas emitted by the engine, the temperature (T_{cl}^{in}) and the mass flow of the cold-producing (m_{cl}).

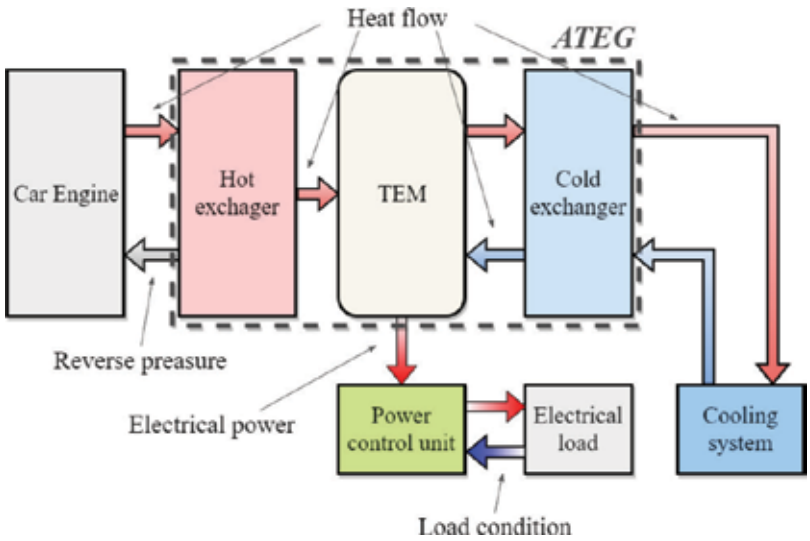

Figure 11. Structural scheme of mathematical model.

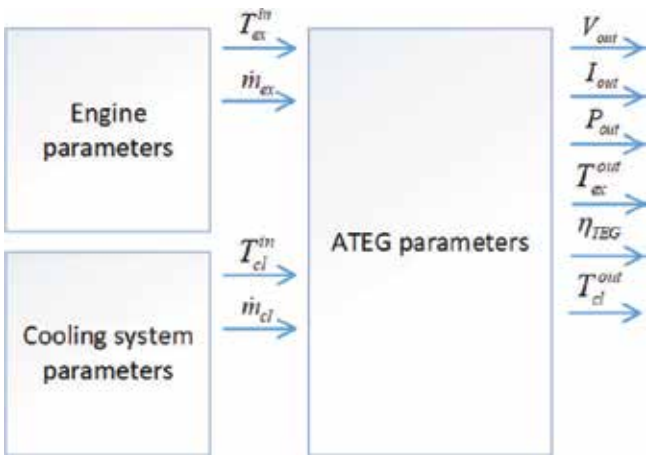

Figure 12. Input and output effects on ATEG.

The output ATEG model impacts, which can be calculated are: generated voltage, current and electrical power output, the temperature of exhaust gas at the exit of ATEG and efficiency (**Figure 12**).

4.2. Physical model ATEG

In general, ATEG consists of several sections through which a flow of hot gas and cold coolant flows. The physical model of the ATEG section contains the following basic elements (**Figure 13**): 1 and 4 - hot and cold heat exchangers; 2 - thermal contact resistances; 3 - thermocouples, 5 - TEM container.

The solution of operation modeling issue for the described system consists of thermal and electric circuits calculations taking into account thermoelectric processes.

The heat problem is solved by finding the distribution of thermal fluxes and temperatures over the entire cross-section of the ATEG section. For this purpose, the heat balance equations are used [46]. The electric current, voltage and power generated by the TEM can be calculated as a function of the electrical load using the Kirchhoff rules in accordance with the proposed electrical connection circuit for the thermoelements [47]. The amount of generated electricity is calculated using classical methods for determining the efficiency of thermoelectric conversion [48]. All characteristic values, such as the Seebeck coefficient, heat and conductivity coefficients, are taken into account.

Since the relationship between vehicle operation modes, the generated heat by exhaust gases and the generated electricity by ATEG are nonlinear, it is necessary to dynamically model these processes. To simulate the operation of ATEG under non-stationary operating conditions, the heat balance equations must be described in a differential form [45].

4.3. Tests of models, city cycles

The ATEG model allows estimating transient processes which makes it possible to use it The New European Driving Cycle (NEDC) is most often used to test the new work models ATEG. There are numerous scientific publications presenting measurements and calculations of thermoelectric generators used in cars on the basis of the NEDC [49]. It is extremely important to consider the dynamic behavior of the thermoelectric system in order to make realistic predictions of the performance of ATEG in the vehicle.

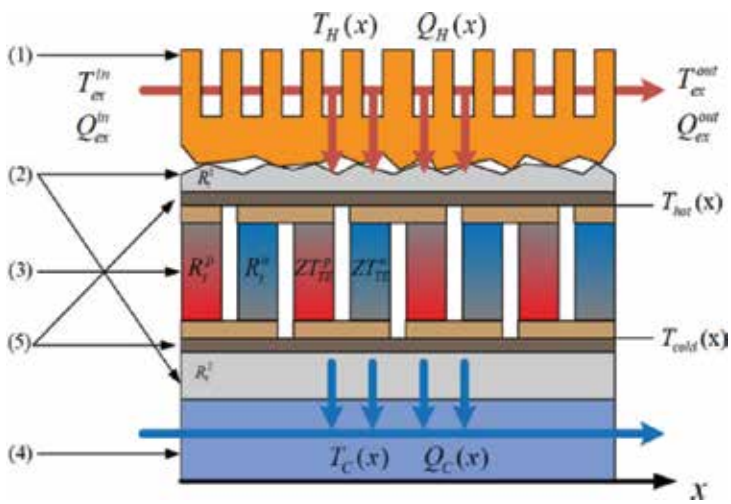

Figure 13. Functional diagram of ATEG section.

5. The ways of ATEG efficiency increasing

5.1. Adapting the design to variable operating modes

ATEG operation is accompanied by frequent volume flow differences and EG temperature changes, and vehicle electrical load is not constant. At the same time, it is necessary to ensure the optimum flow of EG through ATEG, when, on the one hand, there is sufficient intensive heat exchange in the ATEG, and on the other hand, the pressure drop EG is not too great.

Therefore, it is practical to use bypass for removing excessive EG through ATEG or a hot heat exchanger with variable hydraulic resistance of the flowing channel. For example, the patent [50] describes the construction of a heat exchanger using rotatable fins that allows intensifying heat transfer at low shaft speeds and reducing hydraulic resistance at high speeds. In **Figures 14**, 1- turning fins, 2- displacer, 3- TEM, 4- cold heat exchanger, 5- rotational blade-intensifier, 6 - control rod.

5.2. Application of heat pipes

One of the methods to increase the efficiency of ATEG can be the use of heat pipes in its structure [51, 52]. The reduction of the thermal resistance between exhaust gases and hot junctions allows increasing the hot junction temperature and also reduces the counter-pressure in the exhaust system in some cases. In addition, the heat pipes give the possibility of a more flexible approach towards the design of ATEG and there is no need to be limited to only the surface area of the hot heat exchanger. They also help to regulate the temperature of the hot junction by varying their length or by using variable conductance of heat pipes.

5.3. About materials with a phase transition

There is a need to select the operating point in the ATEG design. This fact connected with: variable heat flux through TEM under different operating conditions of the internal combustion engine, the dependence of the TEM semiconductor materials ZT on the junctions' temperature and the limitations on the peak temperature of the hot junction. Optimizing ATEG for obtaining maximum power at the extreme operating conditions of the internal combustion engine leads to low efficiency at low and medium rotational rates with low engine load. In the reverse situation, there is a need to use bypass for not overheating the TEM and not creating a counter-pressure in the exhaust pipe at high engine speeds. The solution to the problem of combining these two extreme situations and, consequently, increasing the efficiency of ATEG under different operating conditions of the ICE can be the use of materials with a phase transition that store heat at high loads on the ICE and give it to ATEG with a heat flux decrease in the exhaust line [53].

5.4. Temperature rise of EG

It is advisable to use EG at high temperatures for efficient ATEG operating which can be achieved through two technical solutions.

Firstly, installing the ATEG on ICE, which has the insulating combustion chamber with protective coatings. Such ICEs are increasingly being used in recent decades and are characterized as a high temperature of EG, low CO and residual hydrocarbons emissions, and fewer loads on the cooling system. Inside the ICE cylinders the operating gas reaches on its highest temperature which is about 2500°C. Mechanical work and temporary averaging of peak values reduce the temperature of the EG at the combustion engine output to 950–1000°C for gasoline internal combustion engines and 800–850°C for diesel engines.

Secondly, a precise thermal insulation of the collector and the exhaust pipe near the TEG location. For example, the authors of this chapter conducted experiments on ATEG which was connected to collector of 0.7 m long with a VAZ 21126 gasoline engine on a test stand. Its power was 72 kW and a volume of 1.6. The EG temperature measurements were made by using Kistler 4049B05DS1–2.0 sensor—installed at the entrance of the ATEG diffuser. It was noted that the insulation coating of the collector with basalt cloth increased the temperature of EG T_{eg} by more than 300°C (**Figure 15**).

Thirdly, to obtain the maximum temperature of EG, it is desirable to install ATEG directly after the internal combustion engine, in front of the catalyst, turbocharger and silencer.

5.5. Reduction of thermal resistance

The thermal resistance of the heat exchanger contacts can greatly reduce heat flow through ATEG [25, 54]. It is shown in [25] that neglect of contact thermal resistances during calculation leads to an overestimation of the generated TEM power by 25–30%. To reduce contact resistance, all possible methods should be taken, including:

- elimination of possible corrosion of contact joints.
- machining with minimal roughness and deviations from flatness.
- the use of graphite grease or high-temperature thermal grease for hot heat exchangers and conventional thermal grease for cold ones.
- installation of elastic expansion joints for temperature deformation to ensure a constant clamping force [54].

When operating ATEG on diesel engine, power may be reduced due to the deposition of soot in the hot heat exchanger. For example, Kajikawa describes an ATEG installed with a diesel engine [55]. During the first 100 h of operation, the heat flow through ATEG fell by 30%, reaching saturation levels due to soot formation, and further, remained almost unchanged for another 100 h. For gasoline engines, soot formation is much less critical.

5.6. Features of electrical load supply

The task of ensuring efficient transmission of TEG power to electrical consumers is significant. Usually, TEG consists of separate TEMs, which can be considered as conventional direct current (DC) sources. As all DC sources, each type of TEM has its own maximum power transfer condition. This condition can be simply described using the equivalent circuit (**Figure 16**).

http://dx.doi.org/10.5772/intechopen.76971

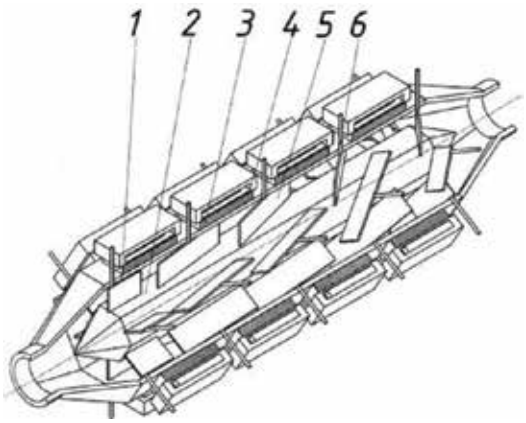

Figure 14. Constructions of hot hexagonal ATEG with variable angle of inclination of heat exchange intensifiers [51].

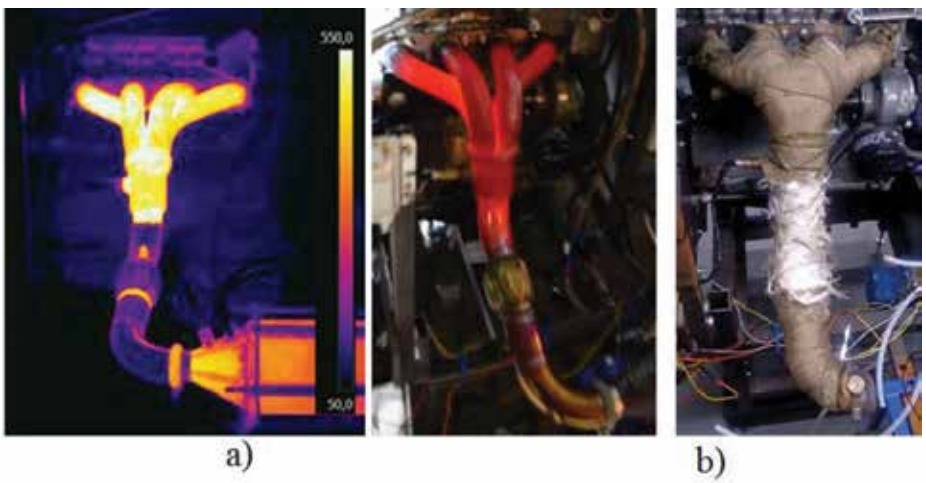

Figure 15. Manifold of the engine influence: (a) thermography and photo without insolation; (b) manifold with basalt fabric.

It is possible to represent the TEM as a power source (V_s) with an internal resistance (R_s). By Ohm's law maximum amount of power dissipates on load resistance (R_L) (Eq. (3)), when the value of the load resistance is exactly equal to the resistance of the power source (**Figure 17**).

$$P = I^2 \cdot R_L = \left(\frac{V_s}{R_S + R_L}\right)^2 \cdot R_L \tag{3}$$

Obtaining required output characteristics from TEMs array is ensuring by connecting TEMs in series or in parallel. The serial connection type is used in the case of increasing the output voltage. The parallel connection allows increasing total current. However, for each ATEG system the choice of connection type should be done attentively, according to modules electrical and temperature consistency.

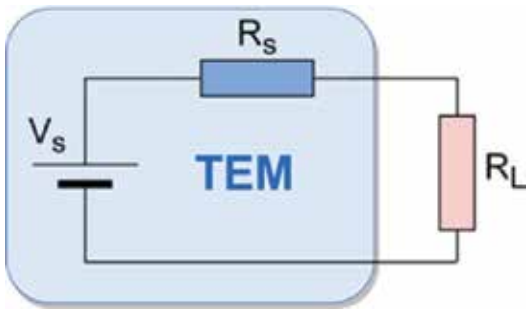

Figure 16. Equivalent circuit schema.

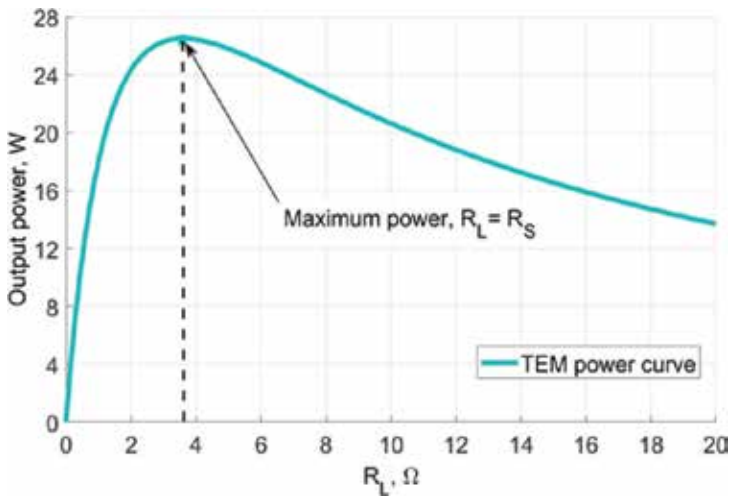

Figure 17. TEM power curve.

Also, heat flux distribution of the ATEG is often not the same all over its surface. Consequently, temperature states of various TEMs may differ. Thereby, it is correct to combine TEMs with equal temperature differences in one electrical circuit.

In the case of steady-state operating conditions, it is natural to connect TEG modules directly to the electrical load. The main parameter, which should be taken into account, is a match between summary electrical resistance of TEMs and a resistance of the electrical load. It allows harvesting maximum output power from TEG, as explained previously.

However, ATEG presents a transient system due to varying engine load conditions. Inconsistency in driving style, speed and torque can lead to changes in TEM temperature difference (**Figure 18**), which affects TEM internal resistance [56]. Consequently, a converter is required to continuously track ATEG power when the engine operates under various working conditions. The solution of this issue is connecting ATEG modules to the vehicle batteries and electrical loads through a DC/DC converter with maximum power point tracking (MPPT) algorithms.

MPPT method is mainly used in photovoltaic applications [57–60]. As solar panels, an operating point of TEM is rarely at peak power, as shown in **Figure 4**. MPPT technique executes continuous

http://dx.doi.org/10.5772/intechopen.76971

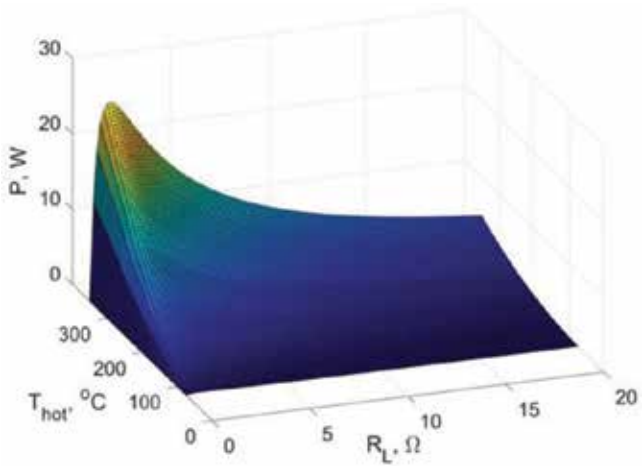

Figure 18. TEM power *P* versus hot-side temperature *T hot* and load resistance *R load* at cold side temperature *T cold* = 50°C.

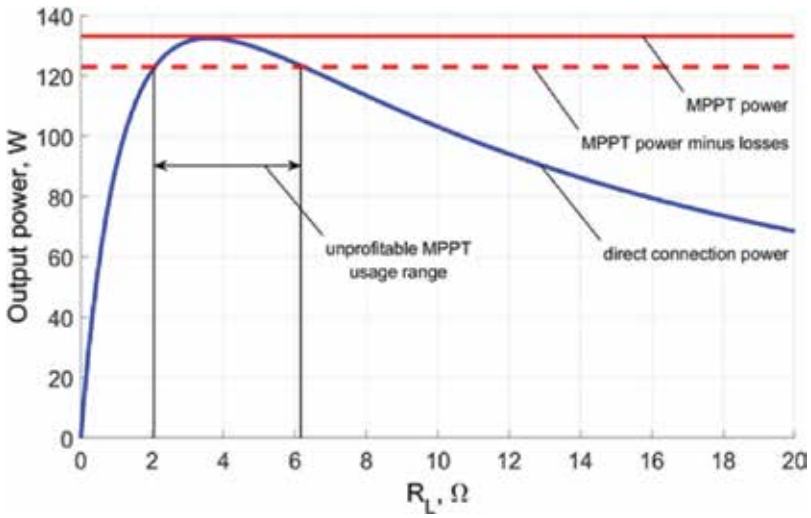

Figure 19. Conversion losses influence.

adjustment of the electrical system resistance to keep it operating at the peak power point under varying conditions. There are many different methods for tracking power point of TEG system: the constant voltage method [61], the perturbation and observation (P&O) method [62], the incremental conductance method [63], the ripple correlation control method [64], the dichotomy method [65] and the gradient method [66]. There are also combinations of several methods, for example, the aggregated dichotomy and gradient (ADG) method [67]. Intelligent methods, such as fuzzy logic [68] and neural network algorithms [69] are also developed for performance enhancement. The appearance and modifying of MPPT algorithms aim to obtain more rapid and accurate tracking of the power point. Some methods are more effective than others; some are easier to implement, but their main goal remains same. In this way, the usage of the DC/DC converter with MPPT function is necessary for such systems as ATEG.

However, ATEG electrical network has conversion losses, which decrease the total efficiency of the system. This fact should be considered while designing DC/DC converter. The function of switching on/off from general schema should be added to converter. When ATEG conditions nearby maximum power, converter with MPPT can be disconnected from ATEG and ATEG should transfer energy directly to the electrical load. It allows avoiding losses on the converter (**Figure 19**).

Also, the electrical network should be equipped with a vehicle battery. The battery provides a constant supply voltage in a range of 12–13 V. According to the principle that in a parallel circuit the voltage is same for all elements and that the voltage of vehicle electrical devices is also 12 V. Using the battery in the electrical network makes it possible to properly power all car systems.

6. Conclusion(s)

Summarizing the analysis of the ATEG development field and its current state, as well as the prospects for the commercial implementation of this technology, the significant progress in this direction, which occurred over the past 20 years, is noted. Many ATEG prototypes have been created. Tests of different vehicle classes with these prototypes in various driving cycles are carried out. That shows the possibility of achieving the specified requirements for reducing fuel consumption and CO_2 emissions, especially for trucks [40]. Developers are increasingly focusing to achieve the possibility of commercializing ATEG, to reduce the cost of electricity watt and to solve reliability issues. This makes them, along with the classic industrially produced TEM materials, consider new promising thermoelectric materials, sacrificing sometimes the efficiency of energy conversion. At the same time, optimization of the ATEG design and technological solutions can significantly reduce the requirements for these materials, and improve the weight and size of the ATEG.

The rapid progress in the development of new thermoelectric materials and the research advancement in this area let us hope that the technology for utilizing the heat of exhaust gases of internal combustion engines in ATEG is capable of reaching a broad practical implementation.

Notes/Thanks/Other declarations

We thank Dmitry Onishchenko, head of the “Piston engine building and special machinery” of Bauman Moscow State Technical University (BMSTU), and his research team for valuable pieces of advice, which helped us to write this chapter.

Also we appreciate PhD student Shehak Sulymani’s participation in the preparation of the final chapter version.

Author details

Alexey Osipkov[1,2]*, Roman Poshekhonov[1,2], Konstantin Shishov[1] and Pavel Shiriaev[1]

*Address all correspondence to: osipkov@bmstu.ru

1 Bauman Moscow State Technical University (BMSTU), Moscow, Russia

2 Peoples' Friendship University of Russia (RUDN University), Moscow, Russia

References

[1] Srivastava DK, Agarwal AK, Datta A, Maurya RK. Advances in Internal Combustion Engine Research. Singapore: Springer; 2017

[2] Kavtaradze RZ. Theory of piston engines. Special chapters: Textbook for high schools. Moscow: Mashinostroenie Publ; 2008

[3] Yang J, Stabler FR. Automotive applications of thermoelectric materials. Journal of Electronic Materials. 2009;**38**(7):1245-1251

[4] Copeland C, Pesiridis A, Martinez-Botas R, Rajoo S, Romagnoli A, Mamat A. Automotive Exhaust Waste Heat Recovery Technologies; 2014

[5] Legros A et al. Comparison and impact of waste heat recovery technologies on passenger car fuel consumption in a normalized driving cycle. Energies. 2014;**7**(8):5273-5290

[6] Singh DV, Pedersen E. A review of waste heat recovery technologies for maritime applications. Energy Conversion and Management. 2016;**111**:315-328

[7] Noor AM, Puteh RC, Rajoo S. Waste heat recovery technologies in turbocharged automotive engine–a review. Journal of Modern Science and Technology. 2014;**2**(1):108-119

[8] Armstead JR, Miers SA. Review of waste heat recovery mechanisms for internal combustion engines. Journal of Thermal Science and Engineering Applications. 2014;**6**(1). DOI: 014001

[9] Zhang QH et al. Thermoelectric devices for power generation: Recent progress and future challenges. Advanced Engineering Materials. 2016;**18**(2):194-213

[10] Hale LE. Thermo-electric battery for motor-vehicles. In: U.S. Patent No. 1,134,452. 6 Apr. 1915

[11] Bauer RH. Auxiliary electric power for an automobile through the utilization of a thermoelectric generator: A critical examination. M of ME Thesis, Department of Mechanical Engineering, Clarkson College of Technology. 1963;**10**

[12] Tomarchio AJ. A Feasibility Study of Replacing an Electrical Generator of a Standard American Automobile with a Thermoelectric Generator. Potsdam, New York: Department of Mechanical Engineering, Clarkson College of Technology; 1964

[13] Goldsmid HJ, Douglas RW. The use of semiconductors in thermoelectric refrigeration. British Journal of Applied Physics. 1954;**5**(11):386

[14] Ioffe AF. Semiconductor Thermoelements [in Russian], Izd. In: MoscowLeningrad. AN SSSR; 1960. p. 129

[15] Birkholt U. Conversion of Waste Exhaust Heat in Automobiles Using FeSi_2 Thermoelements. Proc. 7th Int. conf. Thermoelectric Energy Conv.; 1988

[16] Karri MA. Modeling of an automotive exhaust thermoelectric generator. Mechanical Engineering. 2005:163

[17] Bass JC, Elsner NB, Leavitt FA. Performance of the 1 kW thermoelectric generator for diesel engines. AIP Conference Proceedings. 1994;**316**(1)

[18] Ikoma K et al. Thermoelectric module and generator for gasoline engine vehicles. Thermoelectrics, 1998. Proceedings ICT 98. XVII International Conference on. IEEE; 1998

[19] Ikoma K et al. Thermoelectric generator for gasoline engine vehicles using Bi2Te3 modules. Journal of the Japan Institute of Metals and Materials. Special Issue on Thermoelectric Energy Conversion Materials. 1999;**63**(11):1475-1478

[20] Crane D et al. TEG on-vehicle performance and model validation and what it means for further TEG development. Journal of Electronic Materials. 2013;**42**(7):1582-1591

[21] Jovovic V. Thermoelectric Waste Heat Recovery Program for Passenger Vehicles. Azusa, CA, United States: Gentherm Incorporated; 2015

[22] Magnetto D, Vidiella G. Reduced energy consumption by massive thermoelectric waste heat recovery in light duty trucks. AIP Conference Proceedings. 2012;**1449**(1)

[23] European Commission: CORDIS: Projects & Results Service: Final Report Summary – HEATRECAR (Reduced energy consumption by massive thermoelectric waste heat recovery in light-duty trucks) n.d

[24] Aixala L, Monnet V. Conclusion of RENOTER Project. IAV 3rd Conference on Thermoelectrics; 2012

[25] Poshekhonov RA et al. Development of a mathematical model for optimizing the design of an automotive thermoelectric generator taking into account the influence of its hydraulic resistance on the engine power. Semiconductors. 2017;**51**(8):981-985

[26] Poshekhonov RA, Osipkov AS, Makeev MO. Modelling of physical processes of energy conversion in automobile thermoelectric generators. Global Journal of Pure and Applied Mathematics. 2016;**12**(1):677-690

[27] Wang Y et al. Numerical and experimental investigation for heat transfer enhancement by dimpled surface heat exchanger in thermoelectric generator. Journal of Electronic Materials. 2016;**45**(3):1792-1802

[28] Osipkov A et al. Modeling of thermoelectric generator power characteristics for motorcycle-type engines. Journal of Electronic Materials. 2017;**46**(10):6195-6203

[29] Leontyev AI, Onishchenko DO, Arutyunyan GA. Selecting the optimum method of heat transfer intensification to improve efficiency of thermoelectric generator. Thermophysics and Aeromechanics. 2016;**23**(5):747-754

[30] Onishchenko DO et al. Study of influence of hydraulic thermoelectric generator resistance on gasoline engine efficiency. International Journal of Applied Engineering Research. 2017;**12**(5):721-727

[31] Koppers M, Tatarinov D, Bastian G. Thermoelektrische Generatoranlage zur Energierückgewinnung im Kraftfahrzeug. In: Schritte in die künftige Mobilität. Wiesbaden: Springer Gabler; 2013. pp. 93-110

[32] Massaguer A, Massaguer E, Comamala M, Cabot A, Ricart J, Deltell A. Experimental analysis of an automotive thermoelectric generator under different engine operating regimes. [accessed 2018 February 21]. https://www.researchgate.net/profile/Marti_Comamala/publication/316348918_Experimental_analysis_of_an_automotive_thermoelectric_generator_under_different_engine_operating_regimes/links/596c909b0f7e9b80919c27de/Experimental-analysis-of-an-automotive-thermoelectric-generator-under-different-engine-operating-regimes.pdf

[33] Tatarinov D, Sachau IJ. Charakterisierung und Simulation einer thermoelektrischen Generatoranlage zur Energie-Rekuperation aus Abgasen im Pkw. [accessed 2018 January 10]. https://d-nb.info/1080478833/34

[34] Li Q et al. Compact heat exchangers: A review and future applications for a new generation of high temperature solar receivers. Renewable and Sustainable Energy Reviews. 2011;**15**(9):4855-4875

[35] Su CQ et al. Simulation and optimization of the heat exchanger for automotive exhaust-based thermoelectric generators. Journal of Electronic Materials. 2016;**45**(3):1464-1472

[36] Zohuri B. Compact Heat Exchangers. Cham: Springer; 2017

[37] Hesselgreaves JE, Law R, Reay D. Compact heat exchangers: Selection, design and operation. Oxford: Butterworth-Heinemann; 2016

[38] Isachenko VP, Osipova VA. Teploperedacha./Uchebnik dlja studentov jenergeticheskih vuzov i fakul'tetov. [Heat transfer. /Textbook for students of energy universities and faculties]. In: M-L.: Jenergija. 1965

[39] MusiaŁ M, Borcuch M, Wojciechowski K. The influence of a dispersion cone on the temperature distribution in the heat exchanger of a thermoelectric generator. Journal of Electronic Materials. 2016;**45**(3):1517-1522

[40] Jänsch D et al. Thermoelectrics–An Opportunity for the Automotive Industry?. Conference of Energy and Thermal Management, Air Conditioning, Waste Heat Recovery. Cham: Springer; 2016

[41] Rowe DM. Conversion Efficiency and Figure-of-Merit. In: CRC Handbook of thermoelectrics. Boca Raton, FL: CRC press; 1995. pp. 31-37

[42] Jin Z-H, Wallace TT. Functionally graded thermoelectric materials with arbitrary property gradations: A one-dimensional semianalytical study. Journal of Electronic Materials. 2015;**44**(6):1444-1449

[43] Anatychuk LI, Vikhor LN. Functionally Graded Thermoelectric Materials. Vol. IV. Chernivtsi, 2012; 2012

[44] Crane DT et al. Performance results of a high-power-density thermoelectric generator: Beyond the couple. Journal of Electronic Materials. 2009;**38**(7):1375-1381

[45] Crane DT. An introduction to system-level, steady-state and transient modeling and optimization of high-power-density thermoelectric generator devices made of segmented thermoelectric elements. Journal of Electronic Materials. 2011;**40**(5):561-569

[46] Phillip N et al. Modelling and simulation of a thermoelectric generator for waste heat energy recovery in low carbon vehicles. Environment Friendly Energies and Applications (EFEA), 2012. 2nd ed. International Symposium on. IEEE. 2012

[47] Tatarinov D et al. Modeling of a thermoelectric generator for thermal energy regeneration in automobiles. Journal of Electronic Materials. 2013;**42**(7):2274-2281

[48] Bitschi A. Modelling of thermoelectric devices for electric power generation. Diss. In: ETH Zurich. 2009

[49] Anatychuk LI, Kuz RV. Computer designing and test results of automotive thermoelectric generator. In: Thermoelectrics goes automotive. IAV, Renningen: Thermoelektrik II expert Verlag; 2011

[50] Arutjunjan GA, Basov AO, Onishhenko DO, Safonov RA. Konstruktivnaja shema avtomobil'nogo termojelektricheskogo generatora s teploobmennikom izmenjaemoj geometrii [Constructive scheme of an automobile thermoelectric generator with a heat exchanger of variable geometry]. Patent RF. 2017;**171447**

[51] Orr B et al. A review of car waste heat recovery systems utilising thermoelectric generators and heat pipes. Applied Thermal Engineering. 2016;**101**:490-495

[52] Chi R-G et al. Study on heat pipe assisted thermoelectric power generation system from exhaust gas. Heat and Mass Transfer. 2017;**53**(11):3295-3304

[53] Altstedde K, Mirko FR, Friedrich H. Integrating phase-change materials into automotive thermoelectric generators. Journal of Electronic Materials. 2014;**43**:6

[54] Сакр ХМ, Мансур МХ, Мусса МН. ТЕПЛОВОЙ РАСЧЕТ ТЕРМОЭЛЕКТРИЧЕСКИХ ГЕНЕРАТОРОВ, РАБОТАЮЩИХ НА ВЫХЛОПНЫХ ГАЗАХ АВТОМОБИЛЯ: ЦЕЛИ И ЗАДАЧИ. Термоэлектричество. 2008;**1**:64-73

[55] Kajikawa T. Present status of research and development on thermoelectric power generation technology in Japan. Journal of Thermoelectricity. 2009;**1**:18-29

[56] Mitrani D, Tomé JA, Salazar J, Turó A, García MJ, Chávez JA. Methodology for extracting thermoelectric module parameters. IEEE Transactions on Instrumentation and Measurement. 2005;**54**(4):1548-1552

[57] Kuo YC, Liang TJ, Chen JF. Novel maximum-power-point-tracking controller for photovoltaic energy conversion system. IEEE Transactions on Industrial Electronics. 2001;**48**(3):594-601

[58] Salas V, Olias E, Barrado A, Lazaro A. Review of the maximum power point tracking algorithms for stand-alone photovoltaic systems. Solar Energy Materials and Solar Cells. 2006;**90**(11):1555-1578

[59] Koutroulis E, Kalaitzakis K, Voulgaris NC. Development of a microcontroller-based, photovoltaic maximum power point tracking control system. IEEE Transactions on Power Electronics. 2001;**16**(1):46-54

[60] Esram T, Chapman PL. Comparison of photovoltaic array maximum power point tracking techniques. IEEE Transactions on Energy Conversion. 2007;**22**(2):439-449

[61] Xiong Y, Yu L, Xu JM. MPPT control of photovoltaic generation system combining constant voltage method with perturb-observe method. Electric Power Automation Equipment. 2009;**29**(6):85-88

[62] Femia N, Petrone G, Spagnuolo G, Vitelli M. Optimization of perturb and observe maximum power point tracking method. IEEE transactions on power electronics. 2005;**20**(4):963-973

[63] Kuo YC, Liang TJ, Chen JF. Novel maximum-power-point-tracking controller for photovoltaic energy conversion system. IEEE transactions on industrial electronics. 2001;**48**(3):594-601

[64] Shmilovitz D. On the control of photovoltaic maximum power point tracker via output parameters. IEEE Proceedings-Electric Power Applications. 2005;**152**(2):239-248

[65] Yuan XL, Li SJ, wang C, yan RC. MPPT Arithmetic of Photovoltaic System Based on Dichotomy. Journal of Power Supply. 2011;**6**:012

[66] Li J, Wang H. Maximum power point tracking of photovoltaic generation based on the optimal gradient method. In Power and Energy Engineering Conference, 2009. APPEEC 2009. Asia-Pacific: IEEE; March 2009. pp. 1-4

[67] Fang W, Quan SH, Xie CJ, Tang XF, Wang LL, Huang L. Maximum power point tracking with dichotomy and gradient method for automobile exhaust thermoelectric generators. Journal of Electronic Materials. 2016;**45**(3):1613-1624

[68] Veerachary M, Senjyu T, Uezato K. Neural-network-based maximum-power-point tracking of coupled-inductor interleaved-boost-converter-supplied PV system using fuzzy controller. IEEE Transactions on Industrial Electronics. 2003;**50**(4):749-758

[69] D'Souza NS, Lopes LA, Liu X. An intelligent maximum power point tracker using peak current control. In Power Electronics Specialists Conference, 2005. PESC'05. IEEE 36th. IEEE. June 2005. pp. 172

Section 4

Thermoelectric Cooling: Principles, Effects, Optimization and Applications

Chapter 11

Thermoelectric Refrigeration Principles

Diana Enescu

Additional information is available at the end of the chapter

http://dx.doi.org/10.5772/intechopen.75439

Abstract

This chapter recalls the general principles and main formulations useful in the study of thermoelectric coolers. Starting from the general heat diffusion equation, analytical expressions are introduced for the determination of cooling capacity and rate of heat rejection in steady-state conditions. When dealing with the whole refrigeration system, the limits of the steady-state analysis of the individual thermoelectric elements are pointed out, indicating the need for transient analysis supported by experimental evaluations. Then, the energy indicators are illustrated by considering the electrical power consumption, the thermal performance described by the dimensionless figure of merit, as well as the coefficient of performance. Furthermore, the main methods to enhance the thermoelectric cooler performance in refrigeration units are highlighted, with reference to high-performance materials, design aspects and temperature control systems. Finally, indications are reported on some applications of various thermoelectric refrigeration solutions, considering the technical aspects of the performance of these systems.

Keywords: refrigeration, thermoelectric unit, energy indicators, cooling capacity, coefficient of performance, temperature control, renewable sources

1. Introduction

The thermoelectric effect represents direct conversion of the temperature difference into voltage and vice versa and refers to phenomena with which the current flows through the thermoelements or legs of a thermoelectric module. The thermoelectric effect is formed due to free motion of the charge carriers (free electrons e^- considered as negative charge carriers and holes h^+ considered as positive charge carriers) in metals and semiconductors while carrying energy and electric charge. In this case, the electric effects are accompanied by thermal effects and vice versa [1]. The thermoelectric effects are Peltier effect, Thomson effect and Seebeck effect. The *Peltier effect* is the phenomenon that converts current to temperature and occurs when an

electric current flows through a thermoelectric device. The Peltier effect is a reversible phenomenon, because the Peltier heat depends directly on the direction of the carrier flow or electrical current [2].

There is interdependence between the sense of the electric current and the temperature difference at the hot and cold ends of a thermoelectric device. In other words, if the current flow is changed, the temperature at the hot and cold ends is changed as well.

The heat flow rate is given by

$$\dot{Q}_{\text{Peltier}} = \pi_{\text{AB}} \cdot I \cdot T = (\pi_{\text{B}} - \pi_{\text{A}}) \cdot I \cdot T \tag{1}$$

where $\dot{Q}_{\text{Peltier}}$ is the absorbed or dissipated heat flow rate, in W; I is the electric current that flows through the junctions, in A; π_{AB}, π_{A} and π_{B} are the Peltier coefficients of the thermocouple and conductors A and B, in $\text{W} \cdot \text{A}^{-1}$; and T is the absolute temperature, in K.

The Peltier coefficient π is defined as the amount of heat developed or absorbed at a junction of a thermocouple when a current of one ampere passes through this junction for one second. The Peltier coefficient π is positive for heat absorbed and negative for heat dissipated. The Peltier coefficient determines a cooling effect when the current flows from the N-type semiconductor material to a P-type semiconductor material and a heating effect when the current flows from the P-type semiconductor material to an N-type semiconductor material.

The *Thomson effect* is given by generation or absorption of a heat quantity in a homogeneous conductor by which an electric current flows and where there is a temperature gradient. The heat absorbed or released depends on the electric current direction and the conductor material. The *Thomson effect* is a reversible thermoelectric phenomenon and is observed when the charge carriers change energy levels.

The convention for the Thomson effect is:

- *positive* Thomson effect, when the hot end has a high voltage and the cold end has a low voltage; the heat is generated when the current flows from the hotter junction to the colder junction, while the heat is absorbed when the current flows from the colder end to the hotter end.
- *negative* Thomson effect, when the hot end has a low voltage and the cold end has a high voltage; the heat is generated when the current flows from the colder junction to the hotter junction, while the heat is absorbed when the current flows from the hotter end to the colder end; some metals have negative Thomson coefficients (e.g. Co, Bi, Fe, and Hg) [3].

The Thomson heat flow rate $\dot{Q}_{\text{Thomson}}$ is proportional to the thermal gradient as well as to the intensity of the electric current which flows through the conductor:

$$\dot{Q}_{\text{Thomson}} = -\mu_{\text{AB}} \cdot I \cdot \nabla T = \left(\mu_{\text{B}} - \mu_{\text{A}}\right) \cdot I \cdot \nabla T \tag{2}$$

where μ_{AB} is the Thomson coefficient in $\text{V} \cdot \text{K}^{-1}$, I is the electric current flowing through the circuit supplied by a voltage and $\nabla T = \frac{\text{d}T}{\text{d}x}$ is the temperature gradient along the conductor.

http://dx.doi.org/10.5772/intechopen.75439

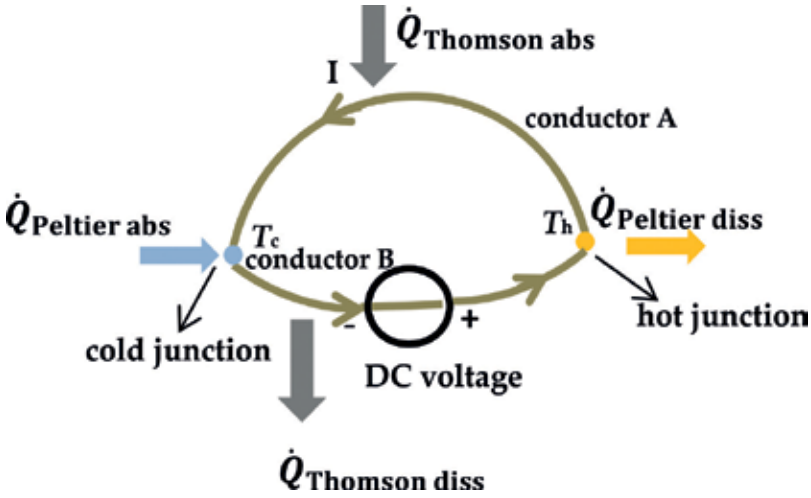

Figure 1. Schematic of Peltier effect and Thomson effect in a thermocouple.

With reference to **Figure 1**, the sign convention of the Thomson coefficient is positive for heat absorbed (conductor A) and negative for heat dissipated (conductor B).

Furthermore, the *Joule* heat $\dot{Q}_{\text{Joule}}$, in W, is irreversible and takes place in a conductor with electrical current flow, regardless of the direction of the current. Its expression is given by

$$\dot{Q}_{\text{Joule}} = R \cdot I^2 \tag{3}$$

where R is the conductor resistance in Ω.

If a current density J exists through a homogeneous conductor, the heat production per unit volume or volumetric heat generation is

$$\dot{q}_{\text{v}} = \underbrace{\rho \cdot J^2}_{\text{Joule heating}} \underbrace{- \mu \cdot J \cdot \nabla T}_{\dot{Q}_{\text{Thomson}}} = \rho \cdot \left(\frac{I}{S}\right)^2 - \mu \cdot \frac{I}{S} \cdot \nabla T \tag{4}$$

where ρ is the electrical resistivity of the material in Ω·m, $J = \frac{I}{S}$ is the current density in $\text{A} \cdot \text{m}^{-2}$ and S is the cross-sectional area in m^2.

The *Seebeck effect* converts temperature to current and occurs like the Peltier effect, but the direction of the electric current is reversed. The Seebeck effect appears when a temperature gradient along a conductor provides a voltage increment. In other words, the Seebeck voltage drives the hole/electron flow due to a temperature difference which does exist in the conductor between the high- and low-temperature regions. The Seebeck voltage appearing at the circuit junctions is

$$\Delta V = \alpha_{\text{AB}} \cdot \Delta T = (\alpha_{\text{A}} - \alpha_{\text{B}}) \cdot (T_{\text{H}} - T_{\text{C}}) \tag{5}$$

where $\alpha_A, \alpha_{\text{B}}$ are the Seebeck coefficients for the conductors A and B, in $\text{V} \cdot \text{K}^{-1}$.

The Seebeck coefficient or thermoelectric power is a very important parameter for the thermoelectric materials, determining the *performance of Peltier elements*. For a good thermoelectric material, the Seebeck coefficient has to be high in order to obtain the desired voltage more easily, the electrical conductivity has to be high, and the thermal conductivity has to be small to reduce the thermal losses in the junctions of the thermocouple [4].

The relationship of the Seebeck coefficient to the electric field E and the temperature gradient ∇T is

$$\alpha_{AB} = \frac{E}{\nabla T} \tag{6}$$

The sign of the Seebeck coefficient depends on the hole and electron flow:

- A negative Seebeck coefficient is obtained in semiconductors negatively doped (e.g. N-type semiconductors).
- A positive Seebeck coefficient is obtained in semiconductors positively doped (e.g. P-type semiconductors).

There is interdependence between the Peltier coefficient and the Seebeck coefficient, as well as between the Seebeck coefficient and the Thomson coefficient, given by the following relationships [5, 6]:

$$\pi_{AB} = \alpha_{AB} \cdot T \tag{7}$$

$$\mu_{AB} = T \cdot \frac{d\alpha_{AB}}{dT} \tag{8}$$

A thermoelectric cooler (TEC) is a semiconductor composed of an electronic component which transforms electrical energy into a temperature gradient. The TEC consists of one or more thermoelectric couples. A thermoelectric couple is a couple having one P-type thermoelectric leg (an excess of holes h^+, positive Seebeck coefficient α_P, electrical resistivity ρ_P and thermal conductivity k_N) and one N-type thermoelectric leg (an excess of free electrons e^-, negative Seebeck coefficient α_N, electrical resistivity ρ_N and thermal conductivity k_N linked to each other by an electrical conductor (a conductive metallic strip) forming a junction. The thermoelectric couples are connected in such a way that when the current flows through the device, both the P-type holes and the N-type electrons move towards the same side of the device.

The two legs are made of two different thermoelectric materials. A thermoelectric material is defined as an alloy of materials that generates thermoelectric properties (thermal conductivity, electric conductivity and Seebeck coefficient). The quality as a semiconductor material to be cooled strictly depends on the transport properties of the material (Seebeck voltage, electrical resistivity and thermal conductivity) as well as the operational temperature field between the cold and hot ends [5]. Considering that the input voltage of a single thermoelectric couple is reduced, many thermoelectric couples are connected to

http://dx.doi.org/10.5772/intechopen.75439

each other by junctions and are sandwiched between two ceramic substrates to form a thermoelectric module (TEM). These ceramic substrates act as insulator from electrical point of view but allow the thermoelectric couples to be thermally in parallel. The number of thermoelectric couples is influenced by the needed cooling capacity and the maximum electric current [5]. When a low voltage DC power source is applied to the free end of the TEM, the heat flow rate is transferred from one side to other side of the device through the N- and P-semiconductor legs and junctions. In this case, one side of the TEM is cooled, and the other side is heated [7]. In the cooling mode, the sense of the electrical current is from the N-type semiconductor to the P-type semiconductor (**Figure 2**). The Seebeck voltage is generated in the device when there is a temperature difference between the junctions of the thermoelements [8].

The direction of the current is then essential to establish the functionality of the device. If the direction of the electrical current is reversed, the compartment would be heated instead of being cooled.

At the top of every junction, the temperature is the same (T_c), and at the bottom of every junction, the temperature is the same (T_h). At the cold junction, the temperature T_c decreases, and the heat $\dot{Q}_c$ is absorbed from the compartment which must be cooled. Through the cold junction, the electrons are transported from a low energy level inside the P-type semiconductor legs to a high energy level inside the N-type semiconductor legs. At the hot junction, the heat $\dot{Q}_h$ is transferred according to the transport electrons. This heat is dissipated at the heat sink (a passive heat exchanger that cools a device by dissipating heat into the environment), and the free electrons flow to an inferior energy level in the P-type semiconductor.

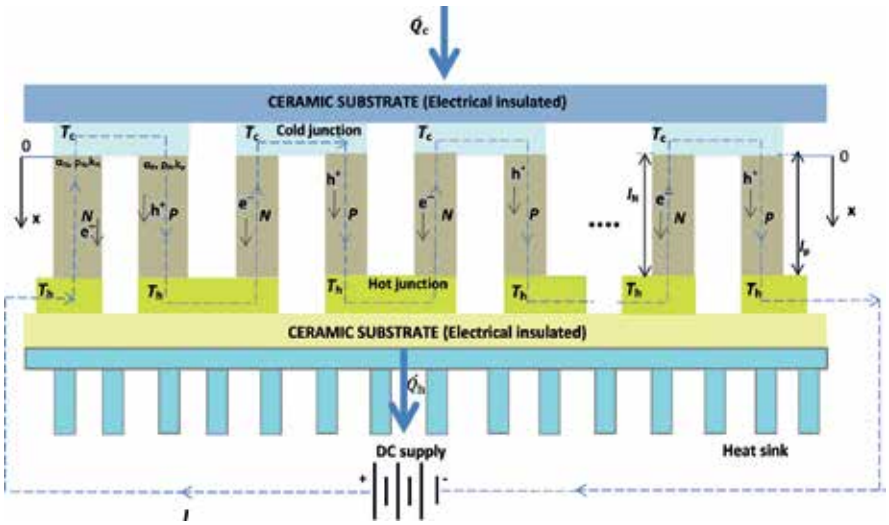

Figure 2. Schematic of a thermoelectric module (TEM) operating in cooling mode.

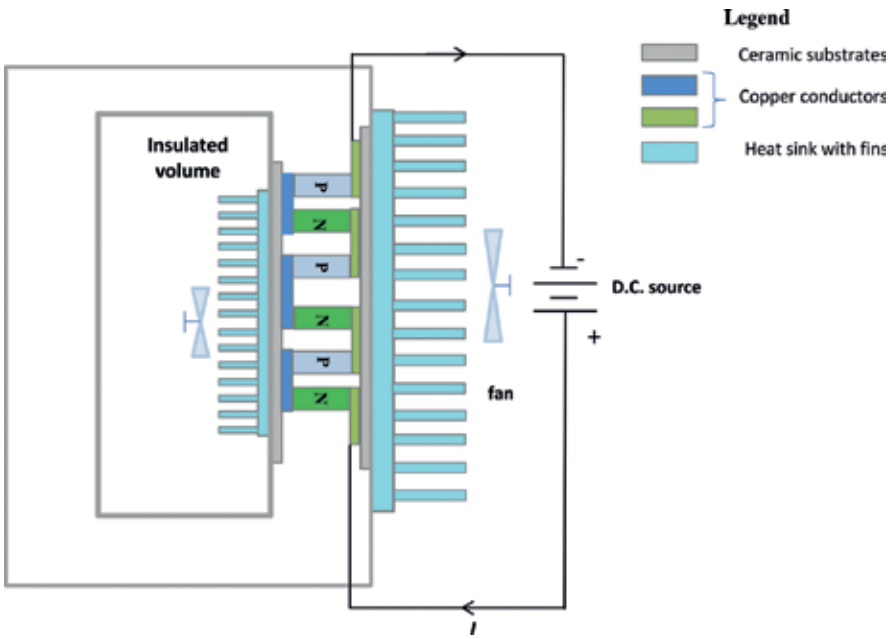

Figure 3. Schematic of a TEM used for the refrigeration unit.

The main components of a refrigeration unit (**Figure 3**) are [7, 9, 10]:

- the insulated refrigerator *cabinet* with thermoelectric technology having variable dimensions (e.g. for a capacity from 5 to 40 l, the thickness is from 5 to 10 cm, and for a capacity less than 5 l the thickness is 4 cm);
- the cooling thermoelectric system with semiconductors (TECs) useful to cool the insulated volume;
- the *heat sink*, considered as a heat exchanger useful to facilitate the heat transfer from the hot side of TEC to the environment. The TEC can operate in a definite operating range of its temperature difference. To keep this temperature difference inside the specific operating range, a TEC is compulsory to have a heat sink at the hot end to dissipate heat from the TEC to environment. Sometimes, another heat sink with fins is fixed inside the compartment to improve the heat transfer from the insulated volume which is cooled (fluid, solid) to the cold side of the TEC. In this case, the heat sink is cooled at a temperature lower than the insulated volume, and the heat flowing between the fins is collected by means of a fan [11–13];
- one or many *fans* which transfer heat through convection and allow the dissipation of heated or cooled air in order to avoid operational problems; the fans are powered by the same external power supply that powers the TEC;
- the control system useful for an accurate temperature control; as the current value is changing, it is possible to directly control the cooling capacity.

http://dx.doi.org/10.5772/intechopen.75439

2. Theoretical assessment of a thermoelectric cooler

2.1. The general heat diffusion equation

Consider a non-uniformly heated thermoelectric material having isotropic properties (the same transport properties in all directions) crossed by a constant current density $\vec{J}$ [2, 14–16]. The continuity equation is

$$\vec{\nabla} \cdot \vec{J} = 0 \tag{9}$$

where $\vec{J}$ is the current density vector and $\vec{\nabla}$ is the gradient vector, a differential operator with respect to the three orthogonal directions:

$$\vec{\nabla} = \vec{i}\,\frac{\partial}{\partial x} + \vec{j}\,\frac{\partial}{\partial y} + \vec{k}\,\frac{\partial}{\partial z} \tag{10}$$

A temperature gradient generates an electric field $\vec{E}$. This electric field depends on the temperature gradient $\vec{\nabla} T$ and on the current density $\vec{J}$ and is expressed as

$$\vec{E} = \underbrace{\rho \cdot \vec{J}}_{\text{Ohm's law}} + \underbrace{\alpha \cdot \vec{\nabla} T}_{\textit{Seebeck voltage}} \tag{11}$$

with the electrical resistivity ρ in Ω·m and the Seebeck coefficient α in $\mathrm{V \cdot K^{-1}}$.

The heat flow rate $\vec{q}$ also depends on the temperature gradient $\vec{\nabla} T$ and is expressed as

$$\vec{q} = \underbrace{-k \cdot \vec{\nabla} T}_{\text{Fourier's law}} + \underbrace{\alpha \cdot T \cdot \vec{J}}_{\text{Peltier heat}} \tag{12}$$

where k is the thermal conductivity in $\mathrm{W \cdot (m \cdot K)^{-1}}$.

The general heat diffusion equation for transient state [14] is

$$-\vec{\nabla} \cdot \vec{q} + \dot{q}_{\text{vol}} = \rho \cdot c_p \cdot \frac{\partial T}{\partial t} \tag{13}$$

where ρ is the electrical resistivity in Ω·m, c_p is the specific heat capacity at constant pressure in $\mathrm{J \cdot (kg \cdot K)^{-1}}$ and $\dot{q}_{\text{vol}}$ is the volumetric heat generation, in $\mathrm{W \cdot m^{-3}}$.

The volumetric heat generation is also given by

$$\dot{q}_{\text{vol}} = \vec{E} \cdot \vec{J} = \left(\rho \cdot \vec{J} + \alpha \cdot \vec{\nabla} T\right) \cdot \vec{J} = \rho \cdot J^2 + \vec{J} \cdot \alpha \cdot \vec{\nabla} T \tag{14}$$

Based on Thomson's relationship and Osanger's relationship, the heat flow rate vector is written as [16]

$$\vec{q} = \alpha \cdot T \cdot \vec{J} - k \cdot \vec{\nabla} T \tag{15}$$

Substituting Eq. (14) and Eq. (15) into Eq. (13), with successive elaborations, yields

$$\rho \cdot \mathrm{J}^2 + \vec{J} \cdot \alpha \cdot \vec{\nabla} T = \vec{\nabla} \cdot \vec{q} + \rho \cdot c_\mathrm{p} \cdot \frac{\partial T}{\partial t}$$

$$\rho \cdot \mathrm{J}^2 + \vec{J} \cdot \alpha \cdot \vec{\nabla} T = \vec{\nabla} \cdot \left(-k \cdot \vec{\nabla} T + \alpha \cdot T \cdot \vec{J} \right) + \rho \cdot c_\mathrm{p} \cdot \frac{\partial T}{\partial t}$$

$$\rho \cdot \mathrm{J}^2 + \vec{J} \cdot \alpha \cdot \vec{\nabla} T = -\vec{\nabla} \cdot \left(k \cdot \vec{\nabla} T \right) + \underbrace{\vec{\nabla} \cdot \left(\alpha \cdot T \cdot \vec{J} \right)}_{T \cdot \vec{J} \cdot \frac{\mathrm{d}\alpha}{\mathrm{d}T} \cdot \vec{\nabla} T + \vec{J} \cdot \alpha \cdot \vec{\nabla} T} + \rho \cdot c_\mathrm{p} \cdot \frac{\partial T}{\partial t} \tag{16}$$

Considering that $\mu = T \cdot \frac{\mathrm{d}\alpha}{\mathrm{d}T}$ is the Thomson coefficient, the heat diffusion equation is

$$\underbrace{\vec{\nabla} \cdot \left(k \cdot \vec{\nabla} T \right)}_{\textit{thermal conduction}} + \underbrace{\rho \cdot \mathrm{J}^2}_{\textit{Joule heating}} - \underbrace{\mu \cdot \vec{J} \cdot \vec{\nabla} T}_{\textit{Thomson effect}} = \underbrace{\rho \cdot c_\mathrm{p} \cdot \frac{\partial T}{\partial t}}_{\text{transient}} \tag{17}$$

2.2. Steady-state and transient approaches

2.2.1. The limits of steady-state analysis

Steady-state analysis for a TEC is typically carried out by resorting to a set of approximations. The simplest model is based on the following assumptions: the Seebeck effect does not depend on temperature, there are no thermal or electrical contact resistances, there are no heat losses, and the Thomson coefficient is zero ($\mu = 0$), so that the Thomson heat is absent [2, 14, 16]. In these conditions, there is no heat transfer from or to the external environment, so that the heat flows occur only between the source and the sink. On these assumptions, Eq. (17) becomes

$$\vec{\nabla} \cdot \left(k \cdot \vec{\nabla} T \right) + \rho \cdot \mathrm{J}^2 = 0 \tag{18}$$

By replacing in Eq. (18) the current density $J = \frac{I}{S}$ and the temperature Laplacian $\nabla^2 T = \vec{\nabla} \cdot \vec{\nabla} T = \vec{i} \frac{\partial}{\partial x} \cdot \vec{i} \frac{\partial T}{\partial x} = \frac{\mathrm{d}^2 T}{\mathrm{d}x^2}$, the one-dimensional differential equation is [2, 14–16]

$$k \cdot S \cdot \frac{\mathrm{d}^2 T}{\mathrm{d}x^2} + \rho \cdot \frac{I^2}{S} = 0 \Rightarrow k \cdot S \cdot \mathrm{d}\left(\frac{\mathrm{d}T}{\mathrm{d}x} \right) = -\rho \cdot \frac{I^2}{S} \mathrm{d}x \tag{19}$$

Let us consider the boundary conditions between the following limits (**Figure 4**):

$$x = 0 \Rightarrow T = T_c \tag{20}$$

$$x = l \Rightarrow T = T_h \tag{21}$$

The heat flow rate at $x = 0$ and $T = T_\mathrm{c}$ is expressed as

$$\dot{Q}_{x=0} = \alpha \cdot I \cdot T_\mathrm{c} - k \cdot S \left. \frac{dT}{dx} \right|_{x=0} \Rightarrow \dot{Q}_{x=0} = \alpha \cdot I \cdot T_\mathrm{c} - \frac{\rho \cdot I^2}{2S} \cdot l - (T_\mathrm{h} - T_\mathrm{c}) \cdot \frac{k \cdot S}{l} \tag{22}$$

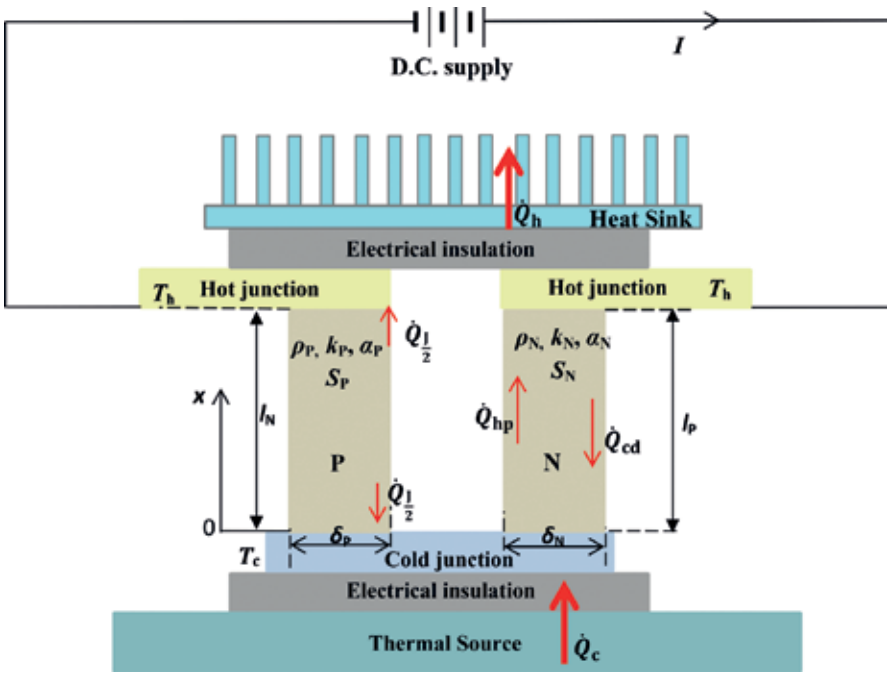

Figure 4. Schematic of a TEC (geometric elements and material properties).

and the heat flow rate at $x = l$ and $T = T_h$ is

$$\dot{Q}_{x=l} = \alpha \cdot I \cdot T_h - k \cdot S \left.\frac{dT}{dx}\right|_{x=l} \Rightarrow \dot{Q}_{x=l} = \alpha \cdot I \cdot T_h + \frac{\rho \cdot I^2}{2S} \cdot l - (T_h - T_c) \cdot \frac{k \cdot S}{l} \tag{23}$$

The heat flow rate at the cold junction is obtained by summing up the contributions of the N-type and P-type elements at $x = 0$:

$$\dot{Q}_c = \dot{Q}_{x=0,P} + \dot{Q}_{x=0,N} \tag{24}$$

$$\dot{Q}_c = (\alpha_P - \alpha_N) \cdot I \cdot T_c - \frac{1}{2} \cdot \left(\frac{\rho_P \cdot l_P}{S} + \frac{\rho_N \cdot l_N}{S} \right) \cdot I^2 - \left(\frac{k_P \cdot S_P}{l_P} + \frac{k_N \cdot S_N}{l_N} \right) \cdot (T_c - T_h) \tag{25}$$

Likewise, the heat flow rate at the hot junction is determined for $x = l$:

$$\dot{Q}_h = \dot{Q}_{x=l,P} + \dot{Q}_{x=l,N} \tag{26}$$

$$\dot{Q}_h = (\alpha_P - \alpha_N) \cdot I \cdot T_h + \frac{1}{2} \cdot \left(\frac{\rho_P \cdot l_P}{S} + \frac{\rho_N \cdot l_N}{S} \right) \cdot I^2 - \left(\frac{k_P \cdot S_P}{l_P} + \frac{k_N \cdot S_N}{l_N} \right) \cdot (T_h - T_c) \tag{27}$$

The total electrical resistance R of the thermoelement pair in series, the total thermal conductance K of the thermoelements in parallel, the Seebeck coefficient α_{NP} of the thermoelectric

couple and the temperature difference ΔT between the hot surface temperature T_h and the cold surface temperature T_c are written as [9]

$$R = \frac{\rho_P \cdot l_P}{S} + \frac{\rho_N \cdot l_N}{S} \tag{28}$$

$$K = \frac{k_P \cdot S_P}{l_P} + \frac{k_N \cdot S_N}{l_N} \tag{29}$$

$$\alpha_{NP} = \alpha_P - \alpha_N \tag{30}$$

$$\Delta T = T_h - T_c \tag{31}$$

Considering that N-type and P-type thermocouples are identical (with the same length), the total electrical resistance is $R = \rho \cdot l \cdot (S)^{-1}$ with $\rho = \rho_P + \rho_N$, the total thermal conductance of the thermoelements is $K = k \cdot S \cdot (l)^{-1}$ with $k = k_P + k_N$ the thermal conductivity corresponding to the N and P thermoelement legs in $W \cdot (m \cdot K)^{-1}$, and σ is the electrical conductivity corresponding to the N and P thermoelement legs with $\sigma = \sigma_P + \sigma_N$ in $S \cdot m^{-1}$. Then, Eq. (24) and Eq. (26) give the cooling capacity (or the rate of heat absorbed at the cold junction) $\dot{Q}_c$ and the rate of heat rejection $\dot{Q}_h$ in W:

$$\dot{Q}_c = \alpha_{NP} \cdot I \cdot T_c - \frac{1}{2} \cdot R \cdot I^2 - K \cdot \Delta T \Rightarrow \dot{Q}_c = \dot{Q}_{hp} - \frac{1}{2}\dot{Q}_J - \dot{Q}_{cd} \tag{32}$$

$$\dot{Q}_h = \alpha_{NP} \cdot I \cdot T_h + \frac{1}{2} \cdot R \cdot I^2 - K \cdot \Delta T \Rightarrow \dot{Q}_h = \dot{Q}_{hp} + \frac{1}{2}\dot{Q}_J - \dot{Q}_{cd} \tag{33}$$

where $\dot{Q}_{hp}$ is the thermoelectric heat pumping at the cold junction, $\dot{Q}_J$ is the Joule heat and $\dot{Q}_{cd}$ is the heat flow conducted from the hot junction to the cold junction.

However, this model can be used only at first approximation for the selection of thermocouple materials [9]. In practice, the semiconductor properties depend on temperature, the contact resistances cannot be avoided, and the Thomson effect cannot be neglected. Moreover, in the steady-state model, the temperatures T_h and T_c are input values that have to be determined accurately. If the object to be cooled is directly in contact with the TEC cold surface, the object temperature has the same value as the temperature of the TEC cold surface T_c. However, if the object to be cooled is not directly in contact with the TEC cold surface, e.g. in a refrigerator compartment, a heat exchanger is required on the TEC cold surface. In this case, the cold surface of the TEC has to be some degrees colder than the desired temperature in the refrigerator compartment, and the temperature T_c is unknown. With a similar reasoning, if a heat exchanger is placed at the hot side, the known value is the ambient temperature, and the temperature T_h is unknown. The temperature distribution of a complex system (refrigerator) with TEC is depicted in **Figure 5**.

Therefore, in practical applications in which the TEC is connected to other components (e.g. heat exchangers), (i) the temperatures T_c and T_h are unknown, (ii) only the external temperatures can be measured accurately, and (iii) the temperature at each point of the system depends

http://dx.doi.org/10.5772/intechopen.75439

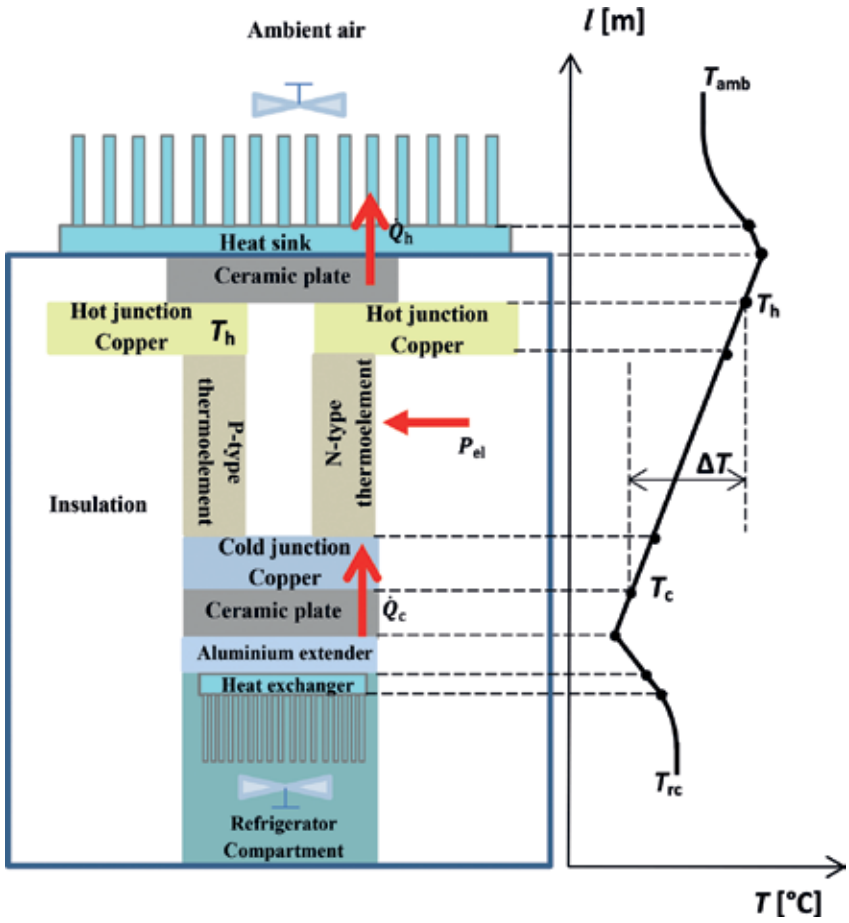

Figure 5. Schematic of temperature profile in a thermoelectric refrigeration system.

on the composition of the whole system and cannot be determined for the individual components. Thereby, the temperatures at the TEC terminals can be determined by using a dedicated model of the interconnected components. These temperatures are calculated from the solution of the overall system equations, in which all the temperature-dependent thermoelectric effects (Peltier, Seebeck, Thomson and Joule) are taken into account [17].

2.2.2. Transient analysis

Thermoelectric refrigerators are controlled devices that operate in transient conditions. Thereby, it is important to formulate a detailed model taking into account all the thermoelectric effects and the dependence of the model parameters on temperature.

Eq. (17) is written in generic transient conditions. The solution of this equation has been obtained in [18] by constructing an electrothermal equivalent model with resistances and capacities (in which the thermoelectric modules are represented through a multi-node structure and the other

components are represented by a single node). The implicit finite difference method has been used to solve the equations. In this model, the input data are the number of modules, the geometric parameters (lengths and cross areas), the structural characteristics of the components, the heat flow rate produced by the heat source, the voltage supply from the electrical system and the environment temperature. The structural characteristics can be given as constant values (density, specific heat, surface electrical resistivity of the thermoelectric elements) or can be expressed as functions of the temperatures (Seebeck coefficient, electrical resistivity and thermal conductivity). Since the model is non-linear, the solution requires an iterative process, so that the initialization of the temperatures at each node of the model has to be provided as well. The outputs of the method (with their evolutions in time) are the temperatures at all the nodes, the heat flow rates in each component, the power produced by the modules and consumed by the fan and the efficiencies of the modules and of the system. This formulation is consistent with an experimental application, such as the one presented in [17].

2.3. Energy indicators for TEC performance

The energy indicators useful for the design and the performance of TEC are the cooling capacity, the rate of heat rejection, the input electrical power, the dimensionless figure of merit ZT and the coefficient of performance (COP).

The temperature difference ΔT created when a current flows through the TEC generates a raising voltage [9]. This voltage depends on the voltage referring to the Seebeck effect $\alpha_{\mathrm{NP}} \cdot \Delta T$ and the voltage at the thermoelectric couple $\alpha_{\mathrm{NP}} \cdot \Delta T$:

$$V = \alpha_{\mathrm{NP}} \cdot \Delta T + R \cdot I \tag{34}$$

The input electrical power P_{el} or electrical power consumption [19] is

$$P_{\mathrm{el}} = \dot{Q}_h - \dot{Q}_c = \alpha_{NP} \cdot I \cdot \Delta T + R \cdot I^2 \tag{35}$$

An important physical property of the TEM is the figure of merit Z. It depends on the transport parameters (Seebeck coefficient of the thermoelectric couple, total electrical resistivity and total thermal conductivity):

$$Z = \frac{\alpha_{\mathrm{NP}}^2}{\rho \cdot k} \tag{36}$$

The thermal performance of a thermoelectric cooler is given by dimensionless figure of merit ZT. The absolute temperature T is the mean device temperature $\overline{T}$ between the hot side and cold sides of the TEC [20, 21]:

$$\overline{T} = \frac{T_{\mathrm{c}} + T_{\mathrm{h}}}{2} \tag{37}$$

Generally the expression ZT is written without indicating the averaging symbol for $\overline{\mathrm{T}}$. The parameter ZT represents the efficiency of the semiconductor materials of N-type and P-type

thermoelements. In this case, a thermoelectric semiconductor with a higher figure of merit is advantageous because it gives a superior cooling power. To obtain a higher figure of merit, a thermoelectric material optimization is required. This means to optimize the ZT dimensionless parameter by a maximization of the power factor, which depends on material properties like electrical conductivity and Seebeck coefficient, as well as a minimization of the thermal conductivity [1].

The best materials with high ZT are high doped semiconductors. Metals have relatively small Seebeck coefficients, and insulators have low electrical conductivity. The thermoelectric cooling materials are alloys which contain bismuth telluride (Bi_2Te_3) with antimony telluride (Sb_2Te_3) (like p-type $Bi_{0.5}Sb_{1.5}Te_3$ composites) [22] and Bi_2Te_3 with bismuth selenide Bi_2Se_3 (like n-type $Bi_2Te_{2.7}Se_{0.3}$) [23], each having $ZT \cong 1$ at room temperature [21]. The thermoelectric materials with good electrical properties and low thermal conductivities are bulk materials and nanostructured materials considering the dimensionless figure of merit $ZT \geq 1$ [24, 25].

The figure of merit of thermoelectric modules rises with the Seebeck coefficient, while the cooling capacity of the heat sink becomes narrow [26]. Much more, the figure of merit of a thermoelectric element limits the temperature differential achieved between the sides of the module, while the length-to-surface ratio for the thermoelements defines the cooling capacity [3].

The number of thermoelements in a thermoelectric module mainly depends on the required cooling capacity and the maximum electric current [9]. An expression for the cooling capacity shows that it also depends on thermal and electrical contact resistances (at both sides of the thermoelectric module), as well as the thermoelement length of the module [20]:

$$\dot{Q}_c = \frac{k \cdot (\Delta T_{\max} - \Delta T)}{l + 2 \cdot r \cdot l_c + r \cdot l_c \cdot COP^{-1}} \tag{38}$$

where l_c is the thickness of the contact layers, r is the thermal contact parameter (which is the ratio between the thermal conductivity of the thermoelements and the thermal conductivity of the contact layers), COP is the coefficient of performance and $\Delta T_{\max}$ the maximum temperature difference.

An insignificant effect of the contact resistances on the cooling capacity is observed for the thermoelements with long lengths, while significant changes of the cooling capacity are obtained when the contact resistances are improved, and this is for the case of short thermoelements [27]. The maximum cooling capacity $\dot{Q}_{c_{max}}$ and the maximum $COP_{\max}$ are used in design to find the operating conditions [28]. The maximum temperature difference $\Delta T_{\max}$ obtainable between the hot and cold sides always occurs at $I_{\max}$, $V_{\max}$ and $\dot{Q}_c = 0$:

$$\Delta T_{\max} = \left(T_h + \frac{1}{Z}\right) - \left[\left(T_h + \frac{1}{Z}\right)^2 - T_h^2\right]^{\frac{1}{2}} \tag{39}$$

The maximum current represents the current which gives the maximum possible temperature difference $\Delta T_{\max}$ which takes place when $\dot{Q}_c = 0$ [4]. Practically, operating under the maximum

current, there is insufficient current to obtain $\Delta T_{\max}$. Working above the maximum current, the power dissipation inside the TEC starts to rise the device temperature and to decrease ΔT. The maximum current is almost constant which is the operating range of the device:

$$I_{\max} = \alpha_{NP} \cdot (T_h - \Delta T_{max}) \cdot R^{-1} \tag{40}$$

The maximum cooling capacity $\dot{Q}_{c_{max}}$ for a TEC is the maximum thermal load obtained when $\Delta T = 0$ and $I = I_{\max}$:

$$\dot{Q}_{c_{max}} = \alpha_{NP}{}^2 \left(T_h^2 - \Delta T_{\max}^2\right) \cdot (2R)^{-1} \tag{41}$$

The maximum voltage represents the DC voltage which gives $\Delta T_{\max}$ at $I = I_{\max}$. In this case *COP* has a minimum value. At maximum voltage the power dissipation inside the TEC starts to rise the device temperature and to decrease ΔT. The maximum voltage depends on the temperature:

$$V_{\max} = \alpha_{NP} \cdot T_h \tag{42}$$

The coefficient of performance (*COP*) represents the heat absorbed at the cold junction or cooling capacity, divided by the input electrical power:

$$COP = \frac{\dot{Q}_c}{P_{el}} \tag{43}$$

Various papers explain the *COP* dependence of the characteristics of the materials on the Thomson effect and on temperature. The TEC performance is improved by raising the figure of merit of the thermoelectric elements and considering the Thomson effect [29]. The validity of the Thomson effect is taken into account in the relationships of the cooling capacity and input electrical power and implicitly in the *COP* relationship, if the dependence on temperature of Seebeck coefficient is considered [30]. In this case the Thomson effect gives a reduction with about 7.1% for the input electrical power and with about 7% for the cooling capacity considering the positive values of the Thomson coefficient; instead, an improvement in both the input electrical power and the cooling capacity is observed for negative values of the Thomson coefficient [31].

The *COP* is also influenced by the thermal and electrical contact resistances. The *COP* of the thermoelectric module can be improved up to 60% by decreasing the electrical contact resistances [27]. Furthermore, the *COP* depends on the thermoelement length. The *COP* rises with the increment of the thermoelement length. For a thermoelement with a shorter length, the contact resistance becomes closer to the resistance of the thermoelement, notably affecting this indicator [27].

The maximum *COP* (indicated as $COP_{\max}$) of a TEC is used for its sizing [9, 20]. The $COP_{\max}$ has the benefit of minimum input electrical power, therefore, minimum total heat to be rejected by the heat sink: $\dot{Q}_h = \dot{Q}_c + P_{el}$.

The $COP_{\max}$ depends on the current and does not depend on the number of TEC pairs [32, 27]:

$$COP_{\max} = \left(R \cdot I^2 + \alpha_{NP} \cdot I \cdot \Delta T\right)^{-1} \cdot \left(\alpha_{NP} \cdot I \cdot T_c - k \cdot \Delta T - \frac{R \cdot I^2}{2}\right) \tag{44}$$

The $COP_{\max}$ and the maximum temperature difference $\Delta T_{\max}$ are affected by the figure of merit. The $COP_{\max}$ is reached at low T_h, high T_c and high Z [33]:

$$COP_{max} = \underbrace{T_c \cdot \Delta T^{-1}}_{COP_C} \cdot \underbrace{\left(\sqrt{1+ZT} - T_h \cdot {T_c}^{-1}\right) \cdot \left(\sqrt{1+ZT} + 1\right)^{-1}}_{COP_r} \tag{45}$$

where COP_C is the (ideal) Carnot COP and COP_r is the relative COP. The COP depends on the temperature difference. Mainly, the COP rises with the reduction of the temperature difference ΔT. For household applications, to obtain an adequate cooling effect, the temperature differential between the sides of TEC is considered to be about $\Delta T = 25 \div 30$ K. In this case, the values $COP = 0.5 \div 0.7$ represent about 50% of the COP of a vapour compressor refrigerator [34].

3. Methods to enhance the TEC performance in refrigeration units

Some methods to enhance the TEC performance are [35]:

- Development of thermoelectric materials with high performance
- TEC design
- Thermal design
- Optimization of the internal temperature controller of the insulated compartment

3.1. Development of thermoelectric materials with high performance

A thermoelectric refrigerator unit operates with COP typically less 0.5 due to the limited cooling temperature to $\Delta T_{\max} \cong 20$ K under the ambient temperature [20]. **Figure 6** shows a comparison of the theoretical COP of a *TEC* with respect to household refrigerators [36]. Refrigerators with thermoelectric modules with materials based on alloys of Bi_2Te_3 have a COP about 1 [9] which is low enough to be competitive to the vapour-compression systems with $COP = 2 \div 4$ [37–39]. The low COP values of TECs are not considered a drawback. These systems are more suitable for a niche market sector (below 25 W) such as military and medical industries, in applications such as temperature stabilization of semiconductor lasers and vaccine cooling. Furthermore, they are also suitable for the civil market (e.g., portable refrigeration, car-seat cooler, high-quality beverage conservators). For these applications, the thermoelectric elements have the advantages that do not suffer vibrations and shocks [21, 40–42].

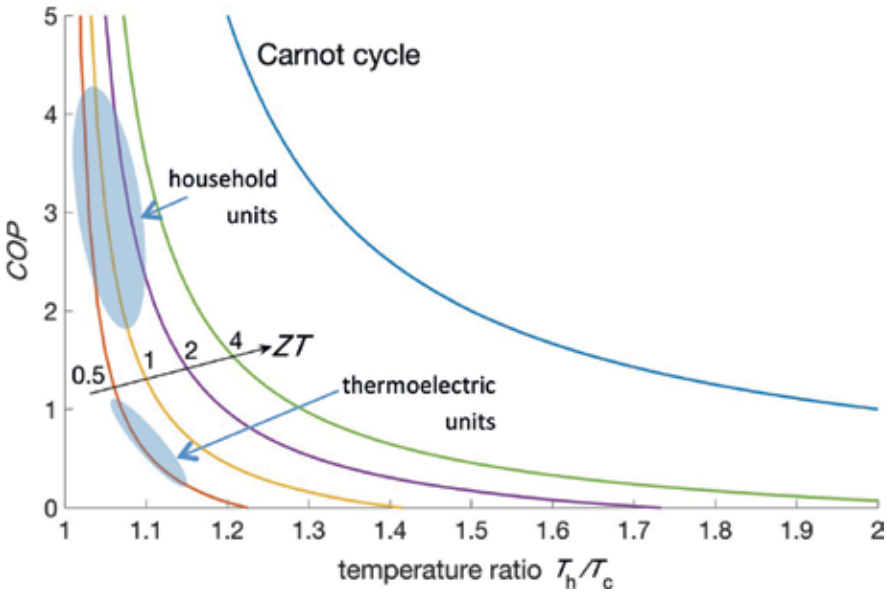

Figure 6. Chart of *COP* vs. temperature ratio for different refrigerators.

3.2. TEC design

TEC design involves the choice of number of thermocouples and thermoelement length and is carried out by looking at the module parameters. For example, for domestic refrigeration the thermoelement length optimization is strongly linked to *COP*, cooling capacity and material consumption. To improve *COP* and cooling capacity, the contact resistances, especially thermal contact resistance, must be reduced.

In devices with long thermoelements, the *COP* is high, and the contact resistances have a little effect on the cooling capacity, while in devices with short thermoelements, the contact resistances have an increased influence on the cooling capacity; in particular, starting from a long thermoelement and reducing its length, the cooling capacity increases up to a maximum value; then it decreases sharply [20].

As mentioned above, the thermal performance of a TEC depends on the thermoelectric material properties which change with the TEC operating temperature. Some manufacturers use the maximum design parameters and the performance chart [43]. The performance chart takes ΔT and $\dot{Q}_c$ as inputs and determines the current and thus the voltage needed to produce the cooling effect. Another possibility is to consider voltage, current and ΔT as known quantities (e.g. measured) in order to find $\dot{Q}_c$. A key aspect of the use of the TEC performance chart is that the module parameters are considered to be known and unchanged for different devices, while actually these parameters change because of the outcomes of the manufacturing process. The design procedure illustrated in [43] is simplified by considering the thermal resistance of the heat sink as one of the key parameters, avoiding the heat transfer analysis of the heat sink.

http://dx.doi.org/10.5772/intechopen.75439

3.3. Thermal design

Thermal design involves the determination of the heat sink geometry considering the thermal resistances and the optimization of the heat sink characteristic.

The heat sink located on the hot side is useful to dissipate heat from the TEC system to the environment and is considered an important factor affecting the TEC performance. Therefore, to enhance the TEC performance, the heat sink must have a low thermal resistance (to be minimized). Important TEC efficiency improvements are obtained by optimization of the different types of heat exchangers at the hot side (water-air system with a cold plate, pump and fan coil, finned heat sink with fan, heat pipe with fan) [44].

A normal heat sink uses fins to increase heat transfer surface. When the thermal resistance of the heat sink is computed, it is necessary to take into account an additional heat thermal resistance of the thermal grease applied to provide a good thermal contact between TEC and heat sink [45]. The design of the heat sinks is presented in [4], where some aspects useful to find the optimal heat sink geometry (fin thickness and position) are detailed.

Sometimes at the hot side of TEC, thermal storage using phase change materials (PCMs) or a heat pipe heat exchanger may take the place of a heat sink with fins in order to reduce the temperature T_c of the TEC.

For *thermal storage*, the heat sink is designed to have a high storage capacity to keep the sink temperature less than the junction temperature. In this case, PCMs are useful to improve the performance of the thermoelectric refrigerator. These high-energy-density materials have the advantage that the heat is transferred at constant temperature. In this case, T_c is constant during the phase change, so that $\dot{Q}_c$ and *COP* remain constant as well. For a conventional refrigerator, the utilization of a heat sink with fins at the cold side of the TEC supposes a fast T_c reduction until ΔT_{max} of the cooler is obtained, while using PCMs a slow reduction of the cold side temperature till ΔT_{max} is obtained. Furthermore, PCMs operate in a wide range of phase change temperatures, providing different alternatives to be used at the hot side and at the cold side of the TEC [46]. These materials are very suitable for different types of thermoelectric refrigerators for food (domestic refrigerators; refrigerators/freezers; hotel room minibar refrigerators preferred for their silent operation; refrigerators for mobile homes, trucks, recreational vehicles, and cars; food service refrigerators for airborne application; and portable picnic coolers) as well as for medicine storage which need precise temperature control [8, 46]. Refrigerators based on PCMs exhibit useful storage capacity behaviour in case of blackout, as they are able to limit the temperature variation during a blackout much more than other materials.

The *heat pipes* are heat exchangers with very high thermal conductivity using ethanol or methanol as refrigerant water. They are used on the both sides of the TEC to dissipate both the cooling and waste heat to the heat sinks. If heat pipes with a thermosiphon are used at the hot side of the TEC, the waste heat is rejected to the environment by natural or forced convection. These systems have a low thermal resistance, leading to reduction of the temperature differential between the hot side temperature of the TEC and the environmental temperature. The heat pipes are used at the cold side of TEC to keep T_c constant during peak and

off-electricity times [46, 47]. Two prototypes of thermoelectric refrigerator are described in [48], one with finned heat sink and the other one with a finned heat sink integrated in an aluminum thermosiphon in which phase change occurs. The thermosiphon depends on the specific latent heat at the phase change from vapour state to liquid state, useful to disperse the heat efficiently to the environment. The results of the experimental heat sink optimization demonstrated that the thermal resistance between the hot side of the TEC and the environment reduced with about 23.8% at 293 K environment temperature and 51.4% at 308 K, with respect to a commercial finned heat sink, and between 13.8% and 45% with respect to an optimized finned heat sink. Much more, the *COP* of this prototype is 26% at ambient temperature of 293 K, achieving 36.5% improvement at 303 K.

3.4. Optimization of the internal temperature controller of the insulated compartment

The operating conditions of a thermoelectric refrigerator depend on parameters as environment temperature, humidity, lower setpoint of the internal temperature and difference between higher and lower setpoints of the internal temperature [49].

In vapour-compression refrigerators, the internal temperature control inside the insulated compartment is generally inaccurate due to the multitude of start and stop cycles made by the compressor, leading to a temperature variation bigger than 8°C, with a negative effect on the quality of the food and on the conservation of the perishable food [50, 51]. This represents a drawback for these refrigerators compared with the thermoelectric refrigerators in which there are no start and stop cycles and the supply voltage gradually increases. However, overall the thermoelectric refrigerators are not competitive with vapour-compression refrigerators in terms of *COP* [10, 11, 48].

Most of the thermoelectric refrigerators have on/off control systems for the internal temperature. This control is critical in the period in which the TEC is switched off, because in this period, the heat stored in the heat sink connected to the hot terminal returns into the refrigerator compartment; in this way, the power consumption of the refrigerator increases and the *COP* decreases [11].

Vian and Astrain [50] carried out a study of the total power consumption on a hybrid thermoelectric system (with vapour freezer and refrigerator compartments and a thermoelectric compartment) at ambient temperature of 25°C. To optimize the system, a thermal bridge (aluminium slab) was used between the freezer compartment and the thermoelectric compartment. This thermal bridge was useful to transfer the heat flow rate from the thermoelectric compartment to the freezer in order to maintain a constant temperature of 0°C inside the thermoelectric compartment. The power consumption in these environmental conditions for each compartment was 0.67 kWh/day for the refrigerator, 0.58 kWh/day for the freezer and 0.2 kWh/day for the thermoelectric system. The results demonstrated that the total electric power consumption reduced from 63.3 W to 49.9 W (20% improvement) due to the thermal bridge. If the environmental conditions are modified (e.g., a rise of the temperature at 30°C), the total power consumption for this unit rises by 30%. Further studies showed that the thermoelectric refrigerator works in any operating condition, but the utilization of on/off

control systems at a maximum voltage decreases the electric power consumption about 40% and raises the *COP* near the maximum value obtained with the control system [11]. In addition, in [49] a reduction of electric power consumption was obtained by experimental optimization of the temperature controller for a thermoelectric refrigerator in stationary state. Their work experimentally demonstrated that the on/off temperature control system used in commercial thermoelectric refrigerators is not so efficient, but is used due to its simplicity and low cost. More efficient temperature control systems applied by the manufacturers to increase the performance of the thermoelectric refrigerator include the use of different voltage supply levels for the modules or the exploitation of proportional-integral-differential control systems. However, these control systems have a higher cost with respect to the on/off control system [11]. A more elaborated idling voltage control system was proposed from experimental optimization in [49], obtaining a 32% reduction of the electric power consumption and a *COP* growth of 64% compared with the normal on/off temperature control system. In this way, in the long term, the savings due to lower consumption compensate for the higher cost of the idling voltage control system with respect to the cost of the on/off control system.

4. Thermoelectric refrigeration unit applications

In spite of their relatively low efficiency with respect to other refrigeration technologies, the TEC technologies are experiencing a period of development, with subsequent efficiency improvement and reduction of the manufacturing costs [52]. One of the drivers that have increased the interest in the development and use of TECs as refrigerators is the absence of environmental pollution in the TEC operation, in particular, the absence of chlorofluorocarbon (CFC) issues. The current trends towards replacement of CFCs consider good solutions with low global warming potential (GWP) using natural refrigerants like CO_2 used at pressures much higher than traditional refrigerants [6, 53]. Further drivers to increase the TEC applications depend on positive aspects of the TECs such as low noise, possibility of operation in different positions, absence of mechanical vibrations, ease of transportation and possibility to obtain accurate temperature control.

Today, thermoelectric refrigerators are the most significant applications at the commercial level [17, 40]. In addition to domestic refrigerators [10, 54, 60], other applications have been developed for food-related services, such as portable refrigerators [55–57], food expositors, refrigerators mounted on vehicles for perishable food transportation as well as low-power refrigerators for minibar, hotel room, offices, boats and aircraft services [8]. Further applications are available for the medical sector (vaccine transportation and instruments for blood coagulators, dew point sensors and others), for the military sector and for scientific devices subject to precise temperature control [58]. In addition, thermoelectric systems are found in the automobile industry for air conditioning or car-seat coolers [59] and in different applications to the microelectronics sector [60, 61].

Besides the applications mentioned above, the present trend towards the use of green energy raises the attention on the possibility of supplying the thermoelectric refrigerator through

energy produced from renewable sources. The refrigerators powered by renewable sources may work in stand-alone of off-grid connection. To connect a thermoelectric refrigerator to the PV module in off-grid mode, the possibilities are [8]:

- the refrigerator is directly powered by the PV panel (the main components are the PV panel, the battery bank, the battery charge controller and the refrigerator); and
- the refrigerator is indirectly powered by the PV panel (the main components are the PV panel, the battery bank, the inverter for AC grid connection and the AC-supplied refrigerator).

Solar-driven thermoelectric refrigerators are of two types, namely, PV-battery thermoelectric systems and PV-PCM thermoelectric systems. The performance of the PV-battery thermoelectric systems depends on the intensity of solar radiation and temperature difference at the hot and cold sides of the TEC. In the case of PV-PCM thermoelectric systems, the PV is directly connected to the TECs having PCMs fixed at the cold side to replace the battery. Thermal storages have generally restricted capacity, and to improve this in some applications, the thermoelectric units use PCM integrated with thermal diodes [62].

Table 1 presents the technical characteristics of some selected thermoelectric refrigeration units with data available from the literature. The selected cases represent various applications with

Ref.	Volume (litres)	ΔT (°C)	Voltage (V)	Cooling capacity (W)	Electrical power input (W)	*COP*	Heat sink at the hot side	Power supply	Applications
[63]	3.6	40	18 (DC)	1.44	12	0.12	With fan	PV	Medicine storage
[64]	40	11.6	110 (AC)	25	13.75	0.69	With fan	Grid	On-grid applications
[55, 56]	—	20	13 (DC)	12	52	0.23	Finned	PV	Cold storage of vaccine, foodstuffs and drinks in remote areas, and outdoor off-grid applications
[10]	115/115/40	10	(DC)	15.6	52	0.3	With fans	Grid	Domestic refrigerator
[57]	13	22	12÷24 (DC)	15.3	95.6	0.16	With fan	PV	Off-grid areas
[65]	225	18.9	12 (DC)	11	48.1	0.23	Thermosiphon with two phase	Grid	Camping vehicles, buses, and special transports for electro medicine
[66]	21.9	40.5 /48.5/ 54.2	8/8/10.3 /11.56	5.2/6.5/ 8.8	20/30.9/40	0.26/0.21/ 0.22	Finned with fan	Grid	Laboratory
[67]	0.83	17.6	18	1.5	15.4	0.1	Finned with fan	DC	Vaccine carrier

Table 1. Technical characteristics and performance of thermoelectric refrigeration units.

different capacities (from a few litres for medicine transportation to some hundreds of litres for food storage), temperature difference, type of heat sink, AC or DC voltage input, powering from electrical grid connection or PV and electrical power input. The performance of these units is indicated with cooling capacity and *COP*.

5. Conclusions

Thermoelectric refrigeration solutions are gaining relevance because of a number of positive aspects, such as long duration, noiseless operation, limited maintenance needs, absence of flammable or toxic refrigerants, possibility of being used in different positions and in movable solutions as well as flexibility of usage through optimized control. This chapter has summarized the principles of thermoelectric refrigeration, by presenting the analytical formulations determining the heat flow rate, cooling capacity and *COP* of a TEC, illustrating the methods to enhance the TEC performance and indicating the current applications of thermoelectric refrigeration. The future improvement of the TEC performance, together with the operational flexibility of the TEC driven by appropriate control systems, will increase the variety of the applications of thermoelectric refrigeration in different contexts, from single units to their inclusion into integrated energy systems.

Author details

Diana Enescu

Address all correspondence to: diana.enescu@valahia.ro

Department of Electronics, Telecommunications and Energy, Valahia University of Targoviste, Targoviste, Romania

References

[1] Zheng JC. Recent advances on thermoelectric materials. Frontiers of Physics in China. 2008;**3**(3):269-279. DOI: 10.1007/s11467-008-0028-9

[2] Sandoz-Rosado EJ. Investigation and Development of Advanced Models of Thermoelectric Generators for Power Generation Applications [thesis]. Rochester Institute of Technology, Rochester NY, USA; 2009. 82 p. Available from: http://scholarworks.rit.edu/theses

[3] Rowe DM. Handbook of Thermoelectrics. Introduction. Boca Raton, FL: CRC Press; 1995 720 p. ISBN: 9780849301469

[4] Lee HS. Thermal Design, Heat Sinks, Thermoelectrics, Heat Pipes, Compact Heat Exchangers, and Solar Cells. NJ: Wiley; 2010. 650 p. DOI: 10.1002/9780470949979

[5] Tritt TM, Subramanian MA. Thermoelectric materials, phenomena, and applications: A Bird's eye view. MRS Bulletin. 2006;**31**:188-198. DOI: org/10.1557/mrs2006.44

[6] Tassou SA, Lewis JS, Ge YT, Hadawey A, Chaer I. A review of emerging technologies for food refrigeration applications. Applied Thermal Engineering. 2010;**30**(4):263-276. DOI: 10.1016/j.applthermaleng.2009.09.001

[7] Riffat SB, Ma X. Thermoelectrics: A review of present and potential applications. Applied Thermal Engineering. 2003;**23**(8):913-935. DOI: 10.1016/S1359-4311(03)00012-7

[8] Enescu D, Ciocia A, Mazza A, Russo A. Solutions based on thermoelectric refrigerators in humanitarian contexts. Sustainable Energy Technologies and Assessments. 2017;**22**:134-149. DOI: 10.1016/j.seta.2017.02.016

[9] Goldsmid HJ. Introduction to Thermoelectricity. Berlin Heidelberg: Springer-Verlag. Springer Series in Material Science. 2010;**121**:242. DOI: 10.1007/978-3-642-00716-3

[10] Min G, Rowe GM. Experimental evaluation of prototype thermoelectric domestic-refrigerator. Applied Energy. 2006;**83**(2):133-152. DOI: 10.1016/j.apenergy.2005.01.002

[11] Astrain D, Martínez A, Gorraiz J, Rodríguez A, Pérez G. Computational study on temperature control Systems for Thermoelectric Refrigerators. Journal of Electronic Materials. 2012;**41**(6):1081-1090. DOI: 10.1007/s11664-012-2002-0

[12] Barbieri J, Colombo E, Ndam Mungwe J, Riva F, Berizzi A, Bovo C, et al. Set 4 food project. Sustainable Energy Technologies for food utilization. 2014. Available from: www.set4food.org [Accessed: December 27, 2017]

[13] Martínez A, Astrain D, Rodríguez A, Aranguren P. Advanced computational model for Peltier effect based refrigerators. Applied Thermal Engineering. 2016;**95**:339-347. DOI: 10.1016/j.applthermaleng.2015.11.021

[14] Lee HS. Thermoelectrics: Design and materials. Western Michigan University, USA: Wiley; 2017. 887p. DOI: 10.1016/j.applthermaleng.2015.11.021

[15] Landau LD, Lifshitz EM, Pitaevskii LP. Electrodynamics of continuous media. 2nd ed. UK: Pergamon Press; 1984. 460 p. ISBN: 9788181477934

[16] Lee HS. The Thomson effect and the ideal equation on thermoelectric coolers. Energy. 2013;**56**:61-69. DOI: 10.1016/j.energy.2013.04.049

[17] Martinez A, Astrain D, Rodriguez A, Aranguren P. Advanced computational model for Peltier effect based refrigerators. Applied Thermal Engineering. 2016;**95**:339-347. DOI: 10.1016/j.applthermaleng.2015.11.021

[18] Martínez A, Astrain D, Rodríguez A. Dynamic model for simulation of thermoelectric self cooling applications. Energy. 2013;**55**:1114-1126. DOI: 10.1016/j.energy.2013.03.093

[19] Parrot JE, Penn AW. The design theory of thermoelectric cooling elements and units. Solid-State Electronics. 1961;**3**:91-99. DOI: 10.1016/0038-1101(61)90062-4

[20] Min G, Rowe DM. Improved model for calculating the coefficient of performance of a Peltier module. Energy Conversion and Management. 2000;**2**(41):163-171. DOI: 10.1016/S0196-8904(99)00102-8

[21] Chen G, Dresselhaus MS, Dresselhaus G, Fleurial JP, Caillat T. Recent developments in thermoelectric materials. International Materials Reviews. 2003;**48**(1):45-66. DOI: 10.1179/095066003225010182

[22] Suh D, Lee S, Hyeona Mun H, Park SH, Lee KH, Kim SW, Choi JY, Baik S. Enhanced thermoelectric performance of Bi0.5Sb1.5Te3-expanded graphene composites by simultaneous modulation of electronic and thermal carrier transport. Nano Energy. 2015;**13**:67-76. DOI: 10.1016/j.nanoen.2015.02.001

[23] Peng QZ, Ye Ko San YK, Samuel Khong S, Jonathan Sim J, Ezhilvalavan S, Ma J, Hoon HH. Advanced Structural and Functional Materials for Protection. In: Proceedings of the International Conference on Materials for Advanced Technologies (ICMAT2011), Symposium W; DOI: 10.4028/www.scientific.net/SSP.185

[24] Nolas GS, Poon J, Kanatzidis M. Recent developments in bulk thermoelectric materials. MRS Bulletin. 2006;**31**(3):199-205. DOI: 10.1557/mrs2006.45

[25] Biswas K, He J, Zhang Q, Wang G, Uher C, Dravid VP, Kanatzidis MG. Strained endotaxial nanostructures with high thermoelectric figure of merit. Nature Chemistry. 2011;**3**:160-166. DOI: 10.1038/nchem.955

[26] Gupta MP, Sayer M, Mukhopadhyay S, Kumar S. Ultrathin thermoelectric devices for on-chip Peltier cooling. IEEE Transactions on Computer, Packaging, and Manufacturing Technology. 2011;**1**(9):1395-1405. DOI: 10.1109/TCPMT.2011.2159304

[27] Rowe DM. Thermoelectrics Handbook: Macro to Nano. Boca Raton, FL: CRC Press Taylor & Francis; 2006 1014 p. ISBN 9780849322648

[28] Elarusi A, Attar A, Lee H. Optimal Design of a Thermoelectric Cooling/heating system for Car seat climate control (CSCC). Journal of Electronic Materials. 2017;**46**(4):1984-1995. DOI: 0.1007/s11664-016-5043-y

[29] Huang MJ, Chou PK, Lin MC. Thermal and thermal stress analysis of a thin-film thermoelectric cooler under the influence of the Thomson effect. Sensors and Actuators A-Physical. 2006;**126**(1):122-128. DOI: 10.1016/j.sna.2005.10.006

[30] Fraisse G, Ramousse J, Sgorlon D, Goupil C. Comparison of different modeling approaches for thermoelectric elements. In Energy Conversion and Management. 2013; **65**:351-356. DOI: 10.1016/j.enconman.2012.08.022

[31] Chen J, Yan Z. The influence of Thomson effect on the maximum power output and maximum efficiency of a thermoelectric generator. Journal of Applied Physics. 1996;**79**: 8823-8828. DOI: 10.1063/1.362507

[32] Chen WH, Liao CY, Hung CI. A numerical study on the performance of miniature thermoelectric cooler affected by Thomson effect. Applied Energy. 2012;**89**:464-473. DOI: 10.1016/j.apenergy.2011.08.022

[33] Bansal P, Vineyard E, Abdelaziz O. Status of not-in-kind refrigeration technologies for household space conditioning, water heating and food refrigeration. International Journal of Sustainable Built Environment. 2012;**1**:85-101. DOI: 10.1016/j.ijsbe.2012.07.003

[34] Zhang HY. A general approach in evaluating and optimizing thermoelectric coolers. Int. Journal of Refrigeration. 2010;**33**(6):1187-1196. DOI: 10.1016/j.ijrefrig.2010.04.007

[35] Gökçek M, Şahin F. Experimental performance investigation of minichannel water cooled-thermoelectric refrigerator. Case Studies in Thermal Engineering. 2017;**10**:54-62. DOI: 10.1016/j.csite.2017.03.004

[36] Chen G, Shakouri A. Heat transfer in nanostructures for solid-state energy conversion. Journal of Heat Transfer. 2001;**124**(2):242-252. DOI: 10.1115/1.1448331

[37] Gauger DC, Shapiro HN, Pate MB. Alternative technologies for refrigeration and air-conditioning applications. United States Environmental Protection Agency. Project Summary EPA/600/SR-95/066; 1995

[38] Bell L. Use of thermal isolation to improve thermoelectric system operating efficiency. In: Proceeding 21st Int. Conf. on Thermoelectrics, ICT'02; 29–29 Aug. 2002; Long Beach, California (USA), p. 477-487. DOI: 10.1109/ICT.2002.1190363

[39] Hermes CJL, Barbosa Jr JR. Thermodynamic comparison of Peltier, Stirling, and vapor compression. Applied Energy. 2012;**91**:51-58. DOI: 10.1016/j.apenergy.2011.08.043

[40] Zhao D, Tan G. A review of thermoelectric cooling: Materials, modeling and applications. Applied Thermal Engineering. 2014;**66**:15-24. DOI: 10.1016/j.applthermaleng.2014.01.074

[41] Enescu D, Virjoghe EO. A review on thermoelectric cooling parameters and performance. Renewable & Sustainable Energy Reviews. 2014;**38**:903-916. DOI: 10.1016/j.rser.2014.07.045

[42] Yeom J, Shannon MA, Singh T. Micro-coolers. In: Reference Module in Materials Science and Materials Engineering. Elsevier; 2017. pp. 2-46. DOI: 10.1016/B978-0-12-803581-8.00568-3

[43] Huang BJ, Chin CJ, Duang CL. A design method of thermoelectric cooler. International Journal of Refrigeration. 2000;**23**:208-218. DOI: 10.1016/S0140-7007(99)00046-8

[44] Astrain D, Aranguren P, Martínez A, Rodríguez A, Pérez MG. A comparative study of different heat exchange systems in a thermoelectric refrigerator and their influence on the efficiency. Applied Thermal Engineering. 2016;**103**:1289-1298. DOI: 10.1016/j.applthermaleng.2016.04.132

[45] Ritzer TM, Lau PG. Economic Optimization of Heat Sink Design. In: Proceedings of the 13th Int. Conference on Thermoelectrics; 30 August-1September; Kansas City, Missouri (USA); 1995; AIP Conference Proceedings 316, 177 (1994). DOI: 10.1063/1.46788

[46] Riffat SB, Omer SA, Ma X. A novel thermoelectric refrigeration system employing heat pipes and a phase change material: An experimental investigation. Renewable Energy. 2001;**23**(2):313-323. DOI: 10.1016/S0960-1481(00)00170-1

[47] Faghri A. Heat Pipe Science and Technology. Taylor & Francis; 1995 859 p. ISBN 978-1560323839

[48] Astrain A, Vián JG, Domínguez M. Increase of COP in the thermoelectric refrigeration by the optimization of heat dissipation. Applied Thermal Engineering. 2003;**23**(17):2183-2200. DOI: 10.1016/S1359-4311(03)00202-3

[49] Martinez A, Astrain D, Rodríguez A, Pérez MG. Reduction in the electric power consumption of a thermoelectric refrigerator by experimental optimization of the temperature controller. Journal of Electronic Materials. 2013;**42**(7):1499-1503. DOI: 10.1007/s11664-012-2298-9

[50] Vián JG, Astrain DD. Development of a hybrid refrigerator combining thermoelectric and vapor compression technologies. Applied Thermal Engineering. 2009;**29**(16):3319-3327. DOI: 10.1016/j.applthermaleng.2009.05.006

[51] He MG, Li TC, Liu ZG, Zhang Y. Testing of the mixing refrigerants HFC152a/HFC125 in domestic refrigerator. Applied Thermal Engineering. 2005;**25**(8–9):1169-1181. DOI: 10.1016/j.applthermaleng.2004.06.003

[52] Sarbu I, Sebarchievici C. Review of solar refrigeration and cooling systems. Energy and Buildings. 2013;**67**:286-297. DOI: 10.1016/j.enbuild.2013.08.022

[53] Aprea C, Greco A, Maiorino A. An experimental evaluation of the greenhouse effect in the substitution of R134a with CO_2. Energy. 2012;**45**:753-761. DOI: 10.1016/j.energy.2012.07.015

[54] Rodríguez A, Vián JG, Astrain D. Development and experimental validation of a computational model in order to simulate ice cube production in a thermoelectric ice-maker. Applied Thermal Engineering. 2009;**29**:2961-2969. DOI: 10.1016/j.applthermaleng.2009.03.005

[55] Dai YJ, Wang RZ, Ni L. Experimental investigation on a thermoelectric refrigerator driven by solar cells. Renewable Energy. 2003;**28**:949-959. DOI: 10.1016/S0960-1481(02)00055-1

[56] Dai Y, Wang J, Ni L. Experimental investigation and analysis on a thermoelectric refrigerator driven by solar cells. Journal of Solar Energy Materials & Solar Cells. 2003;**77**(4): 377-391. DOI: 10.1016/S0927-0248(02)00357-4

[57] Abdul-Wahab SA, Elkamel A, Al-Damkhi AM, Al-Habsi IA, Al-Rubaiey HS, Al-Battashi AK, Ali R, Al-Tamimi AR, Al-Mamari KH, Chutani MU. Design and experimental investigation of portable solar thermoelectric refrigerator. Renewable Energy. 2009;**34**:30-34. DOI: 10.1016/j.renene.2008.04.026

[58] Marlow R, Burke E. Module design and fabrication. In: Rowe DM, editor. Handbook of Thermoelectrics: Introduction. Boca Raton, FL: CRC Press; 1995. p. 591. ISBN 9780849301469

[59] Choi HS, Yun S. Whang K-il. Development of a temperature-controlled car-seat system utilizing thermoelectric device. Applied Thermal Engineering. 2007;**27**(17–18):2841-2849. DOI: 10.1016/j.applthermaleng.2006.09.004

[60] Gordon JM, Ng KC, Chua HT, Chakraborty A. The electro-adsorption chiller: A miniaturized cooling cycle with applications to micro-electronics. International Journal of Refrigeration. 2002;**25**(8):1025-1033

[61] Zhang Y, Christofferson J, Shakouri A, Zeng G, Bowers JE, Croke E. On-Chip high speed localized cooling using Superlattice Microrefrigerators. IEEE Transactions on Components and Packaging Technologies. 2006;**29**(2):395-401

[62] Aste N, Del Pero C, Leonforte F. Active refrigeration technologies for food preservation in humanitarian context-a review. Sustainable Energy Technologies and Assessments. 2017; **22**:150-160. DOI: 10.1016/j.seta.2017.02.014

[63] Field RL. Photovoltaic/thermoelectric refrigerator for medicine storage for developing countries. Solar Energy. 1980;**25**:445-447. DOI: 10.1016/0038-092X(80)90452-1

[64] Bansal PK, Martin A. Comparative study of vapour compression, thermoelectric and absorption refrigerators. International Journal of Energy Research. 2000;**24**(2):93-107. DOI: 10.1002/(SICI)1099-114X(200002)24:2<93::AID-ER563>3.0.CO;2-6

[65] Vián JG, Astrain D. Development of a thermoelectric refrigerator with two phase thermosyphons and capillary lift. Applied Thermal Engineering. 2009a;**29**:1935-1940. DOI: 10.1016/j.applthermaleng.2008.09.018

[66] Jugsujinda S, Vora-ud A, Seetawan T. Analyzing of thermoelectric refrigerator performance. Procedia Engineering. 2011;**8**:154-159. DOI: 10.1016/j.proeng.2011.03.028

[67] Ohara B, Sitar R, Soares J, Novisoff P, Nunez-Perez A, Lee H. Optimization strategies for a portable thermoelectric vaccine refrigeration system in developing communities. Journal of Electronic Materials. 2015;**44**(6):1614-1626. DOI: 10.1007/s11664-014-3491-9

Chapter 12

Thermoelectric Cooling

Raghied M. Atta

Additional information is available at the end of the chapter

http://dx.doi.org/10.5772/intechopen.75791

Abstract

In this chapter, design and analysis study of thermoelectric cooling systems are described. Thermoelectric (TE) cooling technology has many advantages over the conventional vapor-compression cooling systems. These include: they are more compacted devices with less maintenance necessities, have lower levels of vibration and noise, and have a more precise control over the temperature. These advantages have encouraged the development of new applications in the market. It is likely to use TE modules for cooling the indoor air and hence compete with conventional air-conditioning systems. These systems can include both cooling and heating of the conditioned space. In order to improve the performance of the TE cooling systems, the hot side of the TE should be directly connected to efficient heat exchangers for dissipation of the excessive heat. Finally, TE cooling systems can be supplied directly by photovoltaic to produce the required power to run these cooling systems.

Keywords: thermoelectric coolers, heat transfer, heat exchangers, thermal modeling, cooling performance, solar power

1. Introduction

There are three main types of cooling systems used in air conditioners and refrigerators; each has its own advantages and disadvantages [1]. Air conditioners, however, have better performance than refrigerators as only a smaller temperature difference than refrigerators is required [1]. Vapor compression coolers have a high coefficient of performance (COP) and high cooling capacities. However, they have a noisy operation and use refrigerants with high global warming potential (GWP) such as R134a. R513A is a lower GWP alternative of R134a; however, it generally reduces the COP of the cooling systems [2]. Absorption coolers have moderate values of COP with the advantage of recovering waste heat. However, such systems are usually heavy and bulky. Thermoelectric (TE) coolers are portable with no noise, but they have

relatively low COPs. Various studies on thermoelectricity have examined its operation with power directly supplied by photovoltaic to produce the required electricity to run the cooling systems [3, 4]. The electrical current supplied by photovoltaic which is consumed by TE devices, is a direct current so that no DC/AC inverter is required.

Using TE modules, several researchers reported cooling small volumes such as submarines [5]. TE modules have been proposed to be used in building applications using active building envelopes [6, 7]. Such studies underlined the promising future of the TE modules in cooling applications.

General comparison between these three types of coolers for air conditioners is shown in **Table 1** [8].

Recent studies provide two possible directions that can lead to considerable progress in TE cooling [3]:

1. improving intrinsic efficiencies of TE materials, and
2. improving thermal design and optimization of the current available TE cooling modules.

Introducing efficient heat sinks at both the hot and cold side of TE coolers greatly influences the cooling COP. Air cooled heat sink forced convection with fan [9, 10], water cooled heat sink [11] and heat sink integrated with heat pipe [12, 13] are frequently employed techniques. This review will focus on the development of TE cooling with great concerns on advances in materials, modeling and optimization approaches.

	Type	VCAC	AAC (single effect)	TEAC
Cooling	Cooling capacity, W	2500–4500	15–2x104 KW	15–360
	Input electric power, W	750–1670	1.8–54 KW	36–1495
	COPc	2.6–3.0	0.6–0.7	0.38–0.45
	Work permit temperature range, °C	18–45	N/A	0–70
Noise, Db		35–48 Indoor	N/A	N/A
Size		Medium	Big	Small
Life expectancy, years		10–12	≈ 15	≈ 23
Price		Low	High	High

Table 1. Comparison between the three types of coolers for air conditioners.

http://dx.doi.org/10.5772/intechopen.75791

2. Thermoelectric coolers

When two different metals or semiconductors are connected together and the two connections held at different temperatures, there are many irreversible phenomena that can take place at the same time [14]. These are the Joule effect, Fourier effect, Thomson effect, Seebeck effect and Peltier effect. The Peltier effect is the most interesting among them for TE cooling. If a circuit contains two connections between different conductors or semiconductors, applying a DC volt will cause heat to transfer from one junction to the other. For producing the Peltier effect, semiconductor alloy materials, such as Bi_2Te_3 and SiGe, are better than metals [15]. The principle of TE coolers utilizing semiconductor Peltier effects is shown in **Figure 1**. The heat is

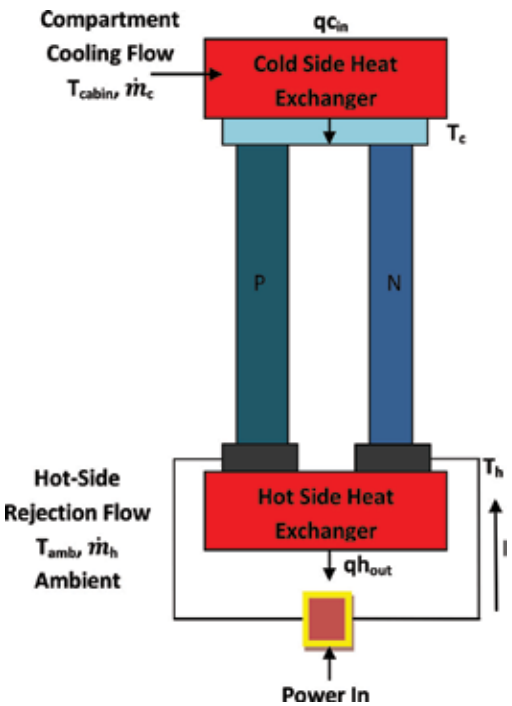

Figure 1. Principle of thermoelectric coolers utilizing semiconductor Peltier effects.

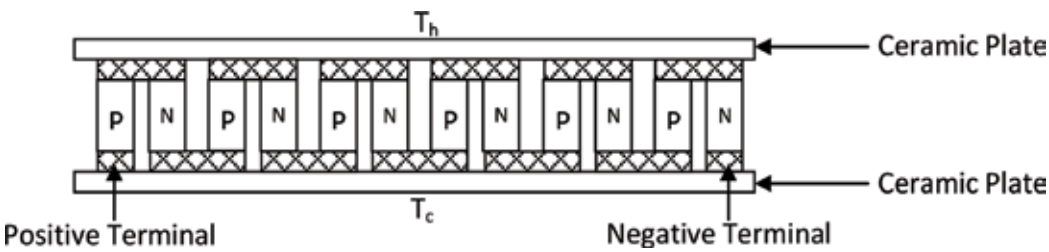

Figure 2. A conventional thermoelectric module with multiple thermoelements.

transferred from the cooled space to the hot-side heat sink through n-type and p-type semiconductor thermoelements which rejects the heat to the environment. The heat flow direction through the semiconductor materials will be reversed if the electric current direction is reversed.

A typical TE module usually consists of a large number of n-type and p-type bulk semiconductor thermoelements that are connected electrically in series and thermally in parallel and sandwiched between two ceramic plates, as illustrated in **Figure 2**.

3. Applications using thermoelectric coolers

Commercially available TE coolers are used in applications where design criteria of the cooling system include factors such as high reliability, low weight, small size, intrinsic safety for hazardous electrical environments and accurate temperature control. TE coolers are more appropriate for unique applications such as space missions, medical and scientific equipment where low COP is not an apparent disadvantage.

TE cooling devices are used for cooling small volumes, such as portable and domestic refrigerator, portable icebox and beverage can cooler [12, 16–21], where the cooling requirements are not too high. In general, the COP for both domestic and portable thermoelectric refrigerators is usually less than 0.5, when operating at an inside/outside temperature difference between 20 and 25°C.

Electronic devices like PC processors produce very large amount of heat during their operation which add great challenge to the thermal management as reliable operation temperature for these electronic devices has to be maintained. TE cooling devices have also been applied to scientific and laboratory equipment cooling for laser diodes and integrated circuit chips [22] to reduce the thermal noise and the leakage current of the electronic components where conventional passive cooling technologies cannot fully meet the heat dissipation requirements. For example, cooling CdZnTe detectors for X-ray astronomy between 30 and 40°C can reduce the leakage current of the detectors and allows the use of pulsed reset preamplifiers and long pulse shaping times, which significantly improves their energy resolution. Integrating thin film TE coolers with microelectronic circuits has been implemented using micromachining technology.

TE cooler appears to be especially favorable for automotive applications [23]. Besides the automobile air-conditioning system and automobile mini refrigerators, researchers also utilized TE device to control car seat temperature to either cooling down or heating up [24].

Some researchers are trying to improve thermoelectric domestic air-conditioning systems [25–27] hoping that these systems can be competitive with the current widely used vapor compression systems. They investigated TE cooling devices for small-scale space's conditioning application in buildings [26]. A TE cooling unit was assembled and generated up to 220 W of cooling capacity with a maximum COP of 0.46 under the input electrical current of 4.8 A for each module.

Active thermal window (ATW) and transparent active thermoelectric wall (PTA) were also introduced for room cooling application in applications where conventional air-conditioning

system is not easy to install [28, 29]. Thermoelectric cooling has also been applied in other occasions, such as generating fresh water [30–33] and active building envelope system [7, 34].

TE systems can be directly connected to a PV panel. Since TE devices are low voltage driven devices, they can accept a power supplied by PV panel without conversion. This advantage makes TE devices attractive for building air-conditioning applications [27, 30]. This solar cooling technique can reduce the energy consumption and the environmental impact issues raised by conventional refrigeration and air-conditioning systems. Batteries can also be used to store DC voltages when sunlight is available while supplying DC electrical energy in a discharging mode in the absence of daylight. A battery charge regulator is needed to protect the battery form overcharging. Solar thermoelectric can be used in cooled ceiling applications to remove of a large fraction of sensible cooling load. In this case, the TE modules are connected in series and sandwiched between aluminum radiant panels and heat pipe sinks in ceilings [35].

4. Analysis of thermoelectric elements

The basic unit of the TE cooler is the n-type and p-type thermoelements. A bottom-up modeling approach is to construct the model at element level with the assumption that both types of thermoelements are exactly the same but opposite direction of the Peltier-Seebeck effect.

In the cooling mode, the cooling capacity $Q_c = (mc_p)_c\,(T_{cout} - T_{cin})$, the heat dissipated in the hot-side heat sink $Q_h = (mc_p)_h\,(T_{hout} - T_{hin})$, the electric input power $W = Q_h - Q_c$, and the cooling COP_c can be expressed by:

$$COP_c = \frac{Q_c}{W} = \frac{1}{\frac{T_{hout} - T_{hin}}{T_{cout} - T_{cin}} C_r - 1} \tag{1}$$

where T_{cin} is the temperature of the inlet fluid in the cold side of the TE system, T_{cout} is the temperature of the outlet fluid in the cold side of the TE system, T_{hin} is the temperature of the inlet fluid in the hot side of the TE system, T_{hout} is the temperature of the outlet fluid in the hot side of the TE system, $(mc_p)_c$ is the thermal conductance of cold side of the TE system, $(mc_p)_h$ is the thermal conductance of hot side of the TE system, m is the mass rate of the fluid, c_p is the specific heat capacity of the fluid and $C_r = \frac{(mc_p)_h}{(mc_p)_c}$ is the heat capacity ratio. In the heating mode, $COP_h = \frac{Q_h}{W} = 1 + COP_c$.

If some of the parameters for TE elements are available, the ideal COP_c ($COP_{C,id}$) and COP_h ($COP_{h,id}$) can be expressed as:

$$COP_{C,id} = \frac{Q_c}{W} = \frac{\alpha_{pn} T_c - \frac{KR\Delta T}{V} - \frac{1}{2} V}{V + \alpha_{pn} \Delta T} \tag{2}$$

$$COP_{h,id} = \frac{Q_h}{W} = \frac{\alpha_{pn} T_h - \frac{KR\Delta T}{V_R} + \frac{1}{2} V}{V + \alpha_{pn} \Delta T} \tag{3}$$

where α_{pn} is the Seebeck coefficient, R is the electrical resistivity, K is the thermal conductivity, V is electrical applied volt and $\Delta T = T_h - T_c$ is the temperature difference between the cold and the hot side of thermoelements at the ceramic plate locations.

For the optimum working voltage *Vopt* and optimum working current *Iopt*,

$$V_{opt} = \frac{\alpha_{pn}\,\Delta T}{\sqrt{1+ZT_m}-1} \tag{4}$$

$$I_{opt} = \frac{V_{opt}}{R} = \frac{\alpha_{pn}\,\Delta T/R}{\sqrt{1+ZT_m}-1} \tag{5}$$

The corresponding maximum $COP_{c,d}$, i.e., $COP_{c,opt}$, will be;

$$COP_{c,\,opt} = \frac{Tc}{T_h - T_c}\frac{\left(\sqrt{1+ZT_m}-\frac{T_h}{T_c}\right)}{\left(\sqrt{1+ZT_m}+1\right)} \tag{6}$$

where T_m is the average temperature of the thermocouple defined as:

$$T_m = \frac{1}{2}(T_h + T_c) \tag{7}$$

Similarly, the optimum coefficient of performance of heating $COP_{h,opt}$ can be expressed as:

$$COP_{h,\,opt} = \frac{T_h}{T_h - T_c}\left(1 - 2\,\frac{\sqrt{1+ZT_m}-1}{ZT_m}\right) \tag{8}$$

A comprehensive parameter that described the thermoelectric characteristics is the figure of merit of the thermocouple Z which can be defined as:

$$Z = \frac{\left(\alpha_p - \alpha_n\right)^2}{(KR)_{min}} = \frac{\alpha_{pn}^2}{(KR)_{min}} \tag{9}$$

This parameter can be made dimensionless by multiplying it by T (the average temperature of the hot side and the cold side of the TE module):

$$ZT = \frac{\alpha_{pn}^2 T}{(KR)_{min}} \tag{10}$$

The value of Z is related only to the physical properties of the thermocouple material. The higher the figure of merit Z for the material, the better the thermoelectric properties it has. The best commercial thermoelectric materials currently have ZT values around 1.0. The highest ZT value reported in research is about 3 at temperature of 550 K [36].

Maximizing Q_c and COP can been obtained by optimizing some parameters like the number of thermoelement pairs for each stage and the applied electrical current [37]. For cascaded

coolers, the expression for the cooling rate q_i per unit area for the i^{th} stage, depending on the COP of the i^{th} stage and on the cooling rate per unit area of the i^{th} stage q_I in connection with the heat source, can be presented by [38]:

$$q_i = q_i\left(1 + COP_I^{-1}\right)\left(1 + COP_{I-1}^{-1}\right)\ldots\left(1 + COP_{I-i}^{-1}\right) \tag{11}$$

In this context, each stage, that is considered from the heat source to the heat sink, must have a cooling capacity higher than the one in the previous stage. Truly, each stage will reject both the extracted heat from the previous stage and the electrical power supplied to the stage. Theoretical study for internally cascaded multistage TE couples showed that an enhancement of a 25.2% in the maximum COP can be achieved by using cascaded 3-stage TE modules [39]. A 1400 W TE air-conditioning system using multiple TE modules was investigated [40].

5. Development of thermoelectric materials

As shown by the primary criterion of merit, a good thermoelectric material should possess high Seebeck coefficient, low thermal conductivity and high electrical conductivity. However, these three parameters are interrelated; hence they have to be optimized to get the maximized *ZT* [41, 42]. The changes in these parameters will unlikely lead to a net increase in *ZT*, since any favorable change in one parameter will be accompanied by an unfavorable change in the other parameters. For instance, if the electrical conductivity is too low, we might like to increase the carrier concentration. However, during increasing the carrier concentration which in turn will increase the electrical conductivity, the Seebeck coefficient will also decrease and the electronic contribution to the thermal conductivity will increase. This dilemma forced the maximum ZT of any thermoelectric material to be held at $ZT = 1$ for many years [43]. The devices made of these materials were operated at a power conversion efficiency of only 4–5%.

Conventional thermoelectric materials are bulk alloy materials such as Bi_2Te_3, PbTe, SiGe and $CoSb_3$. Eventually it was determined that the most efficient bulk thermoelectric materials are high carrier concentration alloyed semiconductors. The high carrier concentration results in a good electrical conductivity while optimizing the electrical properties can be achieved by varying the carrier concentration. Transport of phonons (quantized lattice vibrations which carry heat) can be disrupted by alloying, which results in a reduced thermal conductivity. For this approach, it was discovered that good thermoelectric materials are phonon-glass electron-crystal material [44, 45], where high mobility electrons are free to transport charge and heat but the phonons are disrupted at the atomic scale from transporting heat. The recent trend to optimize the thermoelectric material's performance is achieved by reducing the material thermal conductivity, especially the lattice thermal conductivity [46]. Reducing the lattice thermal conductivity can be achieved by adding low sound velocity heavy elements, such as Bi, Te, and Pb. Examples of commercial thermoelectric alloys include $BixSb_{2\_x}Te_3$ at room temperature, PbTe–PbSe at moderate temperature, and $Si_{80}Ge_{20}$ at high temperature.

A new strategy for high efficiency "phonon-liquid electron-crystal" thermoelectric materials where a crystalline sublattice for electronic conduction is surrounded by liquid like ions was

introduced. The results of an experiment performed on a liquid like behavior of copper ions around a crystalline sublattice of Se in $Cu_{2-x}Se$ showed a very low lattice thermal conductivity which increased the value of *ZT* in this simple semiconductor [47].

The efficiency of TE devices can be further enhanced through nanostructural engineering [44] using two primary approaches: bulk materials containing nano-scale constitutes and nano-scale materials themselves. By the introduction of nanostructures, ZT was pushed to about 1.7 [48] with power conversion efficiency of 11–15%.

Many reviews have summed up progress on thermoelectric materials [49, 50], bulk thermoelectric materials [45] and low-dimensional thermoelectric materials [43, 51, 52]. Low-dimensional materials, including 2-D quantum wells, 1-D quantum wires and 0-D quantum dots, possess the quantum confinement effect of the electron charge carriers that would enhance the Seebeck coefficient and thus the power factor [53]. Furthermore, the introduced various interfaces will scatter phonons more effectively than electrons so that it reduces the thermal conductivity more than the electrical conductivity [18].

Two-dimensional Bi_2Te_3 quantum well improved *ZT* due to the enhancement of thermopower [54]. The *ZT* of Bi_2Te_3 quantum well structures are estimated to be much higher than its bulk material. The highest *ZT* observed was 2.4 using Bi_2Te_3–Sb_2Te_3 quantum well superlattices with a periodicity of 6 nm [55]. Similarly, the highest *ZT* value for its bulk material is only 1.1. Quantum-dot superlattices in the PbTe–PbSeTe system were developed under the quantum confinement may lead to an increased Seebeck coefficient and therefore higher *ZT* [56]. PbSe nanodots were embedded in a PbTe matrix and showed *ZT* of 1.6, which is much higher than their bulk materials of 0.34 [52]. Serial compound $Ag_{1-x}Pb_{18}SbTe_{20}$ has a high *ZT* value of 2.2 at 800 K due to the special nanostructure that is still the most competitive TE material [57] and has ignited broad research interest [58–61]. These new technologies have pushed ZT to 2.4 [62] with predicted increase in the device conversion efficiency to a value between 15 and 20%.

6. Modeling approaches for thermoelectric cooling

Both system cooling power output and cooling COP should be considered for enhancing TE cooling system performance. There are three methods that can possibly lead to this enhancement. First, TE module design and optimization, such as number of thermocouples [63–66], thermoelement length [67–70] and thermoelement length to cross-sectional area ratio [71–73]. Second, cooling system thermal design and optimization [74], which includes investigation of heat sinks' geometry [75–77], identification of the heat transfer area and heat transfer coefficients of both hot and cold side heat sinks [78–80], more effective heat sinks (i.e. heat sink integrated with thermosyphon and phase change material) [16, 81, 82], thermal and electrical contact resistances and interface layer analysis [83–85]. Third, the TE cooling system working conditions (i.e. electric current input [86–88]), heat sink coolant and coolant's mass flow rate [10, 89].

In order to achieve this, a variety of system optimization methods have been adopted. The simplified energy equilibrium model for TE cooler can satisfy many different TE cooling

applications including electronic devices cooling and air conditioning [90–94]. If the TE modules are employed with time-varying temperature distribution and cooling power output, either 1D or 3D transient modeling is needed to better capture the system performance. To capture the module performance, modeling temperature change in all thermoelements is very complicated. Therefore, energy equilibrium model can be applied to simplify the numerical analysis process, especially for those systems which include heat sinks in hot and cold sides.

Positive Thomson coefficient improves TE cooling performance by 5–7% [95], while negative Thomson coefficient reduces cooling performance [96]. However, for commercially available TE coolers, Thomson effect is often small and negligible. Dimensionless analysis is a powerful tool to evaluate the performance of TE cooling system. New dimensionless parameters, such as dimensionless entropy generation number [78], dimensionless thermal conductance ratio and dimensionless convection ratio [64] have been defined.

Both COP and cooling capacity are dependent on the length of thermoelement, and this dependence becomes highly significant with the decrease in the length of thermoelement [97]. As a result, a long thermoelement is preferred to obtain a large COP, while a short thermoelement would be preferable to achieve maximum heat pumping capacity. Therefore, it is obvious that the design of the optimum module will be a tradeoff between the requirements for the COP and the heat pumping capacity. Most commercially available TE modules have thermoelement length range from 1.0 to 2.5 mm. Cooling power density also increases with decreasing the ratio of thermoelement length to the cross-sectional area.

Typical TE modules have a size range from $4 \times 4 \times 3$ mm^3 to about $50 \times 50 \times 50$ mm^3. The development of micro-TE devices to further reduce the dimensions, that is compatible with standard microelectronic fabrication technology [98], has the potential to improve the microelectronic systems performance, achieve considerable reductions in size and improve the TE devices performance, which opens up new commercial applications.

Electrical and thermal contact resistances, especially thermal contact resistance at the thermoelement interface layer, are critical to achieve a further improvement in both TE cooling capacity and COP [84]. An enhanced formula for the COP of a Peltier module which takes into consideration both the electrical and the thermal contact resistances can be written as [34]:

$$\mathrm{COP}_{opt} = \frac{l}{l + 2rl_c}\left(\frac{T_c}{T_h - T_c}\frac{\beta - T_h/T_c}{1+\beta} - \frac{rl_c}{l}\right) \tag{12}$$

where

$\beta = \left(1 + \frac{lZT_M}{n+l}\right)^{1/2}$, $n = \frac{2R_c}{R}$, $r = \frac{k}{k_c}$, l is the thermoelement length, l_c is the thickness of the contact layer, k is the thermal conductivity of the thermoelements, k_c is the thermal conductivity of the contact layers and $T_{\mathrm{M}} = \frac{(T_h + T_c)}{2}$.

In addition, an accurate fabrication technique is needed to provide high-quality and high-performance TE modules. The requirements include: precise measurements of the internal resistance for each module at ambient temperature; determination of the module supply leads

resistance; consideration of optimum values for voltage and current of each module; verification of thermal efficiency of each module and calculations of temperature difference, maximum cooling capacity according to the measurement results, figure of merit and values of internal resistance [99].

Heat sink performance at the hot side is more important than heat sink at the cold side because the heat flux density at hot side is higher. Allocation of the heat transfer area or heat transfer coefficients between hot and cold sides is particularly important. For given hot and cold side fluid temperatures, there exists an optimum cooling capacity which leads to maximum COP [64, 80, 92].

The COP of TE devices could be improved by minimizing the difference in temperature between their hot and cold faces [100]. The hot side of the TE cooler exhibits very high power densities that demands sophisticated cooling infrastructure with high pumping power.

7. Heat transfer analysis of the heat exchanger

To enhance the heat transfer rate between the hot and the cold fluid flows, heat exchangers are commonly applied in air cooling systems. Relations between the hot and the cold side temperatures as well as the optimum heat transfer surface area can be calculated by applying energy balances to both the hot and the cold sides of the TE modules over a differential area [101].

The heat transfer on the hot side of the TE devices can be increased using cross air flow or counter air flow [102]. The COP of TE devices could be improved by minimizing the difference in temperature between their hot and cold faces while applying appropriate electrical power [100]. A TE system used for cooling or warming airflow with a high COP of 1.5 was reported [93]. To achieve such a relatively high COP, the temperature difference between the hot and the cold faces of the TE modules was maintained at 5°C.

Other favorable working strategies using different heat transfer methods such as liquid cooling with phase change materials were also reported [103]. Theoretical and experimental studies were conducted to examine the performance characteristics of TE water cooling system for electronic cooling applications under small heat loads [11]. A TE liquid chiller was developed with 430 ml capacity and a COP ranged between 0.2 and 0.8 for a temperature of 5–15°C below ambient [104]. A cylindrical, water-cooled heat sink for TE air conditioners was designed and characterized [105]. In this context, a thermosyphon with phase change was developed to improve the thermal resistance of the heat exchanger at the hot side of the TE by 36% [12]. This increased the COP of a TE module by 26% at an ambient temperature of 20°C and 36.5% at 30°C. Using evaporative cooling the COP of TE air-conditioning system was improved by 20.9% [106].

TE devices, as electronic components, do not allow direct contact with coolant. Therefore, instead of pumping coolant directly through TE coolers, channels plate liquid cooling system is used. A channels plate block is a heat conductive metal, such as aluminum or copper, which is filled with channels. The base of the water block is a flat metal surface that is placed directly on top of the hot side of the TE module being cooled using thermal paste to improve

http://dx.doi.org/10.5772/intechopen.75791

transferring the heat between the two surfaces. When the TE hot side heats the block, the liquid coolant absorbs the heat as it flows through all the channels, which will be dissipated through a radiator. The same system can be applied at the cold side for the transfer of the cool due to high thermal resistance between the cold side of the TE and the space being cooled.

Recently, heat transfer in mini channels within heat exchangers is drawing substantial attention trying to improve their performance. The proper selection of channel dimensions and nonuniform distribution of the channels can improve the cooling power [107]. Therefore, thermal and hydrodynamic characteristics of channels need to be examined and developed. A TE system using liquid cooling for electronic application using micro-channel heat sink was proposed and its experimental analysis performance was investigated [108]. The effect of channel width, coolant flow rate and heat sink material on the heat transfer rate was also examined [76].

Although micro-channel heat exchangers are able to dissipate higher heat flux densities, the slow flow rate creates a large increase in the temperature alongside the direction of the coolant flow in both channel material and the coolant. Surface roughness also participates in the heat transfer characteristics and the drop of pressure of coolant flow in a channel. Many studies clearly reported that the roughness has an effect on the flow of the coolant and heat transfer characteristics, in addition to the laminar and turbulent transition [109, 110]. Micro channel heat exchangers with different designs and coolants were manufactured and tested and the experimental results confirmed the superiority of this cooling technique [111, 112].

Heat removal through parallel channels involves a complex combination of convection, conduction and coolant flow. In a rectangular channel plate with width W, height H and length L, taking the advantage of the symmetry of the channels, a unit cell containing only one channel with the surrounding metal is chosen. The results obtained can easily be applied to the whole plate. Heat transport in the unit cell is a conjugate problem that mixes heat conduction in the metal and convective heat transfer to the coolant. The dissipated heat in the surrounding regions conducts to the channel side walls, which is then absorbed, through convection, by the coolant and carried away by the circulation.

These parameters can be summarized by stating them as thermal resistances. Conductive resistance, R_{cond}, is determined by thermal characteristics of aluminum that conducts the dissipated heat in the region surrounding the sidewalls of the channel. Convection resistance, R_{conv}, is a result of the convection from sidewalls of the channel to the coolant. Heat resistance, R_{heat}, is a result of heating up of coolant in the downstream direction as the flow is pushed toward the channel exits. These can be expressed as:

$$R_{conv} = \frac{1}{h\,A} \tag{13}$$

where A is the channel surface area. Assuming that heat is transmitted from all the sidewalls, the surface area will be:

$$A = 2\,L(W + H) \tag{14}$$

here h is the convective heat transfer coefficient:

$$h = \frac{N_u K_f}{D_h} \tag{15}$$

where K_f is coolant thermal conductivity, N_u is the Nusselt number calculated with the Dittus-Boelter equation [113],

$$N_u = 0.023\, P_r^{0.4}\, R_e^{0.8} \tag{16}$$

in which P_r is Prandtl number and R_e is Reynolds number. D_h, the hydraulic diameter, is defined as:

$$D_h = \frac{4\,(cross\ sectional\ area)}{perimeter} = \frac{4\,WH}{2\,(W+H)} \tag{17}$$

Hence the convective can be expressed as:

$$R_{conv} = \frac{D_h}{2\,N_u\,K_f L(W+H)} \tag{18}$$

The heat resistances can be expressed as:

$$R_{heat} = \frac{1}{C_p \rho_c f} \tag{19}$$

where C_p is the coolant specific heat and ρ_c is coolant density. f is the volumetric flow rate for each channel which is defined as:

$$f = coolant\ velocity^{*}\ cross\ sectional\ area = v\,W\,H \tag{20}$$

The coolant viscosity and thermal conductivity vary according to the temperature [114]. The conductive resistances can be expressed as:

$$R_{cond} = \frac{W}{k\,L\,H} \tag{21}$$

where k is the thermal conductivity of the channels plates material.

For fluid dynamical and thermal phenomena that occur in the channels with corrugated walls, different heat transfer characteristics can be observed. Generally, the wall corrugation enlarges the surface of the channels and creates turbulence. However, most studies stated that the rise in temperature of the walls along the direction of the flow is almost linear [115–117].

Recently, heat sinks with nano-fluid have shown potential to achieve lower thermal resistance [118, 119]. In addition, cooling technologies based on heat removal from the heat sinks using synthetic jet [120], either single-phase or two-phase flow, are noticeable.

8. Conclusions

In this chapter, a short review of technologies related to the TE cooling was presented. The new methodologies of system design and system analysis have enabled the design of high-performance TE cooling systems. This includes the use of the basic physical properties of TE modules and the flow equations to identify the TE cooling design parameters to maximize the COP of the TE cooling systems. To minimize the energy demands in TE cooling systems and increase their energy effectiveness, solar TE cooling technologies such as active building envelope, solar thermoelectric coolers are suggested to be used in zero-energy environments.

Author details

Raghied M. Atta

Address all correspondence to: ratta@taibahu.edu.sa

Engineering College, Taibah University, Madinah, Saudi Arabia

References

[1] Martin A, Bansal P. Comparative study of vapour compression, thermoelectric and absorption refrigerators. International Journal of Energy Research. 2000;**24**:93-107

[2] Mota-Babiloni A, Makhnatch P, Khodabandeh R. Navarro-Esbrí J:Experimental assessment of R134a and its lower GWP alternative R513A. International Journal of Refrigeration. 2017;**74**:682-688

[3] Xia H, Luo L, Fraisse G. Development and applications of solar-based thermoelectric technologies. Renewable and Sustainable Energy Reviews. 2007;**11**:923-936

[4] Le Pierres N, Cosnier M, Luo L, Fraisse G. Coupling of thermoelectric modules with a photovoltaic panel for air preheating and pre-cooling application; an annual simulation. International Journal of Energy Research. 2008;**32**:1316-1328

[5] Stockolm J, Pujol-Soulet L, Sternat P. Prototype thermoelectric air conditioning of a passenger railway coach. In: 4th International Conference on Thermoelectric Energy Conversion, 10–12 March 1982; Arlington, TX. USA: IEEE. pp. 136-141

[6] Khire R A, Messac A, Van Dessel S: Design of thermoelectric heat pump unit for active building envelope systems. International Journal of Heat and Mass Transfer. 2005;**48**: 4028-4040

[7] Xu X, Van Dessel S, Messac A. Study of the performance of thermoelectric modules for use in active building envelopes. Building and Environment. 2007;**42**:1489-1502

[8] Riffat S, Qiu G. Comparative investigation of thermoelectric air-conditioners versus vapour compression and absorption air-conditioners

[9] Chang Y-W, Chang C-C, Ming-TsunKe S-LC. Thermoelectric air-cooling module for electronic devices. Applied Thermal Engineering. 2009;**29**:2731-2737

[10] Cheinv R, Chenv Y. Performance of thermoelectric cooler integrated with microchannel heat sinks. International Journal of Refrigeration. 2005;**28**:828-839

[11] Huang H, Weng Y, Chang Y, Chen S, Ke M. Thermoelectric water-cooling device applied to electronic equipment. International Communication of Heat and Mass Transfer. 2010; **37**:140-146

[12] Astrain D, Vian JG, Domınguez M. Increase of COP in the thermoelectric refrigeration by the optimisation of heat dissipation. Applied Thermal Engineering. 2003;**23**:2183-2200

[13] Atta R. Solar thermoelectric cooling using closed loop heat exchangers with macro channels. Heat and Mass Transfer. 2017;**53**:2241-2254

[14] Zemansky M, Dittman R. Heat and Thermodynamics. 6th ed. Vol. 1981. McGraw-Hill Book Company. pp. 431-442

[15] Zhao D, Tan G. A review of thermoelectric cooling: Materials, modeling and applications

[16] Min G, Rowe D. Experimental evaluation of prototype thermoelectric domestic-refrigerators. Applied Energy. 2006;**83**:133-152

[17] Vian J, Astrain D. Development of a thermoelectric refrigerator with two phase thermosyphons and capillary lift. Applied Thermal Engineering. 2009;**29**:1935-1940

[18] Dai Y, Wang R, Ni L. Experimental investigation and analysis on a thermoelectric refrigerator driven by solar cells. Solar Energy Materials & Solar Cells. 2003;**77**:377-391

[19] Abdul-Wahab SA et al. Design and experimental investigation of portable solar thermoelectric refrigerator. Renewable Energy. 2009;**34**:30-34

[20] Dai Y, Wang R, Ni L. Experimental investigation on a thermoelectric refrigerator driven by solar cells. Renewable Energy. 2003;**28**:949-959

[21] Astrain D, Vian J, Albizua J. Computational model for refrigerators based on Peltier effect application. Applied Thermal Engineering. 2005;**25**:3149-3162

[22] Mansour K, Qiu Y, Hill C, Soibel A, Yang R. Mid-infrared interband cascade lasers at thermoelectric cooler temperatures. Electronics Letters. 2006;**42**:1034-1036

[23] Yang J, Stabler F. Automotive applications of thermoelectric materials. Journal of Electronic Materials. 2009;**38**:1245-1251

[24] Choi H, Yun S, Whang K. Development of a temperature-controlled car-seat system utilizing thermoelectric device. Applied Thermal Engineering. 2007;**27**:2841-2849

[25] Shen L, Xiao F, Chen H, Wang S. Investigation of a novel thermoelectric radiant air-conditioning system. Energy and Buildings. 2013;**59**:123-132

[26] Gillott M, Jiang L, Riffat S. An investigation of thermoelectric cooling devices for small-scale space conditioning applications in buildings. International Journal of Energy Research. 2010;**34**:776-786

[27] Cheng TC, Cheng CH, Huang Z, Liao G. Development of an energy-saving module via combination of solar cells and thermoelectric coolers for green building applications. Energy. 2011;**36**:133-140

[28] Arenas A, Palacios R, Rodríguez-Pecharromán R, Pagola F: Full-size prototype of active thermal windows based on thermoelectricity. In: Proceedings of ECT2008e6th European Conference on Thermoelectrics, July 24, 2008, O.18.1:O.18.4. Paris, France

[29] Vázquez J, Sanz-Bobi M, Palacios R, Arenas A: An active thermal wall based on thermo-electricity. in: Sixth European Workshop on Thermoelectrics. Freiburg, Germany, Sep 2001

[30] Esfahani J, Rahbar N, Lavvaf M. Utilization of thermoelectric cooling in a portable active solar still – An experimental study on winter days. Desalination. 2011;**269**:198-205

[31] Rahbar N, Esfahani J. Experimental study of a novel portable solar still by utilizing the heat pipe and thermoelectric module. Desalination. 2012;**284**:55-61

[32] Milani D et al. Evaluation of using thermoelectric coolers in a dehumidification system to generate freshwater from ambient air. Chemical Engineering Science. 2011;**66**:2491-2501

[33] Atta R. Solar water condensation using thermoelectric coolers. International Journal of Water Resources and Arid Environments. 2011;**1**:142-145

[34] Dessel S, Foubert B. Active thermal insulators: Finite elements modeling and parametric study of thermoelectric modules integrated into a double pane glazing system. Energy and Buildings. 2010;**42**:1156-1164

[35] Liu Z, Zhang L, Gong G, Li H, Tang G. Review of solar thermoelectric cooling technologies for use in zero energy buildings. Energy and Buildings. 2015;**102**:207-216

[36] Harman T, Walsh M, Laforge B, Turner G. Nanostructured thermoelectric materials. Journal of Electronic Materials. 2005;**34**:19-22

[37] Cheng YH, Shih C. Maximizing the cooling capacity and COP of two-stage thermoelectric coolers through genetic algorithm. Applied Thermal Engineering. 2006;**26**:937-947

[38] Goldsmid J. Introduction to Thermoelectricity. Series in Material Science. Berlin Heidelberg: Springer; 2010

[39] Yu J, Wang B. Enhancing the maximum coefficient of performance of thermoelectric cooling modules using internally cascaded thermoelectric couples. International Journal of Refrigeration. 2009;**32**:32-39

[40] Melero A, Astrain D, Vian JG, Aldave L, Albizua J, Costa C. Application of thermoelectricity and photovoltaic energy to air conditioning. Thermoelectrics, Twenty-Second International Conference on – ICT. 2003:627-630

[41] Zhang X, Zhao L. Thermoelectric materials: Energy conversion between heat and electricity. Journal of Materiomics. 2015;**1**:92-105

[42] Li J, Liu W, Zhao L, Zhou M. High-performance nanostructured thermoelectric materials. NPG Asia Materials. 2010;**2**:152-158

[43] Minnich A,Dresselhaus M, Ren Z, Chen G. Bulk nanostructured thermoelectric materials: Current research and future prospects. Energy & Environmental Science. 2009;**2**: 466-479

[44] Snyder G, Toberer E. Complex thermoelectric materials. Nature Materials. 2008;**7**:105-114

[45] Nolas G, Poon J, Kanatzidis M. Recent developments in bulk thermoelectric materials. Materials Research Society Bulletin. 2006;**31**:199-205

[46] Dresselhaus M, Chen G, Tang M, Yang R, Lee H, Wang D, Ren Z, Fleurial J, Gogna P. New directions for low-dimensional thermoelectric materials. Advanced Materials. 2007; **19**:1043-1053

[47] Liu H, Xu F, Zhang L, Zhang W, Chen L, Li Q, Uher C, Day T, Snyder G. Copper ion liquid-like thermoelectrics. Nature Materials. 2012;**11**:422-425

[48] Hsu KF, Loo S, Guo F, Chen W, Dyck JS, Uher C, et al. Cubic AgPb(m)SbTe(2+m): Bulk thermoelectric materials with high figure of merit. Science. 2004;**303**:818-821

[49] Alam H, Ramakrishna S. A review on the enhancement of figure of merit from bulk to nano-thermoelectric materials. Nano Energy. 2013;**2**:190-212

[50] Tritt T. Thermoelectric phenomena, materials, and applications. Annual Review of Materials Research. 2011;**41**:433-448

[51] Liu W, Yan X, Chen G, Ren Z. Recent advances in thermoelectric nanocomposites. Nano Energy. 2012;**1**:42-56

[52] Chen Z, Han G, Yang L, Cheng L, Zou J. Nanostructured thermoelectric materials: Current research and future challenge. Progress in Natural Science Material International. 2012;**22**:535-549

[53] Medlin D, Snyder G. Interfaces in bulk thermoelectric materials a review for current opinion in colloid and interface science. Current Opinion in Colloid & Interface Science. 2009;**14**:226-235

[54] Hicks LD, Dresselhaus MS. Effect of quantum-well structures on the thermoelectric figure of merit. Physical Review B. 1993;**47**:12727

[55] Venkatasubramanian R, Siivola E, Colpitts T, O'Quinn B. Thin-film thermoelectric devices with high room-temperature figures of merit. Nature. 2001;**413**:597-602

[56] Harman T, Taylor P, Walsh M, LaForge B. Quantum dot superlattice thermoelectric materials and devices. Science. 2002;**297**:2229-2232

[57] Chen N et al. Macroscopic thermoelectric inhomogeneities in (AgSbTe2)x(PbTe)1−x. Applied Physics Letters. 2005;**87**:171903

[58] Wang H, Li J, Zou M, Sui T. Synthesis and transport property of AgSbTe2AgSbTe2 as a promising thermoelectric compound. Applied Physics Letters. 2008;**202106**:93

[59] Wang H et al. High-erformanceAg0.8Pb18+xSbTe20Ag0.8Pb18+xSbTe20 thermoelectric bulk materials fabricated by mechanical alloying and spark plasma sintering. Applied Physics Letters. 2006;**88**:092104

[60] Zhou M, Li J, Kita T. Nanostructured $AgPb_mSbTe_{m+2}$ system bulk materials with enhanced thermoelectric performance. Journal of the American Chemical Society. 2008; **130**:4527-4532

[61] Cai K et al. Preparation and thermoelectric properties of $AgPb_mSbTe_{2+m}$ alloys. Journal of Alloys Compoundd. 2009;**469**:499-503

[62] Pei YZ, Shi XY, LaLonde A, Wang H, Chen LD, Snyder GJ. Convergence of electronic bands for high performance bulk thermoelectrics. Nature. 2011;**473**:66-69

[63] Jing-HuiMeng X-DW, Zhang X-X. Transient modeling and dynamic characteristics of thermoelectric cooler. Applied Energy. 2013;**108**:340-348

[64] Lee H. Optimal design of thermoelectric devices with dimensional analysis. Applied Energy. 2013;**106**:79-88

[65] Huang Y, Wang X, Cheng C, Lin D. Geometry optimization of thermoelectric coolers using simplified conjugate-gradient method. Energy. 2013;**59**:689-697

[66] He W, Su Y, Wang YQ, Riffat SB, Ji J. A study on incorporation of thermoelectric modules with evacuated-tube heat-pipe solar collectors. Renewable Energy. 2012;**37**:142-149

[67] Fraisse G, Lazard M, Goupil C, Serrat J. Study of a thermoelement's behavior through a modeling based on electrical analogy. International Journal of Heat and Mass Transfer. 2010;**53**:3503-3512

[68] Cheng Y, Lin W. Geometric optimization of thermoelectric coolers in a confined volume using genetic algorithms. Applied Thermal Engineering. 2005;**25**:2983-2997

[69] Min G, Rowe D. Improved model for calculating the coefficient of performance of a Peltier module. Energy Conversion and Management. 2000;**41**:163-171

[70] Yazawa K, Shakouri A. Optimization of power and efficiency of thermoelectric devices with asymmetric thermal contacts. Journal of Applied Physics. 2012;**111**:024509

[71] Zhu W, Deng Y, Wang Y, Wang A. Finite element analysis of miniature thermoelectric coolers with high cooling performance and short response time. Microelectronics Journal. 2013;**44**:860-868

[72] Sahin A, Yilbas B. The thermoelement as thermoelectric power generator: Effect of leg geometry on the efficiency and power generation. Energy Conversion and Management. 2013;**65**:26-32

[73] Yang R, Chen G, Snyder G, Fleurial J. Multistage thermoelectric microcoolers. Journal of Applied Physics Junction. 2004;**95**:8226-8232

[74] Lee H. Thermal Design: Heat Sinks, Thermoelectrics, Heat Pipes, Compact Heat Exchangers, and Solar Cells. USA: John Wiley & Sons; Inc; 2010

[75] Wang C, Hung C, Chen W. Design of heat sink for improving the performance of thermoelectric generator using two-stage optimization. Energy. 2012;**39**:236-245

[76] Naphon P, Wiriyasart S. Liquid cooling in the minirectangular fin heat sink with and without thermoelectric for CPU. International Communication of Heat and Mass Transfer. 2009;**36**:166-171

[77] Gao X, Chen M, Snyder G, Andreasen S, Kaer S. Thermal management optimization of a thermoelectric integrated methanol evaporator using a compact CFD modeling approach. Journal of Electronic Materials. 2013;**42**:2035-2042

[78] Wang X, Yu J, Ma M. Optimization of heat sink configuration for thermoelectric cooling system based on entropy generation analysis. International Journal of Heat and Mass Transfer. 2013;**63**:361-365

[79] Zhu L, Tan H, Yu J. Analysis on optimal heat exchanger size of thermoelectric cooler for electronic cooling applications. Energy Conversion and Management. 2013;**76**:685-690

[80] Pan Y, Lin B, Chen J. Performance analysis and parametric optimal design of an irreversible multi-couple thermoelectric refrigerator under various operating conditions. Applied Energy. 2007;**84**:882-892

[81] Qinghai L, Yanjin W, Pengfei Z. A novel thermoelectric airconditioner for a truck cab. In: International Conference on Advances in Energy Engineering (ICAEE), Beijing, China: 19–20 June 2010. IEEE; 2010. p. 178-181

[82] Vian J, Astrain D. Development of a heat exchanger for the cold side of a thermoelectric module. Applied Thermal Engineering. 2008;**28**:1514-1521

[83] Xuan X. Investigation of thermal contact effect on thermoelectric coolers. Energy Conversion and Management. 2003;**44**:399-410

[84] Yamashita O. Effect of interface layer on the cooling performance of a single thermoelement. Applied Energy. 2011;**88**:3022-3029

[85] Silva L. KavianyM: Micro-thermoelectric cooler: Interfacial effects on thermal and electrical transport. International Journal of Heat and Mass Transfer. 2004;**47**:2417-2435

[86] Cheng C, Huang S, Cheng T. A three-dimensional theoretical model for predicting transient thermal behavior of thermoelectric coolers. International Journal of Heat and Mass Transfer. 2010;**53**:2001-2011

[87] Zhang H. A general approach in evaluating and optimizing thermoelectric coolers. International Journal of Refrigeration. 2010;**33**:1187-1196

[88] Taylor R, Solbrekken G. Comprehensive system-level optimization of thermoelectric devices for electronic cooling applications. IEEE Transactions on Components and Packaging Technologies. 2008;**31**:23-31

[89] David B, Ramousse J, Luo L. Optimization of thermoelectric heat pumps by operating condition management and heat exchanger design. Energy Conversion and Management. 2012;**60**:125-133

[90] Chein R, Huang G. Thermoelectric cooler application in electronic cooling. Applied Thermal Engineering. 2004;**24**:2207-2217

[91] Zhang H, Mui Y, Tarin M. Analysis of thermoelectric cooler performance for high power electronic packages. Applied Thermal Engineering. 2010;**30**:561-568

[92] Zhou Y, Yu J. Design optimization of thermoelectric cooling systems for applications in electronic devices. International Journal of Refrigeration. 2012;**35**:1139-1144

[93] Cosnier M, Fraisse G, Luo L. An experimental and numerical study of a thermoelectric air-cooling and air-heating system. International Journal of Refrigeration. 2008;**31**:1051-1062

[94] Seifert W, Ueltzen M, Muller E. One-dimensional modeling of thermoelectric cooling. Physical Status Solidi. 2002;**194**:277-290

[95] Chen W, Liao C, Hung C. A numerical study on the performance of miniature thermoelectric cooler affected by Thomson effect. Applied Energy. 2012;**89**:464-473

[96] Lee H. The Thomson effect and the ideal equation on thermoelectric coolers. Energy. 2013;**56**:61-69

[97] Riffat S, Ma X. Improving the coefficient of performance of thermoelectric cooling systems: A review. International Journal of Energy Research. 2004;**28**:753-768

[98] Gould C, Shammas N. A review of thermoelectric MEMS devices for micro-power generation, heating and cooling applications. In: Takahata K, editor. Micro Electronic and Mechanical Systems. Croatia: INTECH; 2009. pp. 572-581

[99] Anatychuk L, Varych N, Shchedrin A. Methods and means of precise and rapid determinations of thermoelectric cooling and generating modules parameters. 17th International Conference on Thermoelectrics(ICT98); 18 May 1998; Nagoya, Japan: IEEE; 1998. P. 270-272

[100] Rowe D. CRC Handbook of Thermoelectrics. CRC Press; 1995

[101] Chen K, William G. An analysis of the heat transfer rate and efficiency of TE (thermoelectric) cooling systems. International Journal of Energy Research. 1996;**20**:399-417

[102] Buist R, Fenton J, Lee J. A new concept for improving thermoelectric heat pump efficiency. In: Intersociety Energy Conversion Engineering Conference; 12–17 September 1976; New York. American Institute of Chemical Engineers; 1976. p. 1619-1622

[103] Riffat S, Omer S, Ma X. A novel thermoelectric refrigeration system employing heat pipes and a phase change material: An experimental investigation. Renewable Energy. 2001;**23**: 313-323

[104] Faraji AY, Goldsmid HJ, Akbarzadeh A. Experimental study of a thermoelectrically-driven liquid chiller in terms of COP and cooling down period. Energy Conversion and Management. 2014;**77**:340-348

[105] Riffat S, Qiu G. Design and characterization of a cylindrical, water-cooled heat sink for thermoelectric airconditioners. International Journal of Energy Research. 2006;**30**:67-80

[106] Tipsaenporm W, Lertsatitthanakorn C, Bubphachot B, Rungsiyopas M, Soponronnarit S. Improvement of cooling performance of a compact thermoelectric air conditioner using a direct evaporative cooling system. Journal of Electronic Materials. 2012;**41**:1186-1192

[107] Shi B, Srivastava A: Cooling of 3D-IC Using Non-Uniform Micro-channels and Sensor Based Dynamic Thermal Management. In: 49th Annual Allerton Conference Communication, Control, and Computing (Allerton);Septemer2011. p. 1400-1407

[108] Khonsue O. Experimental on the liquid cooling system with thermoelectric for personal computer. Heat and Mass Transfer. 2012;**48**:1767-1771

[109] Kandlikar S, Joshi S, Tian S. Effect of channel roughness on heat transfer and fluid flow characteristics at low reynolds numbers in small diameter tubes. In Proceedings of NHTC'01 35th National Heat Transfer Conference; 10–12 June 2001; Anaheim, California; NHTC01; 2001. p. 12134

[110] Fabbri G. Heat transfer optimization in corrugated wall channels. International Journal of Heat and Mass Transfer. 2000;**43**:4299-4310

[111] Mudawar I, Bowers MB. Ultra-high critical heat flux (CHF) for subcooled water flow boiling—I: CHF data and parametric effects for small diameter tubes. International Journal of Heat and Mass Transfer. 1999;**42**:1405-1428

[112] Ravigururajan T, Cuta J, McDonald C, Drost M. Single-phase flow thermal performance characteristics of a parallel micro-channel heat exchanger. In: ASME proceedings of the 31 national heat transfer conference; 3–6 August 1996; Houston, TX. p. 157-166

[113] Kuan C, Sheng I, Lin H, Lin P, Cheng Y, Chuang J, Liu Y, Tseng T, Chen J. Heat-Transfer Analysis of A Water-Cooled Channel for the Tps Front-End Components. In: Proceedings of Subsystems, Technology and Components IPAC2013; 12 to 17 May 2013; Shanghai, China 2013; p. 3466-3468

[114] Meis M, Varas F, Velázquez A, Vega J. Heat transfer enhancement in micro-channels caused by vortex promoters. International Journal of Heat and Mass Transfer. 2010;**53**: 29-40

[115] Knight R, Goodling J, Hall D. Optimal thermal design of forced convection heat sinks-analytical. ASME Journal of Electronic Packaging. 1991;**113**:313-321

[116] Knight R, Hall D, Goodling J, Jaeger R. Heat sink optimization with application to microchannels. IEEE Trans Components, Hybrids, Manufacturing Technology. 1992;**15**: 832-842

[117] Weisberg A, Bau H, Zemel J. Analysis of microchannels for integrated cooling. International Journal of Heat and Mass Transfer. 1992;**35**:2465-2474

[118] Nnanna A, Rutherford W, Elomar W, Sankowski B. Assessment of thermoelectric module with nanofluid heat exchanger. Applied Thermal Engineering. 2009;**29**:491-500

[119] Putra N, Iskandar F. Application of nanofluids to a heat pipe liquid-block and the thermoelectric cooling of electronic equipment. Experimental Thermal and Fluid Science. 2011;**35**:1274-1281

[120] Chaudhari M, Puranik B, Agrawal A. Heat transfer characteristics of synthetic jet impingement cooling. International Journal of Heat and Mass Transfer. 2010;**53**:1057-1069

Chapter 13

Computational Thermoelectricity Applied to Cooling Devices

Roberto Palma, Emma Moliner and
Josep Forner-Escrig

Additional information is available at the end of the chapter

http://dx.doi.org/10.5772/intechopen.75473

Abstract

This chapter presents a numerical formulation within the finite element method in order to computationally simulate thermoelectric devices. For this purpose, a theoretical formulation based on nonequilibrium thermodynamics with historical notes is previously outlined. Then, a brief description of the finite element is reported to express the thermodynamics governing equations in an amenable form to be numerically discretized. Finally, several applications of cooling thermoelectrics are performed to highlight the benefits of the finite element method. In particular, a commercial thermoelectric device is simulated and several variables such as extracted heat, voltage drop, and temperature distributions inside the thermoelements are represented for different operating conditions. In conclusion, the present numerical tool could be used as a virtual laboratory for the design and optimization of Peltier cells.

Keywords: thermoelectricity, nonequilibrium thermodynamics, finite element method, cooling, Peltier cells

1. Introduction

Thermoelectricity was discovered during the nineteenth century, but it has not been until the decade of 1950 when thermoelectric materials have experimented a quick expansion due to the techniques of doping [1]. Nowadays, the improvement of thermoelectric materials is based on the well-known figure-of-merit Z, which depends on temperature, Seebeck coefficient and thermal and electric conductivities. A high value of Z provides a good thermoelectric material for which the Seebeck coefficient and electrical conductivity are elevated and the thermal conductivity is low.

According to Z, thermoelectric materials can be classified into two groups:

- Bulk materials such as Bi_2Te_3, PbTe, $CoSb_3$, SiGe, which present $Z \leq 1$ [2]. In the last decades, a new range of bulk materials with $Z \leq 1.5$ called nanostructured (for instance, phono-glass electron-crystal material) has emerged. Bulk materials are mainly used in high temperature applications: 700–900 K, [3].
- Low-dimensional materials, such as Sb_2Te_3 superlattices, are based on the quantum confinement effect of the electron charge carriers, which allows to obtain higher values of Seebeck coefficients. The main advantage of these materials is their figure-of-merit ($Z \approx 1.5$); however, they are expensive and not adequate for mass production.

To sum up, despite the fact that values of $Z \approx 3$ have been reached for research applications [4], the best commercial thermoelectric material holds $Z \approx 1$. Therefore, the material science community has a challenge to improve the Z of thermoelectric materials and, consequently, to exploit the potential of these materials.

Regarding thermoelectric applications, there are two operating thermoelectric modes: coolers and generators, see **Figure 1**. Typically, all thermoelectric are composed of thermocouples that are made up of two semiconductors p- and n-type called thermoelements. Furthermore, tin weldings, copper bars for conducting the electric intensity I and alumina for isolating the device are also present, as observed in **Figure 1**. The position of the hot end depends on the operation mode:

- Cooler (**Figure 1** left), heat is extracted from the cold end by applying an electric current.
- Generator (**Figure 1** right), an electric current is produced by the gradient of temperatures between cold and hot ends.

Concerning cooling mode, the devices made out of thermoelectric materials have been restricted, among others, to four specific applications:

1. *Refrigeration*: Thermoelectric coolers present high reliability, no moving parts and reduction in size and weight. Nevertheless, the main drawback of thermoelectric refrigeration is that its efficiency is normally between 0.3 and 0.5 for a gradient of temperature of approximately 20°C, [5].
2. *Electronic devices*: These equipments, such as PC processors, generate considerable quantities of heat that cause troubles if the device junction temperature (approximately 85°C) is exceeded, [2]. Since conventional cooling techniques cannot completely fulfill the requirements of heat dissipation and due to the lack of space in electronic devices, the most adequate refrigeration option consists of using thermoelectric coolers combined with air/liquid cooling systems.
3. *Automotive industry*: Conventional techniques that use refrigerants such as R-134a contribute to global warming. In this connection, thermoelectric coolers could solve the problem. Furthermore, studies show that acceptable efficiency in the range of 0.4–0.8 can be achieved under ambient temperature from 46 to 30°C in the case of a truck cab, [6].

4. *Air-conditioning*: In this field, thermoelectric air-conditioning is not still as efficient as the vapor-compression system. For instance, efficiency of vapor-compression and thermoelectric air-conditioning systems are in the range of 2.6–3.0 and 0.38–0.45, respectively, see [7].

With regard to thermoelectric generator, there exists a great interest in the use of generator devices made out of thermoelectric materials to produce energy from residual sources such as waste heat. These applications are commonly denominated energy harvesting and, nowadays, have a big potential. For this reason, most of the research works focus on thermoelectric generators.

The aim of the present chapter is to develop a numerical formulation within the finite element (FE) method to computationally model thermoelectric devices. Previously, a review of the different numerical techniques that are applied to model thermoelectricity is reported. Then, the FE formulation is introduced and several applications are developed in order to highlight the main advantages of the application of the FE method to thermoelectricity. Notice that this chapter is only focused on cooling applications for the sake of brevity.

This chapter is structured as follows: Firstly, Section 2 presents a state of art on the different numerical techniques to simulate thermoelectricity. Secondly, a thermodynamically consistent formulation within the nonequilibrium thermodynamic formalism is developed in Section 3 to obtain the governing equations, which are composed of balance laws, transport equations and boundary conditions. Thirdly, Section 4 applies the FE method to rewrite the governing equations in an amenable form to be computationally solved. Finally, several examples such as convergence tests, comparisons with analytical solutions and miniaturizations are conducted in Section 5 and the conclusions are summarized in Section 6.

For the sake of clarity, the notation used in the present chapter is shown in **Table 1**.

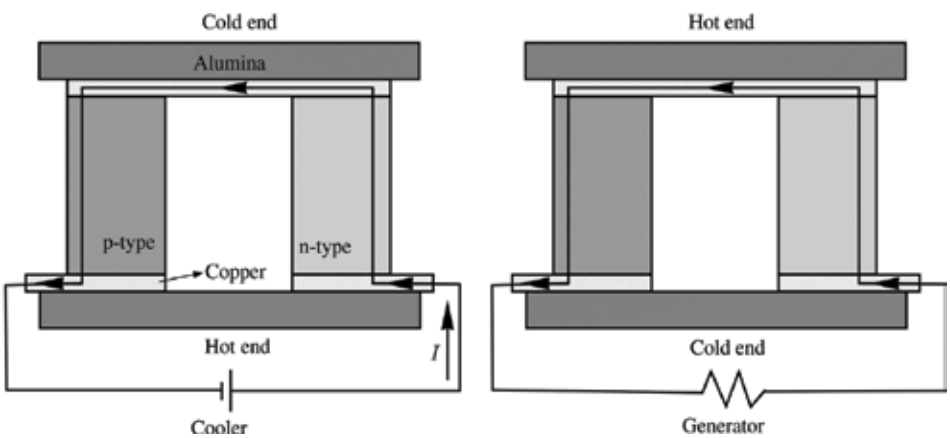

Figure 1. Sketches of thermocouples operating as cooler (left) and generator (right).

Symbol	Description
	Theoretical formulation
Ω, Ω^{∞}, Γ, $\mathbf{n}$	Domain, surrounding, boundary and outward normal
$\rho = \left\{\rho_q^f, \rho_m\right\}$	Free electric charge and mass density
$\mathbf{J} = \{j, j_s\}$	Electric and entropy fluxes
$\Xi = \Sigma_s$	Entropy production
d, δ	Exact differential and variation
t, s, T, V	time, entropy, temperature and voltage
$\boldsymbol{q}, \boldsymbol{x}$,	Heat flux and Cartesian coordinates
c, α, κ, γ	Heat capacity, Seebeck coefficient, and thermal and electric conductivities
	Finite element formulation
$g_a = \left\{\tilde{V}_a, \tilde{T}_a, \dot{\tilde{T}}_a\right\}$	Degrees of freedom
Ω_e, Γ_e	Subdomain and boundary of any finite element
$\mathcal{R}$, $\mathcal{K}$, $\mathcal{C}$	Residual, tangent stiffness and capacity matrices
a, b	Global numbering of elements
k	Newton-Raphson counter
c_1, c_2	Time integration parameters
	Applications
T_c, T_h	Cold and hot temperatures
Q_c, Q_h	Extracted heat at cold and hot ends
I, Z	Intensity and figure-of-merit

Table 1. Table of symbols.

2. Review of numerical methods applied to thermoelectricity

Despite the fact that there exists a large amount of works that use simplified analytical models [8–10] and semi-analytical techniques such as Laplace transforms [11], numerical modeling of thermoelectricity is a fundamental aspect in order to design and optimize sophisticated devices made out of thermoelectric materials. In this connection, there are at least five numerical methods applied to solve the set of two coupled partial differential equations (PDE) of thermoelectricity. For more details, readers are referred to [12], in which some of these numerical methods are compared and discussed.

- *Network or circuit simulator method*, which can be considered as a representation of the natural convection and uses the Kirchhoff's theorems. The main characteristic of this method is the discretization of the spatial coordinates while time is assumed to be a

continuous variable. For instance, the method developed in [13] considers the Thomson effect, which is often neglected in the models for simplicity, and also the temperature-dependency of all material parameters.

- *Finite difference method* is the simplest numerical technique and approximates the set of PDE by using the Taylor's theorem. An example of application can be found in [14]. In this work, the authors study the production of electricity by using the waste heat of a combustion chamber. The temperature and mass flow of the flue gases and the load resistance, which are key parameters for the generation, are included in the model, as well as the elements of the generators (heat exchangers, ceramics, unions) and all the thermoelectric phenomena. As a main novelty of the model, the temperature drop of the flue gases while circulating along the thermoelectric generator is also included. As shown by the authors, this thermoelectric model based on finite differences predicts the thermoelectric generation with a relative error within ±12%. Also in [15] a computational model for thermoelectric self-cooling, based on the implicit finite differences, is presented. The model is capable of simulating both the steady and the transient state of the system and considers all the thermoelectric effects (Seebeck, Thomson, Peltier and Joule) including temperature-dependency of all properties, and exhibits a good correspondence with the experimental measurements (±12% of deviation).

- *Boundary element method* [16] solves the PDE by integral equations and is applied to problems for which Green's functions can be calculated. The main shortcoming of this method is its difficulty for solving nonlinear problems and, for this reason, there are few works in the literature applied to thermoelectricity. For instance, this method is used in [17] to study the two-dimensional temperature distributions in thermoelectric devices.

- *Finite volume method* is also used to evaluate the set of coupled PDE of thermoelectricity in [18]. In this case, the authors numerically study the thermoelectric performance of composite thermoelectric devices, in terms of produced electrical current, Ohmic and Seebeck potentials, power output, heat input and conversion efficiency for various hot surface temperatures, load resistance, semiconductor thickness and convection heat transfer coefficient.

- *FE method* [19] is the most advanced technique for solving PDE in science and engineering. Furthermore, this method is optimal for applying to nonlinear coupled problems as thermoelectricity. In this connection, the authors of the present chapter have extensive experience in developing thermodynamic consistent FE formulations, which are implemented in the research code FEAP [20], see [21–25] and [26]. Regarding commercial FE codes, the authors in [27, 28] use ANSYS to perform a comprehensive numerical analysis focusing on the cooling performance of miniaturized thermoelectric coolers for microelectronics applications. In particular, they study the effects of parameters such as the load current, geometric size. Finally, the software COMSOL is used in [29] to study the thermal stresses in Peltier cells.

In short, the main disadvantage of the boundary element is, as commented, its intrinsic difficulty to solve nonlinear problems. On the contrary, all the other methods can be applied

to solve nonlinear thermoelectricity. The FE and finite volume methods require of complex mathematical developments and they are commonly used by the continuum mechanics community. In contrast, the finite difference method is the most direct approach to numerically solve PDE. Finally, the circuit method is preferably used by the electric engineering community.

Despite the difficulty of the FE method, it is used in the present chapter since it presents two main advantages: i) It is a very general an efficient method, and ii) it is easy to improve the accuracy of the solutions by two approaches: mesh refinement and/or increasing the order of the interpolation functions.

3. Governing equations

Thermoelectricity couples electric and thermal energies by five separated effects: Fourier, Ohm, Seebeck, Thomson and Joule (see historical notes 1 and 2). All of them are thermal and electric fluxes that must satisfy the balances of electric charge and of entropy. The aim of this section is to state both balances and, in addition, to obtain the transport equations that couple electric and thermal energies. Finally, this section reports the boundary conditions that are required for a proper formulation of the set of coupled PDE that governs thermoelectricity.

Historical note 1

- *Jean-Baptiste Joseph Fourier* (1768–1830) was a French mathematician and physicist. Coming of a humble family, he showed such proficiency in mathematics in his early years that he began his career in 1790 as a teacher of mathematics in the school he first attended, the École Royale Militaire of Auxerre. Fourier also joined the local revolutionary committee in his own district promoting the ideals of the French Revolution, and his life was in danger several times for this reason. However, he is best remembered for his work on flow of heat, through his *Théorie analytique de la chaleur* (1872). This work is the basis of what is today known as the Fourier transform.
- *Georg Ohm* (1789–1854) was a German physicist who summarized the most relevant aspects of Ohm's law in his work *Die galvanische kette, mathematish bearbeitet* (1827). At that time he was professor of mathematics at the Jesuits College at Cologne, where he had a well-equipped laboratory in which he started his first experiments with electricity. Despite the great influence of his work in the theory and applications of electric currents, it was not before 1841 when he started to be recognized, being awarded by the Royal Society of London. Also in his honor, the physical unit measuring the electrical resistance *ohm*, was named for him after his death.
- *James Prescott Joule* (1818–1889) was an English physicist best known by his paper *On the production of heat by voltaic electricity* (1840). In this work, he stated the principles of the law that has his name, Joules law: mathematical description of the rate at which the resistance of a circuit converts electric energy into heat. It was also

Joule who formed the basis of the first law of thermodynamics, since he established that the various forms of energy (mechanical, electrical and heat) were in essence the same and could be changed. Other relevant contribution emerged in 1852 when Joule and Thomson discovered the Joule-Thomson effect, which is commonly exploited in thermal machines and played a crucial role in the development of the refrigeration industry in the nineteenth century.

3.1. Balance of electric charges and entropy

The term continuum physics refers to several branches of physics such electromagnetism and nonequilibrium thermodynamic for which the matter consists of material points that are localized by the Euclidean position vector $\boldsymbol{x}$. This fact is mathematically grounded on the continuum hypothesis [30], which allows to work with balance equations that state the conservation, production or annihilation of certain quantities such electric charge and specific entropy.

Consider a closed system of domain Ω, boundary Γ with outward normal $\mathbf{n}$ and its surrounding Ω^{∞}. A general expression of a balance equation for the quantity Υ at time t and in any material point $\boldsymbol{x}$ is given by:

$$\frac{d}{dt}\int_{\Omega}\rho(\Upsilon;\boldsymbol{x},t)\ \ d\Omega\ \ = -\int_{\Omega}\nabla\cdot\mathbf{J}(\Upsilon;\boldsymbol{x},t)\ \ d\Omega\ \ +\int_{\Omega}\Xi(\Upsilon;\boldsymbol{x},t)\ \ d\Omega\ \ , \tag{1}$$

where ρ, $\mathbf{J}$ and Ξ denote the Υ-density, Υ-current density and Υ-production, respectively. This equation balances the quantity Υ since it contains information on:

- The quantity of Υ inside Ω, term on the left-hand side.
- Inflow quantity from Ω^{∞} to Ω through the boundary Γ, first term on the right-hand side (after application of divergence theorem).
- Production/annihilation of Υ inside Ω, second term on the right-hand side.

In thermoelectricity, both electric and thermal fields are present and, consequently, there are two Υ quantities as shown in **Table 2**. As observed, the quantities are the free electric charge ρ_q^f and the specific entropy s; the current densities are the electric $\boldsymbol{j}$ and entropy $\boldsymbol{j}_s$ fluxes. Regarding the production terms, there is not production for the electric field due to the fact that the

Quantity	Υ	Current density	J	Production	Ξ
Free electric charge	ρ_q^f	Electric flux	$\boldsymbol{j}$	–	–
Specific entropy	ρ_ms	Entropy flux	$\boldsymbol{j}_s$	Entropy production	Σ_s

Table 2. Quantities to be balanced in thermoelectricity.

electric charge can neither be created nor destroyed. Consequently, the electric balance becomes a conservation equation. On the contrary, the entropy production Σ_s is due to the irreversibilities (also called dissipations) generated by both the Fourier heat transport and the Joule heating.

In the present chapter, it is assumed that there are not free electric charges; this is a first and good approximation for thermoelectric devices made out of semiconductors. Under this assumption and introducing the quantities of **Table 2** in (1), the thermoelectric balance equations in local forms read:

$$0 = \nabla \cdot \boldsymbol{j}, \qquad \rho_m \dot{s} = -\nabla \cdot \boldsymbol{j}_s - \frac{\boldsymbol{j} \cdot \nabla V}{T}, \tag{2}$$

where the second term on the right-hand side of the right equation represents the Joule heating and V, T denote voltage and temperature, respectively.

The entropy balance of (2) can be manipulated by considering that $\boldsymbol{j}_s = \boldsymbol{q}/T$, where $\boldsymbol{q}$ is the heat flux to give:

$$\rho_m \dot{s} = -\nabla \cdot \left(\frac{\boldsymbol{q}}{T}\right) \underbrace{- \frac{\boldsymbol{q} \cdot \nabla T}{T^2} - \frac{\boldsymbol{j} \cdot \nabla V}{T}}_{\Sigma_s}. \tag{3}$$

Now, the classical heat balance equations can be obtained by manipulating (3) and by taking into account that $\dot{s} = c\dot{T}/T$, where c is the specific heat capacity, to give:

$$\rho_m \, c \, \dot{T} = -\nabla \cdot \boldsymbol{q} - \boldsymbol{j} \cdot \nabla V. \tag{4}$$

As observed, the Joule heating is a heat source since the electric energy is irreversibly converted into heat. In addition, this term is nonlinear due to its quadratic dependency of the ∇V term, as can be observed from (6).

3.2. Transport equations

Within the nonequilibrium thermodynamic formalism [31], the transport equations are obtained from the entropy production Σ_s of (3). Concretely, in a first and good approximation the entropy production can be expressed as the sum of products of fluxes and driving forces. In matrix form:

$$\begin{Bmatrix} -\dfrac{\nabla V}{T} \\ -\dfrac{\nabla T}{T^2} \end{Bmatrix} = \begin{bmatrix} \dfrac{\alpha^2}{\kappa} + \dfrac{1}{\gamma T} & -\dfrac{\alpha}{\kappa T} \\ -\dfrac{\alpha}{\kappa T} & \dfrac{1}{\kappa T^2} \end{bmatrix} \begin{Bmatrix} \boldsymbol{j} \\ \boldsymbol{q} \end{Bmatrix}, \tag{5}$$

where γ, κ and α denote electric and thermal conductivities and Seebeck coefficient, respectively. Finally, the set of two coupled equations of thermoelectricity becomes:

http://dx.doi.org/10.5772/intechopen.75473

$$\boldsymbol{j} = -\gamma(T)\nabla V - \alpha(T)\gamma(T)\nabla T, \qquad \boldsymbol{q} = -\kappa(T)\nabla T + \alpha(T)T\boldsymbol{j}. \tag{6}$$

Historical note 2

The thermoelectric coupling was discovered by *Thomas Johann Seebeck* (1770–1831), *Athanase Peltier* (1785–1845) and *William Thomson* (1824–1907). The former discovered the Seebeck effect in a casual experiment; he initially believed that the deflection experienced by a compass magnet in a circuit made from two different metals with junctions exposed to a temperature gradient was due to magnetism, instead of considering that an electric current was induced by the temperature difference. For that reason, for a century it had no application. The French physicist Peltier realized that the passage of an electric current would induce heating or cooling at the junction of two dissimilar metals. Today, this effect is known called Peltier-Seebeck effect and is the physical basis of thermocouples. Finally, Thomson, later Lord Kelvin, showed the appearance of a temperature gradient when current flows in a material, resulting in a cooling or heating effect of a different nature from Joule effect. Thomson is also best known for giving a comprehensive explanation of the Seebeck and Peltier effects and describing their interrelationships, known as Kelvin relations. The definition of the absolute temperature scale, based on the degree Celsius, was also other of his achievements.

In semiconductors, the material properties γ, κ and α commonly depend on temperature. For instance, for the metal-metalloid alloy Bi_2Te_3 the dependency on temperature of these properties is shown in **Figure 2**. As observed, both γ and κ exhibit a strong temperature dependency that results in a material nonlinearity. Explicitly, the temperature dependency of these material properties can be fitted to second order polynomials to give:

$$\gamma(T) = \gamma_0 + \gamma_1 T + \gamma_2 T^2, \quad \kappa(T) = \kappa_0 + \kappa_1 T + \kappa_2 T^2, \quad \alpha(T) = \alpha_0 + \alpha_1 T + \alpha_2 T^2. \tag{7}$$

Notice that the temperature-dependency of $\alpha(T)$ is the responsible of the Thomson's effect and, consequently, the inclusion of material nonlinearities is a requirement for a proper modeling of thermoelectricity.

3.3. Boundary conditions

The boundary conditions are additional constrains at the boundary Γ that are present at all the boundary value problems. These conditions guarantee the existence of a unique solution and, therefore, the problem is well posed. There exist two types of boundary conditions:

- Dirichlet conditions (also called first-type or essential) specify the value of the degrees of freedom at the boundary.
- Neumann conditions (second-type or natural) give the value of the normal derivative of the fluxes at the boundary.

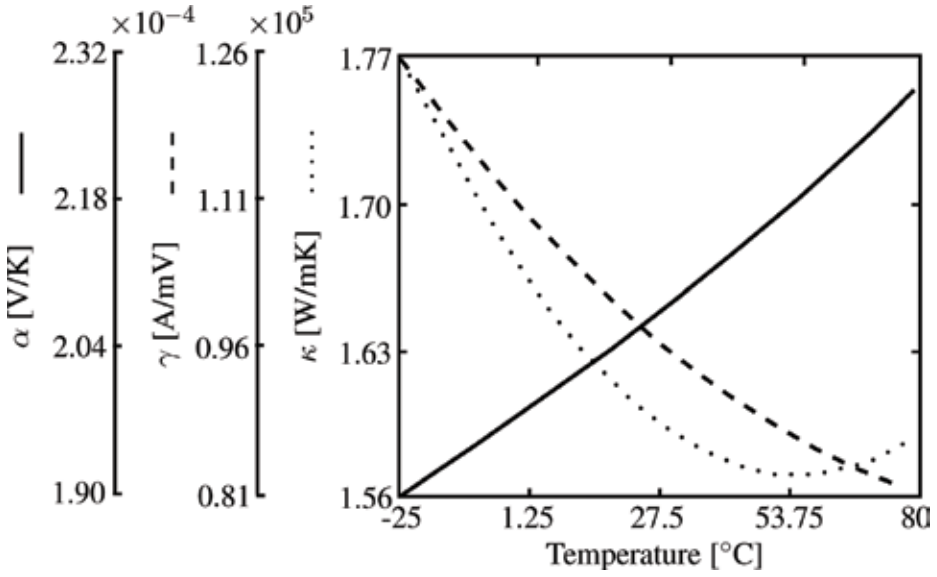

Figure 2. Temperature-dependency of material properties for the Bi_2Te_3 material. Picture taken from [21].

In thermoelectricity, these conditions read:

$$\begin{aligned} \text{Dirichlet type}: \quad & V = \overline{V}, \qquad T = \overline{T}, \\ \text{Neumann type}: \quad & \boldsymbol{j} \cdot \mathbf{n} = \overline{j}, \quad \boldsymbol{q} \cdot \mathbf{n} = \overline{q}, \end{aligned} \tag{8}$$

where $\overline{V}$, $\overline{T}$, $\overline{j}$ and $\overline{q}$ denote prescribed voltage, temperature, electric flux and thermal flux, respectively.

4. Finite element formulation

As commented, the FE is probably the most advanced method for the solution of coupled PDE, but it involves complex mathematical concepts. For the sake of clarity and in order to present a comprehensible FE formulation, this section reports the FE formulation of thermoelectricity by using the following steps:

Historical note 3

The FE method was developed in the 1960s, among others, by the Greek *John Argyris* (1913–2004) at the University of Sttutgart, by the American *Ray William Clough* (1920–2016) at the University of California (Berkeley) and by the Anglo-Polish *Olgierd Zienkiewicz* (1921–2009) at the University of Swansea. The main contribution of the latter was to recognize the general potential of FE to resolve problems in areas outside solid mechanics.

i) The continuum domain Ω is divided into subdomains called finite elements Ω_e interconnected at nodal points a, see **Figure 3**. Mathematically, this discretization is expressed by $\Omega \approx \cup_{e=1}^{n_{el}} \Omega_{e_i}$. There exists a wide amount of finite element types depending on their number of nodes, spatial dimensions, etc. For more details, readers are referred to [19]. In the present work, three-dimensional eight noded elements, as that shown in **Figure 3**, are considered.

ii) The values at nodes are called degrees of freedom $\boldsymbol{g}$ and are the problem unknowns. In thermoelectricity, they are voltage V, temperature T and their time derivatives:

$$\boldsymbol{g}_a = \left\{ \tilde{V}_a, \tilde{T}_a, \dot{\tilde{T}}_a \right\}. \tag{9}$$

iii) A set of functions denominated "shape functions" $\mathcal{N}$ are chosen to interpolate the unknowns and the spatial dimensions within each finite element in terms of their nodal values. Obviously, these functions must satisfy several mathematical requirements that, for the sake of brevity, are not reported in the present work. Furthermore, there are many types of shape functions depending on their polynomial type, degree of interpolation, etc. In this chapter, standard shape functions of Lagragian type, which are linear functions of the degrees of freedom, are used and the numerical interpolations become:

$$\boldsymbol{x} \approx \boldsymbol{\mathcal{N}}_a \tilde{\boldsymbol{x}}_a, \quad V \approx \mathcal{N}_a \tilde{V}_a, \quad T \approx \mathcal{N}_a \tilde{T}_a, \quad \dot{T} \approx \mathcal{N}_a \dot{\tilde{T}}_a, \tag{10}$$

where the Einstein summation convention is used.

iv) The balance and constitutive equations and the boundary conditions reported in Section 3 represent the strong form of the thermoelectric problem; namely, the coupled PDE depend on the second spatial derivatives of V and T. The FE uses "weakened" forms for which V and T are first spatial derivatives. For this purpose, the governing equations must be manipulated by using several approaches such as the principle of virtual work, the weighted residual, Hamilton's principle, etc. In the present work, the weighted residual method is used since it is probably the most systematic approach; it consists of three steps:

a) The balance equations of (2) (left) and (4) are multiplied by test functions of the degrees of freedom δV and δT.

b) The divergence theorem is applied to both arising equation.

c) The Neumann boundary conditions are enforced and the weak forms yield:

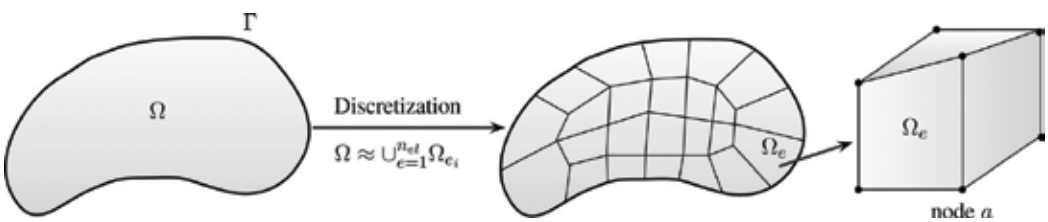

Figure 3. Finite element discretization of a continuum domain and representation of an eight noded element.

$$\begin{aligned} \int_\Omega \nabla\delta V \cdot \quad \boldsymbol{j}\, d\Omega \quad - \oint_\Gamma \delta V \bar{j} \quad d\Gamma \quad &= \quad 0, \\ \int_\Omega \left[\nabla\delta T \cdot \boldsymbol{q} + \delta T\left(\boldsymbol{j}\cdot\nabla V + \rho_m\, c\, \dot{T}\right)\right] \quad d\Omega \quad - \oint_\Gamma \delta T\, \bar{q} \quad d\Gamma \quad &= \quad 0. \end{aligned} \tag{11}$$

v) In this step, similar discretization to those of (10) are applied to the test functions and their spatial derivatives:

$$\begin{aligned} &\delta V \approx \mathcal{N}_a \delta\tilde{V}_a, && \delta T \approx \mathcal{N}_a \delta\tilde{T}_a, \\ &\nabla\delta V \approx \nabla\mathcal{N}_a \delta\tilde{V}_a = \mathcal{B}_a \delta\tilde{V}_a, && \nabla\delta T \approx \nabla\mathcal{N}_a \delta\tilde{T}_a = \mathcal{B}_a \delta\tilde{T}_a. \end{aligned} \tag{12}$$

Introducing these expressions in the weak form of (11), the FE residuals for each finite element of domain Ω_e of boundary Γ_e become:

$$\begin{aligned} \mathcal{R}_b^V &= \int_{\Omega_e} \mathcal{B}_b^{\mathrm{T}} \boldsymbol{j}\, \mathrm{d}\Omega_e - \oint_{\Gamma_e} \mathcal{N}_b\, \bar{j} \quad \mathrm{d}\Gamma_e, \\ \mathcal{R}_b^T &= \int_{\Omega_e} \left[\mathcal{B}_b^{\mathrm{T}} + \mathcal{N}_b\left(\boldsymbol{j}\cdot\nabla V + \rho_m\, c\, \dot{T}\right)\right] \quad \mathrm{d}\Omega_e - \oint_{\Gamma_e} \mathcal{N}_b\, \bar{q} \quad \mathrm{d}\Gamma_e, \end{aligned} \tag{13}$$

vi) Finally, the solution is calculated by solving a set of nonlinear transient equations that involves three steps:

(a) The time interval is divided into small time increments Δt.

(b) The time derivatives are replaced by discrete forms using time integration techniques such as backward or forward finite differences, see [19].

(c) Since the thermoelectric problem is nonlinear due to both the temperature-dependency of the material properties and the Joule heating, the resulting nonlinear algebraic problem is linearized at each time increment by using a numerical algorithm. For instance, the Newton-Raphson algorithm use k iterations for the linearization of the residuals:

$$\mathcal{R}_a\big|^k = -\left.\frac{\partial \mathcal{R}_a}{\partial g_b}\right|^k \mathrm{d}g_b^k \Rightarrow -\left.\frac{\partial \mathcal{R}_a}{\partial g_b}\right|^k \quad = \quad c_1\, \mathcal{K}_{ab} + c_2\, \mathcal{C}_{ab}, \tag{14}$$

where a, b refer the local numbering of two generic FE nodes, the parameters c_1 and c_2 depend on the time integration scheme, see [19], and the consistent tangent matrices $\mathcal{K}$ and the nonzero capacity matrix $\mathcal{C}$ are derived at each iteration as:

$$\begin{aligned} \mathcal{K}_{ab}^{VV} &= -\frac{\partial \mathcal{R}_a^V}{\partial \tilde{V}_b} = -\int_{\Omega_e} \mathcal{B}_a^{\mathrm{T}} \frac{\partial \boldsymbol{j}}{\partial \tilde{V}_b} \quad \mathrm{d}\Omega_e, \\ \mathcal{K}_{ab}^{VT} &= -\frac{\partial \mathcal{R}_a^V}{\partial \tilde{T}_b} = -\int_{\Omega_e} \mathcal{B}_a^{\mathrm{T}} \frac{\partial \boldsymbol{j}}{\partial \tilde{T}_b} \quad \mathrm{d}\Omega_e, \\ \mathcal{K}_{ab}^{TV} &= -\frac{\partial \mathcal{R}_a^T}{\partial \tilde{V}_b} = -\int_{\Omega_e} \left[\mathcal{B}_a^{\mathrm{T}} \frac{\partial \boldsymbol{q}}{\partial \tilde{V}_b} + \mathcal{N}_a \frac{\partial\left(\boldsymbol{j}\cdot\nabla V\right)}{\partial \tilde{V}_b}\right] \quad \mathrm{d}\Omega_e, \\ \mathcal{K}_{ab}^{TT} &= -\frac{\partial \mathcal{R}_a^T}{\partial \tilde{T}_b} = -\int_{\Omega_e} \left[\mathcal{B}_a^{T} \frac{\partial \boldsymbol{q}}{\partial \tilde{T}_b} + \mathcal{N}_a \frac{\partial\left(\boldsymbol{j}\cdot\nabla V\right)}{\partial \tilde{V}_b}\right] \quad \mathrm{d}\Omega_e, \\ \mathcal{C}_{ab}^{TT} &= -\frac{\partial \mathcal{R}_a^T}{\partial \dot{\tilde{T}}_b} = -\int_{\Omega_e} \mathcal{N}_a\, \rho_m\, c\, \mathcal{N}_b \quad \mathrm{d}\Omega_e, \end{aligned} \tag{15}$$

where the derivatives are reported in [24] and are not repeated here for the sake of brevity.

Finally, the solution is updated by using $\boldsymbol{g}_b^{k+1} = \boldsymbol{g}_b^k + d\boldsymbol{g}_b^k$ until the convergence is reached. In particular, the Newton-Raphson algorithm exhibits a quadratic asymptotic rate of convergence. The present FE formulation is coded in the research software FEAP [20], which belongs to the University of California at Berkeley (USA).

5. Numerical examples

As commented, the present numerical tool can be used as a "virtual laboratory" that allows to numerically design and optimize devices made out of thermoelectric materials. In this connection, the aim of this section is to show several features of the FE code. In particular, a commercial Peltier cell for cooling applications is simulated and several variables such as heat extracted, voltage and temperature distributions are analyzed.

A CP1.4-127-045 thermoelectric cooling module composed of 127 thermocouples electrically connected in series, as observed in **Figure 4** (left), and manufactured by LairdTech [32] is modeled. The technical specifications of this device are: maximum intensity $I = 8.7$ (A), maximum extracted heat $Q_c = 82.01$ (W) with voltage drop $V = 15.33$ (V) and under $T_h = T_c = 50\,^{\circ}\mathrm{C}$, where T_c and T_h refer to the temperature at cold and hot ends, respectively.

Numerically, only half of the thermocouple needs to be modeled due to its symmetry and, consequently, the computational time is reduced; the FE mesh composed of 12,670 eight noded elements is shown in **Figure 4** (right). On the one hand, the Neumann boundary conditions, namely, the electric current is enforced by the specific two-dimensional FE developed in [21]. This element can be also used to take into account convection and radiation phenomena among thermocouples; however, both phenomena are ignored in the present chapter. On the other hand, the Dirichlet boundary conditions are applied by setting the voltage reference

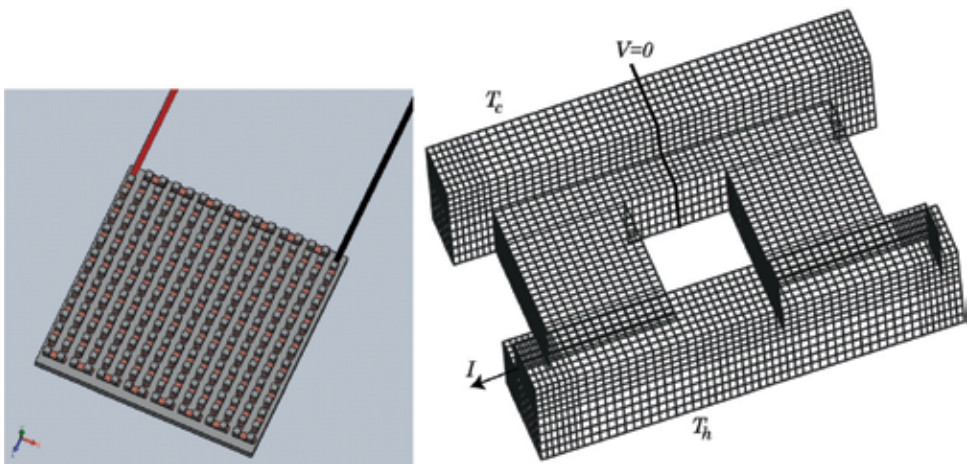

Figure 4. Left: Sketch of the thermoelectric cooling module. Right: Finite element mesh and boundary conditions applied to half of the thermocouple.

$V = 0$ and by prescribing temperatures at cold and hot ends, see **Figure 4** (right). Finally, the coefficients of the temperature-dependent material properties of (7) are also reported in [21].

5.1. Convergence tests

In order to study the accuracy of the FE simulation and since the problem is nonlinear, convergence tests must be carried out. In particular, this section presents two tests: h and residual convergences. The former refers to the improvement of the solution with decreasing the size of the finite elements—this convergence is called h-refinement by the computational mechanics community—and the latter guarantees a proper performance of the Newton-Raphson algorithm to solve the nonlinearities.

For this purpose, the most detrimental operating condition is simulated: the boundary conditions are $T_c = T_h = 50^\circ$C and $I = 8.7$ (A). **Figure 5** shows the h-refinement (left) and residual convergence (right) for the potential drop V (top) and the extracted heat at the cold end Q_c (bottom).

As observed in the left figure, a mesh composed of 12,670 elements gives a perfect convergence for both electrical and thermal variables. The potential drop converges faster than the extracted heat; due to the fact that the voltage is directly calculated while the heat depends on spatial derivatives. Regarding the residual convergence and as observed in the right figure, both electrical and thermal variables require three iterations of the Newton-Raphson algorithm (the residual norm becomes 10^{-16}) to minimize the residual due to the relative nonlinearity of the problem. Notice that each iteration requires 0.46 (s) in a 1.6 (GHz) Intel Core i5 processor.

5.2. Comparisons of extracted heat and voltage drop

The aim of this section is to compare analytical and FE solutions for the commercial cell under $I = 1.7$ (A) and $T_h = 50^\circ$C. The analytical solutions are obtained from [33] and are typically used by designers. For this aim, **Figure 6** shows the voltage drop (left) and the extracted heat (right) versus the temperature at the cold end.

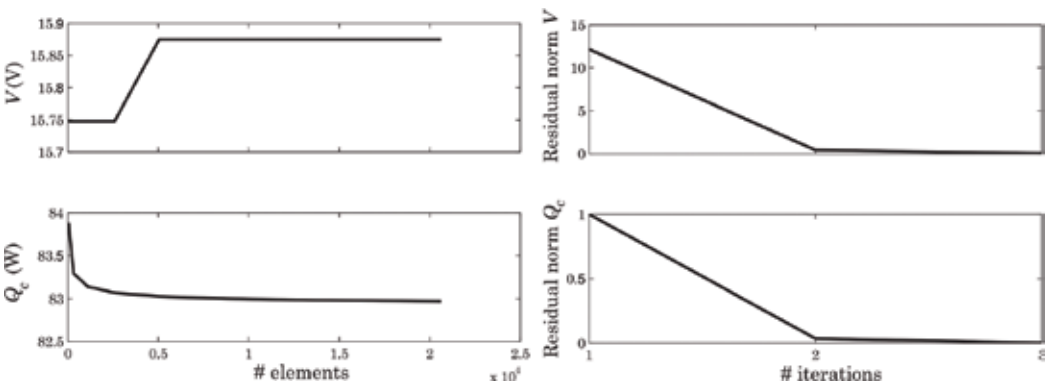

Figure 5. Left: mesh convergence, voltage drop (top) and heat extracted (bottom) vs. number of elements. Right: residual convergence, residual norm of voltage (top) and heat extracted (bottom) vs. number of iterations.

http://dx.doi.org/10.5772/intechopen.75473

As observed, analytical and numerical solutions for the voltage disagree due to the electrical loss at the corners of the thermoelements. This drop loss is captured by the FE but not by the one-dimensional analytical solution, as was concluded in [21] by comparing analytical, numerical and experimental solutions. Therefore, for a proper design of thermoelectric cells the numerical tool is more appropriated than the simple analytical solutions. For the extracted heat, despite the fact that the slope is slightly different, both analytical and numerical solutions agree.

Regarding the drop loss at the corners of the thermoelement, **Figure 7** shows contour plots of the electric currents along horizontal (left) and vertical (right) axes. As observed, the fluxes produce vortices-like phenomena and, consequently, part of the prescribed intensity does not go to the thermoelement.

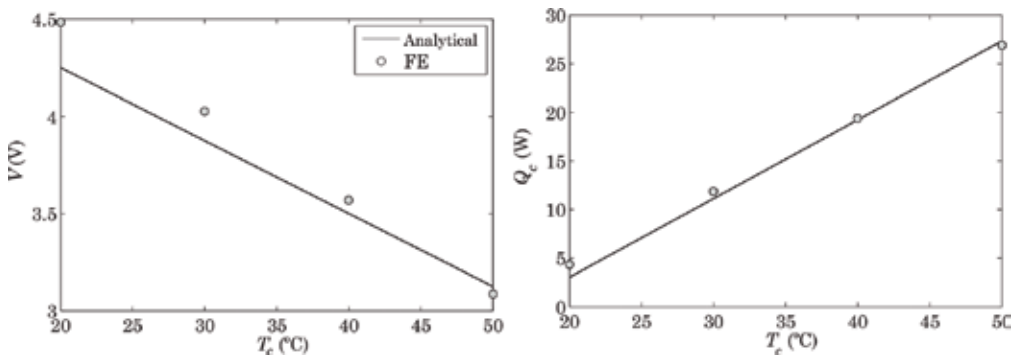

Figure 6. Voltage drop (left) and extracted heat (right) vs. temperature at the cold end for $I = 1.7$ (A), $T_h = 50^\circ$C.

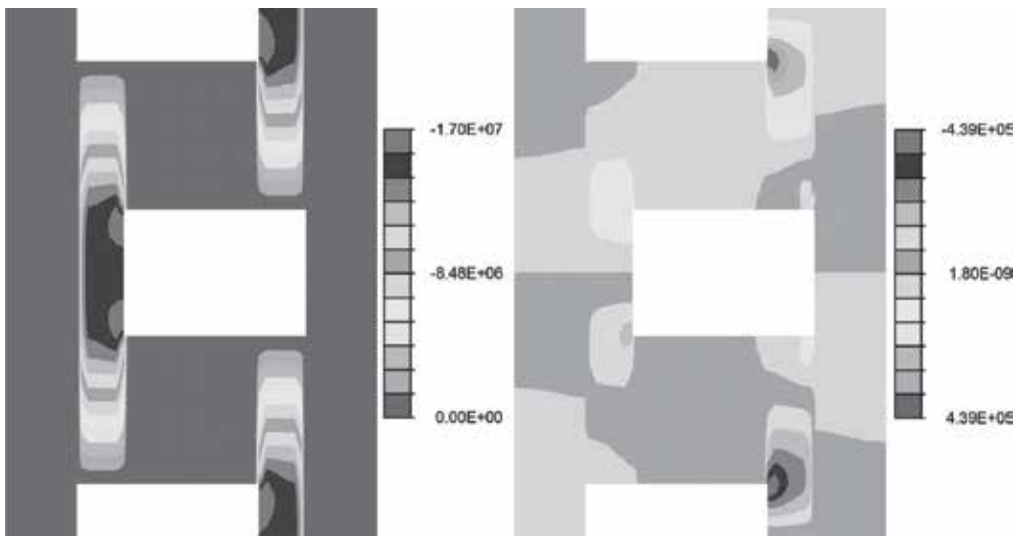

Figure 7. Contour plots of electric current along horizontal (left) and vertical (right) axes for $I = 1.7$ (A), $T_h = T_c = 50^\circ$C.

Another important aspect to be considered for the proper operation of Peltier cells is the maximum temperature inside the thermoelements since an overheating produces thermal stresses that could break the semiconductors from a mechanical point of view. For that matter, **Figure 8** shows the maximum and minimum temperature inside the thermoelements for two operating conditions: $I = 1.7$ and $I = 3$ (A), at $T_h = 50^\circ$C.

As observed, for $I = 3$ (A) the maximum temperature becomes approximately 80°C due to the increasing of the Joule heating that depends on the prescribed intensity. To sum up, the present numerical tool can be used for a proper design and optimization of cooling devices from both thermoelectric and thermomechanic interactions.

5.3. Miniaturization of thermoelements

The last example deals with the minimization of thermoelements. Currently, there exists a trend towards minimization of thermoelectric devices for two reasons: decreasing power consumption and reducing the size of the devices.

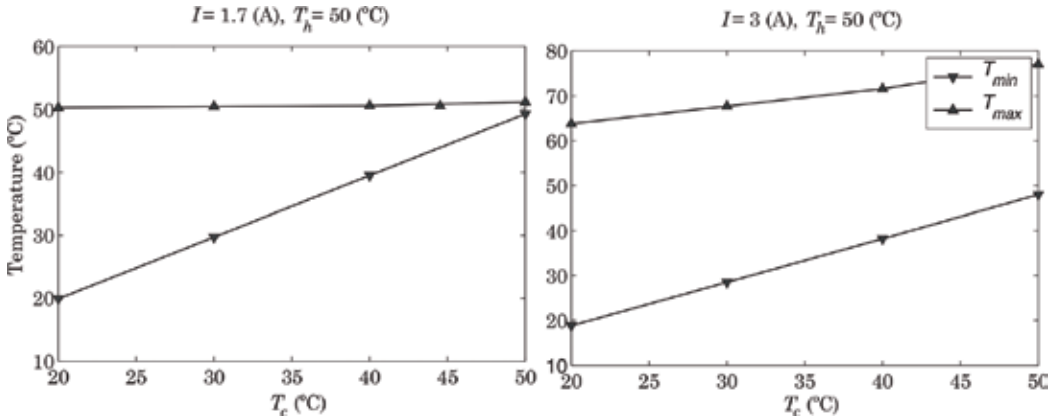

Figure 8. Minimum and maximum temperature inside thermoelements vs. temperature at the cold end for $I = 1.7$ (left) and $I = 3$ (A) (right), $T_h = 50^\circ$C.

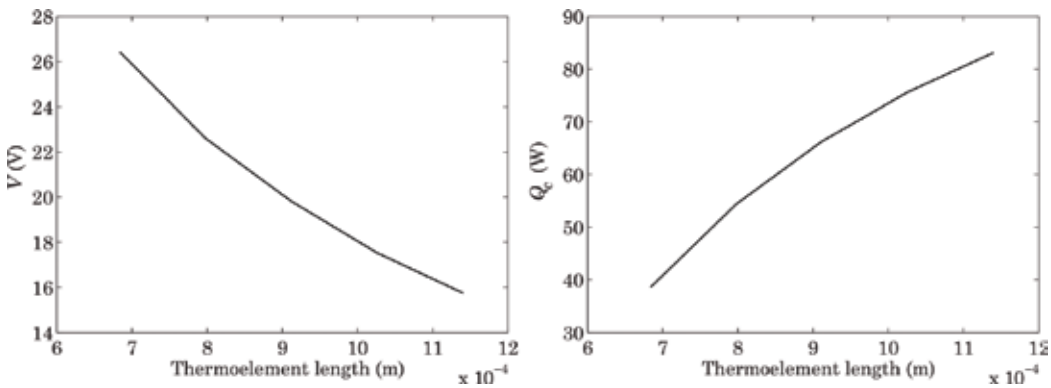

Figure 9. Voltage drop (left) and extracted heat (right) vs. the thermoelement length.

Figure 9 shows the voltage drop (left) and the extracted heat (right) versus the thermoelement length for the detrimental case $I = 8.7$ (A) and $T_c = T_h = 50^\circ$C. As observed, decreasing the size of thermocouple implies to reduce the heat extracted and increase the potential drop. Obviously, both results are detrimental since the coefficient of performance of the cell becomes worse. This fact is due to the Joule heating that is a volumetric effect and, consequently, decreasing the size and maintaining constant the prescribed intensity results in overheating of the thermoelements. Again, the present modeling tool could be used for calibrating the miniaturization of devices by setting the applied intensity in order to achieve an efficient functioning.

6. Concluding remarks

This chapter has presented a thermodynamically consistent formulation to obtain the governing equations of thermoelectricity, from a theoretical point of view. Then, a nonlinear numerical formulation within the finite element method is developed. The nonlinearities emerge from the presence of Joule heating and the temperature-dependence of the material properties and they are numerically solved by the Newton-Raphson algorithm. Notice that this material nonlinearity directly allows the inclusion of the Thomson effect. Furthermore, the formulation is dynamic and monolithic; the former feature is solved by backward finite differences and the latter is carried out by defining a coupled assembled matrix that increases the accuracy of the formulation. Finally, several examples are reported to show the capabilities of the numerical formulation that can be used as a "virtual laboratory." In particular, h-refinements and residual convergence tests are conducted to validate the codification. Then, comparisons between analytical and numerical solutions for cooling thermoelectric cells are reported in order to highlight the advantages of the simulations against the simple one-dimensional analytical solutions. In conclusion, the use of the present numerical tool could be applied for a proper design and optimization of thermoelectric devices. For instance, this tool was used to optimize the shape of a pulsed thermoelectric in [25].

Author details

Roberto Palma*, Emma Moliner and Josep Forner-Escrig

*Address all correspondence to: rpalma@uji.es

Department of Mechanical Engineering and Construction, Universitat Jaume I, Spain

References

[1] Dresselhaus MS, Chen G, Tang MY, Yang RG, Lee HL, Wang DZ, Ren ZF, Fleurial JP, Gogna P. New directions for low-dimensional thermoelectric materials. Advanced Materials. 2007;**19**:1043-1053

[2] Zhao D, Tan G. A review of thermoelectric cooling: Materials, modeling and applications. Applied Thermal Engineering. 2014;**66**:15-24

[3] Alam H, Ramakrishna S. A review on the enhancement of figure of merit from bulk to nano-thermoelectric materials. Nano Energy. 2013;**2**:190-212

[4] Harman TC, Walsh MP, Laforge BE, Turner GW. Nanostructured thermoelectric materials. Journal of Electronic Materials. 2005;**34**(5):19-22

[5] Min G, Rowe DM. Experimental evaluation of prototype thermoelectric domestic-refrigerators. Applied Energy. 2006;**83**:133-152

[6] Qinghai L, Yanjin W, Pengfei Z. A novel thermoelectric air-conditioner for a truck cab. International Conference on Advances in Energy Engineering. 2010

[7] Riffat SB, Qiu G. Comparative investigation of thermoelectric air-conditioners versus vapour compression and absorption air-conditioners. Applied Thermal Engineering. 2004;**24**:1979-1993

[8] Chen L, Li J, Sun F, Wu C. Performance optimization of a two-stage semiconductor thermoelectric-generator. Applied Energy. 2005;**82**(4):300-312

[9] Hsiao YY, Chang WC, Chen SL. A mathematic model of thermoelectric module with applications on waste heat recovery from automobile engine. Energy. 2010;**35**(3):1447-1454

[10] Du C-Y, Wen C-D. Experimental investigation and numerical analysis for one-stage thermoelectric cooler considering Thomson effect. International Journal of Heat and Mass Transfer. 2011;**54**(23):4875-4884

[11] Alata M, Al-Nimr A, Naji M. Transient behavior of a thermoelectric devices under the hyperbolic heat conduction model. International Journal of Thermophysics. 2003;**24**(6): 1753-1768

[12] Fraisse G, Ramousse J, Sgorlon D, Goupil C. Comparison of different modeling approaches for thermoelectric elements. Energy Conversion and Management. 2013;**65**: 351-356

[13] Fraisse G, Lazard M, Goupil C, Serrat JY. Study of a thermoelementâ€™s behaviour through a modelling based on electrical analogy. International Journal of Heat and Mass Transfer. 2010;**53**(17):3503-3512

[14] Aranguren P, Araiz M, Astrain D, Martínez A. Thermoelectric generators for waste heat harvesting: A computational and experimental approach. Energy Conversion and Management. 2017;**148**:680-691

[15] Martínez A, Astrain D, Rodríguez A. Dynamic model for simulation of thermoelectric self cooling applications. Energy. 2013;**55**:1114-1126

[16] Brebbia CA, Domínguez J. Boundary Elements: An Introductory Course. WIT Press/ Computational Mechanics Publications; 1992

[17] S. Kondo, M. Hasak and T. Morimura, Temperature analysis of thermoelectric device of Cu_4SnS_4 with two dimension by boundary element method. 15th International Conference on Thermoelectrics, IEEE. 1996

[18] Reddy BVK, Barry M, Li J, Chyu MK. Mathematical modeling and numerical characterization of composite thermoelectric devices. International Journal of Thermal Sciences. 2013;**67**:53-63

[19] Zienkiewicz OC, Taylor RL, Zhu JZ. The Finite Element Method: Its basis and Fundamentals. 7th ed. Elsevier Butterworth-Heinemann; 2013

[20] Taylor RL. FEAP A Finite Element Analysis Program: User Manual. Berkeley: University of California; 2010

[21] Perez-Aparicio JL, Palma R, Taylor RL. Finite element analysis and material sensitivity of Peltier thermoelectric cells coolers. International Journal of Heat and Mass Transfer. 2012; **55**:1363-1374

[22] Palma R, Perez-Aparicio JL, Taylor RL. Non-linear finite element formulation applied to thermoelectric materials under hyperbolic heat conduction models. Computer Methods in Applied Mechanics and Engineering. 2012;**213**:93-103

[23] Palma R, Perez-Aparicio JL, Bravo R. Study of hysteretic thermoelectric behavior in photovoltaic materials using the finite element method, extended thermodynamics and inverse problems. Energy Conversion and Management. 2013;**65**:557-563

[24] Perez-Aparicio JL, Palma R, Taylor RL. Multiphysics and thermodynamic formulations for equilibrium and non-equilibrium interactions: non-linear finite elements applied to multi-coupled active materials. Archives of Computational Methods in Engineering. 2016; **23**(3):535-583

[25] Perez-Aparicio JL, Palma R, Moreno-Navarro P. Elasto-thermoelectric non-linear, fully coupled, and dynamic finite element analysis of pulsed thermoelectric. Applied Thermal Engineering. 2016;**107**:398-409

[26] Palma R, Moliner E, Perez-Aparicio JL. Elasto-thermoelectric beam formulation for modeling thermoelectric devices. Finite Element in Analysis and Design. 2017;**129**:32-41

[27] Zhu W, Deng Y, Wang Y, Wang A. Finite element analysis of miniature thermoelectric coolers with high cooling performance and short response time. Microelectronics Journal. 2013;**44**(9):860-868

[28] Chen W-H, Wang C-C, Hung C-I, Yang C-C, Juang R-C. Modeling and simulation for the design of thermal-concentrated solar thermoelectric generator. Energy. 2014;**64**:287-297

[29] Wu G, Yu X. A holistic 3D finite element simulation model for thermoelectric power generator element. Energy Conversion and Management. 2014;**86**:99-110

[30] Eringen AC, Maugin GA. Electrodynamics of Continua I. Springer-Verlag New York, Inc; 1990

[31] Callen HB. Thermodynamics and an Introduction to Thermostatistics. John Wiley and Sons, Inc; 1985

[32] Laird. Available from: https://www.lairdtech.com/product-categories/thermal-management/thermoelectric-modules

[33] Rowe DM. CRC Handbook of Thermoelectrics. CRC Press; 1995

Chapter 14

Thermoelectric Cooling: The Thomson Effect in Hybrid Two-Stage Thermoelectric Cooler Systems with Different Leg Geometric Shapes

Pablo Eduardo Ruiz-Ortega,
Miguel Angel Olivares-Robles and
Amado F. Garcia Ruiz

Additional information is available at the end of the chapter

http://dx.doi.org/10.5772/intechopen.75440

Abstract

This chapter aims to analyse the performance of hybrid two-stage thermoelectric cooler systems [two-stage thermoelectric cooling devices (TEC)], which are composed of different thermoelectric materials in each stage with different leg geometric shapes. If we consider a temperature gradient inside a two-stage TEC, then, besides Joule heat, also Thomson heat has to be taken into account. We discuss the out-of-equilibrium thermodynamics equations of a one-dimensional model to provide the performance expressions that govern the system. TEC system performance is analysed in function of the Thomson coefficients ratio of both stages. We describe a recent geometric optimization procedure that includes leg geometry parameters such as ratio of cross-sectional area and length of legs for each stage of the two-stage TEC.

Keywords: ideal equation (IE), Thomson effect, two-stage micro-cooler, Peltier effect

1. Introduction

Thermoelectric cooling devices are based on the Peltier effect to convert electrical energy into a temperature gradient. Thermoelectric effects, such as Seebeck effect, Peltier effect and Thomson effect, result from the interference of electrical current and heat flow in various semiconductor materials [1], and its interaction allows to use thermoelectric effects to generate electricity from a temperature differential; conversely, cooling phenomena occurs when a

voltage is applied across a thermoelectric material. Seebeck and Peltier effects depend on each other, and this dependence was demonstrated by W. Thomson who also showed the existence of a third thermoelectric effect, known as the Thomson effect. Thomson effect describes reversible heating or cooling, in a homogeneous semiconductor material, when there is both a flow of electric current and a temperature gradient [2, 3]. For thermoelectric cooling devices (TECs), a thermocouple consists of a p-type and n-type legs, with Seebeck coefficients (α) values positives and negatives respectively, joined by a conductor metal with low α value; in this chapter, we take this value as zero for calculations. Practical devices make use of modules that contain many thermocouples connected electrically in series and thermally in parallel [4]. TECs suffer from low efficiency, therefore, research on system geometry, for design and fabrication of thermoelectric cooling devices, is investigated in recent days [5, 6]. Coefficient of performance (*COP*) is the most important parameter for a thermoelectric cooling device, which is defined as the heat extracted from the source due an electrical energy applied [7]. Single-stage devices operate between a heat source and sink at a temperature gradient. However, multistage devices provide an alternative for extending the maximum temperature difference for a thermoelectric cooler. Therefore, two-stage coolers should be used to improve the cooling power, Q_c, and *COP*. In recent days, multistage thermoelectric cooling devices have been developed as many as six stages with bismuth telluride-based alloys. Recent works have investigated the ratio of the TE couple number between the stages and the effects of thermocouple physical size and have found that the cooling capacity is closely related to its geometric structure and operating conditions [8, 9]. In this chapter, a thermodynamics analysis and optimization procedure on performance of two-stage thermoelectric cooling devices based on the properties of established materials, system geometry and energy conversion, is analysed. Energy conversion issues in thermoelectric devices can be solved according to material properties: by increasing the magnitude of the differential Seebeck coefficient, by increasing the electrical conductivities of the two branches, and by reducing their thermal conductivities [10]. Several new theoretical and practical methods for the improvement of materials have been put forward and, at last, it seems that significant advances are being made, at least on a laboratory scale. In this work, we consider temperature-dependent properties material (TDPM) systems in calculations to determine the influence of the Thomson effect on performance [11, 12]. Many investigations have been conducted to improve the cooling capacity of two-stage TEC and found that cooling capacity is closely related to geometric structure and operating conditions of TECs. Our analysis to optimize cooling power of a thermoelectric micro-cooler (TEMC) includes a geometric optimization, that is, different cross-sectional areas for the p-type and n-type legs in both stages [13]. We find a novel procedure based on optimal material configurations, using two different semiconductors with different material properties, to improve the performance of a TEMC device with low-cost production.

This chapter is organized as follows: in Section 2, we give an overview of the thermoelectric effects. In Section 3, we apply thermodynamics theory to solve thermoelectric systems, and consequently, a description of the operation of a TEC device is presented. In Section 4, we proposed a two-stage TEC model taken into account Thomson effect for calculations to show its impact on *COP* and Qc. In Section 5, geometric parameters, cross-sectional area (A), and length (L) of a proposed two-stage TEMC system is analysed. For this purpose, constant

http://dx.doi.org/10.5772/intechopen.75440

properties of materials (CPM) models and TDPM models are compared to show Thomson effect's impact on performance. We consider two cases: (a) the same materials in both stages (homogeneous system) and (b) different materials in each stage (hybrid system). We establish optimal configuration of materials that must be used in each stage. Finally, in Section 6, we present a discussion and concluding remarks.

2. Thermoelectric effects

Thermoelectricity results from the coupling of Ohm's law and Fourier's law. Thermoelectric effects in a system occur as the result of the mutual interference of two irreversible processes occurring simultaneously in the system, namely heat transport and charge carrier transport [14]. To define Seebeck and Peltier coefficients, we refer to the basic thermocouple shown in **Figure 1**, which consists of a closed circuit of two different semiconductors. For a thermocouple composed of two different materials a and b, the voltage is given by:

$$V_{ab} = \int_1^2 (\alpha_b - \alpha_a) dT \tag{1}$$

where the parameters α_a and α_b are the Seebeck coefficients for semiconductor materials a and b.

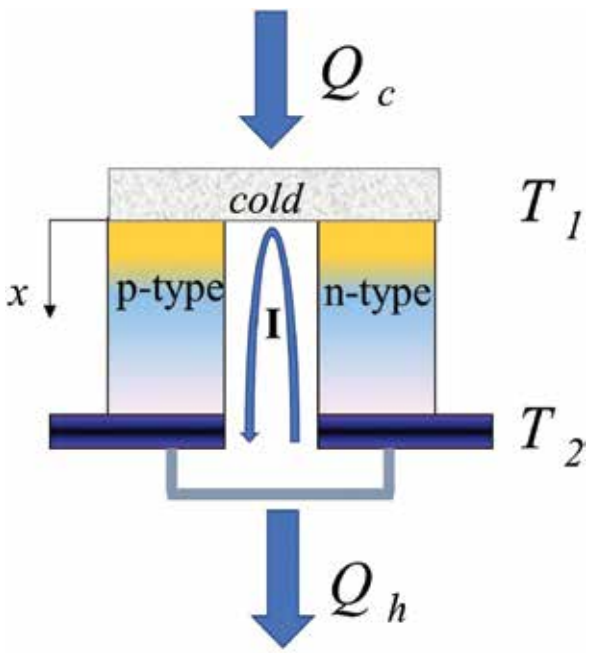

Figure 1. Single thermocouple model for a TEC system.

The differential Seebeck coefficient, under open-circuit conditions, is defined as the ratio of the voltage, V, to the temperature gradient,ΔT

$$\alpha_{ab} = \frac{V}{\Delta T} \tag{2}$$

Electrons move through the n-type element towards the positive pole, attraction effect, while the negative pole of the voltage source repels them. Likewise, in the p-type semiconductor, the holes move to the negative potential of the voltage source, while positive potential acts as repel of the holes and they move in the contrary direction to the flow of electrons. As a result, in p-type semiconductors, α is positive and in n-type semiconductors, α is negative [15]. Peltier coefficient is equal to the rate of heating or cooling, Q, ratio at each junction to the electric current, I. The rate of heat exchange at the junction is

$$Q = \pi_{ab} I \tag{3}$$

Peltier coefficient is regarded as positive if the junction at which the current enters is heated and the junction at which it leaves is cooled. When there is both an electric current and a temperature gradient, the gradient of heat flux in the system is given by

$$\frac{dQ}{dx} = \tau I \frac{dT}{dx} \tag{4}$$

where x is a spatial coordinate and T the temperature. Thomson coefficient, known as the effect of liberate or absorb heat due to an electric current flux through a semiconductor material in which exist a temperature gradient, is given by the Kelvin relation as follows

$$\tau_a - \tau_b = T \frac{d\alpha_{ab}}{dT} \tag{5}$$

When Seebeck coefficient is considered independent of temperature, Thomson coefficient will not be taken into account in calculations, τ is zero.

2.1. Thomson relations

Seebeck effect is a combination of the Peltier and Thomson effects [16]. The relationship between temperature, Peltier, and Seebeck coefficient is given by the next Thomson relation

$$\pi_{ab} = \alpha_{ab} T \tag{6}$$

These last effects have a relation to the Thomson coefficient, τ, given by

$$\tau = T \frac{d\alpha}{dT} \tag{7}$$

To develop an irreversible thermodynamics theory, Thomson's theory of thermoelectricity plays a remarkable role, because this theorem is the first attempt to develop such theory.

3. Thermoelectric refrigeration in nonequilibrium thermodynamics framework

Theory of thermoelectric cooling is analysed according to out-of-equilibrium thermodynamics. Under isotropic conditions, when an electrical current density flows through the semiconductor material with a temperature gradient and steady-state condition, the heat transport and charge transport relations, consistent with the Onsager theory [17], are

$$j_{el} = \sigma E - \sigma\alpha\nabla T \tag{8}$$

and

$$j_q = \alpha T j_{el} - \kappa\nabla T \tag{9}$$

where, α is the Seebeck coefficient, T is the temperature, κ is the thermal conductivity, E is the electric field, j_{el} is the electric current density, j_q is the heat flux and σ is the electric conductivity. Equation (9) is the essential equation for thermoelectric phenomena. The governing equations are

$$\nabla \cdot j_{el} = 0 \quad \text{and} \quad \nabla \cdot j_q = j_{el} \cdot E \tag{10}$$

For one-dimensional model, from Equations (8) and (9), we get for the heat flux

$$\vec{\nabla} \cdot \left(\kappa \vec{\nabla} T\right) + j^2\rho - T\frac{d\alpha}{dT}\vec{J} \cdot \vec{\nabla} T = 0 \tag{11}$$

where ρ is the electrical resistivity $(\rho = 1/\sigma)$ and J is the electric current density. In Equation (11), the first term describes the thermal conduction due to the temperature gradient. According to Fourier's law, the second term is the joule heating and the third term is the Thomson heat, both depending on the electric current density [18]. Now, from Equation (11), the equation that governs the system for one-dimensional steady state is given by:

$$\kappa(T)\frac{\partial^2 T}{\partial x^2} + \frac{d\kappa}{dT}\left(\frac{\partial T}{\partial x}\right)^2 - jT\frac{d\alpha}{dT}\frac{\partial T}{\partial x} = -\frac{j^2}{\sigma(T)} \tag{12}$$

3.1. Cooling power

Thermoelectric coolers make use of the Peltier effect which origin resides in the transport of heat by an electric current. For this analysis, we assume that thermal conductivity, electrical resistivity, and Seebeck coefficient are all independent of temperature, that is, CPM model [19], and the metal that connects the p-type with the n-type leg has a low α value, therefore it is considered as zero. We assume that there is zero thermal resistance between the ends of the branches and the heat source and sink. Thus, only electrical resistance is considered for the thermocouple legs, thereby, the thermocouple legs are the only paths to transfer heat between the source and sink, conduction via the ambient, convection, and radiation are ignored. These

considerations have been addressed in previous studies showing that the *COP* does not depend on the semiconductors length when the electrical and thermal contact resistances are not considered in calculations [20]. To determine the coefficient of performance (*COP*), which is defined as the ratio of the heat extracted from the source to the expenditure of electrical energy, a thermocouple model shown in **Figure 1** is used. Thus, for the p-type and n-type legs, the heat transported from the source to the sink is

$$Q_p = \alpha_p IT - K_p A_p \frac{dT}{dx}; \qquad Q_n = -\alpha_n IT - K_n A_n \frac{dT}{dx} \tag{13}$$

where A is the cross-sectional area, K is the thermal conductivity, and dT/dx is the temperature gradient. Heat is removed from the source at the rate

$$Q_c = \left(Q_p + Q_n\right)|_{x=0} \tag{14}$$

The rate of generation of heat per unit length from the Joule effect is $I^2\rho/A$. This heat generation implies that there is a non-constant thermal gradient

$$-\kappa_p A_p \frac{d^2T}{dx^2} = \frac{I^2\rho_p}{A_p}; \qquad -\kappa_n A_n \frac{d^2T}{dx^2} = \frac{I^2\rho_n}{A_n} \tag{15}$$

Using next boundary conditions: $T = T_1$ at $x = 0$ and $T = T_2$ at $x = L$, we get

$$\kappa_{n,p} A_{n,p} \frac{dT}{dx} = -\frac{I^2\rho_{n,p}\left(x - L_{n,p}/2\right)}{A_{n,p}} + \frac{\kappa_{n,p} A_{n,p}(T_2 - T_1)}{L_{n,p}} \tag{16}$$

where the subscripts n and p are for the n-type and p-type elements, respectively. From Equation (10), we find for the cooling power at the cold side $x = 0$

$$Q_c = \left(\alpha_p - \alpha_n\right)IT_1 - K\Delta T - \frac{1}{2}I^2R \tag{17}$$

where $\Delta T = T_2 - T_1$. The thermal conductance of the two legs in parallel is

$$K = \frac{\kappa_p A_p}{L_p} + \frac{\kappa_n A_n}{L_n} \tag{18}$$

and the electrical resistance of the two legs in series is

$$R = \frac{L_p\rho_p}{A_p} + \frac{L_n\rho_n}{A_n} \tag{19}$$

3.2. Coefficient of performance

The total power consumption in the TEC system is

$$W = (\alpha_p - \alpha_n) I \Delta T + I^2 R \tag{20}$$

then, the coefficient of performance in a TEC system is defined as [21]

$$COP = \frac{Q_c}{W} \tag{21}$$

4. Thomson effect impact on performance of a two-stage TEC

4.1. One-dimensional formulation of a physical two-stage TEC

To determine analytical expressions of cooling power and coefficient of performance in a two-stage TE system, we establish one-dimensional representation model, as shown in **Figure 2**. When a voltage is applied across the device, as a result, an electric current, I, flows from the positive to the negative terminal [22, 23].

$T_1 = T_c$, Q_{c1}, and Q_{h1} are, respectively, cold junction side temperature, amount of heat that can be absorb and amount of heat rejected from stage 1 to 2 of TEC. $T_2 = T_h$, Q_{h2} and Q_{c2} are, respectively, hot junction temperature, amount of heat rejected to the heat source and amount of heat absorbed from stage 1. It should be noted that Q_m is the heat flow from stage 1 to stage 2, that is, $Q_m = Q_{h1} = Q_{c2}$, and T_m is the average temperature in the system. For calculations, we use TDPM model [24] in order to show Thomson effect's role in the system. Arranging pairs of elements in this way allows the heat to be pumped in the same direction.

4.2. TEC electrically connected in series

Considering model from **Figure 2**, we get temperature distributions for p-type and n-type semiconductor legs in each stage. T_{11} and T_{12} are, respectively, the temperatures at the cold side junction for p-type and n-type legs in stage 1. T_{21} and T_{22} are, respectively, the temperatures at the hot side junction for p-type and n-type legs in stage 2 [25]. Solving with next boundary conditions: $T_{11}(0) = T_{12}(0) = T_1$ and $T_{11}(L_{11}) = T_{12}(L_{12}) = T_m$, we have for the first stage

$$T_{1(1,2)} = T_{(1,m)} \mp A_{1(1,2)} x + \frac{\Delta T \pm A_{1(1,2)} L_{1(1,2)}}{1 - e^{\mp \omega_{1(1,2)} L_{1(1,2)}}} (1 - e^{\mp \omega_{1(1,2)} x}), 0 \le x \le L_{1(1,2)} \tag{22}$$

and for the second stage, with $T_{21}(L_{11}) = T_{22}(L_{12}) = T_m$ and $T_{21}(L_{21}) = T_{22}(L_{22}) = T_h$

$$T_{2(1,2)} = T_{(m,2)} \mp A_{2(1,2)} x + \frac{\Delta T \pm A_{2(1,2)} L_{2(1,2)}}{1 - e^{\mp \omega_{2(1,2)} L_{2(1,2)}}} (1 - e^{\mp \omega_{2(1,2)} x}), L_{1(1,2)} \le x \le L_{2(1,2)} \tag{23}$$

where $\omega_{ij} = \frac{\tau_{ij} I}{K_{ij} L_{ij}}$, $A_{ij} = \frac{R_{ij} I}{\tau_{ij} L_{ij}}$, $K_{ij} = \frac{\kappa_{ij} S_{ij}}{L_{ij}}$, $R_{ij} = \frac{L_{ij}}{\sigma_{ij} S_{ij}}$ for $i = 1, 2$ and $j = 1, 2$ when $i \ge j$. The subscripts 1 and 2 describe cold temperature and hot temperature in the junctions. According to the theory of non-equilibrium thermodynamics, for the TEMC, we have for the first stage [26],

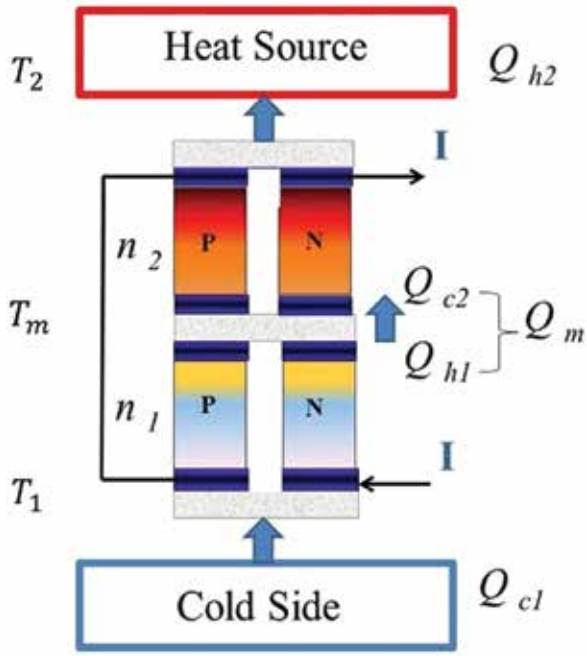

Figure 2. Two-stage thermoelectric cooler (TEC), electrically connected in series.

$$Q_{c1} = \alpha_1^c T_c I - K_1^*(T_m - T_c) - \left(R_1^* + R_1\right)I^2 \tag{24}$$

$$Q_{h1} = \alpha_1^m T_m I - K_1^*(T_m - T_c) - \tau_1(T_m - T_c) - R_1^* I^2 \tag{25}$$

$$Q_{c2} = \alpha_2^m T_m I - K_2^*(T_h - T_m) - \left(R_2^* + R_2\right)I^2 \tag{26}$$

$$Q_{h2} = \alpha_2^h T_h I - K_2^*(T_h - T_m) - \tau_2(T_h - T_m) - R_2^* I^2 \tag{27}$$

with $\alpha_1^k = \alpha_{12}^k - \alpha_{11}^k$, for $k = c, m$ and $\alpha_2^l = \alpha_{22}^l - \alpha_{21}^l$, for $l = m, h$; $R_j = R_{j1} + R_{j2}$; $\tau_j = \tau_{j2} - \tau_{j1}$ and $R_j^* = \left[R_{j1}^* + R_{j2}^* - \left(R_{j1} + R_{j2}\right)\right]$ for $j = 1, 2$. A general solution for the heat fluxes in two-stage system is found in [27] where Thomson effect is studied. The system's coefficient of performance, *COP*, is determined by Q_c and Q_h as follows

$$COP = \frac{\alpha_2^h T_h I - K_2^*(T_h - T_m) - \tau_2(T_h - T_m) - R_2^* I^2}{K_1^*(T_m - T_c) + (T_h - T_m)\left(-\tau_2 I - K_2^*\right) + \left(\alpha_2^h T_h - \alpha_1^c T_c\right)I + \left(R_1^* + R_1 - R_2^*\right)I^2} \tag{28}$$

Performance depends on Thomson coefficients values of both the first stage and the second stage. In our results, we show the role of the ratio values of the Thomson coefficients, $\tau_r = \tau_1/\tau_2$ between stages, on performance. Now solving for T_m, knowing that $Q_m = Q_{h1} = Q_{c2}$, from Equations (25) and (26)

$$T_m = \frac{I^2\left(R_1^* - R_2^* - R_2\right) - T_c\left(K_1^* + \tau_1 I\right) - K_2^* T_h}{I\left(\alpha_1^m - \alpha_2^m - \tau_1\right) - \left(K_1^* + K_2^*\right)} \tag{29}$$

where $K_j^* = K_{j1}^* + K_{j2}^*$, $K_{j1}^* = \frac{\tau_{j1} I}{1 - e^{-\omega_{j1} L_{j1}}}$, $K_{j2}^* = \frac{\tau_{j2} I}{e^{\omega_{j2} L_{j2}} - 1}$, $R_{j1}^* = R_{j1}\left(\frac{1}{1 - e^{-\omega_{j1} L_{j1}}} - \frac{1}{\omega_{j1} L_{j1}}\right)$ and $R_{j2}^* = R_{j2}\left(\frac{1}{\omega_{j2} L_{j2}} - \frac{1}{e^{\omega_{j2} L_{j2}} - 1}\right)$ for $j = 1, 2$. Once again we must notice the relationship that exists between both stages according to average temperature T_m, which also depends on the Thomson effect.

4.2.1. Influence of Thomson effect on performance (COP) and cooling power (Q_c)

Two different materials were used for calculations, thermoelectric properties are shown in **Table 1**, where only Seebeck coefficient is consider that depends on temperature.

With $\alpha_1 = \left[2 \times 10^{-4} + 2 \times 10^{-2}\ (1/T_m - 1/T)\right]$ for material Bi_2Te_3 and $\alpha_2 = [-62675 + 1610\ T - 2.3\ T^2] \times 10^{-6}$ and for material $(Bi_{0.5}Sb_{0.5})Te_3$ [25].

Figure 3 shows the *COP* and the cooling power Q_c, in function of τ_r, at different electric current values Bi_2Te_3 and $(Bi_{0.5}Sb_{0.5})Te_3$ [28]. It is clear that *COP* behaviour is influenced directly by the Thomson effect ratio of both stages. *COP* values increase when there is an increase in the ratio τ_r for lower values of the electric current *I*. We must notice that for lower values of $\tau_r < 1$, *COP* values are very closely one with another, with a maximum difference of 17% as compared an

Property	Bi_2Te_3	$(Bi_{0.5}Sb_{0.5})_2Te_3$	Unit
$\alpha_{1,2}$	197.7×10^{-6} (at 288K)	210.3×10^{-6} (at 288K)	V/K
$\kappa_{1,2}$	1.6	1.35	W/mK
$\rho_{1,2}$	0.7×10^{-5}	1.5385×10^{-5}	Ωm

Table 1. Properties of thermoelectric (TE) elements.

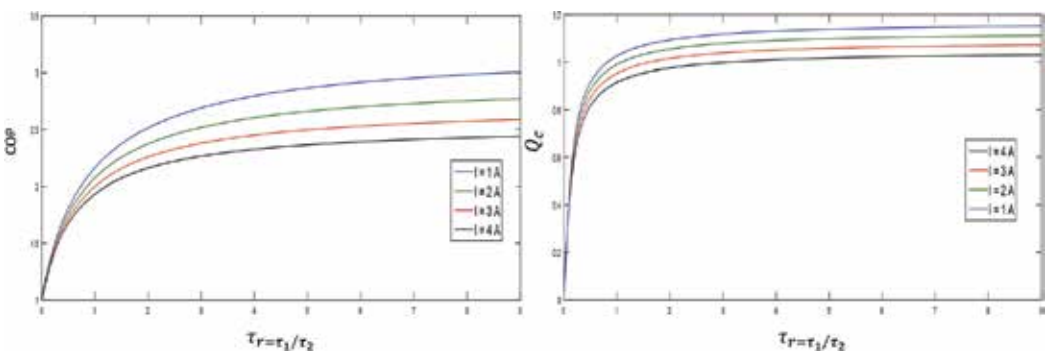

Figure 3. *COP* and Q_c in function of the ratio $\tau_r = \frac{\tau_1}{\tau_2}$, for different electric current values *I*.

electric current value of 1 A with an electric current of 4 A, when $\tau_r = 1$. Moreover, it is observed that from values of $\tau_r > 2$ COP values increase for all the different electric current values.

Similar behaviour, to what happens with the performance COP, happens for the cooling power Q_c, where maximum values are obtained for higher values of τ_r, as shown in **Figure 3**. In this case, Q_c value for an electric current value of 1 A is 11 % higher compared with electric current values of 4 A, when $\tau_r = 1$.

4.3. TECs electrically connected in parallel

Now, we analyse the case in which different electric currents flow in each stage of the system (**Figure 4**). The ratio of electric currents between each stage is given by

$$I_r = \frac{I_1}{I_2} \tag{30}$$

$$Q_c = \alpha_1^c T_c I_1 - K_1^*(T_m - T_c) - \left(R_1^* + R_1\right){I_1}^2 \tag{31}$$

$$Q_{m1} = \alpha_1^m T_m I_1 - K_1^*(T_m - T_c) - \tau_1(T_m - T_c) - R_1^* {I_1}^2 \tag{32}$$

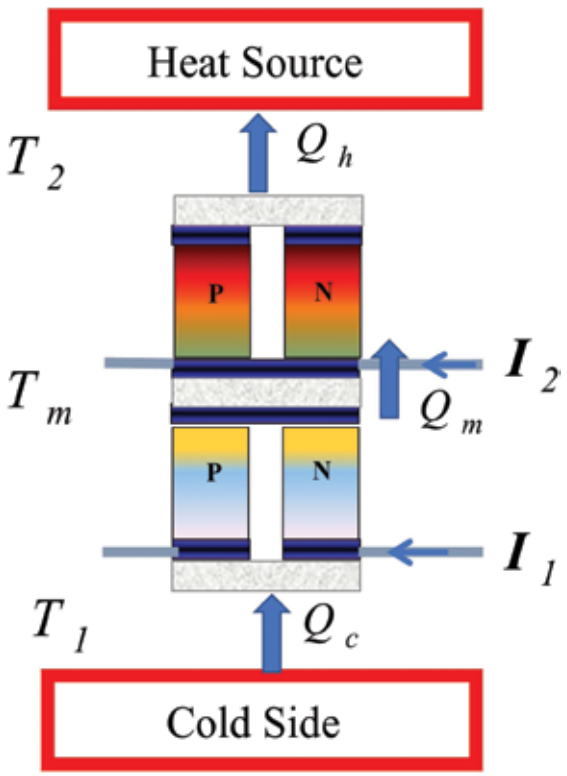

Figure 4. Two-stage thermoelectric cooler (TEC), electrically connected in parallel. Now, in the same way as in the previous section, we solve for the heat fluxes in the system.

$$Q_{m2} = \alpha_2^m T_m I_2 - K_2^*(T_h - T_m) - \left(R_2^* + R_2\right){I_2}^2 \tag{33}$$

$$Q_h = \alpha_2^h T_h I_2 - K_2^*(T_h - T_m) - \tau_2(T_h - T_m) - R_2^* {I_2}^2 \tag{34}$$

where I_1 is the electric current flow in stage 1 and I_2 is the electric current flow in stage 2.

According to the continuity of the heat flow between both stages, $Q_{m1} = Q_{m2}$, from Equations (32) and (33), we solve for the average temperature, T_m

$$T_m = \frac{R_1^* {I_1}^2 - \tau_1 T_c I_1 - K_1^* T_c - K_2^* T_h - \left(R_2^* + R_2\right){I_2}^2}{I_1\left(\alpha_1^m - \tau_1\right) - \left(K_1^* + K_2^*\right) - \alpha_2^m I_2} \tag{35}$$

The system's coefficient of performance, *COP*, is given by

$$COP = \frac{\alpha_2^h T_h I_2 - K_2^*(T_h - T_m) - \tau_2(T_h - T_m) - R_2^* I_2^2}{\left(\alpha_2^h T_h I_2 - K_2^*(T_h - T_m) - \tau_2(T_h - T_m) - R_2^* I_2^2\right) - \alpha_1^c T_c I_1 - K_1^*(T_m - T_c) - \left(R_1^* + R_1\right) I_1^2} \tag{36}$$

In the previous section, it is shown that *COP* increases for higher values of Thomson coefficient ratio between both stages. The behaviour of the *COP* for the case where two different electric currents flow in the system, shown in **Figure 5**, is now analysed. Three different values of

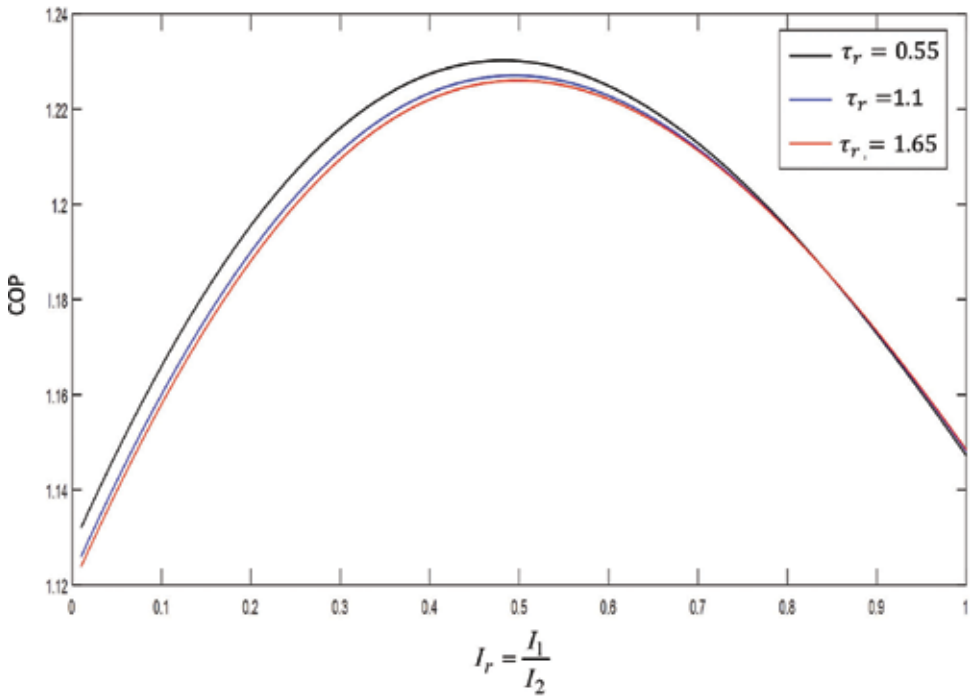

Figure 5. *COP* in function of the ratio $I_r = \frac{I_1}{I_2}$, for different $\tau_r$values.

τ_r	COP_{max}	I_r
0.55	1.23	0.49
1.1	1.227	0.51
1.65	1.228	0.513

Table 2. Maximum values of *COP*.

Thomson coefficients, τ_r, are considered. **Table 2** shows maximum values, from **Figure 5**, for *COP* in function of the electric current ratio between both stages, I_r. Maximum *COP* value is obtained for higher values of the ratio τ_r, that is, a higher value of the electric current $I_2 > I_1$ is desirable to be able to achieve better *COP*.

5. Dimensionless equations of a two-stage thermoelectric micro-cooler

Once it has been investigated the role of the Thomson heat on TEC performance, now a procedure to improve the performance of the micro-cooler based on optimum geometric parameters, cross-sectional area (A) and length (L), of the semiconductor elements is proposed. To optimal design of a TEMC, theoretical basis on optimal geometric parameters (of the p-type and n-type semiconductor legs) is required. Next analysis of a TEMC includes these optimization parameters. The configuration of a two-stage TE system considered in this work is shown in **Figure 2**. Each stage is made of different thermoelectric semiconductor materials. In order to make Equation (12) dimensionless using the boundary conditions $T(0) = T_1$ and $T(L) = T_2$, in accordance with **Figure 2**, we define the dimensionless temperature, θ, and the ξ parameter as,

$$\theta = \frac{T - T_1}{T_2 - T_1} \text{ and } \xi = \frac{x}{L} \tag{37}$$

Dimensionless differential equation corresponding to Equation (12) is given by:

$$\frac{d^2\theta}{d\xi^2} - \beta\big((\theta - 1)\phi + 1\big)\frac{d\theta}{d\xi} + \gamma = 0 \tag{38}$$

where

$$\beta = \frac{IT_2 \frac{d\alpha}{dT}\Delta T}{A\kappa \frac{\Delta T}{L}} \tag{39}$$

that is, β is the relation between Thomson heat with thermal conduction. From Equation (38), if $\beta = 0$, we get the ideal equation (IE) when Thomson effect not considered. Dimensionless parameter, γ, is the relation between Joule heating to the thermal conduction, and the parameter ϕ, which is the ratio of temperature difference to the high junction temperature, defined as:

$$\gamma = \frac{I^2 R}{A\kappa \frac{\Delta T}{L}} \quad \text{and} \quad \phi = \frac{\Delta T}{T_2} \tag{40}$$

5.1. Cooling power: the ideal equation and Thomson effect (τ)

If we consider Seebeck coefficient independent of temperature, Thomson coefficient is negligible ($\beta = 0$), we can obtain the exact result for the cooling power at the cold junction from Equation (14), which is called the ideal equation (IE) for cooling power

$$\dot{Q}_c^{IE} = \overline{\alpha} T_1 I - \frac{1}{2} I^2 R - \frac{Ak}{L}(T_2 - T_1) \tag{41}$$

The resulting equation considering the Thomson effect is given by:

$$\dot{Q}_c^{\beta} = \overline{\alpha} T_1 I - \frac{1}{2} I^2 R - \frac{Ak}{L}(T_2 - T_1) + \beta \frac{Ak}{L}(T_2 - T_1) \tag{42}$$

5.2. Geometric parameter between stages: area-length ratio (W = $w1/w2$)

Figure 6 shows a simple thermocouple with length, L and cross-sectional area, A. Previous studies proved that an improvement on performance of TECs can be achieved by optimizing

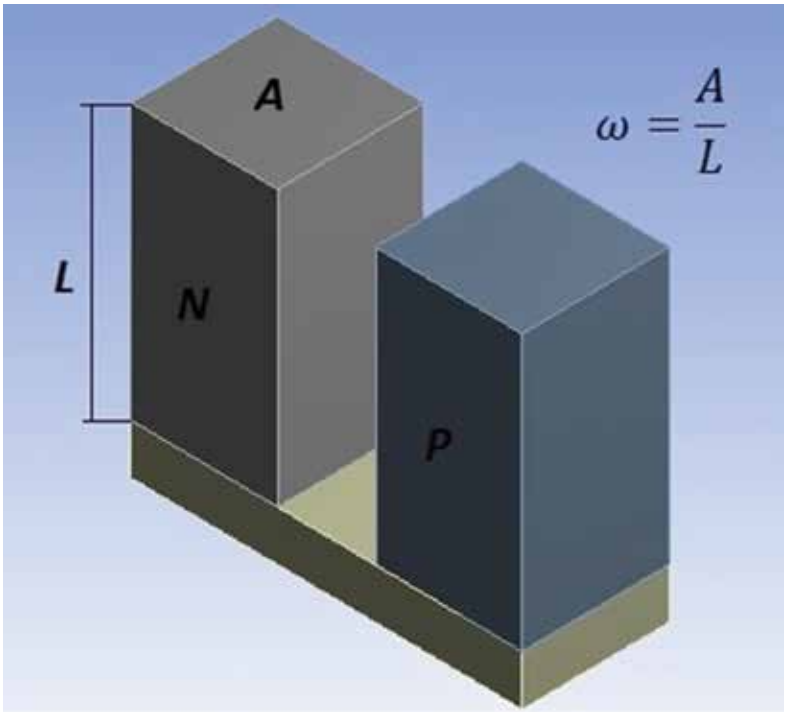

Figure 6. Schematic diagram of a thermocouple.

geometric size of the semiconductor legs [29, 30]. A geometric parameter, ω, is defined as the area-length ratio of the legs in the thermocouple in each stage of the TEMC

$$\omega_1 = \frac{A_1}{L_1} \quad \text{and} \quad \omega_2 = \frac{A_2}{L_2} \tag{43}$$

for the first and second stage, respectively.

We define the geometric parameter, W, which allows us to determine the optimal geometric parameters of the stages, which is expressed as,

$$W = \frac{\omega_1}{\omega_2} \tag{44}$$

In terms of the geometric parameters, ω_1 and ω_2, we get:

$$R = R_p + R_n = \frac{L_p}{\sigma_p A_p} + \frac{L_n}{\sigma_n A_n} = \frac{1}{\sigma_p \omega_1} + \frac{1}{\sigma_n \omega_2} \tag{45}$$

$$K = K_p + K_n = \frac{A_p k_p}{A_p} + \frac{A_n k_n}{A_n} = \omega_1 k_p + \omega_2 k_n \tag{46}$$

We have for the cooling power, in terms of the geometric parameters,$\omega_1$andω_2

$$\dot{Q}_c^{IE} = \alpha\left(T_{avg}\right) T_1 I - \frac{1}{2} I^2 \left(\frac{1}{\sigma_p \omega_1} + \frac{1}{\sigma_n \omega_2}\right) - \left(\omega_1 k_p + \omega_2 k_n\right)\left(T_2 - T_1\right) \tag{47}$$

For ideal equation, $\dot{Q}_c^{IE}$, and Thomson effect, $\dot{Q}_c^{\beta}$, we have

$$\dot{Q}_c^{\beta} = \alpha\left(T_{avg}\right) T_1 I - \frac{1}{2} I^2 \left(\frac{1}{\sigma_p \omega_1} + \frac{1}{\sigma_n \omega_2}\right) - \left(\omega_1 k_p + \omega_2 k_n\right)\left(T_2 - T_1\right) + \beta\left(\omega_1 k_p + \omega_2 k_n\right)\left(T_2 - T_1\right) \tag{48}$$

Finally, we introduce the ratio, M, of the number of thermocouples in the first stage, n_1, to the number of thermocouples in second stage,n_2

$$M = \frac{n_1}{n_2} \tag{49}$$

The total number of thermocouples, N, for both stages is given by,

$$N = n_1 + n_2 \tag{50}$$

5.3. Material properties considerations: CPM and TDPM models

The two different semiconductor materials and their properties are given in **Table 3**: Material M_1, which is obtained from commercial module of laird $CP10 - 127 - 05$ and its properties

Property	Material 1, $CP10-127-05$	Material 2, $(Bi_{0.5}Sb_{0.5})_2Te_3$	Unit
$\alpha_{1,2}$	198.34×10^{-6} (at 288 K)	210.3×10^{-6} (at 288 K)	V/K
$\kappa_{1,2}$	1.6	1.35	W/mK
$\rho_{1,2}$	$1.01\ x\ 10^{-5}$	$1.5385\ x\ 10^{-5}$	Ωm

Table 3. Properties of thermoelectric (TE) elements used in the TEMC device.

were provided by the manufacturer [21], and material M_2, $(Bi_{0.5}Sb_{0.5})_2Te_3$ [17], $T_{avg} = (T_1 + T_2)/2$, where $\overline{\alpha} = \alpha(T_{avg})$ and Seebeck coefficients are dependent on temperature while the electrical resistivity and the thermal conductivity are constant. The sign of n-type elements coefficient is negative while the sign of p-type element coefficients is positive for the Seebeck coefficients values. Then, for materials 1 and 2, we have next equations

$$\alpha_1 = [0.2068\ \ T + 138.78] \times 10^{-6} \quad \text{and} \quad \alpha_2 = \left[-62675 + 1610\ \ T - 2.3\ \ T^2\right] \times 10^{-6} \tag{51}$$

5.4. Special case: single-stage TEMC performance analysis

In this section, we analyse a single-stage system to compare with two-stage system to show the differences between both systems. Thereby, we calculate the two important parameters: *COP* and Q_c versus electric current; and *COP* and Q_c versus geometric parameter (w), for both materials. CPM models are compared with TDPM model, for this purpose, in all figures are shown results obtained considering Thomson effect (solid lines) and results using the ideal equation (dashed lines). **Figure 7** shows the COP_1, $Q_{c,1}$ and COP_2, $Q_{c,2}$ for materials, M_1 and M_2 respectively, as a function of the electric current. The maximum values of *COP* and Q_c are reached when the Thomson effect is considered, better cooling power is obtained with lower values of β. Results show that material M_1 achieves higher values of cooling power Q_c and *COP* than material M_2. The *COP* for material M_1 is 15.1% more than for material M_2 and Q_c for material M_1 is 40.12% more than for materialM_2.

Now, according to optimal electric current values, determined in the previous section, we show the effect of the semiconductor geometric parameters on the *COP*(w) and Qc(w) of the system. **Figure 8** shows that, for *COP* and Q_c, material M_1 has better results in both cases than material M_2. The *COP* of material M_1 is 21.18% higher than that for material M_2 and the Q_c value in material M_1 is 14.85% higher than for materialM_2.

5.5. Hybrid two-stage TEMC system

Now, we analyse a hybrid two-stage TEMC, that is, a system with a different thermoelectric material in each stage. Homogeneous system can also be analysed, this can be achieved by placing the same materials in both stages, as is shown in [27]. We focus on analysing two-stage hybrid systems, where two temperature gradients are generated and, therefore we must

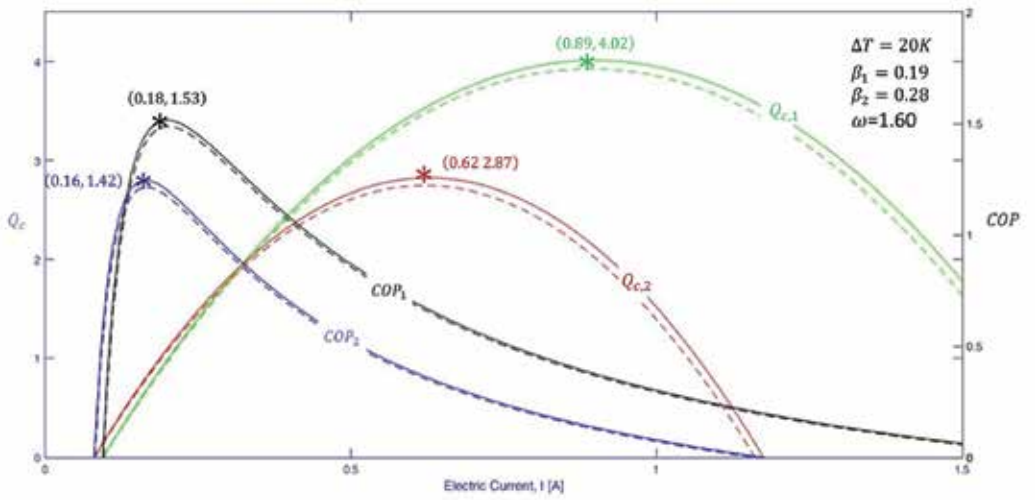

Figure 7. Single-stage coefficient of performance, $COP(I)$, and cooling power, $Q_c(I)$, for both materials M_1 and M_2. Solid lines calculated with Thomson effect and dashed lines considering ideal equation.

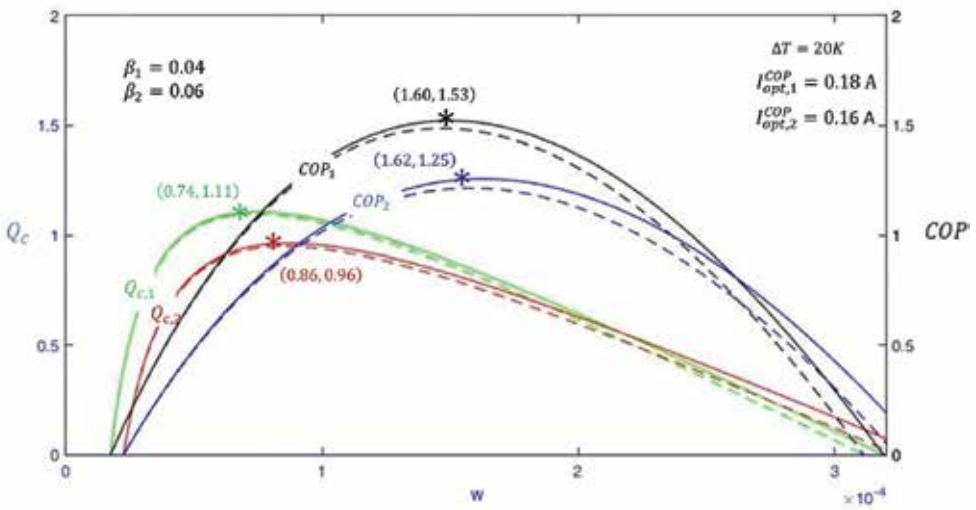

Figure 8. Single-stage $COP(w)$ and $Q_c(\omega)$ for both materials, using optimal electric currents I_{opt}^{cop}. Solid lines calculated with Thomson effect and dashed lines considering ideal equation.

analyse which material works better in each stage. Thus, we determine the optimum thermoelectric material arrangement for the best performance of the TEMC system. For this purpose, two configurations of materials in the hybrid two-stage TEMC model are considered: (a) materials M_1 and M_2 are used in the first and the second stage, respectively; and the inverse system (b) materials M_2 and M_1 are used in the first and the second stage, respectively.

5.5.1. Average system temperature, T_m

A two-stage TEMC consists of n_1 and n_2 thermocouples in the first and second stages, respectively. The heat flux at the cold side, Q_{c1}, and the heat flux at the hot side, Q_{h1}, in the first stage, and for the second stage, Q_{c2} and Q_{h2}, respectively. Thus, heat flux equations in the first stage are [31],

$$Q_{c1} = n_1\left[\alpha_1 I T_{c1} - K_1(T_m - T_{c1}) - 1/2R_1I^2 + \tau_1 I(T_m - T_{c1})\right] \tag{52}$$

$$Q_{h1} = n_1\left[\alpha_1 I T_m - K_1(T_m - T_{c1}) + 1/2R_1I^2 - \tau_1 I(T_m - T_{c1})\right] \tag{53}$$

and for the second stage,

$$Q_{c2} = n_2\left[\alpha_2 I T_m - K_2(T_{h2} - T_m) - 1/2R_2I^2 + \tau_2 I(T_{h2} - T_m)\right] \tag{54}$$

$$Q_{h2} = n_2\left[\alpha_2 I T_{h2} - K_2(T_{h2} - T_m) + 1/2R_2I^2 - \tau_2 I(T_{h2} - T_m)\right] \tag{55}$$

For a hybrid system (different materials in each stage), from equations (53) and (54), we obtain the temperature between stages, Tm,

$$T_m = \frac{-\frac{1}{2}I^2(R_1n_1 + R_2n_2) + \frac{1}{2}I(\tau_2 n_1 T_{h2} - \tau_1 n_1 T_{c1}) - K_2 T_{h2} n_1 - K_1 T_{c1} n_1)}{In_1\left(\alpha_1 - \frac{1}{2}\tau_1\right) + In_2\left(\frac{1}{2}\tau_2 - \alpha_2\right) - K_1 n_1 - K_2 n_2} \tag{56}$$

5.5.2. Dimensionless temperature distribution

For the hybrid two-stage TEMC system, the best configuration of semiconductor thermoelectric materials and its optimal geometric parameters is found in this section. For calculations we use a cross-sectional area of $A_c = 4.9 \times 10^{-9} m^2$ and element length of $L = 15 \mu m$, with a total number of thermocouples of $n_1 = n_2 = 100$ in the first and second stages, respectively. **Figure 9** shows the dimensionless spatial temperature distributions, for cases (a) and (b) mentioned earlier. An important factor to analyse in the graphic is the maximum values of the temperature distribution in each stage. When the value of the derivative is to be $d\theta/d\xi > 0$, the semiconductor material is able to absorb a certain amount of heat, that is, Thomson heat acts by absorbing heat. For the case when the value of the derivative is to be $d\theta/d\xi < 0$, a release of heat occurs in the semiconductor, that is, Thomson heat acts by liberating heat. From **Figure 9**, maximum temperature distribution values in stage 1, $\theta = 1.06$, is near to the junction with stage 2, which is desirable because in the first stage, the system must absorb higher amount of heat to later be released in stage 2. Thereby, dimensionless temperature distribution, θ, as a function of the length, ξ, shows that a lower temperature distribution is required in the first stage and that higher values of temperature distribution are required in the second stage; this is achieved by choosing the optimal arrangement of materials between the two stages. According to this last statement, case (a) is the best configuration of materials to improve the TEMC.

5.5.3. Analysis and coefficient of performance and cooling power (Q_c)

Figure 10 shows COP and Q_c for the TEMC system for cases (a) and (b) described previously. Case (a) reaches best cooling power and coefficient of performance values. Notice that the

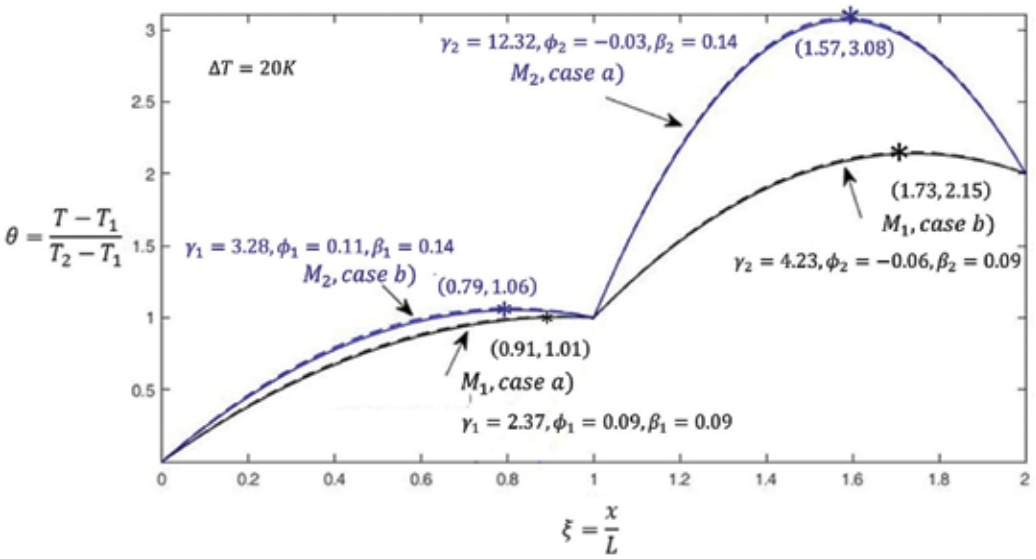

Figure 9. Hybrid two-stage TEMC. Dimensionless temperature distribution, $\theta(\xi)$. Case (a): material M_1 is placed in stage 1 (black line) and material M_2 in stage 2 (blue line). Case (b): material M_2 is placed in stage 1 (blue line) and material M_1 in stage 2 (black line). Solid lines calculated with Thomson effect and dashed lines considering ideal equation.

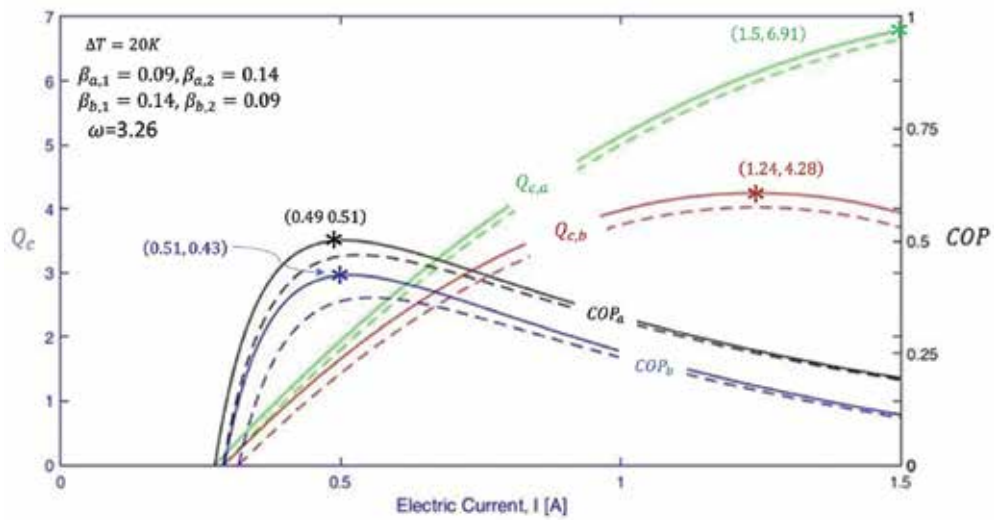

Figure 10. Hybrid two-stage TEMC. $COP(I)$ and $Q_c(I)$ for cases (a) and (b) with $w = w1 = w2$. Solid lines calculated with Thomson effect and dashed lines considering ideal equation.

$COP^{\beta}_{\max}(a)$ is 19.05% better than $COP^{\beta}_{\max}(b)$. It is clear from the graphic that for the same current values, cooling power values for the case (a) are always over those of the case (b).

5.5.4. Optimization analysis according to the geometric parameter W

In this section, we analyse the physical sizes, length and the cross-sectional area of the thermocouples, when the two stages are related each other. We present an optimization procedure of a two-stage TEMC system, on *COP* and Q_c, by introducing a geometric parameter, $W = \omega_1/\omega_2$. The effect of the parameter W on *COP* and Q_c is analysed when (1) $\omega_1 = \omega_2$ and (2) when $\omega_1 \neq \omega_2$. **Figure 11** (a) shows best optimal material configuration for $COP(w)$ and Q_c (w), which turns out to be case (a) where material M_1 is placed in the first stage and material M_2 in the second stage. Results proved that, higher area-length ratio values do not improve Q_c, on the contrary, the cooling power improves for lower values of w. *COP* and Q_c increases by 19 and 10.5%, respectively, from case (a) to case (b). The most relevant case, geometric parameters $\omega_1 \neq \omega_2$, is analysed. In this case, we set $\omega_2 = 3.26 \times 10^{-4}$ m to be a constant value. **Figure 11** (b) shows $COP(W)$ and $Q_c(\omega)$ where it is noted that *COP* increases by 8.9% and Q_c increases 6.27% in case (a) compared with case (b). From this last result, it is important to note that although the performance of TEC systems is affected by combination of different materials, it is also affected by the material configuration and the system geometry as well. These results offer a novel alternative in the improvement of thermoelectric systems, when they are used as coolers. Results shown in this chapter are based only on theory of thermoelectricity to optimize a TEMC system, according to geometric parameters. However, parameters as length and cross-sectional area of the semiconductor elements are based on studies which validated similar results with experimental data [32, 33]. In micro-refrigeration, an important problem is the fact of handle heat flux in a small space and it has been proved that thermal interface resistance has beneficial or detrimental effects on cooling performance [34]. For calculation, contact resistances between stages are not considered, since it is known that thermal resistances exist in the interfaces, which are large when the cross-sectional areas are very dissimilar in the stages and negligible for similar cross-sectional areas [35, 36]. Present work can be useful as theoretical

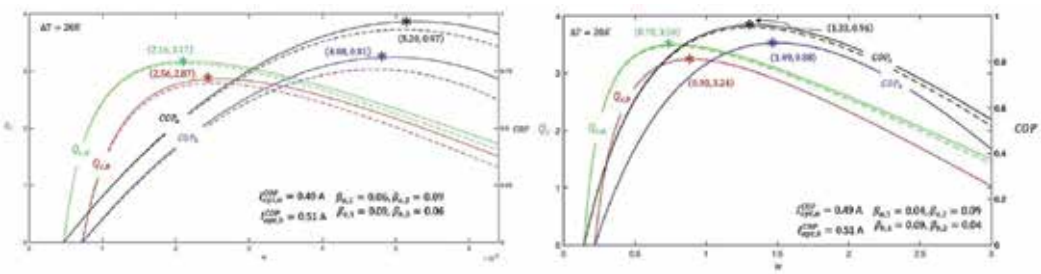

Figure 11. Hybrid two-stage TEMC. (a) $COP(\omega)$ and $Q_c(\omega)$ when $\omega_1 = \omega_2$. (b) $COP(W)$ and $Q_c(\omega)$ when $\omega_1 \neq \omega_2$. Solid lines calculated with Thomson effect and dashed lines considering ideal equation.

basis for future research in the experimental area, development and design of thermoelectric multistage coolers.

6. Conclusions

In this chapter, Thomson effect and leg geometry parameters on performance in a hybrid two-stage TEC were evaluated. For this purpose, the basics of two-stage thermoelectric cooler devices are analysed according to one dimension out-of-equilibrium thermodynamics using TDPM model. Two different semiconductor materials were used in all calculations. Results show, Thomson effect leads to a slight improvement on the performance and when the ratio of Thomson coefficients between both stages, $\tau_r = \tau_1/\tau_2$, increases, more cooling power can be achieved. We show that it is convenient to analyse optimal configuration of materials that must be used in each stage, showing that the material with a higher value of Seebeck coefficient must be place in the first stage. The main interest is to improve cooling power, thereby, a new procedure based on optimum leg geometric parameters of the semiconductor elements, is presented. Our analysis shows that, hybrid system reaches maximum cooling power, 15.9% greater than the one-stage system, for the case when the geometric parameter is $\omega_1 \neq \omega_2$. An important advantage of this work is that result can be confirmed in laboratories, as prototypes are made by mainly using bismuth telluride, which is the basis of the materials we use in all calculations.

Acknowledgements

This work was financially supported by research grant 20180069 of Instituto Politecnico Nacional, México. Pablo Eduardo Ruiz Ortega was financially supported by CONACyT-Mexico (CVU No. 490910). The authors acknowledge the editorial assistance in improving the manuscript.

Conflict of interest

The authors declare no conflict of interest.

Author details

Pablo Eduardo Ruiz-Ortega[1], Miguel Angel Olivares-Robles[1]* and Amado F. Garcia Ruiz[2]

*Address all correspondence to: molivares67@gmail.com

1 SEPI-Esime Culhuacan, Instituto Politecnico Nacional, Ciudad de Mexico, Mexico

2 UPIICSA, Instituto Politécnico Nacional, Ciudad de Mexico, Mexico

References

[1] Julian G, Robert H, Osgood R, Jurgen P, Hans W, editors. Introduction to Thermoelectricity. Springer Berlin: Springer Series in Material Science; 2010. 249 p. DOI: 10.1007/978-3-642-00716-3

[2] Ioffe A. Semiconductor Thermoelements and Thermoelectric cooling. London: Infosearch Limited; 1957. 185 p

[3] Goupil C, Seifert W, Zabrocki K, Muller E, Snyder G. Thermodynamics of thermoelectric phenomena and applications. Entropy. 2011;**13**:1481-1517

[4] Burshteyn A. Semiconductor Thermoelectric Devices. London: Temple Press; 1964

[5] El-Genk M, Saber H, Caillat T. Efficient segmented thermoelectric unicouples for space power applications. Energy Conversion and Management. 2003;**44**:1755-1772

[6] Di L, Fu-Yun Z, Hong-Xing Y, Guang-Fa T. Thermoelectric mini cooler coupled with micro thermosiphon for CPU cooling system. Energy. 2015:1-8

[7] Diana E, Elena O. A review on thermoelectric cooling parameters and performance. Renewable and Sustainable Energy Reviews. 2014;**38**:903-916

[8] Yang R, Chen G, Snyder G, Fleurial J. Multistage thermoelectric microcoolers. Journal of Applied Physics. 2004;**95**:8226-8232

[9] Cheng Y, Shih C. Optimizing the arrangement of two-stage thermoelectric coolers through a genetic algorithm. JSME International Journal. 2006;**49**:831-838

[10] Yang C, Di L, Fu-Yun Z, Jian-Feng T. Performance analysis and assessment of thermoelectric micro cooler for electronic devices. Energy Conversion and Management. 2016;**124**:203-211

[11] Meng F, Chen L, Sun F. Effects of temperature dependence of thermoelectric properties on the power and efficiency of a multielement thermoelectric generator. Energy & Environment. 2012;**3**:137-150

[12] Huang M, Yen R, Wang A. The influence of the Thomson effect on the performance of a thermoelectric cooler. International Journal of Heat and Mass Transfer. 2005;**48**:413-418

[13] Fabián M, Gao M, Alvarez Q. Enhanced performance thermoelectric module having asymmetrical legs. Energy Conversion and Management. 2017;**148**:1372-1381

[14] Callen H. The application of Onsager's reciprocal relations to thermoelectric, thermomagnetic, and galvanomagnetic effects. Physics Review. 1948;**73**:1349-1358

[15] Zemansky M. Heat and Thermodynamics. 5th ed. New York: McGraw-Hill; 1968

[16] Onsager L. Reciprocal relations in irreversible processes. II. Physics Review. 1931;**38**:2265-2279. DOI: 10.1103/PhysRev.38.2265

[17] Seifert W, Ueltzen M, Müller E. One-dimensional modelling of thermoelectric cooling. Physica Status Solidi. 2002;**194**:277-290

[18] Zabrocki K, Müller E, Seifert W. One-dimensional modeling of thermogenerator elements with linear material profiles. Journal of Electronic Materials. 2010;**39**:1724-1729

[19] Rowe DM. CRC Handbook of Thermoelectics. Boca Raton: CRC Press; 1995. pp. 214-219

[20] Min G, Rowe DM. Improved model for calculating the coefficient of performance of a Peltier module. Energy Conversion and Management. 2000;**2**(41):163-171

[21] Lee H. The Thomson effect and the ideal equation on thermoelectric coolers. Energy. 2013; **56**:61-69

[22] Xuan X. Analyses of the performance and polar characteristics of two-stage thermoelectric coolers. Semiconductor Science and Technology. 2002;**17**:414-420

[23] Chen J, Zhou Y, Wang H, Wang J. Comparison of the optimal performance of single- and two-stage thermoelectric refrigeration systems. Applied Energy. 2002;**73**:285-298

[24] Liu J, Wen C. Examination of the cooling performance of a two-stage thermoelectric cooler considering the Thomson effect. Numerical Heat Transfer. 2011;**60**:519-542

[25] Chen J, Yan Z, Wu L. Non-equilibrium thermodynamic analysis of a thermoelectric device. Energy. 1997;**22**:979-985

[26] Goupil C. Continuum Theory and Modeling of Thermoelectric Elements. Berlin: Wiley-VCH; 2016. 353 p. ISBN: 978-3-527-41337-9

[27] Ruiz E, Olivares MA. Analysis of a hybrid thermoelectric microcooler: Thomson heat and geometric optimization. Entropy. 2017;**19**:312. DOI: 10.3390/e19070312

[28] Ruiz E, Olivares MA. Analisis del Calor de Thomson en un Sistema Termoelectrico Unidimensional de dos Etapas. In: Semana Nacional de Ingenieria Electronica. Vol. 108. Celaya Mexico: Pistas Educativas; 2014. pp. 576-593

[29] Matthew M, Kenechi A, Parthib R, Corey E, Reddy B, Minking K. Geometric optimization of thermoelectric elements for maximum efficiency and power output. Energy. 2016;**112**: 388-407

[30] Sahin A, Yilbas B. The thermoelement as thermoelectric power generator: effect of leg geometry on the efficiency and power generation. Energy Conversion and Management. 2013;**65**:26-32

[31] Karimi G, Culham J, Kazerouni V. Performance analysis of multi-stage thermoelectric coolers. International Journal of Refrigeration. 2011;**34**:2129-2135

[32] Snyder GJ, Fleurial J-P, Caillat T, Yang RG, Chen G. Supercooling of Peltier cooler using a current pulse. Journal of Applied Physics. 2002;**92**:1564

[33] Yang R, Chen G, Kumar AR, Snyder GJ, Fleurial JP. Transient cooling of thermoelectric coolers and its applications for microdevices. Energy Conversion and Management. 2005; **46**:1407-1421

[34] Ju YS, Ghoshal U. Study of interfac eeffects in thermoelectric microrefrigerators. Journal of Applied Physics. 2000;**88**(7):4135-4139

[35] Yazawa K, Ziabari A, Kho Y, Shakouri A. Cooling power optimization for hybrid solid-state and liquid cooling in integrated circuit chips with hotspots. IEEE ITHERM Conference; 2012. pp. 99-106

[36] Kho Y, Yazawa K, Shakouri A. Performance and mass optimization of thermoelectric microcoolers. International Journal of Thermal Sciences. 2015;**97**:143-151

Chapter 15

Building-Integrated Thermoelectric Cooling-Photovoltaic (TEC-PV) Devices

Himanshu Dehra

Additional information is available at the end of the chapter

http://dx.doi.org/10.5772/intechopen.75472

Abstract

Photovoltaic driven thermoelectric cooling devices are of great importance in terms of alternative cooling sustainable technologies. Depending on Peltier effect of the thermoelectric cooling (TEC), heating and cooling is achieved by applying a voltage difference in the thermoelectric module. Theoretical design considerations of building-integrated thermoelectric cooling-photovoltaic (TEC-PV) devices are analyzed. System design of a TEC-PV device is investigated with varying fresh outdoor ventilation rates. Integrated design with ceiling suspended, wall mounted, rooftop and active façade TEC-PV devices is considered in the analysis. The effect of voltage, air flow rate and height of fin heat transfer surface is also investigated. Expressions along with results for theoretical exergy of a TEC-PV device are also provided.

Keywords: thermoelectric cooling, TEC-PV device, HVAC, heat sink, solar energy, energy efficiency

1. Introduction

Thermoelectric module is a sold-state energy conversion device made up of thermocouples, which are wired in series electrical circuit and parallel thermal junctions. A thermocouple consists of N-type and P-type semi-conductor elements, so as to generate thermoelectric cooling (viz., Peltier-Seebeck effect) when a voltage difference in appropriate direction is applied through the connected circuit. Thermoelectric cooling has benefits of high reliability, no moving parts, compact size, no requirement of thermo-fluid and light weight of thermoelectric modules. The direct current (DC) required to power thermoelectric cooling (TEC) modules can be easily fed by solar powered photovoltaic (PV) devices. In this way energy conservation is achieved through utilization of available solar energy. With application of low

voltage DC power source in a TEC module, heat transfer takes place from one side to the other side. In this way, TEC module's one side is cooled and other side is heated. In a TEC module, electric current drifts from N-type element to P-type element [1]. The temperature of the cold junction gradually decreases with heat transfer mechanism from environment to cold junction at a lower temperature. This heat transfer mechanism takes place with passing of transport electrons from a low energy level inside the P-type thermocouple element to a high energy level inside the N-type thermocouple element through the cold junction. Simultaneously, transport electrons transmit absorbed heat to hot junction at a higher temperature. This extra generated heat is dissipated to heat sink, whereas transport electrons return to a lower energy level in the P-type semiconductor element, viz., the Peltier effect takes place (see **Figure 1**).

There is constant development and efforts made for making thermoelectric air-conditioning systems in technical competence with vapor-compression technology. The performances of thermoelectric and conventional vapor compression air-conditioners have been compared by Riffat and Qiu [2]. Results have shown that the COPs of vapor compression and thermoelectric air-conditioners are in between 2.6–3.0 and 0.38–0.45, respectively. However, thermoelectric air conditioners have several other capabilities compared to vapor-compression technology. TEC modules can be built into a planar structure on walls and false ceiling and are quiet in operation especially suitable for small offices and mini apartments. Cosnier et al. [3] have presented numerical and experimental results of a thermoelectric air-cooling and air-heating system. The maximum cooling power of 50 W per module, with a COP varying between 1.5 and 2 was reached with electrical current of 4 A and maintaining 5°C temperature difference between the hot and cold sides. Cheng et al. [4] have investigated a solar-driven thermoelectric cooling module with a waste heat regeneration unit for green building applications. Their

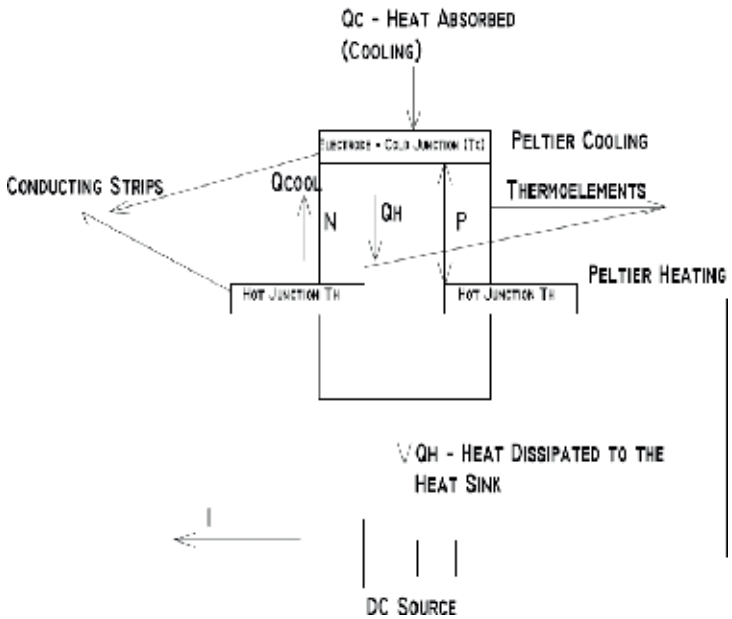

Figure 1. Principle of thermoelectric cooling.

http://dx.doi.org/10.5772/intechopen.75472

results have shown that TEC system was able to produce 16.2°C temperature difference between the ambient and building zone. However, the TEC COP was relatively low, varying from 0.2 to 1.2 in this study.

Gillott et al. [5] investigated TEC devices for small-scale space's air conditioning building application. A thermoelectric cooling unit was built for 220 W cooling capacity with a maximum COP of 0.46 with input electrical current of 4.8 A for each TEC module. Arenas et al. [6] and Vázquez et al. [7] developed an active thermal window (ATW) and transparent active thermoelectric wall (PTA) for room cooling application for building retrofit applications. In these devices, thermoelements embedded on window glass transfer heat through the glass in order to cool the room. A full-size prototype ATW was installed in a window frame (100 × 100 cm), which was able to generate up to 150 W of cooling power while glass transparency decreased by about 20%. Their work was patented [8]. Most of TEC devices directly cool down the indoor air. Shen et al. [9] investigated a novel thermoelectric radiant air-conditioning system (TE-RAC). The TE-RAC system employs thermoelectric modules as radiant panels for indoor cooling, as well as for space heating by easily reversing the input current. Their analysis of a commercial thermoelectric module, TEC1-12706 with a ZT value of 0.765, have obtained a maximum cooling COP of 1.77 with an electric current of 1.2 A while maintaining cold side temperature at 20°C.

The cooling effect in the TEC module is dependent on parameters such as electric current, the hot and cold side temperatures, the electrical contact resistance between the cold side and the surface of TEC device, thermal and electrical conductivities of thermoelement and thermal resistance of the heat sink on the hot side of TEC module. The required cooling capacity with maximum electric current determines the number of thermoelements in a TEC module. The main disadvantage of thermoelectric cooling module is its poor coefficient of performance (COP), predominantly in large capacity applications [10]. The COP and the cooling capacity of the TEC module can be predicted using the standard module theory based on one dimensional (1-D) heat balance equations, with the assumptions of negligible thermal and electrical contact resistances. The COP estimated from the standard module theory is determined from the hot and cold side temperatures of TEC module and figure of merit, ZT of the thermoelectric material. The design of thermoelectric cooling system is based on temperature difference across the hot and cold sides of the TEC module and the required cooling capacity.

In this chapter, one dimensional (1-D) energy balance model is presented for evaluating system design of a prototype thermoelectric cooling – photovoltaic (TEC-PV) device. The prototype consists of an integrated design with ceiling suspended, wall mounted, rooftop and active façade TEC-PV devices.

2. Energy balance model

The total energy efficiency of photovoltaic driven thermoelectric cooling devices can be increased with enhancement of photovoltaic system efficiency and with the use of thermoelectric materials with better performance. The COP of thermoelectric air conditioning devices powered through photovoltaic modules is typically not higher than 0.6 [10]. With consideration of photovoltaic

system efficiency η_{pv}, the total energy efficiency of the system is given by the product of η_{pv} and COP. Mathematically it is written as:

$$E_{TEC-PV} = \eta_{pv} \times COP \tag{1}$$

The values of $E_{TEC\text{-}PV}$ are typically lower than 6%.

Commercial thermoelectric materials are alloys such as Bi_2Te_3, PbTe, SiGe and $CoSb_3$ [11]. Bi_2Te_3 is the most commonly used thermoelectric material. The commercially available thermoelectric materials have highest ZT values around 1.0.

For a particular thermoelectric module with fixed hot/cold side temperatures, the maximum COP at optimum current is given by [11]:

$$COP_{\max,cool} = \frac{T_c}{T_h - T_c} \cdot \frac{\sqrt{1 + ZT_m} - \frac{T_h}{T_c}}{\sqrt{1 + ZT_m} + 1} \tag{2}$$

where ZT_m is the figure-of-merit for thermoelectric material at mean hot and cold side temperature T_m. In calculation of COP, a mean temperature between the hot and cold junction temperatures (with fixed hot side temperature of 300 K with ZT_m = 1) of the thermoelectric module (TEM) is used.

A steady state energy balance model of thermoelectric cooling is used for energy performance assessment. The absorbed (Q_c) heat flux and released (Q_h) heat flux are obtained using Eqs. (3) and (4) respectively. The electric power (P) required to power thermoelectric module (TEM) is obtained from the difference between the absorbed and released heat fluxes (Eq. (5)). In these equations, α, R and K are the Seebeck coefficient, electrical resistance, and thermal conductance of the thermoelectric module. Whereas, *I*, is the electric current and N is the number of thermocouple legs in the thermoelectric module. The TEM is made up of several thermocouple legs. Thermoelectric leg characteristics are responsible for the resulting TEM performance. R and K are calculated using Eqs. (6) and (7) respectively considering the leg length (L), leg section area (S), thermal conductivity (λ) and electrical resistivity (ρ). The coefficient of performance (COP) of the TEM is the ratio between the absorbed heat and total electric power (including fan power) obtained from Eq. (8). In this chapter, a thermocouple leg made of bismuth telluride (Bi_2Te_3) is considered and its properties are shown in **Table 1** [12]. The thermal resistance between the thermoelectric module and fin plate is assumed to be 0.0161 K/W [12].

Conductivity thermal (W/m-K)	$\lambda(T) = \left(62605 - 277.7 \cdot T + 0.4131 \cdot T^2\right)10^{-4}$
Resistivity electrical (Ω·m)	$\rho(T) = \left(5112 - 163.4 \cdot T + 0.6279 \cdot T^2\right)10^{-10}$
Seebeck coefficient (Volts/K)	$\alpha(T) = \left(2224 - 930.6 \cdot T + 0.9905 \cdot T^2\right)10^{-9}$

Table 1. Bismuth telluride (Bi_2Te_3) properties.

$$Q_c = N \cdot \left(\alpha \cdot I \cdot T_C - 0.5 \cdot R \cdot I^2 - K \cdot \Delta T\right) \tag{3}$$

$$Q_h = N \cdot \left(\alpha \cdot I \cdot T_H + 0.5 \cdot R \cdot I^2 - K \cdot \Delta T\right) \tag{4}$$

$$P = Q_h - Q_c = N \cdot \left(\alpha \cdot I \cdot \Delta T + R \cdot I^2\right) \tag{5}$$

$$R = \frac{L}{S} \cdot \rho \tag{6}$$

$$K = \frac{S}{L} \cdot \lambda \tag{7}$$

$$COP_{cooling} = \frac{Qc}{P} \tag{8}$$

In order to investigate the operating energy consumption in summer, a thermoelectric cooling-photovoltaic (TEC-PV) device is simulated for building data as per **Table 2**, representing sunny, hot and humid outdoor air condition. Properties of TEC-PV device is provided in **Table 3**. **Table 4** provides thermal design properties of TEC-PV device.

2.1. Thermoelectric dehumidification

The room sensible heat factor (RSHF) is defined as the ratio of sensible cooling load to total cooling load (Eq. (9)).

$$RSHF = \frac{Q_{sen}}{Q_{sen} + Q_{lat}} \tag{9}$$

Outdoor air condition	Sunny, hot and humid (DBT: 33–35°C, RH: 75%)			
Floor area	9 m^2			
Room volume	27 m^3			
U-value of exterior wall	0.44 W/m^2 K			
U-value of roof	0.126 W/m^2 K			
Window to wall ratio	0.3			
Lighting power density	0.6 W/ft^2			
Infiltration	0.3 ACH			
Operation schedule	07:00 to 17:00 hours			
Indoor air condition	Dry bulb temperature (DBT): 23°C, RH: 55%			
Room sensible heat factor	0.95	0.9	0.8	0.7
Ventilation rate	20 m^3/h	40 m^3/h	90 m^3/h	120 m^3/h
Peak sensible cooling load	1 kW			
Peak latent cooling load	0.05 kW	0.12 kW	0.28 kW	0.48 kW

Table 2. Building data.

TEC module	TEC1-12710		Photovoltaic module	
Operational voltage	12 V DC		Total power required	1.8 kW
Current max	10.5 Amp		Area required	18 m^2
Voltage max	15.2 V		Roof area	9 m^2
Power max	85 W		South façade area	9 m^2
Nominal power	60 W		Nominal power	300 W
Thermocouples	127		Number of PV modules	8
Dimensions	40 × 40 × 3.5 mm		On roof	4
Total number of TEC modules	30		On façade	4
Placement position	Inside ceiling duct	Wall mounted	Battery backup	10.8 kWh
TEC modules	10	20	Battery @ 12 V DC	900 AH

Table 3. Thermoelectric cooling (TEC)-photovoltaic (TEC-PV) device properties.

Relative humidity is a key control parameter for thermal comfort inside a room. The performance of a thermoelectric cooling device depends mainly on optimal positioning and layout of heat exchange & transfer surfaces.

The total heat transfer rate (Q_c) of the fin heat exchanger on the cold side of the thermoelectric module (TEM) is given by [13]:

$$Q_c = h_c \cdot A_c \cdot (t_r - t_c) + m_w \cdot H_c \tag{10}$$

where h_c is the coefficient of convective heat transfer (W/m^2K), A_c is the heat transfer area (m^2), t_r is the room temperature (°C), t_c is average temperature of cold fins (°C) and H_c is the latent heat of condensation (J/kg-K).

The dehumidifying rate (m_w, kg/s) is calculated as [13]:

$$m_w = \frac{m_a \cdot (\phi_1 - \phi_2)}{T_{\text{sec}}} \tag{11}$$

where m_a is the mass of the wet air inside the room (kg), T_{sec} is the dehumidifying period (sec), Φ_1 and Φ_2 are the relative humidity before and after dehumidification (%).

The convective heat transfer coefficient between adjacent fins and room air is given by [14]:

$$h_c = 0.517 \cdot \frac{k_{air}}{H} \cdot Ra^{0.25} \tag{12}$$

where k_{air} is the thermal conductivity of air (W/m-K), H is the height of fin (m) and Ra is the dimensionless Rayleigh number.

Parameter	Values
Thermal resistance of cold side	0.1 K/W
Thermal resistance of hot side	0.7 K/W
TEM thermal conductivity	0.51 W/K
TEM electrical resistance	2.236 Ω
Aluminum thermal conductivity	230 W/m-K
Thickness of aluminum sheet	1.6 mm
Insulation thickness	40 mm
Insulation thermal conductivity	0.05 W/m-K
Insulation specific heat capacity	500 J/kg-K
Thermal contact resistance	0.1 m^2K/W
Fin thickness	1 mm
Fin profile length	20 mm
Fin spacing	3 mm
Number of fins (cold side) per TEC module	10
Number of fins (hot side) per TEC module	10
Thermal resistance (cold side fins)	1.2 K/W
Thermal resistance (hot side fins)	0.76 K/W
Thermal resistance between TEM and fin plate	0.0161 K/W
Height of solar PV wall mounted exhaust duct	3000 mm
Width of solar PV wall mounted exhaust duct	2 Nos.@ 1500 mm
Absorption coefficient of PV panel	0.9
Thickness of PV ventilated exhaust duct	150 mm
Density of PV panel	2300 kg/m^3
Specific heat capacity of PV panel	750 J/kg-K
Thickness of PV panel	5 mm
Number of TEC modules with ceiling suspension duct (position 1)	10 covering 1.60 m^2
Number of TEC modules on wall (position 2)	20 covering 3.60 m^2
Heat transfer fluid	Air
DC power for each fan	1.5 W
Number of DC fans on supply side	2
Number of DC fans on exhaust side	2
Maximum ventilation rate per fan	60 m^3 h^{-1}

Table 4. Thermal design properties of TEC-PV device.

2.2. Exergy expressions

The specific exergy of fresh moist air into the duct is expressed as [15]:

$$ex_{f,in} = \left(c_{pa} + w_{f,in} \cdot c_{pv}\right)\left[T_{f,in} - T_o - T_o \cdot \ln\frac{T_{f,in}}{T_o}\right] + R_a \cdot T_o\left[\left(1 + 1.608 w_{f,in}\right) \cdot \ln\frac{\left(1 + 1.608 w_{f,in}\right)}{\left(1 + 1.608 w_o\right)} + 1.608 \cdot R_a \cdot T_o \cdot w \cdot \ln\frac{w_{f,in}}{w_o}\right] \quad (13)$$

The reference temperature (T_o) and the humidity ratio (w_o) is defined as the indoor air temperature and humidity ratio during hot and humid season. R_a is the thermal resistance of air. c_{pa} is specific heat of moist air and c_{pv} is specific heat inside the duct.

Thus from Eq. (13), total exergy of the fresh air flow into the duct is expressed as:

$$Ex_{f,in} = \rho \cdot M_a \cdot ex_{f,in} \quad (14)$$

where ρ is density of air and M_a is airflow rate m^3/h.

The exergy of the heat transferred between the fresh air and TEM is expressed as:

$$Ex_{Qf} = \left[1 - \frac{T_o}{T_c}\right] \cdot Q_f \quad (15)$$

where Q_f is heat transfer rate (W).

The system exergy efficiency is expressed as:

$$\eta_{Ex} = \frac{Ex_{eff}}{Ex_{sup}} \times 100\% = \frac{\left[Ex_{f,out} - Ex_{f,in}\right]}{Ex_{elec}} \times 100\% \quad (16)$$

where Ex_{eff} is effective Exergy, Ex_{sup} is electrical exergy supplied.

3. Design considerations for thermoelectric cooling photovoltaic (TEC-PV) devices

a. **Building integration parameters:** Thermoelectric cooling (TEC) devices can be fixed in a building on wall and ceiling as radiant cooling panels. Due consideration should be given for placing thermoelectric modules with or without heat sinks. Heat sinks can be placed towards building interior zone and towards exterior zone. The thermoelectric modules can be placed on a cut section of a wall, with provision of cooling the hot side heat sink. The thermoelectric cooling devices can also be fixed on a window or a skylight. Proper protection

has to be ensured from air infiltration and direct solar radiation for TEC devices fixed on windows and skylights. The mode of operation for winter can be reversed by changing the direction of current of thermoelectric modules. TEC devices can also be fixed inside air supply ventilation ducts. Buildings requiring cooling and heating with dual duct ventilation system are good choice for using thermoelectric devices inside ducts.

b. **Thermoelectric module (TEM) system design:** It depends on thermoelement length, number of thermocouple legs, cross sectional area, slenderness ratio. Both COP and cooling capacity of TEC devices are dependent on thermoelement length. Keeping cross sectional area constant, larger length of thermoelectric element achieves greater COP, while shorter length thermoelectric element achieves larger cooling capacity. Commercially available thermoelectric modules have thermoelement length in the range from 1 to 2.5 mm [11]. Cooling power capacity increases with decreasing the ratio of thermoelement length to cross sectional area.

c. **Thermoelectric cooling (TEC) system design:** It depends on cooling system thermal design, heat sinks' geometry, heat transfer area, heat transfer coefficients of hot and cold side heat sinks, thermal and electrical contact resistances, fins placement and design, heat sinks integrated with thermosyphon, heat transfer fluids, phase change materials [16]. Thermal contact resistance at the interface layer of thermocouple legs is critical for its cooling capacity and COP. Because of this reason, it is not essential that increase in ZT of thermoelectric material will increase ZT of a thermocouple leg because of the presence of interface layer. The performance and efficiency of heat sinks at hot and cold side effects the cooling COP. Air cooled heat sink (forced convection with fan, example thermal resistances of 0.54–0.66 K/W [11], water cooled heat sink (thermal resistance of 0.108 K/W [11], and heat sink integrated with heat pipe (thermal resistance 0.11 W/K are most commonly used techniques. It has been found that heat pipes are not preferred as they eventually have to release heat to either air or water eventually. Heat sinks with nanofluid have potential to achieve lower thermal resistance. Hot side heat sink performance is of greater importance due to higher heat flux density in comparison to heat flux at cold side heat sink. Allocation ratios of heat transfer area with heat transfer coefficients between hot and cold sides are important for achieving maximum COP. Typical allocation ratio is around 0.36–0.47 [11]. Maximum COP with optimum cooling capacity can be achieved at given hot and cold sides fluid temperatures.

d. **Photovoltaic (PV) power system design:** The most conventional way is to install PV panels on rooftop and façade of a building with thermoelectric cooling (TEC) devices. In this way, excess power can also be stored in a battery system. In case of non-availability of solar PV power, power can be fed directly from the battery backup. Active façade ventilation can be integrated with TEM and PV devices [17–19]. For heating requirements during winter season, these active façade elements can supplement with heating from TEM and façade integrated PV ventilated devices [20–22].

e. **Performance & operational parameters optimization:** It depends on electric current input, coolants, cooling methods of hot side heat sink, mass flow rate, ventilation requirements. Performance indicators are COP and energy efficiency of devices and systems.

4. System design of thermoelectric cooling-photovoltaic (TEC-PV) device

4.1. Importance of outdoor air ventilation

Indoor air quality improvement is achieved by bringing in outdoor air into the building environment. Introduction of outdoor air increases energy consumption of the conventional air conditioning system. In the conventional air conditioning system, limited energy conservation is achieved through heat recovery ventilators, such as fixed-plate, run-round coil and rotary wheel. In these heat recovery ventilators, passive means are employed through temperature and humidity difference between fresh outdoor air and return air, which are dependent on outdoor weather conditions. However in a thermoelectric cooling-photovoltaic (TEC-PV) device, dedicated outdoor air is cooled and dehumidified by active means through input of solar power. The design is assessed by estimating the cooling capacity for selection of a TEC module according to the temperature difference between the hot and cold side. The current required to operate the TEC module can be obtained from trials and also checked from manufacturer data curve to meet the actual cooling capacity. Energy efficiency of a thermoelectric cooling (TEC) device is defined as the ratio of the cooling capacity to the electrical energy consumed. Exergy analysis is based on quality of energy, used for evaluating energy process with respect to ideal thermodynamic equality. Exergy analysis is used for identifying exergy losses, which is used for understanding of irreversible losses of energy conversion in its system design.

The system design consists of: (i) outdoor fresh air ventilation; (ii) thermoelectric cooling (TEC); (iii) building integration; (iv) photovoltaic power generation; and (v) exhaust air ventilation.

4.2. Operation

The outdoor fresh air is cooled down and dehumidified as it flows over a heat sink/exchanger attached to thermoelectric cooling (TEC) module. The cool air enters the indoor environment which is to be maintained at 23°C and 55% RH. The stale air is taken out through ducted exhaust air ventilation system. The exhaust air also cools down the heat sink/exchanger attached to hot side of thermoelectric module (TEM). The outdoor fresh air is introduced into the single zone building air volume at varying rates as mentioned in **Table 2**. Four DC fans are used to provide power for forced airflow. Two of them are installed on supply fresh air side and other two are installed on exhaust air side. The input power for each fan is 1.5 W with airflow rate at 60 $m^3 h^{-1}$. The maximum fresh air supply in the room is 120 $m^3 h^{-1}$ at full capacity. The outside fresh air is at 33°C and 75% RH. Eight solar PV modules of 300 W each are used to power thirty TEC modules of 60 W each and four DC fans of 1.5 W each. Four solar PV modules are placed on south façade while other four are fixed on roof top. The maximum sensible cooling load in the building zone is 1 kW while maximum latent load varies up to 0.48 kW.

Principle:

Two-stage Dehumidification (Condensation): Depending on dew point of the air, cooling dehumidification and iso-thermal dehumidification can take place on fins inside cooling duct and on wall with TEC modules.

http://dx.doi.org/10.5772/intechopen.75472

Heat transfer process: A steady state is reached when temperature of air remains constant with heat transfer from the cold side fins. Cold side fins are placed both on supply duct and inside room. Hot side fins are placed on exhaust duct and exterior of room wall surface. The height of heat transfer surface inside the duct is 0.5 m and height of heat transfer surface inside the room is 2.5 m. The condensation phenomenon at initial dehumidification will result in rapid temperature drop of cold side fins. The dehumidification will continue further at steady temperature of cold side fins. In order to improve the performance of fins for dehumidification, rapid elimination of condensed water is necessary. This is achieved by specially treated heat transfer surfaces (fins) with superhydrophilic or super water repellant surfaces [13].

The schematic of a building zone with two stage cooling through TEC modules by means of supply duct and wall mounted TEC modules with solar PV façade exhaust duct is illustrated in **Figure 2**. The performance characteristics with voltage variation of analyzed TEC1-12710 modules in TEC calculator is provided in **Figure 3**. The variation in theoretical values of COP (cooling) and temperature (cold) for $ZT_m = 1$ is provided in **Figure 4**. The variation in theoretical values of cooling capacity with temperature difference is provided in **Figure 5**. The variation of theoretical heat transfer coefficient with height of heat transfer surface (fins) is provided in **Figure 6**. The theoretical variation of cooling capacity load served inside room with height of heat transfer surface (fins) is provided in **Figure 7**. The variation of theoretical exergy of air cooled inside the room with cold side temperature and Tout at 306 K is illustrated in **Figure 8**. All the results are based on theoretical values irrespective of actual performance values of the prototype TEC-PV device.

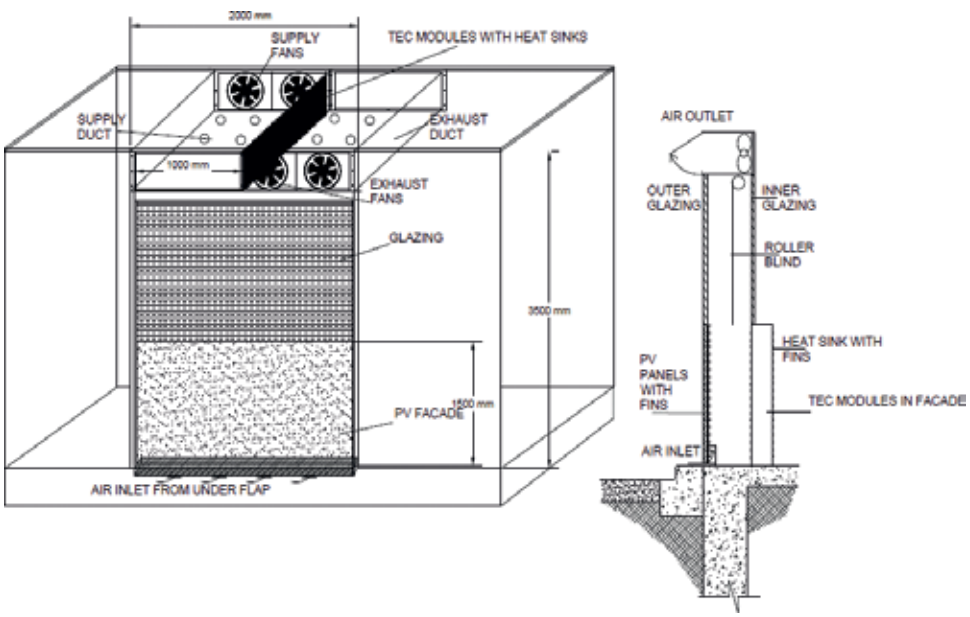

Figure 2. Schematic of a building room zone with TEC modules and PV ventilated façade.

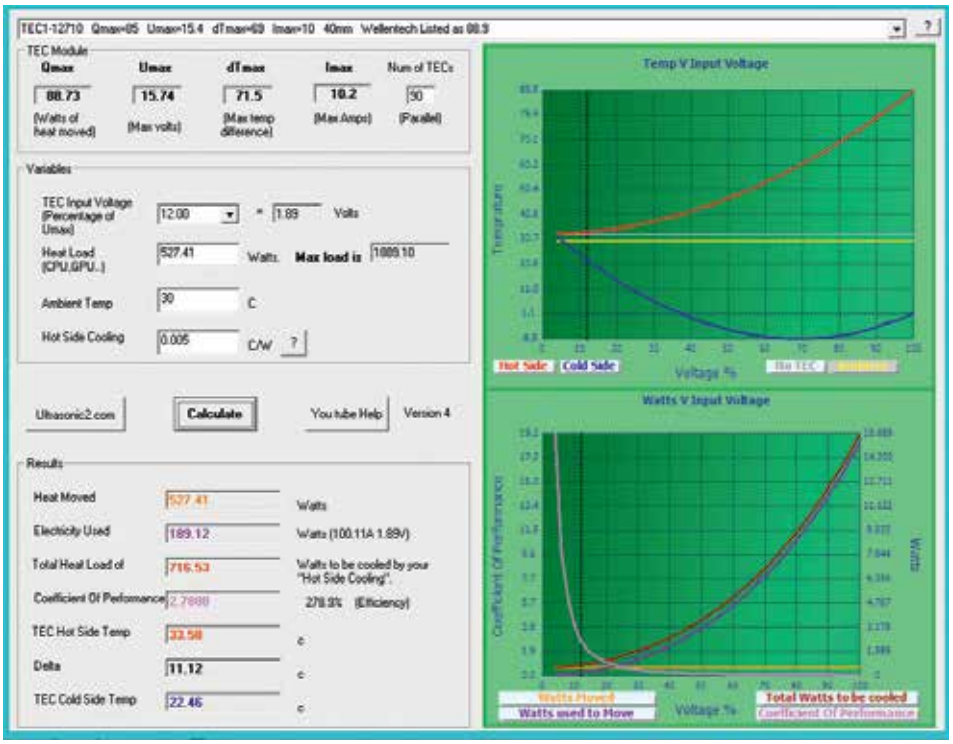

Figure 3. Performance characteristics of TEC1-12710 module with voltage variation analyzed in TEC calculator.

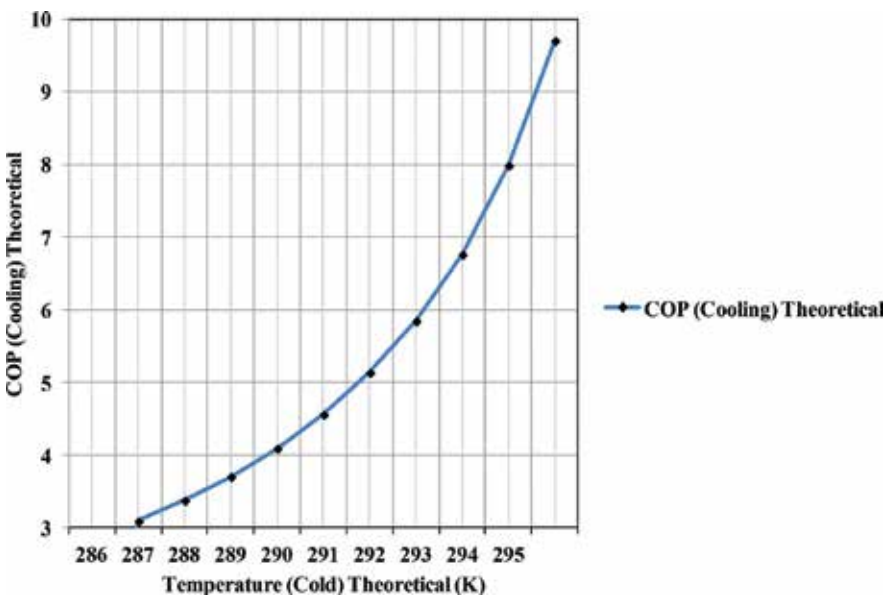

Figure 4. Variation in theoretical values of COP (cooling) and temperature (cold) for $ZT_m = 1$.

http://dx.doi.org/10.5772/intechopen.75472

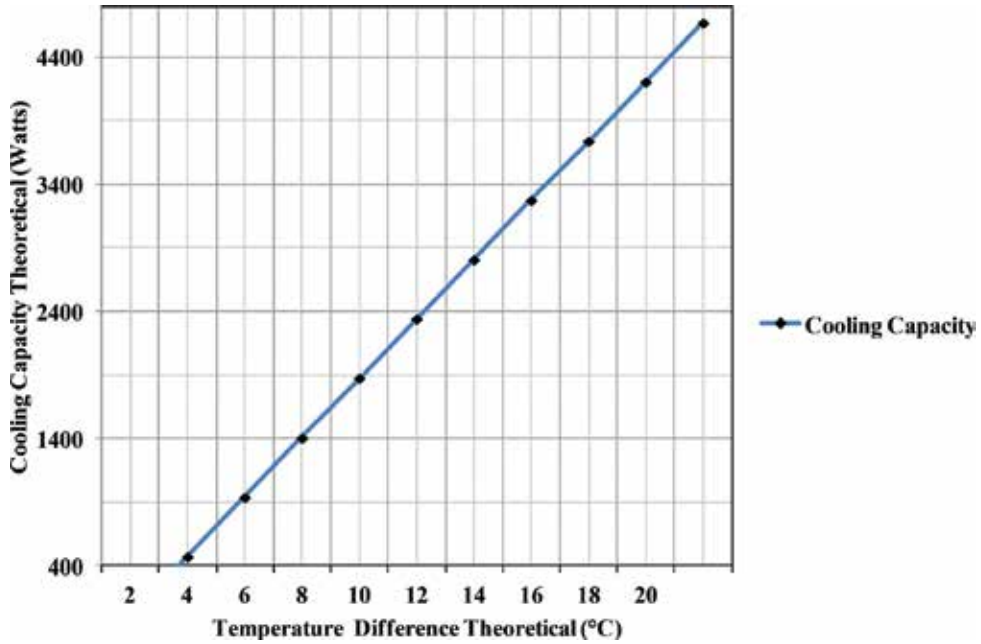

Figure 5. Variation in theoretical values of cooling capacity with temperature difference.

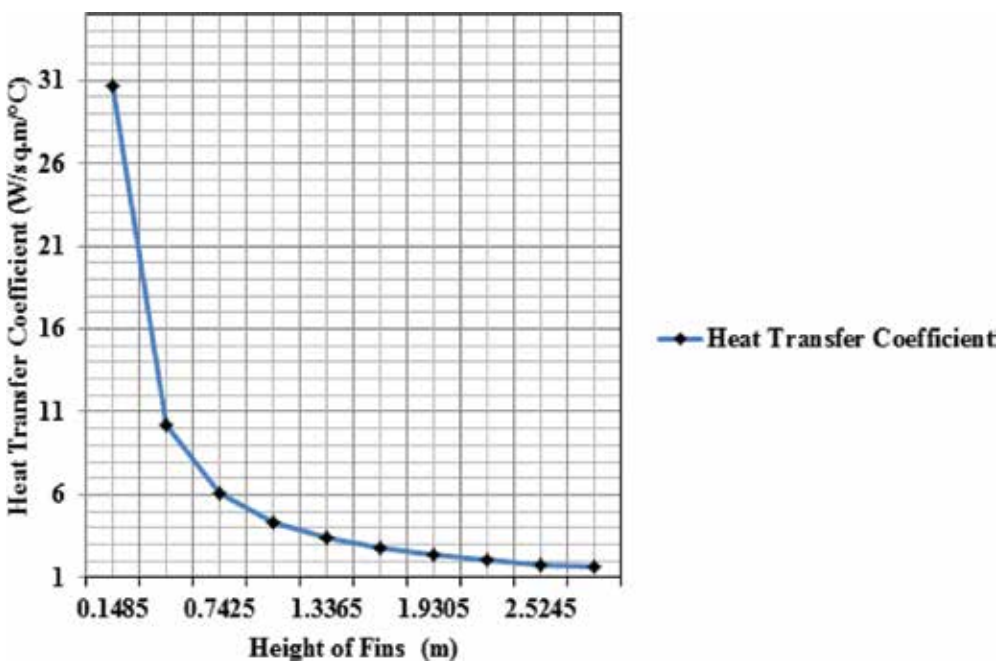

Figure 6. Variation of heat transfer coefficient with height of heat transfer surface (fins).

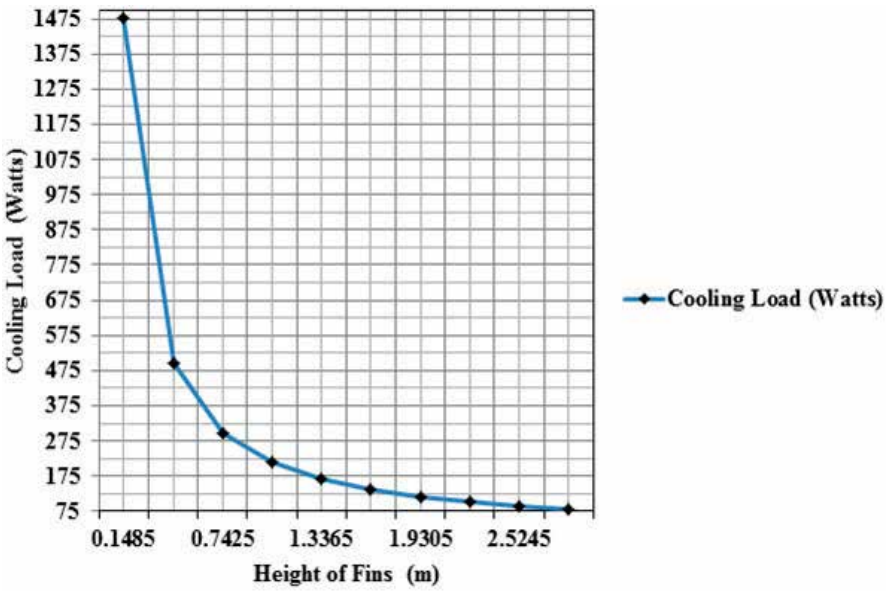

Figure 7. Variation of cooling capacity load served inside room with height of heat transfer surface (fins).

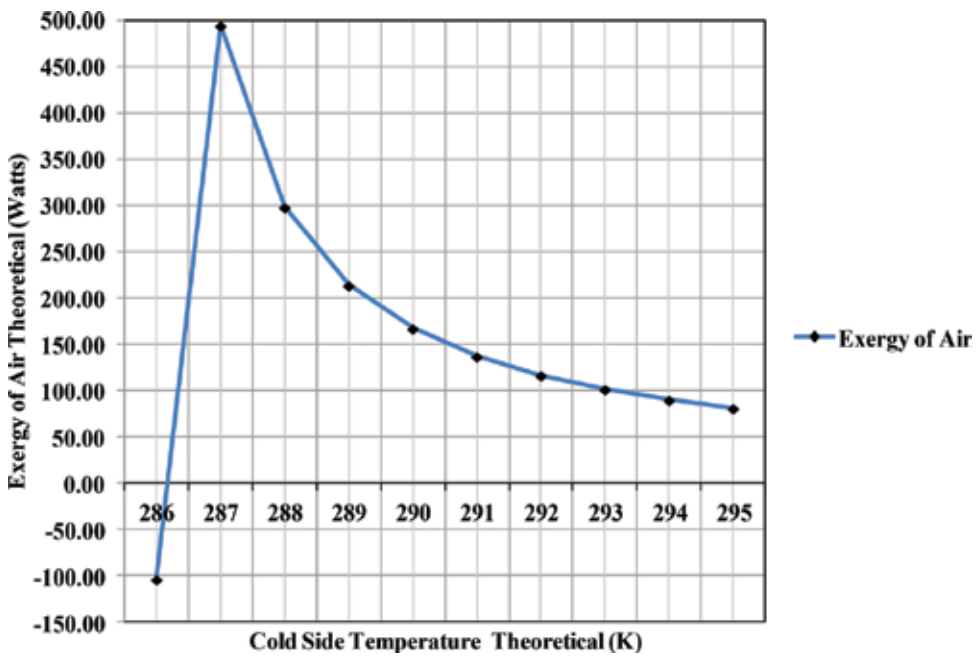

Figure 8. Variation of theoretical exergy of air inside room with cold side temperature and Tout = 306 K.

http://dx.doi.org/10.5772/intechopen.75472

5. Conclusion

Thermoelectric cooling (TEC) is one of the specialized areas in "Thermoelectrics." This chapter has presented the summary of energy balance model parameters representing various performance characteristics of building-integrated thermoelectric cooling-photovoltaic (TEC-PV) devices. The cooling performance of thermoelectric modules for air-conditioning applications is a sustainable technology though not competitive with conventional vapor compression technology. There is significant growing interest level in thermoelectric cooling (TEC) because of their useful control aspects. This is because TEC modules are readily operated at partial load by changing the electric current. Moreover, there is increase in cooling COP with reduction of cooling power. Modular capability is the key merit of thermoelectric cooling (TEC) devices. These devices do not generate noise, thus are of considerable interest in many building applications in which noise is a significant factor. Furthermore, key advantage is the operation of thermoelectric cooling (TEC) devices without requirement of polluting refrigerants.

Air-conditioning of fresh outdoor air for direct indoor use through proper system design of supply air ventilation system and exhaust air ventilation system is another key benefit of thermoelectric cooling (TEC). In addition, photovoltaic (PV) roof-top power generation and photovoltaic (PV) ventilated façade are integrated into the system design, thus making it further sustainably sound in terms of input electricity requirements through green power and active ventilation system for supply and exhaust air. Finally, thermoelectric modules (TEM) offer air-conditioning solutions with flexible electrical loads in contemporary context of smart energy systems for buildings. Thermoelectric modules (TEM) have best advantage of their reversible operation as heating and cooling devices obtained by changing the direction of electric current. The future work comprises of advanced modeling and simulation of the presented prototype through thermoelectric modules (TEMs) operation as heating and cooling devices powered by photovoltaic modules.

Nomenclature

η_{pv}	photovoltaic system efficiency
COP	coefficient of performance
ZT_m	figure-of-merit for thermoelectric material
Q_c	absorbed heat flux, W
Q_h	released heat flux, W
P	electric power, W
α	Seebeck coefficient, Volts/K
R	electric resistance, Ohms

h_c coefficient of convective heat transfer (W/m^2K),

A_c heat transfer area (m^2)

t_r room temperature (°C)

t_c temperature of cold fins (°C)

Φ_1 relative humidity before dehumidification (%)

Φ_2 relative humidity after dehumidification (%)

Ra Rayleigh number

T_o outside temperature (°C)

K thermal conductance, W/m^2K

I electric current, amperes

N number of thermocouple legs

L thermoelectric leg length, m

S leg section area, m^2

λ thermal conductivity, W/m-K

ρ electrical resistivity, Ω·m

Q_{sen} sensible cooling load, W

Q_{lat} latent load, W

H_c latent heat of condensation (J/kg-K)

m_a mass of the wet air inside the room (kg)

T_{sec} dehumidifying period (sec)

k_{air} thermal conductivity of air (W/m-K)

H height of fin (m)

T_c cold side fin temperature (°C)

Ex_{Qf} exergy of fresh air, W

Author details

Himanshu Dehra

Address all correspondence to: anshu_dehra@hotmail.com

Egis Group, Gurugram, India

References

[1] Enescu D, Virjoghe EO. A review on thermoelectric cooling parameters and performance. Renewable and Sustainable Energy Reviews. 2014;**38**:903-916

[2] Riffat SB, Qiu G. Comparative investigation of thermoelectric airconditioners versus vapour compression and absorption air-conditioners. Applied Thermal Engineering. 2004; **24**:1979-1993

[3] Cosnier M, Fraisse G, Luo L. An experimental and numerical study of a thermoelectric air-cooling and air-heating system. International Journal of Refrigeration. 2008;**31**:1051-1062

[4] Cheng T-C, Cheng C-H, Huang Z-Z, Liao G-C. Development of an energy-saving module via combination of solar cells and thermoelectric coolers for green building applications. Energy. 2011;**36**:133-140

[5] Gillott M, Jiang L, Riffat S. An investigation of thermoelectric cooling devices for small-scale space conditioning applications in buildings. International Journal of Energy Research. 2009

[6] Arenas A, Palacios R, Rodríguez-Pecharromán R, Pagola FL. Full-size prototype of active thermal windows based on thermoelectricity. In: Proceedings of ECT2008-6th European Conference on Thermoelectrics; 2-4 July 2008; Paris, France. pp. O.18.1-O.18.4

[7] Vázquez J, Miguel Sanz-Bobi A, Palacios R, Arenas A. An active thermal wall based on thermoelectricity. In: Sixth European Workshop on Thermoelectrics; Sep 2001; Freiburg, Germany

[8] Antonio AA, Transparent Active Thermoelectric Wall (PTA), Spanish Patent, 2151381, Mar 3, 1998

[9] Shen L, Xiao F, Chen H, Wang S. Investigation of a novel thermoelectric radiant air-conditioning system. Energy and Buildings. 2013;**59**:123-132

[10] Jeong ES. A new approach to optimize thermoelectric cooling modules. Cryogenics. 2014; **59**:38-43

[11] Zhao D, Tan G. A review of thermoelectric cooling: Materials, modeling and applications. Applied Thermal Engineering. 2014;**66**:15-24

[12] Kim M-H, Park J-Y, Jeong J-W. Energy saving potential of a thermoelectric heat pump-assisted liquid desiccant system in a dedicated outdoor air system. Energies. 2017;**10**:1306. DOI: 10.3390/en10091306 19 pages

[13] Wang H, Chengying Q. Experimental study of operation performance of a low power thermoelectric cooling dehumidifier. International Journal of Energy and Environment. 2010;**1**(3):459-466

[14] Bejan A, Tsatusaronis G, Moran M. Thermal Design and Optimization. New York: Wiley; 1996

[15] Han T, Gong G, Liu Z, Zhang L. Optimum design and experimental study of a thermoelectric ventilator. Applied Thermal Engineering. 2014;**67**:529-539

[16] Dehra H. A mathematical model of a solar air thermosyphon integrated with building envelope. International Journal of Thermal Sciences. April 2016;**102**:210-227

[17] Luo Y, Zhang L, Jing W, Liu Z, Zhenghong W, He X. Dynamical simulation of building integrated photovoltaic thermoelectric wall system: Balancing calculation speed and accuracy. Applied Energy. 2017;**204**:887-897

[18] Luo Y, Zhang L, Liu Z, Wang Y, Meng F, Jing W. Thermal performance evaluation of an active building integrated photovoltaic thermoelectric wall system. Applied Energy. 2016; **177**:25-39

[19] Irshad K, Habib K, Basrawi F, Saha BB. Study of a thermoelectric air duct system assisted by photovoltaic wall for space cooling in tropical climate. Energy. 2017;**119**:504-522

[20] Dehra H. An investigation on energy performance assessment of a photovoltaic solar wall under buoyancy-induced and fan-assisted ventilation system. Applied Energy. April 2017; **191**(1):55-74

[21] Dehra H. Electrical and thermal characteristics of a photovoltaic solar wall with passive and active ventilation through a room. WASET International Journal of Energy and Power Engineering. May 2017;**11**(5):514-522

[22] Dehra H. A combined solar photovoltaic distributed energy source appliance. Natural Resources. June 2011;(2):75-86 Scientific Research Publishing

Chapter 16

Feasibility and Numerical Analysis of Hybrid Photovoltaic (PV) Panels with Thermoelectric Cooling (TEC) Systems

Arturo Monedero Khouri and
Miguel Angel Olivares Robles

Additional information is available at the end of the chapter

http://dx.doi.org/10.5772/intechopen.75441

Abstract

Photovoltaic-thermoelectric hybrid (PV-TE) systems combine photovoltaic (PV) cells and thermoelectric cooling (TEC) modules to improve the system performance. PV panels efficiency is undesirably influenced by temperature rise, reducing power outlet from PV cells. As a countermeasure, cooling methods have been widely suggested. In this chapter, we provide an overview of both technologies, as well as an analysis of thermoelectric cooling as a possible solution to temperature rise in PV panels. Energy and exergy balances of hybrid system are conducted to determine if the thermoelectric cooling is viable for a self-sustaining system. Our results show that copper indium gallium selenide (CIGS), crystalline silicon (c-Si), amorphous silicon (a-Si), and cadmium tellurium (CdTe) PV panels are unsuitable candidates using the TE cooling. Even though exergy losses diminish with temperature decrease in CIGS, c-Si, and a-Si, the power consumption of the TEC has shown to overcome power generation from PV panels.

Keywords: thermoelectrics, cooling, photovoltaics, hybrid, exergy

1. Introduction

When talking about photovoltaics we are referring to a technology that generates a direct current from semi-conducting materials arranged in cells when they are illuminated by photon particles [1]. These cells generate electrical power for as long as light is shined upon them.

PV effect was first observed by Heinrich Hertz in the late 1800s and has come across power generating devices by early 1900s [2]. It only became more relevant with *positive-negative* (*pn*) junction discovery, consolidating the development of solar photovoltaic panels [1]. Ever since, efficiency has been a paramount factor to be optimized and, as technology advanced and efficiency increased, the diffusion of PV panels has reached worldwide popularity.

1.1. Basic concepts of PV cells

Incident light can be conceived as a stream of photons at a determined frequency. A photon, is a particle of electromagnetic energy, this energy contained by the photon follows the equation:

$$E_{photon} = h\nu \tag{1}$$

where E_{photon} is the energy of the photon, h is Planck's constant ($6.626{*}10^{-34}\ Js$), and ν is the light frequency [3]. When photons with an appropriate frequency, incoming from the shined light, hit a metal surface, electrons in the metal absorb the photons' energy and are knocked off. This energy of the photon transferred to the electron is conserved. An amount is used to knock off the electron (Φ), this term is known as *work function* and varies according to the metal employed, and the remaining energy is transformed into kinetic energy for the electron ($K_{electron}$).

$$E_{photon} = K_{electron} + \Phi \tag{2}$$

This *work function* Φ is the minimum energy required to knock off an electron from a metallic surface, and its value is given by the metallic material. As photons' energy is determined by their frequency, the minimum frequency required to match the *work function* is known as the threshold frequency (ν_0), and for frequencies greater than ν_0, electrons hit will be ejected [3], producing a current flow.

As depicted in **Figure 1**, the frequency of red light (left) is a lesser value than the threshold frequency (ν_0) required to knock off electrons, so none are ejected. The green and blue frequencies of moderate and short wavelengths respectively have ($\nu > \nu_0$) causing photoemission. Higher frequencies correspond to higher kinetic energy acquired by the electrons as they are ejected.

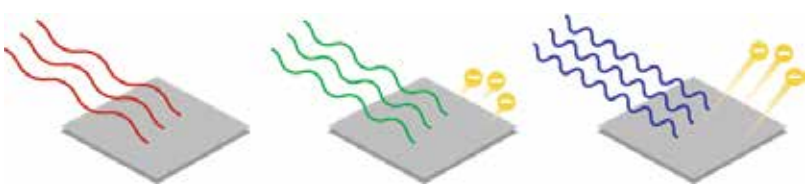

Figure 1. Different frequencies/wavelengths result in none, slower or faster electron ejection from the metal surface as protons collide with it [4].

1.2. PV efficiency as a function of temperature

As discussed before, materials are determinant for the energy amount required to knock off electrons and start a current flow. Different material compounds will possess distinctive photoelectric properties. We can think of this diversity as the stress resistance an alloy possesses; different alloys will have diverse behaviors when submitted to stress conditions, just as different material combinations will allow various photoelectric characteristics.

The paramount property when looking for photoelectric materials is efficiency (η). With higher efficiencies, more incident sunlight will be effectively converted into exploitable electrical power. This relationship between the net electrical power delivered by the PV panel (P_{PV}) and its efficiency (η_{PV}) can be expressed as:

$$P_{PV} = \eta_{PV} Q_{solar} \tag{3}$$

where Q_{solar} is the total incident sunlight shined upon the panel's surface.

Nonetheless, PV panel efficiency is influenced not only by the material's properties, but it can also vary due to temperature changes regardless of the material composition. The drop in efficiency as temperature rises can be traced to the influence upon current and the voltage; as it turns out, the thermally excited electrons begin to dominate the electrical properties of the semi-conductor [5] describing a linear relation for the PV efficiency in the form:

$$\eta_{PV} = \eta_{T_{ref}}\left(1 - \gamma\left(T_{cell} - T_{ref}\right)\right) \tag{4}$$

in which $\eta_{T_{ref}}$ is the cell efficiency at the reference temperature T_{ref}, typically 25°C, and γ represents the temperature coefficient, which can be found in **Table 1** for the several types of PV modules analyzed. These values are usually given by the manufacturer, but can also be calculated with:

$$\gamma = \frac{1}{T_0 - T_{ref}} \tag{5}$$

for which T_0 is the temperature at which the PV panel's efficiency drops to zero.

1.3. Why choose PV panels?

Back in 1997, the largest panels available were 100 W panels, each was around 9% efficient; the cost oscillated around $1300 apiece. Today, solar panels can be up to 24% efficient and cost 25 times less. They also have a higher capacity and a longer life expectancy. Of course, there is more to the installation cost than just the solar panels alone. Cabling, inverters, batteries, mounting brackets and time all cost money, and most of those prices have increased in the past 20 years, but the fact remains that solar has been transformed from an obscure niche product to mainstream energy generation because of incredible leaps in the technology that has made solar more efficient and affordable [6].

Parameters	Symbol	Value
Ambient temperature	T_{amb}	293 K
Area of PV panel	A_{cell}	0.4 m^2
Area of thermoelectric module	A_{TE}	0.04 m^2
Characteristic longitude	L_C	0.6325 m
Efficiency of PV panel at reference temperature	$\eta_{T_{ref}}$	
CdTe		27.9%
CIGS		13.3%
c-Si		12.4%
a-Si		5.0%
Emissivity of the ground	ϵ_{ground}	0.2
Emissivity of the sky	ϵ_{sky}	0.9
Gravity's acceleration	g	9.81 m/s^2
Reference temperature	T_{ref}	298 K
Reflected radiation fraction	ρ_{opt}	0.12
Stephen-Boltzmann constant	σ	$5.6704{*}10^{-8}$ W/m^2K^4
Solar incidence	G	700 W/m^2
Sun temperature	T_{sun}	6000 K
Temperature coefficient	γ	
CdTe		0.00205 K^{-1}
CIGS		0.00353 K^{-1}
c-Si		0.00392 K^{-1}
a-Si		0.00110 K^{-1}
Thermal conductivity (air)	k	0.02587 W/mK
Thermal diffusivity (air)	α	0.00002163 m^2/s
Thermal expansion coefficient (air)	β	0.00324 K^{-1}
Tilt angle	θ	45°
Wind speed	w	2 m/s

Table 1. Parameters of the PV-TEC hybrid system.

Nonetheless, several studies throughout the years have established that temperature increase in PV cells result in efficiency decrease [7–10]. Hence, power output of a PV panel decreases with temperature increment. This is the reason for cooling devices as key component of an integrated hybrid generation system. As PV panels are only capable to convert sunlight or luminous energy into electrical energy, any heat contained in the system will result in an ill temperature rise with counterproductive results. For this purpose, thermoelectric technology

http://dx.doi.org/10.5772/intechopen.75441

has come to our attention, offering a compact solution for the cooling problem that has been previously discussed.

1.4. Thermoelectrics

An electrical potential, also known as voltage, is generated within two dissimilar conducting materials subjected to a temperature gradient. The conversion of this electric voltage differences into temperature gradients and vice versa is known as the thermoelectric effect [11]. It is composed by three different phenomena: the Seebeck effect, the Peltier effect, and the Thomson effect. These can be used to generate electricity, measure temperature, and as a heat source/pump.

1.4.1. The Seebeck effect

An electrical current is originated when an electrical circuit consisting of two dissimilar metals has a temperature difference between its joints. This kind of arrangement is known as *thermocouple* and is usually composed of p-doped and n-doped semiconductors, as depicted in **Figure 2a**.

The Seebeck effect is a typical example of an electromotive force (emf), modifying Ohm's law:

$$V = \propto \Delta T \tag{6}$$

where $\propto$ is the Seebeck coefficient, a property inherent to the local material, also known as themorpower, and ΔT is the temperature gradient between the heat source and the cool side.

1.4.2. The Peltier effect

Complementary to the Seebeck Effect, when a current is passed through an electrical circuit consisting of two dissimilar metals, heat may be generated or removed at the junction as shown in **Figure 2b**. Heat generation or removal will alternate in the junctions if the direction of the current flow is reversed.

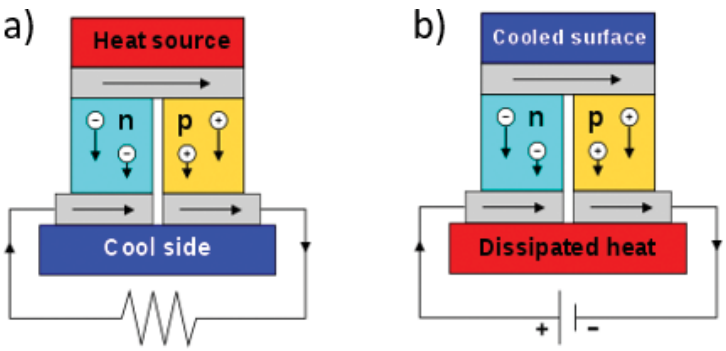

Figure 2. A thermoelectric circuit composed of dissimilar materials, configured as a thermoelectric generator (a) [12] and as a thermoelectric cooler (b) [13].

The Peltier heat generated at the joints per time unit is:

$$\dot{Q} = (\Pi_A - \Pi_B)I \tag{7}$$

where $\dot{Q}$ is the heat flow, Π_A and Π_B are the Peltier coefficients of conductors, and I is the electric current (from A to B).

1.5. TECs performance as a function of temperature

Thermoelectric modules can operate as electrical energy generators or heat pumps, commonly known as cooling devices. The efficiency for these modules benefits from high temperature gradients (ΔT) while generating electrical energy, somewhat around 300°C for most devices. On the other hand, cooling thermoelectric coefficient of performance (COP) is increased when small temperature gradients are present between the body that's been cooled and the ambient temperature.

While on cooling mode, TEC modules consume energy, removing heat from a particular source and releasing it into the medium. This heat removal and energy consumption differ greatly in behavior depending on the thermocouple materials. For the analysis presented here, a commercial module HP-199-1.4-1.15 from TE Technology, Inc. has been implemented. The technical specifications and fitting data were taken from its datasheet presented in **Figure 3**. Equations (8) and (9) have been fitted to this data, considering a hot side temperature of 50°C and 10.2 V circuit voltage.

$$Q_{removed} = -1.4557\Delta T + 67.004 \tag{8}$$

$$I_{TEC} = -0.0185\Delta T + 3.213 \tag{9}$$

Additional to this heat removal, TEC module consumes energy, which is not necessarily the same amount as heat removes. This power consumption is the product of the circuit voltage (V_{TEC}) and the input current (I_{TEC}).

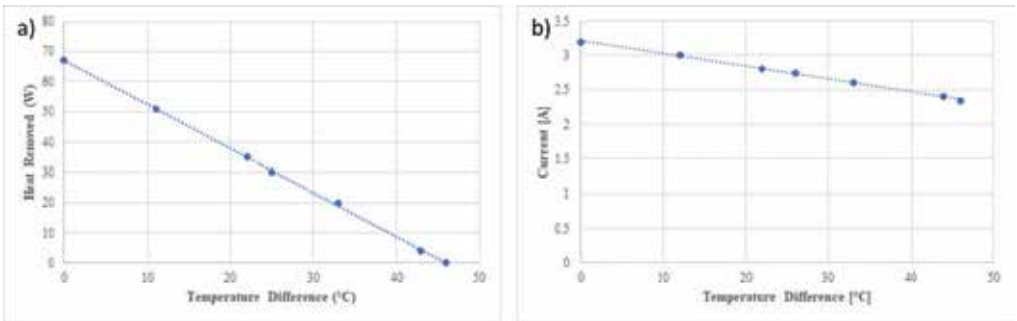

Figure 3. Amount of heat removed (a) and magnitude of current demanded (b) by a commercial HP-199-1.4-1.15 thermoelectric cooler as a function of the temperature gradient between the heat source (T_{cell}) and the heat sink (T_{amb}) as specified by its data sheet.

$$P_{module} = V_{TEC} I_{TEC} \tag{10}$$

Equations (9) and (10) account only for a single TEC module. For calculating the number of TEC modules required, the heat to be removed must be found (Q_{cool}) from Eq. (14). Then the quotient from $Q_{removed}$ and Q_{cool} can be used to determine the number of TEC modules (n_{TEC}) required for the cooling, and then multiplied by each individual consumption to find the total power consumed by the array.

$$n_{TEC} = \frac{Q_{cool}}{Q_{removed}} \tag{11}$$

$$P_{TEC} = P_{module} n_{TEC} \tag{12}$$

where P_{module} is the power consumed by each TEC module, and P_{TEC} is the total power consumed by all TEC modules for cooling.

1.6. Why choose thermoelectrics?

It is established by the Peltier effect that heat is absorbed or liberated when current crosses an interface, given the direction of the current flow, between two different conductors [11], laying the foundations for TEC modules. These constitute miniature devices, unlike conventional vapor systems, energized by a DC power input. Additional to the weight and space savings carried by TECs, their solid-state construction is fluid free to operate and highly reliable, offering also a precise temperature control [14].

In this chapter, we will structure a theoretical frame for the energy inputs and outputs of a PV+TEC hybrid as a brief overview. Then, we will turn out attention to the operational feasibility of the hybrid system, using an energy and exergy balance as assessment. Finally, results of our simulations as well as conclusions will be presented and discussed in depth.

2. Theoretical frame

First, we consider the studied system to be analyzed: a solar PV panel shined upon by sunlight, while cooled through a commercial thermoelectric module (HP-199-1.4-1.15) with previously defined working conditions, see **Figure 4**. Normal convection and radiation take place, as well as sunlight rejection from the PV panel's surface. Also, the system has reached a steady-state condition, meaning that the previously mentioned variables defining the system are unchanging in time.

During steady-state conditions, the total amount of energy remains constant; thus, the total energy change in the system equals zero ($\Delta E_{sys} = 0$) [15]. In consequence, the amount of energy entering the system must be equal to the amount of energy leaving the system. And so, the general energy balance is reduced to:

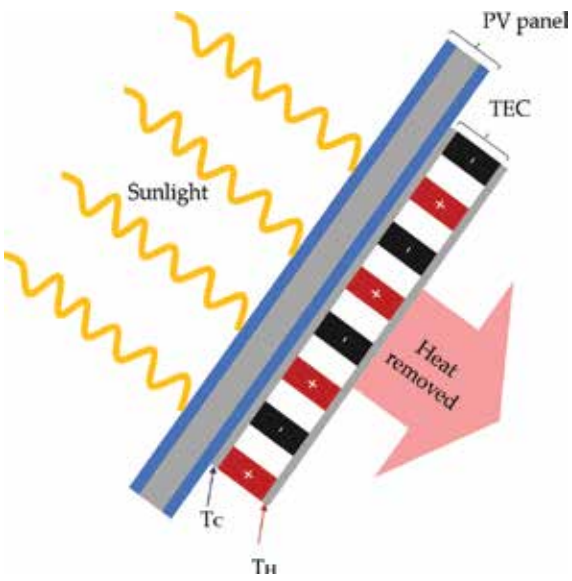

Figure 4. Schematic of the PV+TEC assembly.

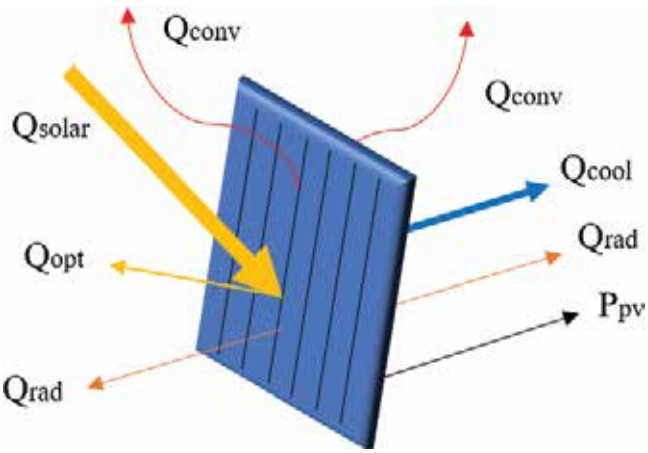

Figure 5. Schematic of the PV+TEC energy inputs and outputs.

$$\dot{E}_{in} - \dot{E}_{out} = 0 \tag{13}$$

Different energy inputs and outputs are outlined entering and leaving the hybrid PV-TEC system, as can be appreciated in **Figure 5**. The sunlight irradiates the panel (Q_{solar}) continuously, this luminous energy is either absorbed or reflected (Q_{opt}) by the PV panel surface. The absorbed fraction is then transformed into electrical energy (P_{PV}) and heat. Some of this heat will be dissipated passively, this means that no energy inputs will be required to extract it from

the system, on each side of the cell by natural cooling mechanisms such as convection (Q_{conv}) and radiation (Q_{rad}).

If we left the system to cool passively, a temperature around 60–80°C is expected to be reached [16]. But in this scenario, a cooling system is implemented to reduce its temperature even more. The thermoelectrical cooler will extract another energy fraction (Q_{cool}) from its contact surface with the PV panel at T_C, while consuming electrical power, and release it to its surroundings passively through its rear end at T_H, no additional components passive or active are considered heat extraction, for example heat exchangers. Thus, considering Eq. (13), the energy balance equation for the hybrid system in steady-state conditions can be written as follows:

$$Q_{solar} = Q_{opt} + Q_{conv} + Q_{rad} + P_{PV} + Q_{cool} \tag{14}$$

Each term is determined by several factors, such as panel characteristics, ambient temperature, wind speed, solar radiation conditions, etc. [17]. These system parameters are shown in **Table 1** and will be employed in further equations. Each term in Eq. (14) is determined by a theoretical model which will be described in the sections to come.

2.1. Solar radiation model

Solar irradiance varies significantly from one place to another and changes throughout the year [6]. The values considered for this model in **Table 1** were selected considering a standard setting for solar irradiance and tilt angle. This selected data is input into the following equation to calculate Q_{solar} and Q_{opt}.

$$Q_{solar} = GA_{cell} \tag{15}$$

It is to be noted that part of Q_{solar} is reflected by the solar panel materials, thus never entering the system. This fraction of reflected radiation is commonly expressed as ρ_{opt} and used to calculate the optical losses (Q_{opt}) of sunlight radiation.

$$Q_{opt} = Q_{solar}\rho_{opt} \tag{16}$$

As stated before, the net solar energy ($Q_{solar} - Q_{opt}$) entering the system will be transformed into electrical power (P_{PV}) and heat. This heat is dissipated by several mechanisms such as convection, radiation, and the thermoelectrical cooling module.

2.2. Convective heat model

As heat accumulates in the system, temperature rises, creating a temperature differential between the system and its surroundings. This originates a heat exchange between the system and the surrounding air known as convective heat loss. There are two phenomena accountable for heat loss: forced and natural convection; these must be considered for the front and the rear faces as the air surrounds the plate from both sides.

Natural convection is related to the temperature difference between the outside air and the panel, which includes the movement of the fluid due to the local density gradients. In calm or little windy days, the contribution of natural convection becomes significant, even more in cold climates where temperature differences between the panel surface and ambient air can be relatively large [17]. Forced convection, in the other hand, relates to the presence of the wind. There are numerous studies on the evaluation of the heat transfer coefficients due to this phenomenon, some are studies in wind galleries, others on field measurements, nonetheless several authors found that the theory usually underestimates the presence of different objects near the panels (other panels, trees, soil, buildings, etc.) [17].

The small area in between the two faces is rendered negligible, and the plate is considered as an isothermal surface for simplification purposes [18]. This allows us to define the convective heat loss as:

$$Q_{conv} = Q_{conv,\,front} + Q_{conv,\,rear} \tag{17}$$

$$Q_{conv,\,front} = h_{conv,\,front} A_{cell} (T_{cell} - T_{amb}) \tag{18}$$

$$Q_{conv,\,rear} = h_{conv,\,rear} A_{cell} (T_{cell} - T_{amb}) \tag{19}$$

where h_{conv} is the overall convective heat coefficient, A_{cell} is the PV panel surface, and $(T_{cell} - T_{amb})$ is the temperature gradient between the cell surface and the ambient temperature. A_{cell}, T_{cell}, and T_{amb} are constant values that can be found in **Table 1** as system parameters. Nonetheless h_{conv} must be calculated, considering natural and forced convection into the same coefficient for each panel side:

$$h_{conv,\,front} = \sqrt[3]{{h_{natural,\,front}}^3 + {h_{forced,\,front}}^3} \tag{20}$$

$$h_{conv,\,rear} = \sqrt[3]{{h_{natural,\,rear}}^3 + {h_{forced,\,front}}^3} \tag{21}$$

To determine forced convection heat transfer coefficient, wind speed (w) is a key variable, this parameter can also be found in **Table 1**. A model developed by Sharples and Charlesworth methodology [19] is applied to the system.

$$h_{forced,\,front} = 3.3w + 6.5 \tag{22}$$

$$h_{forced,\,rear} = 2.2w + 8.3 \tag{23}$$

This leaves natural convection heat transfer coefficient remaining. For it, the Nusselt (Nu) number concept must be analyzed first. The Nusselt number, named after Wilhelm Nusselt, establishes the ratio of convective to conductive heat transfer [20] and, as it may be inferred, it's dimensionless.

$$\overline{Nu} = \frac{Q_{conv}}{Q_{cond}} = \frac{L_c h_{natural}}{k} \tag{24}$$

where $h_{natural}$ is the natural convective coefficient for the fluid, k the fluid's thermal conductivity, and L_c the characteristic longitude of the surface. Nusselt numbers are usually determined empirically for different configurations such as horizontal or inclined flat surfaces, spherical and cylindrical objects, enclosures, etc. The PV panel configuration resembles that of an inclined plane, for which Fujii and Imura model [21] as well as Churchills and Chu's [21] are suggested to be implemented.

$$\overline{Nu}_{front} = 0.14\left[(Ra)^{\frac{1}{3}} - (Ra_{cr})^{\frac{1}{3}}\right] + 0.56(Ra_{cr}\cos\theta)^{\frac{1}{4}} \tag{25}$$

$$\overline{Nu}_{rear} = \left[0.825 + \frac{0.387Ra^{\frac{1}{6}}}{\left[1 + \left(\frac{0.492}{\Pr}\right)^{\frac{9}{6}}\right]^{\frac{8}{27}}}\right]^2 \tag{26}$$

where θ is the tilt angle between the ground and the rear surface of the panel, Ra is the Raleigh number for the fluid's conditions, and Ra_{cr} is the critical Raleigh number at which the Nusselt starts deviating from the laminar relationship ($Ra_{cr} \approx 10^9$).

$$Ra = \frac{g*\beta(T_{cell} - T_{amb}){L_c}^3}{\nu\alpha} \tag{27}$$

where g is gravity's acceleration, β is the fluid's thermal expansion coefficient, ν is the fluid's kinematic viscosity, and α is the fluid's thermal diffusivity. These values are given as system parameters in **Table 1** for air as work fluid.

2.3. Radiation heat model

Thermal radiation is associated with the rate at which matter emits energy as a result of its finite temperature [20]. The assessment of the radiation heat model contemplates radiation emitted to the sky and radiation emitted to the ground from the front and rear faces of the PV panel. This, as seen before in the convective model, divides the heat flow into several components.

$$Q_{rad} = Q_{rad.sky,\,front} + Q_{rad.sky,\,rear} + Q_{rad.ground,\,front} + Q_{rad.ground,\,rear} \tag{28}$$

This radiation emissions are originated by the energy released due to oscillations of the many electrons constituting the matter [20]. Different bodies will emit different amounts of radiation, even at the same temperature, introducing the concept of emissivity (ϵ), which is the ratio between the emitted radiation by a body's surface at a given temperature and the radiation emitted by a *black body* at the same temperature [22]. This *black body* is defined as the perfect emitter and absorber body, emitting a radiation per area unit of:

$$E_b(T) = \sigma T^4 \tag{29}$$

where $\sigma = 5.670*10^{-8}\ W/m^2K^4$, known as the Stephen-Boltzmann constant. Using equation along with emissivity values found in **Table 1**, and a geometrical factor F considering an incline plate, the radiative model components can be written:

$$Q_{rad,\,sky,\,front} = F_{sky,\,front}\epsilon_{sky}\sigma A_{cell}\left({T_{cell}}^4 - {T_{amb}}^4\right) \tag{30}$$

$$Q_{rad,\,sky,\,rear} = F_{sky,\,rear}\epsilon_{sky}\sigma A_{cell}\left({T_{cell}}^4 - {T_{amb}}^4\right) \tag{31}$$

$$Q_{rad,\,ground,\,front} = F_{ground,\,front}\epsilon_{sky}\sigma A_{cell}\left({T_{cell}}^4 - {T_{amb}}^4\right) \tag{32}$$

$$Q_{rad,\,ground,\,rear} = F_{ground,\,rear}\epsilon_{sky}\sigma A_{cell}\left({T_{cell}}^4 - {T_{amb}}^4\right) \tag{33}$$

for which the geometrical factor F is given as:

$$F_{sky,\,front} = \frac{1}{2}(1 + \cos\theta) \tag{34}$$

$$F_{sky,\,rear} = \frac{1}{2}(1 + \cos(\pi - \theta)) \tag{35}$$

$$F_{ground,\,front} = \frac{1}{2}(1 - \cos\theta) \tag{36}$$

$$F_{ground,\,rear} = \frac{1}{2}(1 - \cos(\pi - \theta)) \tag{37}$$

3. The hybrid system

This work's goal is to elaborate a net energy balance between PV generated energy and TEC consumed energy. In fact, we show that TEC's consumed power is greater than PV generated power in all temperature ranges, except for the CdTe PV panel at some temperature ranges. Other works focus in the PV efficiency increase only, disregarding TEC energy consumption associated to it, which makes difficult to assess the energy balance of the hybrid system.

Some of this works can be traced to authors like Najafi and Woodbury [23] who use a modeling approach. Likewise, Borkar, Prayagi and Gotmare [24] report, from a MATLAB simulation model, that increase in life span and efficiency can be achieved by PV + TEC systems without mentioning the net hybrid system energy balance.

Another example of this is the work of Kane and Verma [25] model, with reported results of 0.45% increase in efficiency per °C. This behavior is already expected from a solar PV panel, as explained by Eq. (4), where any temperature decrease will result in a power increase from the module; raising the question: *does the increment in power generation results convenient in comparison with power consumed by TEC cooling to reduce temperature in the PV module?*

Additionally, an experimental montage was elaborated by Benghanem, Al-Masharaqi and Daffallah [26] with a 0.5% of efficiency increase per °C decreased, conducted at Madinah, Saudi Arabia, where panel temperatures rise to 83°C. Results show great resemblance to those of Kane and Verma, but continue to leave aside the analysis for the energy consumption of the active cooler.

Analogue considerations to the work developed by Bjørk and K. Nielsen [27] Analysis for PV and thermoelectric generator (TEG) systems were employed throughout this chapter, where the efficiency of such a hybrid system cannot be considered as single stand-alone units and thus its power generation characteristics are not known. In addition to this approach, it is to be noted that TEGs were replaced with TECs, and real approximation conditions were considered along with an exergy analysis.

A combined PV+TEC system is analyzed regarding a real approximation. The goal for this kind of system is to be a source of electrical power, meaning that power generated by the PV panel must overcome energy consumption from the TEC at all times to ensure its operational validity, otherwise the system will be consuming a greater amount of power than it is able to generate.

$$P_{gen} > P_{cons} \tag{38}$$

$$W_{net} = P_{gen} - P_{cons} > 0 \tag{39}$$

For the proposed system and its limits, as depicted in **Figure 6**, the means for power generation are the PV cells, and the power consuming means are the TECs. The system proposal

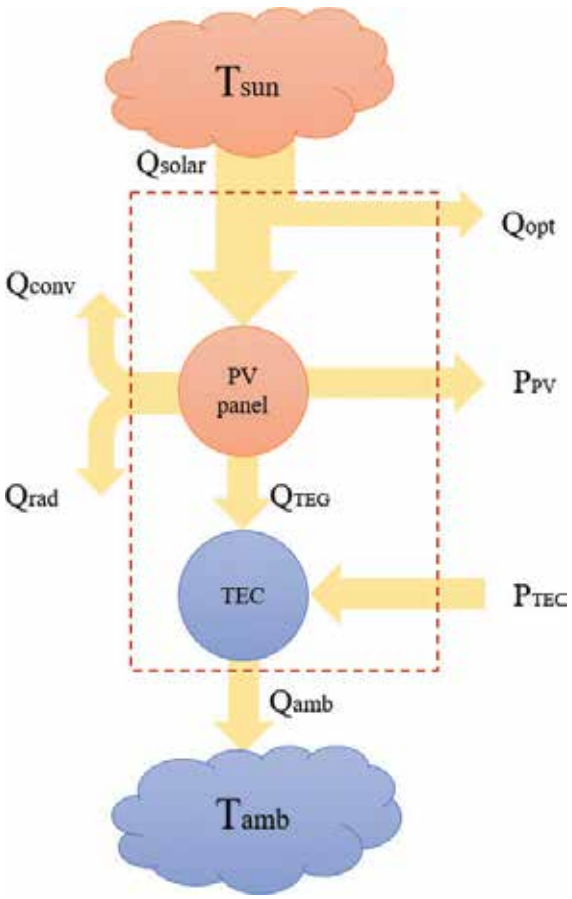

Figure 6. Schematic of the PV+TEC hybrid system limits and energy balance.

intends to assess for the PV panels change in efficiency as temperature is lowered following the working principles of Eqs. (3) and (4) and with the energy consumption of the increasing number of TECs, determined by Eqs. (11) and (12). As active and passive cooling mechanisms extract heat from the hybrid system, energy losses are intended to be found, watching W_{net}'s behavior to determine if the hybrid system is generating enough energy to compensate and justify its active cooling means and account for its feasibility as a power generating system. A net metering method of produced and consumed energy will allow us to determine if $P_{PV} > P_{TEC}$, which must be fulfilled to ensure a $W_{net} > 0$.

3.1. Hybrid system exergy balance

Additional to the energy balance simulations, exergy analysis is undertaken. Considering the same operational temperature range as the energy balance simulations, the temperature of least entropy is intended to be found by the model.

As we know, every engineering processes performance is degraded by system irreversibilities associated to non-ideal conditions. Entropy is a quantitative measure of this irreversibilities; with greater irreversibilities comes greater entropy generation, which means valuable energy is lost in the process [15]. Of course, not all lost energy can be recovered, as the system conditions are not those of a theoretical reversible machine, nonetheless exergy analysis provides a tool for analyzing the minimum entropy generation that can be achieved by a real model, and thus the maximum energy output that can be obtained.

Exergy balance for the PV + TEC hybrid system contemplates all the exergy entering (X_{in}) and exiting (X_{out}) the system, and the destroyed exergy (X_{loss}), by irreversibilities, during the process:

$$X_{in} = X_{out} + X_{loss} \tag{40}$$

The only input to the system, as shown in **Figure 6** and Eq. (14) is solar radiation, expressed as:

$$X_{in} = GA_{cell}\psi_s \tag{41}$$

where ψ_s is the exergy efficiency of solar radiation [28]. This exergy efficiency is the maximum efficiency ratio of the solar emission, and can be calculated with:

$$\psi_s = 1 + \frac{1}{3}\left(\frac{T_0}{T}\right)^4 - \frac{4}{3}\left(\frac{T_0}{T}\right) \tag{42}$$

for this case of study, temperature of the radiation source T, is the Sun's surface temperature (T_s), and T_0 is the baseline temperature at which the system is referred (T_{amb}) [29].

Heat is an unorganized form of energy, and there's just a limited amount that can be transformed into organized energy such as work. It is always possible to produce work from a temperature source whose temperature is higher than the surroundings, in response, this

heat transfer, will always come with exergy transfer [15]. A heat flow Q coming from a thermal source of temperature T will always be accompanied by an exergy transfer X_{heat} of the amount:

$$X_{heat} = \left(1 - \frac{T_0}{T}\right)Q \tag{43}$$

Exergy is a unit for measuring the potential useful work, meaning that any exergy transfer done by work will be equal to the amount of work itself.

$$X_{work} = W \tag{44}$$

Irreversibilities such as friction, mixing, chemical reactions, heat transfer, expansion, compression, etc., will always generate entropy, and everything that generates entropy destroys exergy [15]. Exergy losses represent the wasted work potential, caused by the irreversibility of the process of energy conversion. Any real process will have destroyed exergy, while only ideal scenarios will present $X_{loss} = 0$. The hybrid system involves several exergy losses such as:

$$X_{loss} = X_{loss,\,opt} + X_{loss,\,sur} + X_{loss,\,solar} + X_{loss,\,TEC} \tag{45}$$

Each process in which energy is transferred and transformed presents irreversibilities, thus every term enlisted in Eq. (45) has exergy loss due to these inefficiencies in energy conversion. The first term ($X_{loss,\,opt}$) we called optical loss caused by the absorption and reflection of sunlight. The second term ($X_{loss,\,sur}$) is caused by the heat exchange between the system and its surroundings by the convective phenomenon, both natural and forced. The third term ($X_{loss,\,solar}$) is generated when the high-grade solar radiation is converted into low-grade thermal energy. Finally, the last term is caused by the TEC module consuming electric power, which is defined as exergy itself, and expelling heat from the hybrid system.

$$X_{loss,\,opt} = GA_{cell}\psi_s\boldsymbol{\rho}_{opt} = X_{in}\boldsymbol{\rho}_{opt} \tag{46}$$

The surface of the hybrid system is always at a higher temperature than its surroundings, thus the heat exchange remains continual if sunlight keeps irradiating the PV panel surface. According to the definition of exergy transfer as heat flow, and using the ambient temperature as reference the following can be obtained

$$X_{loss,\,sur} = (Q_{rad} + Q_{conv})\left(1 - \frac{T_{amb}}{T_{cell}}\right) \tag{47}$$

note that the higher the difference between T_{cell} and T_{amb}, the more exergy is lost.

The process of transforming solar radiation into electrical power and thermal energy is an irreversible process, and its exergy loss can be calculated with

$$X_{loss,\,solar} = GA_{cell}\psi_s - X_{loss,\,opt} - X_{loss,\,sur} - P_{PV} - Q_{cool}\left(1 - \frac{T_{amb}}{T_{cell}}\right) \tag{48}$$

Finally, exergy is defined as useful work, and the TEC consumes electrical power to operate, as well as it expels a given heat flow. Thus, an exergy loss is being held at it. To consider this into the balance, the following relation was used

$$X_{loss,\,TEC} = Q_{cool}\left(1 - \frac{T_{amb}}{T_{cell}}\right) + P_{TEC} \tag{49}$$

4. Simulations

We now focus our attention on P_{PV} in Eq. (3), P_{TEC} in Eq. (12), and the energy balance as well as Q_{cool} in Eq. (14). The Q_{cool} heat flux determined by the energy balance of the system will define the amount of TEC modules required to cool the system, enhancing the P_{PV} efficiency as established in Eqs. (3) and (4).

A temperature interval from 333 to 298 K was used for the system evaluation. This interval was chosen regarding the average temperature of a PV panel without cooling (333 K) [16] and a typical value for reference temperature used for PV panel evaluation (298 K).

Based on an energy analysis, the system's feasibility was assessed. We compared the PV panel power generation and the TEC energy consumption for each type of PV module. The power is shown in **Figure 7a** for a TEC+CIGS PV coupling, **Figure 7b** for TEC+c-Si, **Figure 7c** for TEC+a-Si array, and **Figure 7d** for TEC+CdTe. A general PV power generation increase of 10.22% is observed. If we put this quantity in perspective with each °C decreased we'll obtain

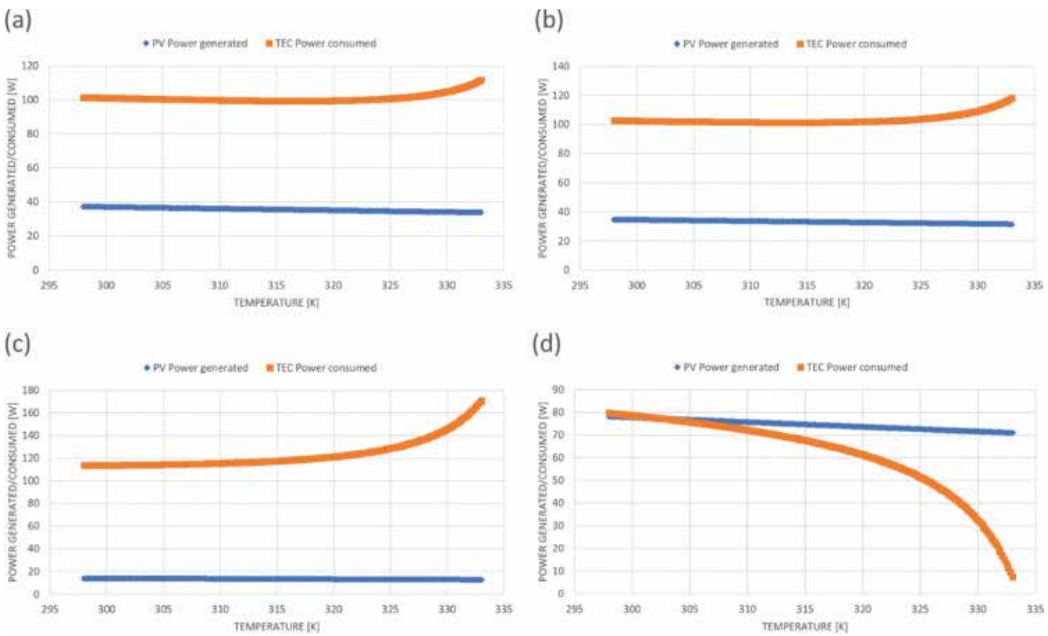

Figure 7. The energy generation for a PV panel compared to the consumption of the TEC in the same system montage. (a) TEC+CIGS power generation vs. consumption, (b) TEC+C-SI power generation vs. consumption, (c) TEC+A-SI power generation vs. consumption, (d) TEC+CDTE power generation vs. consumption.

a 0.292% climb in PV efficiency per °C, comparable to the results found by Kane and Verma [25] and Banghanem, Al-Mashraqi and Daffalah [26].

As can be seen from the figures, except in the case of CdTe, the cooling modules demand a much higher amount of power than what has been produced by the system at all temperatures; even when the efficiency of the PV panel does climb and the TEC consumption decreases, the ratios are not as elevated as it would be necessary for W_{net} to be positive at any point, as intended, according to Eq. (39). The diminishment in TECs power consumption can be traced to net power consumed and number of modules employed, where: CIGS decreased 9.14% the power consumption from the highest to the lowest temperature and reduced 1.238 TECs (n_{TEC}) use needed to cool the system, using Eqs. (8) through (12). These results were consistent with c-Si with 12.97% reduction in power consumption and 1.45 fewer TEC modules, as well as a-Si with 33.43% less power consumption and 3.195 unneeded modules.

Regarding the abnormal behavior of TEC+CdTe system, the curves shown in **Figure 7d** explain that the TEC consumption plummets at high ΔT values. If we concentrate our attention in each term of the system's energy balance (Eq. (14)) we can notice that Q_{solar} and Q_{opt} are not temperature dependent, whereas Q_{conv} and Q_{rad} will contribute in heat dissipation in the same amount for any type of PV+TEC system, leaving P_{PV} and Q_{cool} to account for this odd behavior. After a careful analysis we can only conclude that a small amount of heat removal is required at initial ΔT values. Contrary to the other systems, TEC energy consumption increases when the system approaches (T_{amb}), resulting astoundly counterproductive.

Contrary to the rest of the systems, CdTe doesn't decrease the TECs consumption as it cools, on the opposite, results report almost 9.5 times more energy consumption due to the cooling, and 7.5 more modules required than it did at initial temperatures (333 K). When approximating ambient temperature (298 K) in **Figure 7b**, almost all power generated by the PV panel can be appreciated to be matched by the consumption of the cooling device.

Exergy loss defined in Eq. (45) determines the amount of energy lost due to irreversibilities in the system. **Figure 8a** shows its behavior for the PV+TEC hybrid system as temperature decreases; being obvious that cooling helps reduce the system's exergy losses for three types of PV panels, excepting CdTe. Nonetheless, as shown in **Figure 8a** the total exergy delivered by the system results in a negative amount for CIGS, c-Si, and a-Si. This model is backed by the data found in **Figure 7a**, **b**, and **c**, establishing that, in these cases, the system demands more energy for operation than it generates.

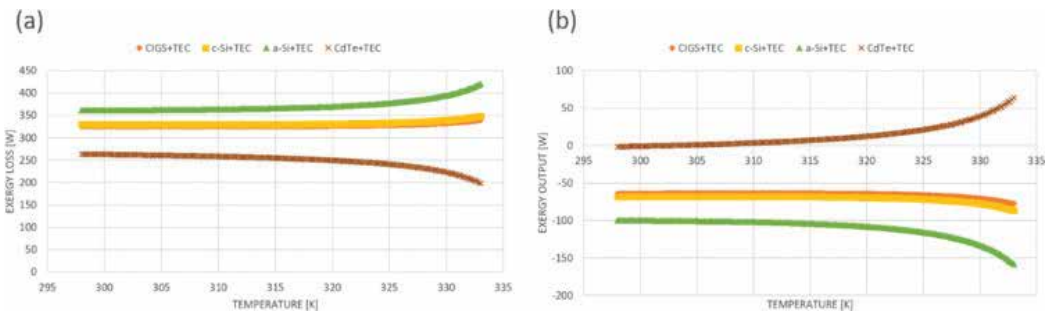

Figure 8. The exergy loss and exergy output for the proposed PV+TEC systems. (a) Exergy loss of OV+TEC systems, (b) Exergy output of OV+TEC systems.

On the other hand, CdTe+TEC system shows to decrease the exergy loss at high ΔT values. The high efficient material properties of the CdTe panel not only locate it in the least exergy loss at all temperature ranges, but also, supported by **Figure 8a** information, indicate that less exergy is used to feed the TEC, as ΔT increases. We must remember that exergy was defined as useful work in Eq. (44), meaning that feeding a cooling system destroys exergy, which is reflected in **Figure 8b**.

These numbers are consistent with the deficit in the exergy output. Only at some ranges, CdTe generates enough energy to result in positive values. TEC consumption increment elevates exergy losses up to a 32.77% at low ΔT values. Furthermore, at high ΔT, exergy loss is decreased, and exergy output is maximized.

For CIGS, c-Si, and a-Si group, cooling increases exergy output generation: 13.69% for CIGS, 21.42% for c-Si, and 36.92% for a-Si as shown in **Figure 8b**. Also, exergy losses can be noted to diminish with the system cooling, 4.03% for CIGS, with a minimum exergy loss temperature range from 313.8 to 305.7 K; 5.34% for c-Si with a minimum exergy loss temperature range from 310.8 to 301.0 K; 13.91% for a-Si with a minimum exergy loss temperature from 298.8 to 298.0 K. It is to be noted that every temperature range where exergy loss is minimal differs from reference or ambient temperatures for PV panels, meaning that excessive cooling can also be counterproductive.

5. Conclusions

In this chapter we have shown that, if we consider the power consumption of the thermoelectric modules, the general energy balance for the whole hybrid PV+TEC system results in a higher energy consumption than energy generation for most systems. Additionally, the exergy analysis shows that for this system there will always be exergy loss, rendering the feasibility of the hybrid PV+TEC system impossible.

Also, the conditions for minimum exergy loss have been determined for diverse types of PV panels, while using thermoelectric cooling modules to decrease temperature. These temperature ranges can be considered as the optimal working conditions, and they all differ from the lowest temperature analyzed for CIGS, a-Si, and c-Si, meaning that reducing the system all the way to ambient temperature (T_{amb}) is not necessarily the best energetic option for the hybrid systems. It is to be noted that this temperature ranges of minimum exergy loss are held within realistic parameters that can be obtained for the system.

We have concluded from these simulation results that the PV+TEC hybrid system is not a viable self-sustaining system. Even though the self-sustenance of the hybrid PV+TEC system is inviable, the conditions for minimum exergy loss allow us to determine the best performance of the system. These optimal operational conditions can be observed from the obtained results, with minimum exergy losses, that can be useful in future studies.

Although the results show that hybrid PV + TEC systems are inviable, thermoelectric technology has a wide range of impact from electronics and telecommunications to medical

equipment. Mostly employed for temperature control of critical parts and components of different lathes and machines; as a cooling method it is precise and reliable technology, with a fluid free compact design requiring only current and voltage for its operation which are easily regulated.

This work shows that a more detailed analysis must be included for the realistic implementation of thermoelectric cooling in photovoltaics. Most works have been realized considering thermoelectric generating (TEG) modules, and just a few around TECs, where an obvious lack of attention has come to the power consumed by the TECs.

Acknowledgements

This work was financially supported by research grant 20180069 of Instituto Politecnico Nacional, México. Arturo Monedero Khouri was financially supported by CONACyT-Mexico (CVU No. 785068). The authors acknowledge the editorial assistance in improving the manuscript.

Author details

Arturo Monedero Khouri and Miguel Angel Olivares Robles*

*Address all correspondence to: olivares@ipn.mx

Instituto Politecnico Nacional, SEPI-ESIME Culhuacan, Coyoacan, Ciudad de Mexico, Mexico

References

[1] Luque A, Hegedus S. Handbook of Photovoltaic Science and Engineering. 1st ed. Chichester: Wiley; 2003

[2] Bellis M. History: Photovoltaics Timeline [Internet]. 2017. Available from: https://www.thoughtco.com/photovoltaics-timeline-1992481 [Accessed: 14-10-2017]

[3] Sears F, Zemansky F, Young H. University Physics. 12th ed. Boston: Addison Wesley; 2009

[4] Khan Academy. Photoelectric Principle [Internet]. 2015. Available from: https://www.khanacademy.org/science/physics/quantum-physics/photons/a/photoelectric-effect [Accesssed: 29-10-2017]

[5] Skopalki E, Palyvos J. On the temperature dependence of photovoltaic module electrical performance: A review of efficiency/power correlations. Solar Energy. 2009;**83**:614-624. DOI: 10.1016/j.solener.2008.10.008

[6] Boxwell M. Solar Electricity Handbook. 11th ed. Birmingham: Greenstream Publishing; 2017

[7] Dorobantu L, Popescu M. Increasing the efficiency of photovoltaic panels through cooling water film. Scientific Bulletin. 2013;**75**:223-232

[8] Irwan Y, Leow M, Irwanto M, Fareq A, Amelia N, Gomesh N, Safwati I. Indoor test performance of PV panel through water cooling method. Energy Procedia. 2015;**79**:604-611. DOI: 10.1016/j.egypro.2015.11.540

[9] Mittleman G, Kribus A, Dayan A. Solar cooling with concentrating photovoltaic/thermal (CPVT) systems. Energy Conversion and Management. 2007;**48**:2481-2490. DOI: 10.1016/j.econman.2007.04.004

[10] Teo H, Li P, Hawlader M. An active cooling for photovoltaic modules. Applied Energy. 2012;**90**:309-315. DOI: 10.1016/j.apenergy.2011.01.017

[11] Rowe D, editor. Handbook of Thermoelectrics. 1st ed. London: CRC Press; 1995

[12] Brazier K. Seebeck Effect [Internet]. 2008. Available from: https://en.wikipedia.org/wiki/File:Thermoelectric_Generator_Diagram.svg [Accesssed: 11-12-2017]

[13] Brazier K. Peltier Effect [Internet]. 2008. Available from: https://en.wikipedia.org/wiki/File:Thermoelectric_Cooler_Diagram.svg [Accesssed: 11-12-2017]

[14] Melcor. Thermoelectric Handbook. 1st ed. Trenton: Laird Technologies; 2015

[15] Cengel Y, Boles M. Thermodynamics, an Engineering Approach. 7th ed. New York: MrGraw Hill; 2011

[16] Van Sark W. Feasibility of photovoltaic-Thermoelectric hybrid modules. Applied Energy. 2011;**88**:2785-2790. DOI: 10.1016/j.apenergy.2011.02.008

[17] Schiro F, Benatto A, Stopatto, Destro N. Improving photovoltaics efficiency by water cooling: Modelling and experimental approach. Energy. DOI: 10.1016/j.energy.2017.04.164

[18] Armstrong S, Hurley W. A model for photovoltaic panels under varying atmospheric conditions. Applied Thermal Engineering. 2010;**30**:1488-1495. DOI: 10.1016/j.applthermaleng.2010.03.012

[19] Sharples S, Charlesworth P. Full-scale measurements of wind-induced convective heat transfer from a roof-roof mounted plate solar collector. Solar Energy. 1998;**83**:187-192. DOI: 10.1016/S0038-092X(97)00119-9

[20] Incropera F, De Witt D. Fundamentals of Heat and Mass Transfer. 7th ed. New Jersey: Wiley; 2011

[21] Kraus A, Bejan A, editors. Heat Transfer Handbook. 1st ed. New Jersey: Wiley; 2003

[22] Cengel Y, Ghajar A. Heat and Mass Transfer. 4th ed. Mexico City: McGraw Hill; 2011

[23] Najafi H, Woodbury K. Optimization of cooling system based on Peltier effect for photovoltaic cells. Solar Energy. 2013;**91**:152-160. DOI: 10.1016/j.solener.2013.01.026

[24] Borkar D, Prayagi S, Gotmare J. Performance evaluation of photovoltaic solar panel using thermoelectric cooling. International Journal of Environmental Research. 2014;**9**:536-539 ISSN: 2319-5013

[25] Kane A, Verma V. Performance enhancement of building integrated photovoltaic module using thermoelectric cooling. International Journal of Renewable Energy Research. 2013;**3**: 320-324 ISSN: 1309-0127

[26] Benghanem A, Al-Mashraqui A, Daffalah K. Performance of solar cells using thermoelectric module in hot sites. Renewable Energy. 2015;**89**:51-59. DOI: 10.1016/j.renene.2015.12.011

[27] Bjørk R, Nielsen K. The performance of a combined photovoltaic (PV) and thermoelectric generator (TEG) system. Solar Energy. 2015;**120**:187-194. DOI: 10.1016/j.solener.2015.07.035

[28] Petela R. Exergy analysis of the solar cylindrical-parabolic cooker. Solar Energy. 2005;**79**: 221-233. DOI: 10.1016/j.solener.2004.12.001

[29] Petela R. Exergy of Heat Radiation. Journal of Heat Transfer. 1964;**86**:187-192. DOI: 10.1115/1.3687092

Chapter 17

Heat Pipe and Thermosyphon for Thermal Management of Thermoelectric Cooling

Thiago Antonini Alves, Larissa Krambeck and
Paulo H. Dias dos Santos

Additional information is available at the end of the chapter

http://dx.doi.org/10.5772/intechopen.76289

Abstract

The heat pipe and thermosyphon are passive heat transfer devices with phase change, which can be applied for thermal management of thermoelectric cooling, such as the TEC hot side. The heat pipes basically consist of a metal tube sealed with capillary structure internally that is embedded with a working fluid. This capillary structure can be made of screen meshes, grooves, or sintered media. The thermosyphon is a heat pipe assisted by gravity, because it has no capillary structure. Then, in this chapter, manufacturing of low cost and easy-to-manufacture heat pipes and thermosyphon is described in detail, and an experimental evaluation of their thermal performance is accomplished. The considered devices were a rod, a thermosyphon, a mesh heat pipe, a grooved heat pipe, and a sintered heat pipe. According to the behavior of the global thermal resistance and the effective thermal conductivity, the passive devices operated satisfactorily with the exception of the rod and the thermosyphon in the horizontal position. The heat pipes were the best among the tested devices and the best position was vertical.

Keywords: heat pipe, thermosyphon, thermoelectric, thermal management, experimental thermal performance, TEC

1. Introduction

Nowadays the advance in the development of computer systems has helped the science to find out computational solutions on understanding phenomena inherent to the problems faced by engineering [1]. The increase of computer system performance has resulted in a high heat generation. On the other hand, the computers' performance can be potentially reduced

due to these high heat flux densities [2]. Therefore, the thermal management of this kind of electronic equipment has become a challenge in order to avoid the overheating and, as a consequence, the hardware failure [3].

According to Sun et al. [4], passive cooling systems such as air, liquid, and heat exchangers with phase change are used to regulate the temperature of CPU and other electronic components at desired levels. Nevertheless, these traditional passive cooling systems are restricted to the working fluid limitations. In this scenario, the thermoelectric cooling (TEC) system can be considered as an alternative to the thermal management of CPU and other electronic components.

A TEC system is composed of a thermoelectric module, a cold, and a hot region. Thermoelectric modules work under the Peltier effect when a DC current passes through a cell made of semiconductor materials; one of the junctions is cooled while the other is heated. In general, the cold region of TEC can be used for cooling the components of personal computers, CPU, graphics processors, and so on. However, its cooling performance is restricted by the thermal resistance at TEC hot region. Besides, TEC is attractive for cooling these devices due to its low weight, compact size, and vibration free characteristics [5].

In order to improve the TEC cooling performance, the heat pipes or thermosyphons can be used as an alternative for TEC hot side cooling [6]. A schematic diagram of a TEC/Heat Pipes (or thermosyphons) system coupled to CPU is shown in **Figure 1**. The principle of this technology is: the heat generated in CPU is transferred to the TEC cold region, where the conversion of electrical energy into thermal energy occurs by Peltier effect, and after this process, the

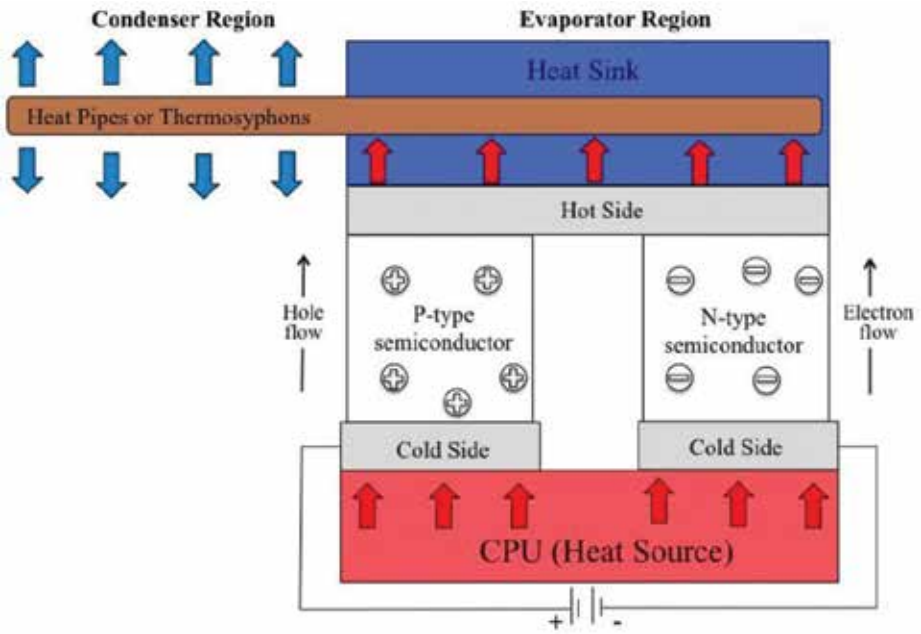

Figure 1. Schematic diagram of a TEC/heat pipes (or thermosyphons) system coupled to CPU.

http://dx.doi.org/10.5772/intechopen.76289

heat is transferred to the TEC hot side. In order to increase the TEC hot side cooling, a heat dissipation system is used, which is composed of a heat sink and heat pipes (or thermosyphons). Thus, the evaporators of heat pipes (or thermosyphons) are fixed in the heat sink and absorb the heat generated by CPU and transfer this heat to the condensers of the heat pipes (or thermosyphons), where finally it is dissipated to the environment.

Heat pipes and thermosyphons are passive heat transfer devices capable of transferring large amounts of heat with a small temperature difference. They became popular in recent decades because of their effectiveness and convenience. These devices are used to improve heat transfer in many industrial fields such as electronics, telecommunications, aerospace, among others [7]. The heat transmitted through these devices is based on phase change. Major advantages of heat pipes include a very high thermal conductance, no pumping power requirements, no moving parts, and relatively low-pressure drops [8]. Furthermore, the heat pipes and thermosyphons are devices relatively simple to manufacture and, therefore, have low cost when their geometry is favorable [9].

The heat pipes and thermosyphons operate according to the following principle [10]: in the evaporator region, heat is transferred to the heat pipe or thermosyphon, vaporizing the working fluid contained inside this region. The steam generated is moved, due to the pressure and density differences, to the cooling regions of the heat pipe or thermosyphon (condenser region) where heat transported is rejected to the cold source. In the heat rejection process, the steam condenses, and the condensate returns back to the evaporator closing the cycle. The adiabatic region, which may have variable dimensions (in some cases it is absent), is located between the evaporator and the condenser being insulated from the external environment. In the heat pipes, the working fluid returns from the condenser to the evaporator due to capillary pumping effect while in the thermosyphon the working fluid returns exclusively by gravity because it has no capillary structure. A schematic diagram of the operating principle of heat pipes is presented in **Figure 2** [11]. More details on the principle of the heat pipes and thermosyphons can be found in [7–10].

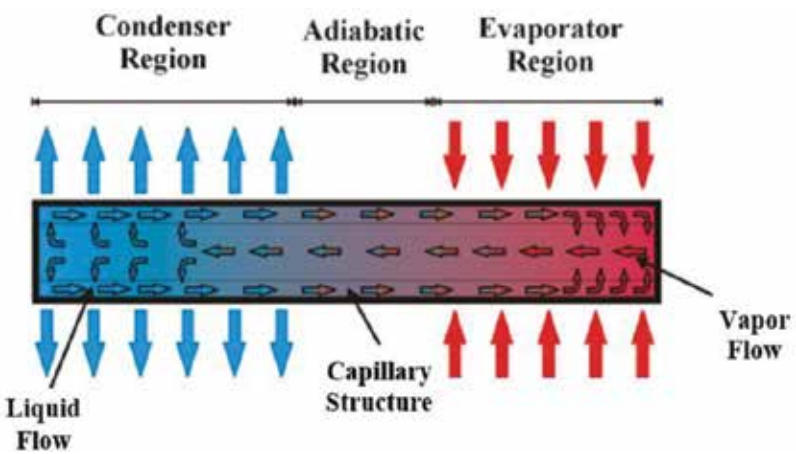

Figure 2. Sketch of the operating principle of a heat pipe [11].

The heat pipes basically consist of a metal tube sealed with capillary structure internally, which is embedded with a working fluid [12]. This capillary structure can be made of screen meshes, grooves, or sintered media [13]. The metal screen is the most commonly used capillary structure because of availability, ease of construction and good capillary pumping [14]. The grooves, as capillary structure, have a high thermal conductivity and good permeability [15]. The sintered metal wicks are manufactured by packing tiny metal particles between the inner heat pipe wall and a mandrel in powder form [16]. As mentioned earlier, the thermosyphon is a heat pipe assisted by gravity, which means that it has no capillary structure to return the working fluid [17]. Some researches available in the literature about thermal management of thermoelectric cooling used heat pipes and thermosyphons [4, 5, 18–20].

Thus, in this chapter, manufacturing of low cost and easy-to-manufacture heat pipes and thermosyphon is described in detail, and an experimental evaluation of the thermal performance is accomplished for several different passive devices that can be used for thermal management of thermoelectric cooling. The considered devices were a rod, a thermosyphon, a mesh heat pipe, a grooved heat pipe, and a sintered heat pipe. In order to evaluate the best passive heat transfer device, their thermal performance was compared.

2. Heat pipe and Thermosyphon manufacturing

In this section, each step of a heat pipe and a thermosyphon manufacturing is described in detail. The proposed procedure has low-cost and the heat transfer passive devices are easy-to-manufacture. The steps are cleaning, assembly, tightness test, evacuation procedure, and filling with the working fluid. These procedures were based on [21–26].

If the operation conditions are favorable to gravity, a thermosyphon can be manufactured. As a result, a capillary structure is not necessary. However, in adverse conditions, a wick should be selected and accommodated in the involucre inner. As mentioned before, the capillary structures can be screen meshes, grooves, sintered powder, among others.

The involucre material, capillary structure (if applicable), and the working fluid depend on the application, and they need to be chemically and mechanically compatible. For thermoelectric cooling, the operation temperature is around 150°C, which makes suitable to use copper and distilled water for involucre and working fluid, respectively.

First of all, the main components of the heat pipe or the thermosyphon have to be prepared. The sintered heat pipe involucre consists of the casing, the closing lids, and the capillary, as shown in **Figure 3**.

2.1. Cleaning process

The cleaning of the heat pipe or the thermosyphon is necessary to ensure the working fluid wettability, the impurity elimination, and the vacuum quality improvement [27]. Consequently,

http://dx.doi.org/10.5772/intechopen.76289

the heat pipe or thermosyphon components need to be thoroughly cleaned, before the introduction of the working fluid. For this purpose, first, the casing, the closing lids, the capillary, and the capillary structure (if applicable) are cleaned with acetone in order to remove larger dirties. Then, they are thoroughly cleaned with a sulfuric acid solution (H_2SO_4 of 0.1 M). After that, these components are taken to an ultrasonic bath, where they remained immersed in acetone for 30 min. Finally, the cleaning is completed. **Figure 4** shows the cleaning of the sintered heat pipe components in an ultrasonic bath.

Figure 3. Sintered heat pipe components.

Figure 4. Cleaning procedure in the ultrasonic bath.

2.2. Assembling of the heat pipes and the thermosyphon

After the cleaning process, the heat pipe or thermosyphon can be properly assembled. As the wick is inside the casing, the closing lids and the capillary are welded to the tube extremities (**Figure 5**). In the case of copper involucres, the welding process can be performed with the aid of a soldering iron and the parts can be brazed using a tin alloy as filler material.

2.3. Tightness test

A tightness test has to be conducted to verify if there was no flaw in the welding process of the heat pipe or thermosyphon. A manual positive displacement pump, a water container (e.g., a sink full of water), and a polymeric tube are necessary to accomplish a low-cost test (**Figure 6**). The polymeric tube makes the connection between the pump and the capillary tube. The heat pipe or thermosyphon is inserted into the water container and the air is pumped into the tube using the positive displacement pump. If there are any flaws in the solder, bubbles will appear in the water. In case of the presence of bubbles, the heat pipe or thermosyphon has to be disassembled, cleaned, welded, and retested.

2.4. Evacuation procedure

First, the heat pipe or thermosyphon is connected to a vacuum pump (*Lab*1000™) that can remove some residual liquid from the cleaning process. Then, the heat pipe or thermosyphon is linked to a vacuum pump *EOS Value*™ i260SV by a polymeric hose. This second pump will do the evacuation process, which the internal pressure should reach at least 90 mbar (9 kPa) – **Figure 7**. To make sure the connections do not leak, the polymeric hose is connected to the capillary with high vacuum grease *Dow Corning*™, prior to starting the vacuum process. The evacuation procedure has a duration of at least 8 h. At the end of the procedure, the polymeric hose is sealed with the assistance of a forceps and the vacuum pump is turned off.

2.5. Filling with working fluid

The amount of working fluid inserted in the heat pipe or thermosyphon is essential for capillary pumping system because the heat transfer depends on that amount of fluid. If there is not enough fluid, the pumping system stop to work and the heat pipe or thermosyphon collapses and as a result, the transferring heat is ceased. As a result, the filling ratio should be carefully chosen. Usually, the filling ratio is based on the evaporator volume.

Figure 5. Assembled heat pipe.

http://dx.doi.org/10.5772/intechopen.76289

To perform the filling procedure with the working fluid, a small filling station has to be developed. The filling station is composed of a universal support, a graduated burette (scale of 0.1 mL) with a capacity of 25 mL, and a forceps (**Figure 8**). The burette and the polymeric hose are completely filled with the working fluid. The evacuated heat pipe or thermosyphon is coupled to the burette by the polymeric hose. Make sure that there are no air bubbles in the tube connecting the burette and the heat pipe or thermosyphon. The next step is to carefully open the burette valve. The forceps are carefully opened to drain the working fluid until the heat pipe or thermosyphon was charged with the correct quantity. It is emphasized that at the moment of filling, great care must be taken; otherwise, the heat pipe or thermosyphon vacuum will be lost. If this happens, the entire vacuum process must be performed again. After charging, the capillary is closed with grip pliers and the capillary end is welded to the completely sealing (**Figure 9**).

Figure 6. Low-cost tightness test.

Figure 7. Evacuation procedure.

Figure 8. Filling station with the heat pipe.

Figure 9. Welding the capillary end.

3. Characteristics of the developed passive devices

The heat pipes and thermosyphon were produced by copper tubes ASTM B-75 Alloy 122 with an outer diameter of 9.45 mm, an inner diameter of 7.75 mm, and a length of 200 mm. The rod was obtained from a full copper bar ASTM B-75 Alloy 122 with the same dimensions of the developed heat pipes and thermosyphon. All the devices had an evaporator of 80 mm

Characteristics	Rod	Thermosyphon	Heat Pipe		
			Mesh	Grooved	Sintered
Inner diameter [mm]	—	7.75	7.75	6.20	7.75
Outer diameter [mm]	9.45	9.45	9.45	9.45	9.45
Evaporator length [mm]	80.0	80.0	80.0	80.0	80.0
Adiabatic section length [mm]	20.0	20.0	20.0	20.0	20.0
Condenser length [mm]	100	100	100	100	100
Working fluid	—	Water	Water	Water	Water
Volume of working fluid [mL]	—	2.26	2.19	1.73	2.26
Filling ratio [%]	—	60	60	60	80
Capillary structure	—	No capillary structure	Phosphor bronze screen mesh #100	Microgrooves by the wire-EDM	Copper powder sintered

Table 1. Main features of the heat transfer passive devices.

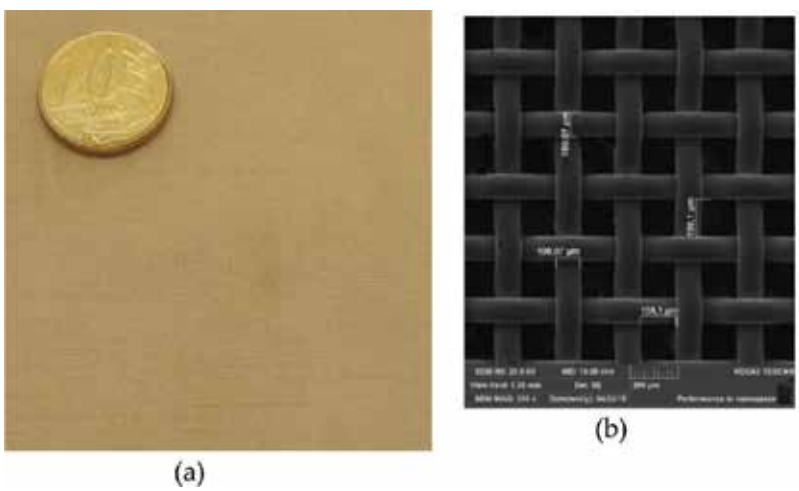

Figure 10. Phosphor bronze screen mesh #100. (a) General view (b) micro-scale image.

in length, an adiabatic region of 20 mm in length, and a condenser of 100 mm in length. The working fluid used is distilled water with filling ratios related to the evaporator volume based on the best performance of each capillary structure. **Table 1** shows the main characteristics of the heat transfer passive devices analyzed in this research.

The mesh heat pipe used one layer of phosphor bronze screen mesh #100 (**Figure 10a**) as capillary structure. A microscale image of screen mesh #100 is shown in **Figure 10b**. The image was obtained by backscattered electron detector (BSD) for scanning electron microscope (SEM). More information about this mesh heat pipe can be found in [23].

The grooved heat pipe shown schematically in **Figure 11a** had 32 microgrooves made by the wire electrical discharge machining (wire-EDM). **Figure 11b** presents the axial microgrooves details with an average diameter of 220 μm by a micro-scale image. The image was obtained by backscattered electron detector (BSD) for scanning electron microscope (SEM). More details about this heat pipe can be found in [24, 28].

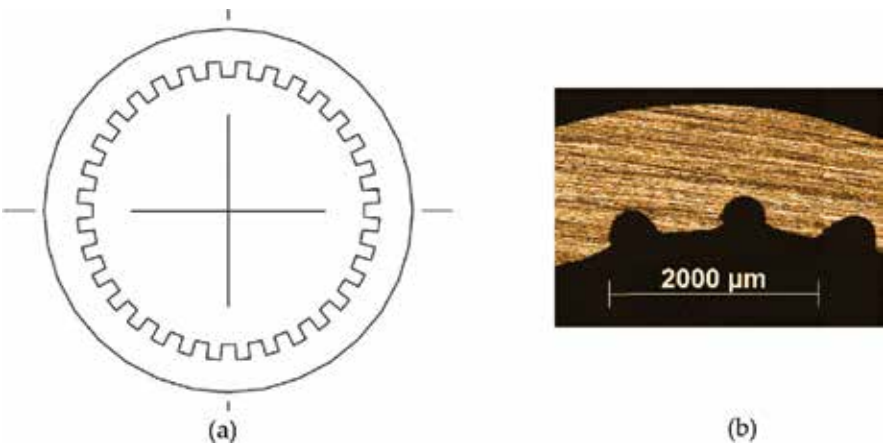

Figure 11. Microgrooves made by wire-EDM. (a) Scheme of microgroove profile and (b) microscale image.

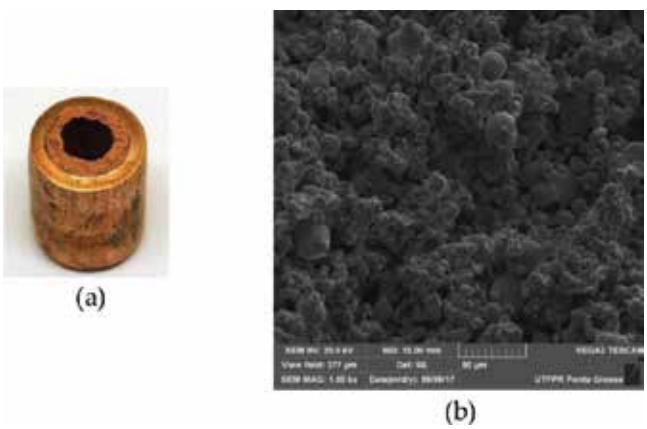

Figure 12. Structure sintered copper powder. (a) General view and (b) microscale image.

The sintered heat pipe was produced by the sintering process with a copper powder and a temporary mandrel. The average diameter of the copper powder particle is 10.9 μm. The porous structure manufactured has a thickness of 1.5 mm (**Figure 12a**). The microscale image of the capillary structure of sintered copper powder is presented in **Figure 12b**. More information about this sintered heat pipe can be found in [26].

4. Experimental tests

To achieve successful results, the experimental tests must reproduce the operation conditions as close as possible to the application for thermal management of thermoelectric cooling. Then, to evaluate the thermal performance of the analyzed passive heat transfer devices, an experimental apparatus and some experimental procedures were used.

4.1. Experimental apparatus

The essential experimental apparatus for the experimental tests, shown in **Figure 13**, is composed of a data logger (*Agilent*™ 34970A with 20 channels), a power supply unit (*Keysight* ™ U8002A), a laptop (*Dell*™), an uninterruptible power supply (*NHS*™), a universal support, and a fan (*Ultrar*™).

For the evaluation of the temperature of the different heat transfer passive devices, K-type thermocouples *Omega Engineering*™ are used. They should be fixed on the outer surface of devices by a thermosensitive adhesive strip *Kapton*™. They should be distributed in the length of the heat pipes and thermosyphon. Thus, there are three thermocouples in the evaporator ($T_{evap,1}$, $T_{evap,2}$, and $T_{evap,3}$), one thermocouple in the adiabatic section (T_{adiab}) e four thermocouples in the condenser ($T_{cond,1}$, $T_{cond,2}$, $T_{cond,3}$, and $T_{cond,4}$) in passive devices (heat pipes and thermosyphon), as shown in **Figure 14**. For the rod, two thermocouples were fixed in the evaporator

Figure 13. Experimental apparatus.

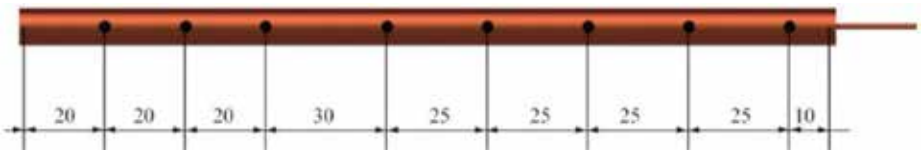

Figure 14. Thermocouple positions in heat pipes.

($T_{evap,1}$ and $T_{evap,2}$), one thermocouple in the adiabatic section (T_{adiab}) and three thermocouples in the condenser ($T_{cond,1}$, $T_{cond,2}$, and $T_{cond,3}$).

As is already known, for the correct operation of the heat pipe and thermosyphon, a heating system is needed in the evaporator and a cooling system in the condenser. The evaporator can be power dissipation in any kind of resistor (strip, cartridge) or a heat source, as the TEC hot side. The cooling system can consist of forced convection by air, water, or coolant, in most of the cases. The adiabatic section may have variable dimensions (in some cases, it is absent) and should be insulated from the external environment.

Thus, in this research, the heating system of the evaporator is conducted by power dissipation from the passage of an electric current in a nickel-chromium alloy power strip resistor *Omega Engineering*™ with 0.1 mm of thickness and 3.5 mm of width. To ensure that the generated heat by Joule effect is transmitted to the evaporator, an aeronautic thermal insulation and a layer of polyethylene are installed in this region. A fiberglass tape is used in adiabatic section as heat insulation between the support and the passive device. The cooling system using air forced convection consisted of a fan in the condenser region.

4.2. Experimental procedure

To ensure the best results and the repeatability of experimental tests, the environment temperature was maintained at 20°C ± 0.5°C. A thermal conditioning system *Carrier*™ was used for this purpose. A detailed check of the equipment and the heat pipe or thermosyphon (fixing thermocouples, thermal insulation, resistor connection, among others) must be made before each experimental test. The heat pipe or thermosyphon was carefully fixed to the universal support bracket in the adiabatic region in the desired position. The cooling system was turned on in the condenser region and set at a speed of 5 m/s controlled by a potentiometer with a combined error of ±0.2 m/s. The data acquisition system was turned on, collecting the temperatures measured by the K-type thermocouples. The temperatures should be verified according to the environment temperature, and if these were stable and approximately 20°C, finally, the heating system can be turned on and adjusted to the dissipation power desired. The initial load was 5 W and, after approximately 15 min, the thermocouples showed stationary values. If it happened, the thermal load has been increased by 5 W. The load increment was made until the maximum temperature of the device reached the critical temperature (150°C), where the melting of the materials could happen. Data were acquired every 5 s, recorded on the desktop by the software *Agilent*™ *Benchlink Data Logger 3*.

5. Data reduction

5.1. Thermal parameters

The thermal performance of the heat pipes and the thermosyphon was analyzed and compared by the operating temperatures (T_{op}), the global thermal resistance (R_{th}), and the effective thermal conductivity (k_{eff}). The analyzed operating temperature is the temperature of the adiabatic region. The global thermal resistance, R_{th}, of a heat pipe and a thermosyphon can be defined as the difficulty of the passive device to transport the heat power and can be calculated by:

$$R_{th} = \frac{\Delta T}{q} = \frac{\left(T_{evap} - T_{\text{cond}}\right)}{q} \tag{1}$$

where, q is the heat transfer capability of the device, T_{evap} and T_{cond} are the mean temperature of the evaporator and the condenser, respectively.

The effective thermal conductivity, k_{eff}, is the property of a certain material to conduct heat. Defined by:

$$k_{eff} = \frac{q\,L_{eff}}{A_{\text{C}}\,\Delta T} = \frac{q\,L_{eff}}{A_{\text{C}}\left(T_{evap} - T_{\text{cond}}\right)} \tag{2}$$

where, L_{eff} is the effective length and A_{C} is the heat transfer cross-sectional area. The effective length can be defined by:

$$L_{eff} = \frac{L_{evap}}{2} + L_{adiab} + \frac{L_{cond}}{2} \tag{3}$$

where, L_{evap} is the evaporator length, L_{adiab} is the adiabatic section length, and L_{cond} is the condenser length.

The heat transfer cross-sectional area can be defined by:

$$A_{\text{C}} = \frac{\left(\pi D_i^2\right)}{4} \tag{4}$$

where D_i is the inner diameter of the heat transfer passive device.

5.2. Uncertainties analysis

In general, the experimental uncertainties are associated to the K-type thermocouples, the data logger, and the power supply unit. The experimental measurement uncertainties were analyzed using the uncertainty combination method described in [29] considering the combination of uncertainties of correlated quantities. They are shown in the obtained

results. It is known that the accuracy of the thermocouples is ±2.2°C and the uncertainty was evaluated as the rectangle type. Thus, the uncertainty values of the temperature sensors were estimated in:

$$u(T) = \frac{\pm 2,2}{\sqrt{3}} = \pm 1,27^{\circ} C \tag{5}$$

The combined uncertainties of the evaporator, adiabatic section, and condenser temperatures were calculated according to the following equations respectively:

$$u\left(T_{evap}\right) = \left|\frac{\partial T_{evap}}{\partial T_{evap,1}}\right| u\left(T_{evap,1}\right) + \left|\frac{\partial T_{evap}}{\partial T_{evap,2}}\right| u\left(T_{evap,2}\right) + \left|\frac{\partial T_{evap}}{\partial T_{evap,3}}\right| u\left(T_{evap,3}\right) \tag{6}$$

$$u\left(T_{adiab}\right) = u(T) = \pm 1,27^{\circ} C \tag{7}$$

$$u\left(T_{cond}\right) = \left|\frac{\partial T_{cond}}{\partial T_{\text{cond},1}}\right| u\left(T_{cond,1}\right) + \left|\frac{\partial T_{cond}}{\partial T_{cond,2}}\right| u\left(T_{cond,2}\right) + \left|\frac{\partial T_{cond}}{\partial T_{cond,3}}\right| u\left(T_{cond,3}\right) + \left|\frac{\partial T_{cond}}{\partial T_{cond,4}}\right| u\left(T_{cond,4}\right) \tag{8}$$

The measurement uncertainties associated with the dissipated power in the evaporator were estimated according to the power supply in the electrical resistance of the tests. The uncertainties were evaluated as the rectangle type, considering the voltage accuracy of 0.35% + 20 mV and the current accuracy of 0.35% + 20 mA. The electrical power dissipated by the electric resistance, P, is calculated as shown below:

$$P = V I \tag{9}$$

where V is the voltage and I is the current.

Considering that thermal losses in the evaporator region are negligible and that all energy is transferred to the wall of the heat pipe, the uncertainty of the heat transfer capacity can be estimated as:

$$u(q) = u(P) = \left|\frac{\partial q}{\partial V}\right| u(V) + \left|\frac{\partial q}{\partial I}\right| u(I) \tag{10}$$

The global thermal resistance uncertainty can be calculated by the following equation:

$$u\left(R_{th}\right) = \left|\frac{\partial R_{th}}{\partial q}\right| u(q) + \left|\frac{\partial R_{th}}{\partial \Delta T}\right| u(\Delta T) \tag{11}$$

where the uncertainty of the temperature difference can be defined as:

$$u(\Delta T) = \left|\frac{\partial \Delta T}{\partial T_{evap}}\right| u\left(T_{evap}\right) + \left|\frac{\partial \Delta T}{\partial T_{cond}}\right| u\left(T_{cond}\right) \tag{12}$$

6. Evaluation of the thermal performance

To summarize the analysis of the thermal performance of the heat pipes and the thermosyphon, different types of passive heat transfer devices were experimentally evaluated and compared. The considered devices were a rod, a thermosyphon, a mesh heat pipe, a grooved heat pipe, and a sintered heat pipe. The analyzed operating positions were vertical and horizontal. The experimental tests were repeated three times and the errors were compared taking into account the difference between the mean values less than 0.5°C. The tests were performed at increasing heat loads of 5 W, ranging from 5 to 45 W for both positions.

6.1. Temperature distribution

Figure 15 shows the temperature distributions as a function of time for the heat pipe with axial microgrooves in the vertical position. The heat pipe starts to work at a temperature of 44° C, for a heat load of 5 W. The maximum dissipated power of the grooved heat pipe was 45 W. **Figure 16** presents the temperature distribution in function of the thermocouple position in the heat pipe length for different heat loads.

6.2. Operation temperature

The behavior of the operating temperature as a function of the dissipated power for different passive devices is shown in **Figure 17**. It may be noted that as the dissipated power increases, the operating temperature also increases for all the devices in both positions.

6.3. Global thermal resistance

Figure 18 presents the global thermal resistance as a function of the power dissipation considering the rod, the thermosyphon, and the heat pipes. The results of two operating positions

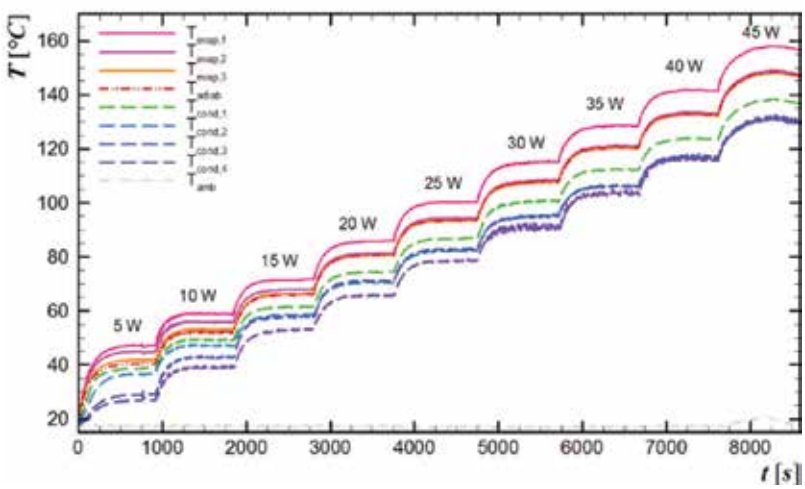

Figure 15. Temperature distribution *versus* time: Grooved heat pipe in vertical.

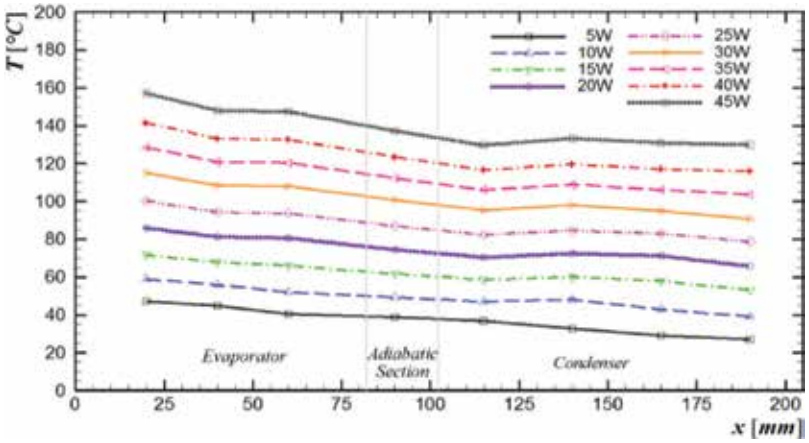

Figure 16. Temperature distribution *versus* thermocouple position: Grooved heat pipe in vertical.

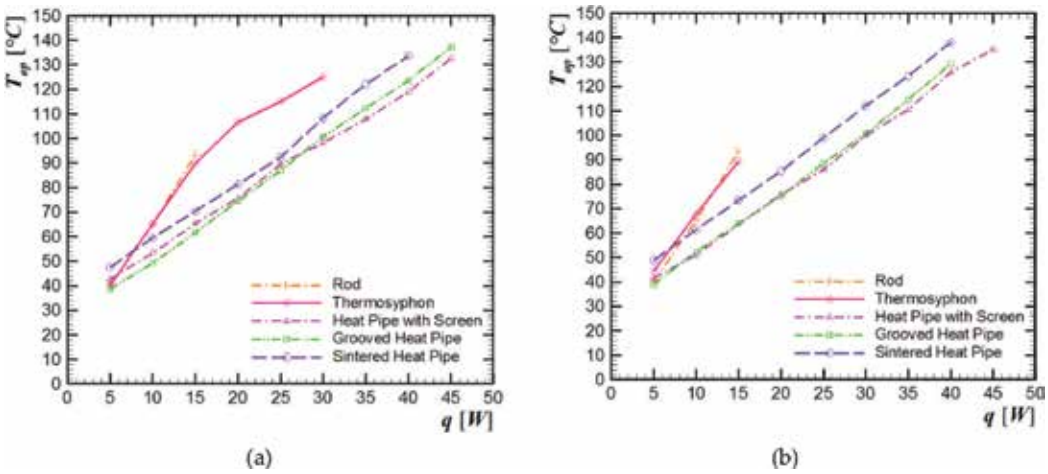

Figure 17. Operating temperature *versus* power dissipation. (a) Vertical and (b) horizontal.

are compared. As the heat dissipation is increased, the thermal resistance decreases for the thermosyphon and the heat pipes in the vertical position. In horizontal, the heat pipes obtain the same behavior; however, the thermosyphon has changed dramatically. It happens due to the necessity of gravity for the fluid return in the thermosyphon. The rod thermal resistance remains almost constant for the entire heat loads in both positions.

As mentioned, the global thermal resistance of the heat pipes and the thermosyphon take into consideration the temperature difference between the evaporator and the condenser and, the dissipated power. However, the processes governing the global thermal resistance are related to the fluid dynamics and the heat transfer. The fluid dynamics is influenced by the gravity and the capillary pumping. In the thermosyphon, the fluid flow from the condenser to the evaporator occurs exclusively by gravity. On the other hand,

http://dx.doi.org/10.5772/intechopen.76289

in the heat pipes, besides gravity, the capillary pumping also has a positive influence on the fluid flow. The heat transfer in the evaporators is governed by boiling, which is facilitated due to the existence of nucleation sites. Thermosyphon nucleation sites happen due to the surface roughness (imperfections). In the heat pipes, the capillary structures (screen meshes, microgrooves, or sintered media) provide the nucleation sites, making the boiling process more efficient. Thus, according to **Figure 18**, the global thermal resistance of the heat pipes is lower than the rod and the thermosyphon. This can be explained by the influence of gravity and the capillary pumping. Also, the boiling process is more efficient due to the existence of more nucleation sites. Finally, note that values of global thermal resistance could be lower if the overall heat transfer coefficient in the condenser of the passive devices were higher, which could be achieved, for example, using fins or liquid cooling.

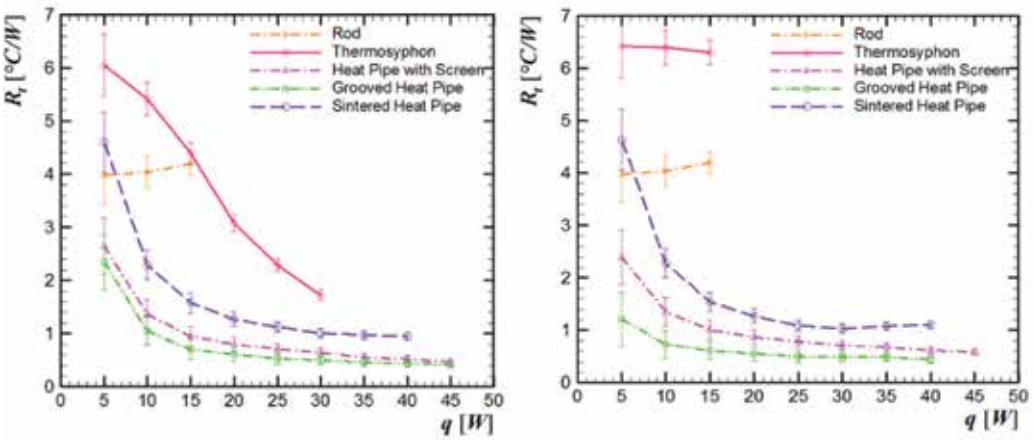

Figure 18. Thermal resistance *versus* power dissipation. (a) Vertical and (b) horizontal.

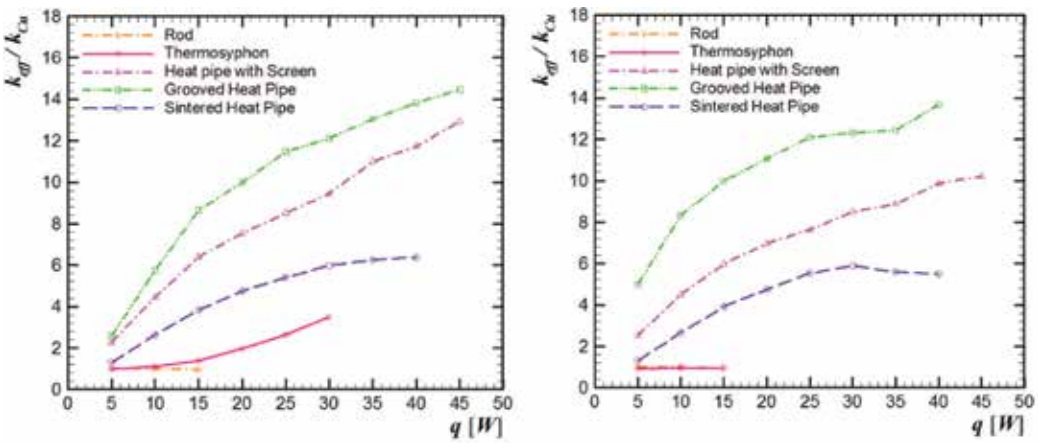

Figure 19. Effective thermal conductivity *versus* power dissipation. (a) Vertical and (b) horizontal.

6.4. Effective thermal conductivity

In **Figure 19**, the behavior of the effective thermal conductivity of the passive heat transfer devices is shown as a function of the power dissipated for vertical (a) and horizontal (b) positions. As expected, it can be seen that the passive devices that use phase change (heat pipes and thermosyphon) have a higher effective thermal conductivity and that this parameter increases with increasing power dissipation.

7. Conclusions

In this research, each step of the heat pipes and the thermosyphon manufacturing (cleaning, assembly, tightness test, evacuation procedure, and filling with the working fluid) was described in detail. The proposed procedure has low-cost and the heat transfer passive devices are easy-to-manufacture. Then, an experimental investigation of the thermal performance of different heat transfer passive devices (solid rod, thermosyphon, mesh heat pipe, grooved heat pipe, and sintered heat pipe) was performed. These passive heat transfer devices were tested in vertical and horizontal positions under thermal loads between 5 and 45 W and worked satisfactorily, except rod and thermosyphon in the horizontal position. The vertical position showed better results than the horizontal one due to gravity. The thermosyphon showed a satisfactory thermal performance in the vertical position. However, in the horizontal, its behavior was worse than a rod. The heat pipes were the devices with the best thermal performance due to the use of the vaporization heat of the working fluid concurrently with the capillary structure. The grooved heat pipe had a better thermal performance based on the lower global thermal resistance or the higher effective thermal conductivity. The experimental results showed that heat pipes and thermosyphon can be successfully used in TEC hot side cooling, and due to the behavior of the global thermal resistance and the effective thermal conductivity, on the other hand, a solid rod cannot be used.

Acknowledgements

Acknowledgments are provided to the CAPES, the CNPq, the PROPPG/UTFPR, the DIRPPG/UTFPR, the PPGEM/UTFPR/Ponta Grossa, and the DAMEC/UTFPR/Ponta Grossa.

Nomenclature

A_C	cross-sectional area, [m^2]
D_i	inner diameter, [m]
I	current, [A]

k	thermal conductivity, [W/mK]
L	length, [m]
P	electrical power dissipated, [W]
q	heat transfer rate, [W]
R_{th}	total thermal resistance, [°C/W]
t	time, [s]
T	temperature, [°C]
V	voltage, [V]
Subscripts	
adiab	adiabatic section
Cu	copper
cond	condenser
eff	effective
evap	evaporator

Author details

Thiago Antonini Alves*, Larissa Krambeck and Paulo H. Dias dos Santos

*Address all correspondence to: thiagoaalves@utfpr.edu.br

Federal University of Technology, Parana, Brazil

References

[1] Antonini Alves T, Altemani CAC. An invariant descriptor for heaters temperature prediction in conjugate cooling. International Journal of Thermal Sciences. 2012;**58**:92-101. DOI: 10.1016/j.ijthermalsci.2012.03.007

[2] Nishida FB, Tadano YS, Antonini AT. Conjugate forced convection-conduction heat transfer in channel flow using different cooling fluids. In: Proceedings of the 15th International Heat Transfer Conference (IHTC-15); 10-15 August 2014; Kyoto/JAP. Connecticut/USA: Begell House; 2014. IHTC15-9594, p. 1957-1970. DOI: 10.1615/IHTC15.eec.009594

[3] Krambeck L, Nishida FB, Aguiar VM, Santos PHD, Antonini Alves T. Thermal performance evaluation of different passive devices for electronics cooling. Thermal Science. 2017; OnLine-First Issue00:300. DOI: 10.2298/TSCI170610300K

[4] Sun X, Zhang L, Liao S. Performance of a thermoelectric cooling system integrated with a gravity-assisted heat pipe for cooling electronics. Applied Thermal Engineering. 2017;**116**:433-444. DOI: 10.1016/j.applthermaleng.2016.12.094

[5] Sun X, Ling L, Liao S, Chu Y, Fan S, Mo Y. A thermoelectric cooler coupled with a gravity-assisted heat pipe: An analysis from heat pipe perspective. Energy Conversion and Management. 2018;**155**:230-242. DOI: 10.1016/j.enconman.2017.10.068

[6] Remeli MF, Kiatbodin L, Singh B, Verojporn K, Date A, Akbarzadeh A. Power generation from waste heat using heat pipe and thermoelectric generator. Energy Procedia. 2015;**75**:645-650. DOI: 10.1016/j.egypro.2015.07.477

[7] Faghri A. Heat pipes: Review, opportunities and challenges. Frontiers in Heat Pipes. 2014; **5**:01-48. DOI: 10.5098/fhp.5.1

[8] Reay DA, Kew PA, McGlen RJ. Heat Pipe: Theory, Design and Applications. 6th ed. Amsterdam/NED: Butterworth-Heinemann; 2014. p. 288

[9] Mantelli MBH. Thermosyphon technology for industrial applications. In: Vasiliev LL, Kakaç S, editors. Heat Pipes and Solid Sorption Transformations. 1st ed. Boca Raton/ USA: CRC Press; 2013. pp. 411-464

[10] Groll M, Rösler S. Operation principles and performance of heat pipes and closed two-phase thermosyphons. Journal of Non-Equilibrium Thermodynamics. 1992;**17**:091-151

[11] Santos PHD, Reis LS, Marquardt LS, Vicence KAT, Alves A. T. Modeling and experimental tests of a copper thermosyphon. Acta Scientiarum Technology. 2017;**39**:59-68. DOI: 10.4025/actascitechnol.v39i1.28957

[12] Santos DLF, Marquardt LS, Santos PHD, Antonini AT. Metallic mesh as capillary structure applied in heat pipe heat exchanger for heat recovery. Advanced Materials Research. 2014;**1082**:309-314. DOI: 10.4028/www.scientific.net/AMR.1082.309

[13] Vasiliev LL. Micro and miniature heat pipes – Electronic component coolers. Applied Thermal Engineering. 2006;**28**:266-273. DOI: 10.1016/j.applthermaleng.2006.02.023

[14] Krambeck L, Nishida FB, Santos PHD, Antonini AT. Configurations of phosphor bronze meshes in heat pipes: An experimental analysis of thermal performance. International Journal of Advanced Engineering Research and Science. 2015;**2**:11-14

[15] Nishida FB, Marquardt LS, Borges VYS, Santos PHD, Antonini Alves T. Development of a copper heat pipe with axial grooves manufactured using wire electrical discharge machining (wire-EDM). Advanced Materials Research. 2015;**1120-1121**:1325-1329. DOI: 10.4028/www.scientific.net/AMR.1120-1121.1325

[16] Webb RL. Next generation devices for electronic cooling with heat rejection to air. Journal of Heat Transfer. 2005;**127**:2-10. DOI: 10.1115/1.1800512

[17] Aguiar VM, Bartmeyer GA, Krambeck L, Santos PHD, Antonini Alves T. Thermal analysis of a finned thermosyphon for heat exchanger applications. International Journal of Science and Advanced Technology. 2018;**5**:18-21. DOI: 10.22161/ijaers.5.1.4

[18] Remeli MF, Kiatbodin L, Singh B, Verojporn K, Date A, Akbarzadeh A. Power generation waste heat using heat pipe and thermoelectric generator. Energy Procedia. 2015;**75**:645-650. DOI: 10.1016/j.egypro.2015.07.477

[19] Liu D, Zhao FY, Yang HX, Tang GF. Thermoelectric mini cooler coupled with micro thermosiphon for CPU cooling system. Energy. 2015;**83**:29-36. DOI: 10.1016/j.energy.2015.01.098

[20] Sun X, Yang Y, Zhang H, Si H, Huang L, Liao S, Gu X. Experimental research of a thermoelectric cooling system integrated with gravity assistant heat pipe for cooling electronic devices. Energy Procedia. 2017;**105**:4909-4914. DOI: 10.1016/j.egypro.2017.03.975

[21] Russo GM, Krambeck L, Nishida FB, Santos PHD, Antonini AT. Thermal performance of thermosyphon for different working fluids. Engenharia Térmica. 2015;**15**:03-08

[22] Aguiar VM. Influence of filling ratio and inclination angle on thermal performance of thermosyphons (in Portuguese). Ponta Grossa/BRA: Federal University of Technology – Parana; 2016

[23] Krambeck L. Experimental investigation of wire mesh thermal performance in heat pipes (in Portuguese). Ponta Grossa/BRA: Federal University of Technology – Parana; 2016

[24] Nishida FB. Development of heat pipes with microgrooves fabricated by wire electrical discharge machining (in Portuguese) [dissertation]. Ponta Grossa/BRA: Federal University of Technology – Parana; 2016

[25] Santo ME. Experimental analysis of different thermosyphon configurations for solar collector application (in Portuguese) [dissertation]. Ponta Grossa/BRA: Federal University of Technology – Parana; 2017

[26] Krambeck L, Bartmeyer GA, Fusão D, Santos PHD, Antonini AT. Experimental research of capillary structure technologies for heat pipes. In: Proceedings of the 24th ABCM International Congress of Mechanical Engineering (COBEM 2017); 3-8 December 2017; Curitiba/BRA; 2017. COBEM-2017-1170

[27] Santos PHD, Krambeck L, Antonini AT. Experimental analysis of a stainless steel heat pipe. International Journal of Science and Advanced Technology. 2014;**4**:17-22

[28] Krambeck L, Nishida FB, Santos PHD, Antonini AT. Heat pipe with axial microgrooves fabricated by wire electrical discharge machining (wire-EDM). In: Proceedings of the 9th World Conference on Experimental Heat Transfer, Fluid Mechanics and Thermodynamics (ExHFC-9); 11-15 June 2017; Foz do Iguaçu/BRA. 2017. PT80

[29] Holman JP. Experimental Methods for Engineers. 8th ed. New York/USA: McGraw-Hill; 2011. p. 768

Edited by Patricia Aranguren

The disproportionate use of fossil fuels has turned into a serious environmental issue. Thus, we are encountering one of the biggest challenges of the twenty-first century, satisfying the energy demand with respect to the environment. Thermoelectricity is an emerging technology, which contributes to reducing the impact of the use of traditional technologies, harvesting the waste heat, and eliminating the use of refrigerants. The book *Bringing Thermoelectricity into Reality* covers the current thermoelectric investigations: the study of novel thermoelectric materials, the development of computational models, the design of proper assemblies, and the optimization of thermal designs, as well as novel thermoelectric generators, coolers, and heating applications. This book looks for the definitive thermoelectric applications applied to everyday life.

Published in London, UK

IntechOpen

ISBN 978-1-83881-565-3